Investigation of Photophysical and Porous Properties of Discrete and Extended Metal-Organic Structures

A Thesis Submitted for the Degree of

Doctor of Philosophy

By

Ritesh Haldar

New Chemistry Unit (NCU)

Jawaharlal Nehru Centre for Advanced Scientific Research

(A Deemed University)

Bangalore – 560064

November, 2014

Dedicated to my family

DECLARATION

I hereby declare that the matter embodied in the thesis entitled "***Investigation of Photophysical and Porous Properties of Discrete and Extended Metal-Organic Structures***" is the result of investigations carried out by me at the New Chemistry Unit (NCU), Jawaharlal Nehru Centre for Advanced Scientific Research (JNCASR), Bangalore, India under the supervision of Dr. Tapas Kumar Maji and that it has not been submitted elsewhere for the award of any degree or diploma.

In keeping with the general practice in reporting the scientific observations, due acknowledgements have been made whenever the work described is based on the findings of other investigators. Any omission that might have occurred due to oversight or error in judgement is regretted.

……

Ritesh Haldar

Date:

Bangalore

CERTIFICATE

I hereby certify that the work described in this thesis entitled "***Investigation of Photophysical and Porous Properties of Discrete and Extended Metal-Organic Structures***" has been carried out by Mr. Ritesh Haldar under my supervision at the New Chemistry Unit (NCU), Jawaharlal Nehru Centre for Advanced Scientific Research (JNCASR), Bangalore, India and that it has not been submitted elsewhere for the award of any degree or diploma.

……..

Dr. Tapas Kumar Maji
(Associate Professor)
(Research Supervisor)

ACKNOWLEDGEMENTS

I wish to express my sincere gratitude to my research supervisor Dr. Tapas Kumar Maji for his kind support, guidance, criticism and invaluable suggestions he has given me all through the course of these investigations. I have learnt so much by interacting with him both professionally and personally. I am thankful to him for giving me an opportunity to work under his guidance.

I thank Prof. C. N. R Rao, FRS, who has been a constant source of inspiration for me. I would also like to thank him as the chairmen of NCU unit for allowing me to use the facilities of the centre.

I would like to thank Prof. H. Ila, Dr. Subi. J. George, Dr. T. Govindraju, Dr. T. K. Maji of JNCASR and Prof. T. N. Guru Row of IISc for their beneficial courses that has been extremely helpful to this study.

I would like to sincerely thank Prof. Balasubramanian Sundaram (CPMU), Dr. Sandeep K. Reddy (CPMU), Mr. Satyanarayana Bonakala (CPMU), Prof. Swapan. K. Pati (TSU), Dr. Pralok Kumar Samanta (TSU), Dr. Siamkhanthang Neihsial (TSU), Prof. Chandrabhas Narayana (CPMU), Ms. Gayatri Kumari, Dr. Subi J George (NCU), Dr. K. V. Rao (NCU), Prof. S. Kitagawa (Kyoto University), Dr. R. Matsuda (Kyoto University), Dr. Satoshi Horike (Kyoto University) and Dr. Debajyoti Ghoshal (Jadavpur University) for fruitful collaborations.

I sincerely acknowledge the help from Dr. Ranjani Viswanatha and Mr. Avijit Saha regarding fluorescence lifetime measurements. I thank the timely help of the technical staffs namely Mr. Anil, Mr. Vasu, Mr. Mahesh and Mr. Srinivas of JNCASR for their help with the various characterization techniques.

I thank JNCASR Library, Complab, Hostel, Health Centre, Academics and Administration staff for providing and maintaining the various facilities that have helped me immensely.

I thank my wonderful lab mates Arpan, Anindita, Suresh, Nivedita, Papri, Syamantak, Komal, and Sohini for their cooperation and help. Also I acknowledge all the visiting scientists and students (POCE and SRF) for their contributions. In particular, I want to thank Komal for her sincere involvement in some of the research problems. I also would like to thank my past lab mates Dr. Prakash Kanoo, Dr. Sudip Mohapatra and Mr. Krishna for their cooperation and help.

My cordial thanks are due to my friends Debabrata Maity, Barun Das, Arup Chattopadhay, Sabyasachi Mukhopadhay, Goutam Chatterjee, Pralok Samanta, Suman Majumdar, Partha Kundu, Dibyajyoti Ghosh, Arkamita Bandopadhay, Somananda Sanyal, Koushik Pal, Sisir Maity, Anirban Mondal, Tarak Karmakar, Rana Saha, Moumita Rana, Abhijit Sen, Rajib Sahoo, Avijit Saha, Amritroop Achari, Chandan Dey, Somanth Ghara, Sudeshna Sen, Soumik Sidhanta, Sumanta Sarkar, Chandradhish Ghosh, Soumyabrata Roy, Arpan Dey, Jiarul Midya, Subhajit Paul, Saikat Chakraborty, Rajkumar Jana and many more. Their support and encouragement have been an indispensable in my Ph. D. life. I would also like to thank my childhood friends Gourab Kundu, Sayak Chakraborty, Sayak Mukherjee, Late Mr. Niloy Kundu for their encouragement.

Last but not least, my heartfelt thanks to my family members for being there for me always. I thank my didi Mrs Suparna Debnath and brother Mr. Sanjoy Debnath for their timely advices and encouragements. This thesis is a humble offering to my parents.

PREFACE

Photophysical properties (and their applications in molecular sensing and light harvesting), porosity, guest induced structural transformation and its related properties in metal-organic materials are the main emphasis of this thesis. This thesis extends in seven chapters. ***Chapter 1*** provides an introduction to metal-organic complexes/frameworks or porous coordination polymers and their various applications in gas storage, separation, catalysis, molecular sensing and light harvesting properties. ***Chapter 2*** is divided in two sections; ***Part 2A*** describes synthesis and characterization of pyrene/anthracene carboxylate based metal-organic complexes and their interesting photophysical properties. These exhibit exciplex emissions which are sensitized through energy transfer from monomer chromophores. One of the complexes with exciplex emission shows ratiometric Al^{3+} sensing properties. In ***Part 2B***, we have synthesized two luminescent frameworks (1D and 3D) just by adjusting the linker stoichiometry and have studied their photophysical properties comprehensively. These frameworks display strong ground state charge transfer (CT) interaction between the linkers (anthracene and phenanthroline) and also bright CT emission. Thus formed CT is further sensitized through energy transfer from monomer chromophores.

Chapter 3 comprises of two parts; ***Part 3A*** describes a discrete molecular complex of pyrene that exhibits preassociated exciplex formation and energy transfer phenomenon. Extending the concept, from an atypical synthetic strategy we obtained a luminescent 1D coordination polymer which self-assembles in 3D porous structure through supramolecular intercations. It shows flexible behaviour upon guest removal or inclusion. We have studied its aromatic amine recognition properties through emission readout and also separation ability of *meta*-xylene isomer from xylene isomer mixture. ***Part 3B*** shows host-guest partial energy transfer in a luminescent supramolecular framework upon fluorescein dye encapsulation and thus originated dual emission feature was exploited for solvent sensing application.

Chapter 4 describes PCPs with highly stable charge separated states and their various properties. The first section, ***Part 4A*** shows 1D coordination polymers with pyrene and anthracene chromophoric linkers; these are flexible, show permanent porosity and biofuel separation ability. DFT calculations and other experimental studies of those

polymers reveal stable charge separated state at ambient condition. In the other section, ***Part 4B*** a luminescent anionic framework with heat mediated reversible electron transfer property has been described. It also exhibits high H_2 storage capacity and selective CO_2 uptake characteristic.

Chapter 5 describes study of structure property relationships in interpenetrated frameworks and their possible applications in selective CO_2 uptake and biofuel separation. In the first section, ***Part 5A*** one cationic two-fold interpenetrated 3D framework shows selective CO_2 uptake properties. Heat mediated removal of one of the linker and subsequent conformational change in the linker transforms the 3D structure to 1D coordination polymer in crystal-to-crystal fashion. In ***Part 5B*** we have synthesized two new amino functionalized PCPs which are structural supramolecular isomers. Two different SBUs give rise to different structural features and selective CO_2 adsorption properties in them. Presence of amino group was exploited for Knoevenagel condensation reaction as catalyst. In ***Part 5c***, another flexible interpenetrated framework has been synthesized and characterized. It shows stepwise CO_2 and C_2H_2 uptake properties. Further it displays selective methanol uptake behaviour, useful for ethanol/methanol separation. Better separation of ethanol was observed in a 1D supramolecular porous structure. Based on the stepwise uptake of solvent vapours it is possible to separate methanol/ethanol or ethanol/water at ambient condition.

Chapter 6 exhibits a flexible Cd(II) based PCP which shows stepwise CO_2 uptake profile at 195 K and also selective O_2 sorption over N_2 at 77 K. Further, solid state ^{113}Cd NMR was exploited as a probe to elucidate the change in Cd(II) metal coordination sphere upon desolvation or guest solvent (methanol) introduction.

Chapter 7 describes interesting phenomena of *in situ* C-N bond formation in porous coordination polymer. An *in situ* C-N bond formation between *trans*-glutaconic acid and 4,4′-azobipyridyl linker result in chiral as well as achiral 3D structures. The chirality obtained was found to be coordination driven and from achiral precursors. The 3D framework (chiral and achiral) shows permanent porosity and high CO_2 uptake property. Replacement of the 4,4′-azobipyridyl linker by 1,2-bispyridylethylene leads to different type of linker and 2D cationic structure through *in situ* C-N bond formation.

Table of contents

Chapter 1

Introduction

1.1 Introduction to coordination polymers (CPs)

Metal-organic structures or coordination polymers (CPs) are versatile hybrid structures in terms of dimensionality and complexity.[1] The porous coordination polymers (PCPs) are well known as metal-organic frameworks (MOFs). It contains inorganic as well as organic subunits and thus possesses merit of both the materials. The inorganic unit can be any metal ion or metal-oxygen cluster (known as secondary building unit (SBU)), whereas organic part can be any bridging organic linkers. These materials are highly crystalline, periodic and modular in nature. As the single crystals of PCPs can be easily obtained, their structural insights are more transparent than conventional organic or inorganic polymers.

Coordination polymer (CP) extends *via* tethering of connectors and linkers in different directions. The connector is inorganic part; any metal ion or metal oxygen clusters (SBU).[2] The coordination sphere (coordination number) of the connector is vital as it can direct the final topology of the polymer. Transition metal ions are widely used as connectors and depending upon their oxidation state and coordination number they give rise to various structures. The geometries formed by them include linear, T- or Y-shaped, tetrahedral, square-planar, square pyramidal, trigonal-bipyramidal, octahedral, trigonal-prismatic, pentagonal-bipyramidal and their distorted forms (Figure 1). The geometries formed also depend on reaction conditions, solvents, counter anions and organic ligands.[3] Other than transition metal ion; lanthanide ions (rare earth elements) also act as connectors and provide comparatively large coordination number from 7 to 10 to give new and unusual network topologies.[4] In some cases, metalloligand connectors are also used to construct CPs.[5] Metal-porphyrin connectors are the most well-known among them and these provide functionally and topologically versatile structures.

Organic ligands can be of wide variety and can be classified in three categories: a) anionic, b) cationic and c) neutral. Anionic linkers can be –COOH, -OH or -SO_3H group functionalized. A list of such possible linkers are shown in Figure 2.[6] Cationic linkers are rare and have been used in specific cases.[7] Neutral linkers contain primarily pyridyl functional groups.[8] Moreover, the disposition of the functional groups in the organic linker can be varied and thus a large library of such linkers can be obtained (Figure 2). Assembly of such connectors and linkers thus can give rise to CPs with different dimensions (1D to 3D) and topology (Figure 3).

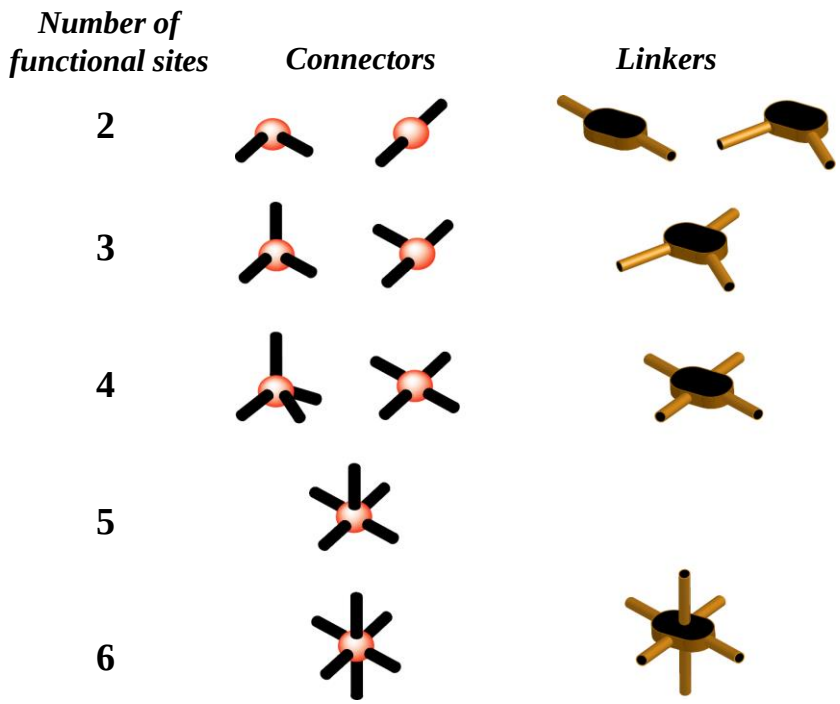

Figure 1: Components of coordination polymers with different number of functional sites.

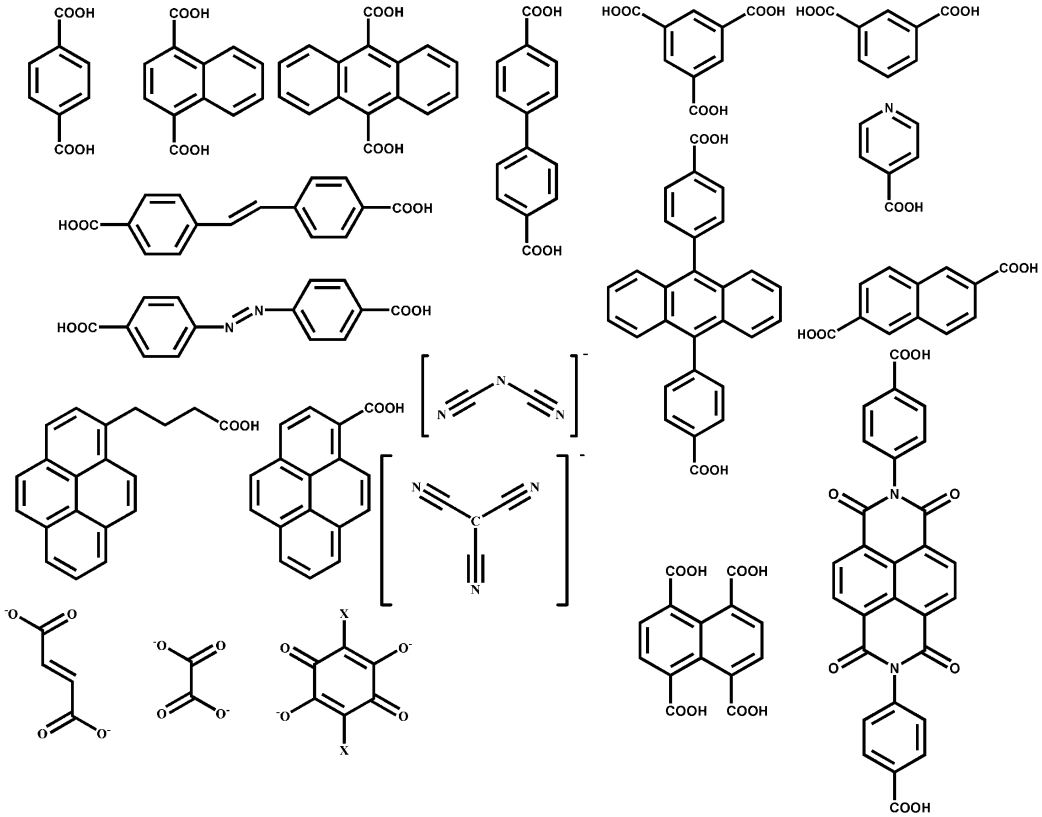

Anionic linkers

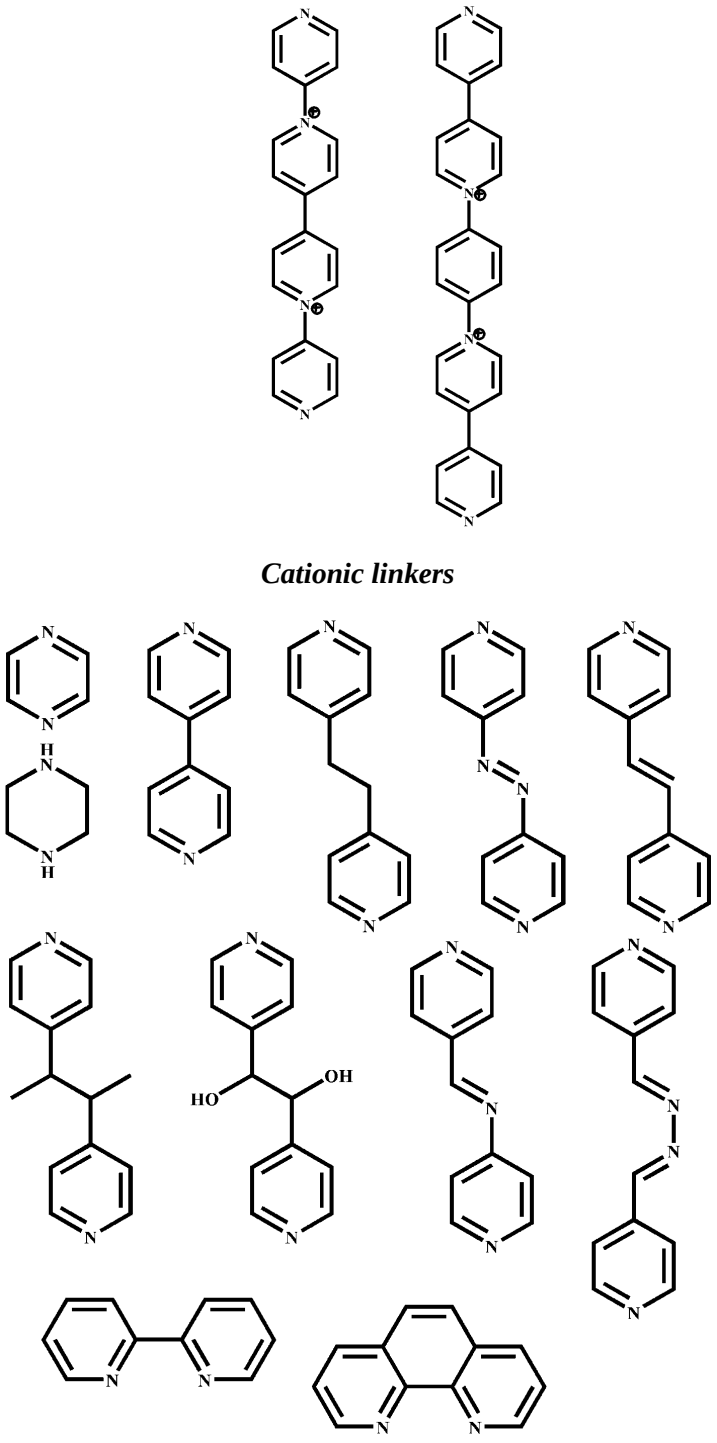

Figure 2: List of anionic, cationic and neutral linkers used for the construction of CPs.

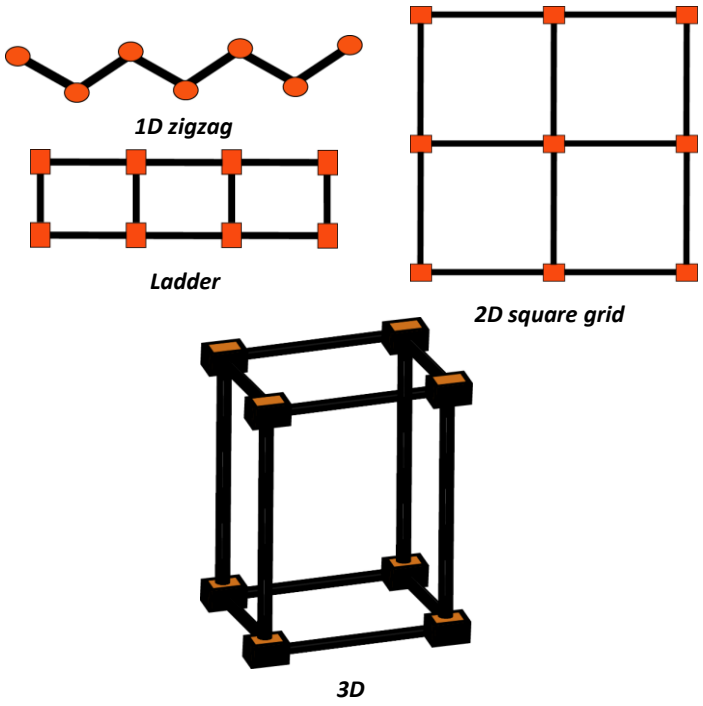

Figure 3: Different dimensionalities of coordination polymers constructed from tethering the connectors and linkers.

1.2 Supramolecular Frameworks

The previous section describes the different dimensionalities in coordination polymers and how linker and connector geometry can modulate or affect the overall structure. The typical coordination bonds and covalent bonds used to construct such structure are very common. Rather use of non-covalent interactions to build such coordination polymers is not well explored.[9]

Among the several possible non-covalent interactions hydrogen bonding, π···π and C-H···π interactions are the most common. Sometimes due to definite shape or functionality of the organic linkers these non-covalent forces are operative. Few possible interaction modes are shown in Figure 4 below. It is expected that these non-covalent interactions do not give sufficient thermal stability which can be obtained by coordination bonds/covalent bonds. But presence of these supramolecular interactions can originate structurally flexible porous structures and interesting photophysical properties. For example, Maji *et. al.* have reported five supramolecular PCPs (MOCPs), $\{[Ni(bipy)(H_2O)_4](2,6\text{-nds})_3\cdot 4H_2O\}$, $\{[Ni(bipy)(H_2O)_4](2,6\text{-nds})_3\cdot 2H_2O\}$, $\{[Ni(bipy)(H_2O)_4](2,6\text{-nds})\}$, $\{[Ni(bipy)(H_2O)_4](2,6\text{-nds})\}$, $\{[Cu(bipy)(H_2O)_4](2,6\text{-nds})\}$ (bipy=4,4′-bipyridine; 2,6-nds=2,6-naphthalenedisulphonate) and characterized them.[10a] $[M(bipy)(H_2O)_4]^{2+}$ is the basic building unit for all the MOCPs and 2,6-nds act as a

counter anion. 2,6-nds interact with water and bipy molecules through strong hydrogen-bonding and π···π interactions to form 3D supramolecular structures. Zaworotko *et. al.* have synthesized Zn^{2+}-4,4′-bipyridine (Zn-bipy) based CPs containing pyrene intercalated between adjacent layers and aromatic solvent molecules incorporated within the framework cavities.[10b] The type of structure obtained depends on the nature of the enclathrated solvent molecule. 1-D ladder architecture was obtained in the case of benzene, toluene, para-xylene and chlorobenzene whereas *o*-dichlorobenzene gives 2-D square grid architecture. The photophysical properties of these coordination polymers were also studied. Same group have reported a coordination polymer $\{[Zn(bipy)_{1.5}(NO_3)_2]\cdot 0.5pyrene\cdot MeOH\}_n$, which contains T-shaped Zn^{2+} nodes and, 4,4′-bipyridine and pyrene as organic components.[10c] Here, pyrene molecules are intercalated between 4,4′-bipyridine forming 2:1 bipy:pyrene exciplex through π···π interactions. In another example, Zeng *et. al.* reported two supramolecular coordination polymers, $[HgI_2(L^1)\cdot 0.5H_2O]_\infty$ (1) and $[HgI_2(L^2)\cdot 0.4CH_3OH]_\infty$ (2) (L^1 = bis[4-(4-pyridylmethyleneamino)phenyl]ether) and L^2 = *N*,*N*′-bis(3-pyridylmethyl)-diphthalicdiimide).[10d] One forms an interestingly infinite cross-linked double helical structure through weak hydrogen bonding (C–H···I), whereas the other forms one-dimensional *zigzag* chains, which are parallel with each other. Different structures can be attributed to the flexibility of ligands. Helical structures have always received attention in coordination chemistry because helicity is an essential element of life and is also important in various applications such as asymmetric catalysis and optical devices. Five neutral infinite Cu^{2+} dicarboxylate coordination polymers, $[Cu(ipa)(2,2'\text{-bpy})]_n\cdot 2nH_2O$, $[Cu_2(ipa)_2(phen)_2H_2O]_n$, $[Cu(oba)(phen)]_n$, $[Cu(oba)(2,2'\text{-bpy})]_n$ and $[Cu(eoba)(phen)]_n$ was synthesized using three V-shaped dicarboxylates (isophthalate (ipa), 4,4′-oxybis(benzoate) (oba) and ethylenedi(4-oxybenzoate) (eoba)) and aromatic chelating ligands.[10e] The bridging ligation of the simple v-shaped dicarboxylate ligands lead to helical chain structures. And interestingly, these helical chains are paired through π···π stacking and hydrogen bonding interactions into double-stranded helices or molecular zippers. Not only polymers, even metal-organic complexes can also extend its structure in higher dimension through non-covalent interactions. Such sort of studies is rare in literature.

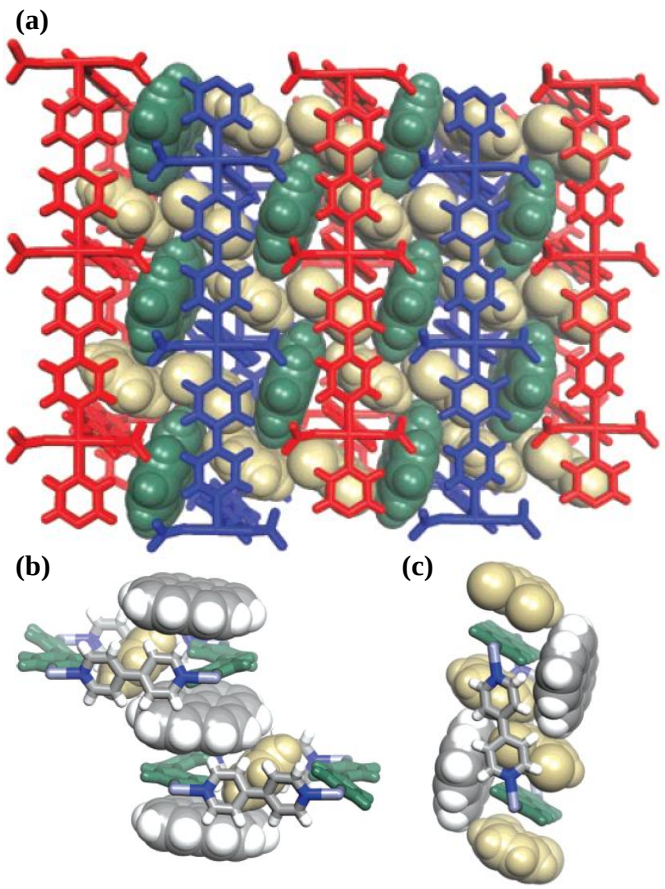

Figure 4: Structural details of ortho-dichlorobenzene (*o*-DCB) and benzene included Zn-bipy CP: (a) Position of pyrene (green) and *o*-DCB (golden) in between the 2D Zn-bipy layers; (b) Face-to-face π···π stacking between pyrene and bipy in benzene included CP; (c) Face-to-edge C-H···π stacking between bipy and pyrene in *o*-DCB included CP. This figure has been reproduced with permission from reference no. 10b.

1.3 Applications of coordination polymers

Porous coordination polymers are not only structurally attractive; they also possess a wide variety of properties. Particularly, porosity, luminescence or magnetism have been studied extensively. Due to the periodicity of the polymeric network the pore size or void space are well defined and also can be systematically tuned. Further functionalization of the pore surface is easy as organic linkers can be easily functionalized or modified. Thus heterogeneous catalysis or separation of gas or industrially important isomers is also possible. A schematic appended below shows the versatile applications in PCPs. In the interest of this thesis mostly the porous and luminescence properties of PCPs have been discussed in detail.

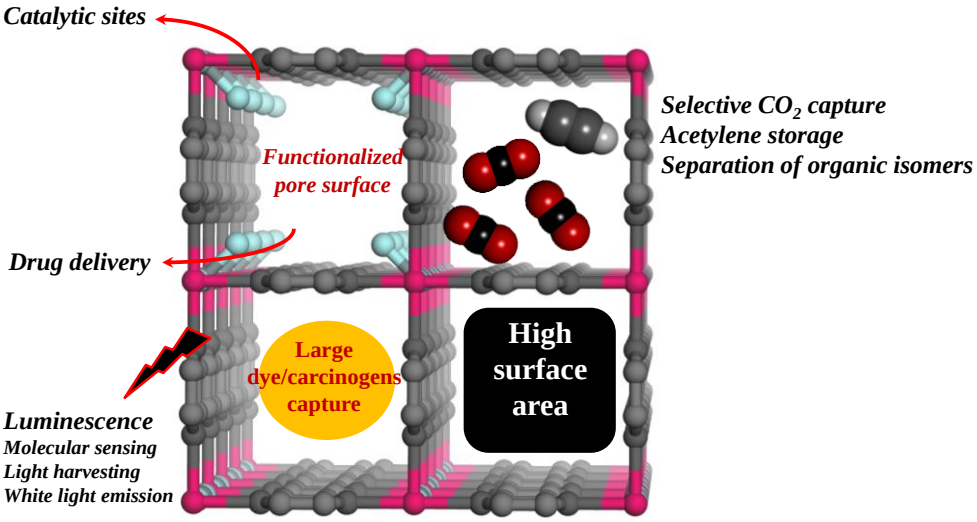

Figure 5: Functional PCPs and its possible applications.

1.3.1 Gas storage and separation, separation of industrially important organic isomers

One of the most extensively studied properties of porous CPs is gas adsorption. Their large internal surface area, modular nature, tunable structures make them good candidates for gas adsorption and separation. Confined nano channels of PCPs can accommodate the guest molecules in high concentration. Till date there are many PCPs that have reported very high surface area compared to the other contemporaries. The highest surface area reported in PCPs till date is 7140 m^2g^{-1} for NU-110 (NU-Northwestern University).[11a] Other landmark examples in this respect are MOF-177 (surface area, 5640 m^2g^{-1}), MIL-101 (surface area, 5900 m^2g^{-1}), UMCM-2 (surface area, 6000 m^2g^{-1}) and MOF-210 (surface area, 6240 m^2g^{-1}).[11b-11e]

PCPs are potential candidates as H_2, CH_4 and C_2H_2 storage materials. As the world faces severe energy related problems, search for alternative energy resources has been in acceleration. H_2 is one of those alternative fuels, but storage and transport of the same have been the main challenges. PCPs are one of those potential materials that can address the problem. For example, mesoporous NU-110 reported by Hupp *et. al*. shows hydrogen storage capacity of 9.05 wt% at 77 K and 56 bar.[12a] PCN-12, another famous PCP reported by Zhou *et. al.* shows 3.05 wt% H_2 uptake at 77 K and 1 atm.[12b] Some of the other potential PCPs with high H_2 uptake capacities are MOF-505 (2.59 wt % at 77 K and 1 atm), HKUST-1 (2.54 wt % at 77 K and 1 atm), PCN-11 (2.59 wt % at 77 K and 1 atm) *etc*.[12c-e] PCN-14, reported by Zhou *et. al.* shows a methane uptake of 230 v/v STP at

290 K and 35 bar, which is 28 % higher than the DOE target and highest value reported till date.[13a] For acetylene storage, Co_2(DHTP) was found to exhibit an uptake of 230 cm^3 (STP)/cm^3 at 298 K, 1 atm.[13b]

Other than storage of gases, sequestration of CO_2, a greenhouse gas, is another important aspect. The rising level of atmospheric carbon dioxide from anthropogenic emissions is one of the greatest environmental threats of today. Carbon capture and sequestration (CCS) is the requirement of present scenario. The CCS process involves the selective removal of CO_2 from gas mixture, the compression of pure CO_2 to a supercritical fluid, transportation to an injection site, and finally permanent subterranean or submarine storage. Significant interest has been directed towards development of solid adsorbents that can selectively adsorb CO_2 at partial pressures applicable to CCS. PCPs are highly tunable which offer greater functionality and has reduced adsorbent mass and volume compared to traditional solid adsorbents. For example, at 35 bar, the volumetric CO_2 adsorption capacity for MOF-177 (Langmuir surface area, 5640 m^2g^{-1}) reaches a storage density of 320 cm^3 (STP)/cm^3.[14a] It is approximately 9 times higher than the quantity stored at this pressure in a container without the PCP and also higher than conventional materials, namely, zeolite 13X and MAXSORB. But at low pressure (1 atm) Mg-MOF-74 shows highest storage capacity of 27.5 wt% at 298 K.[14b] Recently, Zaworotko *et. al*. have shown few fluorinated interpenetrated and noninterpenetrated PCPs that shows excellent performance to separate CO_2 from N_2 at ambient condition (Figure 6).[14c] Their study also reveals that interpentrated PCP with confined space is more efficient at ambient condition for sequestration of CO_2.

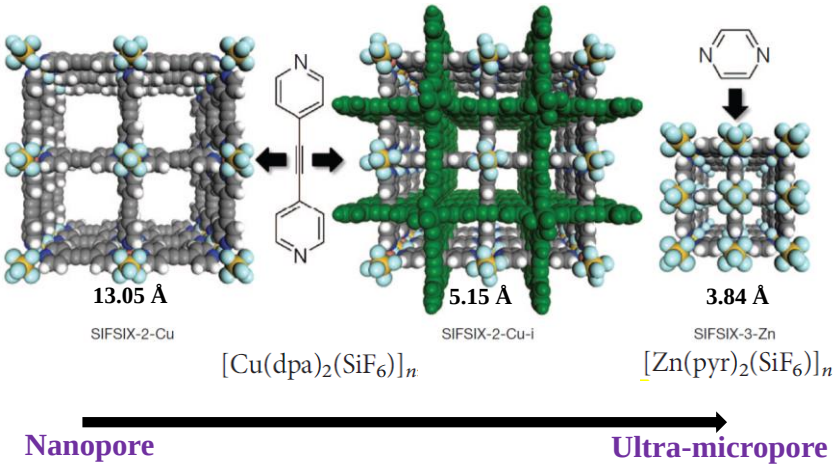

Figure 6: The schematic shows three fluorinated PCPs with their respective molecular formulas and pore sizes. This figure has been reproduced with permission from reference no. 14c.

As PCP contains definite pore size and shape, functionalized pore surface, it can also be used for separation of isomers those are industrially important or carcinogenic. For example, large dye molecules those are water pollutants can be easily separated or captured using mesoporous PCPs. Such scavenging process has been reported in literature.[15] Apart from this, separation of isomers such as xylene isomers has been an interesting topic of study using PCPs. As each xylene isomers (ortho, meta and para) are important industrial precursors, their separation is very important.[16] Using zeolitic materials such separation is presently carried out but PCPs are more potent for such processes. Kinetically and thermodynamically such separation has been possible by PCPs (such as HKUST and MIL-47).[17]

PCPs have also been used for biofuel separation purpose. As mentioned before, alternative energy resources are in high demand, keeping this in mind storage and separation of biofuels such as ethanol has got much attention. PCP is one of the most potential materials to serve the purpose. As the feedstock contains high concentration of water, hence separation of water/ethanol is most challenging. This separation can only be served by any hydrophobic PCP or flexible PCP that shows different gate opening or pore opening pressure for different solvent vapours. Based on this concept several PCPs have been reported till date.[18] Kitagawa *et. al.* have reported one framework, $\{Cu^{2+}(mtpm)Cl_2\}$ (mtpm=tetrakis(*m*pyridyloxymethylene)methane) that shows three different profiles for water, methanol and ethanol vapours leading to clear separation of ethanol and water.[18a] Following this several other PCPs have also been tested for the same.[18b-18c] In the later chapters some improved studies have been shown on flexible PCPs that shows potential for biofuel separation.

1.3.2 Catalysis, magnetism and drug delivery

Heterogeneous catalysts have an advantage of easy recoverability and hence they are important for industrial applications. Because of the presence of well-defined pores and channels which can be easily functionalized, PCPs have the potential for size and shape selective heterogeneous catalysis. Their porosity provides internal surface areas that are relatively large, thereby facilitating their catalytic reactivity and the uniformity of their pore and channel sizes account catalytic selectivity. They are robust because of the presence of inorganic part and are therefore well suited for catalysis under extreme conditions. Catalytic sites in PCP can be obtained during synthesis or postsynthetic way. Generation of unsaturated metal sites (UMSs) in PCPs is an excellent way to create Lewis

acidic catalytic active sites. Among the earliest reports of PCP-based catalysis, in 1994 Fujita *et. al*. reported cyanosilylation of aldehydes by a 2D PCP (layered square grids) of formula $Cd(4,4'\text{-bpy})_2(NO_3)_2$, (bpy = 4,4′-bipyridine).[19a] This work was mainly on size and shape selective clathration. The porous-framework material $[Cu_3(btc)_2(H_2O)_3]$, also known as HKUST-11 and as MOF-199,[19b] contains large cavities having pore dimensions of diameter ~ 6 Å . The Cu^{2+} possesses open sites after the removal of water molecules coordinated to it. Kaskel *et. al.* showed that these Lewis acid sites could catalyse the cyanosilylation of benzaldehyde or acetone.[19c] Kitagawa *et. al*. have reported Knoevenagel condensation reaction using an amide functionalized PCP, $\{[Cd(4\text{-btapa})_2(NO_3)_2]\cdot 6H_2O\cdot 2DMF\}_n$ (4-btapa=1,3,5-benzene tricarboxylic acid tris[*N*-(4-pyridyl)amide]).[19d] The porous structure has three dimensional channels that are decorated by amide groups (Figure 7). These exposed amide groups act as Lewis base catalyst for Knoevenagel condensation reaction.

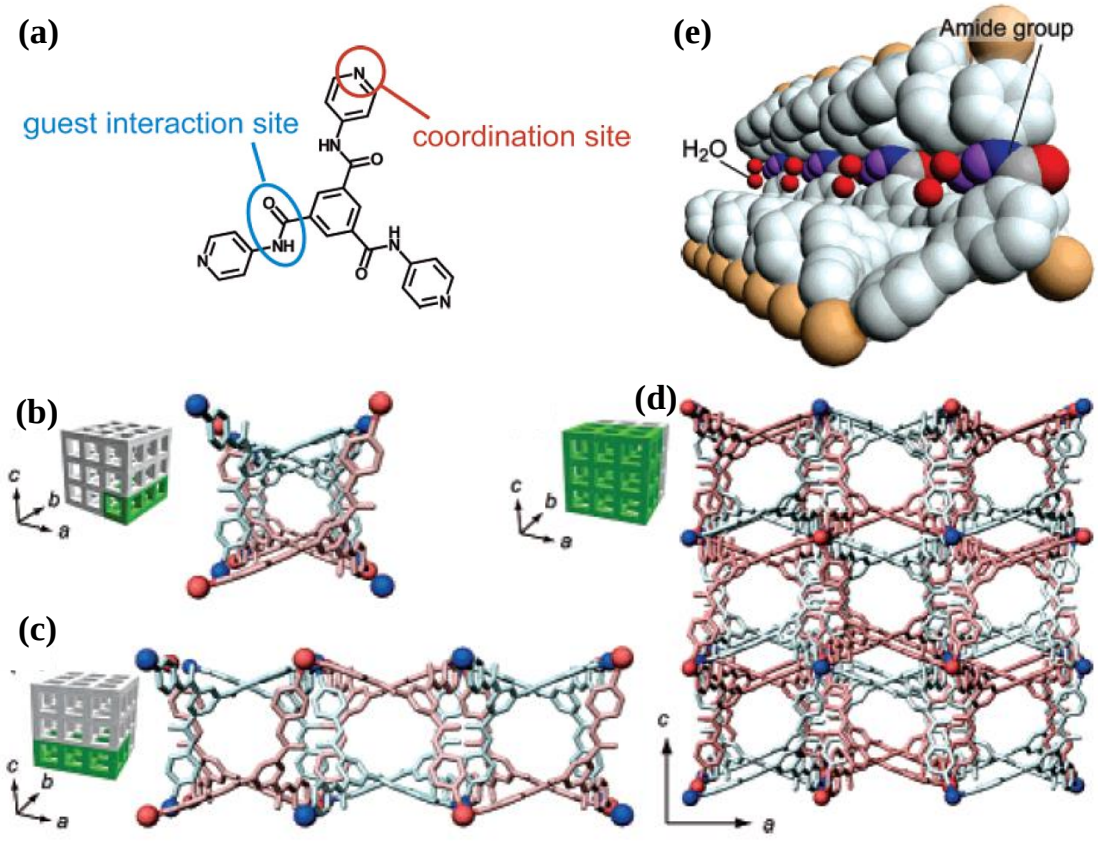

Figure 7: (a) Chemical structure of 1,3,5-benzene tricarboxylic acid tris[*N*-(4-pyridyl)amide]; (b-d) Three dimensionally running channels of dimensions 4.7×7.3 $Å^2$ in $\{[Cd(4\text{-btapa})_2(NO_3)_2]\cdot 6H_2O\cdot 2DMF\}_n$; (e) Ordered amide groups in the channel surface, red balls are the water molecules which are hydrogen bonded to the amide groups. This figure has been reproduced with permission from reference no. 19d.

Incorporation of magnetic moment carriers such as paramagnetic metals or open shell organic ligands or both can induce magnetic properties in PCPs. Magnetism being a cooperative phenomenon, some sort of exchange between the moment carriers is required for material to show magnetic properties. Immobilization of magnetic guests in the framework also conveys magnetism to PCPs. From zero to three dimensions, all sorts of CPs have been exploited to magnetic studies.[20] Coexistence of porosity and magnetism is very unique phenomenon in PCPs as porosity demands long linkers whereas magnetism is a short range phenomenon and requires short linkers to connect the magnetic centers. But such porous magnetic materials also exist and considerable amount of work has been carried out in this direction.[21] Maji *et. al*. have recently reported cyanide-bridged M^{2+}-Ag^{+} bimetallic PCPs, $\{[M^{2+}(pip)\{Ag(CN)_2\}_2]\cdot 5H_2O\}$ (M = Co, **1**; Ni, **2**; pip = piperazine) which show spin canting behaviour and selective CO_2 uptake at 195 K.[21a]

Better techniques of drug administration are always in demand and continuous efforts are being applied by researchers to fulfil the growing demands. PCPs are hybrid materials which combine advantage of organic groups with the inorganic elements to get ordered framework with greater porosity for high drug loading capacity and controlled release. By employing different functional groups in the PCPs, the functionality of the framework and pore size can be tuned to suite different applications. Hence, PCPs show great hope for the development of new therapeutic and diagnostic applications. MIL-88A, MIL-88B-4CH_3 and MIL-100 passed toxicological studies in rats (upto 220 $mgkg^{-1}$) both in vitro and in vivo. They are iron carboxylate based PCPs.[22a] M-CPO-27 or MIL-100 has shown their dissolution and persistence under simulated physiological conditions (eg. Phosphate buffered saline, PBS and bovine serum albumin, BSA) for days to upto three weeks depending on the structure, composition, particle size and formulation.[22b] Another example of drug delivery by PCP is demonstrated by the cationic zinc adeninate PCP for the administration of procainamide (a cationic drug).[22c]

1.3.3 Photophysical Properties of PCPs

Photophysical properties of coordination polymers are of profound interest because of the exotic outcomes such as tunable emissions, molecular sensing, non-linear optical properties and light harvesting applications.[23] Origin of such properties might be associated with the inorganic part (metal ions) or organic linkers or guest molecules (Figure 8). Metal ion based luminescence or charge transfer properties are well studied for zero dimensional molecular complexes also. Lanthanide metal ions are well-known

for their sharp emission with high life time supported by antenna effect. Whereas, for organic chromophoric linkers versatile photophysical properties can be observed. In the following sections such properties and their possible applications have been discussed.

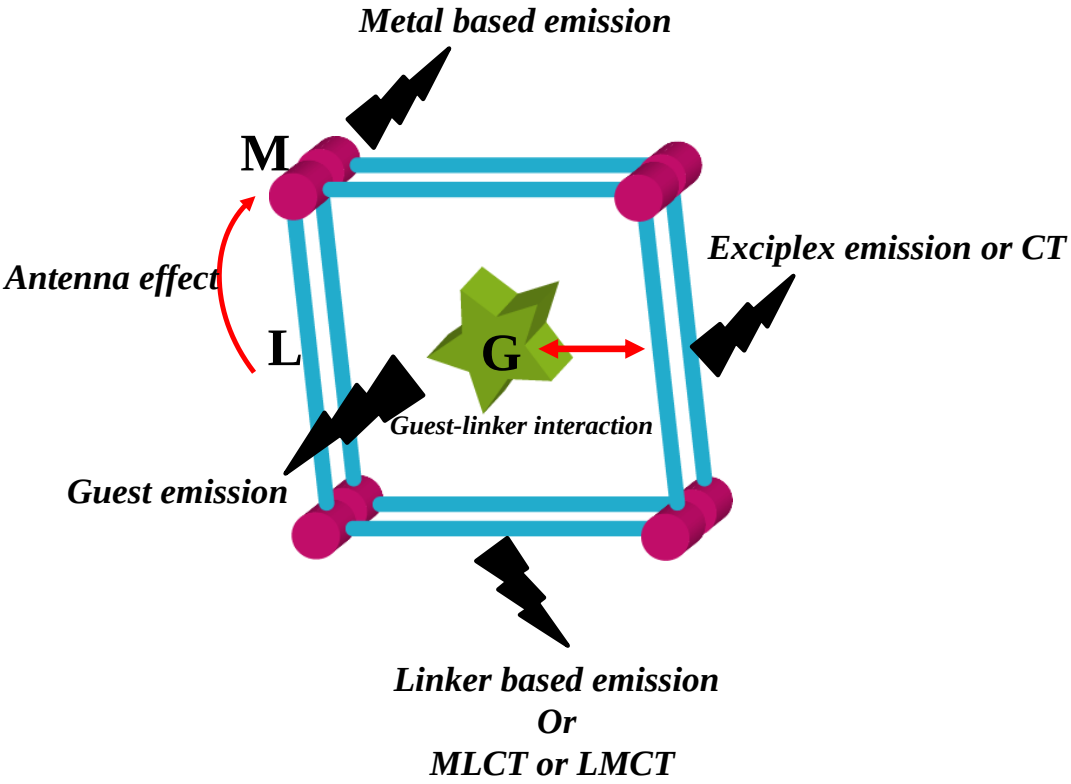

Figure 8: A schematic of different photophysical properties in PCPs.

The trivalent lanthanide ions such as Eu^{3+}, Tb^{3+} and Dy^{3+} are very attractive luminophores as they show very narrow band with emission with high lifetime in solid state as well as in solution state.[24] But, a bare metal ion without a suitable linker do not show significant emission as the 4f orbital is shielded by filled $5s^2 5p^2$ sub-shell and thus screening the 4f-4f electronic transitions. Moreover the electronic transitions are Laporte forbidden and hence results in weak absorption and emission. But by complexation with a suitable organic ligand solves the problem through antenna effect (Figure 9). The organic ligand should have strong absorption and strong vibronic coupling between the organic linker and metal ion that leads to an energy transfer from linker excited state to the metal excited state (Figure 9). In 1942 Weissman first identified such process. Based on such unique emission features of lanthanide ions many possible applications can be found and have been discussed in the later sections.

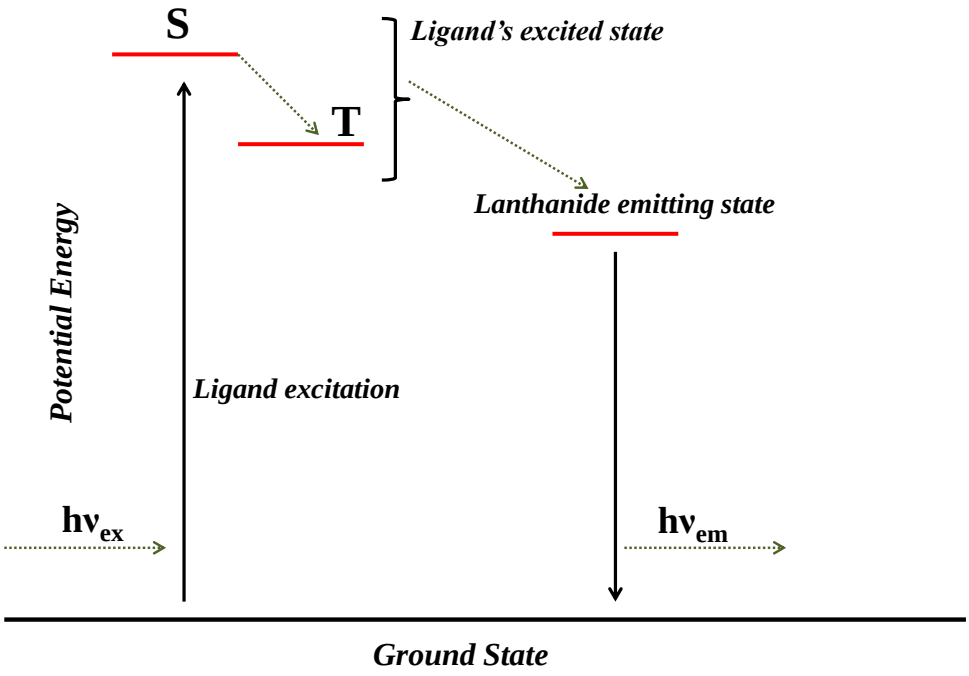

Figure 9: A schematic of antenna effect in lanthanide CPs.

In a typical case, a luminescent CP with organic chromophoric linker mainly shows linker based emission or in certain cases metal-to-ligand or ligand-to-metal charge transfer features. The π-π* or n-π* transitions in an organic ligand of the framework can be easily understood from their emission features as those resemble to the monomer emission of the ligand. In some cases, slight red shift or blue shift (~ 20-30 nm) of linker emission might occur due to variation in the chromophore conjugation due to the metal coordination. It must be mentioned that linker emission generally quench in presence of d^3-d^9 metal ions, as the emission energy is absorbed by the d-d transition. But a large red shift of the emission compared to the monomer emission might involve several excited state processes such as exciplex or excimer or charge transfer (CT) emission. Such processes are very unique in coordination polymers and identification or characterization is done based on emission and absorption spectra profiles, fluorescence life time and excitation spectra. Most importantly, such process involves suitable donor acceptor molecules. A good donor is with low ionization energy and hence easily promotes one electron to the acceptor that has high electron affinity. Combination or stacking of such donor and acceptors can give rise to an exciplex or CT complex. Along with the close stacking, dipole orientation of the chromophores also plays a crucial role. To figure out the several excited state and ground state processes in CPs a schematic has been shown below (Figure 10) that describes the possible pathways.

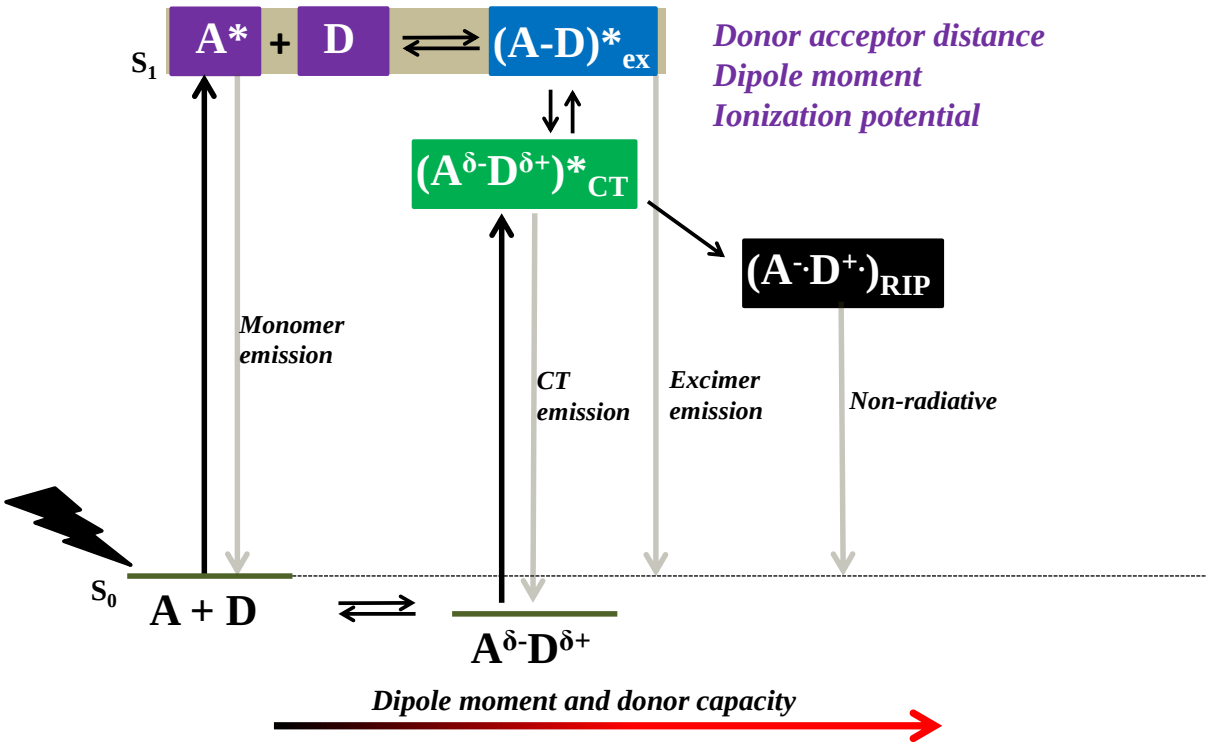

Figure 10: A schematic of various photophysical processes involving donor acceptors in CPs.

Two identical chromophores can combine at the excited state in the following manner: A + hν = A*; A*+ A = (AA)*; where A is the organic chromophore and * denotes excited state. So formed (AA)* is known as excimer. When there are two dissimilar chromophores which can be denoted as acceptor (A) and donor (D), their combination at the excited state is known as exciplex (as represented in Figure 10). On the other hand, donor and acceptor chromophores can also form a stable complex in the ground state ($A^{\delta-}D^{\delta+}$). Stability of such ground state charge transfer (CT) complex depends on the donor and acceptor strengths. Such CT can be identified from the UV-visible spectra as this features a strong band in the visible region of the spectrum. There can also be an excited state CT and this particular state may involve in equilibrium with typical exciplex state. Such studies have been carried out recently by Kitagawa *et. al.*[25] and has also been evidenced in the present work which will be discussed in the later chapters. As the donor and acceptor strength increases further, there can be existence of completely charge separated state or otherwise called as electron transfer. It is worth to mention that exciplex/excimer or CT also involves charge separation. In case of an electron transfer process presence of radical cation or anion is evident and this can be characterized from EPR signal. Evidently such charge separated species are non-radiative in nature due to formation of radical ion pair (RIP). To see such process most cases some

external stimuli such as light or heat is necessary as the activation energy. To understand and get an idea about the donor and acceptor molecules involved in such processes a list of chromophores is appended below (Figure 11).

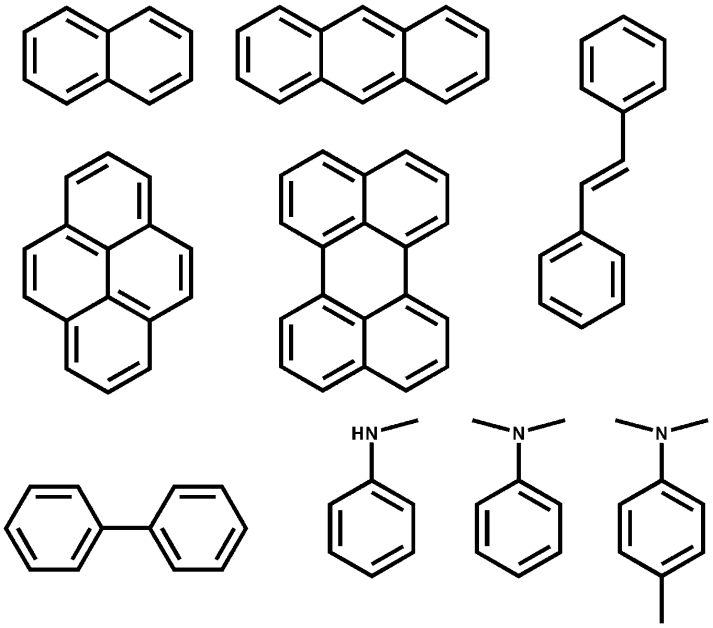

Donor chromophores

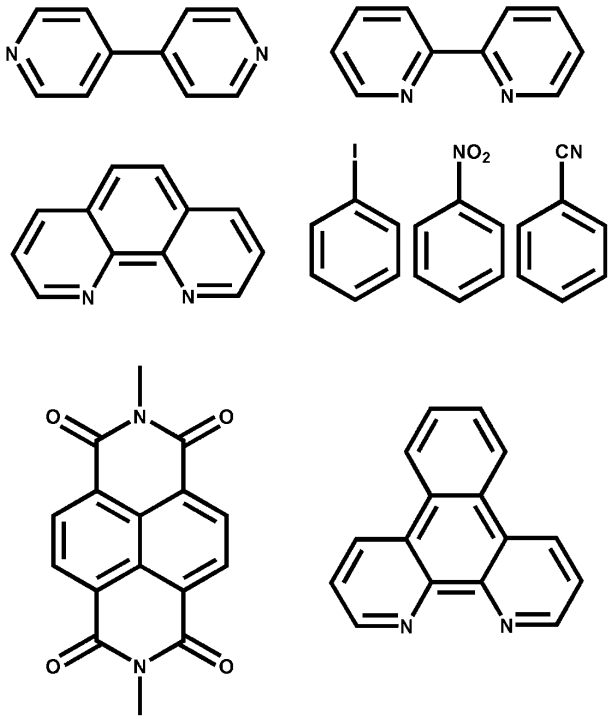

Acceptor chromophores

Figure 11: Donor and acceptor chromophores that can form excimer/exciplex or CT complexes.

Based on such exotic properties of the organic linkers and metal ions various applications can be seen in CPs. Not only the framework struts, guest immobilized inside the nano pores can also induce excellent properties in PCPs. In the following sections such properties are detailed.

1.3.3.1 Molecular sensing

Molecular sensors are those which show significant change in electrical, electronic, magnetic or optical signal when it binds to a specific guest covalently or non-covalently. Few essential features of sensors are as follows:

- It will exhibit specific change in response to an interaction with the analyte
- The change must have some analyte specificity
- Reversible response of the probe
- The change in response to the analyte should be detectable

Such sensing or recognition phenomenon is based on weak interaction between the receptors and substrates. PCPs have been well explored for such application. Sensing of carcinogenic solvents (volatile solvents) or organic molecules, explosive molecules, biologically toxic ions (metal ions or anions such as fluoride) *etc* have been reported till date in literature using PCP as a probe material.[26] Due to a defined pore size and shape, selective recognition is *via*ble; further according to the analyte nature PCPs can be functionalized easily. Figure 12 shows the possible sensing mechanism that operates in CPs.

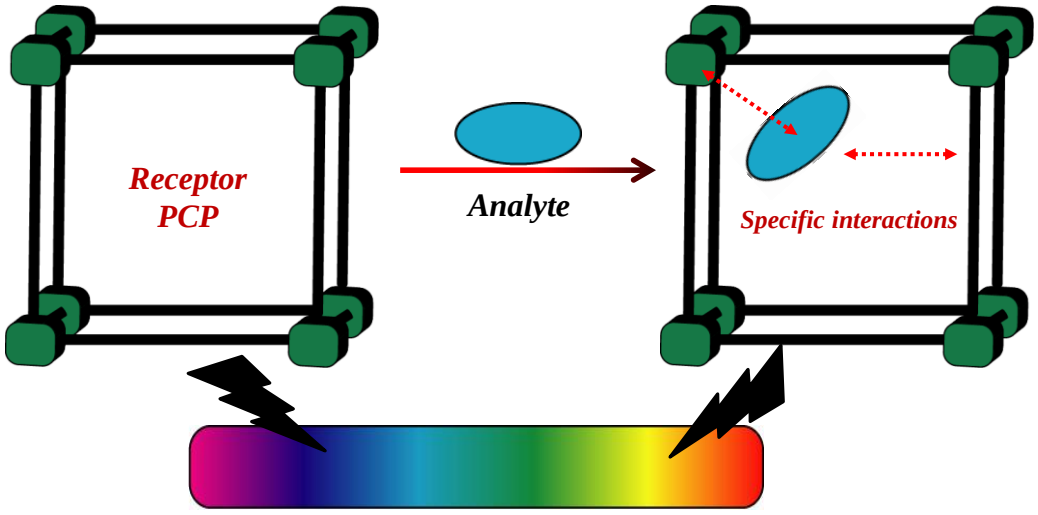

Figure 12: Scheme showing the possible mechanism of sensing through emission property.

PCP based sensory materials can be divided in two primary categories; lanthanide based PCPs and other PCPs which show linker/guest based emission. Lanthanide based PCPs are comparatively less in the literature primarily because it is difficult to synthesize porous lanthanide CPs. Its high coordination number generally leads to condensed non-porous structure but these are very attractive as luminescent material. The emission characteristics and high coordination number have been exploited for several sensing applications. Chen *et. al*. have reported excellent sensing materials based on lanthanide PCPs.[27] A Tb(BTC) (BTC- 1,3,5-benzenetricarboxylate) framework was used as fluoride anion sensor using hydrogen bonding interactions inside the pore surface (Figure 13).[27a] Analogous Eu(BTC) PCP showed solvent responsive emission characteristics, particularly a very small amount of acetone can be easily detected by its luminescence quenching. This is due to the presence of unsaturated Eu^{3+} coordination sites which is available for solvent molecule coordination.[27b] In another example, a PCP {Eu(PDC)DMF} (PDC= pyridine1,3-dicarboxylate) was used for Cu^{2+} sensing applications. Here Cu^{2+} binds to the available pyridyl nitrogen center and thus quenches the Eu^{3+} emission.[27c]

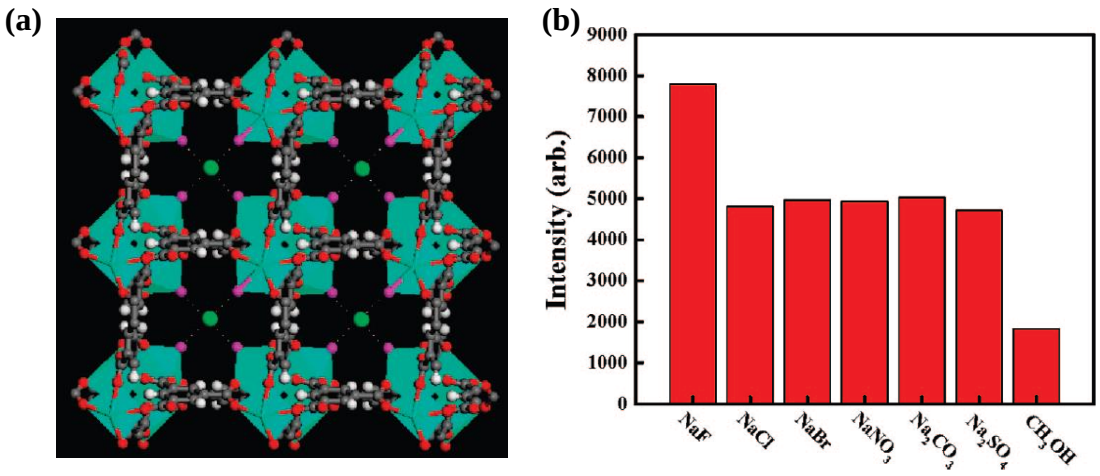

Figure 13: (a) Single crystal structure of Tb(BTC) PCP showing the position of F^- anion inside the pore and hydrogen bonding interaction between methanol and F^-; (b) $^5D_4 \rightarrow {}^7F_5$ transition intensities of activated Tb(BTC) in different types of 10^{-2} NaX and Na_2X methanol solution (λ_{ex} = 353 nm, λ_{mon} = 548 nm). These figures have been reproduced with permission from reference no. 27a.

Based on ligand centered emission several PCPs are reported that show excellent molecular recognition properties. A pyrene linker based luminescent PCP, $[In_2(OH)_2(TBAPy)]\cdot$(guests) was reported by Rosseinsky *et. al.* which showed guest responsive luminescence property.[28a] Pyrene is a good fluorescent probe as its emission is sensitive to its local environment. The monomer and excimer emissions depend on the

relative proximity between pyrene moieties. The pyrene core showed long lived life time and presence of various solvents modulate its emission characteristics. Introduction of luminescent guest molecules in a porous PCP is another way of generating luminescence and in that course complex photophysical processes such as exciplex, excimer or even electron transfer processes are reported. One of the most well-known examples is reported by Kitagawa *et. al.* $[Zn_2(bdc)_2(dpNDI)]_n$, (bdc=1,4-benzene dicarboxylate; dpNDI=N,N′-di(4-pyridyl)-(1,4,5.8-naphthalene diimide)) which contains redox active dpNDI linker and inclusion of various aromatic guests showed different emission colour due to formation of guest:dpNDI exciplex with charge transfer characteristics (Figure 14).[25a] This feature of the PCP is explained as molecular decoding. Another PCP $\{Mg(DHT)(DMF)_2\}_n$, (DHT = 2,5-dihydroxy terepthalic acid) which shows ESIPT (excited state intramolecular proton transfer) phenomenon due to presence of ESIPT active DHT, was used for ammonia sensing in vapour phase.[28b]

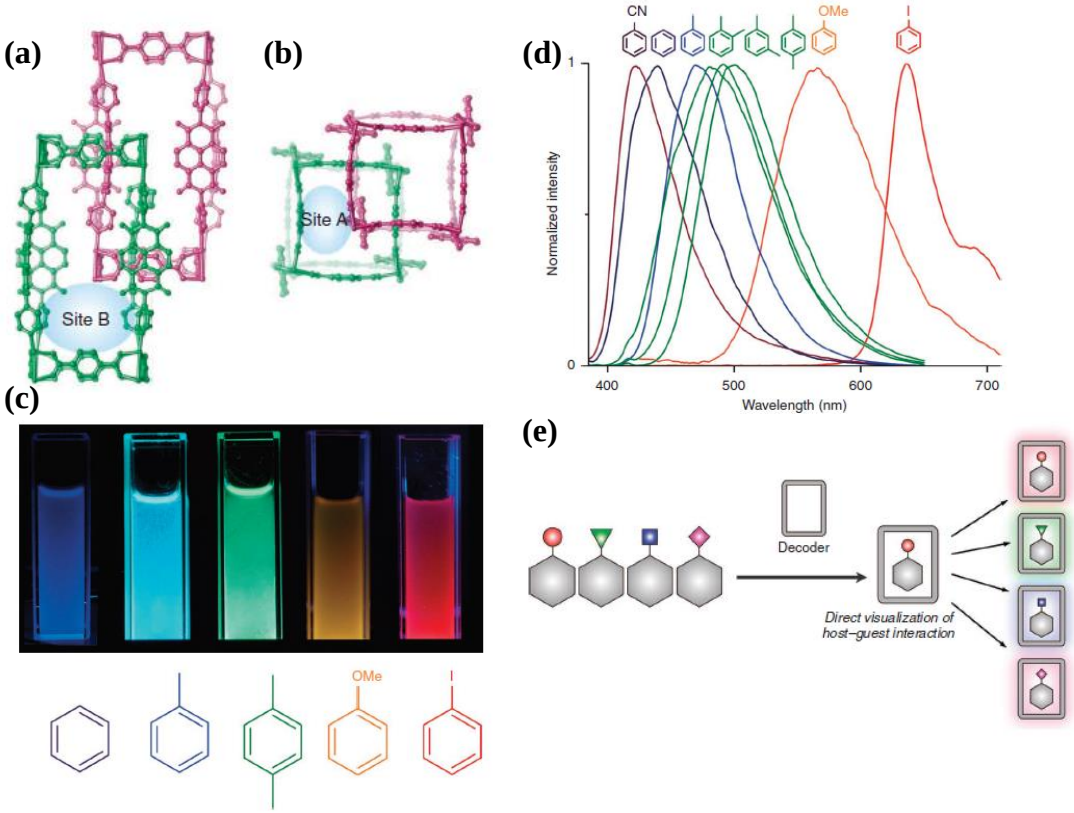

Figure 14: (a,b) View of two different sites in two-fold entangled structure of $[Zn_2(bdc)_2(dpNDI)]_n$, (c) Emission of different VOCs included framework under UV light, (d) Emission spectra of framework with different VOCs incorporated, (e) Schematic of molecular decoding phenomenon. These figures have been reproduced with permission from reference no. 25a.

Sensing of gas such as O_2, CO_2 can also be achieved using luminescent PCP. Chen *et. al.* have reported a framework, $[Zn_4O(bpz)_2(abdc)]\cdot$guest (bpz=3,3′,5,5′-tetramethyl-4,4′-bipyrazole) also known as MAF-X11, which shows bright blue luminescence from abdc linker.[28c] In presence of O_2 this blue emission is almost quenched leading to selective sensing of O_2 gas at ambient condition. Similarly, Kitagawa *et. al.* have also reported a flexible luminescent PCP that can sense CO_2 gas at 195 K.[28d] Sensing of volatile organic compounds has also been carried out by Wu *et. al.*[28e] using a new PCP $[CdL(H_2O)]\cdot 4DMF\cdot 2H_2O$ (L=(E)-4-(2-carboxyvinyl)benzoate) which was found to be suitable for partial loading of Rhodamine B dye. This dye loaded dual emissive framework shows fingerprint emission colours for various volatile aromatic organic compounds. The different ratio of the dual emission intensities is the reason behind the tunable emission colours.

Metal-organic complexes are also useful for such sensing/recognition processes. A 2D coordination compound, $\{[Cu_2(HL)(N_3)]\cdot ClO_4\}_\infty$ (**1**) (H_3L= 2,6-bis(hydroxyethyliminoethyl)-4-methyl phenol) was synthesized by Banerjee *et. al.*.[28f] Each $[Cu(HL)(N_3)]^+$ species is connected to its adjacent unit by a bridging alkoxide oxygen atom of the ligand to form a helical propagation along the crystallographic *a*-axis. These helices are connected by ligand alcoholic oxygen atom along crystallographic *b*-axis to form pleated 2D sheets. The framework dissociates in solution to produce $[Cu_2(HL)_2(H_3L)]\cdot 2H_2O$ (**2**), which act as a metalloligand. Approximately 19–fold Zn^{2+} selective chelation-enhanced fluorescence was observed in HEPES buffer (pH 7.4). Hence, **1** can act as Zn^{2+} selective fluorescent probe for biological applications.

1.3.3.2 Tunable emission

Solid state light emitting materials are interesting and are very important for display and lighting technologies. Tunable emission colours from a single phase matrix and control over the colour stoichiometry can further give rise to white light emission which is very important feature for display devices. Crystalline CPs are an excellent platform for such solid state lighting materials as multi-colour emitting sites can be impeded in the same matrix. Only organic or only inorganic components can cover a part of the visible spectrum. This drawback is overcome by PCPs possessing both organic and inorganic constituents. A variety of PCPs with tunable emission properties and white light emission have been investigated for this purpose.

Lanthanide (Ln) metal containing materials have attracted considerable interest in this field. The red (Eu^{3+}, Pr^{3+}, Sm^{3+}), green (Tb^{3+}, Er^{3+}) and blue (Tm^{3+}, Ce^{3+}, Dy^{3+}) emitting ions when combined judiciously with proper organic ligand or doped in a host, the material can emit across the entire visible spectrum. For example, a family of multifunctional anhydrous Ln-PCPs, LnL (Ln=Y, La-Yb except Pm) was synthesized using ligand (H_3L=4,4′-((2-((4-carboxyphenoxy)methyl)-2-methylpropane-1,3-diyl)bis(oxy))dibenzoic acid).[29a] White light emission was realized by co-doping Dy/Eu or Dy/Sm into analogous Gd compound. Another example include synthesis of two isostructural Ln-Zn (Ln=Eu, Tb) heterometallic PCPs of Eu^{3+} and Tb^{3+} using 4-(1H-tetrazol-5-yl)-biphenyl-3-carboxylic acid as ligand.[29b] Different percentages of Eu^{3+} was doped in the Tb^{3+} PCPs which showed colour tunability leading to nearly white light emissions. CIE coordinate of (0.331, 0.328) was achieved when amount of Eu^{3+} ions was 0.5%.

Encapsulation of functional species in a PCP can also show colour tunability. A mesoporous blue emitting anionic PCP, $[(CH_3)_2NH_2]_{15}[(Cd_2Cl)_3(TATPT)_4]\cdot 12DMF\cdot 18H_2O$ {TATPT= 2,4,6-tris(2,5-dicarboxylphenylamino)-1,3,5triazine} was synthesized by Li *et. al.* which contained two types of pore with dimensions of ~ 2 and 3 nm.[29c] Different concentrations of yellow emissive, $[Ir(ppy)_2(bpy)]^+$ complex was incorporated inside the pores of this framework. 3.5 wt% of the complex in the PCP resulted in white light emitting material with CIE coordinates (0.31, 0.33) (Figure 15). Maji *et. al.* have reported a new phenomenon in PCP known as excited state intramolecular proton transfer using di-hydroxy terepthalic acid as a linker. The $\{Mg(DHT)(DMF)_2\}_n$ PCP shows tunable emission colour in presence of solvents like DMF, methanol, water due to the presence of ESIPT process.[29d]

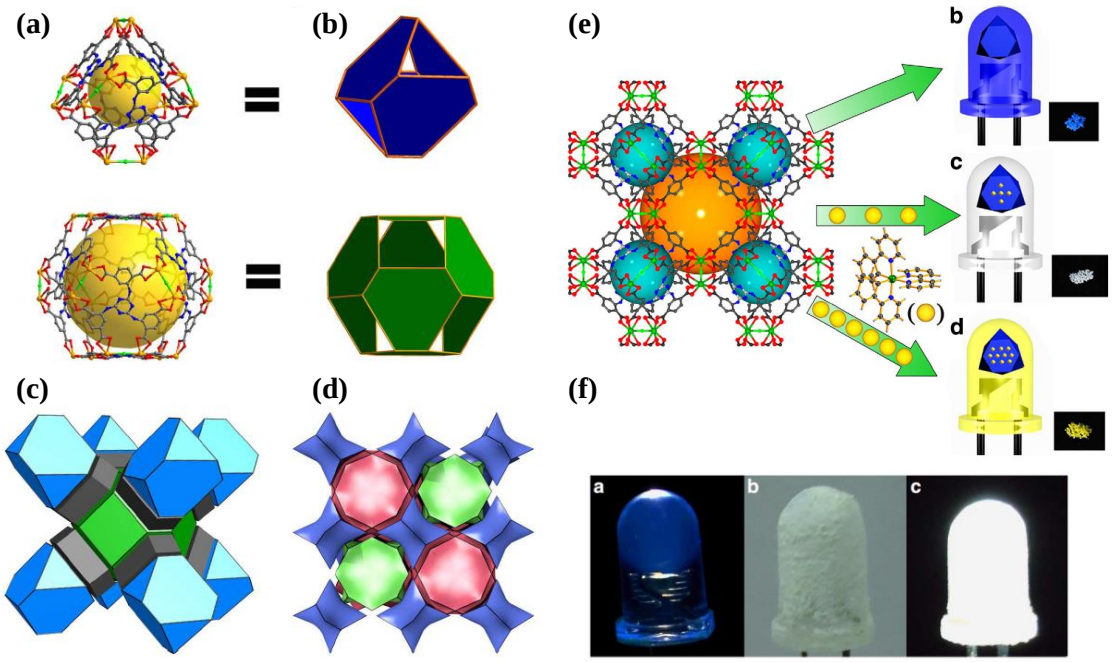

Figure 15: Structural details of $[(CH_3)_2NH_2]_{15}[(Cd_2Cl)_3(TATPT)_4]\cdot 12DMF\cdot 18H_2O$ (**1**) : (a) Truncated tetrahedral and octahedral cages; (b) polyhedra of cages; (c) 3D polyhedral structure; (d) 3,4-connected augmented net; (e) 3D structure , the orange and dark cyan spheres represent the void inside the cages; (f) Photographs of the LEDs, (a) An illuminating 3mm reference ultraviolet LED (turned-on emission has a blue tinge). (b) The same LED coated with a thin layer of sample of 3.5 wt% $[Ir(ppy)2(bpy)]^+$@**1** (not turned on). (c) The coated LED was turned on and illuminates bright white light. These figures have been reproduced with permission from reference no. 29c.

Luminescent metal-organic complexes are also attractive materials. Su *et. al.* have demonstrated the syntheses of 4d-4f heterometallic Ag-Ln complexes; $\{[EuAg_3(3\text{-}TPyMNTB)_2(H_2O)(MeCN)](ClO_4)_6\cdot 4MeCN\}$ (2-Eu-Ag) and $\{[GdAg_3(3\text{-}TPyMNTB)_2(H_2O)(MeCN)](ClO_4)_6\cdot 4MeCN\}$ (2-Gd-Ag), (3-TPyMNTB= tris((pyridin-3-lmethyl)benzoimidazol-2-ylmethyl)amine) through stepwise self-assembly of predesigned Ln^{3+} monomeric complexes $\{[Eu(3\text{-}TPyMNTB)_2](ClO_4)_3\cdot 2.5MeCN$ and $[Gd(3\text{-}PyMNTB)_2](ClO_4)_3\cdot 2MeCN\cdot 2CHCl_3\}$, respectively with the Ag^+ ions.[30a] In 2-Eu-Ag, the ligand centered emission is resensitized by Ag^+ to generate dual emission (the metal-centered f−f emission characteristic of Eu^{3+} ion and ligand-centered excimer emission sensitized by Ag^+ ion) leading to white light emission from single crystal. The complexation of metal ions by conjugated organic molecules can improve structural rigidity which can help in sustaining many excitation-emission cycles. As a result metal-organic complexes can exhibit enhanced fluorescence and can find application in optoelectronic devices. In 2009, Roh *et. al.* studied several green-emitting Zn^{2+} complexes with benzothiazole and its derivatives to produce white-light emission.[30b]

They reported a high luminance (1 cd m^{-2} at 3.5 V, 10400 cd m^{-2} at 14 V) in multilayer electroluminescent devices for one of the fluorenyl-substituted Zn^{2+} complex.

1.3.3.3 Light harvesting

Light harvesting phenomenon is inspired by the nature's photosynthesis process and thus also known as artificial photosynthesis process. This process is basically driven by resonance energy transfer phenomenon in which the excited molecule (donor) transfers its energy very rapidly to adjacent molecule (acceptor) through a non-radiative pathway such that the lifetime of the donor excited state is shortened. This forms the basis of light harvesting. Theodor Förster suggested the mechanism of resonance energy transfer (RET) and the phenomenon is called Förster Resonance Energy Transfer (FRET). This energy transfer occurs *via* coupling of the dipole moments of the donor and acceptor molecules through columbic (electrostatic) interaction. The extent of energy transfer is determined by the distance between the donor and acceptor and the extent of spectral overlap. The typical distance between chromophores for FRET to occur is about 30-100 Å. The efficiency of FRET process is related to the donor and acceptor distance by the following equation:

$\mathbf{E = 1/\{1+(r/R_0)^6\}}$; (r = distance between donor and acceptor; R_0 = Förster distance i.e. the distance at which the energy transfer efficiency is 50%.

Such process can be achieved by suitable designed assembly of chromophores in an ordered matrix. In organic polymers or dendrimers light harvesting is well explored but in coordination polymers this process is yet to be properly studied.[31] As CPs are highly ordered and have well defined structure, hence organization of donor and acceptors can be easily manipulated and hence control over such energy transfer process is more efficient. Possible pathways for energy transfer in PCPs are a) linker-to-linker or strut-to-strut energy transfer; b) host to guest energy transfer. A strut-to-strut energy transfer process was reported by Hupp *et. al.* in a PCP, containing porphyrin as primary chromophore and pyridine functionalized boron dipyromethane (bodipy) as an acceptor antenna.[32a] Bodipy has high fluorescence quantum yield, large molar absorption coefficient, low rate of intersystem crossing, long excited state lifetime and also excellent photo stability. It act as antenna chromophore and excites porphyrin struts collecting most of the light across the visible spectrum through efficient and rapid energy transfer. But porphyrine based PCPs have the drawback of limited coverage of the visible spectrum for light harvesting applications. Hence, Hupp *et. al.* reported porphyrine based PCPs

functionalized with CdSe/ZnS core/shell quantum dots (QDs) for the enhancement of light harvesting efficiency (>80%) through energy transfer from QDs to the PCPs.[32b] Nanocrystalline PCPs are also explored as light harvesting materials. In this case the chromophores are densely embedded within the framework which can increase cross section for light absorption and also the solution processibility of nanocrystals for further applications. One such example was reported by Uvdal *et. al*.[32c] They synthesized highly crystalline Ln-PCP nanoparticles with efficient light harvesting properties. Maji *et. al*. have recently reported a luminescent nano PCP, {Zn(OPE)·2H_2O} (OPE = *oligo*-phenyleneethynylenedicarboxylate) that forms soft vesicular and toroidal nanostructures (Figure 16).[32d] After inclusion of a cationic dye trans-4-[4-(dimethylamino)styryl]-1-methylpyridinium iodide (DSMP) of about 0.02 mol an energy transfer phenomenon was observed from framework to the encapsulated dye molecule. Similar sort of host-to-guest light harvesting was reported using a In^{3+} based porous framework [{In(BCBAIP)}·4DEF·4EtOH] (BCBAIP = 5-(bis(4-carboxybenzyl)amino)-isopthalate) and Coumerin 343 dye as guest.[32e]

In another example light harvesting phenomenon was demonstrated in a metal-organic complex. In 2004, Holten *et. al.* synthesized a triad composed of two porphyrins and an intervening bis(dipyrrinato) zinc complex.[32f] The zinc dipyrrin moiety absorbs light between the absorption of porphyrin (near UV) and visible region and transfers excited state energy to the porphyrins in ~2 ps with 99% yield. Hence, the Zn complex in such triads not only self assembles the linker but also act as an accessory pigment. The excited state characteristics of the complex can be altered by simple substitution for better properties.

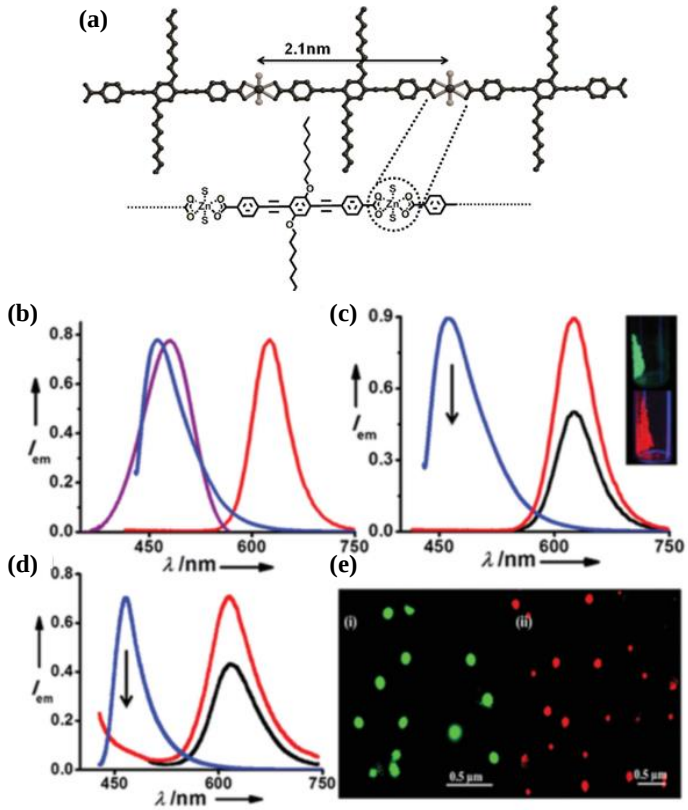

Figure 16: (a) 1D coordination chain of Zn(OPE)·$(H_2O)_2$, below: coordination environment of Zn^{2+} and the linker OPE; (b) Normalized absorption (violet) and emission spectra (red) of DSMP in solution and emission spectrum of Zn(OPE)·$(H_2O)_2$ (blue) in solid state; (c) Normalized emission spectrum of Zn(OPE)·$(H_2O)_2$ excited at 412 nm (blue), dye included PCP Zn(OPE)–DSMP excited at 412 nm (red) and at 480 nm (black, indirect excitation); inset: images of Zn(OPE)·$(H_2O)_2$ (green) and Zn(OPE)–DSMP (red) under UV-lamp. (d) Normalized emission spectra of nanovesicles of Zn(OPE)·$(H_2O)_2$ (blue), and DSMP included nanovesicles excited at 412 nm (red) and 480 nm (black). Confocal microscopy images of (e) (i) nanovesicles of Zn(OPE)·$(H_2O)_2$, (ii) DSMP incorporated nanovesicles of Zn(OPE)·$(H_2O)_2$. These figures have been reproduced with permission from reference no. 32d.

1.4 Scope of the work

Porosity and structural modulation of coordination polymers are not new and development of such properties is already in acceleration. Ligand design and use of SBUs are the key to assemble novel PCPs. Sky high surface area and high gas storage properties has been achieved in these PCPs but selective adsorption and separation has been the major challenge that is yet to be addressed properly. Usage of PCPs in practical condition for sequestration of CO_2, separation of hydrocarbons, biofuel or industrially important xylene isomers has not been achieved so far. Hence, serious amount of work has to be done in this direction. In this thesis some of the PCPs do address such problems. Luminescent PCPs based on lanthanide emission or linker based emission are also well explored but properties like light harvesting or sensing of metal ions or volatile solvents

are comparatively less in literatures. Particularly solution processibility of the sensors and efficiency of light harvesting processes are the key challenges. Use of metal-organic complexes those can be molecularly dissolved in solvents can be used as molecular sensors and such efforts have been described in this thesis. Moreover charge transfer or excimer/exciplex emissions in CPs are studied very less. Better understanding of such photophysical phenomena using different donors and acceptor linkers are yet to be achieved in PCPs. In addition to varieties of such applications characterization of structural change in flexible PCPs is also an important aspect. Apart from X-ray crystallography several other techniques such as IR, NMR *etc* have been employed till date but those are not sufficient. Hence, there is still a need to develop efficient characterization tool to understand structural rearrangement in flexible frameworks.

1.5 Outlook

Prospect of CPs is huge and the ease of the functionalization and modularity make them extremely useful material for versatile applications. Inherent porosity, high surface area and functionalized pore surface lead to applications such as gas storage and separation, separation of biofuels and capture of carcinogenic materials. Porosity also induces possibility of size selective catalysis and drug delivery. Presence of paramagnetic metal centers can also give rise long range ordering in these periodic crystalline materials. The other exciting aspect of PCPs is luminescence and related properties. Several possible photophysical properties have been discussed in the previous section that can be obtained from the PCPS. Such exotic photophysical phenomena such as CT, excimer/exciplex or energy transfer can lead to many important applications such as molecular recognition of solvents, cations or anions *etc*, tunable emission colours and solid state white light emissive materials and artificial photosynthetic systems. In this thesis, most of these features of PCPs and also metal-organic complexes have been exploited for dynamic recognition using flexible PCPs, separation of xylenes, selective capture of CO_2 and biofuel separation. In addition to this interpenetration in PCPs and their structure property relationships and structural characterization have been studied and detailed.

1.5 References

1. a) J. J. Perry IV, J. A. Perman, M. J. Zaworotko, *Chem. Soc. Rev.* **2009**, *38*, 1400; b) J.-R. Li, R. J. Kuppler, H.-C. Zhou, *Chem. Soc. Rev.* **2009**, *38*, 1477; c) Y. Cui, Y. Yue, G.

Qian, B. Chen, *Chem. Rev.* **2012**, *112*, 1126; d) J. Li, J. Sculley, H. Zhou, *Chem. Rev.* **2012**, *112*, 869; e) S. Kitagawa, R. Kitaura, S. Noro, *Angew. Chem., Int. Ed.* **2004**, *43*, 2334; f) D. Farrusseng, S. Aguado, C. Pinel, *Angew. Chem., Int. Ed.* **2009**, *48*, 7502; g) C. Wu, A. Hu, L. Zhang, W. Lin, *J. Am. Chem. Soc.* **2005**, *127*, 8940.

2. D. J. Transchemontangne, J. L. Mendoza-Cortés, M. O'Keeffe, O. M. Yaghi, *Chem. Soc. Rev*. **2009**, *38*, 1257.

3. a) O. M. Yaghi, H. Li, *J. Am. Chem. Soc.* **1996**, *118*, 295; b) T. R. Whitfield, X. Wang, L. Liu, A. J. Jacobson, *Solid State Sciences*. **2005**, *7*, 1096.

4. a) T. Devic, C. Serre, N. Audebrand, J. Marrot, G. Férey, *J. Am. Chem. Soc.* **2005**, *127*, 12788; b) X. Guo, G. Zhu, Z. Li, F. Sun, Z. Yangb, S. Qiu, *Chem. Commun.* **2006**, *3172*.

5. a) M. C. Das, S. Xiang, Z. Zhang, B. Chen, *Angew. Chem., Int. Ed*. **2011**, *50*, 10510; b) V. Chandrasekhar, C. Mohapatra, R. J. Butcher, *Cryst. Growth Des*. **2012**, *12*, 3285; c) R. W. Larsen, L. Wojtas, J. Perman, R. L. Musselman, M. J. Zaworotko, C. M. Vetromile, *J. Am. Chem. Soc.* **2011**, *133*, 10356; d) H. Son, S. Jin, S. Patwardhan, S. J. Wezenberg, N. C. Jeong, M. So, C. E. Wilmer, A. A. Sarjeant, G. C. Schatz, R. Q. Snurr, O. K. Farha, G. P. Wiederrecht, J. T. Hupp, *J. Am. Chem. Soc*. **2013**, *135*, 862.

6. a) R. Yang, L. Li, Y. Xiong, J. Li, H. Zhou, C. Su, *Chem. Asian J*. **2010**, *5*, 2358; b) J. Cheng, S. Zheng, G. Yang, *Inorg. Chem*. **2007**, *46*, 10261.

7. M. Higuchi, K. Nakamura, S. Horike, Y. Hijikata, N. Yanai, T. Fukushima, J. Kim, K. Kato, M. Takata, D. Watanaba, S. Oshima, S. Kitagawa, *Angew. Chem., Int. Ed*. **2012**, *124*, 8494.

8. a) O. Z. Yesxilel, G. Günay, C. Darcan, M. S. Soylu, S. Keskind, S. W. Ng, *CrystEngComm.* **2012**, *14*, 2817; b) T. K. Maji, S. Pal, K. L Gurunatha, A. Govindaraj, C. N. R. Rao, *Dalton Trans.* **2009**, 4426.

9. a) W. Fujita, K. Awaga, R. Kondo, S. Kagoshima, *J. Am. Chem. Soc*. **2006**, *128*, 6016; b) Y. Wang, B. Bredenkötter, B. Riegera, D. Volkmer, *Dalton Trans.* **2007**, 689.

10. a) P. Kanoo, K. L. Gurunatha, T. K. Maji, *Cryst. Growth. Des.* **2009**, *9*, 4147; b) G. J. McManus, J. J. Perry IV, M. Perry, B. D. Wagner, M. J. Zaworotko, *J. Am. Chem. Soc*. **2007**, *129*, 9094; c) B. D. Wagner, G. J. McManus, B. Moulton, M. J. Zaworotko, *Chem. Commun.* **2002**, 2176; d) X. Li, X. Fan, Q. Zeng, *Int. J. Mol. Sci*. **2007**, *8*, 29; e) X. Chen, G. Liu, *Chem. Eur. J.* **2002**, *8*, 4811.

11. a) O. K. Farha, I. Eryazici, N. C. Jeong, B. G. Hauser, C. E. Wilmer, A. A. Sarjeant, Q. Snurr, S. T. Nguyen, A. Ö. Yazaydın, J. T. Hupp, *J. Am. Chem. Soc*. **2012**, *134*, 15016; b) H. K. Chae, D. Y. Siberio-Perez, J. Kim, Y. Go, M. Eddaoudi, A. J. Matzger, M.

O'Keeffe, O. M. Yaghi, *Nature.* **2004**, *427*, 523; c) G. Férey, C. Mellot-Draznieks, C. Serre, F. Millange, J. Dutour, S. Surble, I. Margiolaki, *Science.* **2005**, *309*, 2040; d) K. Koh, A. G. Wong-Foy, A. J. Matzger, *J. Am. Chem. Soc.* **2009**, *131*, 4184; e) H. Furukawa, N. Ko, Y. B. Go, N. Aratani, S. B. Choi, E. Choi, A. O. Yazaydin, R. Q. Snurr, M. O'Keeffe, J. Kim, O. M. Yaghi, *Science*. **2010**, *329*, 424.

12. a) O. K. Farha, A. Ö. Yaza -ydın, I. Eryazici, C. D. Malliakas, B. G. Hauser, M. G. Kanatzidis, S. T. Nguyen, R. Q. Snurr, J. T. Hupp, *Nat. Chem*. **2010**, *2*, 944; b) X.-S. Wang, S. Ma, P. M. Forster, D. Yuan, J. Eckert, J. J. Lopez, B. J. Murphy, J. B. Parise, H.-C. Zhou, *Angew. Chem., Int. Ed*. **2008**, *47*, 7263; c) B. Chen, N. W. Ockwig, A. R. Millward, D. S. Contreras, O. M. Yaghi, *Angew. Chem., Int. Ed.* **2005**, *44*, 4745; d) P. Krawiec, M. Kramer, M. Sabo, R. Kunschke, H. Fröde, S. Kaskel, *Adv. Eng. Mater*. **2006**, *8*, 293; e) X.-S. Wang, S. Ma, K. Rauch, J. M. Simmons, D. Yuan, X. Wang, T. Yildirim, W. C. Cole, J. J. López, A. de Meijere, H.-C. Zhou, *Chem. Mater*. **2008**, *20*, 3145.

13. a) S. Q. Ma, D. F. Sun, J. M. Simmons, C. D. Collier, D. Q. Yuan, H.-C. Zhou, *J. Am. Chem. Soc*. **2008**, *130*, 1012; b) S.-C. Xiang, W. Zhou, Z.-J. Zhang, M. A Green, Y. Liu, B. Chen, *Angew. Chem., Int. Ed*. **2010**, *49*, 4615.

14. a) A. R. Millward, O. M Yaghi, *J. Am. Chem. Soc.* **2005**, *127*, 17998; b) A. G. Wong-Foy, A. J. Matzger, O. M. Yaghi, *J. Am. Chem. Soc*. **2006**, *128*, 3494; c) P. Nugent, Y. Belmabkhout, S. D. Burd, A. J. Cairns, R. Luebke, K. Forrest, T. Pham, S. Ma, B. Space, L. Wojtas, M. Eddaoudi, M. J. Zaworotko, *Nature*. **2013**, *495*, 80.

15. a) M. Du, M. Chen, X. Wang, J. Wen, X.-G. Yang, S.-M. Fang, C.-S. Liu, *Inorg. Chem.* **2014**, *53*, 7074; b) Y. Zhu, Y.-M. Wang, S.-Y. Zhao, P. Liu, C. Wei, Y.-L. Wu, C. K. Xia, J.-M. Xie, *Inorg. Chem*. **2014**, *53*, 7692.

16. a) Ullmann's Encyclopedia of Industrial Chemistry, 6th Ed.; John Wiley & Sons: New York, **2006**; electronic release; b) V. Finsy, H. Verelst, L. Alaerts, D. De Vos, P. A. Jacobs, G. V. Baron, J. F. M. Denayer, *J. Am. Chem. Soc.* **2008**, *130*, 7110.

17. M. A. Moreira, J. C. Santos, A. F. P. Ferriera, J. M. Loureiro, A. E. Rodrigues, *Ind. Eng. Chem. Res.* **2011**, *50*, 7688.

18. a) A. Shigematsu, T. Yamada, H. Kitagawa, *J. Am. Chem. Soc*. **2012**, *134*, 13145; b) R. Plessius, R. Kromhout, A, L. D. Ramos, M. Farbinteanu, M. C. Mittelmeijer-Hazeleger, R. Krishna, R. Rothenberg, S. Tanase, *Chem. Eur. J*. **2014**, *20*, 1; c) H. Furukawa, H. Gandara, Y.-B. Zhang, J. Jiang, W. L. Queen, M. R. Hudson, O. M. Yaghi, *J. Am. Chem. Soc.* **2014**, *136*, 4369.

19. a) M. Fujita, Y. J. Kwon, S. Washizu, K. Ogura, *J. Am. Chem. Soc*. **1994**, *116*, 1151; b) S. S. Chui, S. M. Lo, J. P. Charmant, A. G. Orpen, I. D. Williams, *Science*. **1999**, *283*, 1148; c) L. Alaerts, E. Séguin, H. Poelman, F. Thibault-Starzyk, P. A. Jacobs, D. De Vos, *Chem.–Eur. J*., **2006**, *12*, 7353; d) S. Hasegawa, S. Horike, R. Matsuda, S. Furukawa, K. Mochizuki, Y. Kinoshita, S. Kitagawa, *J. Am. Chem. Soc*. **2007**, *129*, 2607.

20. a) M. Kurmoo, *Chem. Soc. Rev.* **2009**, *38*, 1353; b) K. Zou, J. Zhao, C. Liu, Z. Wang, Z. Li, *Eur. J. Inorg. Chem.* **2013**, *293*; c) T. Aharen, F. Habib, I. Korobkov, T. J. Burchell, R. Guillet-Nicolas, F. Kleizb, M. Murugesu, *Dalton Trans*. **2013**, *42*, 7795.

21. a) A. Chakraborty, R. Haldar, T. K. Maji, *Cryst. Growth. Des*. **2013**, *13*, 4968; b) A. Hazra, P. Kanoo, T. K. Maji, *Chem Commun*. **2011**, *47*, 538; c) C. M. Nagaraja, R. Haldar, T. K. Maji, C. N. R. Rao, *Cryst. Growth. Des*. **2012**, *12*, 975.

22. a) P. Horcajada, T. Chalati, C. Serre, B. Gillet, C. Sebrie, T. Baati, J. F. Eubank, E. Heurtaux, P. Clayette, C. Kreuz, J.-S. Chang, Y. K. Hwang, V. Marsaud, P.-N. Bories, L. Cynober, S. Gil, G. Férey, P. Couvreur, R. Gref, *Nat. Mater*. **2010**, *9*, 172; b) N. J. Hinks, A. C. McKinlay, B. Xiao, P. S. Wheatley, R. E. Morris, *Microporous Mesoporous Mater*. **2010**, *129*, 330; c) J. An, S. J. Geib, N. L. Rosi, *J. Am. Chem. Soc*. **2009**, *131*, 8376.

23. a) B. D. Chandler, D. T. Cramb, G. K. H. Shimizu, *J. Am. Chem. Soc*. **2006**, *128*, 10403; b) Y. Cui, Y. Yue, B. Chen, G. Qian, B. Chen, *Chem. Rev*, **2012**, *112*, 1126; c) D. Liu, K. Lu, C. Poon, W. Lin, *Inorg. Chem*. **2014**, *53*, 1916; d) L. E. Kreno, K. Leong, O. K. Farha, M. Allendorf, R. P. V. Duyne, J. T. Hupp, *Chem. Rev*. **2012**, *112*, 1105.

24. a) Y. Han, X. Li, L. Li, C. Ma, Z. Shen, Y. Song, X. You, *Inorg. Chem.* **2010**, *49*, 10781; b) S. Chen, R. Fan, C. Sun, P. Wang, Y. Yang, Q. Su, Y. Mu, *Cryst. Growth Des.* **2012**, *12*, 1337; c) S. Chen, Y. Ren, W. Wang, S. Gao, *Dalton Trans.* **2010**, *39*, 1552.

25. a) Y. Takashima, V. M. Martinez, S. Furukawa, M. Kondo, S. Shimomura, H. Uehara, M. Nakahama, K. Sugimoto, S. Kitagawa, *Nat. Commun.* **2011**, *2*, 168; b) V. M. Martinez, S. Furukawa, Y. Takashima, I. L. Arbeloa, S. Kitagawa, *J. Phys. Chem. C*. **2012**, *116*, 26084.

26. a) J. Zhou, W. Shi, N. Xu, P. Cheng, *Inorg. Chem*. **2013**, *52*, 8082; b) X. Zhou, L. Li, H. Li, A. Li, T. Yanga, W. Huang, *Dalton Trans*. **2013**, *42*, 12403; c) Z. Chen, Y. Sun, L. Zhang, D. Sun, F. Liu, Q. Meng, R. Wang, D. Sun, *Chem. Commun.* 2013, **49**, 11557.

27. a) B. Chen, L. Wang, F. Zapata, G. Qian, E. B. Lobkovsky, *J. Am. Chem. Soc*. **2008**, *130*, 6718; b) B. Chen, Y. Yang, F. Zapata, G. Lin, G. Qian, E. B. Lobkovsky, *Adv. Mater*. **2007**, *19*, 1693; c) B. Chen, L. Wang, Y. Xio, F. R. Fronczek, M. Xue, Y. Cui, G. Qian, *Angew. Chem., Int. Ed*. **2009**, *48*, 500.

28. a) K. C. Stylianou, R. Heck, S. Y. Chong, J. Bacsa, J. T. A. Jones, Y. Z. Khimyak, D. Bradshaw, M. J. Rosseinsky, *J. Am. Chem. Soc*. **2010**, *132*, 4119; b) N. B. Shustova, A. F. Cozzolino, S. Reineke, M. Baldo, M. Dincă, *J. Am. Chem. Soc.* **2013**, *135*, 13326; c) R. B. Lin, F. Li, S.-Y. Liu, X.-L. Qi, J.-P. Zhang, X.-M. Chen, *Angew. Chem., Int. Ed*. **2013**, *52*, 13429; d) N. Yanai, K. Kitayama, Y. Hijikata, S. Sato, R. Matsuda, Y. Kubota, M. Takata, M. Mizuno, T. Uemura, S. Kitagawa, *Nat. Mater*. **2011**, *10*, 787; e) D. Yan, Y. Tang, H. Lin, D. Wang, *Sci. Rep*. **2014**, *4*, 4337; f) K. Dhara, S. Karan, J. Ratha, P. Roy, G. Chandra, M. Manassero, B. Mallik, P. Banerjee, *Chem. Asian J*. **2007**, *2*, 1091.

29. a) S. Dang, J. Zhang, Z. Sun, *J. Mater. Chem.* **2012**, *22*, 8868; b) Z. Liu, M. Wu, S. Wang, F. Zheng, G. E. Wang, J. Chen, Y. Xiao, A. Wu, G. Guo, J. Huang, *J. Mater. Chem. C*. **2013**, *1*, 4634; c) C. Sun, X. Wang, X. Zhang, C. Qin, P. Li, Z. Su, D. Zhu, G. Shan, K. Shao, H. Wu, J. Li, *Nat. Commun*. **2013**, *4*, 2717; d) K. Jayaramulu, P. Kanoo, S. J. George, T. K. Maji, *Chem. Commun*. **2010**, *46*, 7906.

30. a) Y. Liu, M. Pan, Q. Y. Yang, L. Fu, K. Li, S. Wei, C. Su, *Chem. Mater*. **2012**, *24*, 1954; b) S. Roh, Y. Kim, K. D. Seo, D. H. Lee, H. K. Kim, Y. Park, J. Park, J. Lee, *Adv. Funct. Mater*. **2009**, *19*, 1663.

31. a) D. R. Prasad, G. Ferraudi, *Inorg. Chem*. **1983**, *22*, 1672; b) H. L. Lehtivuori, H. Lemmetyinen, N. V. Tkachenko, *J. Am. Chem. Soc.* **2006**. *128*, 16036; c) D. Kim, A. Osuka, *Acc. Chem. Res*. **2004**, *37*, 735.

32. a) C. Y. Lee, O. K. Farha, B. J. Hong, A. A. Sarjeant, S. T. Nguyen, J. T. Hupp, *J. Am. Chem. Soc.* **2011**, *133*, 15858; b) S. Jin, H. Son, O. K. Farha, G. P. Wiederrecht, J. T. Hupp, *J. Am. Chem. Soc*. **2013**, *135*, 955; c) X. Zhang, M. A. Ballem, Z. Hu, P. Bergman, K. Uvdal, *Angew. Chem., Int. Ed*. **2011**, *50*, 5729; d) V. M. Suresh, S. J. George, T. K. Maji, *Adv. Funct. Mater*. **2013**, *23*, 5585; e) I. V. Sazanovich, C. Kirmaier, E. Hindin, L. Yu, D. F. Bocian, J. S. Lindsey, D. Holten, *J. Am. Chem. Soc*. **2004**, *126*, 2664.

Chapter 2

Luminescent metal-organic complexes and polymers based on pyrene and anthracene chromophores: molecular sensing and energy transfer

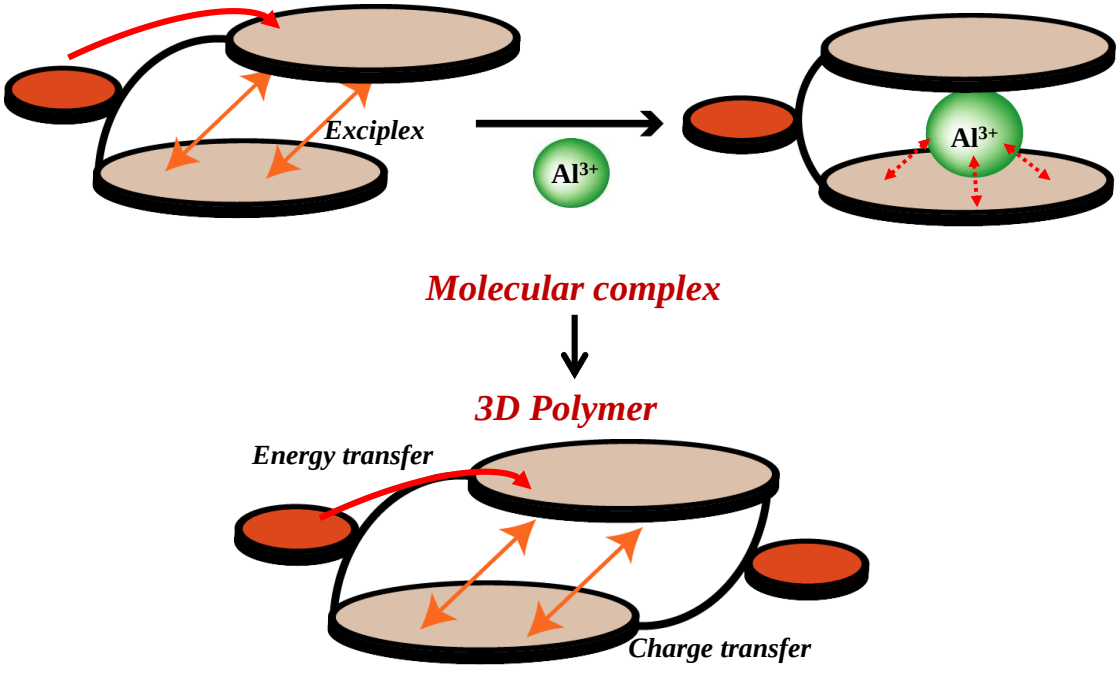

Part: 2A

Metal-organic complexes comprised of pyrene or anthracene chromophores: Exciplex emission, energy transfer and Al^{3+} sensing properties

Summary

Using pyrene and anthracene monocarboxylate chromophores as linker two new metal-organic complexes, $\{[Cd(pma)_2(o\text{-phen})_2]\cdot 2H_2O\cdot MeOH)\}_n$ (**1**) and $\{Cd_2(\mu\text{-}H_2O)(amc)_4(o\text{-phen})_2\}_n$ (**2**) (pma = pyrene monocarboxylic acid; amc = 9-anthracene monocarboxylic acid; *o*-phen = orthophenanthroline) have been synthesized and characterized using single crystal X-ray diffraction. Compound **1** contains a 7-coordinated Cd^{2+} center coordinated by two *o*-phen and two pma, where one pma and *o*-phen pair stacks in a face-to-face fashion and other pma:*o*-phen pair is linked through C-H$\cdots\pi$ interaction. Compound **2** is a dimeric complex of Cd^{2+}, which contains two pairs of face-to-face stacked amc:*o*-phen. Compound **1** shows a red shifted bright cyan emission that can be attributed to pma:*o*-phen exciplex formation. This exciplex emission is further sensitized by another pma through Förster resonance energy transfer process. Similarly in case of **2**, amc:*o*-phen exciplex is sensitized through Förster resonance energy transfer from the other amc linker in solid state, while in methanol such energy transfer process is perturbed resulting in a dual emission related to monomer of amc and exciplex of amc:*o*-phen. Density functional theory based calculations provide clear evidence of ground state interactions between pma:*o*-phen and amc:*o*-phen in **1** and **2**, respectively. Interestingly, blue emission of **2** dispersed in methanol changes to bright cyan-green emission upon addition of Al^{3+} and remains almost unchanged or slightly affected with other metal ions leading to selective chemosensing of Al^{3+}.

1. R. Haldar, K. Prasad, P. K. Samanta, S. K. Pati, T. K. Maji, To be Submitted.

2A.1 Introduction

The design and synthesis of luminescent metal-organic complexes, polymers or supramolecular frameworks are gaining interest as they find applications in molecular sensing, tunable emission for various light emitting devices and light harvesting.[1] Presence of organic as well as inorganic building blocks makes these hybrids thermally more robust and versatile in terms of functionality. In such hybrids, luminescence may originate from metal ions such as lanthanides (Tb^{3+}, Sm^{3+}, Eu^{3+} *etc*) or from organic chromophoric ligands.[2] Due to wide variety of available organic chromphores, ligand based luminescence is exploited affluently.[3] Versatile photophysical properties such as charge transfer (CT), exciplex or excimer emission and energy transfer process can be realized with suitable choice of donor acceptor pairs in metal-organic system.[4] Luminescence efficiency (based on CT and exciplex) or energy transfer processes are highly dependant on the spatial disposition of the organic chromophores in the metal-organic structure. As the non-covalent interactions (C-H$\cdots\pi$ or $\pi\cdots\pi$) govern such processes, hence chromophores with large aromatic π surface or with electron rich or deficient nature are more often used to construct such systems. Thus formed donor-acceptor pairs are also sensitive to the microenvironment and hence can be used as sensing tool for targeted analyte.[5]

To name few organic chromophores those show excellent photophysical properties are naphthalene, anthracene, pyrene or perylene. These all can form excited state dimer (excimer), can act as good donor chromophore to form exciplex or CT complex, have high quantum yield and also high fluorescence life time.[6] Using these chromphores, particularly anthracene and pyrene very few metal-organic complexes have been reported till date.[7] However, all these reports do not discuss any potential sensing applications, such as biologically toxic metal ion (Al^{3+}, Cu^{2+} *etc*) sensing. Al^{3+} is one of the most abundant in the bio-system and known for its toxicity.[8] Diseases like headaches, anaemia, speech problem, softening of bone, rickets, colic, and Alzheimer can be caused by extreme Al^{3+} exposure.[9] Hence, to develop an effective method to detect such toxic Al^{3+} is important and to serve this purpose various molecular probes have been reported in literatures.[10] In most cases mechanistic pathway involves charge transfer, electron transfer or energy transfer phenomena.[10] Apart from purely organic based probes there are no reports with metal-organic hybrid systems for potential Al^{3+} sensing. It is envisioned that these issues can be addressed by exploiting the exotic photophysical

properties of the organic ligand chromophores in metal-organic hybrid system. It is worth to mention that inorganic complexes based on Ru^{3+}/Os^{3+} are known for sensing applications.[11] Here, instead of constructing an extended polymeric structure, it was sought to synthesize molecular complexes for ease of solution processibility. As the ditopic linkers would lead to polymeric structure, pyrene and anthracene chromophore based two linkers; pyrene monocarboxylic acid (pma) and 9-anthracene monocarboxylic acid (amc) have been chosen. Additionally a chelating ligand with extended aromatic π-surface, orthophenanthroline (*o*-phen) was selected. Co-assembly of these linkers will not produce extended coordination polymer rather a molecular complex can be achieved. Cd^{2+} has been chosen as a metal ion for its flexible coordination geometry and assembled with pma/amc and *o*-phen to obtain two metal-organic complexes; $\{[Cd(pma)_2(o\text{-}phen)_2]\cdot 2H_2O\cdot MeOH)\}_n$ (**1**) and $\{Cd_2(\mu\text{-}H_2O)(amc)_4(o\text{-}phen)_2\}_n$ (**2**). **1** and **2** both show preassociated exciplex emission of pma:*o*-phen and amc:*o*-phen, respectively. Evidences of ground state interactions in pma:*o*-phen and amc:*o*-phen were supported from density functional theory (DFT) calculations. Interestingly, the exciplex emissions are sensitized through Förster resonance energy transfer (FRET) process from pendant pma and amc subunit, in case of **1** and **2**, respectively. Furthermore, **2** dispersed in methanol shows ratiometric fluoroscence response for Al^{3+} among other metal ions. The selective sensing of Al^{3+} can be attributed to the changes in spatial arrangement of the pendant amc linker that inhibits the monomer emission.

2A.2 Experimental section

2A.2.1 Materials

All the reagents employed were commercially available and used as provided without further purification. $Cd(NO_3)_2\cdot 6H_2O$ was obtained from Spectrochem, pyrene monocarboxylic acid and orthophenanthroline were obtained from Sigma Aldrich chemicals. 9-anthracene monocarboxylic acid was prepared following previously reported methods.[12]

2A.2.2 Physical measurements

Elemental analyses were carried out using a Thermo Fischer Flash 2000 Elemental Analyzer. FT-IR spectra were recorded on a Bruker IFS 66v/S spectrophotometer using KBr pellets in the region 4000-400 cm^{-1}. Powder XRD pattern

of the products were recorded by using Mo-K_α radiation (Bruker D8 Discover; 40 kV, 30 Ma). Electronic absorption spectra were recorded on a Perkin Elmer Lambda 900 UV-VIS-NIR spectrometer and emission spectra were recorded on Perkin Elmer Ls 55 Luminescence Spectrometer. UV-Vis and emission spectra were recorded in 1 mm path length cuvette. Fluorescence decay was recorded in a time correlated single-photon counting spectrometer of Horiba-Jobin Yvon with 350-450 nm picosecond Ti-saphhire laser.

2A.2.3 Synthesis of $\{[Cd(pma)_2(o\text{-phen})_2]\cdot 2H_2O\cdot MeOH\}_n$ (1)

An aqueous solution (25 mL) of pma (1 mmol, 0.288 g) was mixed with a methanolic solution (25 mL) of *o*-phen (1 mmol, 0.184 g) and stirred for 30 min to mix well. $Cd(NO_3)_2\cdot 6H_2O$ (0.5 mmol, 0.151 g) was dissolved in 50 mL of water and then ligand solution (2 mL) was layered above the metal solution (2 mL) and after 10-12 days light yellow colour rod shaped crystals of **1** were found at the walls of the tube. A good quality single crystal was picked up from the mother liquor and immediately covered with paraffin oil and crystal data was collected at 293 K. To prepare the compound in bulk ligand solution was directly mixed with metal solution and stirred for 48 h. The poly-crystalline bulk compound was filtered off, washed several times with methanol and dried under vacuum. The PXRD pattern of the bulk powder matches well with simulated PXRD pattern of **1** indicating phase purity (Figure 1). Yield: 67%, relative to Cd^{2+}. Anal. Calcd. for $C_{59}H_{42}CdN_4O_7$: C, 71.78; H, 5.52; N, 3.22. Found: C, 71.11; H, 5.17; N, 3.01. FT-IR (KBr pellet, 4000-400 cm^{-1}) (Figure 2): 3037(b), 1588(s), 1614(s), 1565(s), 1514(s), 1427(s), 1342(s), 1314(s), 1178(s), 1151(s), 1100(s), 1046(s), 841(s), 787(s), 723(s).

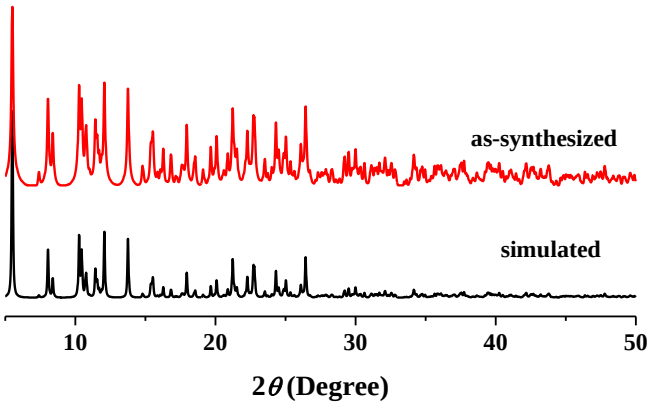

Figure 1: Simulated and as-synthesized PXRD patterns of compound **1**.

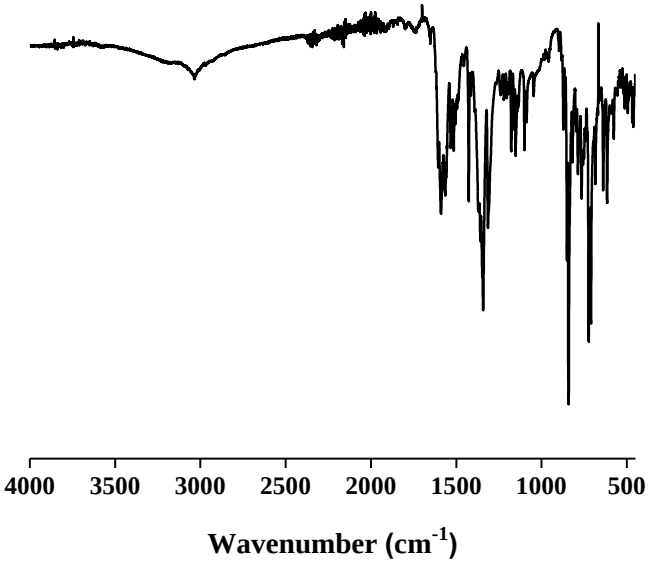

Figure 2: FT-IR spectrum of **1**.

2A.2.4 Synthesis of $\{Cd_2(\mu\text{-}H_2O)(amc)_4(o\text{-}phen)_2\}_n$ (2)

Compound **2** is synthesized following similar methodology as used for **1**, except amc was used instead of pma. Light yellow colour crystals were observed after 10-15 days and bulk powder compound was prepared by direct mixing. PXRD patterns of the bulk polycrystalline compound and simulated patterns match well confirming phase purity of the bulk sample (Figure 3). Yield: 71%, relative to Cd^{2+}. Anal. Calcd. for $C_{84}H_{52}Cd_2N_4O_9$: C, 67.88; H, 3.50; N, 3.77. Found: C, 67.49; H, 3.11; N, 3.59. FT-IR (KBr pellet, 4000-400 cm^{-1}) (Figure 4): 3049(w), 2365(w), 1570(s), 1518(s), 1428(s), 1387(s), 1322(s), 1269(s), 1221(s), 843(s), 725(s), 668(s), 637(s).

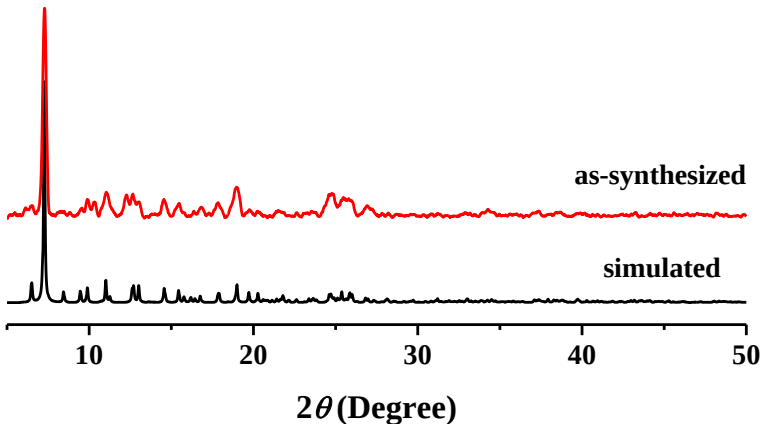

Figure 3: Simulated and as-synthesized PXRD patterns of compound **2**.

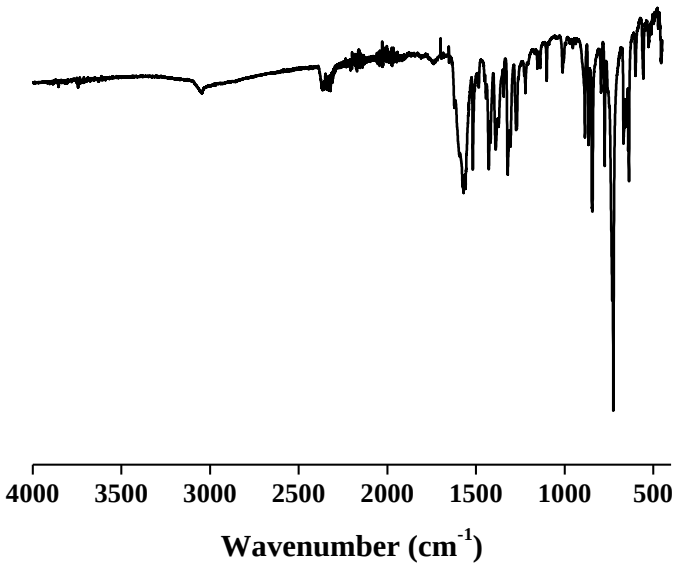

Figure 4: FT-IR spectrum of **2**.

2A.2.5 X-ray Crystallography

X-ray single crystal structural data of **1** and **2** were collected on a Bruker Smart-CCD diffractometer equipped with a normal focus, 2.4 kW sealed tube X-ray source with graphite monochromated Mo-*Kα* radiation (λ = 0.71073 Å) operating at 50 kV and 30 mA. The program SAINT[13] was used for integration of diffraction profiles and absorption correction was made with SADABS[14] program. All the structures were solved by SIR 92[15] and refined by full matrix least square method using SHELXL-97.[16] All the hydrogen atoms were geometrically defixed and placed in ideal positions. All crystallographic and structure refinement data of **1** and **2** are summarized in Table 1. Selected bond lengths and angles for **1** and **2** are given in Table 2-3, respectively. All calculations were carried out using SHELXL 97,[16] PLATON,[17] SHELXS 97[18] and WinGX system, Ver 1.70.01.[19]

2A.2.6 Computational details

Electronic properties of each molecules were calculated with the help of *ab initio* Density Functional Theory (DFT) combined with time-dependant DFT (TD-DFT) as implemented in Gaussian 09 program package.[20] For the DFT and TD-DFT calculations B3LYP[21-23] exchange and correlation functional with 6-31g(d) basis set for all atoms except for Cd atoms for which LANL2DZ, a widely used effective core potential (ECP)-type basis set was used.[24-26] For these calculations, the X-ray crystallographic structures were considered and only the H-atoms position was optimized using DFT. Then the optical properties are calculated using TD-DFT methods.

2A.3 Results and discussion

2A.3.1 Structural description of $\{[Cd(pma)_2(o\text{-phen})_2]\cdot 2H_2O\cdot MeOH)\}_n$ (1) and $\{Cd_2(\mu\text{-}H_2O)(amc)_4(o\text{-phen})_2\}_n$ (2)

Compound **1** crystallizes in triclinic $P\bar{1}$ space group and the asymmetric unit contains one Cd^{2+}, two pma, two *o*-phen, guest water and methanol molecules. The Cd^{2+} metal center is seven coordinated; two carboxylate oxygen atoms (O1 and O2) coordinate from one chelating pma (denoted as pma(I)), one oxygen atom (O3) from a carboxylate group of other pma (pma(II)) and rest of the four coordination sites are occupied by the four nitrogen atoms (N1-N4) from two chelated *o*-phen (*o*-phen I and II) ligands (Figure 5). The Cd^{2+}-O and Cd^{2+}-N bond distances are in the range of 2.242(4)-2.569(6) Å and 2.359(3)-2.426(5) Å, respectively. In the molecular complex unidentate pma(II) is stacked in face-to-face ($\pi\cdots\pi$ ~ 3.547 Å) fashion with *o*-phen(II); the other pma(I) (chelated) undergoes C-H$\cdots\pi$ interaction (~ 2.747 Å) with *o*-phen(I). Two such complexes are tethered through several supramolecular interactions. Figure 6a shows two neighbouring complexes are attached *via* $\pi\cdots\pi$ (3.849 Å) interaction between two *o*-phen(II) and C-H$\cdots\pi$ (~ 3.00 Å) interactions between *o*-phen(I) and *o*-phen(II). On the other hand, one *o*-phen(II) of one unit and pma(I) of other unit interacts *via* C-H$\cdots\pi$ interaction (2.627 Å)

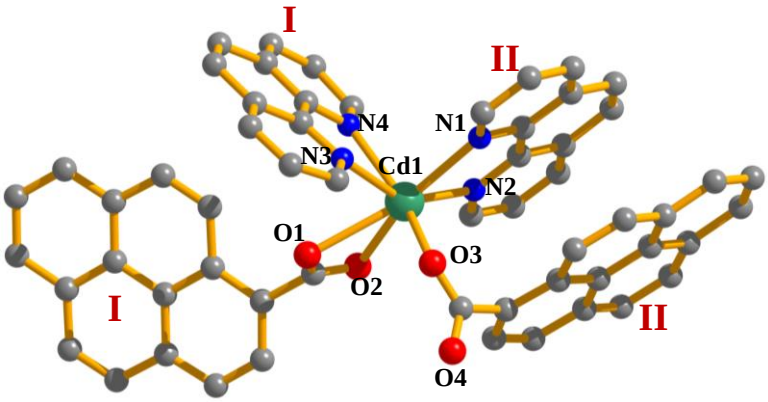

Figure 5: Coordination environment of Cd^{2+} in complex **1**.

and all these interactions together form a 2D supramolecular layer along *ab* plane (Figure 6b-c). The compound also contains non-coordinated solvent water and methanol molecules which are held through several hydrogen bonding intercations. The pendant free oxygen (O4) of the carboxylate group from pma(II) forms strong hydrogen bonds with guest O1W and O2W (2.741 and 2.959 Å, respectively) (Figure 7a). Several other hydrogen bonds between O3$\cdots$O2W (2.987 Å), O1$\cdots$O2W (2.983 Å) and O2$\cdots$O1W

(3.007 Å) hold two monomeric complexes together in the 2D layer (Figure 7b). The methanol molecule is also hydrogen bonded to the guest water O2W (O3W···O2W ~ 2.724 Å) (Figure 7a). These 2D supramolecular layers stack along *c*-direction *via* pma(I):pma(I) off-set stacking (~ 4.00 Å) and thus forming a 3D supramolecular structure (Figure 8).

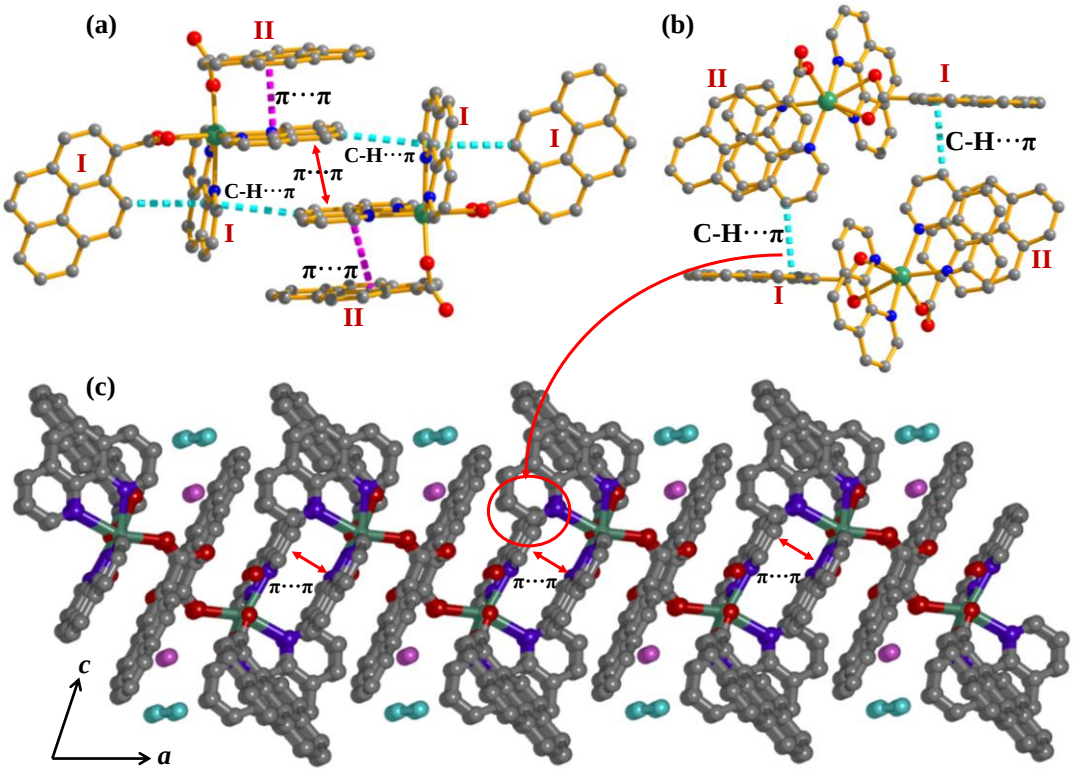

Figure 6: Structural details of **1** (a) Two of the monomers interact through π···π and C-H···π interactions; (b) Two monomers interacts *via* C-H···π interaction; (c) 2D supramolecular layer formed in *ab* plane.

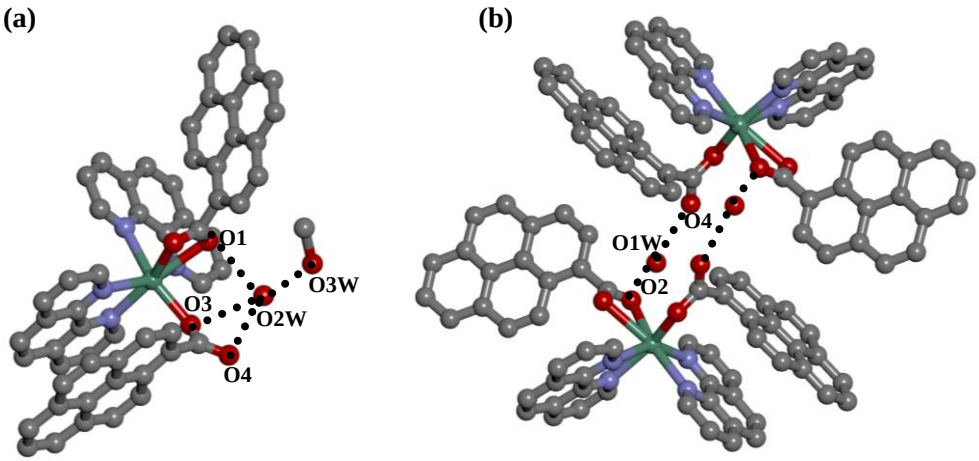

Figure 7: Hydrogen bonds (dotted black lines) in **1**: (a) O3···O2W, O4···O2W, O1···O2W and O2W···O3W hydrogen bonds keep the guest solvents attached; (b) O4···O1W and O2···O1W hydrogen bonds hold two monomer complexes.

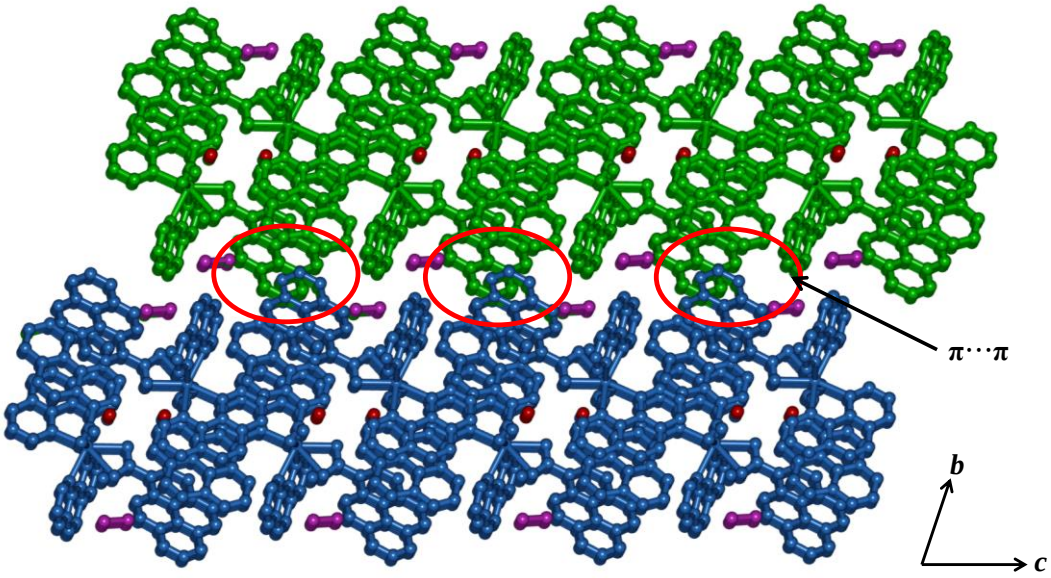

Figure 8: π···π stacked 2D layers (shown in two different colours) of **1** to form 3D supramolecular framework.

Compound **2** crystallizes in monoclinic, *C*2/*c* space group and the asymmetric unit contains two Cd^{2+} centers, four amc, two *o*-phen and one bridging water molecule (Figure 9a). Each Cd^{2+} center is in a distorted octahedral geometry; four oxygens from three carboxylate groups of amc and one water molecule, and two nitrogens from one *o*-phen occupy the six coordination sites of the metal center. Two Cd^{2+} centers are bridged by oxygen (μ-oxo) atoms from two different amc carboxylate groups and one water molecule to form a dimeric complex (Figure 9a). There are two types of amc ligands marked as amc(I) and amc(II); amc(I) is acting as a monodentate ligand whereas amc(II) acting as a bridging bidentate ligand and binds two Cd^{2+} through μ-oxo bridge. Therefore both amc linkers have one pendant carboxylate oxygen atom. Interestingly, the chelating *o*-phen and bridging amc(II) stacks in a face-to-face fashion in the dimer and the monodentate amc(I) does not show any close contact in the dimer except hydrogen bonding between bridging water molecule (O2) and pendant carboxylate oxygen O4 (O2···O4 ~ 2.629 Å). One such dimer is connected to the neighbouring dimer *via* several non-covalent interactions such as, C32-H···π between (~ 2.8 Å) amc(II) aromatic hydrogen with amc(I) aromatic ring of other dimer and offset π···π stacking (~ 3.56 Å) between *o*-phen. In addition hydrogen bonding between amc(I) carboxylate oxygen (O3) and aromatic C10-H of *o*-phen (~ 2.525 Å) also extends the supramolecular structure (Figure 9b). Presence of these close distance supramolecular interactions finally led to formation of a 3D extended closely packed supramolecular structure (Figure 10).

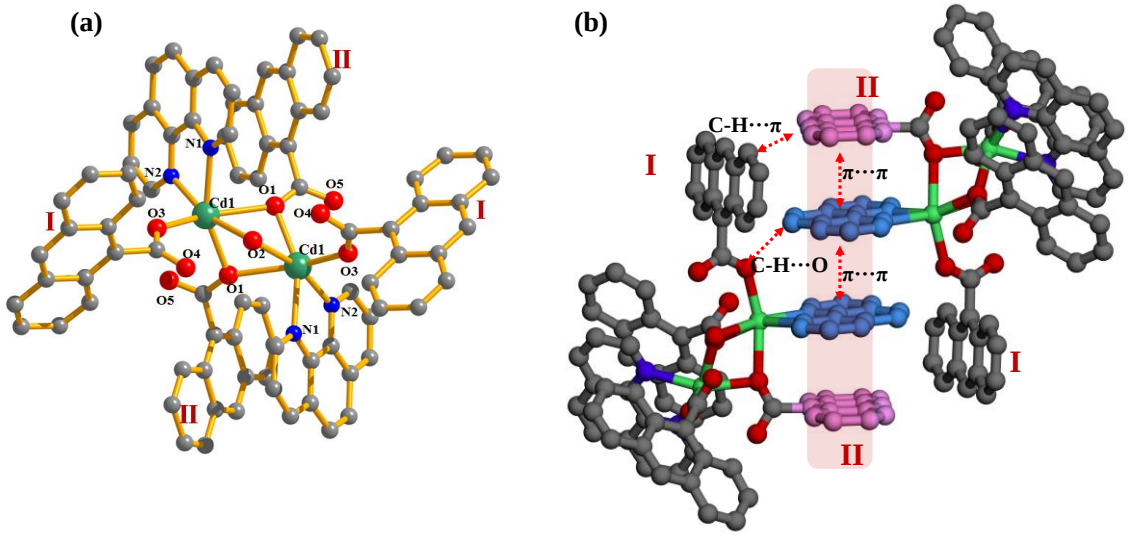

Figure 9: (a) Coordination environment of Cd^{2+} in dimeric complex **2**; (b) View of the non-covalent interactions between two dimers in complex **2**.

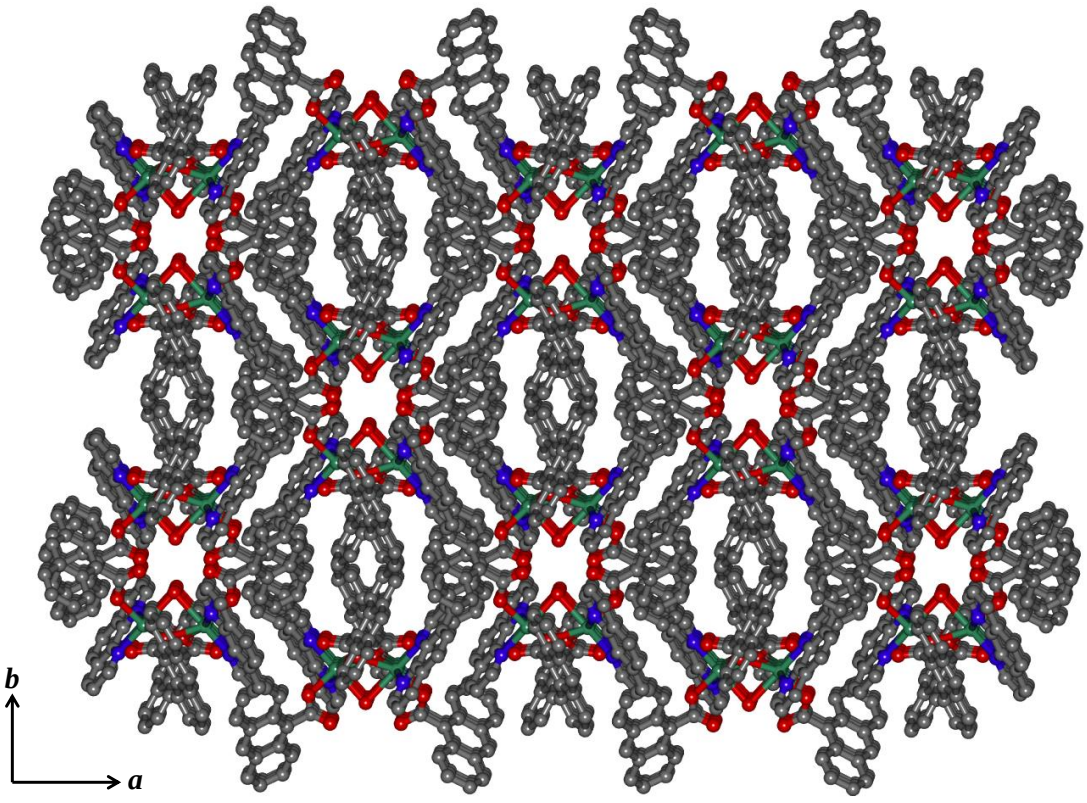

Figure 10: View of the 3D close packed structure of complex **2** along *c*-direction.

Table 1: Crystal data and structure refinement parameters of compound **1** and **2**.

Parameters	**1**	**2**
Empirical formula	$C_{59}H_{42}CdN_4O_7$	$C_{84}H_{52}Cd_2N_4O_9$
M	1031.31	1486.12
Crystal system	Triclinic	Monoclinic
Space group	*P*$\bar{1}$	*C*2/*c*
***a* (Å)**	11.4286(8)	22.8800(5)
***b* (Å)**	12.8633(10)	17.8769(4)
***c* (Å)**	17.8410(13)	17.9672(4)
***α* (deg)**	110.488(4)	90
***β* (deg)**	104.772(4)	113.907(1)
***γ* (deg)**	91.007(4)	90
***V* (Å^3)**	2359.1(3)	6718.5(3)
Z	4	4
***T*(K)**	293	150
***λ* (Mo K$_α$)**	0.71073	0.71073
***D*$_c$ (g cm^{-3})**	1.441	1.469
***μ* (mm^{-1})**	0.524	0.698
***θ*$_{max}$ (deg)**	28.4	29.6
total data	35336	56477
unique reflection	9772	9479
***R*$_{int}$**	0.080	0.055
data [*I* > 2σ(*I*)]	5708	5891
***R*^{a}**	0.0504	0.0419
***R*$_w$^{b}**	0.1419	0.1111
GOF	0.88	1.01

^{a} $R = \Sigma||F_o| - |F_c||/\Sigma|F_o|$. ^{b} $R_w = [\Sigma\{w(F_o^2 - F_c^2)^2\}/\Sigma\{w(F_o^2)^2\}]^{1/2}$.

Table 2: Selected bond lengths (Å) and angles (°) for {[Cd(pma)$_2$(*o*-phen)$_2$]·2H$_2$O·MeOH)}$_n$ (**1**).

Cd1-O1	2.569(6)	Cd1-O2	2.475(6)
Cd1-O3	2.242(4)	Cd1-N1	2.403(4)
Cd1-N2	2.359(3)	Cd1-N3	2.386(3)
Cd1-N4	2.426(5)		
O1-Cd1-O2	50.50(17)	O1-Cd1-O3	84.57(16)
O1-Cd1-N1	155.70(16)	O1-Cd1-N2	133.85(17)

O1-Cd1-N3	84.60(16)	O1-Cd1-N4	68.51(18)
O2-Cd1-O3	102.43(15)	O2-Cd1-N1	153.72(14)
O2-Cd1-N2	83.55(15)	O2-Cd1-N3	87.42(15)
O2-Cd1-N4	116.46(17)	O3-Cd1-N1	87.93(13)
O3-Cd1-N2	113.33(12)	O3-Cd1-N3	155.40(12)
O3-Cd1-N4	86.22(13)	N1-Cd1-N2	70.18(13)
N1-Cd1-N3	92.98(13)	N1-Cd1-N4	87.98(15)
N2-Cd1-N3	89.94(12)	N2-Cd1-N4	149.27(14)
N3-Cd1-N4	69.26(12)		

Table 3: Selected bond lengths (Å) and angles (°) for $\{Cd_2(\mu\text{-}H_2O)(amc)_4(o\text{-phen})_2\}_n$ (**2**).

Cd1-O1	2.213(3)	Cd1-O2	2.513(2)
Cd1-O3	2.206(3)	Cd1-N1	2.328(3)
Cd1-N2	2.301(2)	Cd1-O1_a	2.387(3)
O1-Cd1-O2	74.25(9)	O1-Cd1-O3	106.12(10)
O1-Cd1-N1	156.46(10)	O1-Cd1-N2	116.93(10)
O1-Cd1-O1_a	72.57(10)	O2-Cd1-O3	84.32(7)
O2-Cd1-N1	93.44(7)	O2-Cd1-N2	164.95(6)
O1_a-Cd1-O2	71.44(9)	O3-Cd1-N1	92.18(9)
O3-Cd1-N2	101.03(9)	O1_a-Cd1-O3	155.26(10)
N1-Cd1-N2	72.45(9)	O1_a-Cd1-N1	84.59(10)
O1_a-Cd1-N2	101.33(10)		

a = 2-x,y,3/2-z

2A.3.2 Photophysical properties of 1: Exciplex emission and energy transfer

The absorption spectrum of **1** in solid state shows a broad profile ranging from 300-425 nm (Figure 11a). Excitation of **1** at 350 nm shows a broad featureless spectrum with maximum at 450 nm corresponding to cyan emission (Figure 11b). This red shifted spectrum compared to blue emission of pma monomer in methanol can be attributed to exciplex emission from face-to-face stacked *o*-phen(II):pma(II) (Figure 11c). Evidently, the face-to-face stacked *o*-phen(II):pma(II) gives rise to such emissive state. The fluorescence life time monitored at 470 nm suggest a high life time of ~ 3.7 ns compared

to that of pma dissolved in methanol (~ 1.6 ns) (Figure 12a). This high life time further indicates the presence of exciplex emission. Interestingly, the excitation spectrum monitored at 480 nm shows high intensity at ~ 435 nm and weak intensity at ~ 340 nm (Figure 12b). The distinct intensity in the visible region which is much red shifted compared to the pma absorbance might be due to ground state interaction between *o*-phen(II):pma(II) indicating preassociated nature of the exciplex. To get an insight *ab initio* Density Functional Theory (DFT) based calculations combined with Time-Dependant DFT (TDDFT) as implemented in Gaussian 09 program package was carried out for **1**. Calculation suggests three low energy peaks at 314.4, 343.6 and 381.5 nm (Figure 13). The transition at 314.4 nm is located on the C-H···π tethered pma(I) and the other red shifted transition (343.6 nm) corresponds to pma(II) involved in exciplex formation. These absorption bands are attributed to π-π* transitions. Whereas the low energy band at 381.5 nm clearly suggests a ground state interaction between pma(II) and *o*-phen(II). This evidently indicates the preassociated nature of the exciplex. Surprisingly, any spectroscopic signature of pma(I) remains absent in the emission spectrum. As there are no other quenching paths available, it can be concluded that exciplex emission is sensitized by the pma(I) emission through energy transfer process. This is also supported by the good overlap between free pma emission and exciplex excitation spectra, and also high fluoroscence life time value observed for the exciplex (Figure 12b). Such sensitization of exciplex emission through energy transfer from the pma(I) is a rare phenomenon and similar observations have been reported by our group previously.[27]

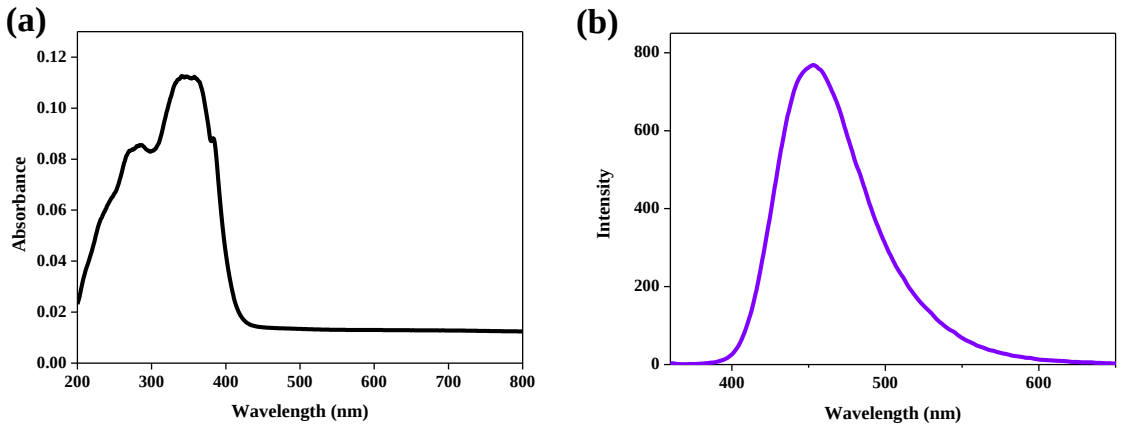

Figure 11: (a) Absorption spectrum of **1**; (b) Emission spectrum of **1** upon excitation at 350 nm; (c) Emission spectrum of pma dissolved in methanol upon excitation at 350 nm.

Moreover, emission spectra of **1** in different solvents, like chloroform, methanol and benzene (DMF) were studied. Upon excitation at 350 nm blue shifted structured emission profiles at ~ 400 nm as of PMA monomer emission was observed (Figure 14). Absence of

exciplex emission hints that the complex might have disintegrated in those solvents or the face-to-face stacking arrangement of *o*-phen(II):pma(II) changes drastically.

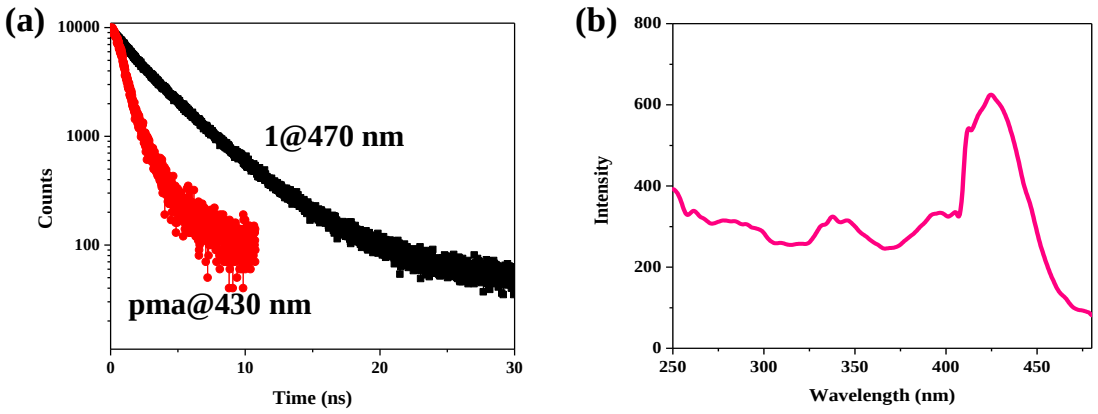

Figure 12: (a) Fluorescence decay profiles of **1** and pma dissolved in methanol observed at 470 and 430 nm, respectively; (b) Excitation spectrum of **1** monitored at 480 nm.

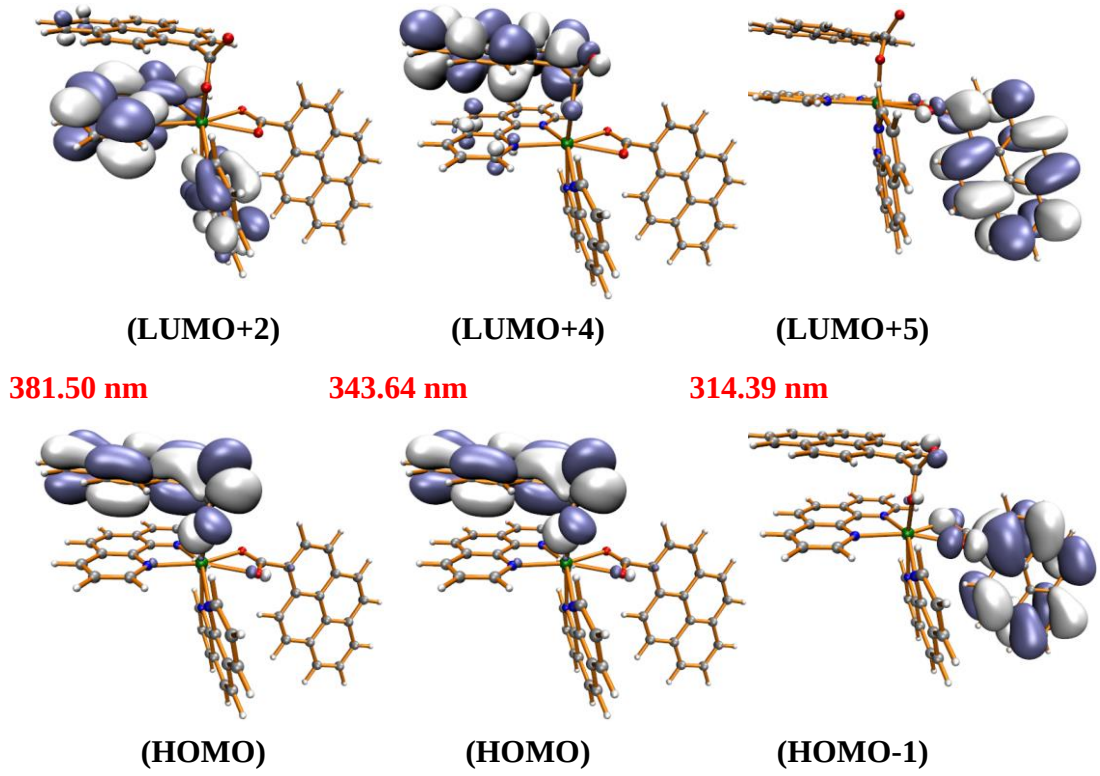

Figure 13: DFT studies of **1**: Frontier molecular orbitals of HOMO and LUMO and corresponding transition wavelengths.

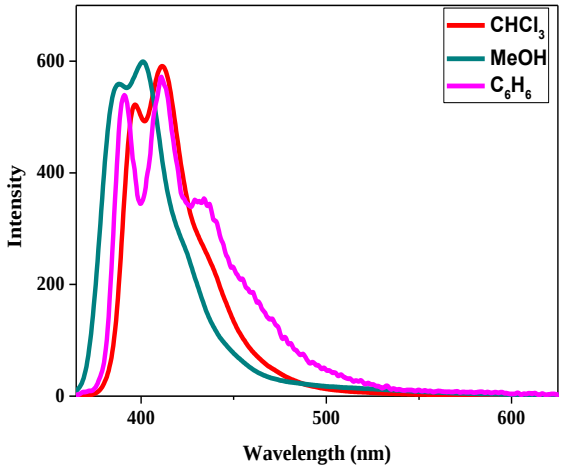

Figure 14: Emission spectra of **1** dispersed in chloroform, methanol and benzene upon excitation at 350 nm.

2A.3.3 Photophysical properties of 2: Exciplex emission and energy transfer

The photophysical characteristics of **2** in solid as well as in solvent dispersed state were examined. The absorption spectrum of **2** in solid state shows a relatively broad profile with a λ_{max} ~ 400 nm and a small shoulder in the visible region (~ 430 nm) (Figure 15a). Compound **2** when excited at 350 nm shows a broad featureless spectrum with maximum at 450 nm corresponding to cyan emission which is red shifted compared to amc monomer emission (~ 400 nm) in methanol (Figure 15b). These features suggest exciplex emission attributed to the amc(II):*o*-phen. This emission feature is similar to the one observed in case of **1**; although the donor is different.

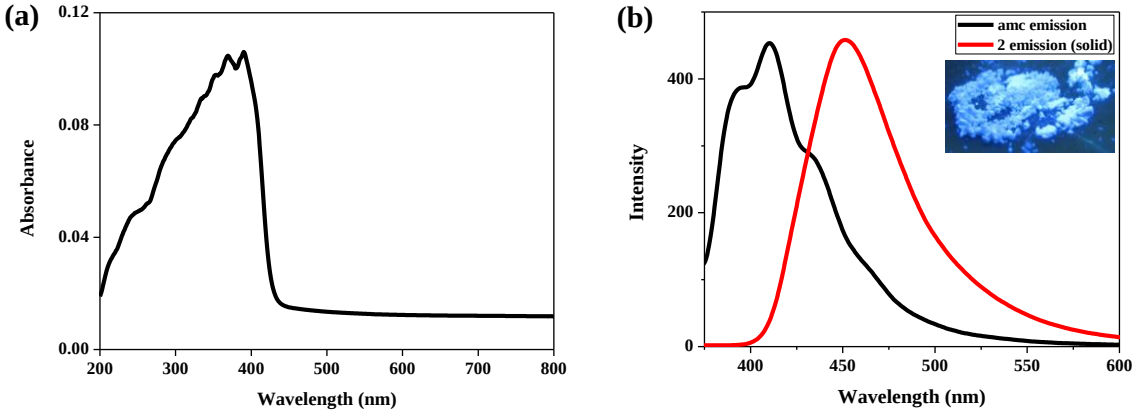

Figure 15: (a) Absorption spectrum of **2**; (b) Emission spectrum of **2** in solid state and amc in methanol upon excitation at 350 nm; Inset: Photograph of solid crystalline **2** under UV light.

The fluoroscence life time observed for the exciplex is sufficiently high (~ 4.1 ns) compared to monomer amc indicating exciplex emission (Figure 16a). The excitation spectrum monitored at 510 nm shows distinct three intensities at ~ 320, 370 and 390 nm,

as has been observed for **1** (Figure 16b). Here also DFT calculations of the complex were carried out in gas phase, similarly as in case of **1**. Three low energy transitions at 356.7, 333.2 and 323.6 nm are observed; among these three transitions 333.2 and 323.6 nm absorption bands are due to π-π* transitions (Figure 17). The red shifted transition at 356.7 nm was found to be due to amc(II):*o*-phen ground state interaction and thus indicates preassociated nature of exciplex, similar to that in **1**. In the emission spectrum of **2**, no signature of amc(I) was observed. This is probably due to the energy transfer from amc(I) to the exciplex of amc(II):*o*-phen. Such energy transfer process is very similar to that observed in compound **1**.

The emission spectrum changes clearly when compound **2** is dispersed in methanol. In addition to the exciplex emission at ~ 450 nm, a distinct peak of lower intensity at 416 nm suggests emission from the monomer amc linker (Figure 18a). Such dual emission suggests subtle perturbation in the energy transfer process from pendant anthracene to the anthracene:*o*-phen exciplex. As methanol is a polar solvent it can readily interact with **2**, which contains several pendant oxygens. This might lead to rotation of the anthracene ring due to interaction of the carboxylate groups with methanol leading to change in the dipole direction and hence perturbed energy transfer process. Possibility of complete breaking of the complex can be ruled out as the excitation spectrum monitored at 550 nm and exciplex emission remains almost similar as that of solid state (Figure 18b).

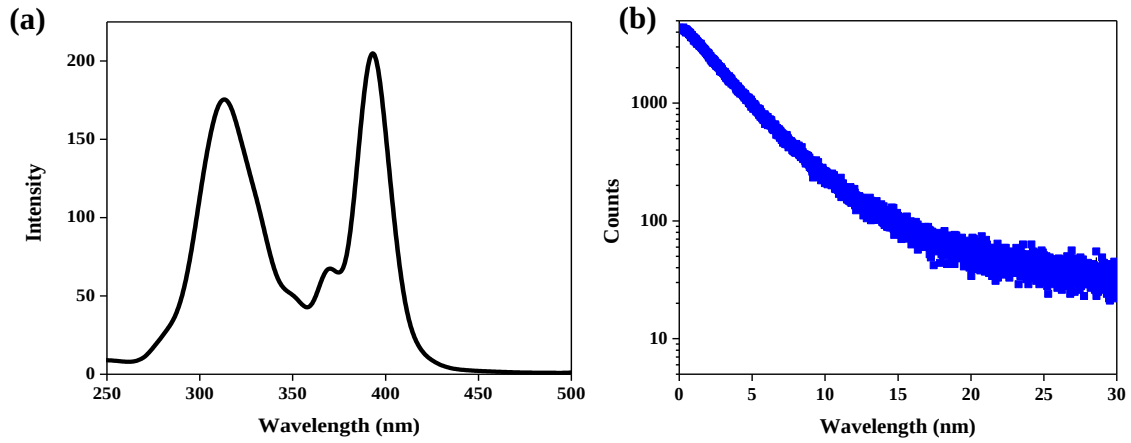

Figure 16: (a) Excitation spectrum of **2** monitored at 500 nm; (b) Fluorescence decay profile of **2** monitored at 470 nm.

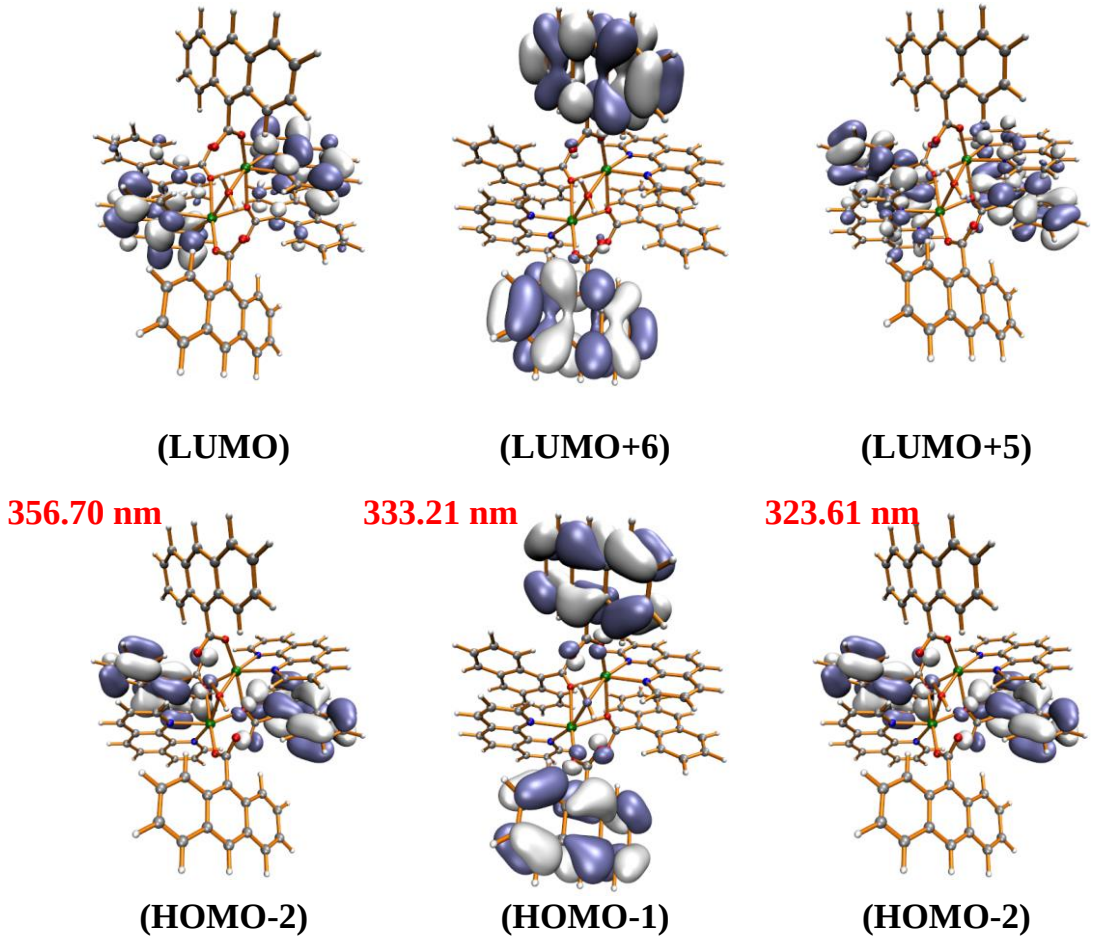

Figure 17: DFT studies of **2**: Frontier molecular orbitals of HOMO and LUMO of compound **2** and corresponding transition wavelengths.

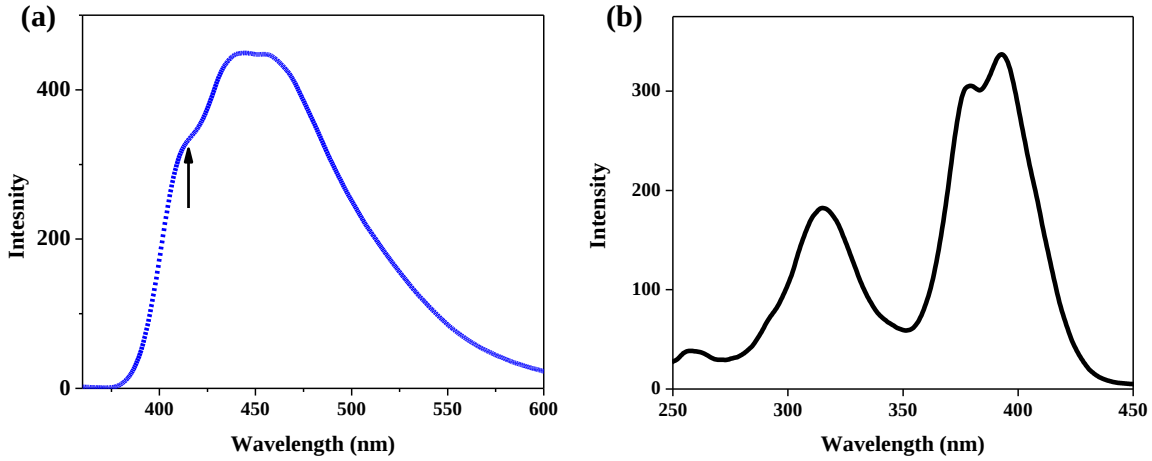

Figure 18: (a) Emission spectrum of **2** dispersed in methanol upon excitation at 350 nm; (b) Excitation spectrum monitored at 550 nm for **2** dispersed in methanol.

2A.3.4 Emission properties upon metal ion addition: Selectivity towards Al^{3+}

As mentioned earlier, the emission properties of compound **1** change drastically in solvents like methanol. While for compound **2** in methanol a dual emission feature leading to blue emission was observed. Moreover, **2** contains non-coordinated free oxygens from the carboxylate groups and hence these are available for interaction with different cations. It was envisaged that metal ions of suitable size and charge might interact with those pendant oxygens from carboxylate groups and thus emission characteristics might alter. Therefore, the emission properties of **2** upon addition of several metal ions such as Zn^{2+}, Cd^{2+}, Cu^{2+}, Ni^{2+}, Co^{2+}, Fe^{3+}, Mn^{2+}, Mg^{2+}, Ca^{2+}, Pb^{2+}, Li^{+}, Na^{+}, K^{+} and Eu^{3+} were studied (Figure 19a-19b). After addition of 100 μM of different metal ions to the methanolic solution of **2**, emission band at 416 nm remains almost as it is while in some cases exciplex emission at ~ 450 nm enhances or decreases (Figure 20a). In all cases dual emission characteristics with variable intensities were observed. Thus the emission colour remains unchanged (blue). Surprisingly for Al^{3+}, the emission peak at 416 nm slowly quenched and the exciplex emission shifted further to 466 nm with distinct enhancement (Figure 20b). Hence, the dual emission nature changes and a bright cyan-green emission can be observed upon Al^{3+} addition. The other metal ions of this group Ga^{3+} and In^{3+} show similar trend but change in intensity of emission remains very low compared to that in case of Al^{3+} (Figure 20c). The diminishing emission intensity at 416 nm corresponds to the anthracene monomer emission. The I_{470}/I_{411} vs Al^{3+} shows slow a sigmoidal type curve (Figure 21). From these observations it can be speculated that Al^{3+} addition renders efficient energy transfer from amc(I) to the exciplex. The excitation spectrum monitored at 500 nm after addition of Al^{3+} does not show significant change compared to that of only **2** in methanol (Figure 22). This reiterates that the complex does not involve in any ground state interaction with the metal ion. In presence of other metal ions also Al^{3+} shows similar change in the emission spectrum leading to cyan emission. To rationalize the observations initially the metal ion concentration was quantified. After addition of around double amount of Al^{3+} fluoroscence intensity saturates indicating each complex can accommodate two Al^{3+} ions. Further to confirm the presence of Al^{3+} in the complex EDAX and elemental analysis were carried out. EDAX shows presence of Al^{3+} along with Cd^{2+} in 1:1 Al^{3+}:Cd^{2+} ratio (Figure 23). The FT-IR spectrum also shows change in the carboxylate binding mode; the –C-O ν_{asym}(COO) str*et*ching frequency shifts

at lower wavenumber indicating binding towards Al^{3+}; secondly the presence of -NO_3^- ions as counter anion of Al^{3+} can be seen in the spectrum (Figure 24). This made us believe that hard Al^{3+} interacts with the complex probably through the hard pendant oxygen coordination and does not disintegrate the complex (Figure 25). The reason of selectivity towards the Al^{3+} ion is due to the specific arrangement of the pendant oxygen atoms in the dimeric unit.

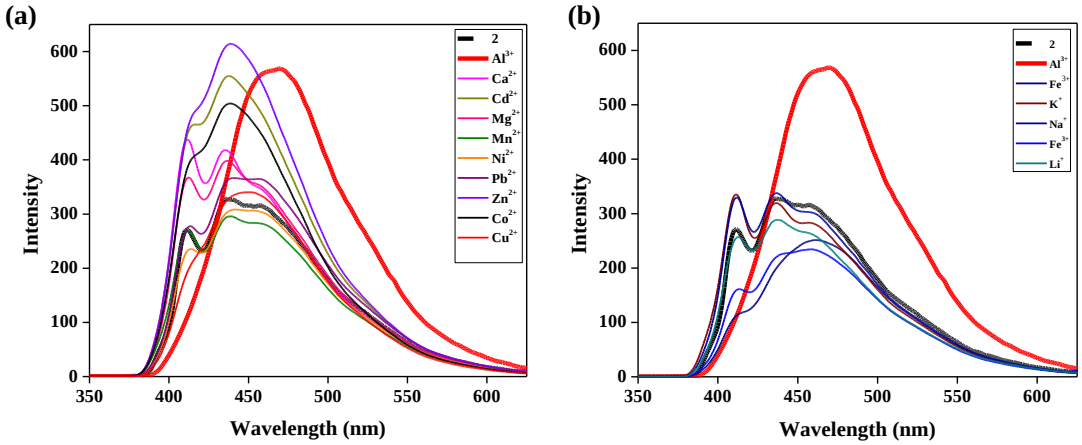

Figure 19: (a and b) Emission spectra of **2** in methanol before and after addition of various metal ions.

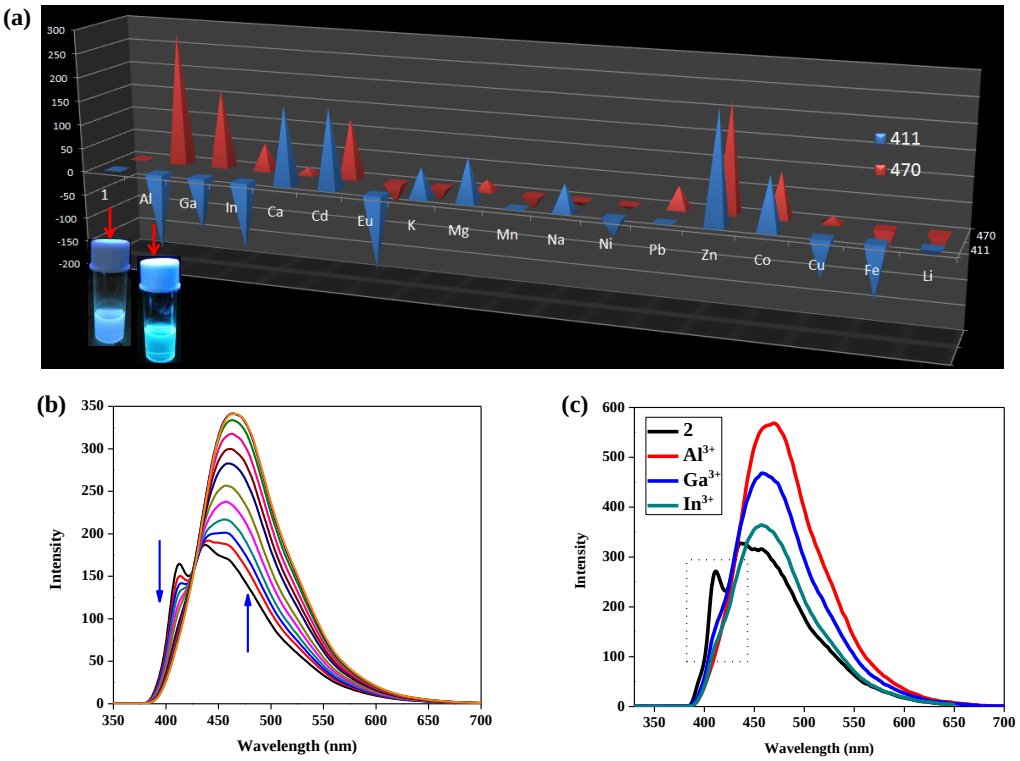

Figure 20: (a) Fluoroscence response of **2** upon addition of different metal ions: plotted intensities are observed at 411 and 470 nm (λ_{ex} = 350 nm); (b) Emission spectra of **2** after addition of Al^{3+} upon excitation at 350 nm; (c) Fluoroscence response of **2** upon addition of Al^{3+}, Ga^{3+} and In^{3+} (λ_{ex} = 350 nm); Inset shows 380-430 nm region of the emission profiles indicating the presence of monomer amc emission.

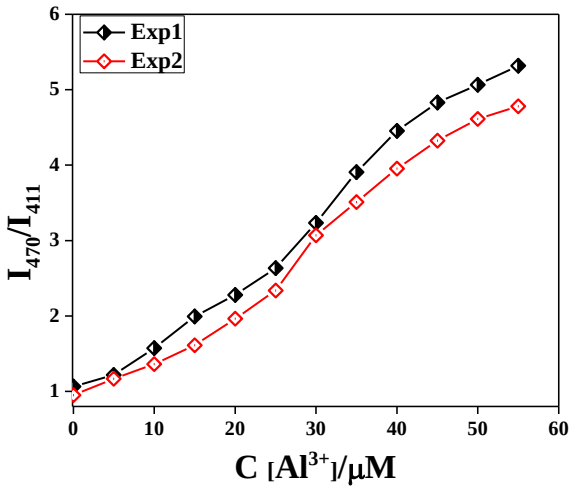

Figure 21: Ratiometric fluorescence intensity [I_{470}/I_{411}]as a function of Al^{3+} concentration in **2** solution.

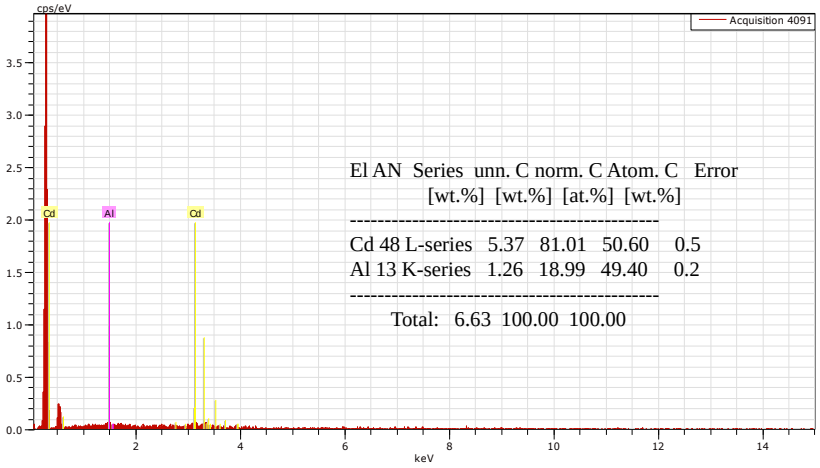

Figure 23: EDAX spectra showing the Al^{3+} and Cd^{2+} abundancy in **2** after Al^{3+} addition.

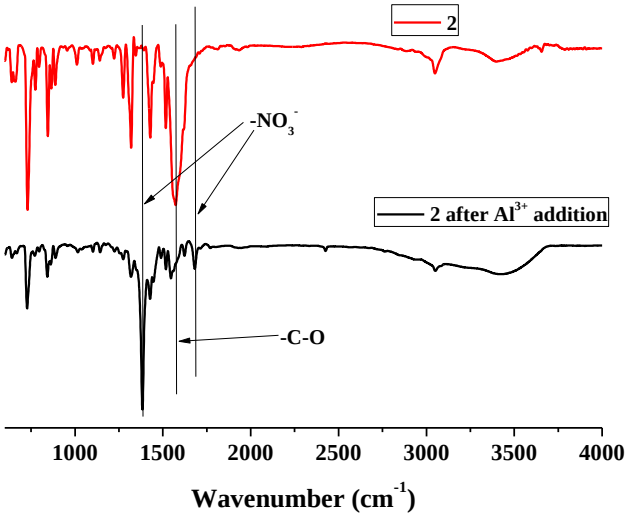

Figure 24: FT-IR spectrum of **2** and **2** after Al^{3+} addition.

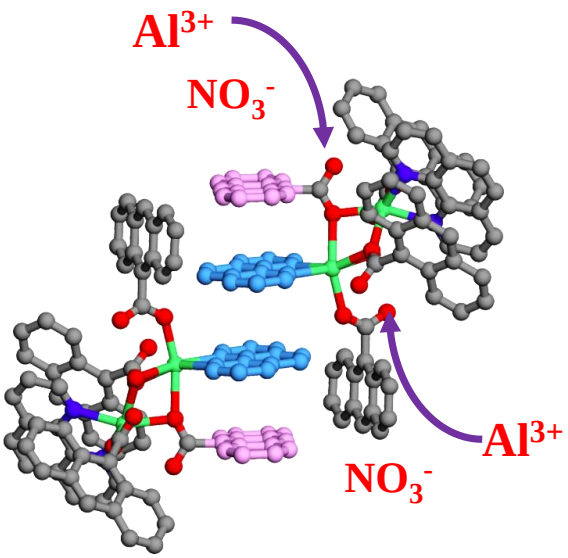

Figure 25: Possible interaction pathway of Al^{3+} with the pendant oxygens in complex **2**.

2A.4 Conclusions

In conclusion, two new metal-organic complexes, using pyrene and anthracene chromophores as building unit were synthesized. Presence of such electron rich chromophores and acceptor chromophore *o*-phen through coordination restrains give rise to preassociated exciplex formation with bright cyan-blue emissions in **1** and **2**. Interestingly, in **1** and **2**, exciplex emissions are sensitized through Förster energy transfer from pma and amc monomer, respectively. Such photophysical processes have not been studied earlier. **2** shows slightly different emission spectrum in methanol as the energy transfer process is altered through change in spatial reorientation of the linker. The blue emission of **2** in methanol turns to cyan-green selectively for Al^{3+} leading to efficient ratiometric sensing of Al^{3+} in micro-molar concentration. Change in emission spectrum upon addition of Al^{3+} occurs through coordination of Al^{3+} to the pendant oxygen atoms of the complex **2**. This sort of ratiometric highly efficient sensing of Al^{3+} using a metal-organic complex is unprecedented in literature. Following this work, molecular sensing/recognition platform based on metal-organic systems can be developed in future.

2A.5 References

1. a) K. C. Stylianou, R. Heck, S. Y. Chong, J. Bacsa, A. J. T. Jones, Y. Z. Khimyak, D. Bradshaw, M. J. Rosseinsky, *J. Am. Chem. Soc*. **2010**, *132*, 4119; b) G. J. McManus, J. J. Perry IV, M. Perry, B. D. Wagner, M. J. Zaworotko, *J. Am. Chem. Soc*. **2007**, *129*, 9094; c) C. Y. Lee, O. K. Farha, B. J. Hong, A. A. Sarjeant, S. T. Nguyen, J. T. Hupp, *J. Am.*

Chem. Soc. **2011**, *133*, 15858; d) B. Chen, S. Xiang, G. Qian, *Acc. Chem. Res*. **2010**, *43*, 1115; e) K. Jayaramulu, P. Kanoo, S. J. George, T. K. Maji, *Chem. Commun*. **2010**, *46*, 7906; f) D. Liu, K. Lu, C. Poon, W. Lin, *Inorg. Chem*. **2014**, *53*, 1916; g) L. E. Kreno, K. Leong, O. K. Farha, M. D. Allendorf, R. P. V. Duyne, J. T. Hupp, *Chem. Rev*. **2012**, *112*, 1105.

2. a) J. Heine, K. Müllar-Buschbaum, *Chem. Soc. Rev*. **2013**, *42*, 9232; b) L. V. Meyer, F. Schönfeld, K. Müllar-Buschbaum, *Chem. Commun*. **2014**, 10.1039/C4CC00848K; (c) B. Chen, Y. Yang, F. Zapata, G. Lin, G. Qian, E. B. Lobkovsky, *Adv. Mater*. **2007**, *19*, 1693.

3. a) M. J. Dong, M. Zhao, S. Ou, C. Zou, C. D. Wu, *Angew. Chem. Int. Ed.* **2013**, *52*, 1; b) P. Falcaro, S. Furukawa, *Angew. Chem. Int. Ed.* **2012**, *51*, 2.

4. a) B. D. McCarthy, E. R. Hontz, S. R. Yost, T. V. Voorhis, M. Dincă, *J. Phys. Chem. Lett*. **2013**, *4*, 453; b) J. K. Sun, L.-X. Cai, Y.-J. Chen, Z.-H. Li, J. Zhang, *Chem. Commun*. **2011**, *47*, 6870; c) Y. Zeng, S. Liao, J. Dai, Z. Fu, *Chem. Commun*. **2012**, *48*, 11641; d) V. Martínez-Martínez, S. Furukawa, Y. Takashima, I. L. Arbeloa, S. Kitagawa, *J. Phys. Chem. C*. **2012**, *116*, 26084.

5. a) S. Nishizawa, Y. Kato, N. Teramae, *J. Am. Chem. Soc*. **1999**, *121*, 9463; (b) D. Maity, V. Kumar, T. Govindaraju, *Org. Lett*. **2012**, *14*, 6008.

6. a) L. B. Picraux, B. T. Weldon, J. K. McCusker, *Inorg. Chem*. **2003**, *42*, 273; b) P. K. Lekha, E. Prasad, *Chem. Eur. J*. **2010**, *16*, 3699; c) F. M. Winnik, *Chem. Rev*. **1993**, *93*, 587; d) T. M. Figueira-Duarte, K. Müllen, *Chem. Rev*. **2011**, *111*, 7260.

7. a) D. Maity, C. Bhaumik, D. Mondal, S. Baitalik, *Inorg. Chem.* **2013**, *52*, 13941; b) S. Gonell, E. Peris, *Acs Catal*. **2014**, *4*, 2811.

8. a) E. Delhaize, P. R. Ryan, *Plant Physiol*. **1995**, *107*, 315; b) D. L. Godbold, E. Fritz, A. Huttermann, *Proc. Natl. Acad. Sci. U.S.A.* **1988**, *85*, 3888.

9. a) G. D. Fasman, *Coord. Chem. Rev*. **1996**, *149*, 125; b) G. Berthon, *Coord. Chem. Rev*., **2002**, *228*, 319; c) C. S. Cronan, W. J. Walker, P. R. Bloom, *Nature*. **1986**, *324*, 140.

10. a) A. B. Othman, J. W. Lee, Y.-D. Huh, R. Abidi, J. S. Kim, J. Vicens, *Tetrahedron*. **2007**, *63*, 10793; b) D. Maity, V. Kumar, T. Govindaraju, *Chem. Commun*. **2010**, *46*, 4499; c) D. Maity, V. Kumar, T. Govindaraju, *Inorg. Chem. Commun*. **2010**, *49*, 7229.

11. a) S. J. Payne, G. L. Fiore, C. L. Fraser, J. N. Demas, *Anal. Chem*. **2010**, *82*, 917; b) A. Gulino, T. Gupta, P. G. Mineo, M. E. van der Boom, *Chem. Commun*. **2007**, 4878.

12. D. Tanaka, S. Horike, S. Kitagawa, M. Ohba, M. Hasegawa, Y. Ozawa, K. Toriumi, *Chem. Commun.* **2007**, 3142.

13. SMART (V 5.628), SAINT (V 6.45a), XPREP, SHELXTL; Bruker AXS Inc. Madison, Wisconsin, USA, **2004**.

14. G. M. Sheldrick, Siemens Area Detector Absorption Correction Program, University of Götingen, Götingen, Germany, **1994**.

15. A. Altomare, G. Cascarano, C. Giacovazzo, A. Gualaradi, *J. Appl. Cryst*., **1993**, *26*, 343.

16. G. M. Sheldrick, SHELXL-97, Program for Crystal Structure Solution and Refinement; University of Götingen, Götingen, Germany, **1997**.

17. A. L. Spek. *J. Appl. Crystallogr*. **2003**, *36*, 7.

18. G. M. Sheldrick, SHELXS 97, Program for the Solution of Crystal Structure, University of Götingen, Germany, **1997**.

19. L. J. Farrugia, WinGX-A Windows Program for Crystal Structure Analysis, *J. Appl. Cryst*. **1999**, *32*, 837.

20. Gaussian 09, Revision A.1, M. J. Frisch, G. W. Trucks, H. B. Schlegel, G. E. Scuseria, M. A. Robb, J. R. Cheeseman, G. Scalmani, V. Barone, B. Mennucci, G. A. Petersson, H. Nakatsuji, M. Caricato, X. Li, H. P. Hratchian, A. F. Izmaylov, J. Bloino, G. Zheng, J. L Sonnenberg, M. Hada, M. Ehara, K. Toyota, R. Fukuda, J. Hasegawa, M. Ishida, T. Nakajima, Y. Honda, O. Kitao, H. Nakai, T. Vreven, Jr. J. A. Montgomery, J. E. Peralta, F. Ogliaro, M. Bearpark, J. J. Heyd, E. Brothers, K. N. Kudin, V. N. Staroverov, R. Kobayashi, J. Normand, K. Raghavachari, A. Rendell, J. C. Burant, S. S. Iyengar, J. Tomasi, M. Cossi, N. Rega, N. J. Millam, M. Klene, J. E. Knox, J. B. Cross, V. Bakken, C. Adamo, J. Jaramillo, R. Gomperts, R. E. Stratmann, O. Yazyev, A. J. Austin, R. Cammi, C. Pomelli, J. W. Ochterski, R. L. Martin, K. Morokuma, V. G. Zakrzewski, G. A. Voth, P. Salvador, J. J. Dannenberg, S. Dapprich, A. D. Daniels, Ö. Farkas, J. B. Foresman, J. V. Ortiz, J. Cioslowski, D. J. Fox, Gaussian, Inc., Wallingford CT **2009.**

21. A. D. Becke, *J. Chem. Phys*. **1993**, *98*, 5648.

22. C. T. Lee, W. T. Yang, R. G. Parr, *Phys. Rev. B*. **1988**, *37*, 785.

23. B. Miehlich, A. Savin, H. Stoll, H. Preuss, *Chem. Phys. Lett*. **1989**, *157*, 200.

24. P. J. Hay, W. R. Wadt, *J. Chem. Phys*. **1985**, *82*, 270.

25. P. J. Hay, W. R. Wadt, *J. Chem. Phys*. **1985**, *82*, 299.

26. W. R. Wadt, P. J. Hay, *J. Chem. Phys*. **1985**, *82*, 284.

27. R. Haldar, K. V. Rao, S. J. George, T. K. Maji, *Chem. Eur. J*. **2012**, *148*, 5848.

Part: 2B

Stoichiometry controlled 1D and 3D coordination polymers based on orthophenanthroline and anthracene chromophores: Tunable exciplex emission amplified by energy transfer

Summary

Following the results presented in the previous section, it was aimed to synthesize coordination polymers based on ditopic anthracene dicarboxylic acid (adc) linker. This section reports syntheses, structural characterizations and photophysical properties of 1D and 3D coordination polymers, $\{[Zn(adc)_{0.5}(o\text{-phen})_2]\cdot Hadc\cdot H_2O\}_n$ (**1**) and $\{[Zn_4(adc)_4(o\text{-phen})_2(DMF)_2]\cdot 2DMF\cdot 13H_2O\}_n$ (**2**), respectively, composed of adc and orthophenanthroline (*o*-phen) linkers just by varying the linker stoichiometry. Compound **1** contains $\{Zn_2(COO)_2(o\text{-phen})_4\}$ secondary building unit (SBU) which is extended by adc linkers resulting a cationic 1D coordination polymer where each adc is stacked in between two *o*-phen fragments. The guest Hadc forms a 1D chain with guest water molecules through hydrogen bonding and this chain stacks with 1D cationic chain by $\pi\cdots\pi$ interaction. **1** shows *o*-phen:adc 2:1 exciplex emission which is sensitized through Förster resonance energy transfer (FRET) from guest Hadc. Compound **2** contains $\{Zn_2(CO_2)_3(\mu\text{-OCO})(o\text{-phen})\}$ SBU which is connected in all three directions by adc linker resulting in a 3D porous structure. It shows similar *o*-phen:adc 2:1 exciplex emission which is sensitized through FRET from remaining adc linkers. It also shows selective uptake of CO_2 over N_2 and 0.43 wt% of H_2 uptake at 77 K at high pressure.

1. R. Haldar, S. Kitagawa, T. K. Maji, To be submitted.

2B.1 Introduction

Assembly of donor acceptor chromophores and control of their spatial disposition (dipole orientation) is very vital for their versatile photophysical properties, particularly to form any excited state complex such as excimer/exciplex or charge transfer complex.[1] An emissive CT complex is even more interesting as it can absorb light from the visible region of the spectrum and it is also be emissive. Materials with such feature might be useful for solar cell or visible light photocatalysis applications.[2] However, such complexes are rare and have been studied very recently.[3] On the other hand, spectral overlap of donor emission and acceptor absorption and their suitable spatial organization can also lead to energy transfer process. Such donor-acceptor organization is very vital and is explored for light harvesting applications.[4] Efforts of mimicking nature's photosynthetic process through light harvesting have been an important area of research and several materials have been tested for the same. Self-assembly of such chromophores in solution state is worth to study but it is challenging to get any information on the exact spatial disposition of the chromophores. Instead, chromophores embedded in polymer matrix have been studied more often and charge transfer characteristics or light harvesting properties have been reported.[5] Other way to assemble multichromophoric system is using metal-coordination approach as such process rigidifies the system and exact location/arrangement of chromophores can be identified through crystallography.[4a] In this context synthesis of discrete metal-organic complexes or higher dimensional structures (1D, 2D or 3D) based on specific chromophores those can form donor-acceptor complexes at excited state is an important topic of study.[6]

The recent development of luminescent coordination polymers is bound to the metal-based (Eu^{3+}, Tb^{3+} *etc*) or linker-based emission properties;[7] whereas very few report other photophysical properties such as light harvesting phenomenon, CT or non-linear optics *etc*. Some of the recent studies show host-guest photophysical property studies by encapsulating dye chromophores inside the pores of the frameworks.[8] Whereas strut-to-strut energy transfer process has been reported solely by Hupp *et. al*.[4a] Doping of quantum dots inside the framework matrix has also been reported by the same group.[4b] Moreover, emission properties of the organic linkers are generally explained as exciplex or excimer emission through close contacts but an emissive CT state is a rare phenomenon. This chapter shows such unique photophysical phenomena that have not been accounted in the coordination polymers till date. Following the work mentioned in

the previous section, ditopic anthracene dicarboxylate (adc) linker is used to extend the coordination network in higher dimensions. Two new coordination polymers $\{[Zn(adc)_{0.5}(o\text{-phen})_2]\cdot Hadc\cdot H_2O\}_n$ (**1**) and $\{[Zn_4(adc)_4(o\text{-phen})_2(DMF)_2]\cdot 2DMF\cdot 13H_2O\}_n$ (**2**) have been synthesized and characterized using single crystal X-ray diffraction. **1** is a 1D coordination polymer with one cationic 1D chain of $[Zn(adc)_{0.5}(o\text{-phen})_2]^+$ and an anionic counterpart chain formed by uncoordinated Hadc and guest water molecules. It features a *o*-phen:adc 2:1 exciplex emission with charge transfer characteristics sensitized through Förster energy transfer from guest anions, Hadc. **2** is a 3D porous honeycomb type structure with large 1D channel. It also shows similar *o*-phen:adc 2:1 exciplex emission with charge transfer characteristics sensitized through FRET from remaining adc linkers. It shows selectivity towards CO_2 over N_2 and 0.43 wt% of H_2 uptake at 77 K at high pressure.

2B.2 Experimental Section

2B.2.1 Materials

All the reagents employed were commercially available and used as provided without further purification. The $Zn(NO_3)_2\cdot 6H_2O$ metal salt was obtained from Spectrochem, 9,10-anthracenedicarboxylic acid and orthophenanthroline were obtained from Sigma Aldrich chemicals.

2B.2.2 Physical Measurements

Elemental analyses were carried out using a Thermo Fischer Flash 2000 Elemental Analyzer. FT-IR spectra were recorded on a Bruker IFS 66v/S spectrophotometer using KBr pellets in the region 4000-400 cm^{-1}. Powder XRD pattern of the products were recorded by using Mo-K_α radiation (Bruker D8 Discover; 40 kV, 30 Ma). The TG analysis was carried out using a Rigaku Thermo plus TG 8120 apparatus (Rigaku) in the temperature range of 303–773 K under flowing N_2 gas at a heating rate of 10 K min^{-1}. Electronic absorption spectra were recorded on a Perkin Elmer Lambda 900 UV-VIS-NIR Spectrometer and emission spectra were recorded on Perkin Elmer Ls 55 Luminescence Spectrometer. Fluorescence decay was recorded in a time correlated single-photon counting spectrometer of Horiba-Jobin Yvon with 350-450 nm picosecond Ti-saphhire laser. The fluorescence quantum yields were measured using an absolute photoluminescence quantum yield measurement system (Hamamatsu, C9920-02).

2B.2.3 Synthesis of $\{[Zn(adc)_{0.5}(o\text{-phen})_2]\cdot Hadc\cdot H_2O\}_n$ (1)

0.026 g (0.1 mmol) anthracene dicarboxylic acid and 0.018 g (0.1 mmol) orthophenanthroline were dissolved in 6 mL of DMF and sonicated for 5-10 min to mix well. 0.03 g (0.1 mmol) of $Zn(NO_3)_2\cdot 6H_2O$ was added to the ligand solution and mixed well before keeping in a 20 mL Teflon-lined vessel. This vessel was placed in a stainless steel autoclave, sealed and heated to 120 $^{\circ}$C under autogenous pressure for 24 h and cooled to room temperature with cooling rate of 5 °C/h. Yellow rod shaped crystals of **1** were isolated and washed with DMF before the X-ray single crystal diffraction measurement. Yield: 47%, relative to Zn^{2+}. Anal. Calcd. for $C_{48}H_{31}ZnN_4O_7$: C, 68.44; H, 3.68; N, 6.65. Found: C, 69.01; H, 3.19; N, 6.71. FT-IR (KBr pellet, 4000-400 cm^{-1}) (Figure 1): 3481(b), 3284(w), 2326(s), 2238(m), 2128(m), 1614(s), 1562(s), 1502(s), 1428(s), 1310(w), 1228(s), 1068(s), 1020(s), 912(w), 874(w), 820(s).

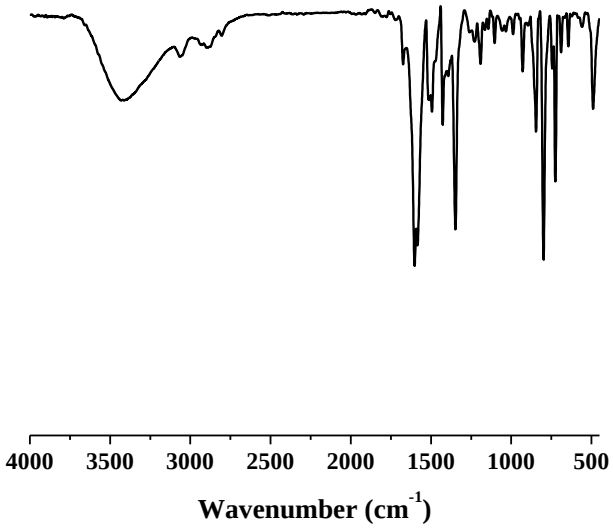

Figure 1: FT-IR spectrum of **1**.

2B.2.4 Synthesis of $\{[Zn_4(adc)_4(o\text{-phen})_2(DMF)_2]\cdot 2DMF\cdot 13H_2O\}_n$ (2)

2 is synthesized following similar methodology as used for **1**, except orthophenanthroline amount was reduced to 0.05 mmol, 0.009 g. Yellow crystals were isolated and washed properly with DMF before the X-ray single crystal diffraction measurement. Yield: 61%, relative to Zn^{2+}. Anal. Calcd. for $C_{96}H_{92}Zn_4N_6O_{33}$: C, 54.36; H, 4.38; N, 3.96. Found: C, 54.89; H, 4.75; N, 4.09. FT-IR (KBr pellet, 4000-400 cm^{-1}) (Figure 2): 3481(b), 3284(w), 2326(s), 2238(m), 2128(m), 1614(s), 1562(s), 1502(s), 1428(s), 1310(w), 1228(s), 1068(s), 1020(s), 912(w), 874(w), 820(s).

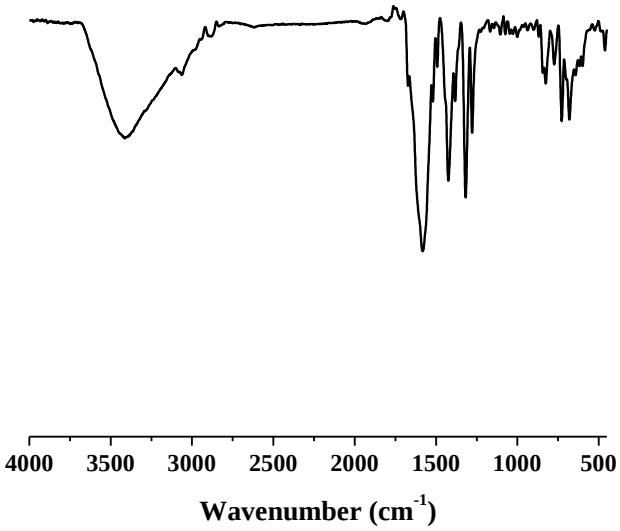

Figure 2: FT-IR spectrum of **2**.

2A.2.5 X-ray Crystallography

X-ray single crystal structural data of **1** and **2** were collected on a Bruker Smart-CCD diffractometer equipped with a normal focus, 2.4 kW sealed tube X-ray source with graphite monochromated Mo-*Kα* radiation (λ = 0.71073 Å) operating at 50 kV and 30 mA. The program SAINT[9] was used for integration of diffraction profiles and absorption correction was made with SADABS[10] program. All the structures were solved by SIR 92[11] and refined by full matrix least square method using SHELXL-97.[12] All the hydrogen atoms were geometrically defixed and placed in ideal positions. All crystallographic and structure refinement data of **1** and **2** are summarized in Table 1. Selected bond lengths and angles for **1** and **2** are given in Table 2-3, respectively. All calculations were carried out using SHELXL 97,[12] PLATON,[13] SHELXS 97[14] and WinGX system, Ver 1.70.01.[15]

2B.2.6 Adsorption study

The adsorption isotherm of CO_2 and N_2 (195 K) using the dehydrated sample of **2 (2a)** were measured by using QUANTACHROME QUADRASORB-*SI* analyzer. In the sample tube the adsorbent sample (~100-150 mg) was placed which had been prepared at 453 K under a 1×10^{-1} Pa vacuum for about 6 h prior to measurement of the isotherms. Helium gas (99.999% purity) at a certain pressure was introduced in the gas chamber and allowed to diffuse into the sample chamber by opening the valve. The amount of gas adsorbed was calculated readily from pressure difference (P_{cal} - P_e), where P_{cal} is the calculated pressure with no gas adsorption and P_e is the observed equilibrium pressure.

All operations were computer-controlled and automatic. High pressure H_2 adsorption measurement at 273 K was carried out on a fully computer controlled volumetric BELSORP-HP, BEL JAPAN high pressure instrument. H_2 gas used for the measurement is scientific/research grade with 99.999% purity. For the measurements, approximately 100 mg sample was taken in a stainless-steel sample holder and degassed at 453 K for a period of 12 h under 0.1 Pa vacuum. Dead volume of the sample cell was measured with He gas of 99.999% purity. Non-ideal correction for H_2 gas was made by applying virial coefficients at 298 K.

2B.3 Results and Discussion

2B.3.1 Structural description of $\{[Zn(adc)_{0.5}(o\text{-phen})_2]\cdot Hadc\cdot H_2O\}_n$ (1) and $\{[Zn_4(adc)_4(o\text{-phen})_2(DMF)_2]\cdot 2DMF\cdot 13H_2O\}_n$ (2)

Compound **1** crystallizes in monoclinic $P2_1/c$ spacegroup. In the asymmetric unit there are one Zn^{2+}, two *o*-phen, two adc and one crystalline water molecule. The hexacoordinated Zn^{2+} metal center is connected to four nitrogen atoms (N1, N2, N3 and N4) from two *o*-phen and two oxygen atoms (O1 and O2) from two adc linkers. Two such Zn^{2+} centers are bridged by the carboxylate (*syn-anti*) of two adc linkers to form a dimeric cationic building unit $\{Zn_2(o\text{-phen})_4(COO)_2\}$ and further extended by adc linker along *a*-axis to form a cationic 1D chain like structure (Figure 3a-3b). In this chain the adc linkers are sandwiched between two chelated *o*-phen ligands through π···π interactions (cg···cg ~ 3.495 Å). To neutralize the charge of the cationic 1D chain a monoanionic Hadc molecule resides next to the 1D chain (Figure 3c). These Hadc guest molecules form a 1D linear chain like structure along *a*-axis through hydrogen bonding interactions between carboxylate groups and guest water molecules (Figure 3c). There are no close contacts between the cationic chains along *bc* plane. But the anionic hydrogen bonded chain connects the cationic chain along *bc* plane through several non-covalent interactions. The *o*-phen rings of cationic 1D chain undergo moderate C-H···π and π ···π interactions with the Hadc anions of the anionic 1D chain to stabilize the whole 3D supramolecular framework (Figure 4a-b). A supramolecular structure with such two ionic 1D chains aligned in parallel fashion is unique from structural point of view (Figure 4b).

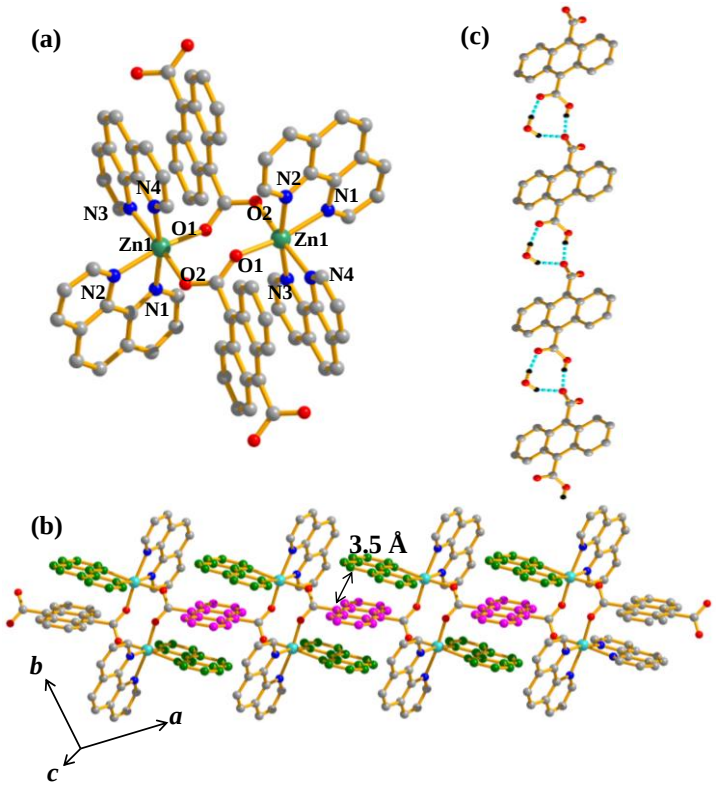

Figure 3: Structural details of **1**: (a) Basic building unit showing the coordination environment of Zn^{2+}; (b) 1D cationic chain of $[Zn(adc)_{0.5}(o\text{-phen})_2]^+$; (c) 1D hydrogen bonded chain formed by uncoordinated Hadc and guest water molecules.

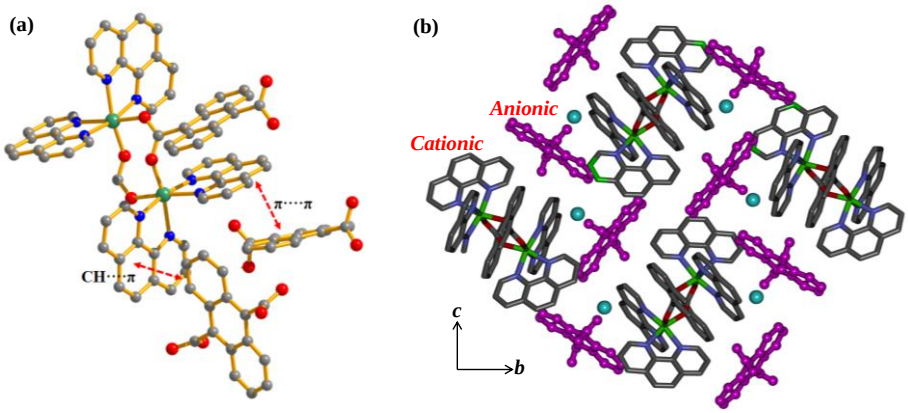

Figure 4: (a) C-H···π and π···π intercations in **1** between Hadc anions and *o*-phen of the cationic chain; (b) View of the cationic and anionic parts along *a*-direction.

Compound **2** was synthesized using similar precursors as that of **1**, in a different condition. It crystallizes in monoclinic *C*2/*c* spacegroup. **2** contains two crystallographically distinguishable Zn^{2+} centers Zn1 and Zn2 which are hexacoordinated (Figure 5a). Zn1 is coordinated to six oxygen atoms (O1, O3, O4, O5, O7 and O8) from four different adc linkers (two bridging adc and two chelating adc); Zn2 is coordinated to three oxygen atoms (O2, O6 and O7) from three bridging adc linkers, one oxygen atom

from one DMF (O1w) and two nitrogen atoms (N1 and N2) of *o*-phen (Figure 5a). The two metal centers form a {$Zn_2(CO_2)_3$(μ-OCO)(*o*-phen)} secondary building unit (SBU) which is connected through four adc linkers in three dimensions in a tetrahedral fashion (Figure 5b). Such tetrahedral disposition of the SBU lead to a 3D framework with one dimensional distorted hexagonal (8×8 $Å^2$) channels running along *c*-axis (Figure 5c).[16] These 1D channels are occupied with water and guest DMF molecules removal of which gives a void space of 25% of total cell volume (4000 $Å^3$) as calculated using PLATON.[13] Topological analysis of the 3D structure using TOPOS 4.0 suggests a honeycomb type (2-c)2(4-c) net with *Schläfli* symbol {12^6}{12}2 (Figure 6a-6b).[17] Though the precursors used do not contain any tetrahedral center, the *in situ* formed SBU directs the formation of honeycomb lattice. Similar to **1**, in **2** also several non-covalent interactions are present between the adc and *o*-phen aromatic rings. Viewed along *b*-axis shows a column of face-to-face π···π stacked (*o*-phen:adc:*o*-phen) repeating units (Figure 7). The cg···cg distances between successive *o*-phen rings and *o*-phen and adc rings are 3.5 and 3.6 Å, respectively. Interestingly, only one among four adc linkers participate in the stacking mentioned above, while other three do not undergo any close interaction.

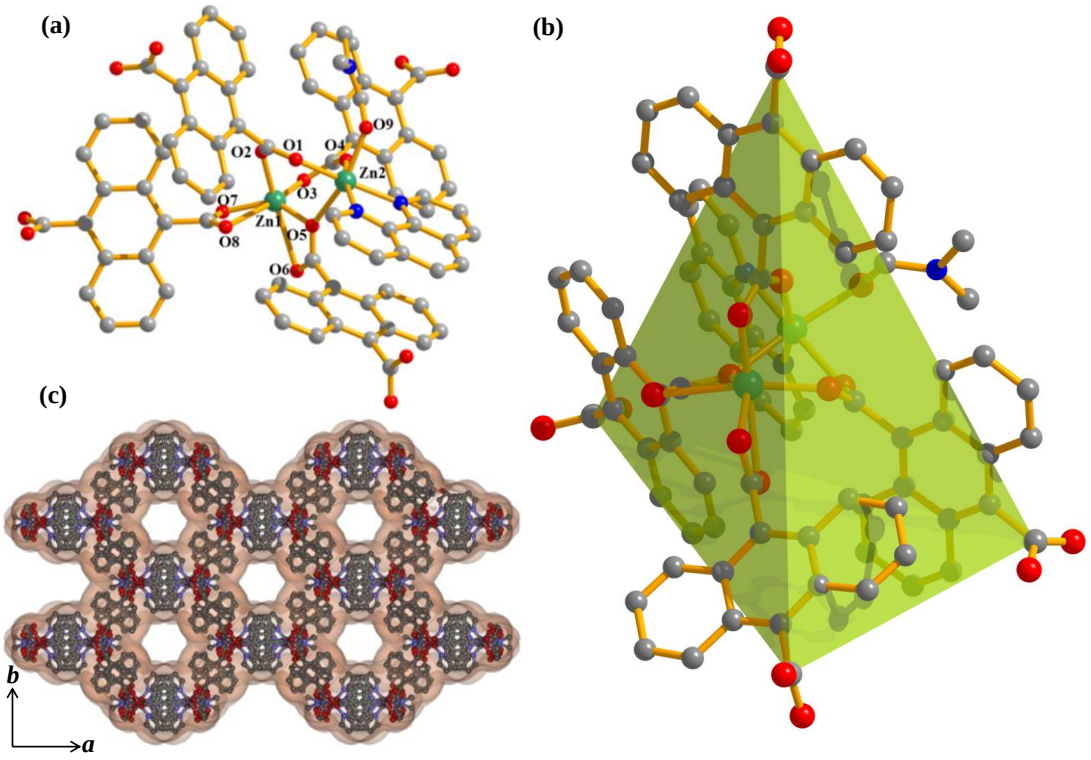

Figure 5: Structural details of **2**: (a) Basic building unit with Zn^{2+} coordination environment; (b) Tetrahedral unit formed by unique linker disposition; (c) View of the 1D pore along *c*-direction.

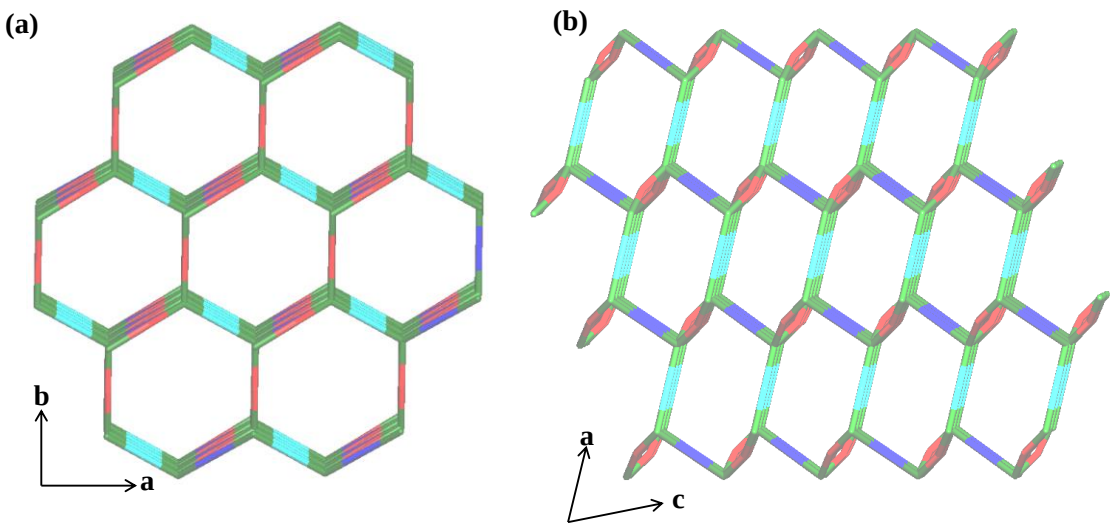

Figure 6: Topological analysis of **2**: (2-c)2(4-c) net along (a) *c*-direction; (b) *b*-direction.

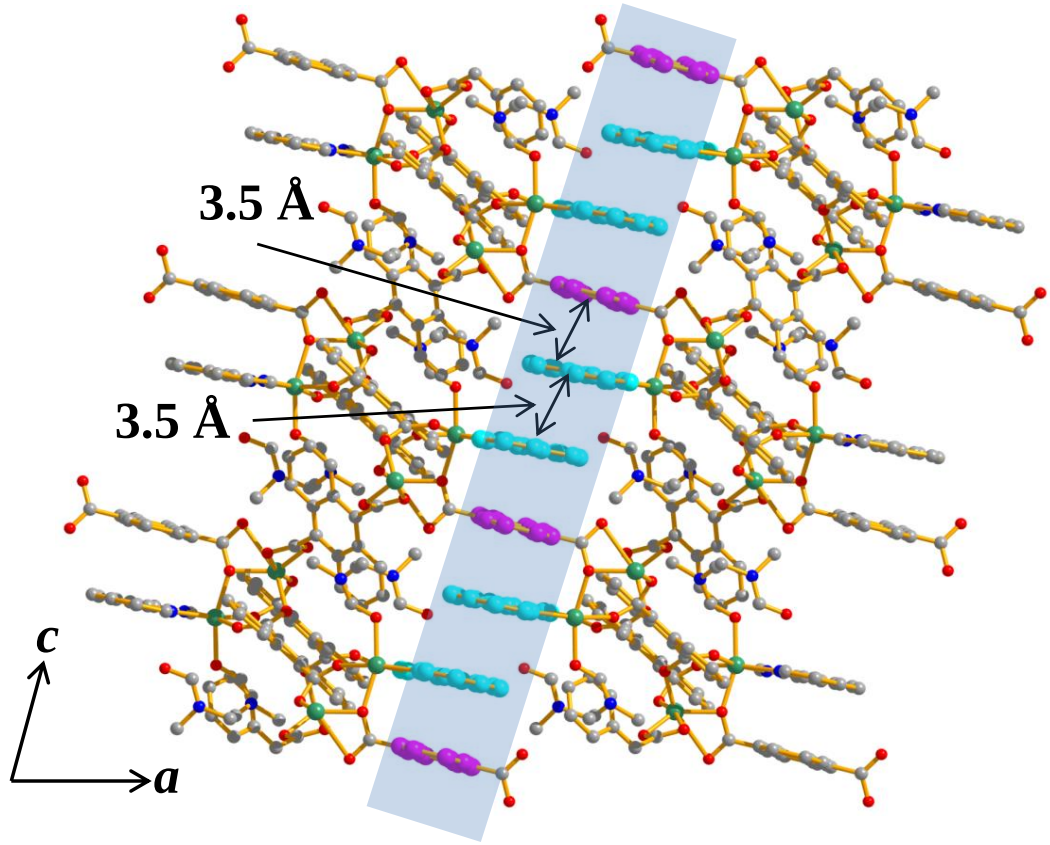

Figure 7: View of 2:1 *o*-phen:adc stacking along *b*-direction in **2**.

Table 1: Crystal data and structure refinement parameters of compound **1** and **2**.

Parameters	1	2
Empirical formula	$C_{48}H_{31}ZnN_4O_7$	$C_{96}H_{92}Zn_4N_6O_{33}$
M	841.16	2119.69
Crystal system	Monoclinic	Monoclinic
Space group	$P2_1/c$	$C2/c$
***a* (Å)**	9.6122(19)	30.510(6)
***b* (Å)**	25.571(5)	17.8000(4)
***c* (Å)**	15.211(3)	21.230(4)
***α* (deg)**	90	90
***β* (deg)**	97.87(3)	108.54(3)
***γ* (deg)**	90	90
***V* (Å^3)**	3703.6(13)	10931(4)
Z	4	8
***T*(K)**	293	293
***λ* (Mo $K_α$)**	0.71073	0.71073
***D*$_c$ (g cm^{-3})**	1.509	1.390
***μ* (mm^{-1})**	0.728	0.955
***θ*$_{max}$ (deg)**	27.5	29.0
total data	30817	49395
unique reflection	8496	14105
***R*$_{int}$**	0.132	0.054
data [*I* > 2σ(*I*)]	4870	10501
***R*^{a}**	0.0852	0.0965
***R*$_w$^{b}**	0.1678	0.2977
GOF	1.06	1.17

^{a} $R = \Sigma||F_o| - |F_c||/\Sigma|F_o|$. ^{b} $R_w = [\Sigma\{w(F_o^2 - F_c^2)^2\}/\Sigma\{w(F_o^2)^2\}]^{1/2}$.

Table 2: Selected bond lengths (Å) and angles (°) for $\{[Zn(adc)_{0.5}(o\text{-phen})_2]\cdot Hadc\cdot H_2O\}_n$ (**1**).

Zn1-O1	2.076(3)	Zn1-N1	2.190(4)
Zn1-N2	2.180(4)	Zn1-N3	2.116(4)
Zn1-N4	2.189(4)	Zn1-O2_a	2.103(3)
O1-Zn1-N1	165.47(14)	O1-Zn1-N2	88.84(14)
O1-Zn1-N3	100.23(14)	O1-Zn1-N4	88.77(14)

O1-Zn1-O2_a	97.05(12)	N1-Zn1-N2	76.64(16)
N1-Zn1-N3	94.25(16)	N1-Zn1-N4	93.13(15)
O2_a-Zn1-N1	82.10(14)	N2-Zn1-N3	168.73(16)
N2-Zn1-N4	96.07(16)	O2_a-Zn1-N2	87.54(14)
N3-Zn1-N4	77.60(16)	O2_a-Zn1-N3	97.87(14)
O2_a-Zn1-N4	173.23(14)		

a = 1-x,-y,1-z

Table 3: Selected bond lengths (Å) and angles (°) for $\{[Zn_4(adc)_4(o\text{-phen})_2(DMF)_2]\cdot 2DMF\cdot 13H_2O\}_n$ (**2**).

Zn1-O2	2.034(3)	Zn1-O3	1.975(3)
Zn1-O5	1.988(3)	Zn1-O6	2.597(4)
Zn1-O7	1.955(4)	Zn1-O8	2.560(4)
Zn2-O1	2.053(4)	Zn2-O4	2.196(3)
Zn2-O5	2.141(3)	Zn2-O9	2.089(4)
Zn2-N1	2.124(4)	Zn2-N2	2.128(5)
O2-Zn1-O3	99.15(14)	O2-Zn1-O5	104.10(14)
N1-Zn2-N2	78.26(18)	O2-Zn1-O6	156.31(14)
O2-Zn1-O7	94.36(15)	O2-Zn1-O8	81.91(13)
O3-Zn-O5	106.85(14)	O3-Zn1-O6	98.29(13)
O3-Zn1-O7	110.55(15)	O3-Zn1-O8	167.68(14)
O5-Zn1-O6	55.21(14)	O5-Zn1-O7	134.70(15)
O5-Zn1-O8	84.64(13)	O6-Zn1-O7	94.40(15)
O6-Zn1-O8	84.46(12)	O7-Zn1-O8	57.16(14)
O1-Zn2-O4	103.16(14)	O1-Zn2-O5	86.90(14)
O1-Zn2-O9	83.01(18)	O1-Zn2-N1	168.21(16)
O1-Zn2-N2	91.49(18)	O4-Zn2-O5	82.96(13)

2B.3.2 Thermal stability and PXRD

The thermal stability of both the compounds is found to be high as realized from the Thermogravimetric analysis. Compound **1** loses the guest water molecules at ~ 150 °C and is stable upto 300 °C (Figure 8). After this temperature weight loss is very sharp indicating loss of one of the linker from the framework. Compound **2** loses the guest water and DMF molecules at 130 °C and further weight loss in the range 150-250 °C is due to the coordinated DMF molecules. The desolvated compound (**2a**) is stable upto 300 °C. PXRD of the phase pure compound **1** is shown in Figure 9a. The desolvated (heated at 180° C) PXRD pattern of **2** (**2a**) is quite dissimilar compared to that of as-synthesized **2** (Figure 9b). This suggests structural rearrangement after desolvation. As the coordinated DMF molecules are released from the SBU the adc spatial disposition might alter leading to structural change.

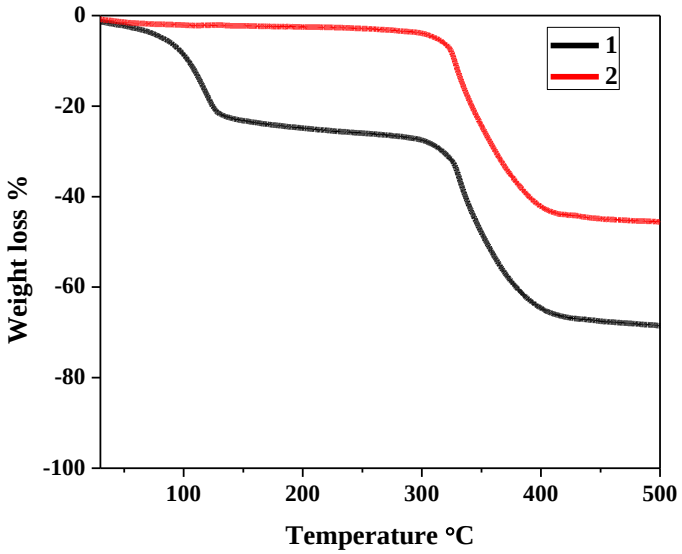

Figure 8: TGA profiles of **1** and **2** under N_2 atmosphere with heating rate of 3 °C/min in the temperature range of 30-500 °C.

2B.3.3 Photophysical properties of 1 and 2: Exciplex emission and energy transfer

The absorption spectrum of **1** shows a broad nature ranging from 300-460 nm (Figure 10a). Reasonably high absorption in the visible region (400-460 nm) suggests possibility of ground state interaction in the framework. Excitation of **1** at 400 nm shows a broad featureless emission spectrum with a maximum at 472 nm (cyan emission; Figure 10b). Evidently this spectrum is much red shifted from expected anthracene emission (~400 nm) which is suggesting some other photophysical phenomena operating in the

system. As was seen in the previous section 2A, formation of excited state complex between adc:*o*-phen might be a possibility. But the excitation spectrum monitored at 480 nm shows a high intensity in the visible region of the spectrum (430 nm) and this is clear evidence of exciplex with charge transfer (CT) characteristics (Figure 10c). Further, the excitation spectrum clearly advocates that the origin of emission is exciplex with CT characteristics. Careful analysis of the structure shows one adc is sandwiched between two *o*-phen rings and hence it can be postulated that a 2:1 *o*-phen:adc exciplex has been formed. It is worth to mention that this exciplex is from the cationic 1D chain whereas the anionic Hadc emission is not observed in the emission spectrum. As a possible explanation I conjecture that Hadc acts as a donor to further sensitize exciplex emission through a FRET that amplified exciplex emission. A high intensity peak at ~ 337 nm in the excitation spectrum retells the contribution from Hadc. Further overlap of adc monomer emission and excitation spectrum of **1** at 480 nm supports the existence of

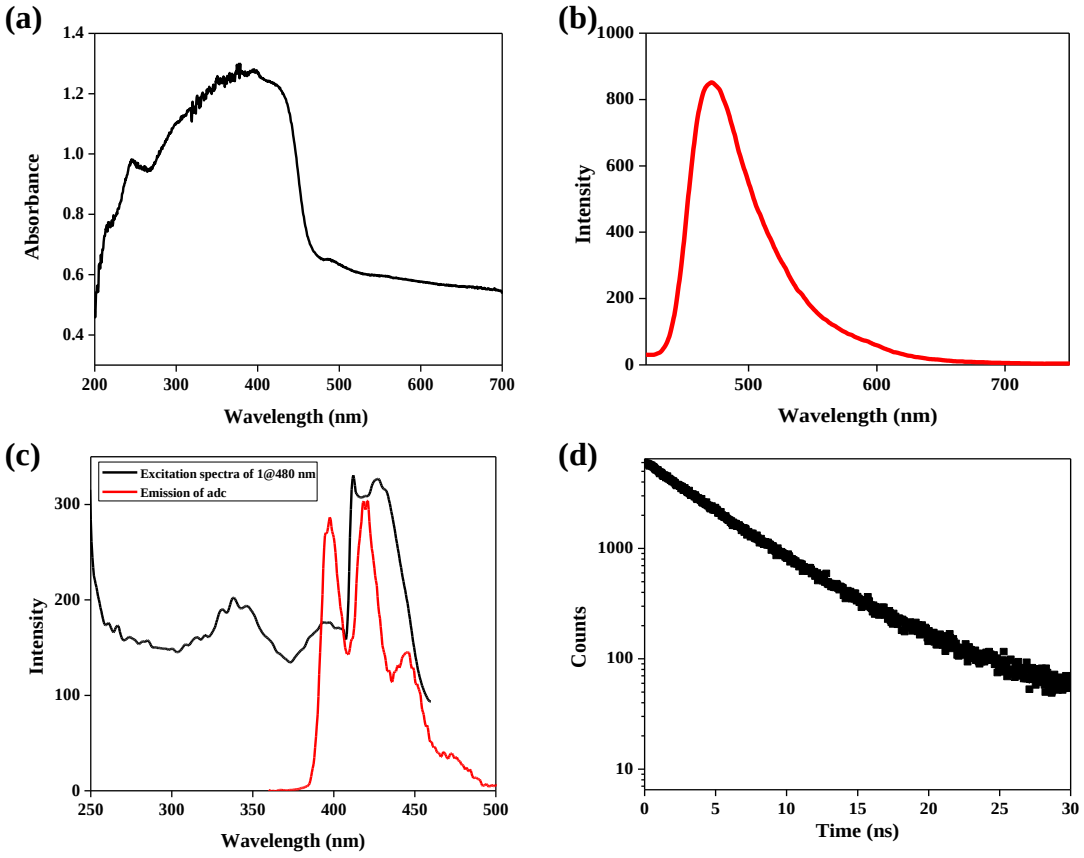

Figure 10: (a) Absorption spectrum of **1**; (b) Emission spectrum of **1** upon excitation at 400 nm; (c) Overlap of excitation spectrum of **1** monitored at 480 nm and emission spectrum of adc in methanol upon excitation at 340nm; (d) Fluorescence life time profile monitored at 480 nm.

FRET process (Figure 10c). This sort of energy transfer process is presented in the previous section. The fluoroscence life time spectrum of **1** monitored at 480 nm shows a

very high life time of ~ 5.6 ns, which is cumulative effect of exciplex formation and the presence of FRET process (Figure 10d). The absolute quantum yield (ϕ_f %) of **1** is ~ 4 which is reasonable for such systems (Figure 11).

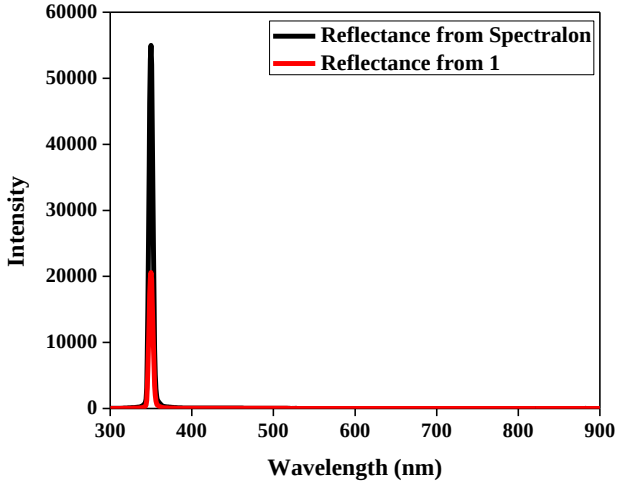

Figure 11: Quantum yield of **1** measured at room temperature in solid state.

In case of **2**, the absorption spectrum is similarly broad as that in case of **1** (Figure 12a). Excitation of **1** at 400 nm shows a very broad emission spectrum with maximum at 510 nm (Figure 12b). This clearly advocates presence of different photophysical process as this spectrum is red shifted and broad in nature compared to adc emission. The structural insight tells possible *o*-phen:adc stacking in 2:1 ratio, similar to that in **1**. Excitation spectrum monitored at 520 nm looks very similar to that in **1**; a high intensity peak in the visible region of the spectrum (400-460 nm) and small intensity peak at ~ 330 nm (Figure 12c). The peak at visible region of the spectrum advocates formation of an exciplex with CT characteristics. This feature is similar to the 1D CP but the emission profile is slightly red shifted compared to that of **1**. This might be due to subtle difference in dipole orientations of the donor-acceptor molecules; although the $\pi\cdots\pi$ distances do not vary much.

As described in the structural description of **2**, out of four adc linkers only one participates in the exciplex formation and hence a high intensity adc emission is expected. But similar to previous cases no such emission from adc can be seen. This made us believe that the photophysical pathways are similar to that in **1**. Here, three adc linkers act as donor and the 2:1 *o*-phen:adc exciplex complex is the acceptor. The major difference between **1** and **2** is the donor acceptor ratios are 1:1 and 3:1, respectively. The fluorescence life time observed for **2** at 520 nm is ~ 6.5 ns, slightly higher than that in **1**

(Figure 12d). Also the absolute quantum yield (ϕ_f %) increases to ~ 7 which is reasonably high for such system (Figure 13). The inference can be drawn from the above mentioned results that changing the superstructure from 1D to 3D strengthens the CT emission in terms of life time and quantum yield. Also form 1D to 3D the donor-acceptor ratio changes leading to a better light harvesting system.

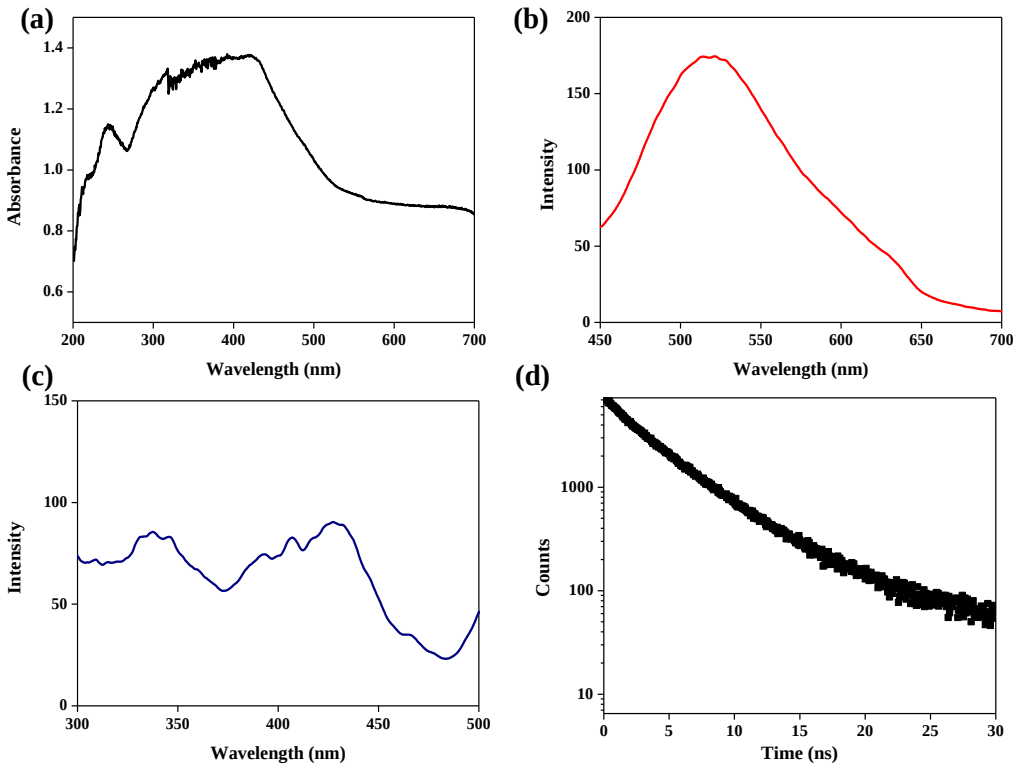

Figure 12: (a) Absorption spectrum of **2**; (b) Emission spectrum of **2** upon excitation at 400 nm; (c) Excitation spectrum of **2** monitored at 520 nm; (d) Fluorescence life time profile monitored at 520 nm.

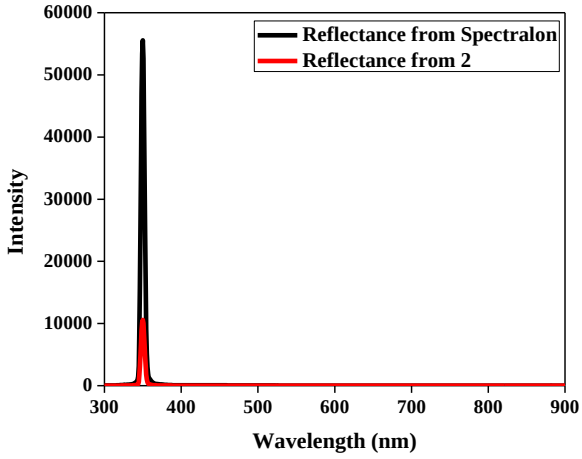

Figure 13: Quantum yield of **2** measured at room temperature in solid state.

2B.3.4 Gas adsorption studies

Compound **1** is a 1D coordination polymer and extended to 3D supramolecular framework through guest Hadc and water molecules. It does not show any possible void space for gas adsorption properties. Rather compound **2** is a 3D framework with 1D channels filled with guest DMF and water molecules. Therefore, N_2 (77 K) and CO_2 (195 K) gas adsorption studies have been performed to establish the permanent porosity. It does not show any N_2 uptake at 77 K indicating non-porous nature (Figure 14a). It is expected as after guest solvent removal framework undergoes contraction realized form the PXRD patterns. Surprisingly, at 195 K **2a** shows a reasonable CO_2 uptake of 32 mL/g (Figure 14a). As the kinetic diameter[18] of CO_2 (3.3 Å) is lesser than N_2 (3.64 Å) and quadrupole moment of CO_2 can interact with the aromatic electron rich pore surface of **2a** such selectivity is expected.[19] H_2 adsorption at 77 K for **2a** shows an uptake amount of 0.43 wt% (Figure 14b).

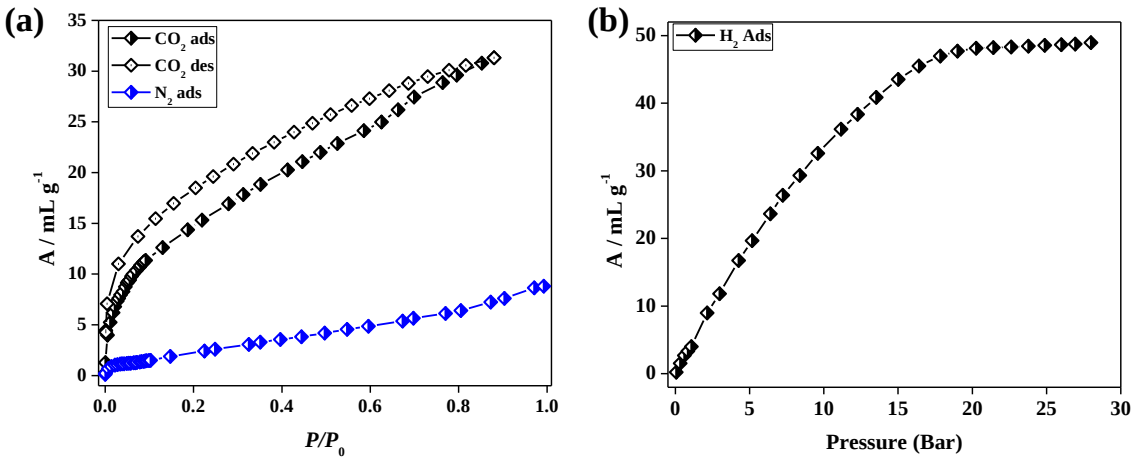

Figure 14: Adsorption isotherms of **2a**: (a) CO_2 and N_2 adsorption isotherms at 195 and 77 K; (b) H_2 adsorption isotherm at high pressure at 77 K.

2B.4 Conclusions

In conclusion, changing the stoichiometry of adc and *o*-phen linkers two coordination polymers with different dimensionality, 1D (**1**) and 3D (**2**) were synthesized. **1** is a 1D coordination polymer with cationic 1D chain and an anionic Hadc counterpart. While **2** is a 3D structure with honeycomb type lattice and possesses 1D hexagonal channels. **1** shows strong CT emission from a 2:1 *o*-phen:adc and this is sensitized by the anionic Hadc linker through Förster energy transfer process. In case of **2** also, similar 2:1 *o*-phen:adc CT formation was observed and this CT is sensitized by three remaining adc

linkers through Förster energy transfer process. This work shows that by increasing the dimensionality one can have increased exciplex emission life time, quantum yield and also better light harvesting system because the donor-acceptor ratio increases to 3:1 (3D) from 1:1 (1D). Such synthetic strategy and frameworks with exciting photophysical properties can be promising for the development of new luminescent metal-organic systems in future.

2B.5 References

1. a) G. De Santis, L. Fabbrizzi, M. Licchelli, C. Mangano, D. Sacchi, *Inorg. Chem.* **1995**, *34*, 3581; b) A. Jover, F. Meijide, E. R. Núñez, J. V. Tato, *Langmuir* **1996**, *12*, 1789; c) J. K. Klosterman, M. Iwamura, T. Tahara, M. Fujita, *J. Am. Chem. Soc.* **2009**, *131*, 9478; d) D. Gust, T. A. Moore, A. L. Moore, *Acc. Chem. Res*. **2001**, *34*, 40; e) T. J. Meyer, *Acc. Chem. Res*. **1989**, *22*, 163.

2. T. Zhang, W. Lin, *Chem. Soc. Rev*. **2014**, DOI: 10.1039/C4CS00103F.

3. a) C. Vijaykumar, V. K. Praveen, A. Ajayaghosh, *Adv. Mater*. **2009**, *21*, 2059; b) A. Ajayaghosh, V. K. Praveen, C. Vijayakumar, *Chem. Soc. Rev*. **2008**, *37*, 1090.

4. a) C. Y. Lee, O. K. Farha, B. J. Hong, A. A. Sarjeant, S. T. Nguyen, J. T. Hupp, *J. Am. Chem. Soc.* **2011**, *133*, 15858; b) S. Jin, H. Son, O. K. Farha, G. P. Wiederrecht, J. T. Hupp, *J. Am. Chem. Soc*. **2013**, *135*, 955.

5. a) V. M. Martinez, S. Furukawa, Y. Takashima, I. L. Arbeloa, S. Kitagawa, *J. Phys. Chem. C*. **2012**, *116*, 26084; b) V. M. Suresh, S. J. George, T. K. Maji, *Adv. Funct. Mater*. **2013**, *23*, 5585.

6. a) G. J. McManus, J. J. Perry IV, M. Perry, B. D. Wagner and M. J. Zaworotko, *J. Am. Chem. Soc.* **2007**, *129*, 9094; b) B. D. Wagner, G. J. McManus, B. Moulton, M. J. Zaworotko, *Chem. Commun.* **2002**, 2176.

7. D. Liu, K. Lu, C. Poon, W. Lin, *Inorg. Chem*. **2014**, *53*, 1916.

8. D. Yan, Y. Tang, H. Lin, D. Wang, *Sci. Rep*. **2014**, *4*, 4337.

9. SMART (V 5.628), SAINT (V 6.45a), XPREP, SHELXTL; Bruker AXS Inc. Madison, Wisconsin, USA, **2004**.

10. G. M. Sheldrick, Siemens Area Detector Absorption Correction Program, University of Götingen, Götingen, Germany, **1994**.

11. A. Altomare, G. Cascarano, C. Giacovazzo, A. Gualaradi, *J. Appl. Cryst*., **1993**, *26*, 343.

12. G. M. Sheldrick, SHELXL-97, Program for Crystal Structure Solution and Refinement; University of Götingen, Götingen, Germany, **1997**.

13. A. L. Spek. *J. Appl. Crystallogr*. **2003**, *36*, 7.

14. G. M. Sheldrick, SHELXS 97, Program for the Solution of Crystal Structure, University of Götingen, Germany, **1997**.

15. L. J. Farrugia, WinGX-A Windows Program for Crystal Structure Analysis, *J. Appl. Cryst*. **1999**, *32*, 837.

16. The sizes of the channels were calculated considering the van der Waals radii of the atoms.

17. a) V. A. Blatov, L. Carlucci, G. Ciani, D. M. Proserpio, *CrystEngComm*. **2004**, *6*, 377; b) V. A. Blatov, A. P. Shevchenko, V. N. Serezhkin, *J. Appl. Crystallogr*. **2000**, *33*, 1193.

18. C. E. Webster, R. S. Drago, M. C. Zerner, *J. Am. Chem. Soc*. **1998**, *120*, 5509.

19. a) T. Ahnfeldt, N. Guillou, D. Gunzelmann, I. Margiolaki, T. Loiseau, G. Férey, J. Senker, N. Stock, *Angew. Chem., Int. Ed*. **2009**, *48*, 5163; b) X.-Y. Chen, B. Zhao, W. Shi, J. Xia, P. Cheng, D.–Z. Liao, S.–P. Yan, Z.–H. Jiang, *Chem. Mater*. **2005**, *17*, 2866; c) A. L. Grzesia, F. J. Uribe, N. W. Ockwig, O. M. Yaghi, A. J. Matzger, *Angew. Chem., Int. Ed*. **2006**, *45*, 2553; d) X. Si, C. Jiao, F. Li, J. Zhang, S. Wang, S. Liu, Z. Li, L. Sun, F. Xu, Z. Gabelica, C. Schick, *Energy Environ Sci*. 2011, **4**, 4522; e) J. An, S. J. Geib, N. L. Rosi, *J. Am. Chem. Soc*. **2010**, *132*, 38; f) Y, Zhao, H. Wu, T. J. Emge, Q, Gong, N, Nijem, Y. S. Chabal, L. Kong, D. C. Langreth, H. Liu, H. Zeng, J. Li, *Chem. Eur. J*. **2011**, *17*, 5101; g) Z. Zhang, Y, Zhao, Q, Gong, J. Li, *Chem Commun*. **2013**, *49*, 653.

Chapter 3

Metal-organic complex and polymers: Study of photophysical properties, molecular recognition and separation

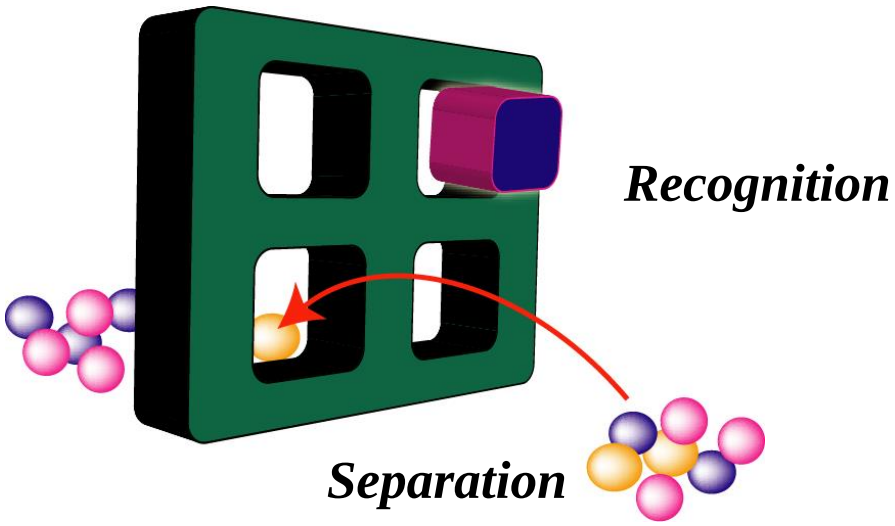

Part: 3A

Discrete and extended metal-organic structures: Study of charge transfer emission, molecular recognition and separation

Summary

This chapter reports a bottom up approach to build luminescent supramolecular nano pores for recognition and separation purposes. The synthetic concept borrowed from the last chapter was exploited for synthesis of a pyrene based molecular complex, {[Mg(*o*-phen)(H_2O)$_4$](2PBA)(H_2O)} (**1**) (PBA = Pyrene butyric acid; *o*-phen = 1,10-phenanthroline) which shows pyrene:*o*-phen exciplex emission. Further, this exciplex emission is sensitized *via* energy transfer process from a PBA monomer attached to the complex. In crystalline as well as in solution state (in benzene) the energy transfer process is equally efficient. Similar photophysical phenomenon is exploited in a supramolecular 3D structure, {[Zn(ndc)(*o*-phen)]·DMF}$_n$ (**2**) (ndc = 2,6-napthalenedicarboxylate) for various aromatic amine recognition. **2** has confined nanospaces that can accommodate different electron donating aromatic amine guests with selective turn-on emission signalling, ensuing a molecular recognition platform through the emission read out process. Such unprecedented tunable emission with different amines is attributed to its emissive CT complexation with *o*-phen linkers. In certain cases this CT emission is further amplified by energy transfer from the chromophoric linker ndc, as evidenced by proper structural characterization. Further, the nanospace of **2** shows excellent selectivity and separation capability for meta-xylene isomer among other xylene isomers (ortho and para). Structure determination through single crystal X-ray diffraction of the xylene adsorbed phase distinctly shows the preferential interactions with meta-xylene. Computational studies further validate the experimental observations.

1. R. Haldar, K. V. Rao, S. J. George, T. K. Maji, ***Chem. Eur. J***. **2012**, *18*, 5848.
2. R. Haldar, R. Matsuda, S. Kitagawa, S. J. George, T. K. Maji, ***Angew. Chem., Int. Ed.*** **2014**, *53*, 11772.
3. R. Haldar, S. Bonakala, S. Balasubramanian, T. K. Maji, To be submitted.

3A.1 Introduction

Supramolecular organization of donor and acceptor chromophores has been a prolific area of investigation, because of their crucial role in the excited state photophysical processes such as energy transfer and for the formation of excited state complexes (exciplex/excimer).[1] The development of artificial photosynthetic systems and extracting better performance for organic electronic devices definitely requires fundamental understanding of energy transfer in supramolecularly organized donor-acceptor assemblies.[2] On the other hand there has been an increased interest in the design of various exciplex based optoelectronic materials with the development of sensors and light emitting diodes.[3] However, an inorganic-organic hybrid approach towards this direction using metal-organic assembly in coordination complexes or extended frameworks is a relatively unexplored area.[4] The coordination driven spatial organization of chromophores appears to be advantageous, because such hybrid materials would exhibit interesting optoelectronic properties coupled with enhanced thermal and mechanical properties.[5] Furthermore, metal–directed self-assembly would constrain different donor-acceptor fluorophores in a close proximity and thus furnish rigidity in the lattice that are not typically observed for free organic molecule in solution. Keeping these advantages in mind, organic-inorganic design principle have been recently used for the synthesis of hybrid materials exhibiting efficient Förster resonance energy transfer[6] and tunable fluorescence properties.[7]

Along with the luminescence properties, another aspect of coordination polymers is porosity.[8] The bimodal nature of such porous luminescent coordination polymers can be useful for guest recognition/sensing or light harvesting applications.[9] Imparting flexibility in such materials can lead to adaptable behaviour towards encapsulating different guest molecules.[10] In this context, it can be perceived that porosity moulded by the soft supramolecular interactions (π-π or C-H$\cdots\pi$) between 1D coordination polymers consisting of aromatic linkers would be dynamic contrary to their higher dimensional counterparts formed solely by metal-linker coordination bonds. The unique guest/stimuli responsive behaviour of PCPs compared to conventional porous materials are advantageous for applications such as selective adsorption/separation, molecular recognition and sensing properties.[9,11] Such flexible nanospaces would allow the accommodation of various guest molecules through specific host-guest interactions. However chemical affinity of the coordination spaces limits the appropriate guest

inclusion and hence pore structure functionalization is crucial. Flexible nanospaces constructed from luminescent chromophoric organic linkers would also provide fast fluorescence readout of the dynamic recognition processes leading to sensory PCPs. This fluorescence transduction mechanism is highly sensitive to environment and hence accommodation of various guests in the nanospace can lead to either change in emission wavelength, enhanced/decreased intensity or even new emission as a result of charge transfer (CT) or exciplex/excimer formation.[12] All these features of a material can be used in recognition of carcinogenic analytes such as aromatic amines. Aromatic amines are of immense importance for syntheses of drugs and in the field of polymers but these are also carcinogenic to the human health.[13] Therefore easy detection and capture of aromatic amines are of paramount importance for health and environment. Furthermore, flexible PCPs can also be used for separation purposes. Separation of positional isomers, such as ortho/meta/para-xylenes is immensely important from industrial point of view and there is insufficient amount of work carried out to address this issue.[14] Still energy efficient separation process need to be developed. Adsorptive based separation is one of such energy efficient process where specific interaction between host and guest directs the selective uptake of a particular isomer in presence of other isomers.

In this chapter, a bottom up approach has been reported for design and synthesis of a discrete molecular complex to an extended porous framework and their different photophysical and adsorption properties. A molecular complex {[Mg(*o*-phen)(H_2O)$_4$](2PBA)(H_2O)} (**1**) (PBA=Pyrene butyric acid; *o*-phen=orthophenanthroline) shows bright pyrene:*o*-phen exciplex emission which is amplified by energy transfer (FRET) from a non-coordinated PBA monomer (Scheme

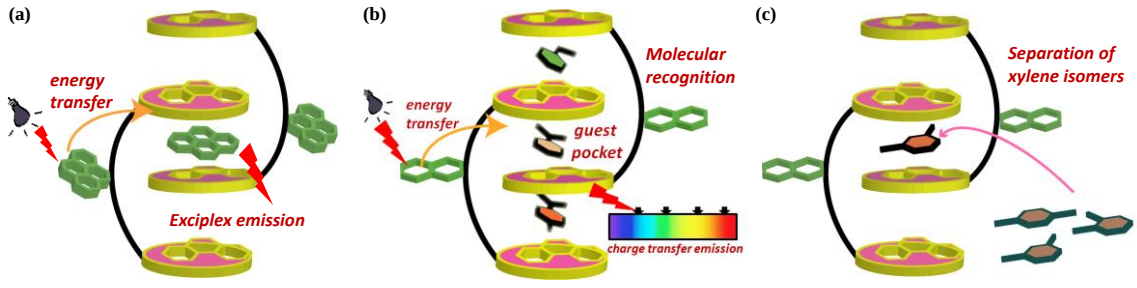

Scheme 1: (a) Schematic of a pyrene based exciplex sensitized through energy transfer from another pyrene; (b) Schematic of a fluorescent porous coordination polymer and its adaptable nanospace for recognition of aromatic guest through emission readout process; (c) Schematic of xylene isomers separation using a porous coordination polymer.

1a). {[Zn(ndc)(*o*-phen)]·DMF}$_n$ (**2**) (ndc = 2,6-napthalenedicarboxylate) is a 1D coordination polymer that self-assembles to a 3D porous supramolecular framework through non-covalent interactions. The framework contains 1D channels and exhibits guest responsive structural flexibility realized PXRD coupled CO_2 adsorption study and solvent vapour adsorption study. The structural dynamics and π-electron rich coordination nanospaces of **2** were exploited for the recognition of different aromatic amines; aniline (AN), *N*-methyl aniline (NMA), *N,N′*-dimethyl aniline (DMA) and *N,N′*-dimethyl-*p*-toluidine (DMPT) through visible and emission colour change (Scheme 1b). This selective turn-on emission with aromatic amines is attributed to charge transfer complexation of *o*-phen ligands with aromatic amines, which in certain cases is further sensitized by energy transfer from ndc chromophores, as evidenced by proper structural characterization. Such unprecedented turn-on aromatic amine recognition in PCPs is yet to be accounted. Further, the nanospace of **2** is also found to be efficient for separation of xylene isomers (Scheme 1c). Meta-xylene is found to be preferentially adsorbed by **2** over ortho and para isomers. Single crystal X-ray diffraction and density functional theory calculations give a proper insight into such unprecedented selectivity.

3A.2 Experimental Section

3A.2.1 Materials

All the reagents employed were commercially available and used as provided without further purification. $Mg(NO_3)_2·6H_2O$ and $Zn(NO_3)_2·6H_2O$ were obtained from Spectrochem; pyrene butyric acid, 2,6-naphthalene dicarboxylic acid, orthophenanthroline, aniline, *N*-methyl aniline, *N,N′*-dimethyl aniline, *N,N′*-dimethyl paratoluedene, nitrobenzene, toluene, cyanobenzene, iodobenzene, ortho-xylene (*o*X), meta-xylene (*m*X) and para-xylene (*p*X) were obtained from Sigma Aldrich chemicals.

3A.2.2 Physical Measurements

Elemental analyses were carried out using a Thermo Fischer Flash 2000 Elemental Analyzer. FT-IR spectra were recorded on a Bruker IFS 66v/S spectrophotometer using KBr pellets in the region 4000-400 cm^{-1}. Powder XRD pattern of the products were recorded by using Cu-K_α radiation (Bruker D8 Discover; 40 kV, 30 mA). Electronic absorption spectra were recorded on a Perkin Elmer Lambda 900 UV-VIS-NIR Spectrometer and emission spectra were recorded on Perkin Elmer Ls 55

Luminescence Spectrometer. UV-Vis and emission spectra were recorded in 1 mm path length cuvette. Fluorescence spectra were recorded in front face geometry with 350 nm excitation wavelength. NMR spectra were obtained with a Bruker AVANCE 400 (400 MHz) Fourier transform NMR spectrometer with chemical shifts reported in parts per million (ppm). Fluorescence decay was recorded in a time correlated single-photon counting spectrometer of Horiba-Jobin Yvon with 350-450 nm picosecond Ti-saphhire laser.

3A.2.3 Synthesis of {[Mg(*o*-phen)$(H_2O)_4$](2PBA)(H_2O)} (1)

An aqueous solution (25 mL) of PBA (1 mmol, 0.288 g) was mixed with a methanol solution (25 mL) of *o*-phen (1 mmol, 0.184 g) and stirred for 30 min to mix well. $Mg(NO_3)_2 \cdot 6H_2O$ (0.5 mmol, 0.146 g) was dissolved in 50 mL of water and then ligand solution (2 mL) was layered above the metal solution (2 mL) and after 5-6 days beautiful light yellow colour rod shaped crystals were found at the walls of the tube. Crystals were separated, washed with water and dried. A good quality single crystal was picked up from the mother liquor and immediately covered with paraffin oil and crystal data was collected at 293 K. The bulk compound is prepared by direct mixing of ligand solution and metal solution and phase purity was checked from the PXRD patterns (Figure 1). TG analysis was also carried out to see the thermal stability (Figure 2). Yield: 61%, relative to Mg. Anal. Calcd. for $C_{52}H_{48}MgN_2O_9$: C, 71.78; H, 5.52; N, 3.22. Found: C, 71.11; H, 5.17; N, 3.01. FT-IR (KBr pellet, 4000-400 cm^{-1}) (Figure 3): 3481(b), 3284(w), 2326(s), 2238(m), 2128(m), 1614(s), 1562(s), 1502(s), 1428(s), 1310(w), 1228(s), 1068(s), 1020(s), 912(w), 874(w), 820(s).

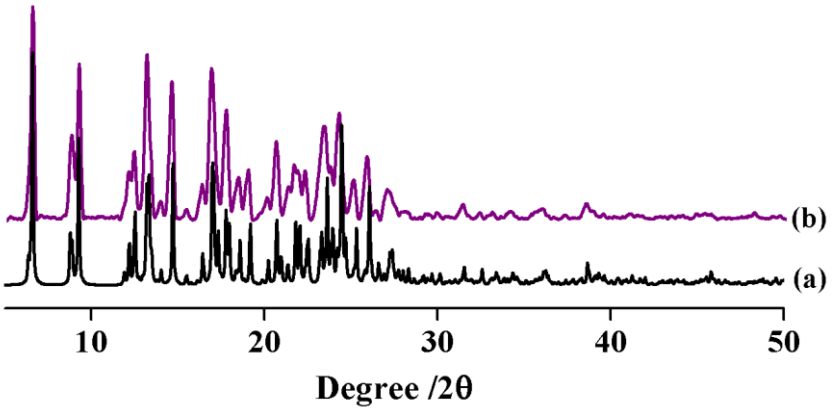

Figure 1: PXRD patterns of compound **1**: a) simulated, b) as-synthesized.

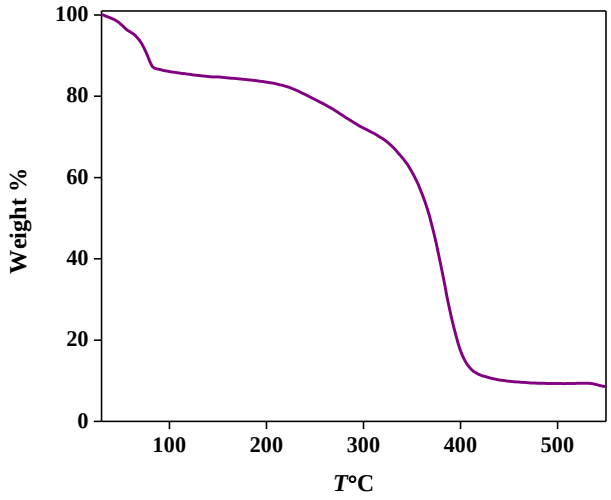

Figure 2: TG analysis of compound **1** with a heating rate of 3 °C/min under N_2 atmosphere.

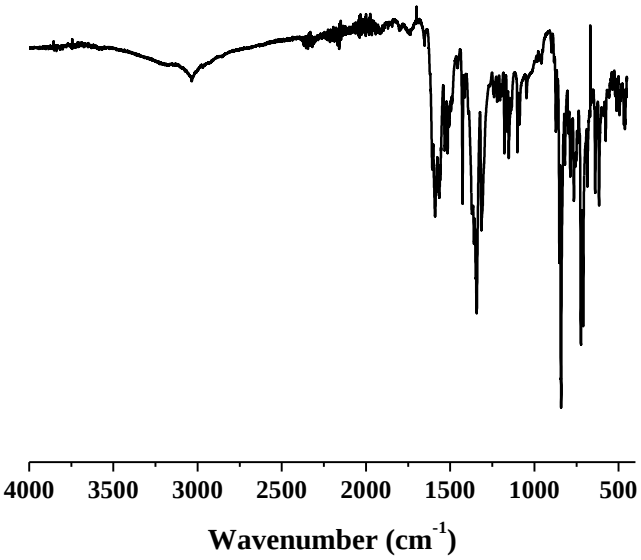

Figure 3: FT-IR spectrum of compound **1**.

3A.2.4 Synthesis of {[Zn(ndc)(*o*-phen)]·DMF)}$_n$ (2)

2,6-naphthalenedicarboxylic acid (0.022 g, 0.1 mmol) and orthophenanthroline (0.020 g, 0.1 mmol) were dissolved in 5 mL of dimethyl formamide and mixed well. 0.030 g (0.1 mmol) of $Zn(NO_3)_2 \cdot 6H_2O$ was added to the ligand solution and sonicated before the sealed glass vial was kept in an oven at 120 °C for 36 h. Good quality transparent crystals of **2** were isolated and washed with fresh DMF before taking for single-crystal X-ray diffraction measurement. Yield of **2**: 78 %; Anal. Calcd. for $C_{27}H_{21}N_3O_5Zn$: C, 60.91; H, 3.94; N, 7.89. Found C, 61.31; H, 4.13; N, 7.56. FT-IR (KBr pellet, 4000-400 cm^{-1}) (Figure 4): 3069(w), 2932(w), 1675(s), 1602(s), 1560(m), 1415(s), 1190(s), 1080(s), 930(s), 853(s), 793(s), 727(s), 645(s).

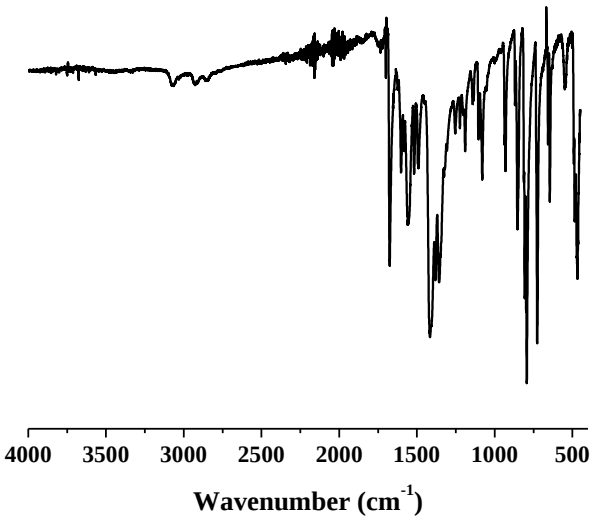

Figure 4: FT-IR spectrum of compound **2**.

3A.2.5 Syntheses of 2a-2h:

As-synthesized compound **2** was activated at 170 °C under vacuum for 18-20 h. This activated compound **2′** (0.030 g) was immersed in 2 mL of different solvents; such as aniline, *N*-methyl aniline, *N,N′*-dimethyl aniline, *N,N′*-dimethyl-*p*-toluidine, nitrobenzene, cyanobenzene and iodobenzene for 72 h to get **2a, 2b, 2c, 2d, 2f, 2g** and **2h**, respectively. These compounds were filtered, washed several times with DMF and dried under vacuum before doing PXRD and ^{1}H-NMR experiments (Figure 5-11).

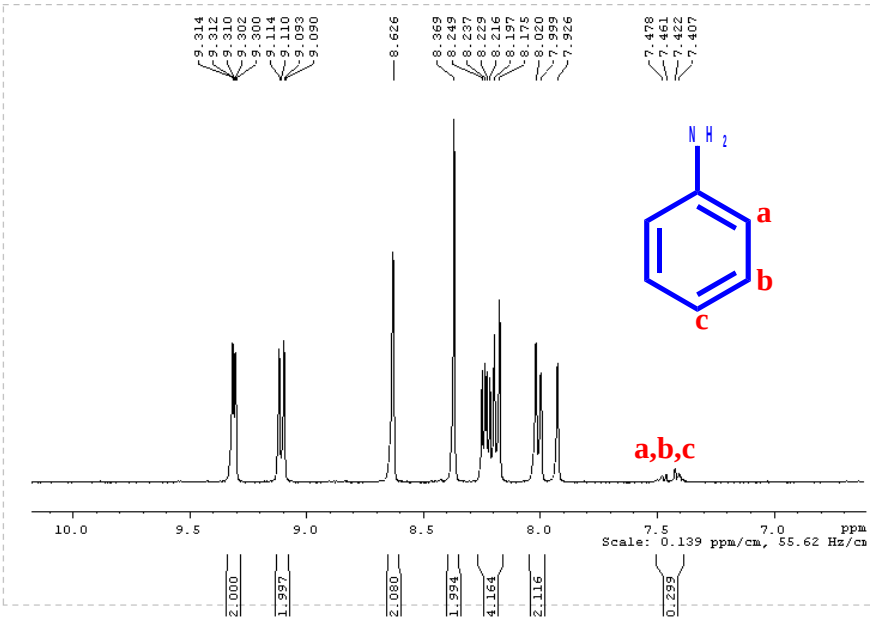

Figure 5: ^{1}H-NMR spectrum of compound **2a** in d_6-DMSO solvent.

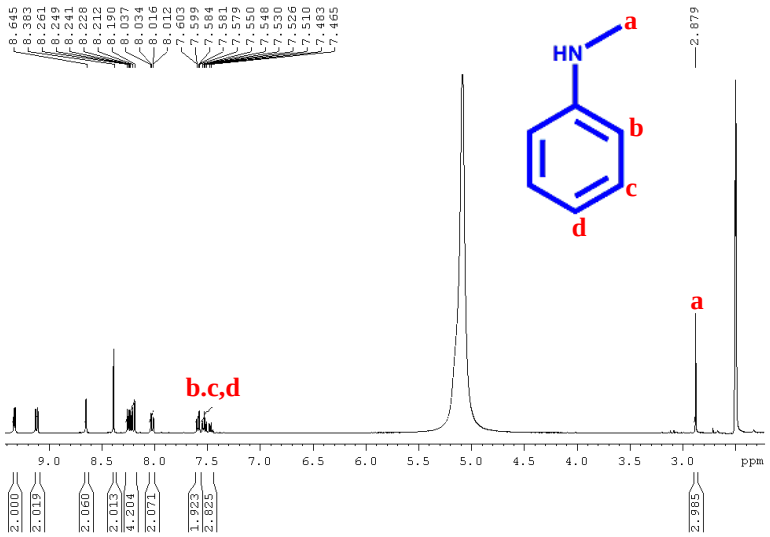

Figure 6: ^{1}H-NMR spectrum of compound **2b** in d_6-DMSO solvent.

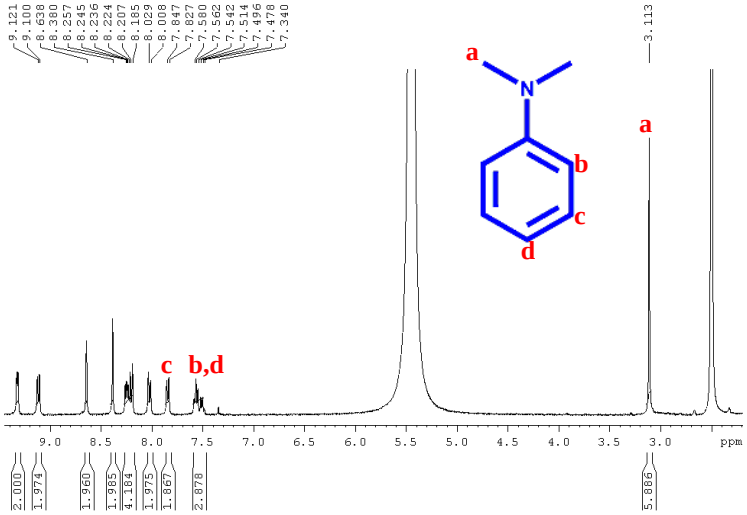

Figure 7: ^{1}H-NMR spectrum of compound **2c** in d_6-DMSO solvent.

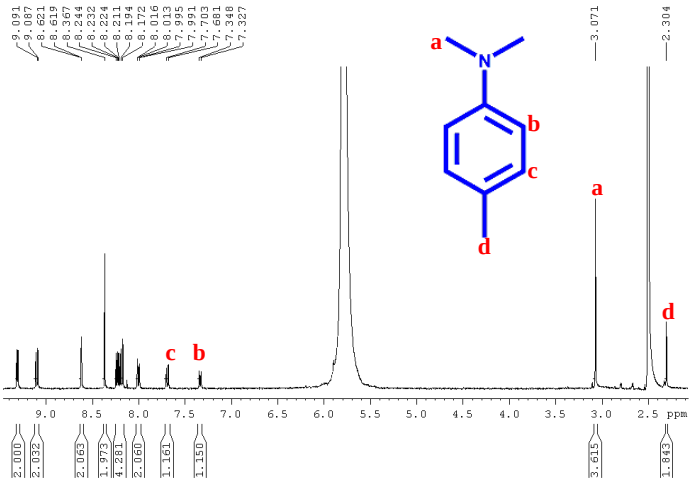

Figure 8: ^{1}H-NMR spectrum of compound **2d** in d_6-DMSO solvent.

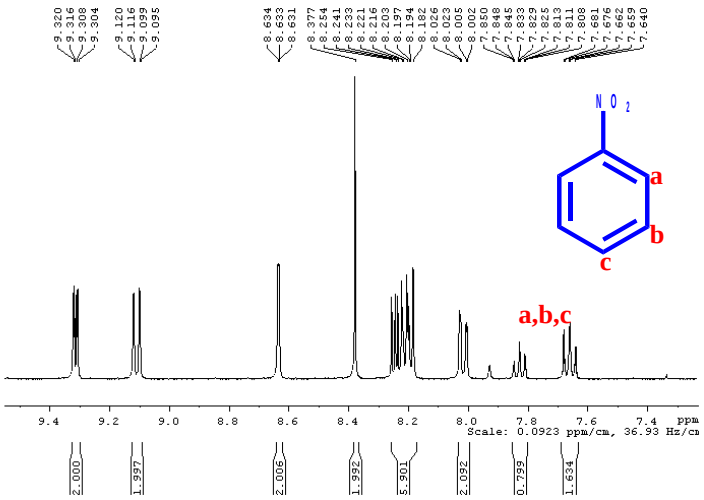

Figure 9: ^{1}H-NMR spectrum of compound **2f** in d_6-DMSO solvent.

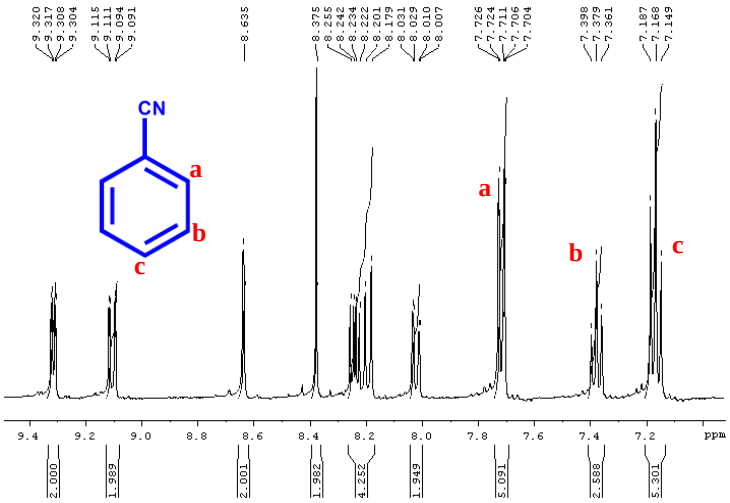

Figure 10: ^{1}H-NMR spectrum of compound **2g** in d_6-DMSO solvent.

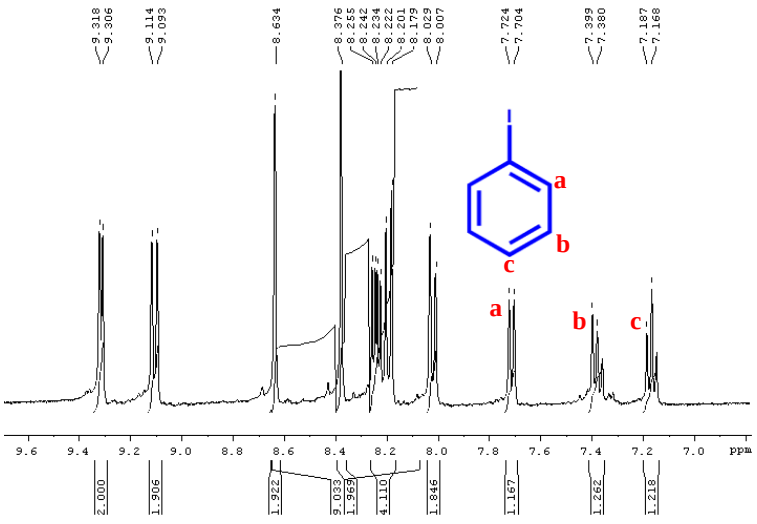

Figure 11: ^{1}H-NMR spectrum of compound **2h** in d_6-DMSO solvent.

3A.2.6 Syntheses of 2b′, 2c′, 2d′ and 2e:

2,6-naphthalenedicarboxylic acid (0.022 g, 0.1 mmol) and orthophenanthroline (0.020 g, 0.1 mmol) were dissolved in 5 mL of dimethyl formamide (DMF) and mixed well. 0.030 g (0.1 mmol) of $Zn(NO_3)_2 \cdot 6H_2O$ was added to the ligand solution and sonicated for 10 min. 1 mL of N-methylaniline was added to this clear solution before the sealed glass vial was kept in an oven at 120 °C for 36 h. Good quality light yellow color crystals of **2b′** were isolated and washed with fresh DMF before taking for single-crystal X-ray diffraction measurement. Yield of **2b′**: 72 %; Anal. Calcd. for $C_{31}H_{23}N_3O_4Zn$: C, 65.73; H, 4.06; N, 7.42. Found C, 65.98; H, 4.25; N, 7.11.

2c′, **2d′** and **2e** were synthesized following similar methodology except *N*-methylaniline was replaced by *N*,*N*′-dimethyl aniline, *N*,*N*′-dimethyl-*p*-toluedene and toluene, respectively. Yield of **2c′**: 69 %; Anal. Calcd. for $C_{32}H_{25}N_3O_4Zn$: C, 66.09; H, 4.30; N, 7.23. Found C, 65.71; H, 4.23; N, 7.56. Yield of **2d′**: 76 %; Anal. Calcd. for $C_{33}H_{27}N_3O_4Zn$: C, 68.16; H, 4.64; N, 7.23. Found C, 68.94; H, 4.60; N, 7.29. Yield of **2e**: 71 %; Anal. Calcd. for $C_{31}H_{22}N_2O_4Zn$: C, 67.40; H, 3.98; N, 5.07. Found C, 67.57; H, 3.91; N, 5.63.

3A.2.7 Syntheses of {[Zn(ndc)(*o*-phen)]·ortho-xylene)}$_n$ (3a), {[Zn(ndc)(*o*-phen)]·meta-xylene)}$_n$ (3b) and {[Zn(ndc)(*o*-phen)]·para-xylene)}$_n$ (3c)

2,6-naphthalenedicarboxylic acid (0.022 g, 0.1 mmol) and orthophenanthroline (0.020 g, 0.1 mmol) were dissolved in 5 mL of dimethyl formamide (DMF) and mixed well. 0.030 g (0.1 mmol) of $Zn(NO_3)_2 \cdot 6H_2O$ was added to the ligand solution and sonicated for 10 min. 1 mL of ortho-xylene was added to this clear solution before the sealed glass vial was kept in an oven at 120 °C for 36 h. Good quality light yellow color crystals of **3a** were isolated and washed with fresh DMF before taking for single-crystal X-ray diffraction measurement. Yield of **3a**: 72 %; Anal. Calcd. for $C_{31}H_{23}N_3O_4Zn$: C, 65.73; H, 4.06; N, 7.42. Found C, 65.98; H, 4.25; N, 7.11.

3b and **3c** were synthesized following similar methodology except ortho-xylene was replaced by meta-xylene and para-xylene, respectively. Yield of **3b**: 69 %; Anal. Calcd. for $C_{32}H_{25}N_3O_4Zn$: C, 66.09; H, 4.30; N, 7.23. Found C, 65.71; H, 4.23; N, 7.56. Yield of **3c**: 76 %; Anal. Calcd. for $C_{33}H_{27}N_3O_4Zn$: C, 68.16; H, 4.64; N, 7.23. Found C, 68.94; H, 4.60; N, 7.29.

3A.2.8 X-ray Crystallography

X-ray single crystal structural data of **1**, **2**, **2b′**, **2c′**, **2d′**, **2e**, **3a**, **3b**, **3c** were collected on a Bruker Smart-CCD diffractometer equipped with a normal focus, 2.4 kW sealed tube X-ray source with graphite monochromated Mo-*Kα* radiation (λ = 0.71073 Å) operating at 50 kV and 30 mA. The program SAINT[15] was used for integration of diffraction profiles and absorption correction was made with SADABS[16] program. All the structures were solved by SIR 92[17] and refined by full matrix least square method using SHELXL-97.[18] All the hydrogen atoms were geometrically defixed and placed in ideal positions. All crystallographic and structure refinement data of **1**, **2**, **2b′**, **2c′**, **2d′**, **2e**, **3a**, **3b**, **3c** are summarized in the respective sections. Selected bond lengths and angles for **1**, **2**, **2b′**, **2c′**, **2d′**, **2e**, **3a**, **3b**, **3c** are given in the respective sections. All calculations were carried out using SHELXL 97,[18] PLATON,[19] SHELXS 97[20] and WinGX system, Ver 1.70.01.[21]

3A.2.9 Adsorption study

Adsorption isotherms of CO_2 (195 K) H_2 and N_2 (77 K) were recorded using the dehydrated samples of **2** (**2′**) by using a QUANTACHROME QUADRASORB-*SI* analyzer. In the sample tube the adsorbent samples (~ 100-150 mg) were placed which had been prepared at 170 °C under a 1×10^{-1} Pa vacuum for about 12 h prior to measurement of the isotherms. Helium gas (99.999% purity) at a certain pressure was introduced in the gas chamber and allowed to diffuse into the sample chamber by opening the valve. The amount of gas adsorbed was calculated from the pressure difference (P_{cal}-P_e), where P_{cal} is the calculated pressure with no gas adsorption and P_e is the observed equilibrium pressure. All the operations were computer-controlled.

The PXRD coupled adsorption measurements were carried out using on a Rigaku Ultima-IV with Cu-Kα radiation connected with BELSORP-18 volumetric adsorption equipment (BEL Japan Inc.).

Adsorption isotherms of benzene and xylene vapours at 298 K and kinetics of xylene isomers were measured for the dehydrated **2** (**2′**) by using a BELSORP-aqua-3 analyzer. A sample of about ~ 100–150 mg was prepared by heating at 170 °C for about 12 h under vacuum (1×10^{-1} Pa) prior to measurement of the isotherms. The solvent molecules used to generate the vapour were degassed fully by repeated evacuation. Dead volume was measured with helium gas. The adsorbate was placed into the sample tube,

then the change of the pressure was monitored and the degree of adsorption was determined by the decrease in pressure at the equilibrium state. All operations were computer controlled and automatic.

3A.2.10 Computational details

Periodic density functional theory calculations (DFT) were performed using CP2K software.[22] Cell parameter and geometry optimization were carried out the QUICKSTEP module of CP2K. Optimization calculations were carried out for the following systems (with the size of supercells in parantheses): meta-xylene (2×2×1), para-xylene (2×1×1) and ortho-xylene (2×1×1). The valence electrons were treated with either the BLYP functional in a double zeta basis set[23-25] or the PBE functional. In addition, empirical van der Waals correction prescribed by Grimme (both D2 and D3 varieties) were adopted.[26] Electron density was described with an energy cut off of 280 Ry and the effect of core electrons and nuclei were represented using norm-conserving pseudopotentials of Goedecker-Teter-Hutter.[27] The component of maximum forces on every atom during cell parameter and geometry optimization was fixed to be less than 4.5×10^{-4}. The optimized cell parameters, energy density and binding energy are described in the respective section. Various DFT functionals were employed to identify their performance in reproducing the experimental crystal structure. Binding energy was calculated as: $\Delta E = E(PCP+Xylene) – E(PCP) – E(Xylene)$.

3A.3 Results and Discussion

3A.3.1 Structural description of {[Mg(*o*-phen)(H_2O)$_4$](2PBA)(H_2O)} (1)

Compound **1** crystallizes in monoclinic $P2_1/n$ space group (Table 1). Here, Mg^{2+} was chosen as the metal ion for the co-ordination directed assembly, as it possesses a [Ne] electronic configuration and therefore does not significantly quench the fluorescence emission of PBA. X-ray single crystal structure determination reveals that discrete molecular complex of Mg^{2+} is chelated to one *o*-phen and connected to other four water molecules (Figure 12). The two PBA carboxylates (PBA1 and PBA2) are non-coordinated and neutralize the charge of the $[Mg(o\text{-phen})(H_2O)_4]^{2+}$ complex. The Mg^{2+}-N and Mg^{2+}-O bond distances are in the range of 2.221(4)–2.254(3) Å and 2.027(3)–2.037(3) Å, respectively (Table 2). The degree of distortion from the ideal octahedral geometry of Mg^{2+} is reflected in the *cisoid* (range 74.25(11)–100.95(12)°) and *transoid*

angles (range 165.37(13)–177.73(13)°) (Table 2). The PBA1 are intercalated between the cationic complex $[Mg(o\text{-phen})(H_2O)_4]^{2+}$ through π···π interactions with the *o*-phen (cg···cg distances are in the range of 3.697(4)-4.466(4) Å) resulting in a 1D supramolecular array along the crystallographic *b*-axis (Figure 13a). The carboxylate group of PBA1 alternatively connects two cationic complexes *via* H-bonding interactions with the coordinated water molecules (O1···O1w/O4w (in the range of 1.795-1.895 Å) providing extra stability and support to the 1D supramolecular chains (Figure 13a). Two such 1D chains interact in a face-to-face manner endorsed by bifurcated H-bonding interactions between carboxylate oxygen (O4) of another PBA (*i.e* PBA2) and coordinated water molecules (O3w) (1.804-1.855 Å) of two different chains ensuing a double 1D chain like structure (Figure 13b). The double 1D chains are further linked by guest water molecules O5w through H-bonding interactions with the coordinated water molecules O2w and carboxylate oxygen O2 from PBA1 resulting a 2D bilayer galleries where PBA2 is intercalated between 1D chains. PBA2 is oriented perpendicular to PBA1, which is supported by several C-H···π interactions (3.155-4.408 Å) (Figure 14). The nearest neighbour $Mg^{2+}\cdots Mg^{2+}$ distance in the 1D H-bonded chain and between the chains are 7.559 and 7.203 Å, respectively.

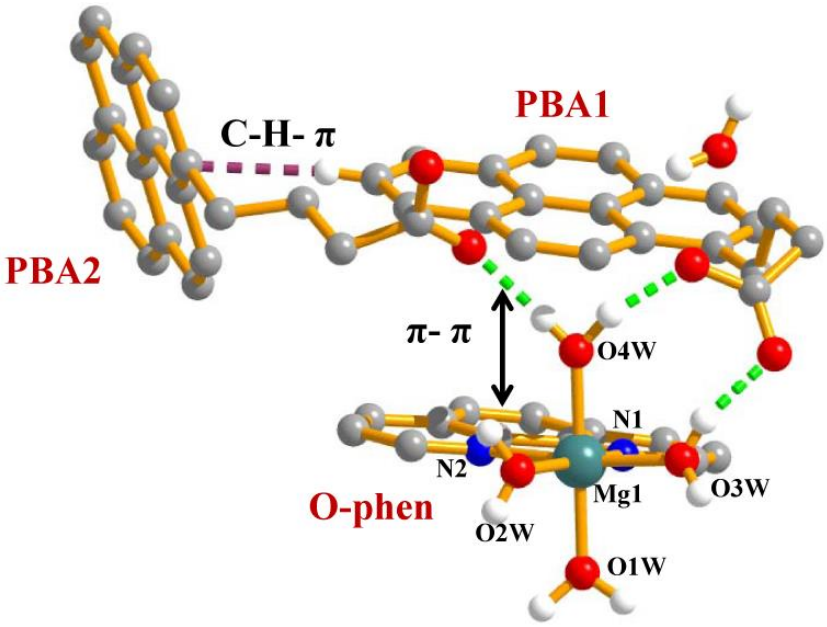

Figure 12: View of the asymmetric unit of **1** showing the orientation and assembly of PBA1, PBA2 and *o*-phen. (Dotted lines indicate H-bonds).

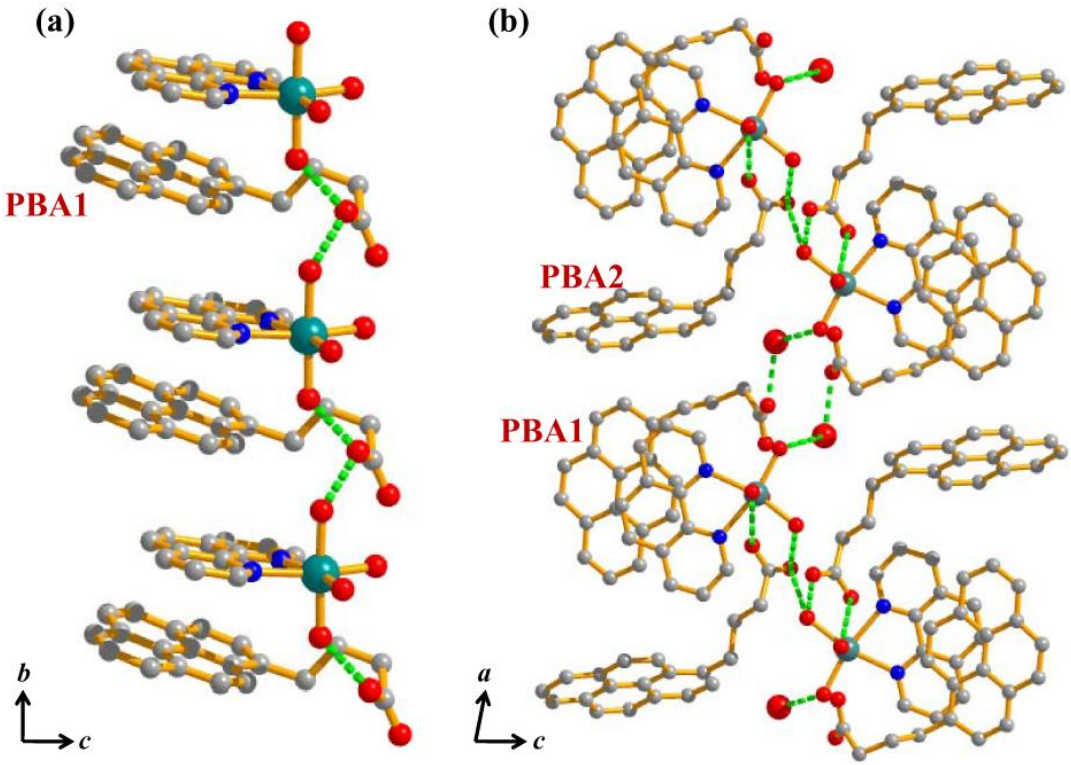

Figure 13: (a) 1D chain formed by π···π stacking of PBA1 and *o*-phen along *b*-axis. The chain is supported by H-bonding interactions of the pyrene carboxylate groups with the coordinated water molecules; (b) Top view of the PBA1-*o*-phen π-stacked columns, which are separated by orthogonally oriented PBA2 molecules. The guest water molecules and PBA2 help to grow 1D chain to higher dimension.

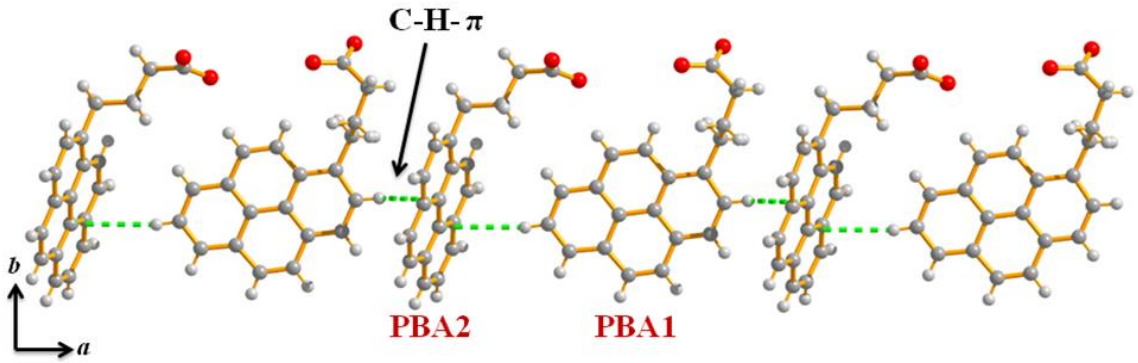

Figure 14: C-H···π interaction between two different **PBA** molecules of **1** along *a*-axis.

Table 1: Crystal data and structure refinement parameters of compound **1**.

Parameters	**1**
Empirical formula	$C_{52}H_{48}N_2MgO_9$
M	869.23
Crystal system	Monoclinic
Space group	$P2_1/n$ (14)
***a* (Å)**	14.527(5)
***b* (Å)**	7.559(5)
***c* (Å)**	39.797(5)
***β* (deg)**	93.069(5)
***V* (Å^3)**	4364(3)
Z	4
***T*(K)**	293
***λ* (Mo K$_α$)**	0.71073
***D*$_c$ (g cm^{-3})**	1.441
***μ* (mm^{-1})**	0.103
***θ*$_{max}$ (deg)**	32.110
total data	106131
unique reflection	15220
***R*$_{int}$**	0.215
data [*I* > 2σ(*I*)]	4929
***R*^{a}**	0.0826
***R*$_w$^{b}**	0.2602
GOF	0.96

^{a} $R = \Sigma||F_o| - |F_c||/\Sigma|F_o|$. ^{b} $R_w = [\Sigma\{w(F_o^2 - F_c^2)^2\}/\Sigma\{w(F_o^2)^2\}]^{1/2}$.

Table 2: Selected bond lengths (Å) and angles (°) for **1**.

Mg1-N2	2.221(4)	Mg1-O3W	2.032(3)
Mg1-O1W	2.037(3)	Mg1-O2W	2.027(3)
Mg1-O4W	2.030(3)	Mg1-N1	2.254(3)
O1W-Mg1-N2	90.75(12)	O2W-Mg1-N1	165.37(13)
O2W-Mg1-O3W	100.95(12)	O2W-Mg1-N2	92.15(12)
O3W-Mg1-N1	92.89(11)	O3W-Mg1-O4W	90.81(11)
O4W-Mg1-N1	85.72(11)	O3W-Mg1-N2	166.73(12)
N1-Mg1-N2	74.25(11)	O4W-Mg1-N2	91.45(12)

O1W-Mg1-O3W	87.18(11)	O1W-Mg1-O2W	90.04(12)
O1W-Mg1-N1	95.41(11)	O1W-Mg1-O4W	177.73(13)
O2W-Mg1-O4W	89.33(12)		

3A.3.2 Photophysical properties of 1: Exciplex emission and energy transfer

In the solid state, compound **1** has a broad absorption spectrum with subtle difference from that of free PBA and *o*-phen (Figure 15a). Upon excitation of **1** at 345 nm, it does not show any emission corresponding to PBA monomer or *o*-phen, rather a red shifted broad featureless emission at 452 nm was observed (Figure 15b). The broad and structureless features of the emission band are diagnostic of intermolecular exciplex emission and are similar to the exciplex fluorescence of analogous pyrene-bipyridine complexes.[12e] This exciplex formation can be envisaged to have formed by the self-assembly of PBA1 and *o*-phen into π···π stacked 1-D columns in [{Mg(*o*-phen)$(H_2O)_4$}(PBA1)}]$^+$ as indicated by the corresponding absorption changes. Evidently, between PBA1 and *o*-phen a 1:1 complex has been formed where PBA1 acts as a donor and coordinated *o*-phen as an acceptor chromophore. The crystal structure clearly advocates that the *o*-phen and PBA1 which are in close vicinity are in perfect spatial disposition to make such kind of donor–acceptor π-complex (exciplex), in an analogous way to previous reports of excimer/exciplex formation upon excitation of van der Waals dimers of aromatic molecules.[28] In addition, the excitation spectrum collected at the exciplex emission (λ_{mon} = 452 nm), showed a maximum at 370 nm, which is red-shifted compared to the spectrum (λ_{max} = 332 nm) collected at the monomer pyrene emission (λ_{mon} = 378 nm), indicating the preassociated nature of the pyrene and phenanthroline chromophores in the ground state (Figure 15b-c).[29] Time-resolved single photon counting experiments of the crystals of **1** upon excitation at 345 nm and monitoring the emission at 454 nm (Figure 15d) showed long lived bi-exponential decay (τ_1 = 0.32 ns (6%), τ_2 = 6.9 ns (94%)). The long lifetime is substantially high, which might not have formed within the life time of the excited state but rather arise from the preassociated chromophores in the one-dimensional assemblies. This further reiterates the preassociated nature of the exciplex formed. The exciplex emission showed by compound **1** is blue shifted (452 nm) compared to that of earlier reported exciplexes based on pyrene or pyrene derivatives

with aromatic compound having N-atom, which could be due to a slight off-set in the co-facial organization of donor and acceptor molecules in the present case. For example 1:1 and 2:1 bipyridine/pyrene complexes and 1:1 di-methylaniline/pyrene complex which show emission maxima at 520 nm, 540 nm and 496 nm respectively.[12e,30]

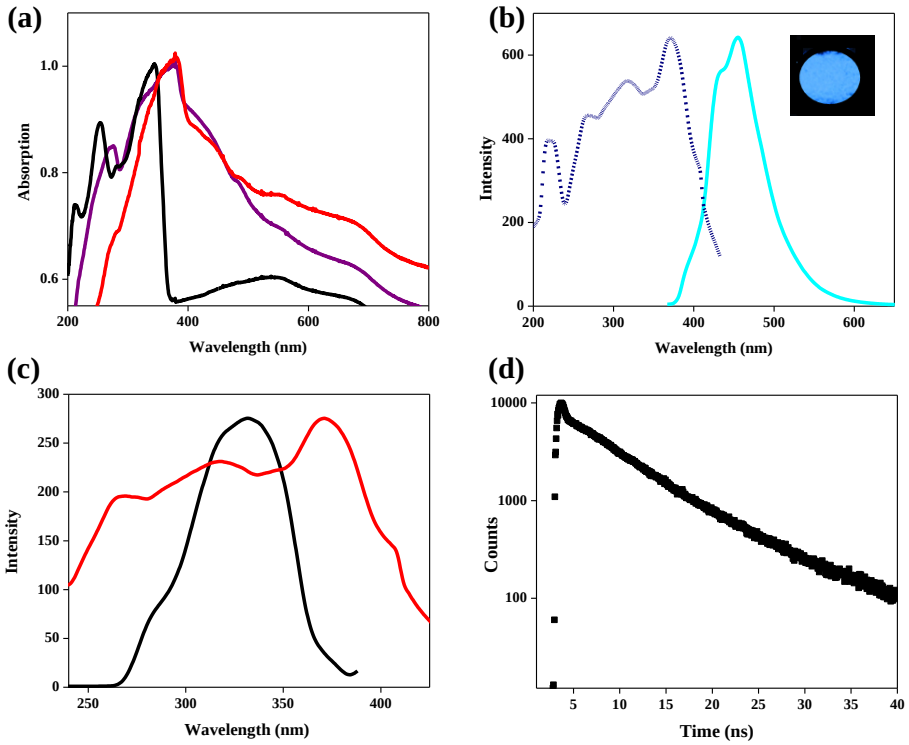

Figure 15: (a) Absorption spectrum of compound **1** (purple), free PBA (red) and *o*-phen (black); (b) Excitation spectrum (monitored at 452 nm, dotted lines) and emission spectrum (λ_{ex} = 345 nm) of the crystals of **1**, Inset shows the photograph of the powder of **1** under UV light; (c) Excitation spectrum (red) of compound **1** monitored at the exciplex emission (λ_{mon}= 452 nm) and PBA monomer emission (black) (λ_{mon}= 378 nm) in benzene solution; (d) Fluorescence lifetime decay profile of **1** (λ_{ex} = 345 nm) while monitoring the emission at 454 nm.

Surprisingly, emission corresponding to the pyrene monomer emission (378 nm) is quenched in **1**, despite the presence of isolated PBA2 chromophore in extended arrays, which does not interact with *o*-phen and undergoes only weak edge-to-face C-H$\cdots\pi$ interaction with PBA1. The quenching of PBA2 emission can be considered due to self-absorption at higher concentrations or due to energy transfer process from the PBA2 to the exciplex formed by PBA1-*o*-phen 1:1 complex in the 1-D self-assembled array. However, the possibility of quenching of emission due to self-absorption is ruled out by performing fluorescence measurements with front-face geometry and by the controlled measurements of the complex **1** in solution. In light of this, energy transfer can be considered as a possible cause for the absence of characteristic PBA2 emission in **1**,

which is further supported by the perfect spectral overlap of the excitation spectra of **1** with that of typical PBA monomer emission as shown in Figure 16a. (In benzene solution: Figure 16b; discussed in the next paragraph). This type of complex excited process in coordination complex is unprecedented.

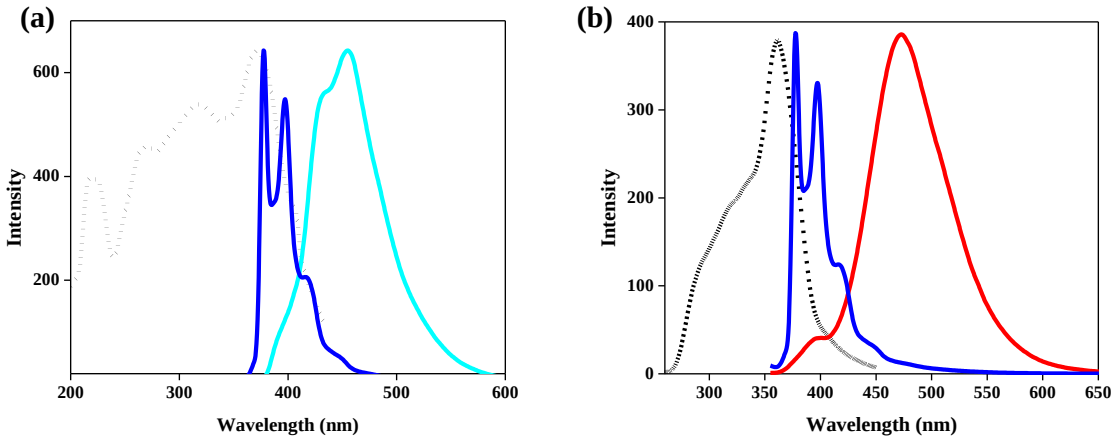

Figure 16: Overlap of emission spectrum of PBA monomer (λ_{ex} = 345 nm) (blue) with excitation spectrum of **1** (black dotted line) in (a) solid state and (b) benzene solution; Cyan line in (a) and red line in (b) are the emission spectra in solid and solution state, respectively.

Further photophysical properties of **1** were studied in different solvents to see the effect of polarity on the stability of the complex and the exciplex emission. Interestingly in non-polar aromatic solvents like benzene, toluene and xylene the exciplex emission is retained, (Figure 17) indicating that the complex is stable in solution, although the extended 1D columns may be absent. In benzene the exciplex emission of **1** is more intense and slightly red shifted (λ_{em} = 472 nm) compared to that of in the crystal, when excited at 345 nm. This could be due to the enhanced π···π interaction between PBA1 and *o*-phen as a result of solvophobic interaction by non-polar aromatic solvent molecules. The formation of this stable exciplex in benzene solution is further evident from the time-resolved emission measurements which showed a life-time of 11 ns when monitored at 480 nm, which is higher than that of observed in the solid state (Figure 17; inset a). Furthermore, in benzene solution the characteristic vibronic bands of PBA is absent rather a featureless small hump appears at around 400 nm. This again indicates that PBA2 is indeed a part of the complex and that energy transfer from this pyrene to the exciplex occurs even in the solution state (Figure 16b). The stability and integrity of the compound **1** in solution could be further proved by NOESY experiments in C_6D_6 which showed through space interactions between PBA1 and *o*-phen and PBA1 and PBA2 (Figure 18-19). The sharp peaks of **1** from the ^{1}H-NMR spectra in C_6D_6, further suggest that the **1** exists in solution as a discrete entity rather than an extended array as in the solid state.

The integrity of the complex in solution is further confirmed by the mass-spectroscopy analysis. MALDI-TOF-MS spectrum of the **1**, made from toluene solution showed the presence of stable complex, with all the chromophores intact (Figure 20). On the other hand, NOESY experiments in CD_3OD confirm the instability of **1** in polar solvents (Figure 21). MALDI-TOF-MS spectrum of the **1**, in another polar solvent acetonitrile clearly shows the fragmented portions (Figure 22).

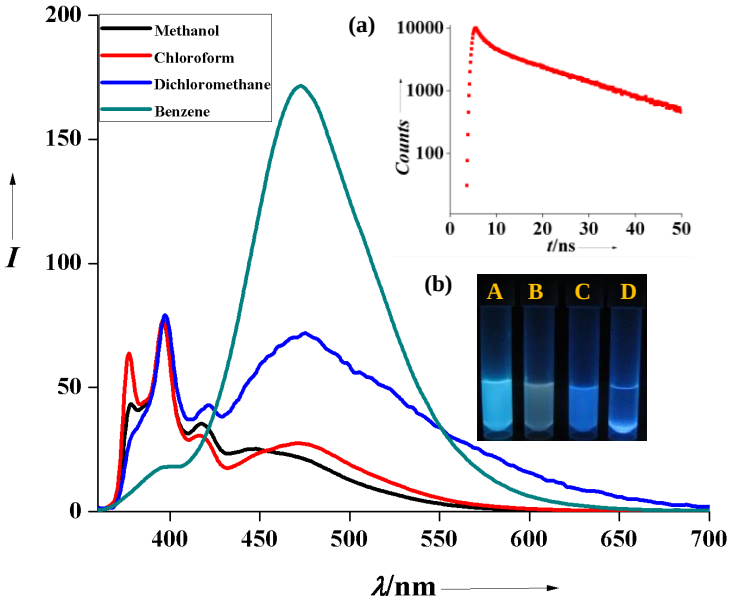

Figure 17: Emission spectra of compound **1** (λ_{ex} = 345 nm) in different solvents. Inset figure a) Fluorescence lifetime decay profile of **1** in benzene (λ_{ex} = 345 nm) while monitoring the emission at 480 nm, b) Photographs of compound **1** in different solvents under UV light: a) Benzene, b) Dichloromethane, c) Methanol, d) Chloroform.

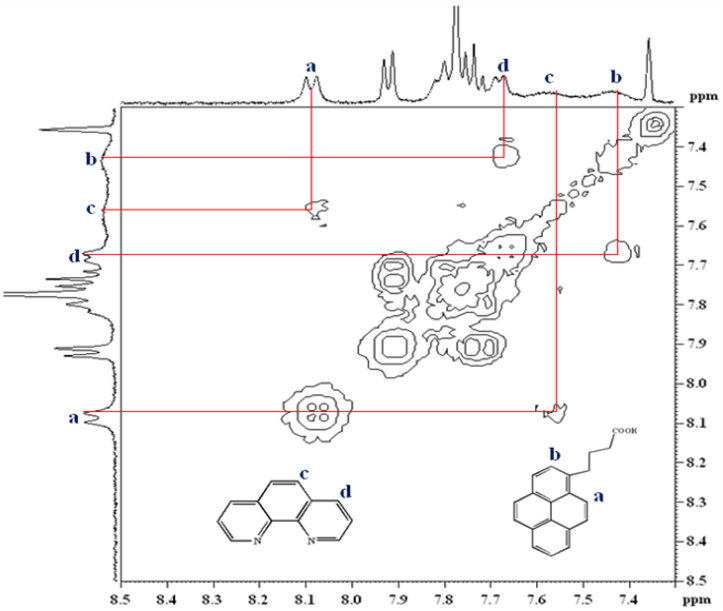

Figure 18: NOESY spectra of compound **1** in C_6D_6 solvent.

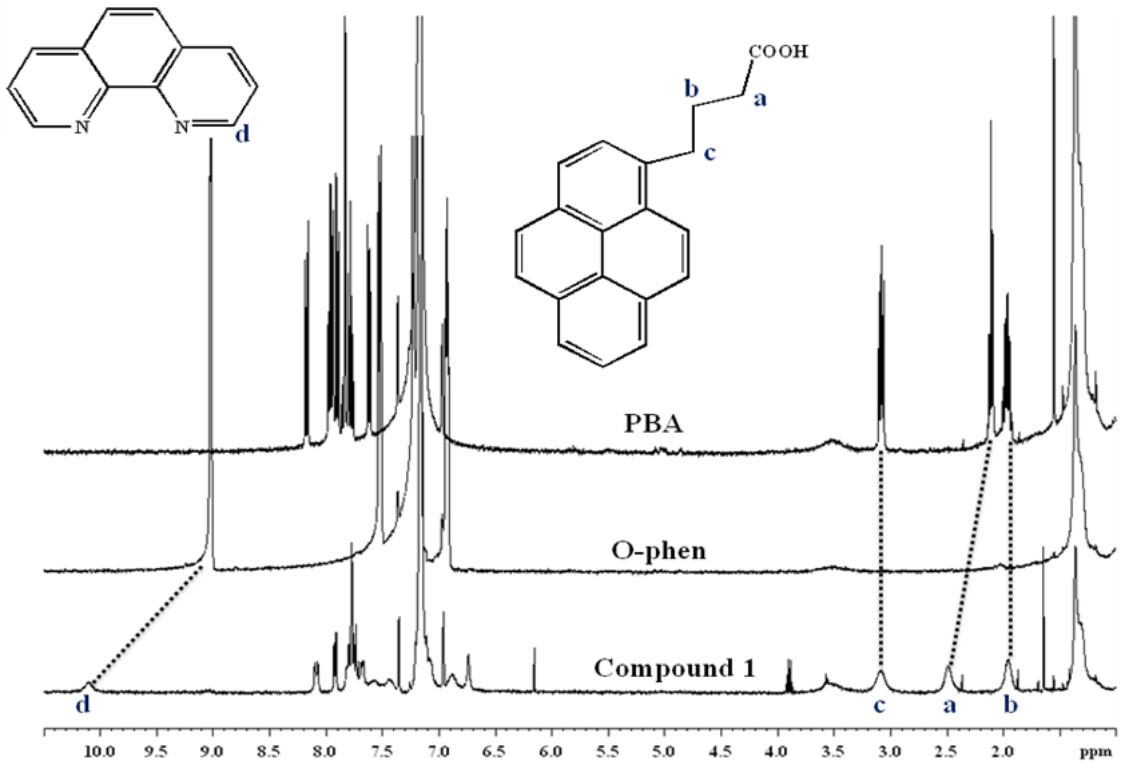

Figure 19: ^{1}H-NMR spectra of compound **1** with relative shifting of peaks from free PBA and *o*-phen in C_6D_6 solvent.

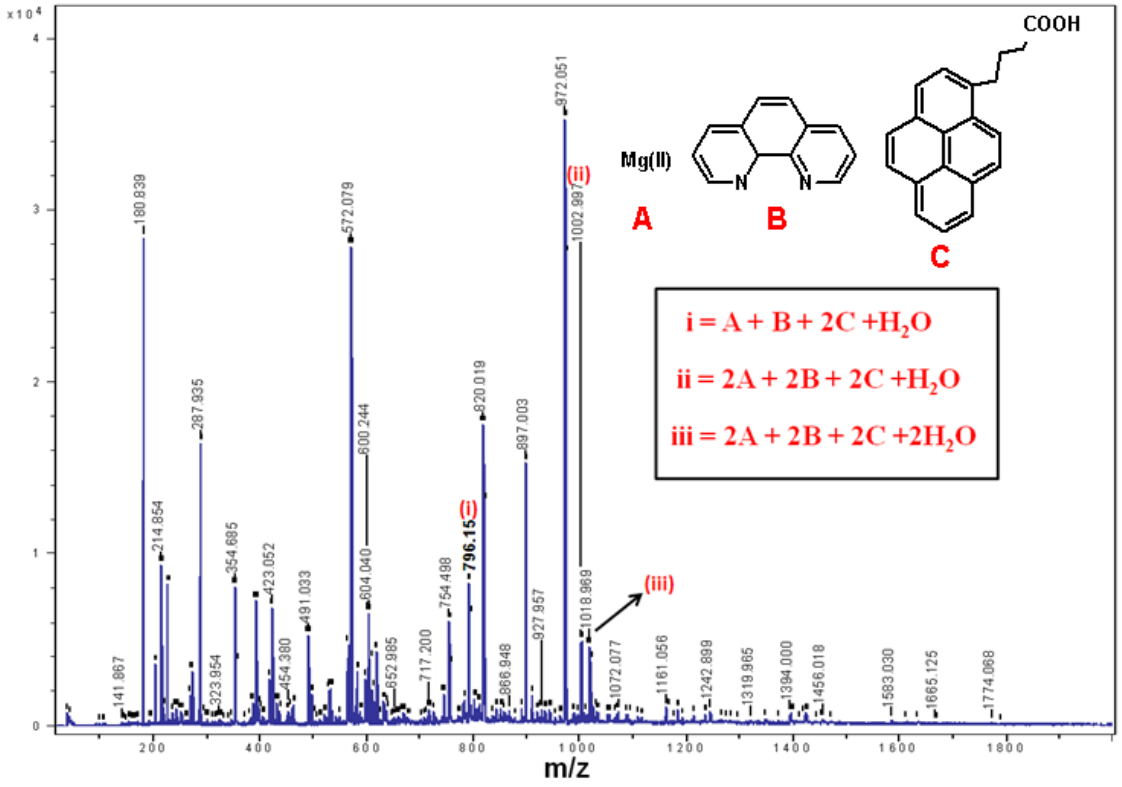

Figure 20: MALDI-TOF-MS spectrum of compound **1** in toluene showing the masses corresponding to different associated molecular complexes.

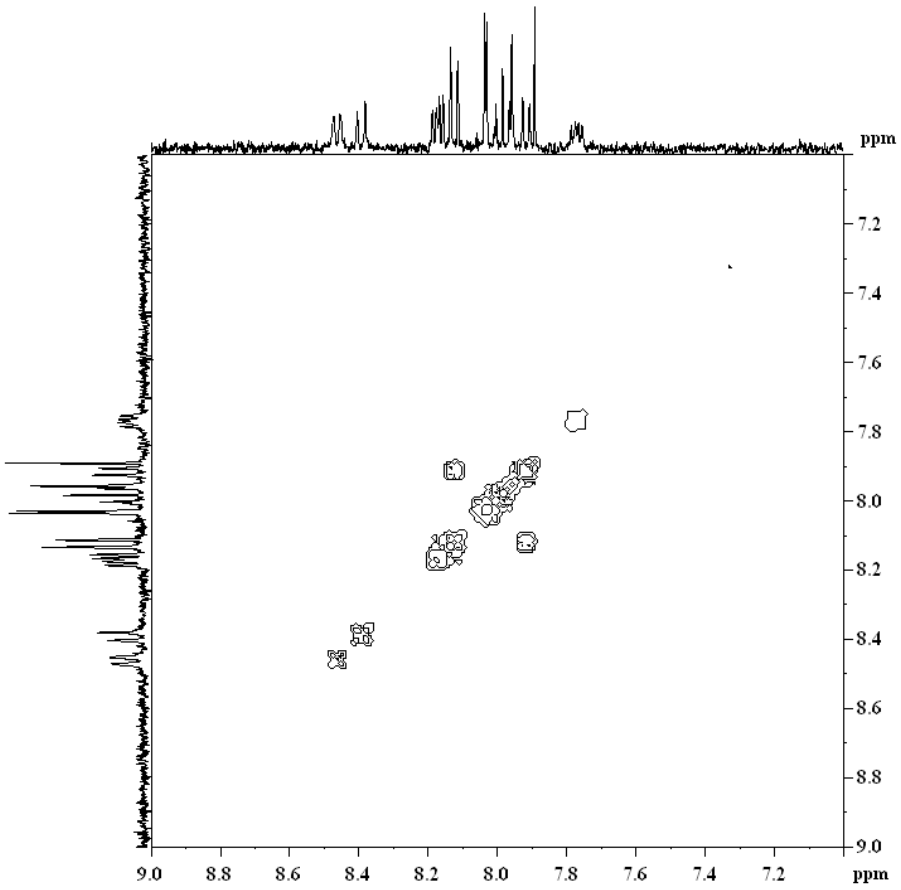

Figure 21: NOESY spectra of compound **1** in CD_3OD solvent.

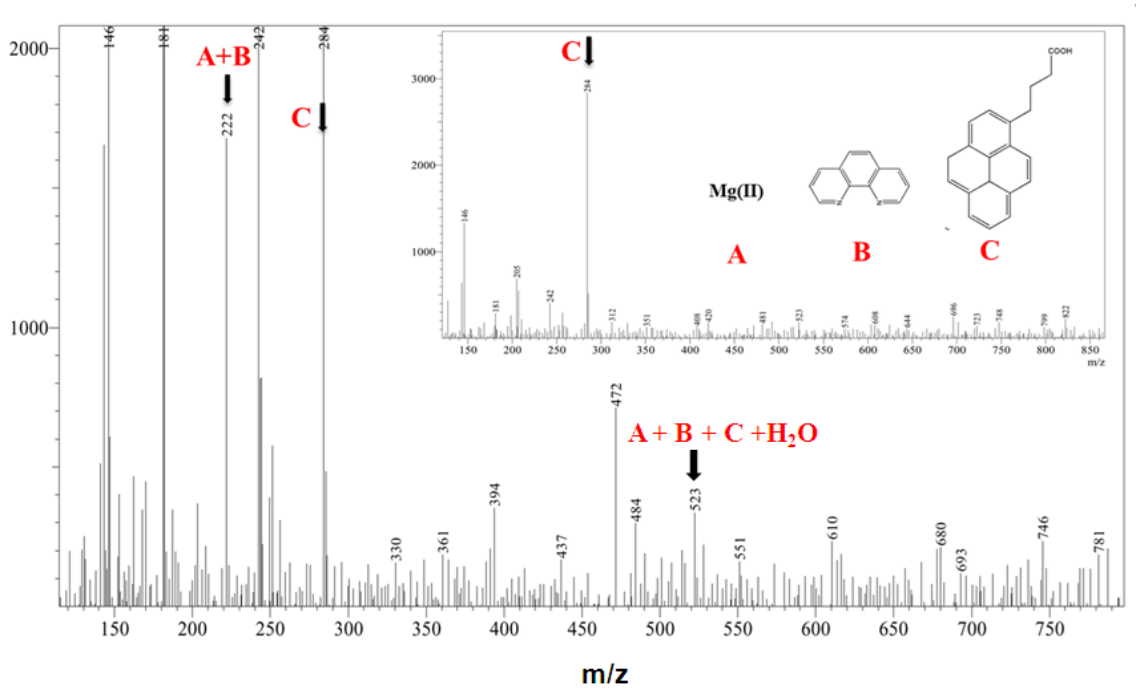

Figure 22: ESI-MS spectra of compound **1** in acetonitrile. (Inset figure shows spectrum of only pyrene butyric acid).

To support our hypothesis of energy transfer from PBA2 to the exciplex emission titration of PBA versus compound **1** solution in benzene was done. A 10^{-6} M benzene solution of PBA was quantitatively added to the benzene (10^{-6} M) solution of **1** and the corresponding emission spectra were measured. With the increase of free PBA in the benzene solution of **1**, the intensity of PBA monomer emission (λ_{em} = 395 nm) increases linearly and the intensity of exciplex emission remains same. A plot of the optical density increase versus the intensity of emission at 378 nm shows a straight line (Figure 23) which indicates that additionally added PBA does not have any contribution to the exciplex emission properties of **1**. This experiment unequivocally proves that the PBA2 is indeed in the complexed state in solution and exists in its quenched state due to the energy transfer to the exciplex state.

The association constant of complex **1** in benzene was found to be very high. This is evident from the dilution experiments of **1** in benzene, which showed the appearance of free PBA emission, characteristic of the breaking of the complex, only at very low concentrations (>2 × 10^{-6} M) (Figure 24). This breaking up of the complex at lower concentrations is also evident from the time resolved emission decay profiles which showed a fast decay component (0.73 ns, 81%) corresponding to the free pyrene emission, apart from the exciplex life time (9.7 ns, 19%) (Figure 24 inset). Similarly, in polar solvents like MeOH, $CHCl_3$ and CH_2Cl_2 compound **1** shows monomer emission of PBA and the corresponding intensity of exciplex emission significantly decreases indicating that the compound is unstable in such polar protic or aprotic solvents (Figure 17).

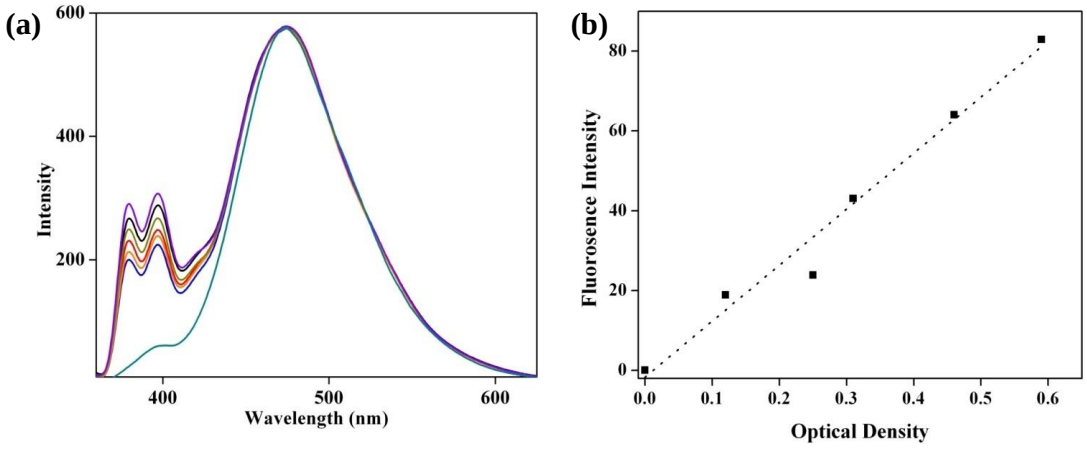

Figure 24: (a) Emission spectra recorded on 345 nm excitation by the successive addition of 10^{-6} (M) benzene solution of **PBA** to 10^{-6} (M) benzene solution of compound **1**; (b) Plot of excess optical density of added PBA monomer and emission intensity.

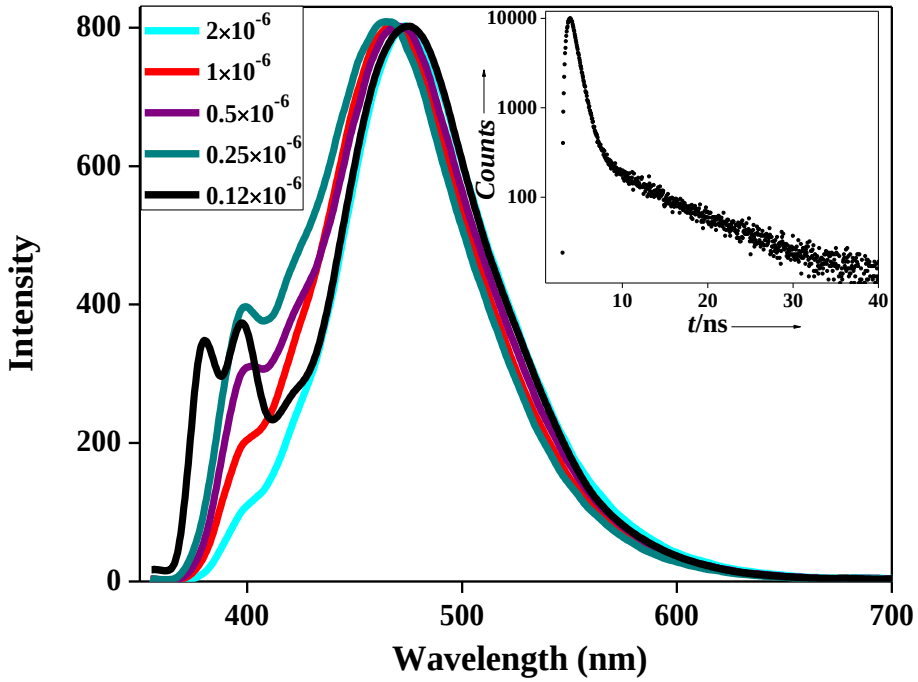

Figure 25: Emission spectra of compound **1** (λ_{ex} = 345 nm) in benzene at different dilution. Inset figure shows fluorescence lifetime decay profile of **1** in benzene **(**0.12 × 10^{-6} M) (λ_{ex} = 345 nm) while monitoring the emission at 472 nm.

3A.3.3 Structural description of {[Zn(ndc)(*o*-phen)]·DMF)}$_n$ (2)

Compound **2** was synthesized by the co-assembly of $Zn(NO_3)_2 \cdot 6H_2O$, ndc and *o*-phen under solvothermal condition. Structure determination using single crystal x-ray diffraction reveals that **2** crystallizes in monoclinic, *P*2/*n* space group (Table 3 and 4). The asymmetric unit contains two metal centers Zn1 and Zn2, two ndc, two *o*-phen and one guest DMF. The hexa-coordinated Zn^{2+} metal centers are chelated to two carboxylate groups of two ndc and other two coordination sites are furnished by a *o*-phen. Zn1 is coordinated to N2, N2* (from *o*-phen), O2, O2*, O6 and O6* (from ndc); Zn2 is coordinated to N1, N1* (from *o*-phen), O1, O1*, O5 and O5* (from ndc) (Figure 26). The Zn^{2+} centers are connected by ndc linker along (101) plane to form a 1D *zigzag* chain (Figure 27a). These chains are parallelly aligned through C-H···OCO (~ 2.76 Å) interactions between ndc linkers resulting in a 2D corrugated sheet lying in the crystallographic *ac* plane (Figure 27b). Further, these sheets are tethered *via* C-H(*o*-phen)···π (ndc) (~ 3.58-3.60 Å) and C-H(*o*-phen)···O(ndc) interactions resulting in a 3D supramolecular structure with distorted rectangular shaped 1D channels of dimensions[31] 3.5 × 4.2 $Å^2$ along *a*-axis (Figure 27c). These channels are filled with guest DMF molecules and removal of them shows a void space of 28% of total cell volume.[19] It is

worth mentioning that along the *c*-axis 1D column of DMF and {Zn(*o*-phen)} formed by alternative packing of one 2D sheet which protrude in to the groove of another 2D sheets composed of similar column (Figure 27d). Such arrangement results in a herring-bone type packing in the *ac* plane (Figure 27b).

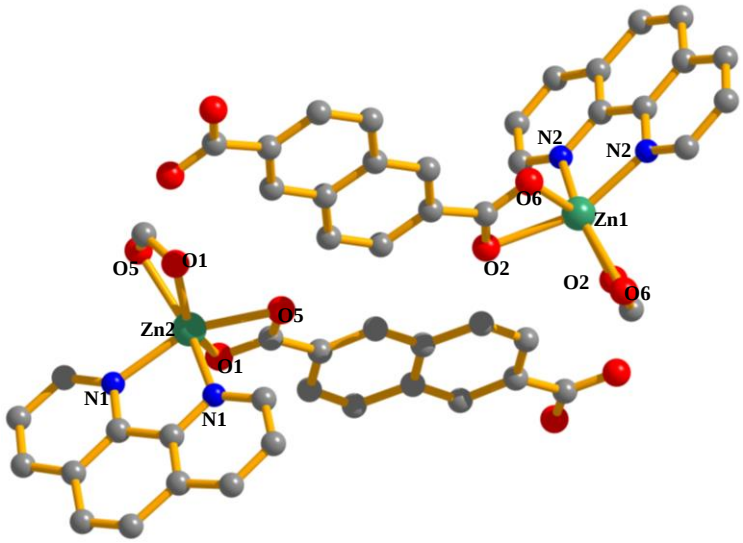

Figure 26: Coordination environment of Zn1 and Zn2 in compound **2**.

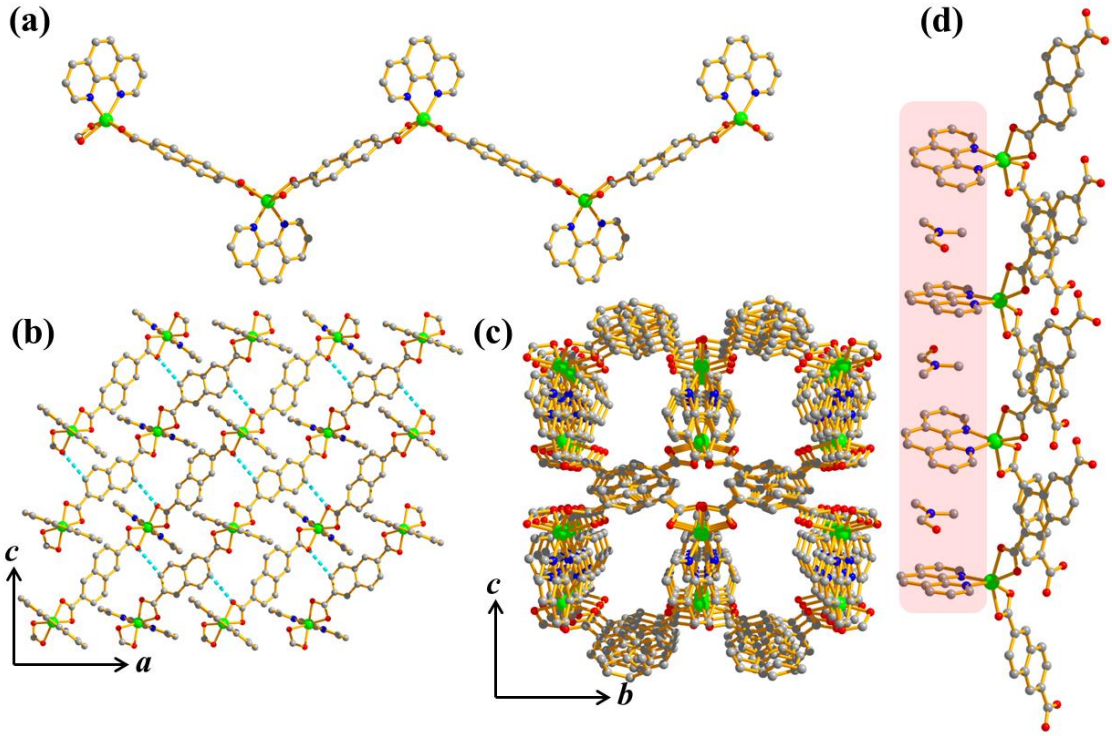

Figure 27: Structural details of **2**: (a) 1D *zigzag* chain of compound **2**, (b) 2D corrugated sheet, (c) View of the rectangular channels along *a*-axis formed by supramolecular organization of 1D chains, (d) Columnar stacking of {Zn(*o*-phen)} and guest DMF.

Table 3: Crystal data and structure refinement parameters of compound **2**, **2b′**, **2c′**, **2d′** and **2e**.

Empirical formula	$C_{27}H_{21}ZnN_3O_5$ **(2)**	$C_{31}H_{23}ZnN_3O_4$ **(2b′)**	$C_{32}H_{25}ZnN_3O_4$ **(2c′)**	$C_{33}H_{27}ZnN_3O_4$ **(2d′)**	$C_{31}H_{22}ZnN_2O_4$ **(2e)**
M_r	531.85	565.91	580.94	594.97	551.90
crystal System	monoclinic	Monoclinic	orthorhombic	orthorhombic	monoclinic
space group	*P*2/*n* (No. 13)	$P2_1/c$ (No. 14)	$Pna2_1$ (No. 33)	$Pc2_1b$ (No. 29)	$P2_1/c$ (No. 14)
***a* (Å)**	14.7676(6)	7.545(5)	15.422(3)	7.991(5)	7.8978(4)
***b* (Å)**	9.8557(4)	19.699(5)	22.456(5)	17.376(5)	19.3282(11)
***c* (Å)**	16.6713(6)	16.739(5)	7.5597(15)	19.323(4)	16.4646(8)
α (deg)	90	90	90	90	90
β (deg)	95.332(2)	90.339(5)	90	90	92.812(4)
γ (deg)	90	90	90	90	90
***V* (Å^3)**	2415.93(16)	2487.9(19)	2618.1(9)	2683.00(19)	2510.3(2)
Z	4	4	4	4	4
***T* (K)**	293	293	293	100	293
D_c (g cm^{-3})	1.462	1.511	1.474	1.473	1.460
μ (mm^{-1})	1.060	1.032	0.983	0.961	1.020
***F* (000)**	1092	1164	1200	1232	1136
θ_{max} (deg)	32.2	31.2	31.2	29.0	26.4
λ (Mo Kα)(Å)	0.71073	0.71073	0.71073	0.71073	0.71073
tot. data	37441	23421	9996	23277	30267
unique data, R_{int}	7767, 0.065	7356, 0.040	4967, 0.141	5992, 0.040	5150, 0.218
data [$I > 2\ \sigma(I)$]	4011	6112	2282	5297	2108
***R*[a],**	0.0442	0.0597	0.0981	0.0397	0.0635
R_w[b]	0.1152	0.1610	0.2780	0.0929	0.1444
GOF	0.86	1.06	1.00	1.06	0.95

[a] $R = \Sigma||F_o| - |F_c||/\Sigma|F_o|$. [b] $R_w = [\Sigma\{w(F_o^2 - F_c^2)^2\}/\Sigma\{w(F_o^2)^2\}]^{1/2}$.

Table 4: Selected bond lengths (Å) and angles (°) for **2**.

Zn2-O1	2.0933(15)	Zn2-O5	2.1973(15)
Zn2-N1	2.1175(19)	Zn2-O1_a	2.0933(15)

Zn2-O5_a	2.1973(15)	Zn2-N1_a	2.1175(19)
Zn1-N2_d	2.111(2)	Zn1-O6	2.2516(16)
Zn1-N2	2.111(2)	Zn1-O2	2.0732(17)
Zn1-O6_d	2.2516(16)	Zn1-O2_d	2.0732(17)
O1-Zn2-O5	61.73(6)	O1-Zn2-N1	106.95(7)
O1-Zn2-O1_a	151.55(6)	O2_d-Zn1-O6_d	60.66(6)
O1-Zn2-O5_a	100.15(6)	O2_d-Zn1-N2_d	93.91(8)
O1-Zn2-N1_a	95.07(7)	O6_d-Zn1-N2_d	153.17(8)
O5-Zn2-N1	92.92(7)	O1_a-Zn2-O5	100.15(6)
O6-Zn1-N2_d	98.04(7)	O5-Zn2-O5_a	105.52(6)
O5-Zn2-N1_a	152.19(7)	O2_d-Zn1-N2	106.19(8)
O2-Zn1-O6	60.66(6)	O1_a-Zn2-N1	95.07(7)
O2-Zn1-N2	93.91(8)	O5_a-Zn2-N1	152.19(7)
N1-Zn2-N1_a	78.78(7)	O2-Zn1-O2_d	153.81(7)
O2-Zn1-O6_d	100.64(6)	O2-Zn1-N2_d	106.19(8)
O6-Zn1-N2	153.17(8)	O1_a-Zn2-O5_a	61.73(6)
O2_d-Zn1-O6	100.64(6)	O1_a-Zn2-N1_a	106.95(7)
O6-Zn1-O6_d	95.26(6)	O5_a-Zn2-N1_a	92.92(7)
O6_d-Zn1-N2	98.04(7)	N2-Zn1-N2_d	80.04(8)

a =3/2-x,y,1/2-z; d =1/2-x,y,1/2-z

3A.3.4 PXRD and thermal stability of 2

TG analysis suggests that guest DMF solvent molecules are released at 170 °C under vacuum and the desolvated state (**2′**) is stable till 340 °C (Figure 28a). **2′** shows noteworthy changes in the PXRD pattern compared to that of the as-synthesized framework **2** (Figure 28b). The Bragg's diffractions for (101) and (10-1) planes, which are passing through the ndc linker and Zn^{2+} metal center, shifts to higher angles after exclusion of the guest solvent molecules implying shrinkage in the framework. Indexing of the PXRD pattern of desolvated **2** (**2′**) shows reduced cell volume (1990 $Å^3$) compared

to that of **2** (Figure 29, Details given below). It is anticipated that a 3D supramolecular structure, built up by non-covalent interactions, would be flexible and structure can be modulated by removal or reintroduction of guest solvents molecules.[32]

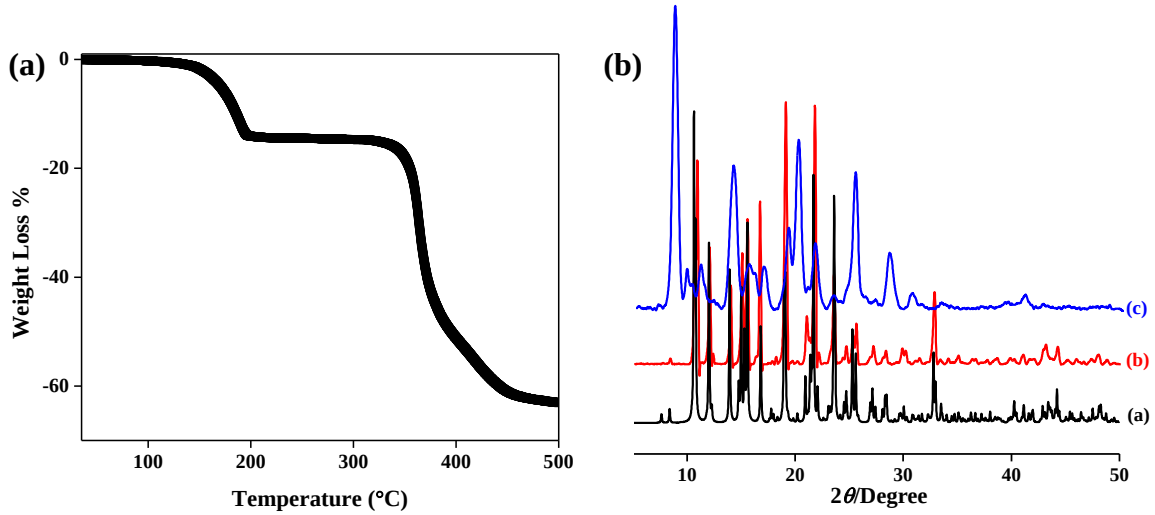

Figure 28: Thermal stability of **2**: (a) TGA profile in the tempearture range of 35-500 °C under N_2 atmosphere; (b) PXRD patterns of **2**: a) simulated, b) as-synthesized and c) heated at 170 °C.

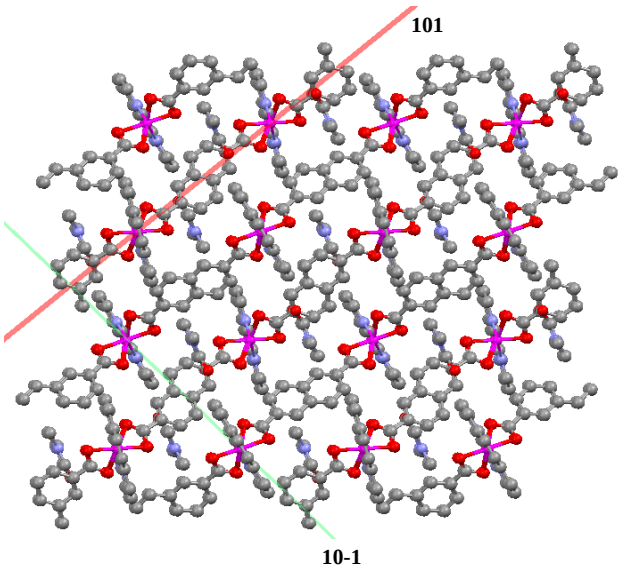

Figure 29: (101) and (10-1) planes passing through ndc and Zn^{2+} metal centers in **2**.

PXRD indexing results of 2′:

Cell parameters: a = 13.6549 Å, b = 10.5617 Å, c = 14.0516 Å , β = 93.531°, V = 1900.562Å

H	K	L	DOBS	DCAL	DOBS-DCAL	QOBS	QCAL	2TH.OBS	2TH.CAL	DIF.2TH.
1	1	-1	7.53190	7.55937	-.02747	.01763	.01750	11.740	11.697	.043
1	0	1	6.84653	6.83994	.00659	.02133	.02137	12.920	12.932	-.012
2	0	-2	6.20604	6.21669	-.01065	.02596	.02588	14.260	14.235	.025

2	1	-1	6.21595	-.00991	.02588	14.237	.023		
1	1	1	5.56247	5.55510	.00737	.03232	.03241	15.920	15.941	-.021
2	1	0	5.57768	-.01521	.03214	15.876	.044		
0	0	2	5.36822	5.37807	-.00985	.03470	.03457	16.500	16.470	.030
1	1	-2	5.26680	5.27214	-.00533	.03605	.03598	16.820	16.803	.017
0	2	0	4.76152	4.76064	.00088	.04411	.04412	18.620	18.623	-.003
3	1	-2	4.53936	4.54588	-.00652	.04853	.04839	19.540	19.512	.028
0	2	1	4.35835	4.35331	.00504	.05264	.05277	20.360	20.384	-.024
3	1	0	4.12976	4.13328	-.00352	.05863	.05853	21.500	21.481	.019
1	1	2	3.89715	3.89875	-.00160	.06584	.06579	22.800	22.791	.009
1	1	-3	3.73871	3.73348	.00523	.07154	.07174	23.780	23.814	-.034
3	1	1	3.34347	3.34195	.00151	.08946	.08954	26.640	26.652	-.012
5	0	-3	3.19752	3.19516	.00236	.09781	.09795	27.880	27.901	-.021
4	0	-4	3.10376	3.10834	-.00458	.10381	.10350	28.740	28.697	.043
4	2	-2	3.10798	-.00421	.10352	28.700	.040		

NUMBER OF OBS. LINES = 15

NUMBER OF CALC. LINES = 15

M(15)= 11 AV.EPS.= .0000274

F 15= 15.(.01369, 31)

3A.3.5 Flexibility of 2: CO_2 and solvent vapour adsorption

The structural flexibility of **2′** was further comprehended from the CO_2 adsorption (195 K) measurement (Figure 30a). CO_2 uptake increases gradually up to P/P_0 ~ 0.18 (point B) followed by a sudden rise, which ended with an uptake amount of 48 mL/g (~ 0.9 molecules/formula) (point C). Desorption path does not retrace the adsorption path showing large hysteretic sorption profile. Such hysteritic profile in a flexible PCP of this kind is expected but studied very little. Here, to obtain an appropriate insight of such adsorption behaviour *in situ* PXRD measurements coupled with CO_2 adsorption was studied and diffraction patterns of **2′** at each adsorption point were recorded. Noteworthy observations were noted from the PXRD patterns at points A-E in the isotherm (Figure

30b). Indexing the diffraction patterns at these points show continuous increase in the cell volume from point A to C (2143 (point A) to 2963 Å^3 (point C)) suggesting expansion of the framework structure to accommodate CO_2 molecules (Details of indexing given below, Table 5). This rearrangement might be driven by the CO_2···aromatic π-electron cloud interactions. Finally, at the last desorption point (E) which shows ~ 6 mL/g CO_2 retention in the pores, the structure does not revert back to contracted desolvated phase **2′** as evident from the cell volume (2836 Å^3). Hence, unless the framework is completely evacuated (CO_2 removed) the open form remains stable. The high pressure adsorption profile at 273 K also shows a double step uptake indicating similar CO_2 induced structural rearrangement (Figure 31a). Whereas, increasing the temperature to 293 K gives a type-I uptake profile. On the other side N_2 at 77 K is unable to diffuse into the pores, possibly due to high diffusion barrier imposed by weak interaction between the framework and N_2 or contracted pore size which is not sufficient for N_2 accommodation (Figure 32b). H_2 adsorption at 77 K also shows no uptake. Such selectivity towards CO_2 is possibly due to preferential CO_2···aromatic π-electron cloud interactions (Figure 31b).[33]

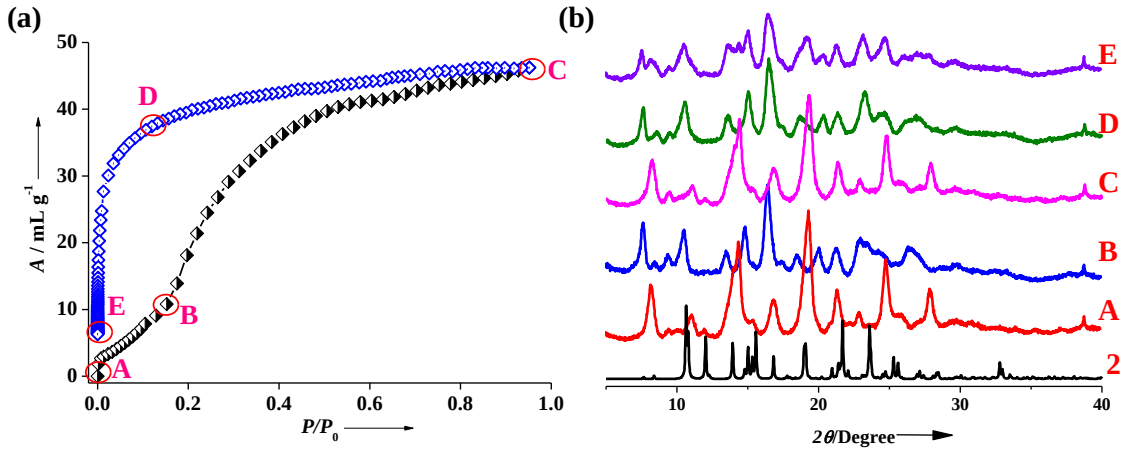

Figure 30: CO_2 Adsorption details: (a) CO_2 adsorption isotherm at 195 K; (b) PXRD patterns at different points during adsorption process.

Then benzene solvent vapour adsorption was studied which reiterates the flexible nature of the framework (Figure 32). A gated sorption profile (threshold pressure P/P_0 ~ 0.1) with benzene was observed and the final uptake amount indicates commensurate adsorption of one molecule of benzene per formula of **2′**. This suggests structural rearrangement during adsorption and such expansion of the framework is driven by specific π···π interactions with host and benzene molecules. The commensurate benzene adsorption made us believe that similar aromatic molecules can be encapsulated in the coordination nanospace based on CT interaction with electron donating guest molecules.

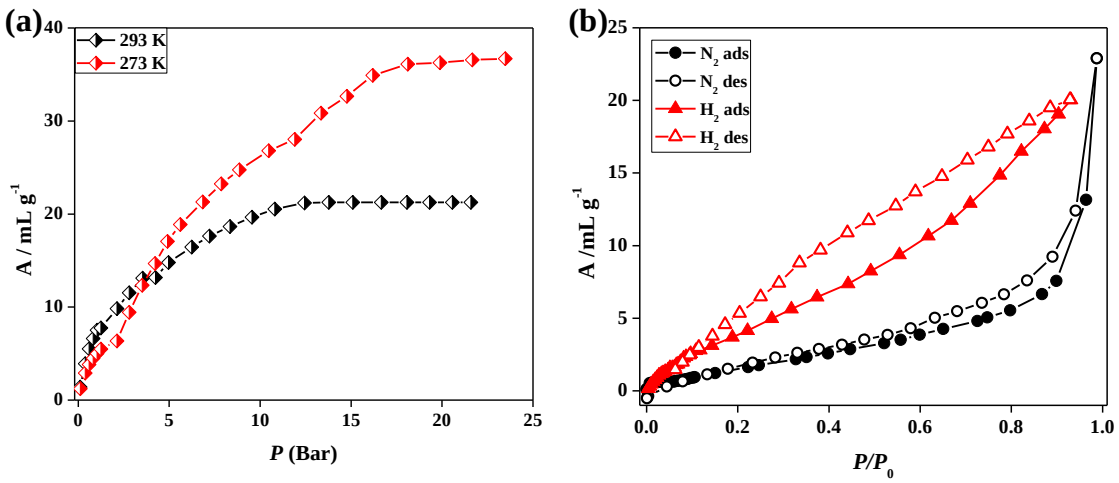

Figure 31: Adsorption details of **2′**: (a) CO_2 adsorption isotherms at 293 and 273 K at high pressure; (b) N_2 and H_2 adsorption isotherms at 77 K.

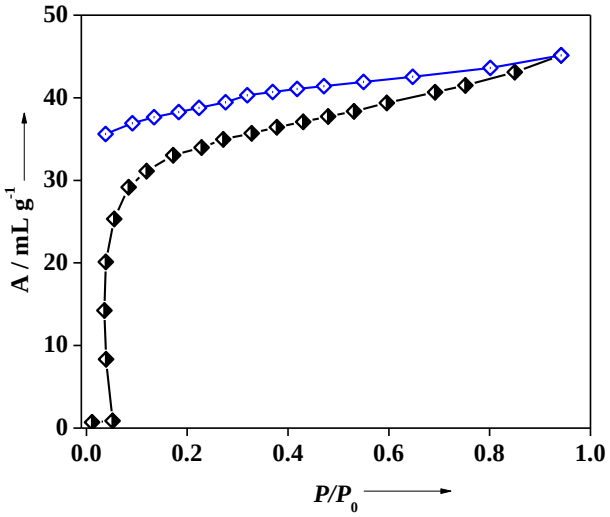

Figure 32: Benzene vapour adsorption profile of **2′** at 293 K.

PXRD indexing results at Point A during CO_2 adsorption:

Cell parameters: a = 14.1938 Å, b = 11.1734 Å, c = 14.0679 Å , β = 92.861°, V = 2143.839 Å^3

H	K	L	SST-OBS	SST-CALC	DELTA	2TH-OBS	2TH-CALC	D-OBS	FREE PARAM.
-1	0	1	.005548	.005567	-.000019	8.543	8.558	10.3421	0
-2	0	1	.007079	.007098	-.000019	9.653	9.666	9.1556	0
0	1	0	.007809	.007772	.000036	10.139	10.116	8.7172	0
1	1	0	.009115	.009081	.000034	10.957	10.936	8.0685	0
-2	1	1	.014798	.014870	-.000073	13.974	14.009	6.3324	0
-4	0	1	.017986	.018011	-.000025	15.415	15.425	5.7437	0

1	1	1	.018128		15.476				
-3	1	1	.019040	.019018	.000021	15.862	15.853	5.5825	0
			.021272		16.773		5.2815	0	
-5	0	1	.027397	.027393	.000004	19.055	19.053	4.6538	0
-2	1	2	.030064	.030040	.000024	19.970	19.962	4.4426	0
1	0	2	.032709		20.839				
5	0	0	.032729	.032712	.000017	20.846	20.840	4.2579	0
			.034878		21.527		4.1246	0	
1	1	2	.040303	.040481	-.000178	23.162	23.214	3.8370	0
5	1	0	.040485		23.215				
2	2	1	.047755	.047766	-.000011	25.245	25.248	3.5249	0

NUMBER OF OBS. LINES = 14

NUMBER OF CALC. LINES = 15

M(14)= 11 AV.EPS.= .0000384

F 14 = 15.(.016295, 59)

PXRD indexing results at Point B during CO_2 adsorption:

Cell parameters: a = 16.0299 Å, b = 14.6001 Å, c = 11.4344 Å , V = 2677.754 Å^3

H	K	L	SST-OBS	SST-CALC	DELTA	2TH-OBS	2TH-CALC	D-OBS	FREE PARAM.
0	1	1	.010318	.010320	-.000002	11.660	11.661	7.5834	0
			.011795		12.470		7.0926	0	
0	0	2	.015535	.015538	-.000003	14.320	14.321	6.1802	0
2	1	0	.018730		15.732				
-2	1	1	.018844	.018845	-.000001	15.780	15.781	5.6115	0
-2	0	2	.020294	.020293	.000001	16.380	16.380	5.4073	0
-1	1	2	.021290	.021278	.000012	16.780	16.775	5.2793	0
2	1	1	.026395	.026384	.000011	18.700	18.696	4.7413	0
1	2	0	.028796	.028817	-.000021	19.540	19.547	4.5394	0
1	1	2	.028817		19.547				

-1	2	1	.030814	.030816	-.000003	20.220	20.221	4.3882	0
3	1	0	.034091	.034097	-.000006	21.280	21.282	4.1720	0
2	0	2	.035369	.035371	-.000002	21.680	21.680	4.0959	0
-2	2	1	.038152			22.527			
-3	1	2	.038261	.038327	-.000066	22.560	22.580	3.9381	0
-2	1	3	.042379	.042382	-.000002	23.760	23.761	3.7418	0
-3	2	1	.051635			26.268			
-4	1	1	.051912	.051957	-.000045	26.340	26.352	3.3809	0
-3	1	3	.052095			26.387			
0	3	0	.057922			27.852			
-1	2	3	.058117	.058123	-.000006	27.900	27.901	3.1953	0
0	2	3	.060703			28.527			
3	1	2	.060943			28.584			
1	3	0	.061009	.060996	.000013	28.600	28.597	3.1186	0
2	2	2	.061114			28.625			
2	1	3	.064994	.064998	-.000004	29.540	29.541	3.0215	0
1	3	1	.066765			29.949			
4	1	1	.066987	.067035	-.000048	30.000	30.011	2.9762	0

NUMBER OF OBS. LINES = 12

NUMBER OF CALC. LINES = 14

M(14)= 11 AV.EPS.= .0000356

F 14 = 15.(.020156, 39)

PXRD indexing results at Point C during CO_2 adsorption:

Cell parameters: a = 22.9235 Å, b = 12.1651 Å, c = 10.3915 Å , V = 2963.505 Å^3

H	K	L	SST-OBS	SST-CALC	DELTA	2TH-OBS	2TH-CALC	D-OBS	FREE PARAM.
0	0	1	.004485	.004393	.000092	7.680	7.601	11.5021	0
2	1	0	.005383			8.415			
1	0	1	.005395			8.424			
0	2	0	.005492	.005505	-.000013	8.500	8.510	10.3942	0
1	1	1	.006742	.006771	-.000029	9.420	9.440	9.3810	0

2	0	1	.008373	.008400	-.000028	10.500	10.517	8.4184	0
2	2	1	.013856	.013905	-.000049	13.520	13.544	6.5440	0
0	3	1	.016767	.016780	-.000013	14.880	14.886	5.9488	0
4	0	1	.020442	.020421	.000021	16.440	16.432	5.3877	0
2	1	2	.022932	.022956	-.000024	17.420	17.429	5.0867	0
1	4	0		.023022			17.454		
0	2	2		.023078			17.476		
3	3	1	.025783	.025795	-.000012	18.480	18.484	4.7973	0
4	2	1		.025926			18.532		
2	4	1	.030393	.030420	-.000027	20.080	20.089	4.4185	0
5	2	0		.030548			20.132		
2	3	2	.033964	.033967	-.000002	21.240	21.241	4.1797	0
1	5	1	.039816	.039801	.000014	23.020	23.016	3.8604	0

NUMBER OF OBS. LINES = 12

NUMBER OF CALC. LINES = 18

M(12)= 9 AV.EPS.= .0000270

F 12 = 10.(.016056, 83)

PXRD indexing results at Point D during CO_2 adsorption:

Cell parameters: a = 20.7952 Å, b = 12.3019 Å, c = 11.5803 Å , V = 2899.546 Å^3

H	K	L	SST-OBS	SST-CALC	DELTA	2TH-OBS	2TH-CALC	D-OBS	FREE PARAM.
0	0	1	.004984	.004980	.000004	8.096	8.093	10.9114	0
1	0	0	.007333	.007375	-.000042	9.825	9.853	8.9953	0
1	0	1	.008406	.008413	-.000007	10.521	10.525	8.4015	0
0	-2	2		.009618			11.256		
1	1	0	.009784	.009785	-.000001	11.353	11.354	7.7877	0
-1	1	0	.015792	.015903	-.000111	14.438	14.489	6.1298	0
-1	-2	1		.015965			14.518		
-1	-2	2		.018759			15.744		
1	1	1	.018876	.018866	.000011	15.794	15.789	5.6066	0

1	-2	3	.020198	.020096	.000102	16.341	16.299	5.4201	0
1	-2	1		.020317			16.389		
0	2	0	.021975	.021873	.000102	17.050	17.010	5.1964	0
				.024357			17.958	4.9357	0
1	-1	3	.024693	.024763	-.000070	18.082	18.108	4.9020	0
				.027459			19.077	4.6486	0
				.033417			21.066	4.2138	0
1	1	2	.037841	.037906	-.000065	22.434	22.454	3.9599	0
2	2	0	.039135	.039138	-.000003	22.820	22.821	3.8938	0
0	2	1	.042922	.042940	-.000018	23.914	23.919	3.7181	0
2	-3	3	.045827	.045842	-.000015	24.722	24.726	3.5983	0
-2	-1	2	.048448	.048452	-.000003	25.431	25.432	3.4996	0
2	0	3	.050758	.050666	.000092	26.040	26.016	3.4191	0
2	2	1	.052293	.052321	-.000028	26.438	26.445	3.3685	0
2	-3	2	.052680	.052959	-.000279	26.538	26.609	3.3561	0
0	-1	4	.052874	.052969	-.000095	26.587	26.612	3.3500	0
-1	-2	4	.054242	.054226	.000017	26.936	26.931	3.3074	0

NUMBER OF OBS. LINES = 22

NUMBER OF CALC. LINES = 23

M(20)= 6 AV.EPS.= .0000560

F 20 = 13.(.019525, 83)

M(22)= 6 AV.EPS.= .0000560

PXRD indexing results at Point E during CO_2 adsorption:

Cell parameters: a = 23.0919 Å, b = 12.1312 Å, c = 10.1279 Å , V = 2836.1295 Å^3

H	K	L	SST-OBS	SST-CALC	DELTA	2TH-OBS	2TH-CALC	D-OBS	FREE PARAM.
0	0	1	.004392	.004413	-.000021	7.600	7.618	11.6230	0
1	1	0	.005160	.005148	.000012	8.239	8.229	10.7235	0
1	0	1	.006857	.006988	-.000130	9.500	9.590	9.3022	0
				.008436			10.540	8.3866	0

			.014143		13.660	6.4773	0	
			.015839		14.460	6.1206	0	
2	1	1	.017218	.017284	-.000066	15.080	15.109	5.8704	0
2	2	0	.020640	.020593	.000047	16.520	16.501	5.3618	0
1	1	2	.022880	.022802	.000078	17.400	17.370	5.0925	0
2	0	2	.027927	.027950	-.000024	19.240	19.248	4.6095	0

NUMBER OF OBS. LINES = 10

NUMBER OF CALC. LINES = 7

M(10)= 15 AV.EPS.= .0000539

F 10 = 21.(.029091, 17)

Table 9: Cell parameters obtained after indexing of the PXRD patterns.

	1	1′	A	B	C	D	E
a/Å	14.77	13.65	14.19	16.03	22.92	20.79	23.09
b/Å	9.86	10.56	11.17	14.60	12.16	12.30	12.13
c/Å	16.67	14.05	14.07	11.43	10.39	11.58	10.13
α/°	90	90	90	90	90	90	90
β/°	95.33	93.5	92.86	90	90	90	90
γ/°	90	90	90	90	90	90	90
V/Å^3	2415.93	1900.56	2143.84	2677.75	2963.50	2899.5	2836.12

3A.3.6 Recognition of aromatic amines

Absorption spectrum of **2** shows a broad profile with λ_{max} ~ 350 nm (Figure 33a). Upon excitation at 350 nm it shows bright blue emission with a maximum at 427 nm due to the presence of naphthalene chromophore (Figure 33b). Hence, inclusion of strong electron donor, such as aromatic amines might interfere with emission characteristics of **2**. Following our notion four aromatic amines; AN, NMA, DMA and DMPT, with

different electron donating capabilities and variable sizes were selected. The synthetic procedure has been discussed in the experimental section. The guest encapsulated compounds of **2′** exhibited sharp colour change and **AN@2′** (**2a**), **NMA@2′** (**2b**), **DMA@2′** (**2c**) and **DMPT@2′** (**2d**) inclusion compounds showed light brown, fade yellow, yellow and orange colour, respectively. ^{1}H-NMR spectroscopic studies suggest 0.81, 0.99, 0.98 and 0.61 molecules of AN, NMA, DMA and DMPT were encapsulated in the framework, respectively (Figure 5-8). PXRD patterns of the inclusion compounds are quite different compared to **2′** indicating structural reorganization after amine encapsulation (Figure 34). The intense colours observed for **2a-2d** are clearly perceptible from the UV-vis spectra where strong charge transfer (CT) bands are observed (Figure 35a). Furthermore, the emission characteristics are more interesting, where red shifted broad emission spectra are observed in all four compounds. **2a** shows a slightly shifted emission maximum at 450 nm while **2b** shows dual emission with maxima at 425 and 546 nm when excited at 350 nm (Figure 35b). In **2c** and **2d**, the emission maxima are 576 and 595 nm. Noticeably, as the donors strength increases from AN<NMA<DMA<DMPT, emission maxima also shifted to higher wavelengths.

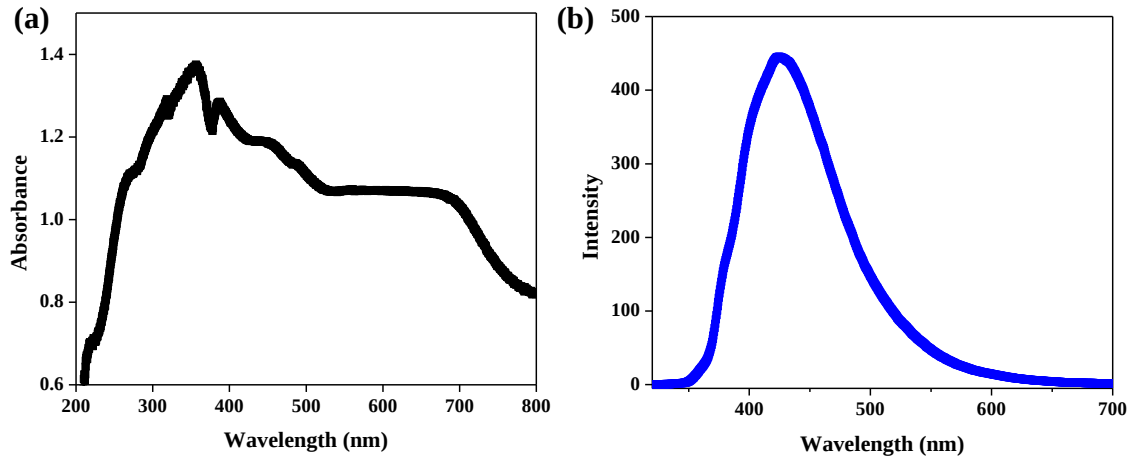

Figure 33: Photophysical properties of **2**: (a) Absorption spectrum; (b) Emission spectrum upon excitation at 350 nm.

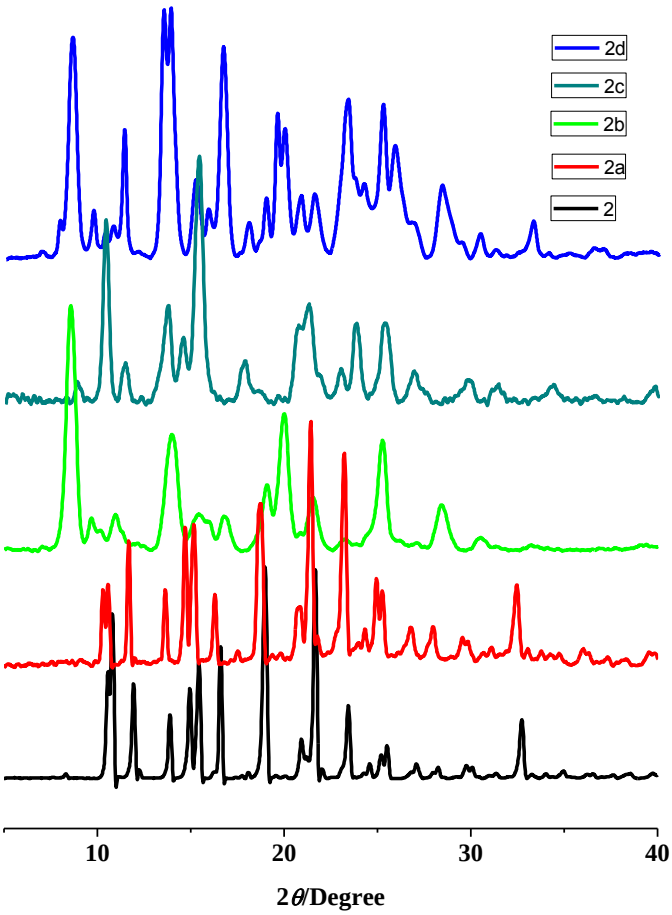

Figure 34: PXRD patterns of **2** and **2a-2d**.

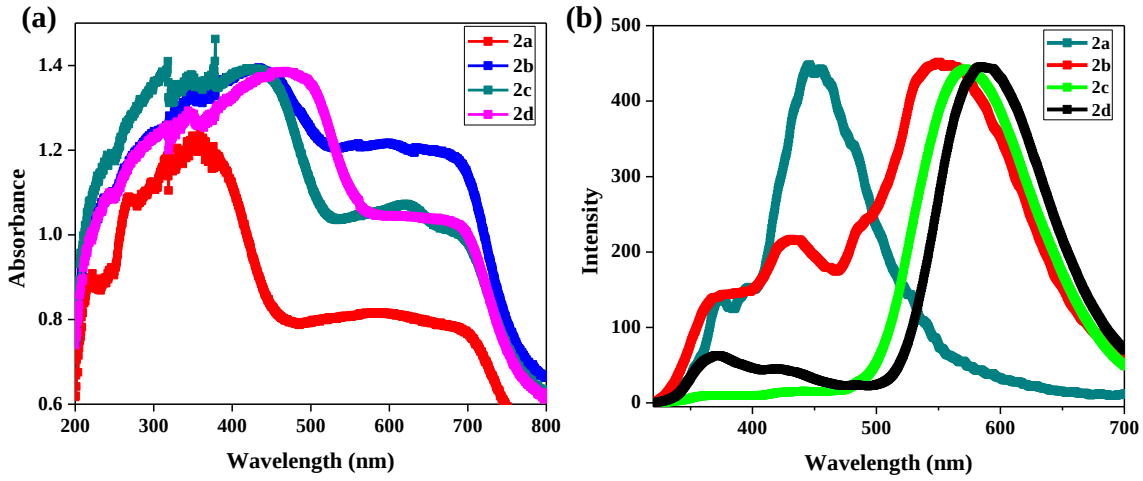

Figure 35: Photophysical properties of **2a-2d**: (a) Absorption spectra; (b) Emission spectra upon excitation at 350 nm.

Hence, for each aromatic amine characteristic visible colour change and turn-on emission was observed and this can be counted as an efficient and easy recognition method (Figure 36a). I conjecture that featureless broad emissions in **2b-2d** are originated from the CT interaction between guest and host framework as realized from the excitation

spectra (Figure 36b). Excitation spectra showed the presence of ground state interactions, thus ruling out the possibility of exclusive excited-state exciplex emission.

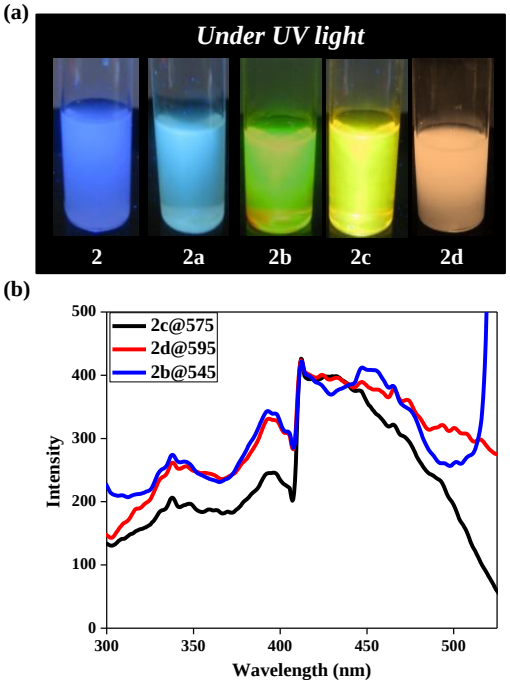

Figure 36: (a) Pictures of **2**, **2a-2d** dispersed in methanol under UV light; (b) Excitation spectra of **2b-2d** monitored at 545, 575 and 595 nm, respectively.

But the whole phenomena would not be conspicuous unless the precise molecular arrangements of the guests and their interactions with ndc and *o*-phen are known. Therefore I tried to crystallize the guest encapsulated framework. As after guest DMF removal at 170 °C structure undergoes major disruption, single crystallinity of **2′** is not good. Hence, postsynthetically it was not possible to get a good single crystal. Here *in situ* methodology was adopted and details are given in the experimental section. By this method it was possible to grow good quality single-crystals and determine crystal structures of guest encapsulated compounds; {[Zn(ndc)(*o*-phen)]·NMA}$_n$ (**2b′**), {[Zn(ndc)(*o*-phen)]·DMA}$_n$ (**2c′**) and {[Zn(ndc)(*o*-phen)]·DMPT}$_n$ (**2d′**) except with aniline due to very poor single crystallinity (Table 3; Details of bond lengths and angles in Table 6-8). All the compounds show similar 1D coordination chain as that in **2** where guest DMF molecules are replaced by the respective amines and molecular packing remains almost similar (Figure 37a-37c). In all three frameworks guest molecules are arranged in a face-to-face fashion with *o*-phen and the π···π distances indicate strong interactions (centroid···centroid distances = **2b′**: 3.56 Å; **2c′**: 3.55 Å; **2d′**: 3.65 Å; Figure 37d-37f). Interestingly, the naphthalene (ndc) chromophores do not interact with guest amines molecules strongly and rather remains tethered to the *o*-phen by similar C-H···π

interactions, similar to that in **2**. Further, to accommodate larger size guests the ndc linkers bent (bow shape) and guest orientation differs in each case (Figure 38). Therefore, to accommodate various sizes of guests the supramolecular pores are modified and expanded accordingly to encapsulate the various guests, suggesting highly dynamic and adaptive nature of the framework.

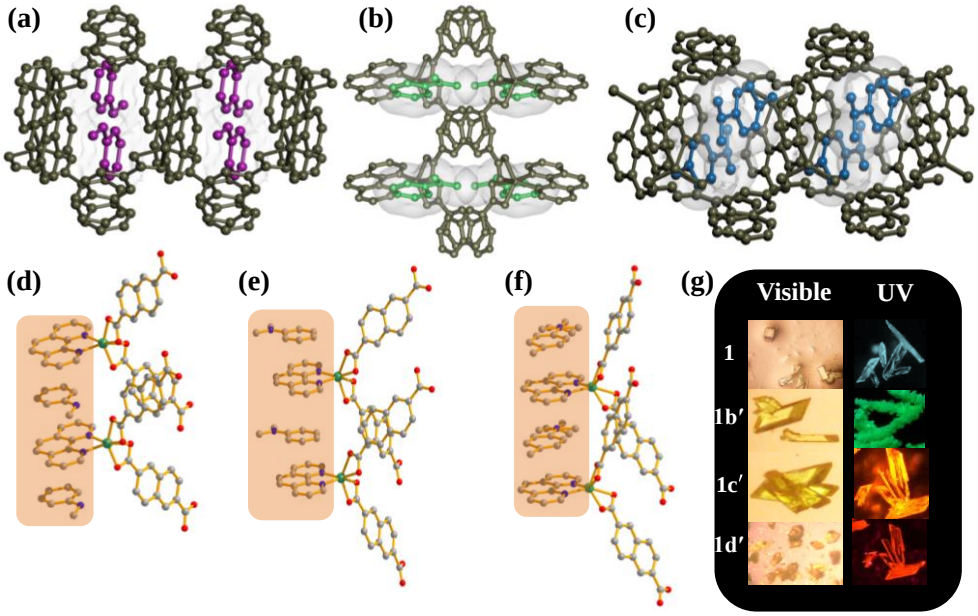

Figure 37: (a-c) Structural characterization showing the location of guest molecules in the coordination nanospaces of **2b′-2d′**; (d-f) Face-to-face stacked aromatic amines with *o*-phen in **2b′-2d′**; (g) Microscopic images of crystals of **2** and **2b′-2d′** under visible and UV light.

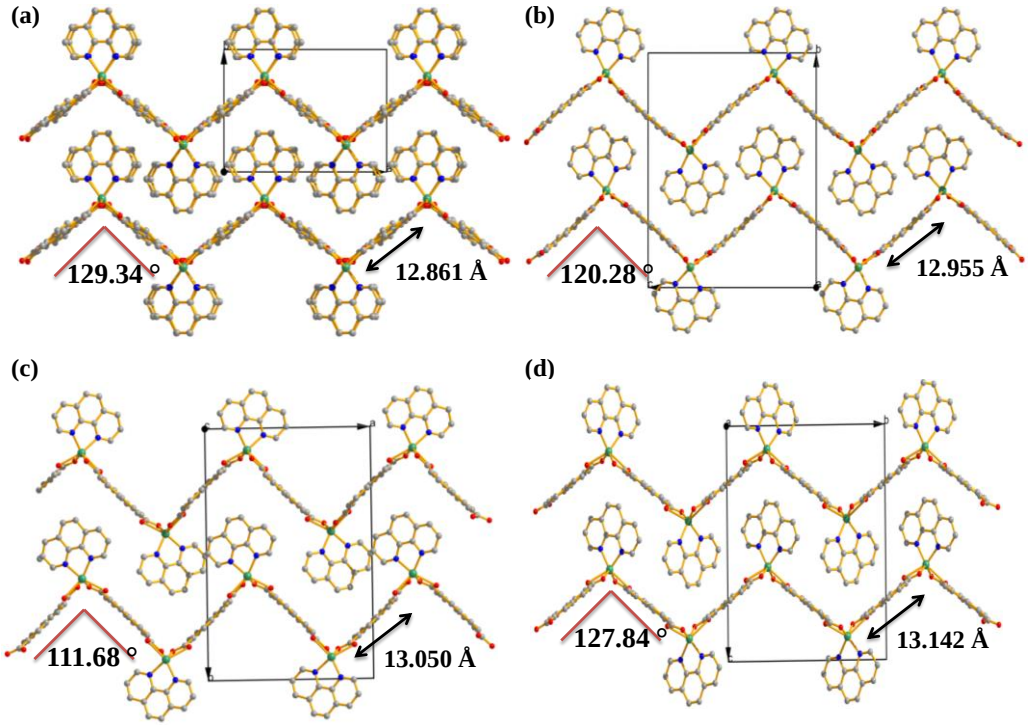

Figure 38: Arrangement of 1D coordination polymers (a) **2**; (b) **2b′**; (c) **2c′** and (d) **2d′**.

The compounds **2b′-2d′** are light yellow, yellow and orange coloured similar to **2b-2d**, respectively (Figure 37g). The absorption and emission spectra obtained for **2b′-2d′** were exactly similar to that observed for **2b-2d** which suggest the post-synthetic inclusion compounds (**2b-2d**) have similar molecular arrangements to that of *in situ* synthesized **2b′-2d′**. (Figure 39). From the single crystal structures now it is evident that there is a *o*-phen:amine CT complexation, which is reflected in the featureless broad red shifted emissions and broad absorbance in visible region. It is expected that aniline will assemble in a similar fashion inside the nano pores as these are structurally similar.

Interestingly, any naphthalene monomer emission was not observed for **2c′** and **2d′** (negligible), but for **2b′** emission of naphthalene (λ_{em}= 425 nm) and also CT emission (λ_{em}= 546 nm) were observed (Figure 39b). Such quenching of emission of naphthalene in **2c′** and **2d′** was surprising as the ndc chromophore remains intact in the framework without undergoing any strong interaction with the encapsulated guest. The most reasonable explanation of such quenching would be the energy transfer from the excited monomer (ndc) to the guest:*o*-phen CT complex (in **2b′** and **2c′**) and this is in line with the case of compound **1**. The distances between the ndc and CT complex are in the range of 3.58 - 3.60 Å, which is suitable for such energy transfer process to occur. Further confirmation of the proposed energy transfer process came from the time-resolved single photon counting experiments of **2c′** and **2d′** upon excitation at 370 nm and monitoring the emission at 576 and 595 nm, respectively (Figure 40a). Both cases bi-exponential decay was observed and the life times are substantially high, *i.e,* 48.5 and 18.5 ns for **1c′** and **1d′**, respectively. Further, the excitation spectra of **2c′-2d′** (λ_{mon}= 650 nm) show a maxima around 330 nm which corroborates to framework absorbance (precisely, naphthalene) and this phenomena refers to energy transfer from ndc to the CT emission (Figure 40b). Lifetime values observed at 410 nm for **2c′** and **2d′** (donor emission i.e. ndc emission) is found to be negligible suggesting efficient energy transfer. It is worth to mention that life time for as-synthesized framework (**2**) monitored at 420 nm is 2.36 ns. In case of **2b′** such energy transfer is not efficient as can be realized from the dual emission and also from the fluoroscence life time profile (Figure 40a and 40c). Excitation of **2b′** at 370 nm and monitoring at 420 and 546 nm shows life time 1.98 ns and 9 ns, respectively (Figure 40b). Life time observed at 420 nm is for the monomer ndc emission and this data matches well with as-synthesized frameworks (**2**). For **2a**, life time observed at 470 and 400 nm are ~ 3 and 2 ns, respectively. This indicates absence of energy transfer and efficient charge tranfer interaction in **2a**. As mentioned previously the

orientation of guest amines is not same in all cases; hence the energy transfer efficiency is tuned in **2b′-2d′**. Such tuning of CT emission and energy transfer process imposed high emission life time of organic chromophores is unprecedented in PCPs. Further, it takes merely 5-10 seconds to recognize the amine by the framework due to the fast diffusion process (Figure 41).

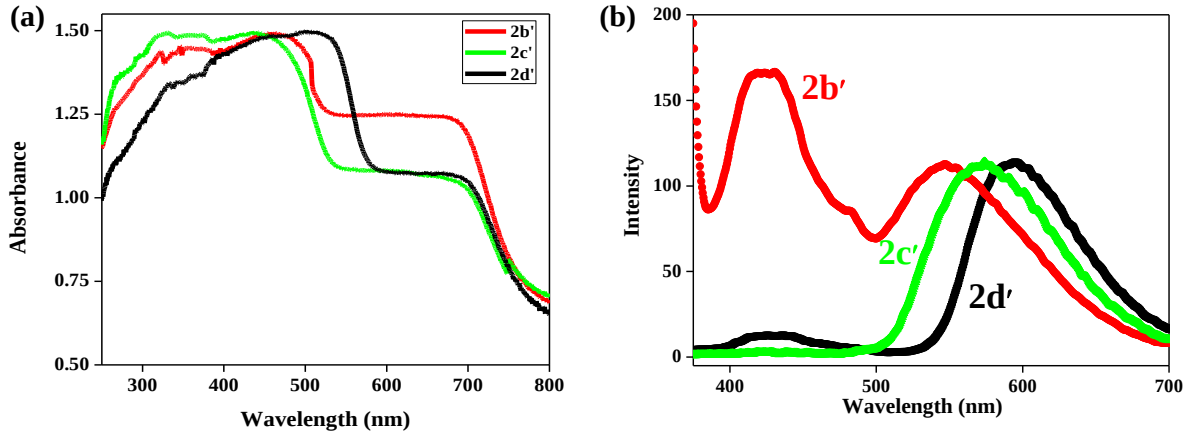

Figure 39: (a) Absorbance spectra of **2b′-2d′**; (b) Emission spectra of **2b′-2d′** upon excitation at 350 nm.

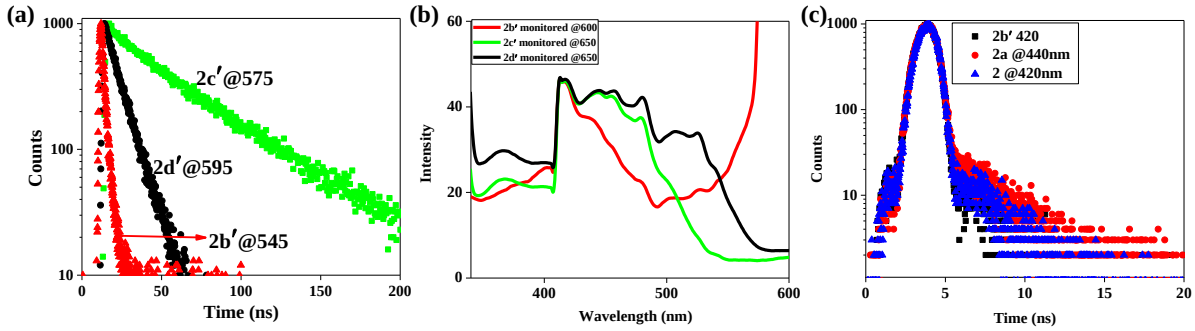

Figure 40: (a) Fluorescence decay profiles for **2b′-2d′**; (b) Eexcitation spectra of **2b′-2d′**; (c) Fluorescence decay profiles for **2**, **2a** and **2b′**.

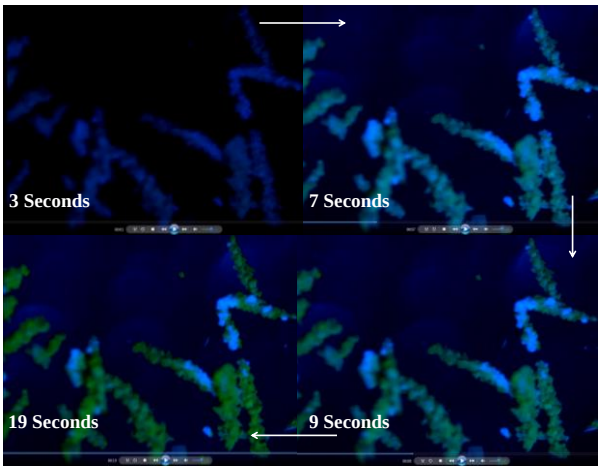

Figure 41: Snapshots of a video recorded under optical microscope: A drop of DMA on **2′** crystals was added and subsequent chnages in emission was recorded.

Apart from those amines, various other aromatic guests like toluene (**2e**), nitrobenzene (**2f**), cyanobenzene (**2g**) and iodobenzene (**2h**) were also encapsulated (See experimental section). These all have higher ionization potential compared to AN and hence weak electron donating capabilities. But still I find that toluene included framework (**2e**) to have similar molecular arrangement to that of **2b′-2d′** (Figure 42). Crystal structure of **2e** shows toluene is in face-to-face arrangement with *o*-phen with a π···π stacking distance 3.556 Å (Table 3 and 9; Figure 43a). Interestingly, toluene or other guests (nitrobenzene, cyanobenzene and iodobenzene) do not form any CT complex rather solvatochromic shifts were observed in their emission spectra (Figure 43a). Time-resolved single photon counting experiments show life time in the range of 2 ns which are originated from the ndc monomer (Figure 43b).

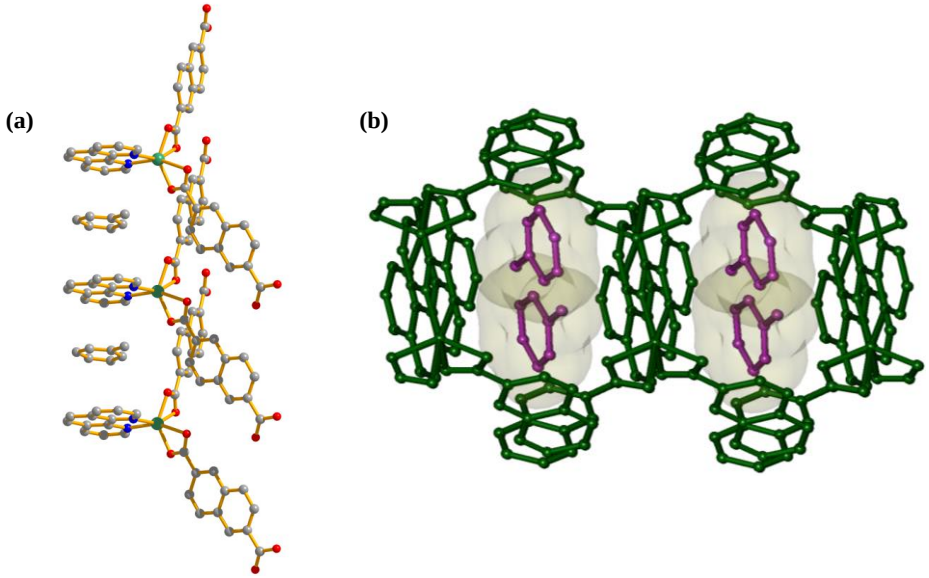

Figure 42: Structural details of **2e**: (a) π···π columner stacking of toluene and *o*-phen; (b) View of the guest toluene molecules inside the supramolecular pores.

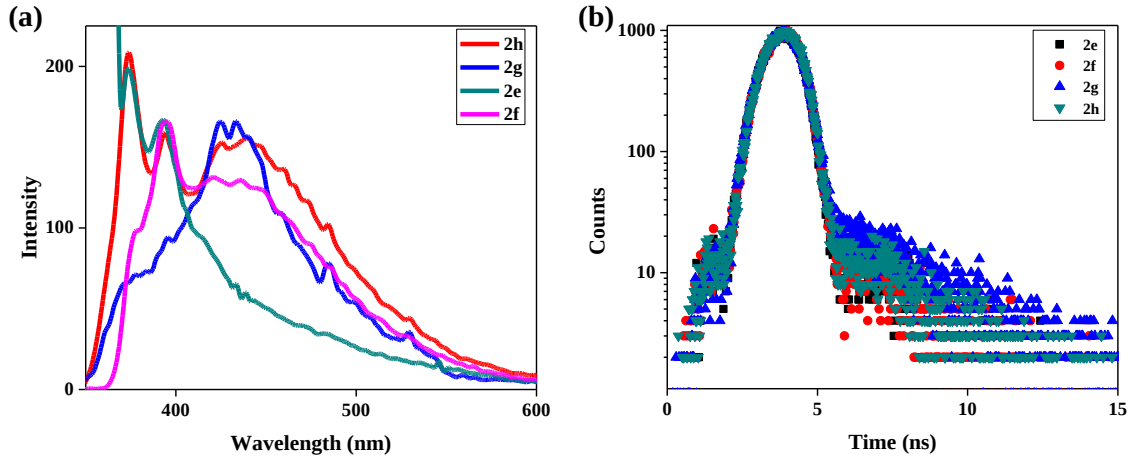

Figure 43: (a) Emission spectra of **2e-2h**; (b) Fluorescence decay profile of **2e-2h** observed at 420 nm.

Table 6: Selected bond lengths (Å) and angles (°) for **2b′**.

Zn1-O1	2.045(2)	Zn1-O2	2.312(3)
Zn1-O3	2.302(3)	Zn1-O4	2.047(2)
Zn1-N1	2.103(3)	Zn1-N2	2.103(3)
O1-Zn1-O2	97.01(8)	O1-Zn1-O3	60.63(6)
O1-Zn1-O4	146.84(7)	O1-Zn1-N1	99.30(8)
O1-Zn1-N2	105.47(8)	O2-Zn1-O3	102.36(7)
O2-Zn1-O4	60.34(8)	O2-Zn1-N1	94.58(8)
O2-Zn1-N2	157.40(8)	O3-Zn1-O4	98.52(7)
O3-Zn1-N1	154.89(8)	O3-Zn1-N2	90.88(8)
O4-Zn1-N1	105.98(8)	O4-Zn1-N2	99.95(8)
N1-Zn1-N2	79.70(8)	O2-Zn1-O3	102.36(7)

Table 7: Selected bond lengths (Å) and angles (°) for **2c′**.

Zn1-O1	1.972(9)	Zn01-O2	2.418(9)
Zn01-N1	2.091(11)	Zn01-N2	2.112(9)
Zn01-O3_a	2.441(8)	Zn01-O4_a	2.001(9)
O1-Zn01-O2	60.0(4)	O1-Zn01-N1	100.4(4)
O1-Zn01-N2	108.4(4)	O1-Zn01-O3_a	95.1(3)
O1-Zn01-O4_a	136.0(4)	O2-Zn01-N1	151.8(4)
O2-Zn01-N2	87.6(3)	O2-Zn01-O3_a	108.2(3)
O2-Zn01-O4_a	92.5(4)	N1-Zn01-N2	79.6(4)
O3_a-Zn01-N1	92.6(3)	O4_a-Zn01-N1	114.7(4)
O3_a-Zn01-N2	156.2(3)	O4_a-Zn01-N2	103.5(4)
O3_a-Zn01-O4_a	59.3(3)		

a =-1/2+x,1/2-y,1+z

Table 8: Selected bond lengths (Å) and angles (°) for **2d′**.

Zn1-O3	1.946(4)	Zn1-O4	2.648(5)
Zn1-N1	2.089(4)	Zn1-N2	2.079(4)
Zn-O1_a	2.672(5)	Zn1-O2_a	1.936(4)
O3-Zn1-O4	55.56(14)	O3-Zn1-N1	114.31(15)

O3-Zn1-N2	104.90(15)	O1_a-Zn1-O3	96.29(13)
O2_a-Zn1-O3	126.98(15)	O4-Zn1-N1	85.83(14)
O4-Zn1-N2	148.00(14)	O1_a-Zn1-O4	120.27(13)
O2_a-Zn1-O4	98.18(14)	N1-Zn1-N2	80.22(14)
O1_a-Zn1-N1	148.25(13)	O2_a-Zn1-N1	107.33(15)
O1_a-Zn1-N2	84.08(14)	O2_a-Zn1-N2	113.40(15)
O1_a-Zn1-O2_a	54.89(13)		

a =-1+x,1/2+y,1/2-z

Table 9: Selected bond lengths (Å) and angles (°) for **2e**.

Zn1-O3	1.963(4)	Zn1-O4	2.503(5)
Zn1-N1	2.085(6)	Zn1-N2	2.087(5)
Zn1-O1_a	2.508(4)	Zn1-O2_a	1.968(4)
O3-Zn1-O4	57.13(14)	O3-Zn1-N1	110.58(17)
O3-Zn1-N2	104.87(17)	O1_a-Zn1-O3	97.03(14)
O2_a-Zn1-O3	137.51(16)	O4-Zn1-N1	90.30(17)
O4-Zn1-N2	155.05(17)	O1_a-Zn1-O4	110.90(13)
O2_a-Zn1-O4	98.21(14)	N1-Zn1-N2	79.9(2)
O1_a-Zn1-N1	151.62(16)	O2_a-Zn1-N1	102.75(17)
O1_a-Zn1-N2	86.90(17)	O2_a-Zn1-N2	106.30(17)
O1_a-Zn1-O2_a	57.03(14)		

a =-1+x,1/2-y,1/2+z

3A.3.7 Separation of meta-xylene isomer

3A.3.7.1 Importance of separation

Separation technology is of high importance to the chemical, petrochemical and pharmaceutical industry for large scale production of pure compounds. The organic isomers (such as xylenes, long chain hydrocarbons *etc*) with similar physical properties and diverse industrial importance are particularly of interest. Till date distillation process based on difference in boiling points has been the key method in compound purification in the industries.[34] But an alternate solution with cheaper cost and efficiency is adsorption based separation or purification. Porous inorganic resins, silica, porous carbon or zeolites are already accepted[35] as efficient adsorbents but keeping the selectivity and efficiency in consideration porous coordination polymers (PCP) or metal-organic framework (MOF) is

fur more promising.[36] These hybrid materials have high and tunable surface area, periodic well defined structures and most importantly these are modular in nature.[37] Based on these features many promising applications such as gas storage, separation, catalysis and molecular sensing have been achieved and have studied well in the recent years.[9,38] Hence, PCPs can be very effective in adsorption based separation techniques; particularly selective sorption of structural isomers such as industrially important aromatic hydrocarbons, olefins, paraffins and also *ortho*/*meta*/*para*-xylenes.

All three xylene isomers are important raw materials for several useful and industrially important materials.[39] The para-xylene (*p*X) isomer is an important precursor in the synthesis of polyester; similarly meta-isomer (*m*X) is the precursor for isopthalic acid which is used as a copolymerizing monomer for polyethylene terephthalate (PET) synthesis; ortho-xylene (*o*X) is used for pthalic anhydride synthesis which is used as plasticizer. But all these three has very similar physical properties and hence separation becomes tricky and challenging. PCPs have recently been explored for such separation; MIL-47, MIL-53(Al) and HKUST-1 have been found to be very effective for such process.[39b,40] Later on many other PCPs have been studied and mostly these favour para or ortho isomers.[34] Few cases selectivity has been rigorously studied through structural characterization. But a deep insight of the selectivity is rare. In this case it was envisaged that framework **2′** might be a good candidate for separation of xylene isomers as the framework is dynamic and can encapsulate aromatic molecules commensurately through specific host guest intercations.

3A.3.7.2 Xylene vapour adsorption studies and their separation

The single component vapour adsorption experiments of xylene isomers were carried out at 298 K. Unlike the gate opening type adsorption profile of benzene, I have observed stepwise uptake in all three isomers (Figure 44a). After relative pressure P/P_0 ~ 0.05 the *o*X uptake rises sharply to reach final uptake amount of 74.7 mmol per mol. For *p*X a steep uptake occurs at P/P_0 ~ 0.03 and the final uptake amount is 86.3 mmol per mole. In case of *meta* isomer the step is observed at P/P_0 ~ 0.03 and after this pressure uptake is very sharp compared to that of other isomers and the final uptake amount is 92.4 mmol per mol. In every case the adsorbed molecules are not released even at very low pressure suggesting that all the isomers are strongly encapsulated in the host framework. The slightly higher and steep uptake for m*X* at low pressure region compared to *o*X/*p*X indicates that framework has higher affinity towards binding of *m*X in the supramolecular

pores. This provoked us to carry out the diffusion kinetics measurement of all three isomers in the vapour phase. The kinetics measurements were carried out at 293 K and the data were fitted using linear driving force mass transfer model (LDF),[41] which provides satisfactory descriptions in most cases of the adsorption kinetics of various gases/vapors on carbon molecular sieves, active carbons, and even PCPs. This model can be described by the following equation: M_t/M_e = 1 - exp(-kt); where M_t is the mass uptake at time *t*, M_e is the mass uptake at equilibrium, and *k* is the kinetic rate constant. The plot of M_t/M_e vs *t* clearly shows faster mass diffusion for *m*X and similar mass diffusion for ortho and para isomers (Figure 44b). The kinetic rate constant values obtained at pressure P/P_0 ~ 0.074, 0.078 and 0.063 for ortho, para and meta isomers are 7.8×10^{-3}, 6.5×10^{-3} and 2.1×10^{-2} s^{-1}, respectively. Thus the difference of mass diffusion is almost of one magnitude higher for meta isomer compared to other two isomers. Such kinetic selectivity for *m*X is unique as most of the framework structure prefers para or ortho isomers. These results encouraged us to study the competitive experiments for separation of *m*X in presence of *o*X and *p*X.

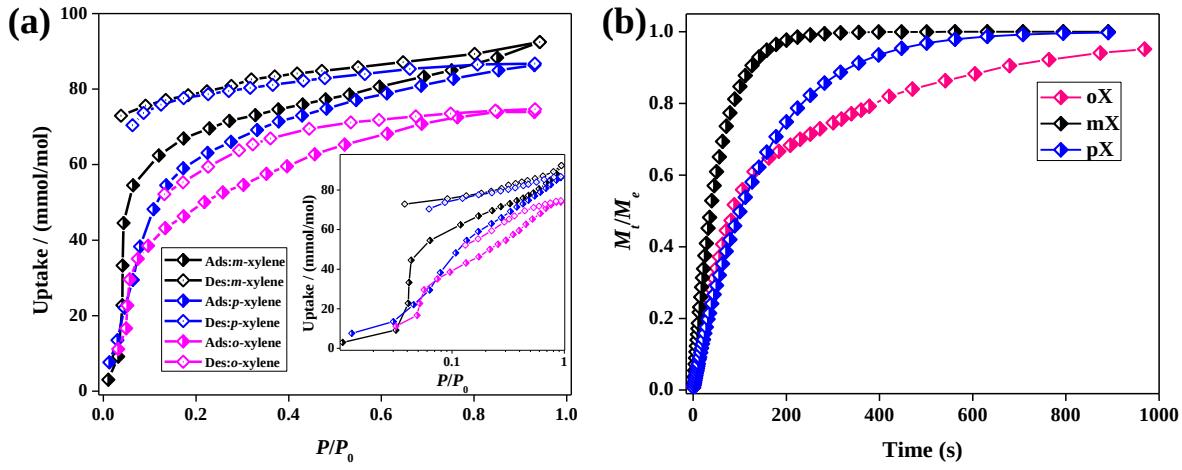

Figure 44: (a) Xylene isomers vapour adsorption profiles for compound **2′** at 293 K; (b) Kinetic plots of xylene isomers vapour diffusion in compound **2′** at 293 K.

Both batch and chromatographic separation experiments of the isomers were carried out. Activated **2′** (100 mg) was immersed in 1:1:1 mixture of the *m*/*p*/*o*-xylene isomers (0.1 mL each) in 3 mL hexane and stirred at RT condition. Several fractions of solvent mixtures are collected at different time intervals (5 min, 15 min, 45 min and 2 h) and GC experiments were carried out to find out the relative ratios of the isomers (Figure 45). With increasing time *m*X isomer % decreases in the mixture; while the other two isomer ratio does not change much. Within 2 h *m*X uptake saturates indicating very fast

diffusion of *m*X into the supramolecular pores of **2′**. This experiment clearly indicates that even in presence of all three isomers **2′** is selective towards *m*X.

(a)

	oX	*mX*	*pX*
5 min	*33/33*	*33/33*	*33/33*
15 min	*45/41*	*13/16*	*42/43*
45 min	*47/46*	*7/9*	*46/45*
2 h	*48/46*	*6/7*	*46/47*

(b)

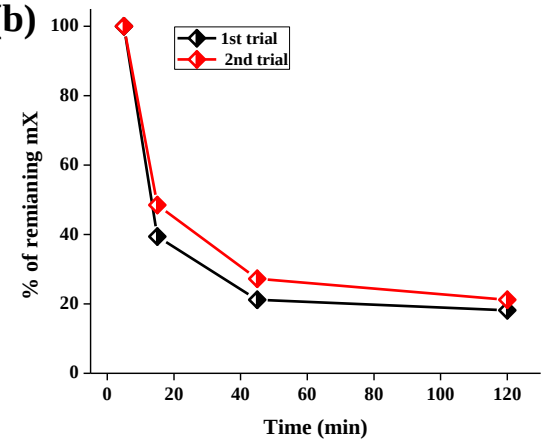

Figure 45: (a) Percentages of each xylene isomer found after different time intervals from two set of batch experiments; (b) Plot of % of unadsorbed *m*X *vs* time for two set of experiments; % of each isomers were obtained from GCMS experiments.

Further, a fixed bed column of **2′** using a glass pipe was made. The diameter of the column is 0.5 cm and length is 4 cm (Figure 46a). This column is prepared using adsorbent **2′** and held by cotton plug from both side. Column was packed using hexane as eluent and the stability of the packed column was tested by continuous flow of hexane for several minutes. 0.6 mL of xylene isomers mixture (1:1:1) in 0.5 mL hexane was added from the top and held 45 minutes for complete diffusion. 7 fractions at 5, 10, 15, 20, 25, 30 and 45 min were collected to check the xylene isomer percentages. The GC experiments clearly shows presence of no meta isomer till 10 min (breakthrough time); after that fractions collected till 45th minutes, meta isomer concentration increases and finally saturates. Thus it can be concluded that till 10 min the column can separate the meta isomer efficiently from the xylene mixtures. The breakthrough time can be increased by changing the column length accordingly.

All these experiments clearly advocate the separation ability of **2′** at ambient condition. The amount adsorbed may not be very high but the selectivity observed for meta isomer is very unique. Hence, it is very important to look into the structure of the xylene adsorbed frameworks and locate the interaction sites.

(a) ***Chromatographic separation***

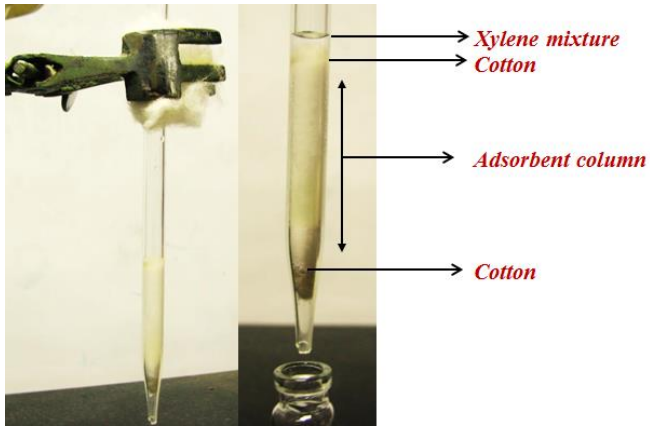

(b)

	oX	*mX*	*pX*
5 min	*51/53*	*---*	*49/47*
10 min	*52/49*	*---*	*48/51*
15 min	*48/49*	*6/6*	*46/45*
20 min	*43/44*	*15/11*	*42/45*
25 min	*41/38*	*21/22*	*38/40*
30 min	*35/37*	*29/30*	*36/33*
45 min	*33/33*	*33/33*	*33/33*

(c)

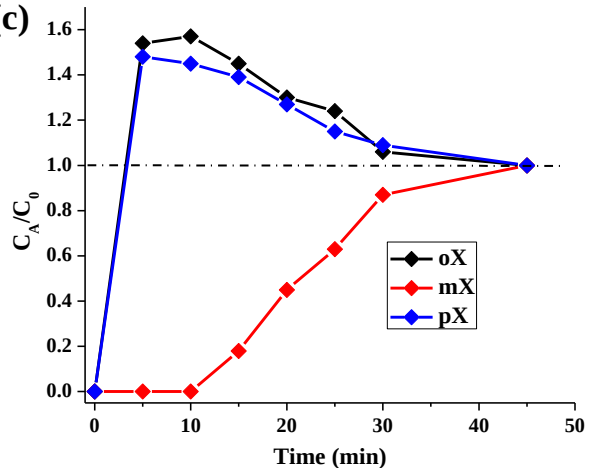

Figure 46: (a) A column packed with the activated framework **2′**; (b) Percentages of each xylene isomer found in the eluent at different time intervals from two set of experiments; (b) Breakthrough plot of *m*X; % of each isomers were obtained from GCMS experiments.

3A.3.7.3 Locating the xylene molecules using single crystal X-ray diffraction

In a postsynthetic way it was not possible to get the single crystals of xylene encapsulated frameworks. Hence, an *in situ* methodology was adopted to get single crystals of xylene included framework and it has been described in section 3A.2.7. The single crystal X-ray diffraction revealed the position of the xylene isomers in the supramolecular pocket. Compound **3a**, the ortho xylene encapsulated framework *crystallizes* in orthorhombic *Pbca* space group and the asymmetric unit contains one Zn^{2+}, one ndc, one *o*-phen and one guest *o*X (Table 11 and 12). The structure exactly resembles mother compound **2**; only dissimilarity is instead of DMF molecules *o*X is sandwiched between the *o*-phen rings. The other two frameworks with meta and para isomers (**3b** and **3c**, respectively) crystallize in orthorhombic *Pc* and $P2_1/c$ space group, respectively (Table 11 and 13-14). The positions of the xylene isomers in the supramolecular pocket

are similar in all the cases (Figure 47). Although the π···π distances are almost same between xylene isomers and *o*-phen (3.649 (*o*x), 3.568 (*m*x) and 3.679 Å (*p*x)), the methyl group directions are different and shown in figure 48.

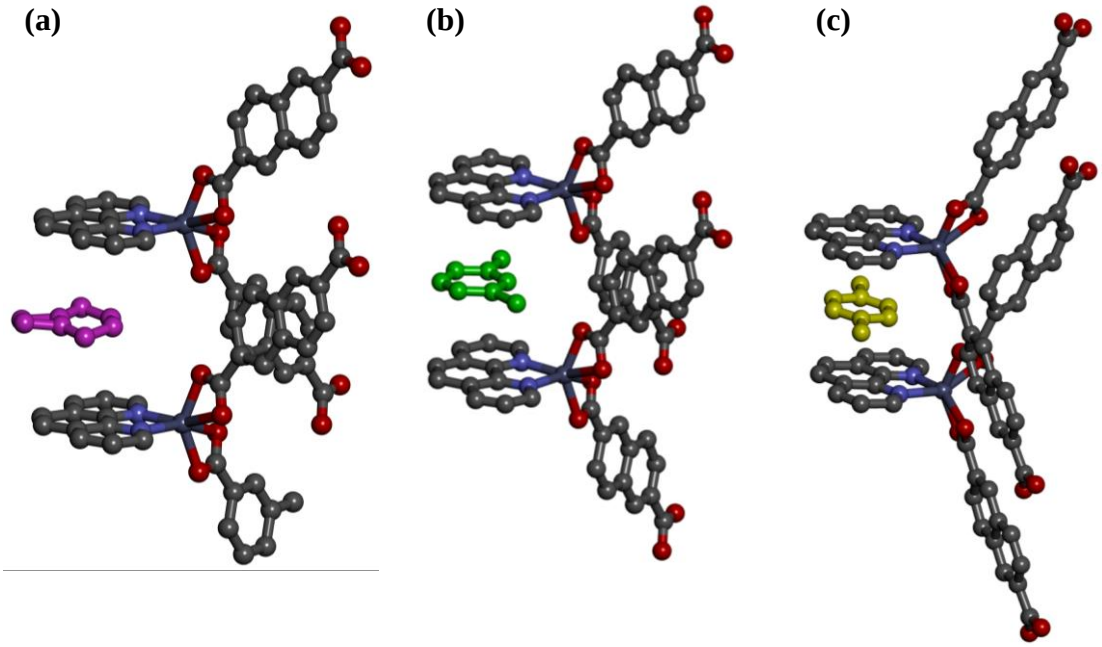

Figure 47: Spatial position of the ortho, meta and para-xylene isomers in compounds (a) **3a**, (b) **3b** and (c) **3c**, respectively.

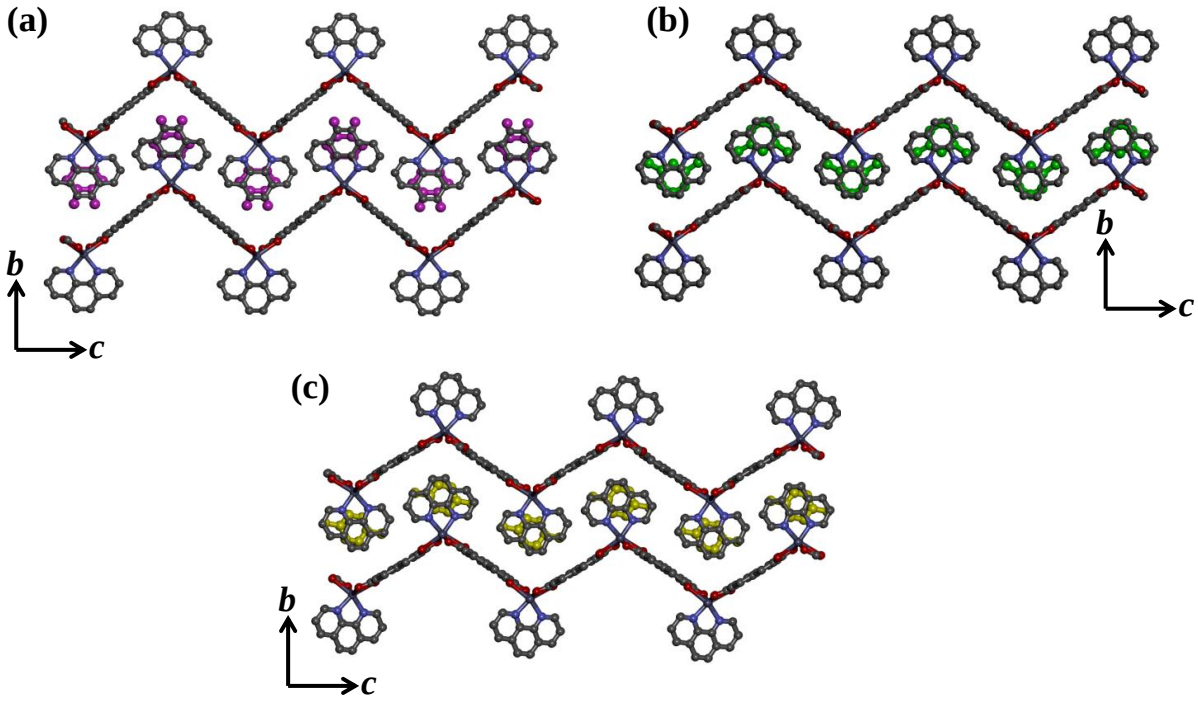

Figure 48: Orientation of the methyl groups of ortho, meta and para-xylene isomers in compounds (a) **3a**, (b) **3b** and (c) **3c**, respectively along *a*-axis.

Table 11: Crystal data and structure refinement parameters of compounds **3a-3c**.

Empirical formula	**$C_{32}H_{24}ZnN_3O_4$ (3a)**	**$C_{32}H_{24}ZnN_3O_4$ (3b)**	**$C_{32}H_{24}ZnN_2O_4$ (3c)**
M_r	565.92	565.92	565.92
crystal System	orthorhombic	Monoclinic	monoclinic
space group	*Pbcn* (No. 60)	*Pc* (No. 7)	$P2_1/c$ (No. 14)
***a* (Å)**	7.554(5)	7.674(5)	7.798(5)
***b* (Å)**	21.865(5)	9.814(5)	19.568(5)
***c* (Å)**	16.015(5)	17.059(4)	16.966(5)
α (deg)	90	90	90
β (deg)	90	90.727(5)	90.805(5)
γ (deg)	90	90	90
***V* (Å^3)**	2645(2)	1284.7(11)	2588.6(19)
Z	4	2	4
***T* (K)**	293	100	293
D_c (g cm^{-3})	1.396	1.468	1.452
μ (mm^{-1})	0.969	0.999	0.991
***F* (000)**	1128	586	1168
θ_{max} (deg)	28.3	28.4	28.4
λ (Mo Kα)(Å)	0.71073	0.71073	0.71073
tot. data	37199	20695	39821
unique data, R_{int}	3282, 0.058	6275, 0.042	6106, 0.089
data [$I > 2\ \sigma(I)$]	2248	4500	2782
R^a,	0.0774	0.0384	0.0478
R_w ^{b}	0.2739	0.1118	0.1310
GOF	1.06	1.03	0.88

^{a} $R = \Sigma||F_o| - |F_c||/\Sigma|F_o|$. ^{b} $R_w = [\Sigma\{w(F_o^2 - F_c^2)^2\}/\Sigma\{w(F_o^2)^2\}]^{1/2}$.

Table 12: Selected bond lengths (Å) and angles (°) for **3a**.

Zn1-O1	2.013(4)	Zn1-O2	2.359(5)
Zn1-N1	2.110(5)	Zn1-O1_a	2.013(4)

Zn1-O2_a	2.359(5)	Zn1-N1_a	2.110(5)
O1-Zn1-O2	96.49(13)	O1-Zn1-N1	104.95(16)
O1-Zn1-O1_a	141.27(14)	O1-Zn1-O2_a	59.49(13)
O1-Zn1-N1_a	104.76(16)	O2-Zn1-N1	157.61(16)
O1_a-Zn1-O2	59.49(13)	O2-Zn1-O2_a	106.94(15)
O2-Zn1-N1_a	89.75(16)	O1_a-Zn1-N1	104.76(16)
O2_a-Zn1-N1	89.75(16)	N1-Zn1-N1_a	78.74(18)
O1_a-Zn1-O2_a	96.49(13)	O1_a-Zn1-N1_a	104.95(16)
O2_a-Zn1-N1_a	157.61(16)		

a = -x,y,3/2-z

Table 13: Selected bond lengths (Å) and angles (°) for **3b**.

Zn1-O1	2.359(7)	Zn1-O2	1.999(6)
Zn1-N1	2.094(7)	Zn1-N2	2.130(7)
Zn1-O3_a	2.043(6)		
Zn1-O4_a	2.365(7)	O1-Zn1-O2	59.0(2)
O1-Zn1-N1	154.1(2)	O1-Zn1-N2	89.4(2)
O1-Zn1-O3_a	96.6(2)	O1-Zn1-O4_a	109.0(2)
O2-Zn1-N1	102.3(2)	O2-Zn1-N2	107.4(3)
O2-Zn1-O3_a	141.1(2)	O2-Zn1-O4_a	97.7(2)
N1-Zn1-N2	78.9(3)	O3_a-Zn1-N1	108.3(2)
O4_a-Zn1-N1	90.2(2)	O3_a-Zn1-N2	101.6(3)
O4_a-Zn1-N2	154.2(2)	O3_a-Zn1-O4_a	59.5(2)

a = -1+x,1-y,-1/2+z

Table 14: Selected bond lengths (Å) and angles (°) for **3c**.

Zn1-O1	1.972(3)	Zn1-O2	2.495(3)
Zn1-N1	2.109(3)	Zn1-N2	2.102(3)
Zn1-O3_b	1.981(3)	Zn1-O4_b	2.457(3)
O1-Zn1-O2	57.48(9)	O1-Zn1-N1	106.34(11)
O1-Zn1-N2	110.24(11)	O1-Zn1-O3_b	136.32(10)
O1-Zn1-O4_b	97.21(9)	O2-Zn1-N1	155.19(10)
O2-Zn1-N2	88.62(10)	O2-Zn1-O3_b	96.39(9)
O2-Zn1-O4_b	111.68(9)	N1-Zn1-N2	79.52(11)
O3_b-Zn1-N1	107.38(11)	O4_b-Zn1-N1	87.62(10)
O3_b-Zn1-N2	102.54(11)	O4_b-Zn1-N2	151.97(10)

b = 1+x,1/2-y,-1/2+z

3A.3.7.4 Computational study: Selectivity towards meta-xylene

To find out the origin of the selectivity towards *m*X isomer periodic density functional theory (DFT) calculations were performed. The computational details are

described in section 3A.2.10. The lattice parameters of the guest removed framework **2** as well as those loaded with isomers of xylene are best predicted using the plain PBE functional. It appears that the D2 and the D3 corrections overestimate the crystal density, whereas the plain PBE functional underestimates it, albeit by a smaller magnitude. However, I have observed (in agreement with many others in the literature)[42-43] that van der Waals corrections are crucial in obtaining reasonable binding energies between the adsorbate molecule and the framework. Specifically, it was found that the D2 corrections are the most appropriate for reproducing the experimental enthalpies of adsorption. Based on binding energy calculations (Table 15-17), the framework favours *m*X over *p*X/*o*X, consistent with experimental observations. The optimized crystal structures are shown in Figure 49. The difference (around 15 kJ/mol) is attributed to the presence of C-H···π interactions in *m*X. The methyl groups in *m*X are oriented in a manner so as to enable the proton in C-H (of the methyl) to interact with the π-cloud of ndc in the framework. This is not so in the case of *p*X and *o*X. Further, confirmation of these observations from periodic density functional theory calculations comes from quantum chemical calculations of relevant fragments of the framework interacting with the isomers of xylene which is described below.

The electron density difference maps were calculated to delineate the interactions between xylene isomers with the PCP using periodic density functional theory calculations. These were performed on the structures which were optimized using PBE-D3 method in CP2K. The electron density difference were calculated using the relation,

$$\Delta\rho = \rho(\text{PCP-xylene isomer}) - \rho(\text{PCP}) - \rho(\text{xylene isomer})$$

Where Δρ, ρ(framework-xylene isomer), ρ(framework) and ρ(xylene isomer) are the electron density difference of the system, total electron density of the framework with xylene isomer, individual electron density of the framework and isolated xylene isomer respectively. These maps are shown in Figure 50a-c. Orange and cyan regions indicate the increased and decreased electron densities. The main interactions are one involving between frameworks atoms and xylene isomers: i) π-π interaction between phenyl ring of xylene isomers with ndc linker of the framework, ii) C-H···π interactions between phenyl C-H, methyl C-H of xylene isomers and π-electron cloud of ndc linkers of framework, and iii) H-bond interaction between C-H of methyl group of *o*X and carboxylate oxygen of ndc from the PCP. The binding energies of *o*-, *m*-, and *p*X isomers in the framework are 133.412, 144.096, and 135.126 kJ/mol which are tabulated in Table 15. *m*X

participate the methyl C-H···π interaction with the ndc linkers which are absent in *o*X leads to the less binding energy than *m*X or *p*X.

Plane wave based codes such as CPMD or CP2K does not handle hybrid exchange-correlation functionals efficiently. For instance, the B3LYP or M06 functionals have been shown to properly account for dispersion interactions. These are however implemented efficiently in codes such as Gaussian[44] which use a localized basis set. Unfortunately, periodic calculations cannot be carried out with such an approach. However, one can identify regions of the framework which are proximal to the adsorbed xylene isomers and can consider such a fragment, and terminate it sensibly with hydrogen atoms. It should then be possible to obtain binding energies of the adsorbate with this fragment and also identify various interactions contributing to it. Here, I identify two such critical interactions between xylene and the framework: i) π···π and b) C-H···π interactions. The latter can arise either from the xylene aromatic C-H or from the xylene methyl C-H. Calculations were carried out using the functional M06[45] which treats non-covalent interactions well.[46] The 6-31g(d,p) basis set was employed. SCF energies were calculated for isolated xylene isomers, framework fragments and for xylene isomers interacting with the fragments (Figure 51). The framework fragments were chosen from the respective experimental crystal structures. The interaction strengths of xylene isomers with the fragments of the framework are also shown in Figure 51. *m*X interacts the strongest, confirming the periodic PBE-D2 calculations.

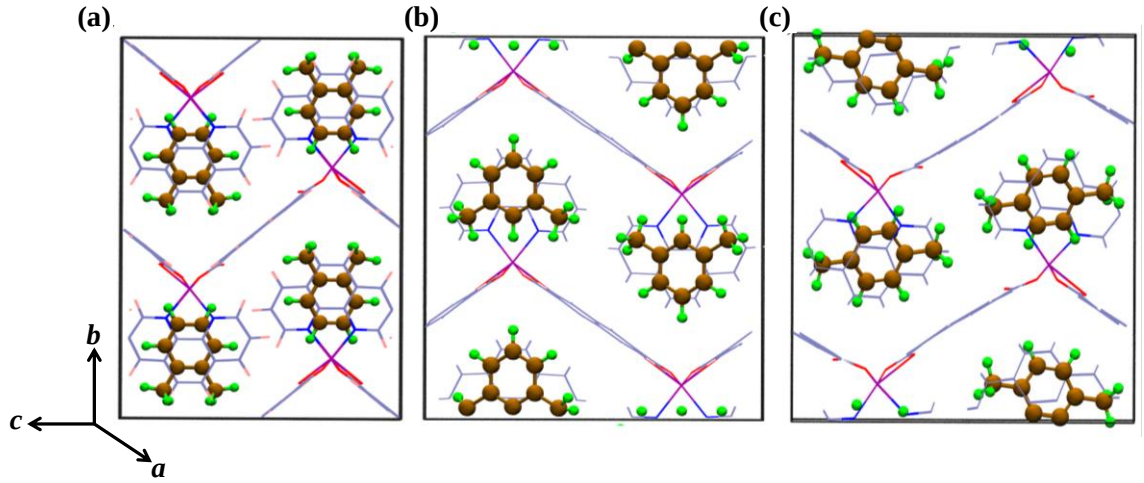

Figure 49: a, b, c are the optimized geometries of ortho, meta and para-xylene isomers in **3a**, **3b** and **3c**, respectively using PBE-D3 level of theory. Xylene isomers are represented in ball and stick model and the framework is in line representation. Color scheme: Xylene isomers: C-ochre and H-green; Framework: C-iceblue, H-pink, O-red and Zn-violet.

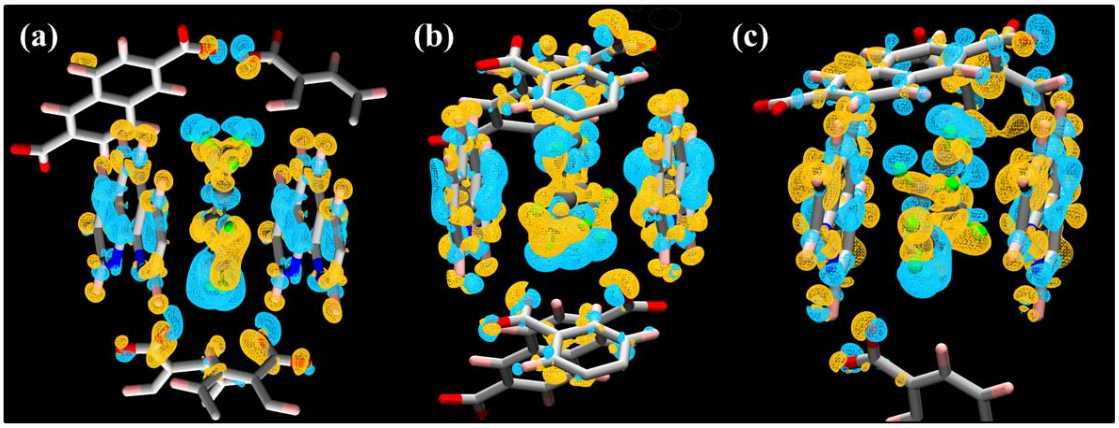

Figure 50: a, b, and c are the electron density difference maps of *o*-xylene, *m*-xylene and *p*-xylene in **3a**, **3b** and **3c**, respectively. Orange and cyan regions indicate the increased and decreased electron density, respectively. Representations: Framework atoms are in stick and xylenes are in ball and stick. Color scheme: Framework atoms: C-silver, H-pink and O-red; Xylene isomers: C-gray and H-green. The electron density difference has been calculated for the entire framework. However, only the region around xylene isomers is shown for clarity.

Table 15: Binding energy calculation results using PBE-D3 method.

Compound		***a* (Å)**	***b* (Å)**	***c* (Å)**	***β* (°)**	**Volume Error %**	**Binding energy (kJ/mol)**
3c (2×1×1)	Expt.	15.596	19.568	16.966	90.805	-2.700	-135.729 (12.407)
	Theory	15.316	19.368	16.976	91.805		
3b (2×2×1)	Expt.	15.348	19.628	17.059	90.727	-3.210	-144.096 (12.988)
	Theory	15.008	19.428	17.058	89.567		
3a (2×1×1)	Expt.	15.108	21.805	16.015	90.000	-1.600	-133.412 (10.531)
	Theory	14.908	21.795	15.965	90.000		

Table 16: Binding energy calculation results using PBE-D2 method.

Compound		***a* (Å)**	***b* (Å)**	***c* (Å)**	***β* (°)**	**Volume Error %**	**Binding energy (kJ/mol)**
3c (2×1×1)	Expt.	15.596	19.568	16.966	90.805	-5.060	-128.610
	Theory	15.126	19.178	16.956	92.135		

Compound		***a* (Å)**	***b* (Å)**	***c* (Å)**	***β* (°)**	**Volume Error %**	**Binding energy (kJ/mol)**
							(13.349)
3b (2×2×1)	Expt.	15.348	19.628	17.059	90.727	-4.160	-143.290 (13.999)
	Theory	14.908	19.368	17.058	89.467		
3a (2×1×1)	Expt.	15.108	21.805	16.015	90.000	-2.600	-123.437 (10.504)
	Theory	14.908	21.645	15.915	90.000		

Table 17: Binding energy calculation results using PBE method.

Compound		***a* (Å)**	***b* (Å)**	***c* (Å)**	***β* (°)**	**Volume Error %**	**Binding energy kJ/mol**
3c (2×1×1)	Expt.	15.596	19.568	16.966	90.805	2.400	-2.800 (11.303)
	Theory	15.726	19.758	17.076	91.065		
3b (2×2×1)	Expt.	15.348	19.628	17.059	90.727	1.980	-3.470 (11.854)
	Theory	15.468	19.758	17.480	90.287		
3a (2×1×1)	Expt.	15.108	21.805	16.015	90.000	3.260	-6.325 (9.511)
	Theory	15.278	22.095	16.135	90.00		

Following Sanders *et. al.*[47] report, the binding energies can be explained as follows: In *m*X, the C-H bond from the aromatic ring is oriented along the centroid of the framework ndc π system, whereas in *p*X and *o*X, the C-H bond of the aromatic ring of xylene molecules does not point to the centroid of π system of the framework fragment. Hence *m*X has more binding energy (113 kJ/mol) than *p*X and *o*X. Binding energies of *p*X and *o*X with the framework fragments were calculated to be 100 and 85 kJ/mol, respectively. It is gratifying to note that the magnitudes of binding energies between the

bulk and fragment calculations are comparable. Further, both calculations predict a deeper binding for *m*X with the framework.

In order to obtain the contribution of π···π and C-H···π (aromatic C-H or methyl C-H) interactions to the stabilization energy, fragment calculations similar to the one described above were carried out but with certain regions/groups masked. The energy contributions from each of the masked segment as discussed in Figure 52 are shown in Table 18.

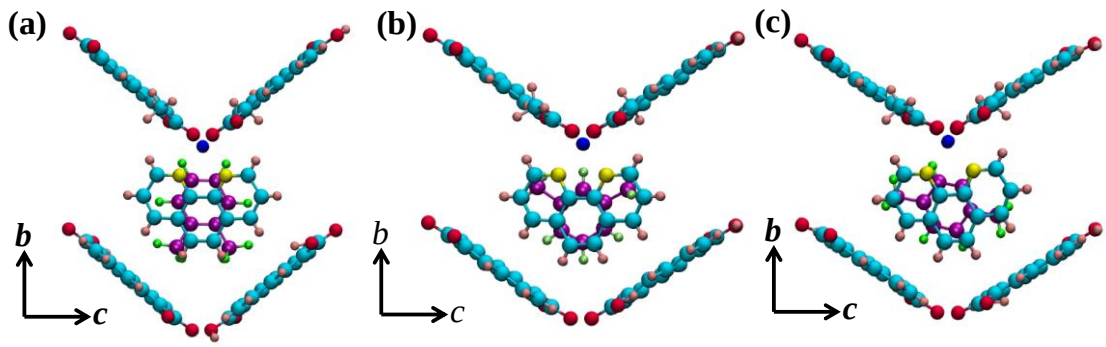

Figure 51: Orientation of the methyl groups of *o*X, *m*X and *p*X isomers in compounds (a) **3a**, (b) **3b** and (c) **3c**, respectively along *a*-axis.

The π···π interactions are more in *m*X rather than *p*X and *o*X due to preferable orientation with framework π-cloud. Interactions between the aromatic ring C-H group and the π cloud of the framework are present in *m*X and *p*X with strengths of 12 and 13 kJ/mol. These values are comparable to those reported by Severance *et. al.*[48] In *o*X, the strength of the interaction between methyl group C-H and the π cloud of framework is around 6.2 kJ/mol, which is comparable to that reported by Tsuzuki *et. al.*[49] In *m*X, the distance between C-H and the centroid of the closest π systems is within 3.45 Å whereas in *p*X and *o*X, the distances can be beyond 5 Å. Thus, those methyl C-H bonds will not participate in C-H···π interactions, decreasing the stability of the corresponding xylene isomers.

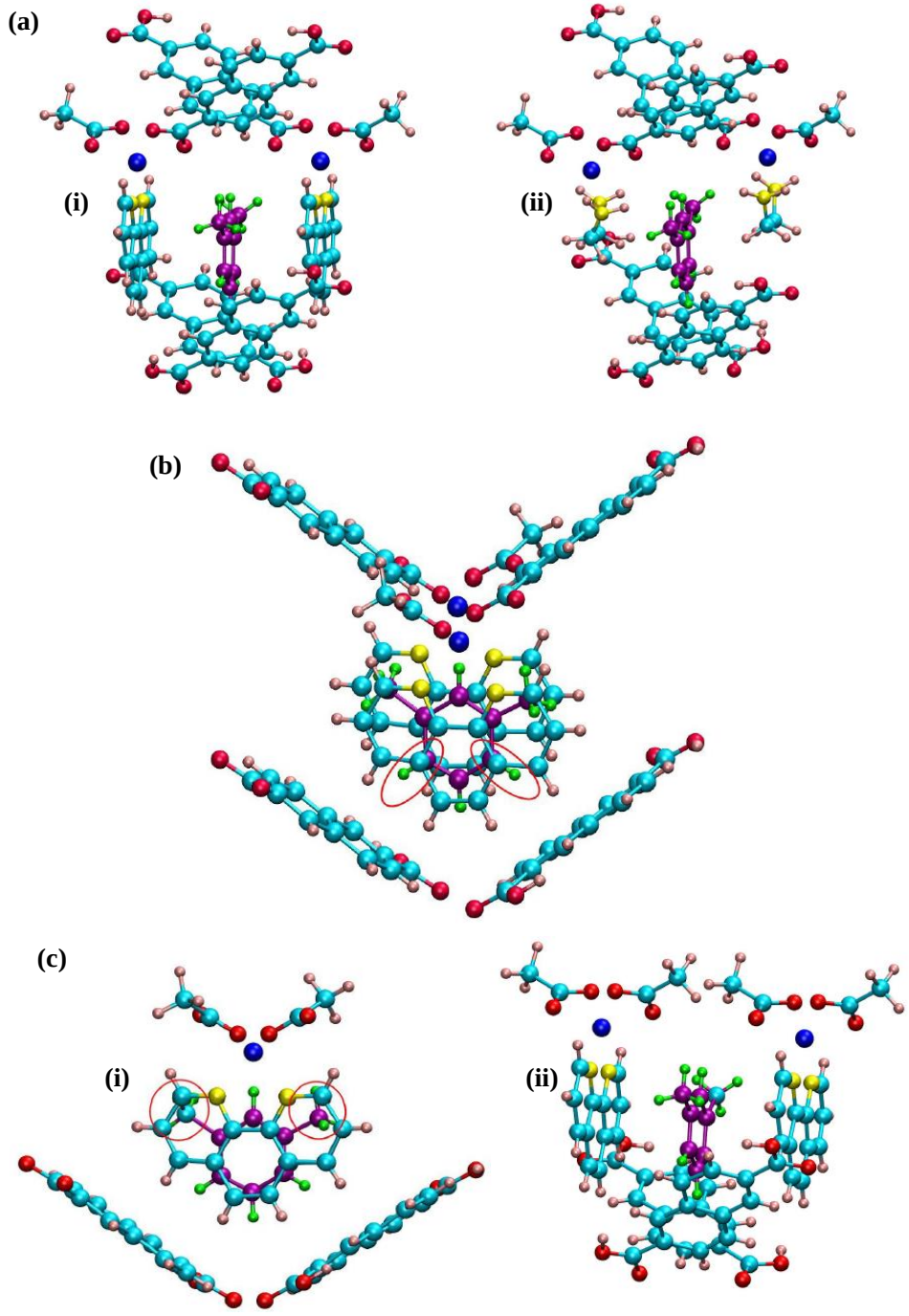

Figure 52: These fragments used in masked calculations: (a) Identifying contributions from π···π and methyl C-H···π interactions (i) original complete fragment (same as seen in Figure 50). Two π systems of the framework can be seen on either side of the central *m*X (ii) the two π systems discussed in (i) are changed to H_2N-CH_2-CH_2-NH_2. In this process, the π···π interactions between these two π systems and *m*X is removed. Further, the interaction between the methyl C-H and the π systems is also removed; (b) Interaction between the aromatic C-H of *m*X with the framework π systems. The former, oriented towards the latter are circled. The contribution of this interaction to the stabilization energy is obtained by masking out the two π systems of the framework that are shown below *m*X on its left and right; (c) Contribution for methyl C-H of xylene and π system of framework. Two orientations are shown. In (i), the specific methyl C-H bonds which pointed to these π systems are circled, In (ii), The π systems on top of the xylene are changed to acetate which coordinate the zinc atom.

Table 18: Energy contributions from the masked calculations.

Xylene Isomers	**Energy contribution from interaction (a) (kJ/mol)**	**Energy contribution from interaction (b) (kJ/mol)**	**Energy contribution from interaction (c) (kJ/mol)**
meta-xylene	-66.872	-24.402	-4.109
para-xylene	-25.098	-27.424	-4.375
ortho-xylene	-3.893	-3.741	-12.672

3A.4 Conclusions

In conclusion, a luminescent molecular complex {[Mg(*o*-phen)$(H_2O)_4$](2PBA)(H_2O)} (**1**) has been synthesized and it shows pyrene:*o*-phen preassociated exciplex emission. This emission was found to be amplified by an energy transfer process from the other PBA subunit. Further, a 1D supramolecular luminescent porous framework, {[Zn(ndc)(*o*-phen)]·DMF}$_n$ (**2**) was synthesized using similar concept. The dynamic and nanoporous nature of the framework, confirmed from PXRD coupled CO_2 adsorption experiment and benzene vapour adsorption is exploited for recognition of aromatic amines. For aniline and other substituted anilines red shifted CT emissions of guest amines and *o*-phen were observed. The structural characterization using single crystal X-ray diffraction revealed presence of CT emission which is further amplified by FRET process from ndc linker. Following this work, this supramolecular framework **2′** was exploited for kinetic separation of *m*X from *p*X and *o*X. Chromatographic and batch experiments confirmed the separation ability of the framework. Single crystal structures of xylene isomers included frameworks and computational studies clearly show the interaction sites and origin of selectivity. Such semi-covalent approach to build supramolecular porous structure is new and has been exploited for the first time. Moreover, this porous supramolecular PCP is the first example which shows aromatic amine sensing with such CT emission properties. The *m*X selectivity for a PCP system is also rare and thus this porous supramolecular structure has bimodal recognition and separation capability. Based on this concept several other PCP materials can be developed for recognition or separation purposes.

3A.5 References

1. a) D. R. Prasad, G. Ferraudi, *Inorg. Chem*. **1983**, *22*, 1672; b) H. L. Lehtivuori, H. Lemmetyinen, N. V. Tkachenko, *J. Am. Chem. Soc.* **2006**. *128*, 16036; c) D. Kim, A. Osuka, *Acc. Chem. Res*. **2004**, *37*, 735; d) G. De Santis, L. Fabbrizzi, M. Licchelli, C. Mangano, D. Sacchi, *Inorg. Chem.* **1995**, *34*, 3581; e) A. Jover, F. Meijide, E. R. Núñez, J. V. Tato, *Langmuir* **1996**, *12*, 1789; f) J. K. Klosterman, M. Iwamura, T. Tahara, M. Fujita, *J. Am. Chem. Soc.* **2009**, *131*, 9478; g) D. Gust, T. A. Moore, A. L. Moore, *Acc. Chem. Res*. **2001**, *34*, 40; h) T. J. Meyer, *Acc. Chem. Res*. **1989**, *22*, 163.

2. a) C. Vijaykumar, V. K. Praveen, A. Ajayaghosh, *Adv. Mater*. **2009**, *21*, 2059; b) A. Ajayaghosh, V. K. Praveen, C. Vijayakumar, *Chem. Soc. Rev*. **2008**, *37*, 1090; c) C. Vijayakumar, V. K. Praveen, K. K. Kartha, A. Ajayaghosh, *Phys. Chem. Chem. Phys.* **2011**, *13*, 4942.

3. a) S. L. Lai, M. Y. Chan, Q. X. Tong, M. K. Fung, P. F. Wang, C. S. Lee, S. T. Lee, *Appl.Phys. Lett*. **2008**, *93*, 143301; b) H. Zhu, X. Zheng, Z. Fuzun, Z. Suling, D. Song, *Appl. Surf. Sci.* **2006**, *54*, 5511; c) W. E. B. Shepherd, A. D. Platt, M. J. Kendrick, M. A. Loth, J. E. Anthony, O. J. Ostroverkhova, *Phys. Chem. Lett.* **2011**, *2*, 362.

4. M. D. Allendorf, C. A. Bauer, R. K. Bhakta, R. J. T. Houk, *Chem. Soc. Rev*. **2009**, *38*, 1330.

5. a) B. Chen, L. Wang, F. Zapata, G. Qian, E. B. Lobskovsky, *J. Am. Chem. Soc*. **2008**, *130*, 6718; b) C. A. Kent, B. P. Mehl, L. Ma, J. M. Papanikolas, T. J. Meyer, W. Lin, *J. Am. Chem. Soc*. **2010**, *132*, 112767; c) G. Calzaferri, S. Huber, H. Maas, C. Minkowski, *Angew. Chem. Int. Ed.* **2003**, *42*, 3732; d) G. Calzaferri, K. Lutkouskaya, *Photochem. Photobiol. Sci.* **2008**, ***7***, 879; e) N. Mizoshita,T. Taniab, S. Inagaki, *Chem. Soc. Rev.* **2011**, *40*, 789; f) H. Xu, F. Liu, Y. Cui, B. Chen, G. Qian, *Chem. Commun*. **2011**, *47*, 3153; g) S. J. K. Pond, O. Tsutsumi, M. Rumi, O. Kwon, E. Zojer, J.–L. Brédas, S. R. Marder, W. J. Perry, *J. Am. Chem. Soc*. **2004**, *126*, 9291; h) X. Zhang, M. A. Ballem, M. Ahrén, A. Suska, P. Bergman, K. Uvdal, *J. Am. Chem. Soc*. **2010**, *132*, 10391; i) W. Lin, W. Rieter, K. M. L. Taylor, *Angew. Chem. Int. Ed*. **2009**, *48*, 650; j) A. Lan, K. Li, H. Wu, D. H. Olson, T. J. Emge, W. Ki, M. Hong, J. Li, *Angew. Chem. Int. Ed*. **2009**, *48*, 2334.

6. a) S. Inagaki, O. Ohtani, Y. Goto, K. Okamoto, M. Ikai, K. Yamanaka, T. Tani, T. Okada, *Angew. Chem. Int. Ed.* **2009**, *48*, 4042; b) K. V. Rao, K. K. R. Datta, M. Eswaramoorthy, S. J. George, *Angew. Chem. Int. Ed.* **2011**, *50*, 1179; c) K. A. White, D.

A. Chengelis, K. A. Gogick, J. Stehman, N. L. Rosi, S. Petoud, *J. Am. Chem. Soc*. **2009**, *131*, 18069; d) C. Y. Lee, O. K. Farha, B. J. Hong, A. A. Sarjeant, S. T. Nguyen, J. T. Hupp, *J. Am. Chem. Soc*. **2011**, *133*, 15858; e) K.–L. Wong, G.–L. Law, Y.-Y. Yang; W.-T. Wong, *Adv. Mater*. **2006**, *18*, 1051; f) X. Zhang, M. A. Ballem, Z.-J. Hu, P. Bergman, K. Uvdal, *Angew. Chem. Int. Ed.* **2011**, *50*, 5729.

7. a) C.–C. Tsai, T.–T. Luo, J.–F. Yin, H.–C. Lin, K.–L. Lu, *Inorg. Chem*. **2009**, *48*, 8650; b) G. A. Pereira, J. A. Peters, F. A. A. Paz, J. Rocha, C. F. G. C. Geraldes, *Inorg. Chem*. **2010**, *49*, 2969; c) K. Jayaramulu, P. Kanoo, S. J. George, T. K. Maji, *Chem. Commun*. **2010**, *46*, 7906.

8. a) H. -S. Choi, M. P. Suh, *Angew. Chem. Int. Ed*. **2009**, *48*, 6865; b) R. Kitaura, K. Seki, G. Akiyama, S. Kitagawa, *Angew. Chem. Int. Ed*. **2003**, *43*, 428; c) R. Haldar, S. K. Reddy, V. M. Suresh, S. Mohapatra, S. Balasubramanian, T. K. Maji, *Chem. Eur. J*. **2014**, *20*, 4347; d) S.-I. Noro, Y. Hijikata, M. Inukai, T. Fukushima, S. Horike, M. Higuchi, S. Kitagawa, T. Akutagawa, T. Nakamura, *Inorg. Chem*. **2013**, *52*, 280.

9. a) B. D. Chandler, D. T. Cramb, G. K. H. Shimizu, *J. Am. Chem. Soc*. **2006**, *128*, 10403; b) Y. Cui, Y. Yue, B. Chen, G. Qian, B. Chen, *Chem. Rev*. **2012**, *112*, 1126; c) D. Liu, K. Lu, C. Poon, W. Lin, *Inorg. Chem*. **2014**, *53*, 1916; d) L. E. Kreno, K. Leong, O. K. Farha, M. Allendorf, R. P. V. Duyne, J. T. Hupp, *Chem. Rev*. **2012**, *112*, 1105; e) G. Lu, J. T. Hupp, *J. Am. Chem. Soc*. **2010**, *132*, 7832; f) D. Ma, B. Li, X. Zhou, Q. Zhou, K. Liu, G. Zeng, G. Li, Z. Shi, S. Feng, *Chem. Commun*. **2013**, *49*, 8964; g) Z. Xai, L. Ma, K. E. deKrafft, A. Jin, W. Lin, *J. Am. Chem. Soc*. **2010**, *132*, 922; h) R.-B. Lin, F. Li, S.-Y. Liu, X.-L. Qi, J.-P. Zhang, X.-M. Chen, *Angew. Chem. Int. Ed*, **2013**, *52*, 13429.

10. a) Y. Takashima, V. M. Martinez, S. Furukawa, M. Kondo, S. Shimomura, H. Uehara, M. Nakahama, K. Sugimoto, S. Kitagawa, *Nat. Commun.* **2011**, *2*, 168; b) C.-Y. Sun, X.-L. Wang, X. Zhang, C. Qin, P. Li, Z.-M. Su, D.-X. Zhu, G.-G. Shan, K.-Z. Shao, H. Wu, J. Li, *Nat. Commun.* **2013**, *4*, 168; c) D. Yan, Y. Tang, H. Lin, D. Wang, *Sci. Rep*. **2014**, *4*, 4337.

11. a) R. Haldar, T. K. Maji, *CrystEngComm*. **2012**, *14*, 684; b) P. Kanoo, R. Sambhu, T. K. Maji, *Inorg. Chem*. **2011**, *50*, 400.

12. a) D. Tanaka, S. Horike, S. Kitagawa, M. Ohba, M. Hasegawa, Y. Ozawa, K. Toriumi, *Chem. Commun*. **2007**, 3142; b) P. L. Feng, K. Leong, M. D. Allendorf, *Dalton Trans*. **2012**, *41*, 8869; c) Y. Zeng, Z. Fu, H. Chen, C. Liu, S. Liao, J. Dai, *Chem. Commun*. **2012**, *48*, 8114; d) V. M. Martinez, S. Furukawa, Y. Takashima, I. L. Arbeloa,

S. Kitagawa, *J. Phys. Chem. C*. **2012**, *116*, 26084; e) G. J. McManus, J. J. Perry IV, M. Perry, B. D. Wagner, M. J. Zaworotko, *J. Am. Chem. Soc*. **2007**, *129*, 9094.

13. a) M. D. Hall, H. R. Mellor, R. Callghan, T. W. Hambley, *J. Med. Chem*. **2007**, *50*, 3403; b) H. Kanazawa, M. Higuchi, K. Yamamoto, *Macromolecules*. **2006**, *39*, 138; c) H. Li, L. S. Lee, *Environ. Sci. Technol*. **1999**, *33*, 1864; d) D. Nikolic, R. B. van Breeman, *Chem. Res. Toxicol*. **2001**, *14*, 351.

14. J.-R. Lee, J. Sculley, H.-C. Zhou, *Chem. Rev.* **2012**, *112*, 869.

15. SMART (V 5.628), SAINT (V 6.45a), XPREP, SHELXTL; Bruker AXS Inc. Madison, Wisconsin, USA, **2004**.

16. G. M. Sheldrick, Siemens Area Detector Absorption Correction Program, University of Götingen, Götingen, Germany, **1994**.

17. A. Altomare, G. Cascarano, C. Giacovazzo, A. Gualaradi, *J. Appl. Cryst*. **1993**, *26*, 343.

18. G. M. Sheldrick, SHELXL-97, Program for Crystal Structure Solution and Refinement; University of Götingen, Götingen, Germany, **1997**.

19. A. L. Spek, *J. Appl. Cryst*. **2003**, *36*, 7.

20. G. M. Sheldrick, SHELXS 97, Program for the Solution of Crystal Structure, University Götingen, Germany, **1997**.

21. L. J. Farrugia, WinGX-A Windows Program for Crystal Structure Analysis, *J. Appl. Cryst.* **1999**, *32*, 837.

22. J. VandeVondele, M. Krack, F. Mohamed, M. Parrinello, T. Chassaing, X. Hutter, *J. Compt. Phys. Commun*. **2005**, *167*, 103.

23. J. VandeVondele, J. Hutter, *J. Chem. Phys*. **2007**, *127*, 114105.

24. A. D. Becke, *Phys. Rev. A.* **1988**, *38*, 3098.

25. C. Lee, W. Yang, R. G. Parr, *Phys. Rev. B*. **1988**, *37*, 785.

26. S. Grimme, *J. Comp. Chem*. **2006**, *27*, 1787.

27. C. Hartwigsen, S. Goedecker, J. Hutter, *Phys. Rev. B*. **1998**, *58*, 3641.

28. M. D. Pandey, A. K. Mishra, V. Chandrashekhar, S. Verma, *Inorg. Chem*. **2010**, *49*, 2020; b) B. Manimaran, L.–J. Lai, P. Thanasekaran, J.–Y. Wu, R. T. Liao, T.–W. Tseng, Y.–H. Liu, G.–H. Lee, S.–M. Peng, K.–L. Lu, *Inorg. Chem*. **2006**, *45*, 8070; c) S. S. Babu, V. K. Praveen, S. Prasanthkumar, A. Ajayaghosh, *Chem. Eur. J*. **2008**, *14*, 9577.

29. a) M. Kumar, S. J. George, *Chem. Eur. J*. **2011**, *17*, 11102; b) M. Kumar, S. J. George, *Nanoscale.* **2011**, *3*, 2130.

30. R. J. Hartley, L. R. Faulkner, *J. Am. Chem. Soc*. **1985**, *107*, 3436.

31. The sizes of the channels were calculated considering the van der Waals radii of the atoms.

32. H. J. Park, M. P. Suh, *Chem. Commun*. **2010**, *46*, 610.

33. A. M. Plonka, D. Banerjee, W. R. Woerner, Z. Zhang, N. Nijem, Y. J. Chabal, J. Li, J. B. Parise, *Angew. Chem. Int. Ed*. **2013**, *52*, 1692.

34. R. M. Lima, I. E. Grossmann, *AIChE J*. **2009**, *55*, 354.

35. a) H. A. Mohameed, B. A. Jdayil, K. Takrouri, *Chem. Eng. Process.* **2007**, *46*, 25; b) V. Cottier, J.-P. Bellat, M.-H. Simonot-Grange, A. Methivier, *J. Phys. Chem. B.* **1997**, *101*, 4798; c) W. Yuan,Y. S. Lin, W. Yang, *J. Am. Chem. Soc.* **2004**, *126*, 4776.

36. a) Z. R. Herm, E. D. Bloch, J. R. Long, *Chem. Mater.* **2014**, *26*, 323; b) Z. R. Herm, B. M. Wiers, J. A. Mason, J. M. van Maten, M. R. Hudson, P. Zajdel, C. M. Brown, N. Masciocchi, R. Krishna, J. R. Long, *Science*. **2013**, *340*, 960.

37. a) S. Kitagawa, R. Kitaura, S.–I. Noro, *Angew. Chem., Int. Ed.* **2004**, *43*, 2334; b) O. M. Yaghi, *Nat. Mater*. **2007**, *6*, 92.

38. a) R. Banerjee, A. Phan, B. Wang, C. Knobler, H. Furukawa, M. O'Keeffe, O. M. Yaghi, *Science*. **2008**, *319*, 939; b) H. Hayashi, A. P. Côté, H. Furukawa, M. O'Keeffe, O. M. Yaghi, *Nat. Mater*. **2007**, *6*, 501; c) R. K. Das, A. Aijaz, M. K. Sharma, P. Lama, P. K. Bharadwaj, *Chem. Eur. J*. **2012**, *18*, 6866.

39. a) Ullmann's Encyclopedia of Industrial Chemistry, 6th Ed.; John Wiley & Sons: New York, **2006**; electronic release; b) V. Finsy, H. Verelst, L. Alaerts, D. De Vos, P. A. Jacobs, G. V. Baron, J. F. M. Denayer, *J. Am. Chem. Soc.* **2008**, *130*, 7110.

40. M. A. Moreira, J. C. Santos, A. F. P. Ferriera, J. M. Loureiro, A. E. Rodrigues, *Ind. Eng. Chem. Res.* **2011**, *50*, 7688.

41. N. Sikdar, A. Hazra, T. K. Maji, *Inorg. Chem.* **2014**, *53*, 5993.

42. P. Kanoo, S. K. Reddy, G. Kumari, R. Haldar, C. Narayana, S. Balasubramanian, T. K. Maji, *Chem. Commun*. **2012**, *48*, 8487.

43. D. Fairen-Jimenez, R. Galvelis, A. Torrisi, A. D. Gellan, M. T. Wharmby, P. A. Wright, C. Mellot-Draznieks, T. Düren, *Dalton. Trans*. **2012**, *41*, 10752.

44. M. J. Frisch, G. W. Trucks, H. B. Schlegel *et. al*. GAUSSIAN 09, Revision A.1, Gaussian Inc. Wallingford, CT, **2009**.

45. Y. Zhao, D. G. Truhlar, *Theor. Chem. Acc.* **2008**, *120*, 215.

46. Y. Zhao, D. G. Truhlar, *Acc. Chem. Res*. **2008**, *41*, 157.

47. C. A. Hunter, J. K. M. Sanders, *J. Am. Chem. Soc*. **1990**, *112*, 5525.

48. W. L. Jorgensen, D. L. Severance, *J. Am. Chem. Soc.* **1990**, *112*, 4168.

49. S. Tsuzuki, K. Honda, T. Uchimaru, M. Mikami, K. Tanabe, *J. Am. Chem. Soc*. **2000**, *122*, 3746.

Part: 3B

Flexible supramolecular framework for dye encapsulation, host-guest energy transfer and solvent sensing

Summary

In this chapter, a 1D coordination polymer $\{[Zn(ndc)(2,2'\text{-bpy})]\cdot 2DMF\}_n$ (**1**) (ndc = 2,6-napthalenedicarboxylate; 2,2′-bpy = 2,2′-bipyridyl) has been synthesized following previously established synthetic protocols shown in section 3A. **1** self-assembles to 3D supramolecular structure with large distorted 1D rectangular channel and shows structural rearrangement upon guest solvent removal. The desolvated (**1′**) framework shows stepwise CO_2, C_2H_2 and solvent vapour uptake profiles indicating dynamic nature of the framework. Fluorescein dye was encapsulated into the supramolecular pores of **1′** to obtain a dual emissive (blue and green) inclusion compound **1a**. **1a** emits yellow and small amount of dye inclusion further allows adsorption of different solvent vapours. **1a** shows different types of dual emission characteristics in solvents of different polarities. Such emission colour tuning is possibly due to structural change during solvent vapour diffusion that tunes energy transfer efficiency from framework to the encapsulated dye fluorescein (host to guest energy transfer).

1. R. Haldar, K. Prasad, T. K. Maji, To be submitted.

3B.1 Introduction

Porous metal-organic polymers or coordination polymers (PCPs) are well-known for their highly crystalline and modular nature.[1] Thus, their structure and functionalities can be readily tuned and in some cases predictable. Such unique features of PCPs give rise to applications in gas storage and separation, catalysis, drug delivery etc.[2] Apart from these; luminescent PCPs are also very promising for molecular sensing, light harvesting and nonlinear optics.[3] Using luminescent linkers many such PCPs are reported those show solvent sensing, explosive sensing, metal ion sensing or volatile organic chromophore sensing.[4] All these are mostly dependent on change in luminescence intensity from single transition, and hence may not be accurate enough as absolute intensity in the solid state is variable. In addition quenching or enhancement of emission intensity, as in most sensing processes are observed, is not as effective as shift in the emission profile which leads to direct visual readout.[5] Hence, a dual emissive platform is much more effective to build an easy readout sensory material. Till date using PCPs such efforts are rare.[6]

To synthesize a dual emissive material use of host-guest chemistry is fruitful; a luminescent framework which can encapsulate large dye molecules is most suitable one.[7] Further, a partial overlap of emission spectrum of host framework with the absorption spectrum of encapsulated dye may lead to energy transfer phenomenon; a complete energy transfer might lead to complete quenching of emission from the host and hence to get dual emission feature perfect spectral overlap is not suitable. In addition it was envisioned a flexible host PCP that adapts the pore structure to accommodate incoming dye molecules through specific host-guest interaction.[8] To synthesize such PCP a methodology was adopted that is described in the previous PART-3A and a luminescent 1D coordination polymer $\{[Zn(ndc)(2,2'\text{-bpy})]\cdot 2DMF)\}_n$ (**1**) was synthesized. This 1D coordination polymer forms a 3D supramolecular structure with large 1D channels occupied by guest DMF molecules. This shows avid flexibility as realized from the gas (CO_2 and C_2H_2) and solvent vapour (MeOH and C_6H_6) adsorption studies. Considering the large pore size and partial overlap of the emission spectrum of **1** with absorption spectrum of fluorescein dye, fluorescein encapsulated PCP (**1a**) which shows dual emission feature was prepared. **1a** shows variable dual emission intensities leading to different emission in presence of solvents with different polarities (Scheme 1). Such

change in emission was found to be effective to recognize the solvents in vapour phase also. Details study suggests diffusion of the solvent vapours into the pores of **1a** which lead to structural change as well as modulation of energy transfer process.

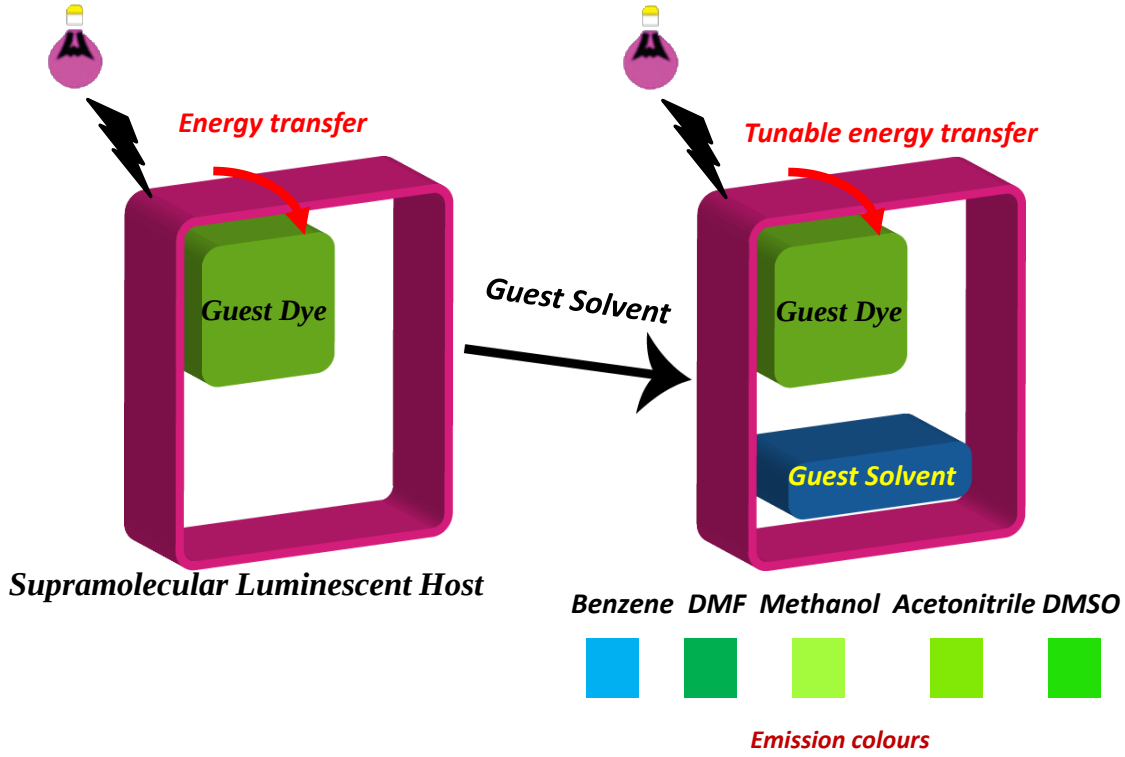

Scheme 1: Schematic of a guest encapsulated supramolecular porous coordination polymer and its dual emission nature for recognition of solvents of different polarity and size.

3B.2 Experimental Section

3B.2.1 Materials

All the reagents employed were commercially available and used as provided without further purification. $Zn(NO_3)_2 \cdot 6H_2O$ were obtained from Spectrochem; 2,6-naphthalenedicarboxylic acid, 2,2′-bipyridyl and fluorescein were obtained from Sigma Aldrich chemicals.

3B.2.2 Physical Measurements

Elemental analyses were carried out using a Thermo Fischer Flash 2000 Elemental Analyzer. FT-IR spectra were recorded on a Bruker IFS 66v/S spectrophotometer using KBr pellets in the region 4000-400 cm^{-1}. Powder XRD pattern of the products were recorded by using Cu-K_α radiation using Bruker D8 Discover (40

kV, 30 mA). Electronic absorption spectra were recorded on a Perkin Elmer Lambda 900 UV-vis-NIR Spectrometer and emission spectra were recorded on Perkin Elmer Ls 55 Luminescence Spectrometer. UV-Vis and emission spectra were recorded in 1 mm path length cuvette. NMR spectra were obtained with a Bruker AVANCE 400 (400 MHz) Fourier transform NMR spectrometer with chemical shifts reported in parts per million (ppm). Fluorescence decay was recorded in a time correlated single-photon counting spectrometer of Horiba-Jobin Yvon with 350-450 nm picosecond Ti-saphhire laser.

3B.2.3 Synthesis of {[Zn(ndc)(2,2′-bpy)]·2DMF)}$_n$ (1)

2,6-naphthalenedicarboxylic acid (0.022 g, 0.1 mmol) and 2,2′-bipyridyl (0.016 g, 0.1 mmol) were dissolved in 5 mL of *N*,*N*′-dimethyl formamide (DMF) and mixed well. 0.030 g (0.1 mmol) of $Zn(NO_3)_2 \cdot 6H_2O$ was added to the ligand solution and sonicated before the sealed glass vial was kept in an oven at 120 °C for 36 h. Good quality transparent crystals of **1** were isolated and washed with fresh DMF before taking for single-crystal X-ray diffraction measurement. Yield of **2**: 73 %; Anal. Calcd. for $C_{28}H_{28}N_4O_6Zn$: C, 57.79; H, 4.81; N, 9.63. Found C, 58.11; H, 4.96; N, 9.51. FT-IR (4000-450 cm^{-1}) (Figure 1): 3441(b), 3050(w), 1660(s), 1599(s), 1565(s), 1473(s), 1407(s), 1354(s), 1250(s), 1188(s), 1089(s), 1027(s), 925(s), 796(s).

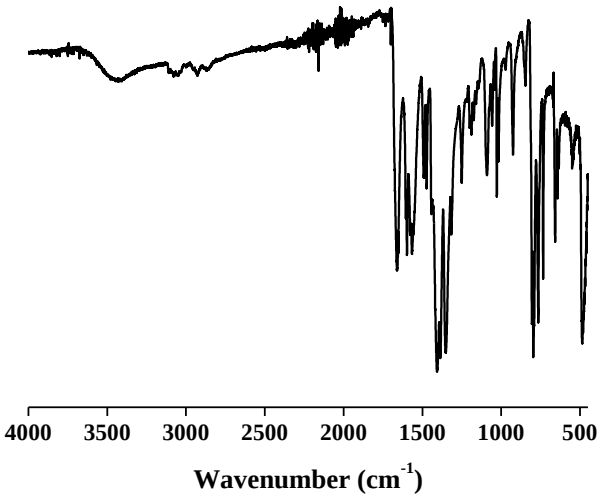

Figure 1: FT-IR spectrum of compound **1**.

3B.2.4 Synthesis of 1a:

As-synthesized compound **1** was activated at 170 °C under vacuum for 18-20 h. This activated compound **1′** (0.100 g) was immersed in 3 mL methanol solution of

fluorescein (0.010 g) and stirred for 2 days. The solid compound was filtered, washed several times with methanol and dried under vacuum before doing ^{1}H-NMR experiment (Figure 2). FT-IR ((4000-450 cm^{-1}) (Figure 3): 3431(b), 3092(w), 1605(s), 1566(s), 1474(s), 1414(s), 1356(s), 1249(s), 1192(s), 1027(s), 924(s), 797(s), 765(s), 652(s), 480(s).

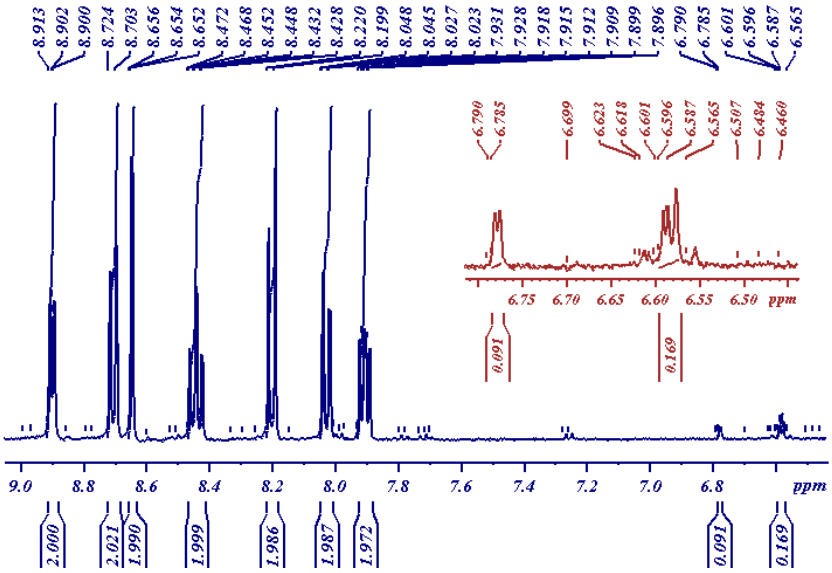

Figure 2: ^{1}H-NMR spectrum of compound **1a** in d_6-DMSO solvent.

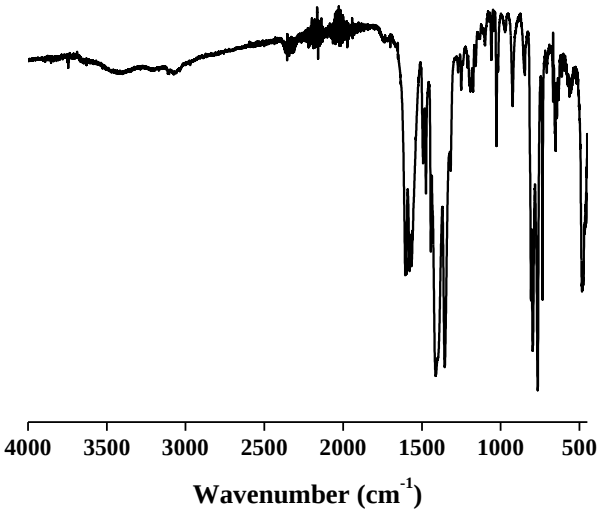

Figure 3: FT-IR spectrum of compound **1a**.

3B.2.5 X-ray Crystallography

X-ray single crystal structural data of **1** was collected on a Bruker Smart-CCD diffractometer equipped with a normal focus, 2.4 kW sealed tube X-ray source with graphite monochromated Mo-*Kα* radiation (λ = 0.71073 Å) operating at 50 kV and 30

mA. The program SAINT[9] was used for integration of diffraction profiles and absorption correction was made with SADABS[10] program. All the structures were solved by SIR 92[11] and refined by full matrix least square method using SHELXL-97.[12] All the hydrogen atoms were geometrically defixed and placed in ideal positions. All crystallographic and structure refinement data of **1** is summarized in Table 1. Selected bond lengths and angles for **1** is given in Table 2. All calculations were carried out using SHELXL 97,[12] PLATON,[13] SHELXS 97[14] and WinGX system, Ver 1.70.01.[15]

3B.2.6 Adsorption study

Adsorption isotherms of CO_2 (195 K), C_2H_2, H_2 and N_2 (77 K) were recorded using the dehydrated samples of **1** (**1′)** by using a QUANTACHROME QUADRASORB-*SI* analyzer. In the sample tube the adsorbent samples (~100-150 mg) were placed which had been prepared at 170 °C under vacuum (1×10^{-1} Pa) for about 12 h prior to measurement of the isotherms. Helium gas (99.999% purity) at a certain pressure was introduced in the gas chamber and allowed to diffuse into the sample chamber by opening the valve. The amount of gas adsorbed was calculated from the pressure difference (P_{cal} - P_e), where P_{cal} is the calculated pressure with no gas adsorption and P_e is the observed equilibrium pressure. All the operations were computer-controlled.

Adsorption isotherms of methanol (293 K) and benzene vapour (298 K) were measured for the dehydrated **1** (**1′)** by using a BELSORP-aqua-3 analyzer. A sample of about ~100–150 mg was prepared by heating at 443 K for about 12 h under vacuum (1×10^{-1} Pa) prior to measurement of the isotherms. The solvent molecules used to generate the vapor were degassed fully by repeated evacuation. Dead volume was measured with helium gas. The adsorbate was placed into the sample tube, then the change of the pressure was monitored and the degree of adsorption was determined by the decrease in pressure at the equilibrium state. All operations were computer controlled and automatic.

3B.3 Results and discussion

3B.3.1 Structural description of {[Zn(ndc)(2,2′-bpy)]·2DMF)}$_n$ (1)

Structure determination using single crystal X-ray diffraction suggests that **1** crystalizes in monoclinic *C*2/*c* space group and the asymmetric unit contains one Zn^{2+}

metal center, one ndc and one 2,2′-bpy. The hexa-coordinated Zn^{2+} metal center is coordinated by four oxygen atoms (O1, O2, O1* and O2*) from two carboxylate groups of ndc and two nitrogen atoms (N1 and N1*) from one 2,2′-bpy (Figure 4). The ndc linkers connect two metal centers and 2,2′-bpy binds in chelating fashion to form a 1D *zigzag* chain (Figure 4). These 1D chains are held together on the *ac* plane through hydrogen bonding interactions between C2-H···O1 to form a undulated 2D layer like structure (Figure 5a). These 2D layers stack along *c*-axis through face-to-face π···π interaction (3.518 Å) between 2,2′-bpy moieties resulting in a 3D supramolecular framework (Figure 5b). This 3D supramolecular framework contains large dumbell-rectangular shaped 1D channels with dimensions of 14.5×9 $Å^2$ (Figure 6).[16] These channels are filled with guest DMF molecules, confirmed from TGA, elemental analysis and ^{1}H-NMR (Figure 7 and 8). Calculated void space after removal of guest DMF molecules using PLATON is 44% of the total cell volume.[13]

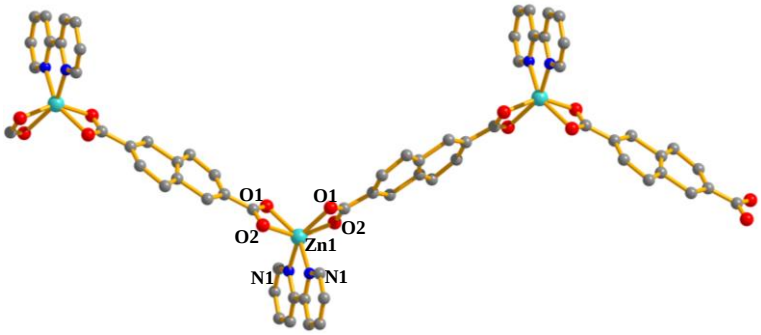

Figure 4: 1D chain like structure of **1** and the coordination environment of Zn^{2+} metal center.

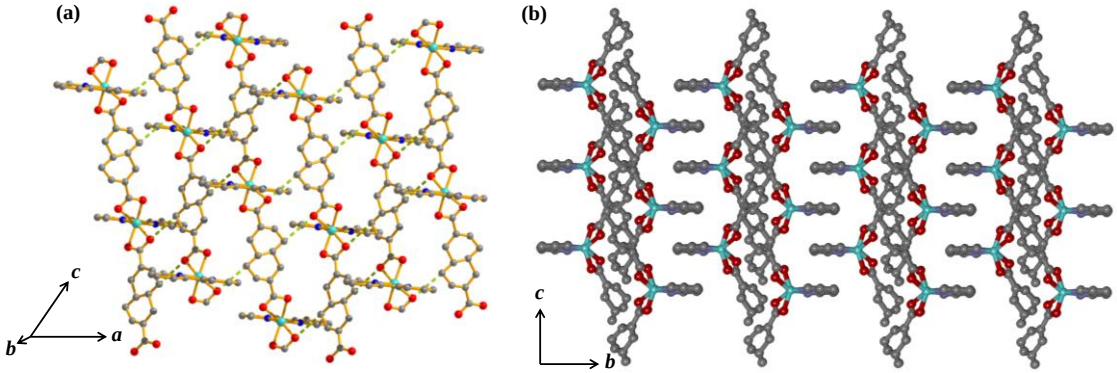

Figure 5: Structural description of **1**: (a) 1D chains are hydrogen bonded through C2-H···O1 to form a 2D undulated sheet like structure in the *ac* plane; (b) The 2D sheets are stacked along *c*-axis through face-to-face stacking of 2,2′-bpy.

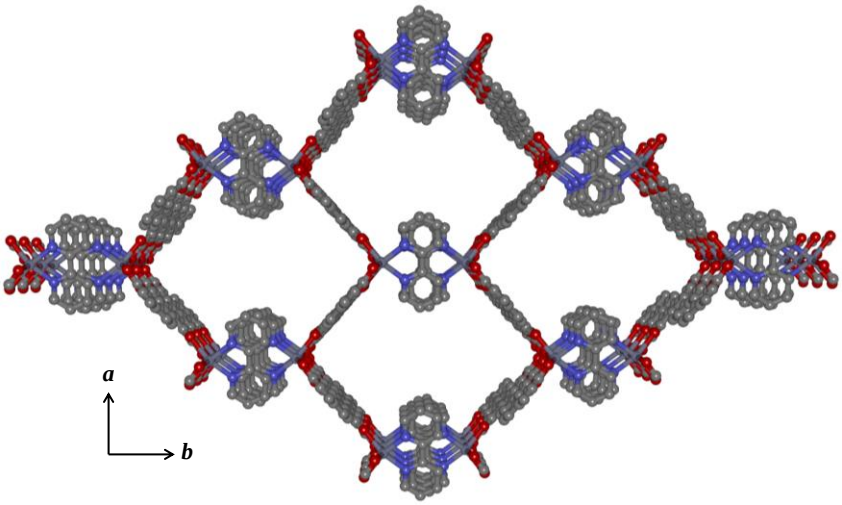

Figure 6: View of the dumbell-shaped pores in **1** along *c*-axis.

Table 1: Crystal data and structure refinement parameters of compound **1**.

Parameters	**1**
Empirical formula	$C_{28}H_{28}N_4ZnO_6$
M	581.38
Crystal system	Monoclinic
Space group	*C*2/*c* (15)
***a* (Å)**	15.6069(8)
***b* (Å)**	24.6985(16)
***c* (Å)**	8.3123(4)
***β* (deg)**	117.408(3)
***V* (Å^3)**	2844.5(3)
Z	4
***T*(K)**	293
λ (Mo K$_\alpha$)	0.71073
D_c (g cm^{-3})	1.298
μ (mm^{-1})	0.908
θ_{max} (deg)	26.4
total data	12556
unique reflection	2676
R_{int}	0.082
data [$I > 2\sigma(I)$]	1558
R^a	0.0987
$R_w{}^b$	0.2796
GOF	0.95

^{a} $R = \Sigma||F_o| - |F_c||/\Sigma|F_o|$. ^{b} $R_w = [\Sigma\{w(F_o^2 - F_c^2)^2\}/\Sigma\{w(F_o^2)^2\}]^{1/2}$

Table 2: Selected bond lengths (Å) and angles (°) for **1**.

Zn1-O1	2.240(8)	Zn1-O2	2.042(6)
Zn1-N1	2.101(6)	Zn1-O1_a	2.240(8)
Zn1-O2_a	2.042(6)	Zn1-N1_a	2.101(6)
O1-Zn1-O2	59.2(3)	O1-Zn1-N1	94.6(3)
O1-Zn1-C6	29.0(4)	O1-Zn1-O1_a	103.5(3)
O1-Zn1-O2_a	98.5(3)	O1-Zn1-N1_a	151.8(3)
O2-Zn1-N1	109.4(3)	O1_a-Zn1-O2	98.5(3)
O2-Zn1-O2_a	145.9(3)	O2-Zn1-N1_a	97.1(3)
O1_a-Zn1-N1	151.8(3)	O2_a-Zn1-N1	97.1(3)
N1-Zn-N1_a	78.2(2)		

a = -x,y,1/2-z

3B.3.2 Thermal stability and PXRD analysis of 1

Crystallographically it was not possible to locate the guest molecules. But the TG analysis and ^{1}H-NMR suggested presence of two DMF as guest molecules which are released at ~ 170 °C under vaccum (Figure 7 and 8). The desolvated state (**1′**) is stable till 340 °C and further heating probably disintegrates the framework (Figure 7). The PXRD pattern of **1′** is distinctly different from that of **1**, suggesting structural rearrangement upon desolvation (Figure 9). Such chages are expected in this framework as the superstructure is tethered through π···π, C-H···π and H-bonding interactions. Similar observation was noted with the framework shown in chapter 3A, where a 1D coordination chain self-assembles in 3D structure.

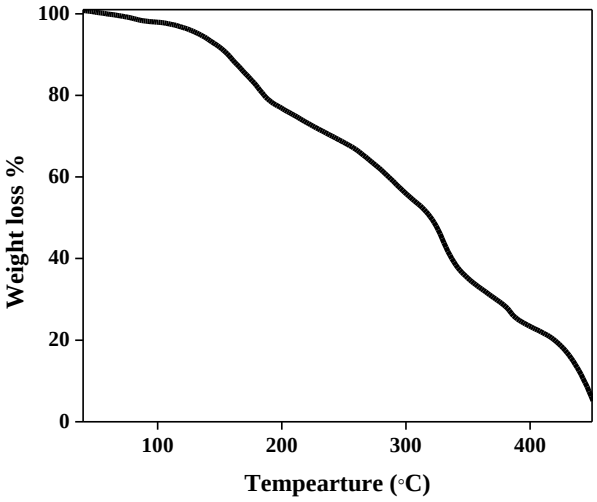

Figure 7: TG analysis of compound **1** under N_2 atmosphere.

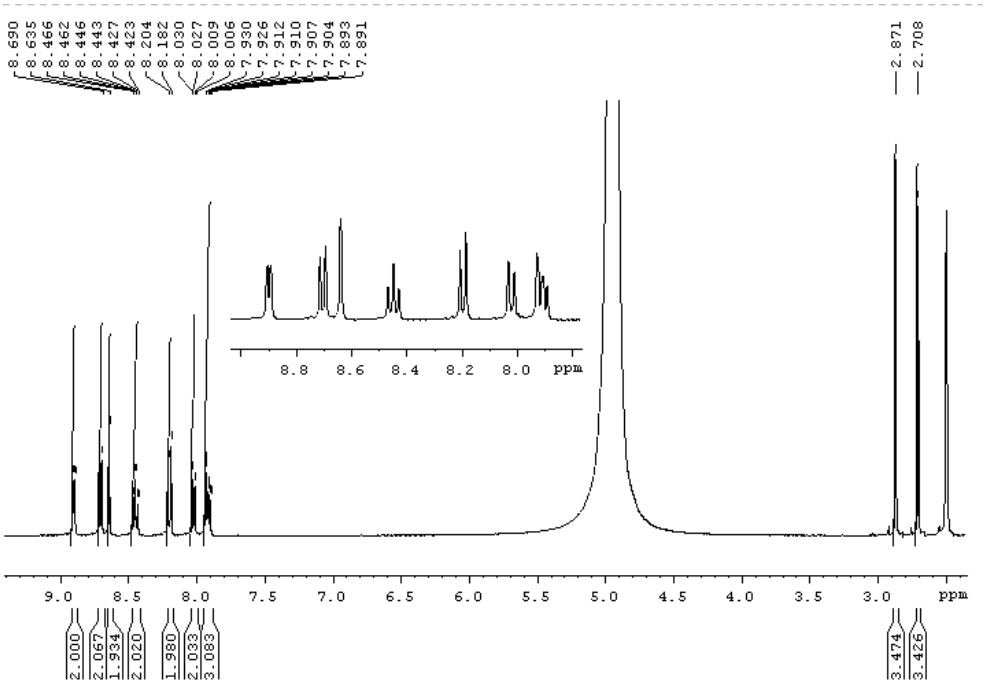

Figure 8: ^{1}H-NMR spectrum of compound **1** in d_6-DMSO solvent.

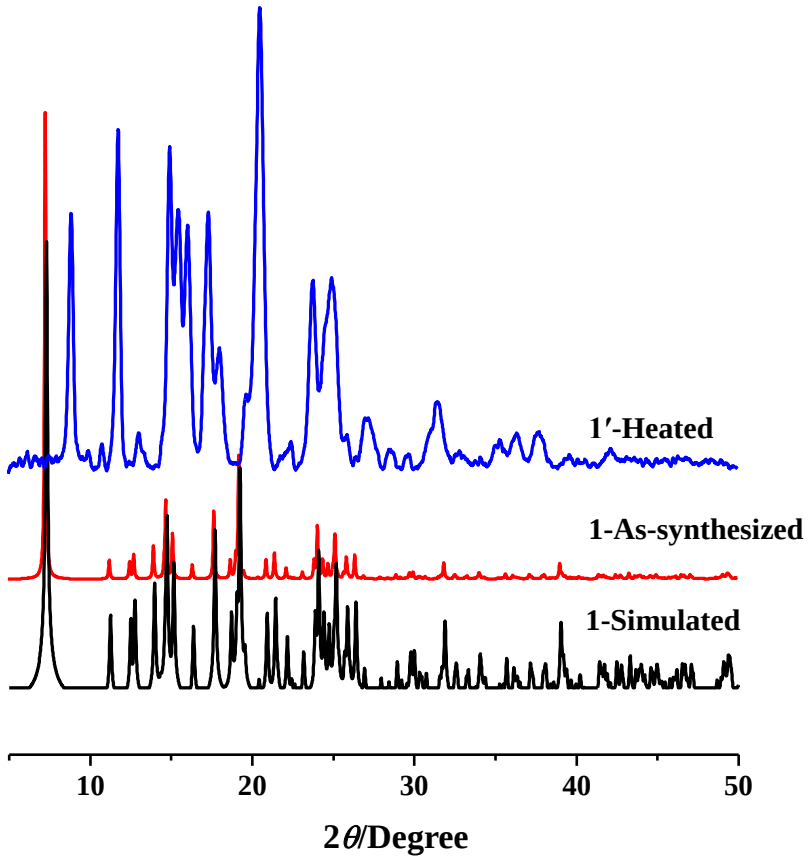

Figure 9: PXRD patterns of compound **1** and its desolvated phase.

3B.3.3 Gas and solvent vapour adsorption

To check the porous properties of **1′** N_2 adsorption measurement at 77 K was carried out. It shows a type-II profile suggesting only surface adsorption. After guest solvent removal structral contraction might be the reason of no uptake. Similarly, H_2 also can not diffuse into the pores of **1′** at 77 K (Figure 10). Surprisingly, at 195 K CO_2 and C_2H_2 show stepwise uptake profiles (Figure 11). A double-step uptake profile was obtained for CO_2; initially (till P/P_0 ~ 0.2) uptake is slow and after following a distinct step the uptake amount reaches to 57 mL/g. The desorption path creates a huge hysterisis loop suggesting either strong interaction of CO_2 with the framework or kinetic trapping. Here, the quadrapole moment of CO_2 might interact strongly with the aromatic π electrons present at the pore surface.[17] In case of C_2H_2 also initial upatake is low (8 mL/g) and after P/P_0 ~ 0.1 uptake profile rises sharply to 47 mL/g. Similar to CO_2 adsorption profile, the desorption curve shows a clear hysterisis. Here the acetylene functionality possibly interacts strongly with the aromatic π electrons present at the pore surface and thus such stepwise uptake and large hysterisis occurs. Evidently the stepwise uptake profile indicates structural rearrangement during adsorption. Such phenomena are usually observed in case of flexible framework structures.[18]

To understand the nature of pore surface in more details methanol and benzene vapour adsorption for **1′** were carried out (Figure 12). Methanol vapour sorption isotherm shows a three-step uptake profile at 293 K; till P/P_0 ~ 0.36 relative pressure a type-I nature profile was observed with 51 mL/g uptake which corresponds to one methanol per formula. With increasing pressure uptake rises sharply to reach 115 mL/g (2.2 methanol molecules per formula) at P/P_0 ~ 0.73. Another steep uptake after this pressure reaches a saturation amount of 173 mL/g which corresponds to a total 3.32 molecules of methanol per formula. The desorption curve creates large hysterisis with retention of ~ 1.5 molecules methanol per formula. Similar stepwise uptake profile was obtained for benzene vapour; after P/P_0 ~ 0.12 pressure it rises sharply to reach final uptake amount 60 mL/g which corresponds to ~ 1.1 benzene molecules per formula (Figure 12). Here also the desoprtion curve creates a distinct hysterisis which might be due to strong aromatic interactions. The stepwise uptake profiles for methanol and benzene reiterates the fleibility in the framework and also suggest aromatic electron rich polar pore surface.

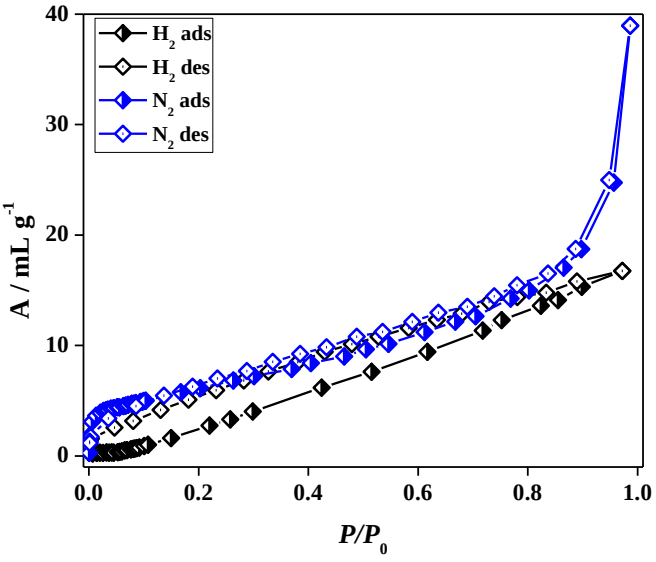

Figure 10: N_2 and H_2 adsorption profiles at 77 K for **1′**.

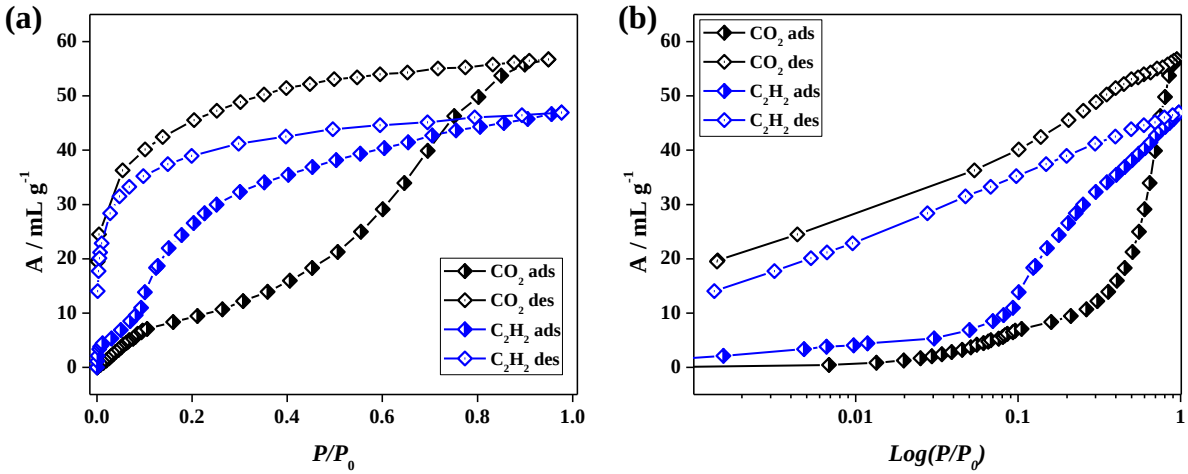

Figure 11: (a) CO_2 and C_2H_2 adsorption isotherms of **1′** at 195 K; (b) CO_2 and C_2H_2 adsorption isotherms of **1′** at 195 K with logarithmic scale plot.

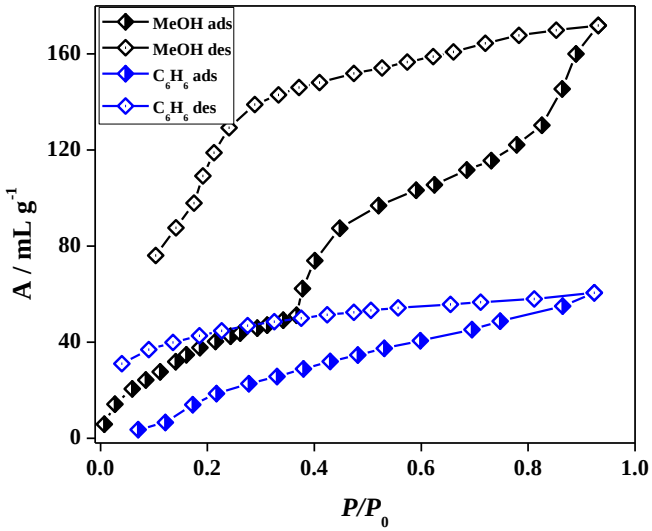

Figure 12: Methanol and benzene vapour adsorption profiles of **1′** at 293 and 298 K, respectively.

3B.3.4 Photophysical properties: Dye loading and solvent sensing

The absorbance spectrum of **1** shows a broad feature with λ_{max} ~ 330 nm (Figure 13). Excitation of **1** at 330 nm shows emission with maximum at ~ 430 nm (Figure 14). This blue emission is red shifted compared to that of only ndc emission probably due to molecularly organized state upon metal coordination.

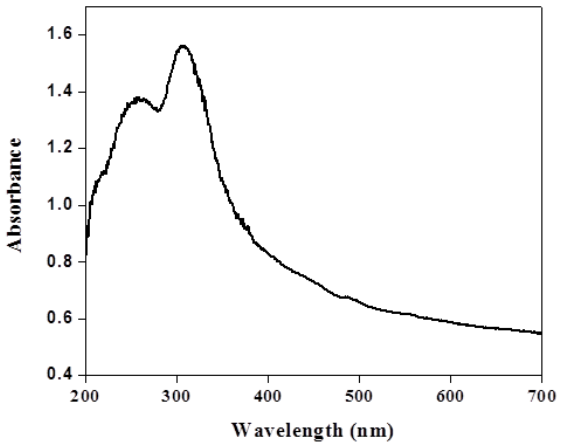

Figure 13: Absorption spectrum of **1**.

Study of porosity, particularly benzene adsorption profile clearly indicates that the pore surface favours diffusion of aromatic molecules. Moreover, the framework is dynamic and is also blue emissive in nature due to presence of naphthalene chromophore based linker ndc. These features provoked us to carry out dye loading experiment in **1′**. With a suitable dye molecule one can observe partial or complete energy transfer from donor framework to the acceptor dye and this can lead to dual emission. Further, this dual emission can be tuned using different solvent templates those can affect the energy transfer process. Following these ideas fluorescein dye was selected, as its molecular size matches well with the pore size of **1** and its absorbance spectrum overlaps partially with the framework emission (Figure 14). Only 0.04 molecule of fluorescein dye was encapsulated into the framework **1′** and inclusion was confirmed from ^{1}H-NMR, CO_2 and solvent vapour adsorption studies (Figure 2 and 15). Inclusion compound **1a** shows only ~ 20 mL/g uptake of CO_2 which suggest decreased void space due to dye inclusion (Figure 15a). It also shows two-step uptake of methanol with uptake amount of 94 mL/g (1.9 methanol per formula) and exhibits approximately 0.6 molecules of benzene uptake per formula of **1′** (Figure 15b). The absorbance spectrum of **1a** shows a new absorbance ~ 500 nm along with framework absorbance at 330 nm. The absorbance ~ 500 nm is attributed to the encapsulated fluorescein dye (Figure 16a). Excitation of **1a** at 330 nm

shows two distinct emission bands with maxima at ~ 432 and 535 nm, which are attributed to the framework and encapsulated dye, respectively (Figure 16b). Such dual emission leads to yellow green emission of **1a** (Figure 16b Inset). Direct excitation of **1a** at 490 nm shows comparatively low intensity at 535 nm which suggests a partial energy transfer from donor framework to the fluorescein dye (Figure 16b). Excitation spectrum of **1a** monitored at 550 nm reiterates the energy transfer process (Figure 17a). Further the fluorescence life time of framework in **1a** (~ 1.9 ns) decreases significantly compared to as-synthesized **1** (~ 2.8 ns) when monitored at 400 nm (Figure 17b). On the other hand, the fluoroscence life time of encapsulated fluorescein dye is ~ 4.8 ns (monitored at 550 nm) which is slightly higher compared to that of free fluorescein (~ 4.1 ns) (Figure 17c). These life time data clearly advocate presence of partial energy transfer from framework to the encapsulated dye.

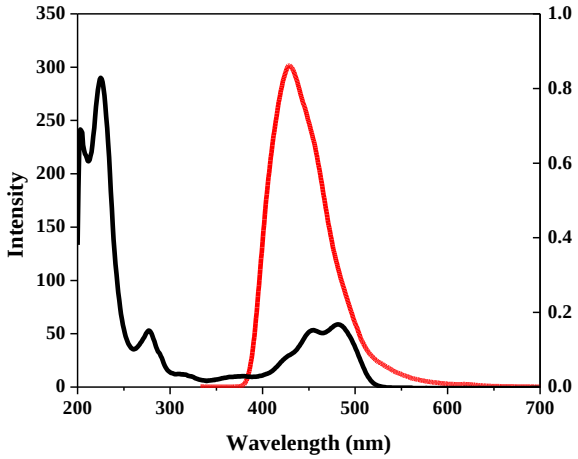

Figure 14: Overlap spectra of framework **1** emission (red) and absorbance of fluorescein dye in methanol (black).

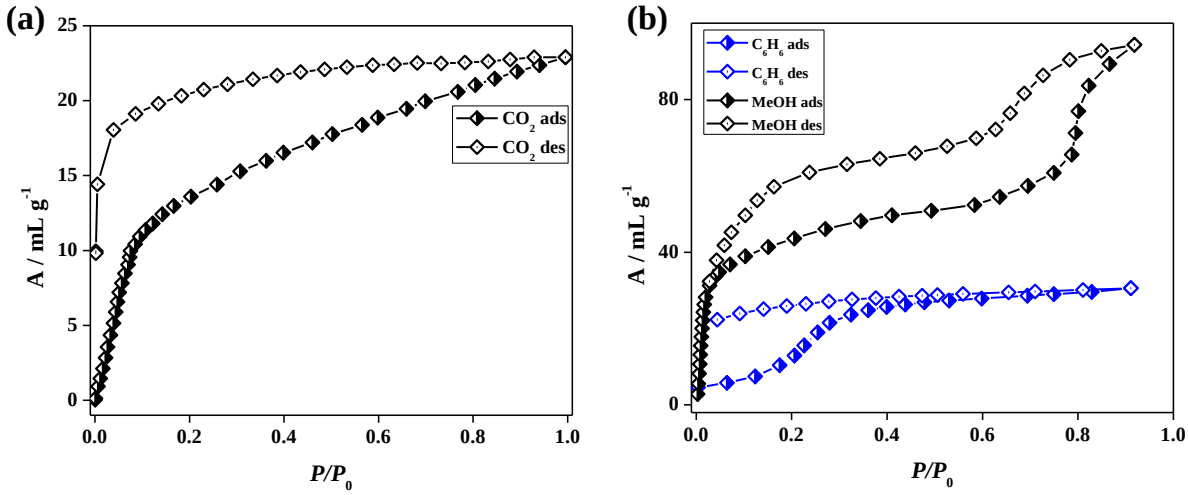

Figure 15: Adsorption studies of **1a**: (a) CO_2 adsorption profile at 195 K; (b) Methanol and benzene vapour adsorption profiles at 293 and 298 K.

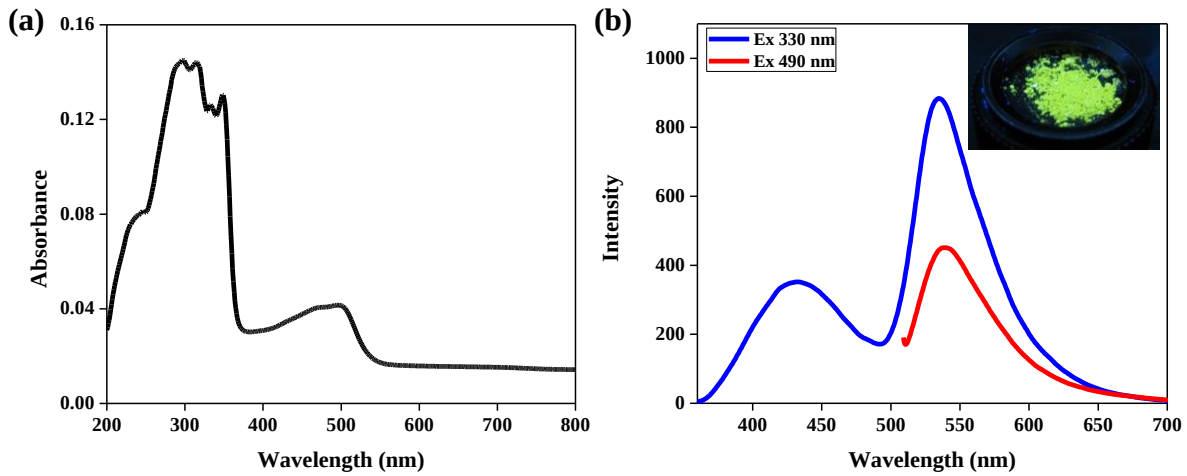

Figure 16: (a) Absorption spectrum of **1a**; (b) Emission spectrum of **1a** upon excitation at 330 and 490 nm; Inset: Photograph of **1a** under UV light.

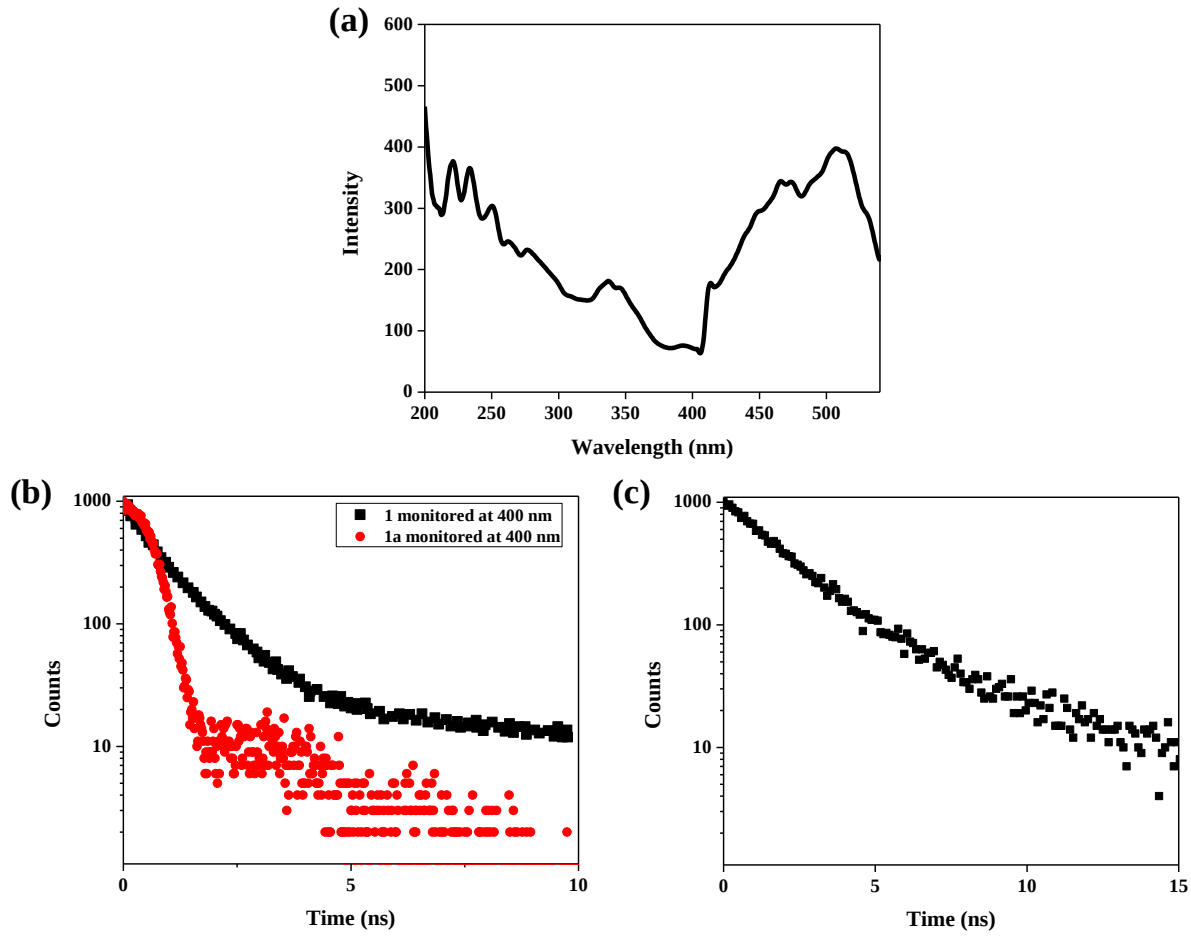

Figure 17: (a) Excitation spectrum of **1a** monitored at 560 nm; (b) Fluorescence life time profiles of **1** and **1a** monitored at 400 nm; (c) Fluorescence life time profiles of **1a** monitored at 550 nm.

The dual emissive **1a** was exploited as a probe material for various solvent sensing. Initially, **1a** was dispersed in solvents like methanol, acetonitrile, DMF, DMSO

and benzene. Their emission spectra feature distinct I_{435}/I_{535} ratios; i.e. different emission colours (Figure 18). The emission spectra in these solvents are different in nature; only I_{435}/I_{535} ratios are 0.53 (methanol), 0.98 (acetonitrile), 0.71 (DMF), 0.83 (DMSO) and 2.37 (benzene) (Figure 19). Such change in emission colors in presence of different solvents of different polarity is unique in framework systems and dye encapsulated compound **1a** can be used as a fingerprint sensing material. Further, emission spectra of **1a** upon exposure to all these solvent vapours were examined (Figure 20). Similar sort of spectral change were observed in all cases. The slight change in the intensity ratio compared to that in solution might be due to different amount of solvent vapour inclusion compared to the solution state.

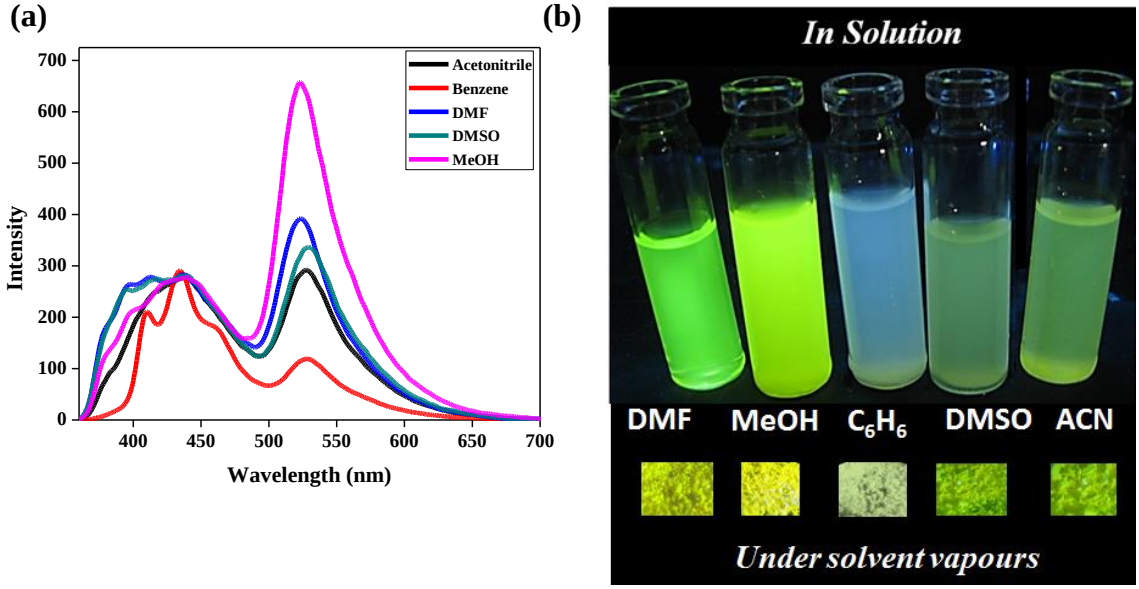

Figure 18: (a) Emission spectra of **1a** dispersed in various solvents excited at 330 nm; (b) Photographs of **1a** dispersed in various solvents and in solid state under UV light.

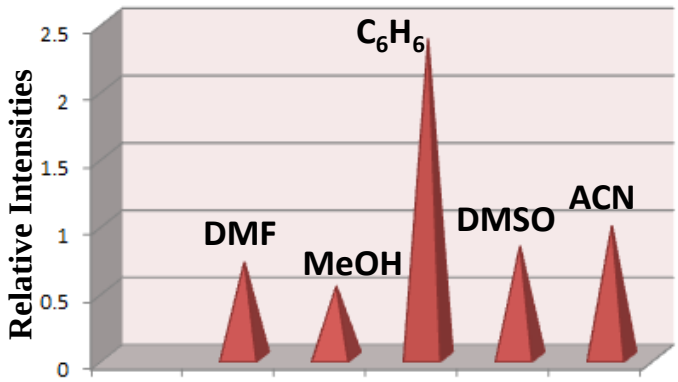

Figure 19: Plot of relative emission intensities (I_{435}/I_{535}) in different solvents.

Diffusion of the solvent vapours can be confirmed from the methanol and benzene vapour adsorption profiles. Hence, the spectral change is possibly induced by the structural change upon solvent vapour diffusion. As the structure is flexible, solvents might rearrange the structure and this leads to different arrangement of fluorescein dye inside the supramolecular pores of **1a**. To confirm the structural integrity, **1a** was dipped into the respective solvents (minimum amount) and PXRD patterns were collected in wet condition (Figure 21). PXRD patterns clearly suggest structural change upon solvent diffusion into the supramolecular pores. Such change also tunes the energy transfer process from host framework to the guest dye and hence the emission properties are tuned leading to fingerprint recognition of each solvent in vapour phase.

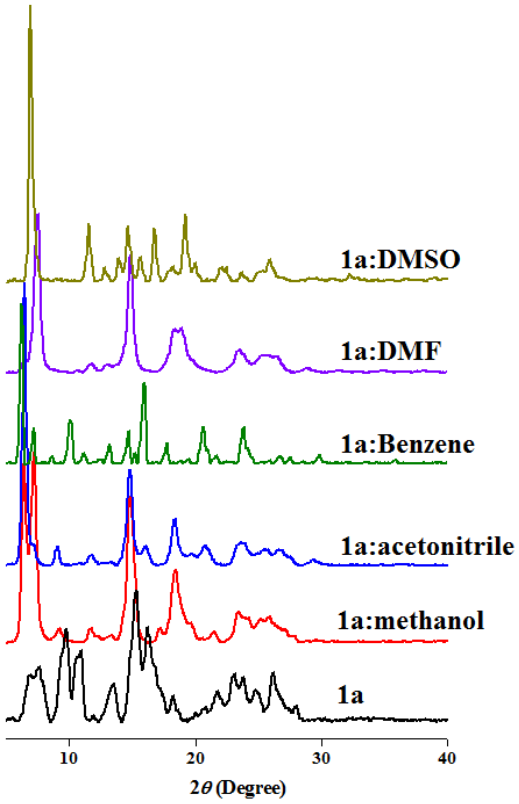

Figure 21: PXRD patterns of compound **1a** upon exposure to different solvent vapours.

3B.4 Conclusions

In conclusion, a 3D supramolecular framework (**1**) from non-covalent organization of 1D coordination polymer has been synthesised. It possesses large 1D channels which contract after guest solvent removal. Dynamic nature of the framework was realized from CO_2, C_2H_2 and solvent vapour adsorption studies. Benzene vapour

adsorption indicates aromatic π electron rich pore surface and hence fluorescein dye could be encapsulated inside the supramolecular pores. The dye encapsulated framework (**1a**) shows dual emission characteristic with yellow-green emission. Moreover, a partial energy transfer phenomenon was observed from the host framework to the guest dye. Interestingly, **1a** in vapour phase and in dispersed state in different solvents like methanol, acetonitrile, DMF, DMSO and benzene show characteristic emission leading to recognition of each solvent. Solvent induced structural change is the most plausible factor that tunes the dual emission intensity ratios. Such host-guest systems with dual emission nature would be promising material as a platform for sensory devices.

3B.5 References

1. a) S. Kitagawa, R. Kitaura, S.-I. Noro, *Angew. Chem. Int. Ed*. **200**4, *43*, 2334; b) H. Furukawa, K. E. Cordova, M. O'Keeffe, O. M. Yaghi, *Science.* **2013**, *341*, 1230444; c) N. Stock, S. Biswas, *Chem. Rev*. **2013**, *112*, 933.

2. a) Thematic issue on metal-organic framework, *Chem. Rev*. 2013, **112**, 703-932; b) S. Qiu, M. Xue, G. Zhu, *Chem. Soc. Rev*. **2014**, *43*, 6116; c) M. Yoon, R. Srirambalaji, K. Kim, *Chem. Rev*. **2013**, *112*, 1196; d) J. Liu, L. Chen, H. Cui, J. Zhang, L. Zhang, C.-Y. Su, *Chem. Soc. Rev*. **2014**, *43*, 6011; e) P. Horcajada, R. Gref, T. Baati, P. K. Allan, G. Maurin, P. Couvreur, G. Férey, R. Morris, C. Serre, *Chem. Rev*. **2013**, *112*, 1232.

3. a) M. D. Allendorf, C. A. Bauer, R. K. Bhakta, R. J. T. Houk, *Chem. Soc. Rev*. **2009**, *38*, 1330; b) Z. Hu, B. J. Deibert, J. Li, *Chem. Soc. Rev*. **2014**, *43*, 5815; c) L. E. Kreno, K. Leong, O. K. Farha, M. Allendorf, R. P. V. Duyne, J. T. Hupp, *Chem. Rev*. **2013**, *112*, 1105; d) V. M. Suresh, S. J. George, T. K. Maji, *Adv. Funct. Mater*. **2013**, *23*, 5585; e) T. Zhang, W. Lin, *Chem. Soc. Rev*. **2014**, *43*, 5982; f) R. Haldar, K. V. Rao, S. J. George, T. K. Maji, *Chem. Eur. J.* **2012**, *18*, 5848.

4. a) B. Chen, S. Xiang, G. Qian, *Acc. Chem. Res*. **2010**, *43*, 1115; b) B. Chen, L. Wang, F. Zapata, G. Qian, E. B. A. Lobkovsky, *J. Am. Chem. Soc*. **2008**, *130*, 6718; c) Z. Guo, H. Xu, S. Su, J. Cai, S. Dang, S. Xiang, G. Qian, H. Zhang, M. O'Keeffe, B. Chen, *Chem. Commun*. **2011**, *47*, 5551; d) Y. Li, S. Zhang, D. Song, *Angew. Chem. Int. Ed*. **2013**, *52*, 710; e) V. M. Suresh, S. Chatterjee, R. Modak, V. Tiwari, A. B. Patel, T. K. Kundu, T. K. Maji, *J. Phys. Chem. C*. **2014**, *118*, 12241.

5. a) Y. Takashima, V. M. Martinez, S. Furukawa, M. Kondo, S. Shimomura, H. Uehara, M. Nakahama, K. Sugimoto, S. Kitagawa, *Nat. Commun.* **2011**, *2*, 168; b) D. Yan, Y. Tang, H. Lin, D. Wang, *Sci. Rep*. **2014**, *4*, 4337.

6. M.-J. Dong, M. Zhao, S. Ou, C. Zou, C.-D. Wu, *Angew. Chem., Int. Ed.* **2014**, *53*, 1575.

7. a) R. Grünker, V. Bon, A. Heerwig, N. Klein, P. Müller, U. Stoeck,I. A. Baburin, U. Mueller, I. Senkovska, S. Kaskel, *Chem. Eur. J*. **2012**, *18*, 13299; b) S. Wuttke, C. Dietl, F. M. Hinterholezinger, H. Hintz, H. Langhals, T. Bein, *Chem. Commun.* **2014**, *50*, 3599.

8. C.-Y. Sun, X.-L. Wang, X. Zhang, C. Qin, P. Li, Z.-M. Su, D.-X. Zhu, G.-G. Shan, K.-Z. Shao, H. Wu, J. Li, *Nat. Commun.* **2013**, *4*, 168.

9. SMART (V 5.628), SAINT (V 6.45a), XPREP, SHELXTL; Bruker AXS Inc. Madison, Wisconsin, USA, **2004**.

10. G. M. Sheldrick, Siemens Area Detector Absorption Correction Program, University of Götingen, Götingen, Germany, **1994**.

11. A. Altomare, G. Cascarano, C. Giacovazzo, A. Gualaradi, *J. Appl. Cryst*. **1993**, *26*, 343.

12. G. M. Sheldrick, SHELXL-97, Program for Crystal Structure Solution and Refinement; University of Götingen, Götingen, Germany, **1997**.

13. A. L. Spek, *J. Appl. Cryst*. **2003**, *36*, 7.

14. G. M. Sheldrick, SHELXS 97, Program for the Solution of Crystal Structure, University Götingen, Germany, **1997**.

15. L. J. Farrugia, WinGX-A Windows Program for Crystal Structure Analysis, *J. Appl. Cryst.* **1999**, *32*, 837.

16. The sizes of the channels were calculated considering the van der Waals radii of the atoms.

17. A. M. Plonka, D. Banerjee, W. R. Woerner, Z. Zhang, N. Nijem, Y. J. Chabal, J. Li, J. B. Parise, *Angew. Chem. Int. Ed*. **2013**, *52*, 1692.

18. a) S. Yang, L. Liu, J. Sun, K. M. Thomas, A. J. Davies, M. W. George, A. J. Blake, A. H. Hill, A. N. Fitch, C. C. Tang, M. Schröder, *J. Am. Chem. Soc*. **2013**, *135*, 4954; b) M. K. Sharma, P. K. Bharadwaj, *Inorg. Chem*. **2011**, *50*, 1889; c) D. Tanka, K. Nakagawa, M. Higuchi, S. Horike, Y. Kubota, T. C. Kobayashi, M. Takata, S. Kitagawa, *Angew. Chem., Int. Ed*. **2008**, *47*, 3914

Chapter 4

Extended supramolecular metal-organic structures with long-lived charge separated states at ambient condition: Control over charge transfer and porosity

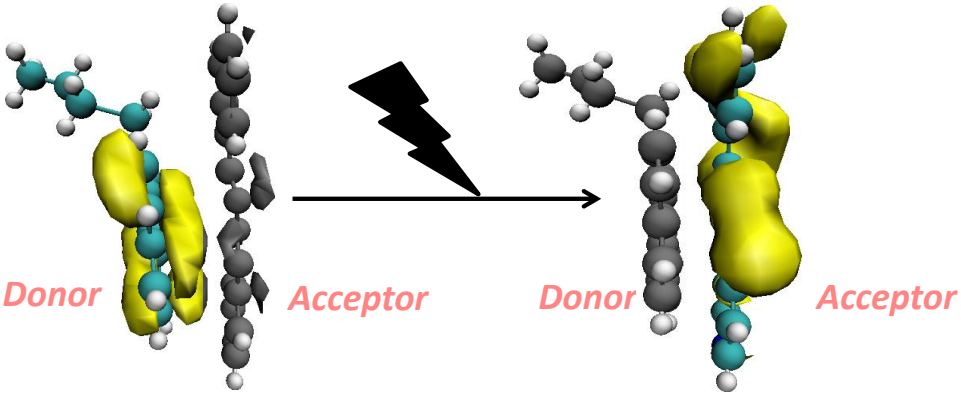

Part 4A

Coordination driven highly stable charge separated state in supramolecular coordination frameworks: Controllable porosity and charge transfer

Summary

This chapter reports syntheses and structural characterizations of two Cd^{2+} based 1D coordination polymers (CPs), [{$Cd(pma)_2(bphz)$}] (**1**) and [{$Cd(pba)_2(bphz)$}·$5H_2O$] (**2**) (Hpma = Pyrene monocarboxylic acid; Hpba = Pyrene butyric acid; bphz = 1,2-bis-(4-pyridylmethylene)hydrazine) composed of pyrene based electron rich chromophores and an imine based electron acceptor linker. Both the polymers are restricted to 1D due to mono-carboxy functional linkers, but the 1D chains interdigitate via π···π and C-H···π interactions to form 3D supramolecular structure. Due to the flexible alkyl chain of pba linker framework **2** possess 1D supramolecular pore while framework **1** is nonporous. The flexibility of **2** can be realized from the structural contraction and expansion upon desolvation/resolvation of the framework. It also shows stepwise solvent vapour (water, methanol and ethanol) uptake profiles and can be promising for biofuel separation. Both the compounds are non-emissive in nature although those contain emissive pyrene chromophores. Due to the interdigitation between the 1D polymeric networks pyrene and bphz linkers stack in a face-to-face fashion to promote stable charge separated state at room temperature. DFT calculations and replacement of bphz linker by 4,4′-bipyridine (bpy) further confirm the presence of charge separated state between pyrene and bphz units.

1. R. Haldar, S. Neihsial, A. Chakraborty, S. K. Pati, T. K. Maji, To be submitted.

4A.1 Introduction

Organic chromophores with high quantum yield have huge applications in molecular sensing or recognition and other light emitting device fabrication.[1] Pyrene is one of the most well-known chromophores which shows long lived excited state emission and high quantum yield. It has large aromatic π surface and the bright emission can be tuned by changing the microenvironment around it.[2] Due to such interesting emission properties it has been utilized for various sensing applications, for light harvesting processes and also in nanotechnologies.[3] The nanostructures fabricated using pyrene cores can show exciting electronic properties and can be used as semiconductor and field effect transistors.[4] Apart from the emission properties, strong absorption in the visible region of the spectrum due to ground state charge transfer (CT) or electron transfer (ET) is also an interesting topic of study.[5] A complete charge separation or ET induced by external stimuli such as pressure, heat or light can be very useful for practical applications such as organic photovoltaics, solar energy conversion, molecular photonics, transistors *etc*.[6] But such sort of stimuli responsive redox behaviour or photochromic behaviour are rare in literature. The key factor would be the organization of donor and acceptor chromophores in close vicinity where electron transfer can be easily tuned by external stimuli. Moreover, stability and reversibility of such radical ion pairs generated by electron transfer process is vital. In this case along with pyrene which is a strong donor, a strong acceptor chromophore is the primary requirement. Metal-directed self-assembly of those organic chromophores can give interesting charge separated complexes that might show interesting redox properties.[7] Although such sort of studies are mostly done in solution state or in organic polymers, but using a metal-coordination driven self-assembly approach is yet to be studied.[8] Coordination polymers (CPs) constructed from assembly of metal ions and organic linkers can be a suitable platform to study the above mentioned properties.

Porous CPs are a well-known class of porous material and show outstanding surface area and tunable adsorption properties.[9] Constructed from organic and inorganic building units it can show versatile topologies and numerous applications such as catalysis, molecular sensing, selective gas adsorption, drug delivery *etc*.[10] Here, to synthesize porous CT crystal, it was envisioned of a metal directed self-assembly of mono-carboxyl functional pyrene and imine based exo-bidentate linkers which will act as donor and acceptor, respectively. The deliberate choice of monocarboxylate pyrene linker is to extend the structure through non-covalent interactions between donor and acceptor. Here, two pyrene based chromophoric

linkers, Pyrene monocarboxylic acid (pma) and pyrene butyric acid (pba) were used as donors and 1,2-bis-(4-pyridylmethylene)hydrazine (bphz) was used as an acceptor chromophore.[11] Self-assembly of Cd^{2+}, pma and bphz resulted a 1D interdigitated coordination polymer $[Cd(pma)_2(bphz)]_n$ (**1**) which is nonporous in nature. Further to tune the structure we have introduced a flexible alkyl chain containing linker, pyrene butyric acid (pba) and we could synthesize similar 1D interdigitated flexible porous structure of $[\{Cd(pba)_2(bphz)]\}\cdot 5H_2O]_n$ (**2**). **2** shows structural contraction and expansion upon desolvation-resolvation, respectively realized from crystal structure determination using single crystal X-ray diffraction. Moreover solvent vapour adsorption profiles show **2** can be useful for biofuel separation. Interestingly, both the structures are non-emissive in spite of presence of pyrene chromophores. Details study shows formation of stable charge separated state at ambient condition between pma:bphz and pba:bphz in **1** and **2**, respectively. Further density functional theoretical calculations supported the observation. Replacement of bphz linker by 4,4′-bipyridine (bpy) in a similar 1D CP, $[Cd(pma)_2(bpy)]_n$ (**3**) shows pyrene excimer emission further support that bphz is acting as an acceptor chromophore.

4A.2 Experimental Section

4A.2.1 Materials

All the reagents employed were commercially available and used as provided without further purification. The $Cd(NO_3)_2\cdot 6H_2O$ was obtained from Spectrochem, pyrene monocarboxylic acid and pyrene butyric acid were obtained from Sigma Aldrich chemicals. 1,2-bis-(4-pyridylmethylene)hydrazine was prepared following previously reported methods.[12]

4A.2.2 Physical measurements

Elemental analyses were carried out using a Thermo Fischer Flash 2000 Elemental Analyzer. FT-IR spectra were recorded on a Bruker IFS 66v/S spectrophotometer using KBr pellets in the region 4000-400 cm^{-1}. Powder XRD pattern of the products were recorded by using Cu-K_α radiation (Bruker D8 Discover; 40 kV, 30 mA). Electronic absorption spectra were recorded on a Perkin Elmer Lambda 900 UV-VIS-NIR Spectrometer and emission spectra were recorded on Perkin Elmer Ls 55 Luminescence Spectrometer. UV-Vis and emission spectra were recorded in 1 mm path length cuvette. NMR spectra were obtained

with a Bruker AVANCE 400 (400 MHz) Fourier transform NMR spectrometer with chemical shifts reported in parts per million (ppm).

4A.2.3 Synthesis of $\{[Cd(pma)_2(bphz)]\}_n$ (1)

A basic aqueous solution (1 mmol NaOH in 25 mL water) of pma (1 mmol, 0.246 g) was mixed with a methanolic solution (15 mL) of bphz (0.5 mmol, 0.105 g) and stirred for 30 min to mix well. $Cd(NO_3)_2 \cdot 6H_2O$ (0.5 mmol, 0.151 g) was dissolved in 40 mL of water and then ligand solution (2 mL) was layered above the metal solution (2 mL) and after 10-12 days light yellow colour rod shaped crystals of **1** were found at the walls of the tube. A good quality single crystal was picked up from the mother liquor and immediately covered with paraffin oil and crystal data was collected at 293 K. To prepare the compound in bulk ligand solution was directly mixed with metal solution and stirred for 36 h. The poly-crystalline bulk compound was filtered of, washed several times with methanol and dried under vacuum. The PXRD pattern of the bulk powder matches well with the simulated PXRD pattern of **1** indicating phase purity (Figure 1). Yield: 55%, relative to Cd^{2+}. Anal. Calcd. for $C_{46}H_{28}CdN_4O_4$: C, 67.88; H, 3.44; N, 6.88. Found: C, 67.97; H, 3.07; N, 6.59. FT-IR (KBr pellet, 4000-400 cm^{-1}) (Figure 2): 3021(b), 1581(s), 1609(s), 1567(s), 1511(s), 1419(s), 1329(s), 1319(s), 1113(s), 1111(s), 1101(s), 1013(s), 841(s), 781(s), 720(s).

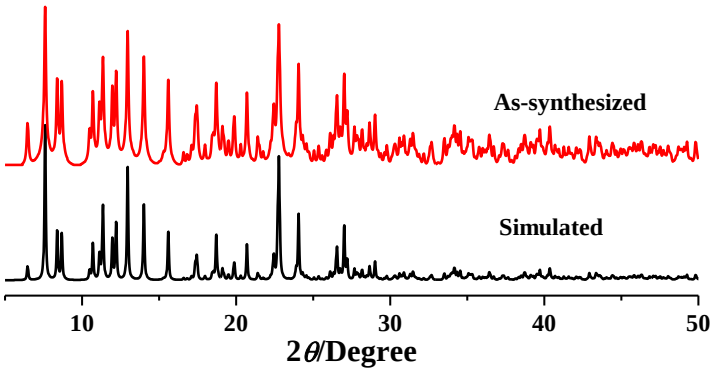

Figure 1: Simulated and as-synthesized PXRD patterns of compound **1**.

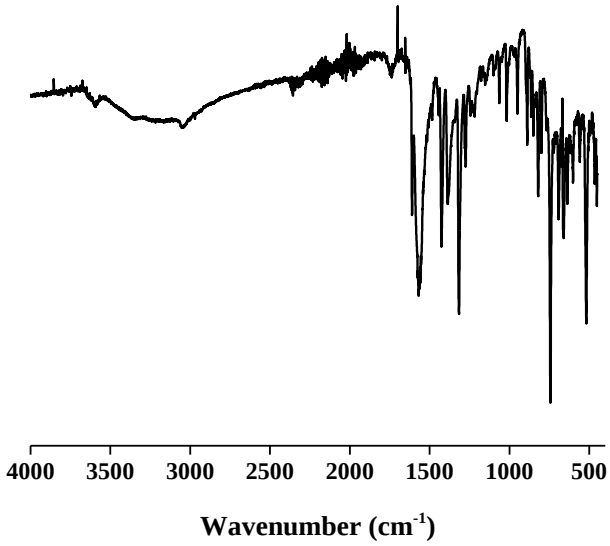

Figure 2: FT-IR spectrum of **1**.

4A.2.4 Synthesis of $[\{Cd(pba)_2(bphz)\}\cdot 5H_2O]_n$ (2)

Compound **2** is synthesized following similar methodology as used for **1**, except pba was used instead of pma. Light yellow colour crystals were observed after 10-15 days and bulk powder compound was prepared by direct mixing. PXRD patterns of the bulk polycrystalline compound and simulated patterns match well confirming phase purity of the bulk sample (Figure 3). Yield: 49%, relative to Cd^{2+}. Anal. Calcd. for $C_{52}H_{50}CdN_4O_9$: C, 63.20; H, 5.06; N, 5.67. Found: C, 63.57; H, 5.09; N, 5.31. FT-IR (KBr pellet, 4000-400 cm^{-1}) (Figure 4): 3449(b), 1576(s), 1509(s), 1438(s), 1383(s), 1315(s), 1267(s), 1210(s), 849(s), 720(s), 663(s), 639(s).

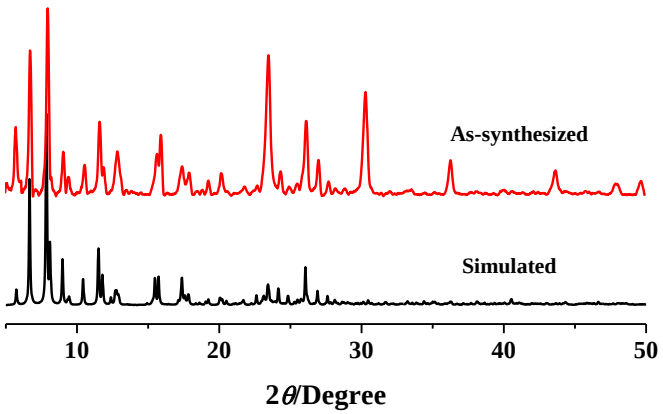

Figure 3: Simulated and as-synthesized PXRD patterns of compound **2**.

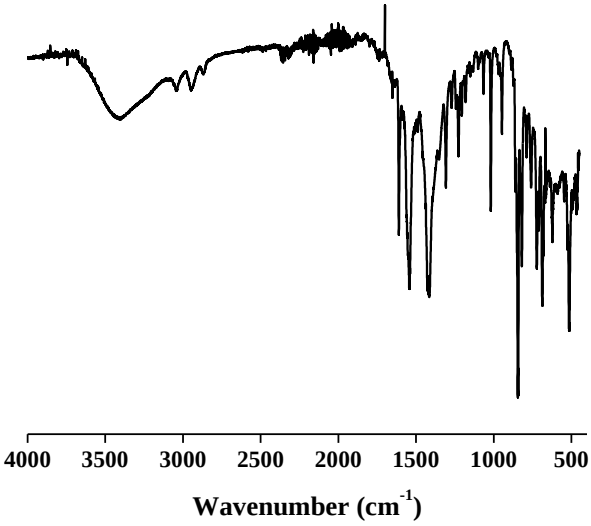

Figure 4: FT-IR spectrum of **2**.

4A.2.5 Synthesis of $\{[Cd(pma)_2(bpy)]\}_n$ (3)

Compound **3** is synthesized following similar methodology as used for **1**, except bpy was used instead of pma. Colorless crystals were observed after 10-12 days and bulk powder compound was prepared by direct mixing of ligand and metal solutions. PXRD patterns of the bulk polycrystalline compound and simulated patterns match well confirming phase purity of the bulk sample (Figure 5). Yield: 49%, relative to Cd^{2+}. Anal. Calcd. for $C_{44}H_{26}CdN_2O_4$: C, 69.55; H, 3.42; N, 3.68. Found: C, 70.10; H, 3.17; N, 3.65. FT-IR (KBr pellet, 4000-400 cm^{-1}) (Figure 6): 3040(w), 2360(w), 1589(s), 1511(s), 1375(s), 1319(s), 1263(s), 1217(s), 819(s), 731(s), 659(s), 628(s).

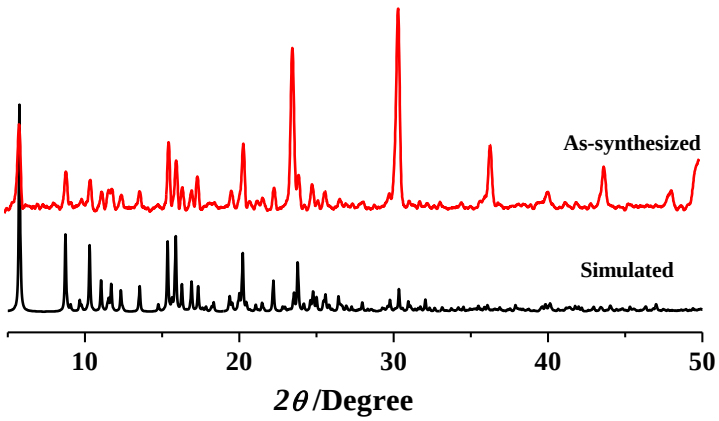

Figure 5: Simulated and as-synthesized PXRD patterns of compound **3**.

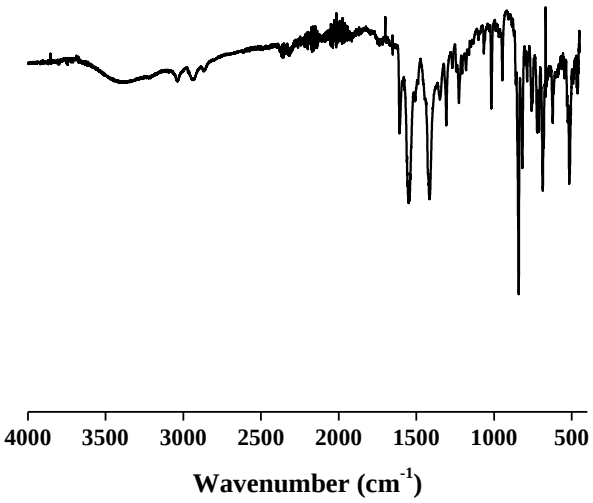

Figure 6: FT-IR spectrum of **3**.

4A.2.6 X-ray Crystallography

X-ray single crystal structural data of **1**, **2**, **2a**, **2b** and **3** were collected on a Bruker Smart-CCD diffractometer equipped with a normal focus, 2.4 kW sealed tube X-ray source with graphite monochromated Mo-*Kα* radiation (λ = 0.71073 Å) operating at 50 kV and 30 mA. The program SAINT[13] was used for integration of diffraction profiles and absorption correction was made with SADABS[14] program. All the structures were solved by SIR 92[15] and refined by full matrix least square method using SHELXL-97.[16] All the hydrogen atoms were geometrically defixed and placed in ideal positions. All crystallographic and structure refinement data of **1**, **2**, **2a**, **2b** and **3** are summarized in Table 1. Selected bond lengths and angles for **1-3** are given in Table 2-4, respectively. All calculations were carried out using SHELXL 97,[16] PLATON,[17] SHELXS 97[18] and WinGX system, Ver 1.70.01.[19]

4A.2.7 Adsorption measurements

The adsorption isotherms of CO_2 at 195 K and N_2 at 77 K using the dehydrated sample of **2 (2′)** were measured by using AUTOSORB-*IQ2* instrument. In the sample tube the adsorbent sample (~100-150 mg) was placed which had been prepared at 453 K under a 1×10^{-1} Pa vacuum for about 12 h prior to measurement of the isotherms. Helium gas (99.999% purity) at a certain pressure was introduced in the gas chamber and allowed to diffuse into the sample chamber by opening the valve. The amount of gas adsorbed was calculated readily from pressure difference (P_{cal} - P_e), where P_{cal} is the calculated pressure with no gas adsorption and P_e is the observed equilibrium pressure. All operations were computer-controlled and automatic.

The adsorption of different solvents like MeOH at 293K and H_2O, EtOH at 298 K were measured in the dehydrated sample of **2** (**2′**) in the vapour state by using BELSORP-aqua-3 analyzer. The sample of about ~100–150 mg was prepared by heating at 453 K for about 12 hours under vacuum (1×10^{-1} Pa) prior to measurement of the isotherms. The different solvent molecules used to generate the vapor were degassed fully by repeated evacuation. Dead volume was measured with helium gas. The adsorbate was placed into the sample tube, then the change of the pressure was monitored and the degree of adsorption was determined by the decrease in pressure at the equilibrium state. All operations were computer controlled and automatic.

4A.2.8 Computational details

Theoretical calculations of the compounds **1**, **2** and **3** are carried out using Gaussian 09 package[20-21] employing a DFT method of M06 hybrid functional and 3-21g levels. The Natural Bonding Orbitals (NBO)[22] analysis using NBO 3.1 program[23] is used to study the intra- and intermolecular bonding and interaction among bonds and for investigating charge transfer in molecular systems . The second-order Fock matrix was used to evaluate the donor-acceptor interactions in the NBO basis.[23] The optical properties were explained using Time-Dependent DFT (TDDFT) calculations as implemented in Gaussian 09.[24]

4A.3 Results and Discussion

4A.3.1 Structural description of $\{Cd(pma)_2(bphz)_2\}_n$ (1) and $[\{Cd(pba)_2(bphz)]\cdot5H_2O\}]_n$ (2)

Compound **1** crystallizes in triclinic *P*ī space group. The asymmetric unit contains one Cd^{2+}, two pma and one bphz linker. The seven coordinated Cd^{2+} center is connected to another by Cd^{2+} by μ-oxo bridge to form a $\{Cd_2(\mu\text{-}OCO)_2\}$ secondary building unit (SBU) (Figure 7a). Among seven coordination sites, five equatorial positions are occupied by carboxylate oxygens (O1, O2, O4, O4* and O6) from three pma and other two axial sites are occupied by two nitrogen atoms (N2 and N5) from two bphz linker. The Cd^{2+}-O and Cd^{2+}-N bond distances are in the range of 2.238(16)-2.606(16) and 2.354(18)-2.367(17) Å, respectively. The oxo bridged SBUs are extended along (110) plane through bphz pillars to form a bipillared 1D columnar structure (Figure 7b). As the pma has mono-carboxyl functionality, 1D columns are not extended along other directions through any covalent bonds rather H-bonding, π···π and C-H···π interactions between pyrene aromatic rings and

bphz pillars direct the formation of 3D supramolecular structure. The 1D bi-pillared chains form a 2D sheet like structure along (-110) direction through hydrogen bonding between carboxylate oxygen and C-H from bphz linker (C63-H···O6 ~ 3.509 Å) (Figure 8a). These are further interdigitated through face-to-face stacking (π···π ~ 3.614 Å) between pma units along *c*-axis to form a supramolecular 3D structure (Figure 8b-c). The pma ligand of one 1D chain also interacts with the bphz linker of neighbouring 1D chain through C-H···π interaction (~ 3.695 Å) (Figure 8d).

Compound **2** also crystallizes in triclinic *P*$\bar{1}$ space group and the basic structure resembles to that of **1**. But the replacement of pma linker by pba which has flexible alkyl chains modulates the final structure to a porous framework. The Cd^{2+} center is seven coordinated and forms similar μ-oxo bridged $\{Cd_2(\mu\text{-}OCO)_2\}$ secondary building unit (SBU). The coordination environment of metal center is similar to that of Cd^{2+} in **1**; five equatorial positions are occupied by carboxylate oxygen atoms (O1, O1*, O2, O3 and O4) from three pba and the axial positions are filled by two nitrogens (N1 and N4) from two bphz (Figure 9). The Cd^{2+}-O and Cd^{2+}-N bond distances are in the range of 2.310(6)-2.467(5) and 2.315(5)-2.317(3) Å, respectively. Similar to framework **1**, the 1D bipillared chain formed *via* connecting the SBUs through bphz linkers extends along *c*-axis (Figure 10a). Here, the spatial disposition of pyrene rings of pba is very unique. Among four pba that are connected to one SBU, two aligns upwards and the other two downwards (Figure 9). This arrangement helps to keep two neighbouring columns together through interdigitation which is supported by a continuous face-to-face stacking of pba:bphz:bphz:pba (Figure 10a-b). Here the pba:pba and pba:bphz π···π distances are 3.589 and 3.601 Å, respectively. Further one bphz also interacts to pba of neighbouring 1D chain *via* C-H···π interaction (Figure 10c). Such interdigitated stacking of the 1D chains along *a* and *b*-axes lead to a 3D supramolecular structure with 1D irregular shaped pore channels with dimensions 1.5×3.2 $Å^2$ along *c*-direction (Figure 11).[25] The void space is occupied by five guest water molecules. The total void space calculated using PLATON[17] after removing the guest water molecules is 15% of total cell volume.

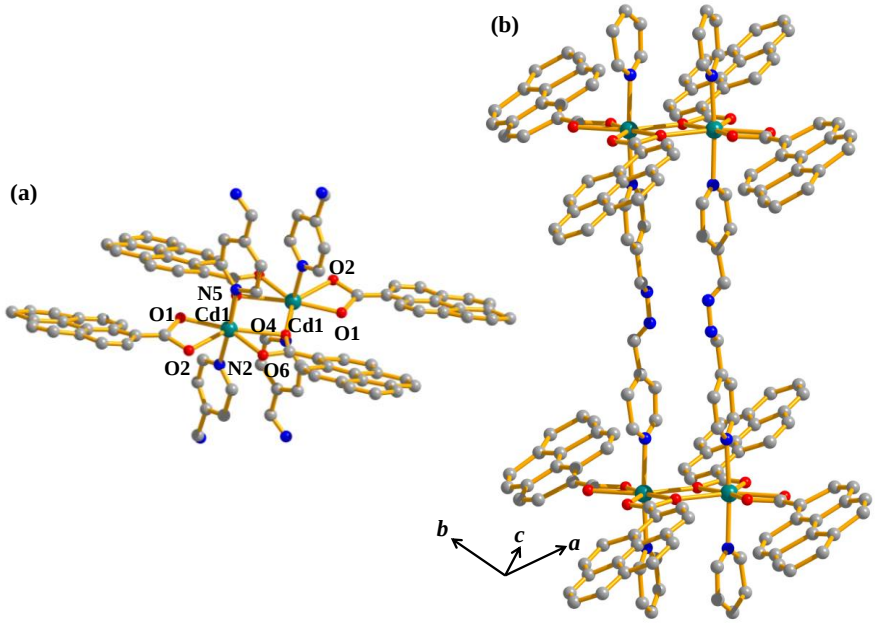

Figure 7: (a) Coordination environment of Cd^{2+} in framework **1**; (b) 1D bipillared chain of **1**.

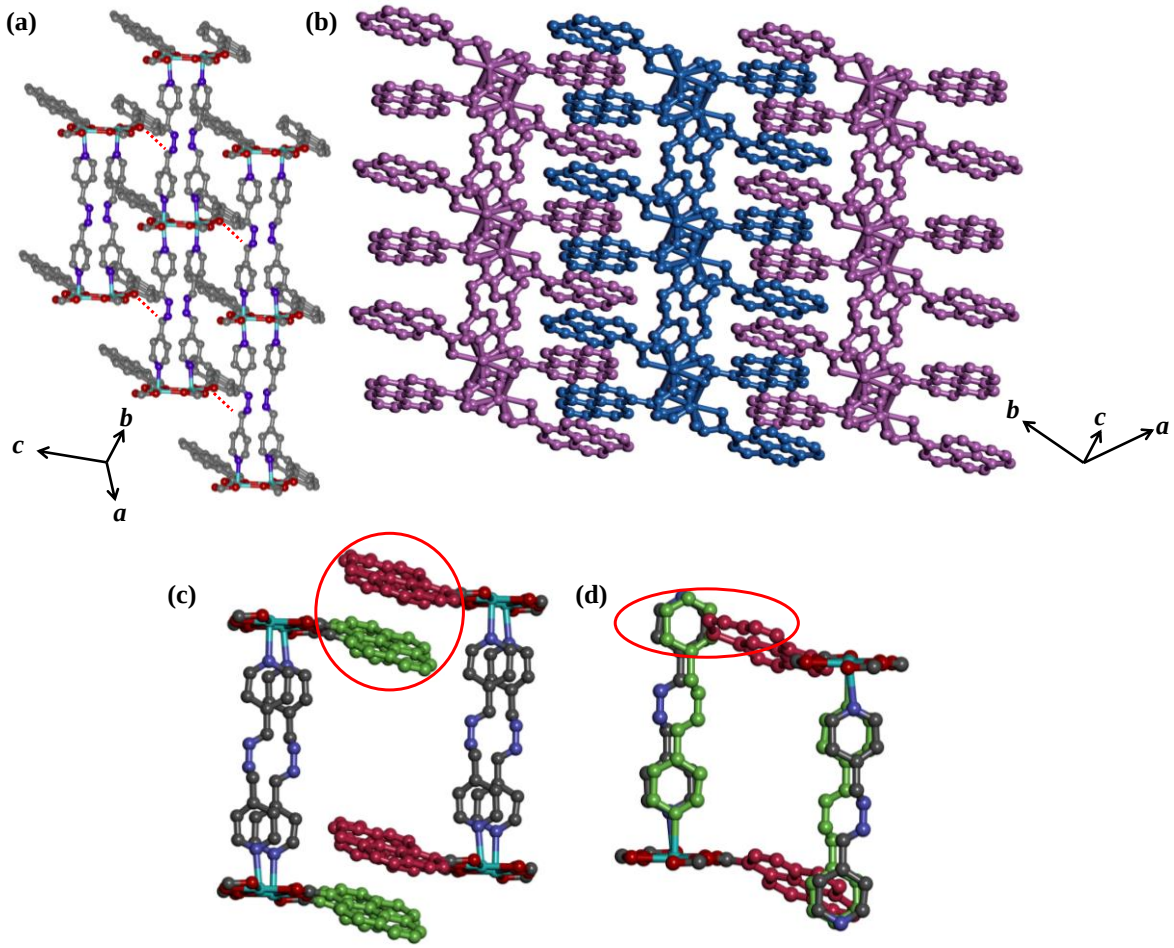

Figure 8: Structural details of **1**: (a) 2D layer formed by hydrogen bonding shown in red dotted lines; (b) Interdigitation between the 1D chains; (c) face-to-face π···π stacking of pma of neighbouring 1D chains; (d) C-H···π interaction between bphz and pma of neighbouring 1D chains.

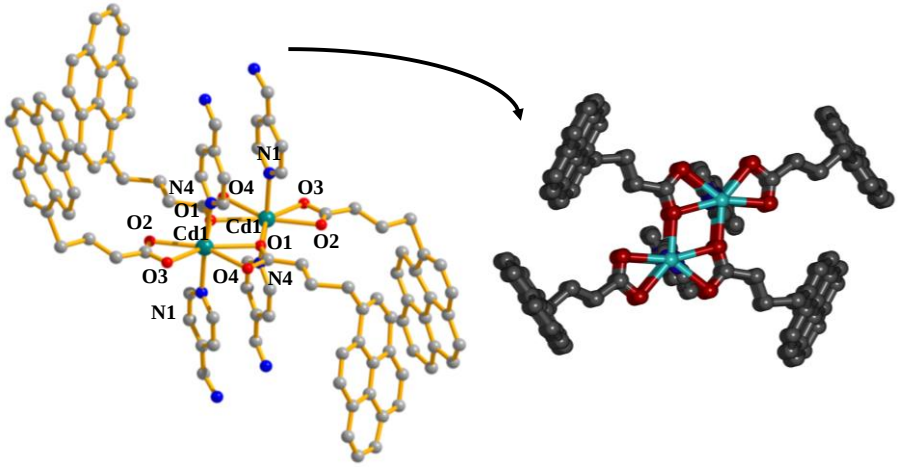

Figure 9: Coordination environment of Cd^{2+} in compound **2**; Right side: View of the 1D chain along the bi-pillar which shows the four pba arms of the 1D chain.

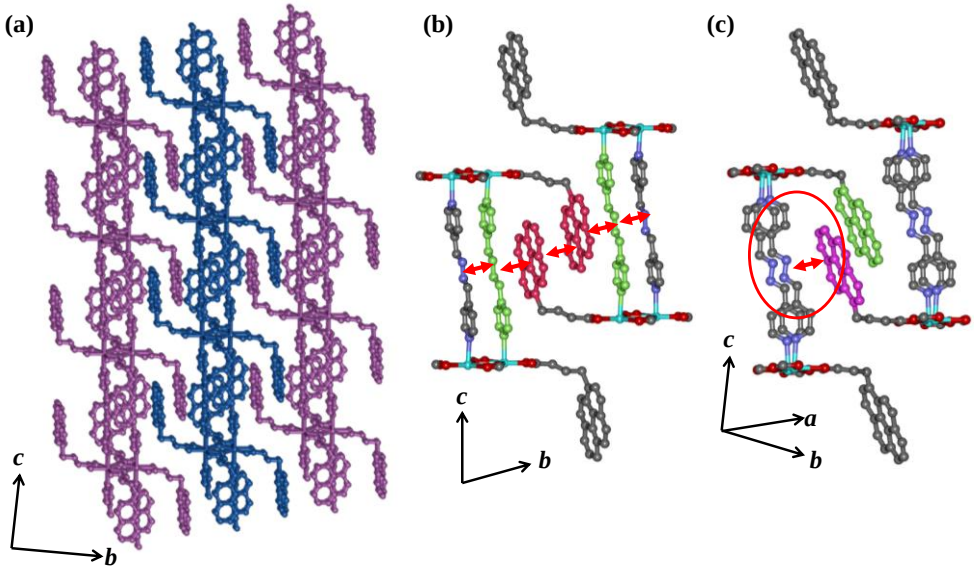

Figure 10: (a) View of the interdigitated 1D bipillared chains of **2** along *a*-axis; Similar interdigitation occurs along *b*-axis; (b) Continuous face-to-face stacking of pba:bphz:bphz:pba; (c) C-H···π interaction between the bphz pillars with the pba ring of neighbouring 1D chain.

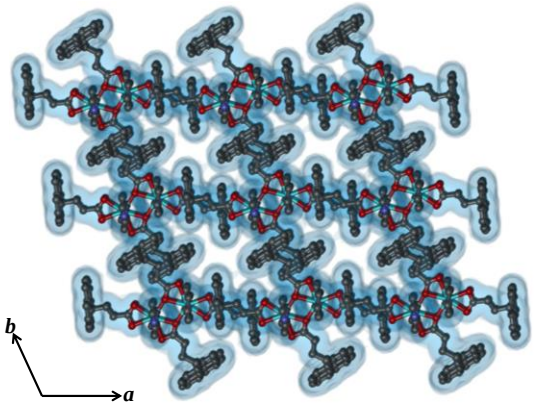

Figure 11: van der Waals surface added view of 1D channels along *c*-axis in compound **2**.

Table 1: Crystal data and structure refinement parameters of compound **1**, **2**, **2a**, **2b** and **3**.

Parameters	1	2	2a	2b	3
Empirical formula	$C_{46}H_{28}CdN_4O_4$	$C_{52}H_{50}CdN_4O_9$	$C_{52}H_{42}CdN_4O_5$	$C_{52}H_{54}CdN_4O_{11}$	$C_{44}H_{26}CdN_2O_4$
M	811.96	977.29	905.011	1014.16	759.08
Cryst. system	Triclinic	Triclinic	Triclinic	Triclinic	Triclinic
space group	*P*ī	*P*ī	*P*ī	*P*ī	*P*ī
***a* (Å)**	10.1365(3)	11.7806(5)	18.5462(9)	18.5114(7)	10.223(5)
***b* (Å)**	11. 01269(3)	13.9045(5)	20.0824(10)	21.0115(8)	11. 637(5)
***c* (Å)**	14.2362(5)	15.7871(2)	8.7759(5)	8.7093(3)	15.998(5)
***α* (deg)**	91.659(3)	78.956(2)	77.516(3)	78.853(4)	101.780(5)
***β* (deg)**	101.993(5)	86.961(8)	89.196(5)	85.539(8)	95.206(5)
***γ* (deg)**	96.369(7)	75.263(5)	75.296(6)	74.298(1)	115.530(5)
***V* (Å^3)**	1725.023(8)	2524.261(9)	2317.961(5)	2759.124(4)	1646.4(12)
Z	4	4	4	4	4
***T*(K)**	150	150	100	100	293
***λ* (Mo K$_α$)**	0.71073	0.71073	0.71073	0.71073	0.71073
***D*$_c$ (g cm^{-3})**	1.342	1.199	1.338	1.306	1.531
***μ* (mm^{-1})**	0.820	0.797	0.818	0.589	0.713
***θ*$_{max}$ (deg)**	25.5	26.4	27.5	32.1	25.5
total data	18296	19272	17049	23902	18296
unique reflection	2979	3285	3683	1950	2979
***R*$_{int}$**	0.040	0.039	0.090	0.051	0.040
data [*I* > 2σ(*I*)]	2583	2644	2444	4115	2583
***R*^{a}**	0.0587	0.0815	0.0809	0.0669	0.048
***R*$_w$^{b}**	0.1836	0.2764	0.2649	0.2256	0.1248
GOF	1.11	1.15	1.09	1.07	0.92

^{a} $R = \Sigma||F_o| - |F_c||/\Sigma|F_o|$. ^{b} $R_w = [\Sigma\{w(F_o^2 - F_c^2)^2\}/\Sigma\{w(F_o^2)^2\}]^{1/2}$.

Table 2: Selected bond lengths (Å) and angles (°) for [{Cd(pma)$_2$(bphz)}] (**1**).

Cd1-O1	2.256(18)	Cd1-O2	2.497(15)	Cd1-O4	2.432(17)
Cd1-N5_b	2.367(17)	Cd1-O4_c	2.606(16)	Cd1-O6_c	2.238(16)
O1-Cd1-O2	51.3(6)	O1-Cd1-O4	89.9(6)	O1-Cd1-N2	87.6(7)
O1-Cd1-N5_b	88.9(7)	O1-Cd1-O4_c	168.7(6)	O1-Cd1-O6_c	141.7(6)
O2-Cd1-O4	141.0(6)	O2-Cd1-N2	92.3(6)	O2-Cd1-N5_b	89.9(5)
O2-Cd1-O4_c	139.9(6)	O2-Cd1-O6_c	90.8(6)	O4-Cd1-N2	89.6(6)
O4-Cd1-N5_b	84.7(6)	O4-Cd1-O4_c	78.8(5)	O4-Cd1-O6_c	128.2(6)
N2-Cd1-N5_b	173.4(7)	O4_c-Cd1-N2	92.7(6)	O6_c-Cd1-N2	89.5(7)

O4_c-Cd1-N5_b	89.6(6)	O6_c-Cd1-N5_b	96.8(6)	O4_c-Cd1-O6_c	49.6(6)

Table 3: Selected bond lengths (Å) and angles (°) for [{Cd(pma)$_2$(bphz)}] (**1**).

Cd1-O1	2.310(6)	Cd1-O004	2.467(5)	Cd1-O2	2.381(10)
Cd1-N1	2.315(5)	Cd1-N4	2.317(3)	Cd1-O1_c	2.459(6)
O1-Cd1-O004	124.7(2)	Cd1-O1-Cd1_c	107.5(3)		
O1-Cd1-O3	143.4(3)	O1-Cd1-N1	89.98(19)		
O1-Cd1-C39	115.8(5)	O1-Cd1-O1_c	72.5(2)		
O004-Cd1-O3	91.8(3)	O004-Cd1-N1	87.61(19)		
O004-Cd1-C39	119.5(5)	O1_c-Cd1-O004	52.2(2)		
O2-Cd1-N1	94.3(2)	O2-Cd1-N4	89.9(2)		
O1_c-Cd1-O2	161.2(3)	O3-Cd1-N1	88.9(2)		
O3-Cd1-C39	27.7(5)	O1_c-Cd1-O3	144.0(3)		
N1-Cd1-C39	90.7(3)	O1_c-Cd1-N1	88.66(18)		
O1_c-Cd1-N4	88.00(16)	O1_c-Cd1-C39	171.6(5)		

Table 3: Selected bond lengths (Å) and angles (°) for {[Cd(pma)$_2$(bpy)]}$_n$ (**3**).

Cd1-O1	2.369(6)	Cd1-O2	2.435(5)	Cd1-O3	2.337(6)
Cd1-N2_b	2.341(6)	Cd1-O3_c	2.583(5)	Cd1-O4_c	2.342(5)
O1-Cd1-O2	53.83(19)	O1-Cd1-O3	145.93(16)		
O1-Cd1-C11	27.0(2)	O1-Cd1-N2_b	87.45(19)		
O1-Cd1-O4_c	85.93(17)	O2-Cd1-O3	92.51(19)		
O2-Cd1-C11	27.2(2)	O2 -Cd1-N2_b	78.5(2)		
O2-Cd1-O4_c	138.15(18)	O3-Cd1-N1	86.6(2)		
O3-Cd1-N2_b	90.94(19)	O3-Cd1-O3_c	76.42(17)		
N1-Cd1-C11	102.1(2)	N1 -Cd1-N2_b	177.5(2)		
O4_c-Cd1-N1	91.73(19)	N2_b-Cd1-C11	79.0(2)		
O4_c-Cd1 -C11	111.3(2)	O3_c-Cd1-N2_b	96.28(19)		
O3_c-Cd1-O4_c	51.97(17)				

4A.3.2 Thermal stability structural flexibility

Compound **1** does not contain any potential void space due to the closed packed structure. But compound **2**, due to the flexible alkyl chain of pba linker possess reasonable void space and a 1D channel along *c*-direction. The thermogravimetric analysis profile of **2** suggests loss of all the guest molecules in the temperature range of 30-80° C (Figure 12a). Further heating leads to some unknown phase. The PXRD pattern of desolvated compound **2** (**2′**) shows slight changes compared to that of as-synthesized **2**, indicating structural rearrangement upon guest removal (Figure 12b).

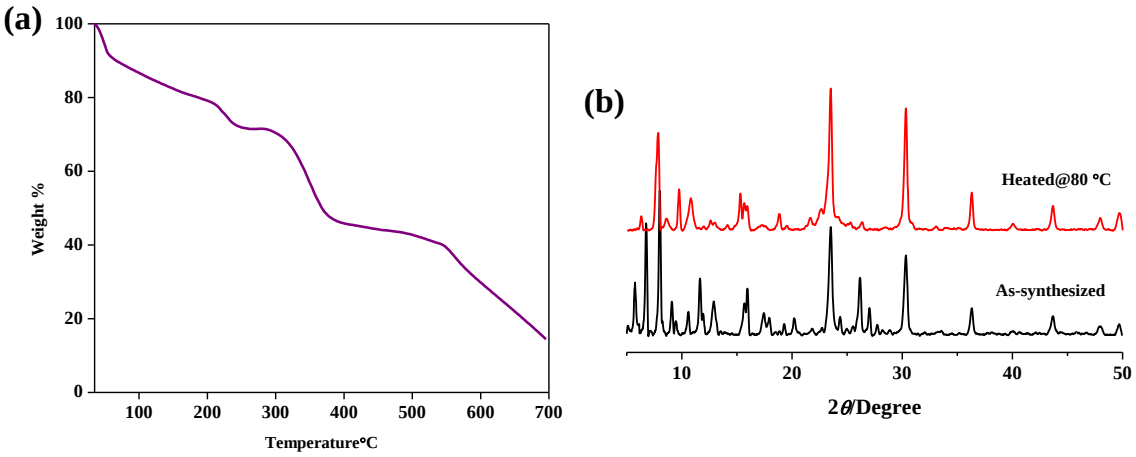

Figure 12: (a) TGA profile of compound **2** in the temperature range of 30-700 °C at heating rate of 3 °C/min under N_2 atmosphere.

Further to get an insight of the structural rearrangement process, single crystals of **2** were desolvated at a controlled heating condition at 70 °C under vacuum for 16 h. Most of the crystals become polycrystalline while few good quality crystals were selected for single crystal X-ray diffraction. After several attempts we could get a partially desolvated structure, $[\{Cd(pba)_2(bphz)\}\cdot H_2O]_n$ (**2a**) which has a slightly contracted cell volume compared to that of **2** (Figure 13). All of the guest water molecules could not be removed after several attempts as the crystallinity of the crystals degrade drastically. Further, resolvation of **2a** crystals under water vapour for 2-3 days yields a framework, $[\{Cd(pba)_2(bphz)\}\cdot 7H_2O]_n$ (**2b**) with more number of guest water molecules than in **2**. Interestingly, the cell volume is even more than **2** indicating structural expansion of the framework. Such contraction and expansion phenomena are possible due to the π···π stacked interdigitated 1D chains of compound **2**. The cell parameters are tabulated in Table 1.

4A.3.3 Porosity of compound 2: Selective stepwise adsorption

To check the permanent porosity of the compound **2′** we have carried out N_2 and CO_2 gas adsorption measurements at 77 and 195 K (Figure 14). **2′** does not show any uptake of N_2 possibly due to small pore dimension which is not sufficient for N_2. But at 195 K **2′** adsorbs ~30 mL/g CO_2 suggesting porous nature of the PCP. Such selectivity towards CO_2 is possibly due to interaction between CO_2 quadrupole and aromatic π electrons in the pore surface.

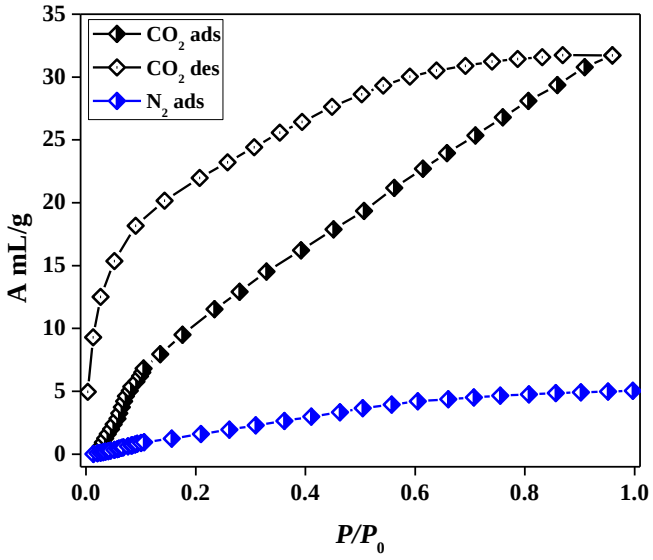

Figure 14: CO_2 and N_2 adsorption profiles of **2′** at 195 and 77 K, respectively.

Much more interesting features were realized in different solvent vapour adsorption experiments. At 298 K the diffusion of H_2O solvent vapour increases gradually upto P/P_0 ~ 0.53 and that corresponds to ~ 2.2 molecules/formula uptake (Figure 15). After that with a sudden jump uptake amount reaches to ~ 8 molecules/formula. This sort of double step uptake profile with a steep uptake at higher pressure reveals the guest induced structural transformation. Moreover the desorption curve creates a large hysteresis loop revealing strong interaction with the framework or kinetic trapping in the confined channels. The MeOH solvent vapour uptake profile was quite different from that of H_2O vapour. It was anticipated that due to increased kinetic diameter and less polarity the uptake amount will be less and no such steep rise of adsorption will be observed. But a double step uptake profile is observed and at relatively lower pressure (P/P_0 ~ 0.1) a sharp uptake was realized revealing the structural change or gate opening phenomenon. The final uptake amount is 4.5 molecules/formula and a large hysteresis which again indicates the possibility of kinetic trapping. Even at P/P_0 ~ 0.05 3 molecules of methanol/formula retains inside the pores. In

case of EtOH vapour, till P/P_0 ~ 0.8 no uptake was observed and after this with a sudden jump in uptake reaches the final amount 3.4 molecules/formula. Similar to MeOH the desorption curve creates a hysteresis and the till P/P_0 ~ 0.05 2.5 molecules/formula retain in the framework. The onset pressure for EtOH is higher than MeOH and H_2O which is due to higher kinetic diameter and also possibly less polarity. The retention of EtOH molecules can be attributed to the strong confinement inside the channels. The huge difference in the onset pressure of uptake in MeOH and EtOH makes this framework a potential material for separation of these solvent mixtures. Moreover, the Table 5 shown below gives the sepration factors of the water/ethanol and methanol/ethanol which clearly indicates the potential of this framework for separation of ethanol, a biofuel which has immense importance as an alternative energy source.[26]

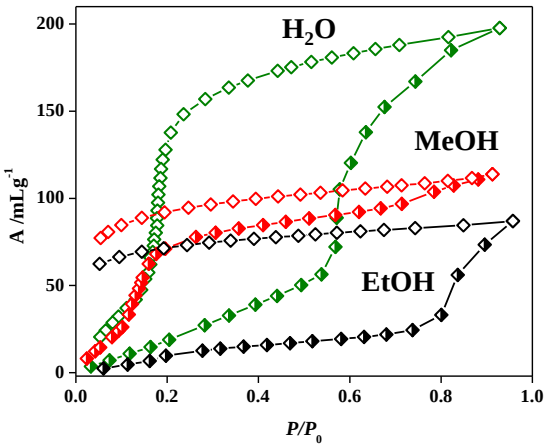

Figure 15: Water, methanol and ethanol vapour adsorption profiles for **2′**.

Table 5: Separation factors of water/ethanol and methanol/ethanol at different vapour pressures calculated based on uptake amounts.

	Separation factors	
Relative vapour pressure	Water/ethanol	methanol/ethanol
~ 0.05	~ 2.4	~ 7.2
~ 0.1	~ 2.5	~ 5.8
~ 0.3	~ 2.7	~ 5.8
~ 0.7	~ 7	~ 4.3

4A.3.3 Photophysical properties of 1 and 2: Stable charge separated state

The UV-vis spectrum of **1** shows a broad absorption band from 200 to 400 nm and a weaker band in 400-500 nm range (Figure 16a). Upon excitation at 400 nm we have observed no emission spectrum which is unexpected as the framework contains luminescent pyrene chromophore. Such quenching of emission is possible in the following ways: a) aggregation based quenching of pyrene or b) any ground state charge transfer between the pyrene and bphz linker or c) due to some other non-radiative path. Possibility of aggregation based quenching can be overruled as pyrene is well-known to show excimer emission in aggregated state. The partial or long lived charge separation between the pba and bphz is another possibility but due to broad nature of the absorbance spectrum it was not clear. To understand the photophysical phenomenon behind this quenching we carried out EPR experiment of **1** and found a single radical peak with g value 2.0009 (Figure 16b). This confirms that there is an existence of charge separated species and pyrene is involved in this process. Interesting feature of this process is that no energy was provided for the process which means the charge separated state is stable at RT condition. Close look at the structure reveals that the pyrene core of pba and bphz linker of neighbouring 1D chain are in close contact through C-H···π interaction, hence through space electron transfer is possible. The other possibility is through coordination bonds. But confirmation of such process is difficult to establish. Unique feature of this process is the charge separated state exists between two 1D chains those are interdigitated but not in a single 1D chain of **1**. Further details of its charge separated state in **1** come from theoretical calculations. We have taken a fragment of the structure that contains pma unit and bphz unit from other neighbouring 1D chain and these two are in close contact through C-H···π interactions. The Time-dependent Density Functional Theory (TDDFT) calculations suggested two low energy peaks at 397.6 and 456.7 nm (Figure 17a). These transitions correspond to π-π* transition of pba and a complete charge transfer from pba to the bphz, respectively (Figure 17b). Hence the weak absorption band observed in the absorption spectrum of **1** is clearly due to the charge separated state that exists between pba and bphz.

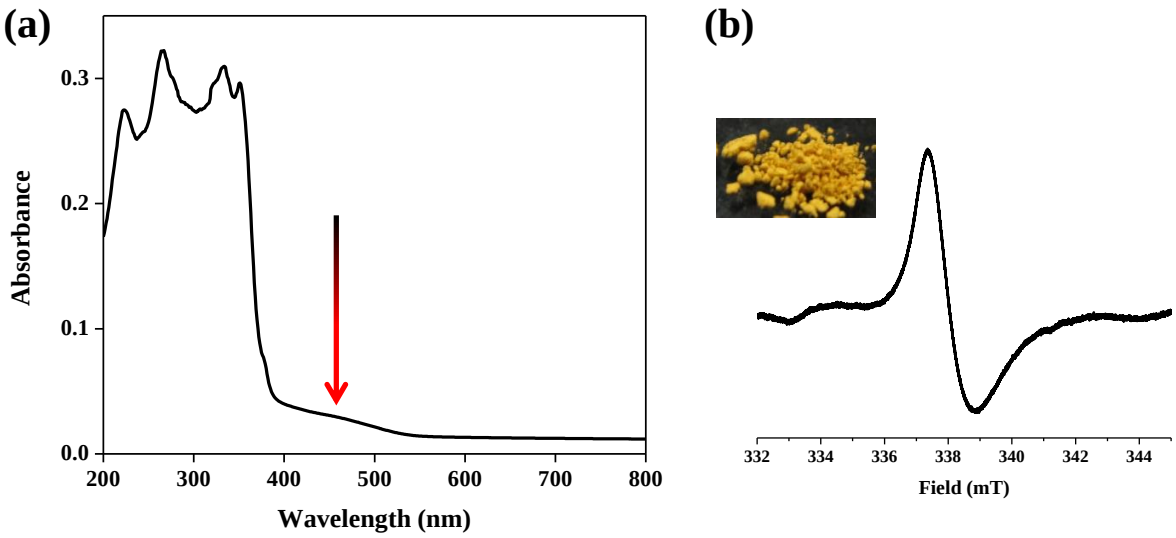

Figure 16: (a) Absorption spectrum of **1**; (b) EPR spectrum of **1**, Inset: Photograph of compound **1** in daylight.

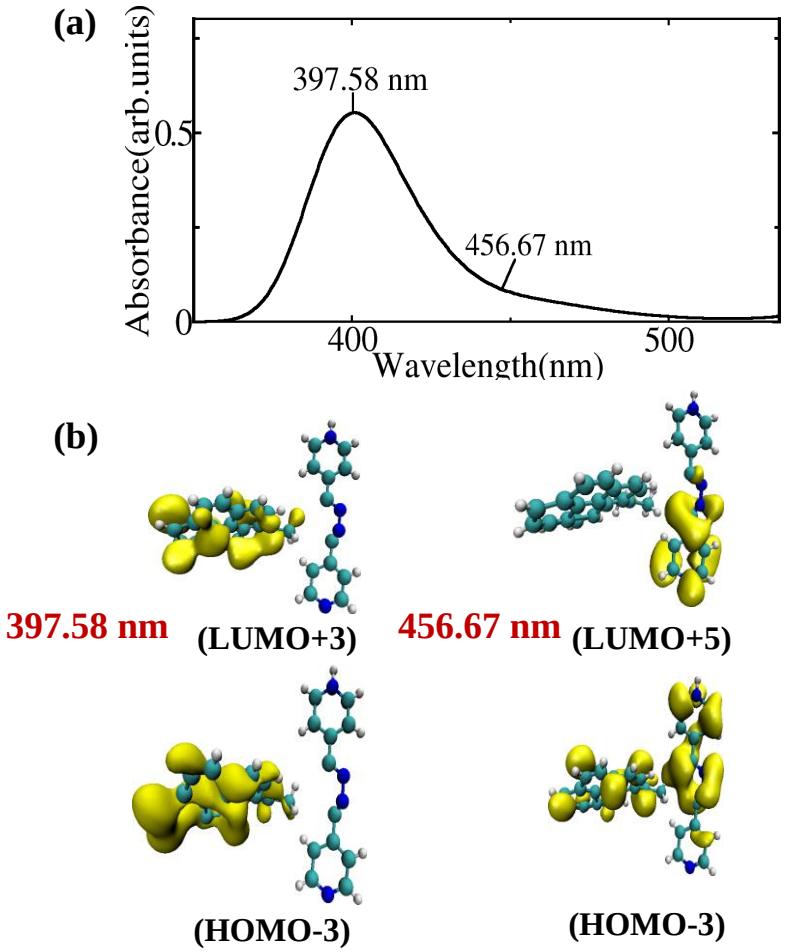

Figure 17: DFT studies of **1**: (a) Calculated absorption spectrum; (b) Frontier molecular orbitals of HOMO and LUMO and their corresponding transition wavelengths.

Compound **2**, also shows no emission and an absorption spectrum similar to that of **1**. In addition to a broad absorption from 200 to 400 nm a significant band at 400-500 nm exists in absorption spectrum of **2** (Figure 18a). EPR experiment of **2** clearly shows a single radical peak at g = 2.0021 (Figure 18b). This reiterates the presence of similar charge separated state between pba and bphz. In this case the pba chromophores stack in face to face fashion with each other. Further the bphz linkers are also in similar arrangement with pba, i. e. face to face stacked. Evidently the possibility of through electron transfer is very much viable here. To consolidate the fact we have done calculation with two different fragments. In one case we have considered only the π···π stacked pba from two different 1D chains; another case π···π stacked pba and bphz from other 1D chain. In the first case only one low energy transitions at 330.6 nm but no obvious transitions in the visible region of the spectrum was observed (Figure 19a). This 330.6 nm transition corresponds to purely π-π* transition (Figure 19b). For the second fragment, we have observed two distinct low energy transitions at 404.5 and 450.6 nm (Figure 20a). The high energy transition (404.5 nm) corresponds to π-π* whereas the low energy transition in the visible region comes from the charge separated state between the pba and bphz (Figure 20b). This particular transition matches well with the observed weak absorption peak of **2** in the visible region of the spectrum. It is worth to mention that like compound **1** here also the charge separated state exists between two interdigitated 1D chains. Hence such interesting photophysical process is induced by the structural constrains.

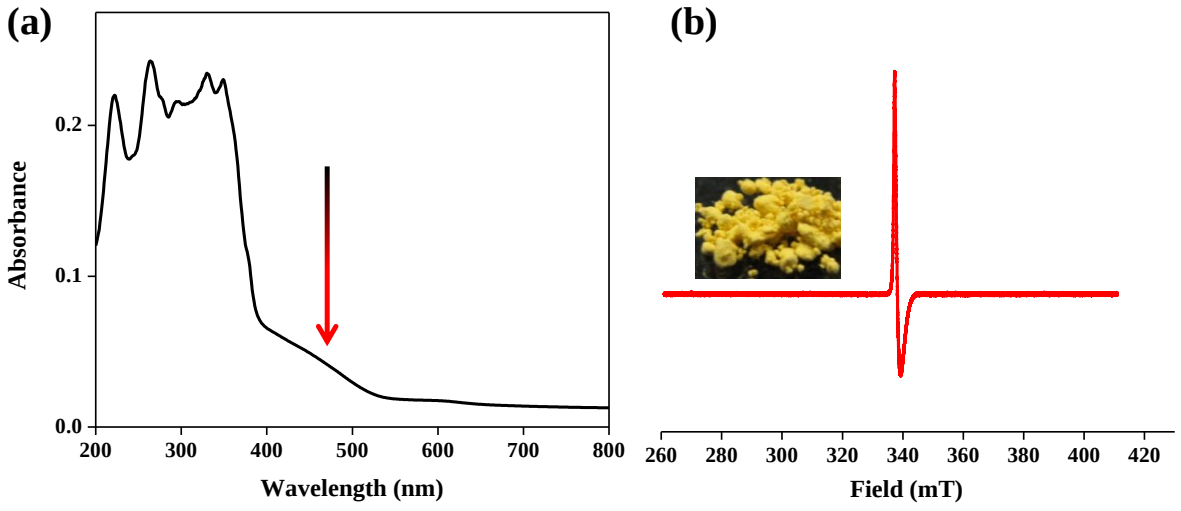

Figure 18: (a) Absorption spectrum of **2**; (b) EPR spectrum of **2**, Inset: Photograph compound **2** in solid state in daylight.

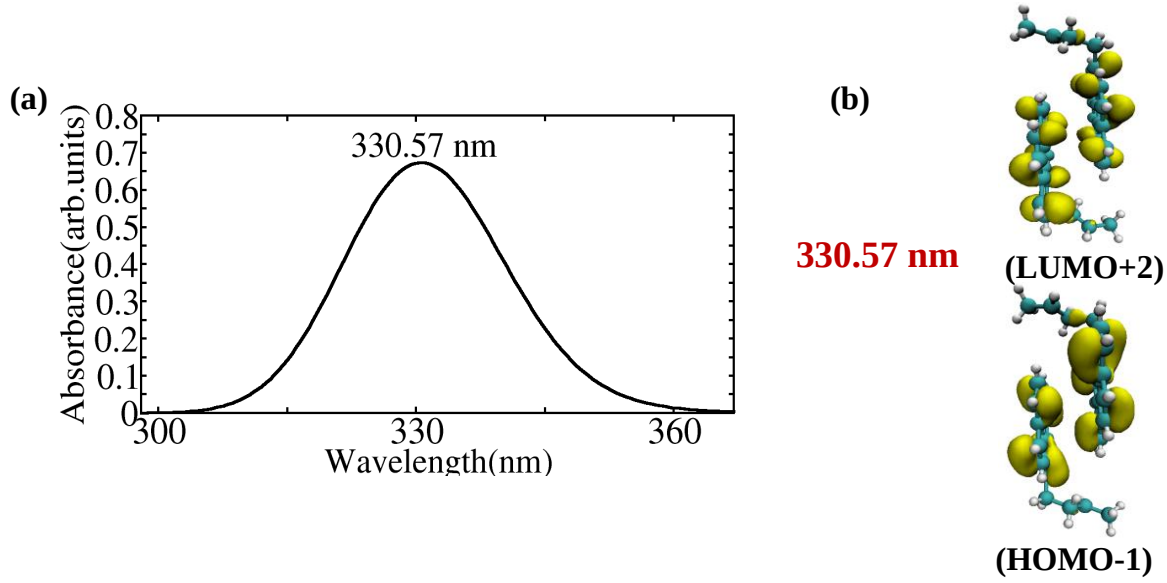

Figure 19: DFT studies of **2** (face to face stacked pba units): (a) Calculated absorption spectrum; (b) Frontier molecular orbitals of HOMO and LUMO and their corresponding transition wavelengths.

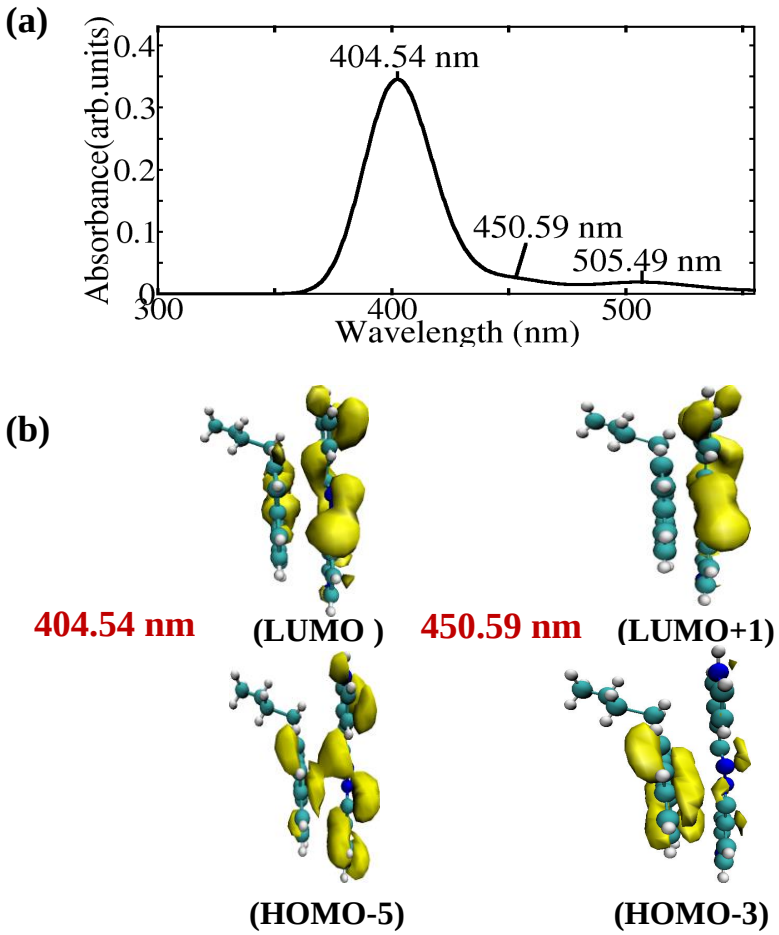

Figure 20: DFT studies of **2** (face to face stacked pba and bphz): (a) Calculated absorption spectrum; (b) Frontier molecular orbitals of HOMO and LUMO and their corresponding transition wavelengths.

In both the compounds the donor and acceptor chromophores are similar but their spatial arrangements are not same. Bphz linker contains imine functionality which can act as an electron acceptor but has not been explored in PCPs before. In the present case the close distances of pyrene based linkers and bphz induced by framework interdigitation is the key factor for such stable charge separated state formation.

4A.3.5 Compound 3 as a model compound of 1: Role of bphz linker

As mentioned before in compound **3**, the pillar linker is bpy and the rest if the structure remains very similar to compound **1**. It also crystallizes in triclinic *P*ī spacegroup and the asymmetric unit contains one Cd^{2+}, two pma and one bpy linker. The seven coordinated Cd^{2+} metal center is coordinated by 5 equatorial oxygen atoms (O1, O2, O3, O3* and O4) from two pma and other two axial positions are occupied by two nitrogen atoms (N1 and N2) from two bpy linkers (Figure 21). The Cd^{2+}-O and Cd^{2+}-N bond distances are in the range of 2.238(16)-2.606(16) and 2.354(18)-2.367(17) Å, respectively. Similar to that in **1**, a dinuclear μ-oxo bridged $\{Cd_2(\mu\text{-}OCO)_2\}$ SBU is formed and further connected by bpy along (1-10) plane to form a bipillared 1D chain. These 1D chains are stacked to the next 1D chain through mainly C-H···π interactions between bpy:pma and pma:bpy (3.756 and 3.698 Å, respectively) (Figure 22a). In addition to that, pma:pma C-H···π interaction (3.985 Å) can also be found that holds the 1D chain to form the final 3D supramolecular structure (Figure 22b and 23). Similar to **1**, here also we could see interaction between pma and the pillar linker, here it is bpy. This structure does not contain any void space as was observed in case of **1**.

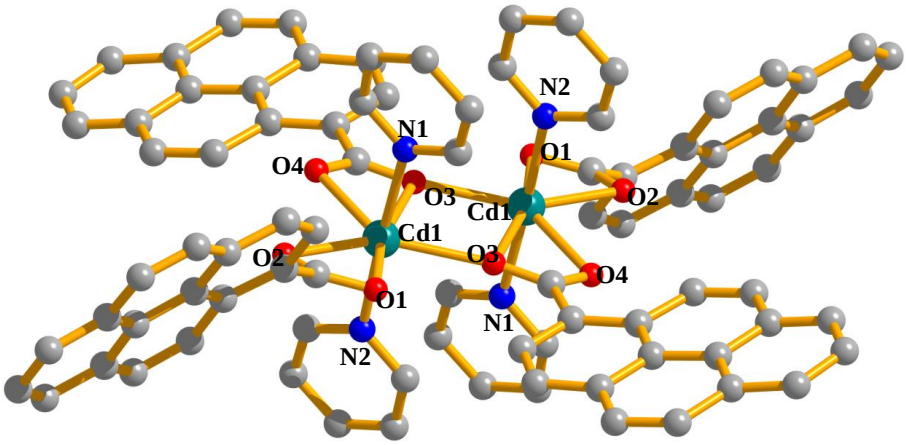

Figure 21: Coordination environment of Cd^{2+} in compound **3**.

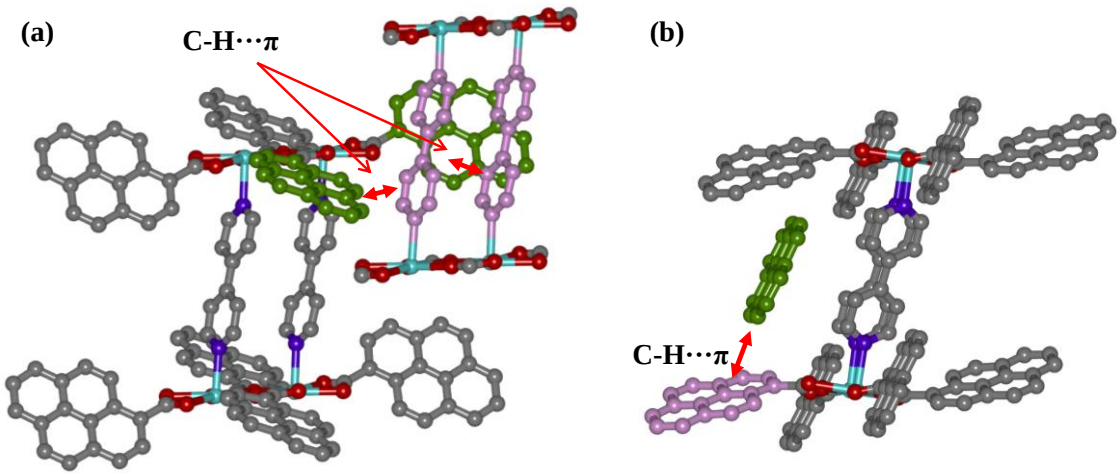

Figure 22: Structural details of compound **3**: (a) C-H···π interaction between the pma and bpy of neighbouring 1D chains; (b) C-H···π interaction between pma of neighbouring 1D chains.

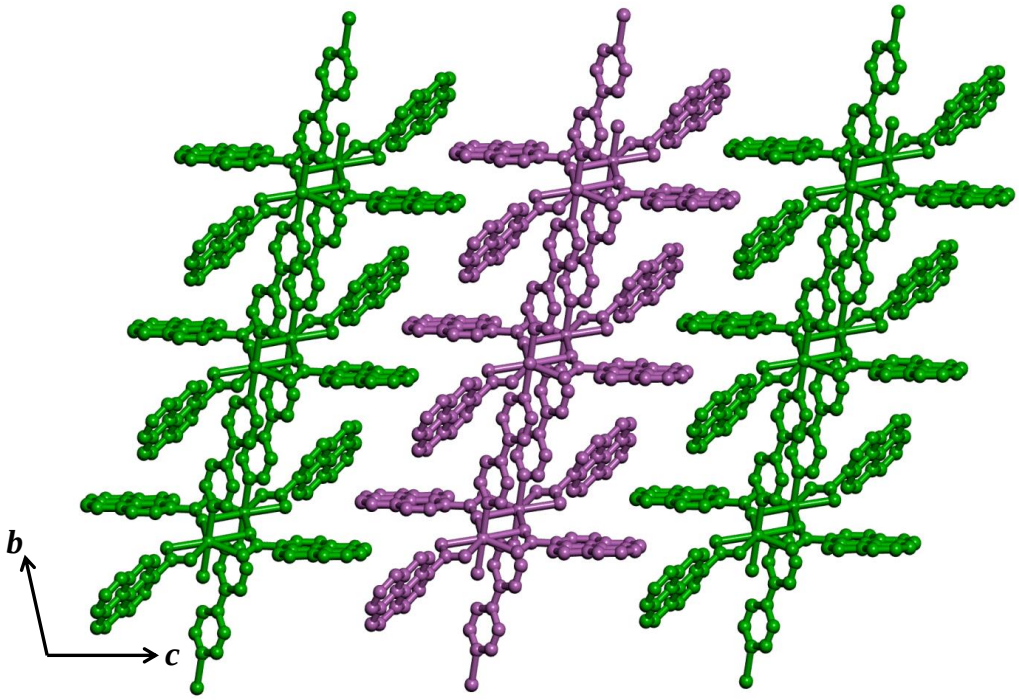

Figure 23: View of the packed 1D structure of compound **3** along *a*-direction.

Interestingly, the absorption spectrum of **3** does not show any band in the visible region and excitation at 400 nm clearly shows a broad emission spectrum with maximum at 471 nm (Figure 24). This emission spectrum is much red shifted to typical pma monomer emission indicating presence of excited state complex formation. But even more interesting fact is, replacement of bphz by bpy linker brings back the emission and no such ground state interaction exists. This observation reiterates that bphz acts as an electron acceptor in **1** and **2**. Further, TDDFT calculations considering the C-H···π connected pma and bpy fragment

shows a low energy transition at 335.7 nm and this transition corresponds to π-π* transition of pma as can be seen from localized electron density (Figure 25). No strong transitions were observed in the visible region of the spectrum suggesting absence of ground state interactions.

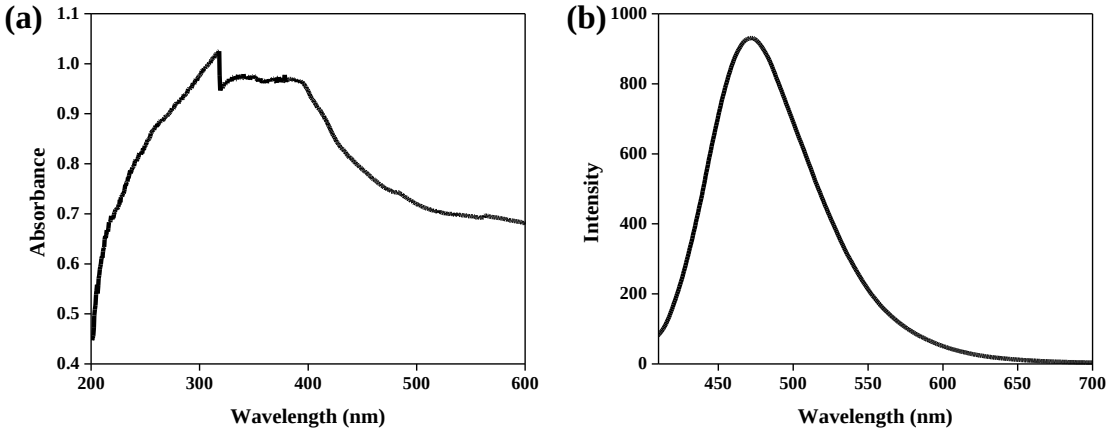

Figure 24: (a) Absorption spectrum of **3**; (b) Emission spectrum of **3** upon excitation at 400 nm.

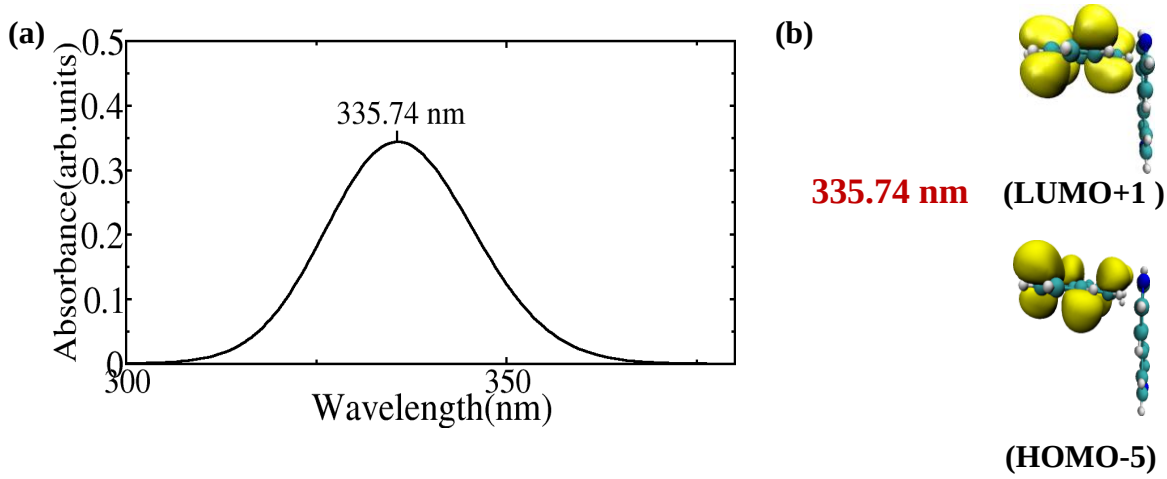

Figure 25: DFT studies of **3**: (a) Calculated absorption spectrum; (b) Frontier molecular orbitals of HOMO and LUMO and their corresponding transition wavelengths.

4A.4 Conclusions

In conclusion, in this chapter two new 1D coordination polymers using pyrene as an electron rich chromophore and a new electron acceptor chromophore bphz have been synthesized. Self-assembly of pma and bphz with Cd^{2+} yields a 1D interdigitated nonporous framework **1**, whereas changing the linker from pma to pba gives a porous 1D interdigitated structure **2**. Such tuning of nonporous to porous structure through linker modification is unique. Further, framework **2** shows structural contraction and expansion upon desolvation/resolvation process. Interestingly, the desolvated structure shows stepwise

solvent vapour adsorption profiles suggesting potential application in biofuel separation process. Both the frameworks show stable charge separated complex of pma:bphz and pba:bphz due to interdigitation between the 1D coordination polymers. Such interdigitation induced stable charge separated state formation at room temperature is unprecedented. Further, DFT calculations support the above mentioned observation. Participation of bphz as an acceptor in both compounds was further proved by a model compound consisting of bpy as a replacement to bphz. This model compound shows bright pyrene excimer emission and no ground state interaction confirming that bphz acts as an acceptor in compound **1** and **2**. Pyrene based coordination polymers are rare in literature and such sort of stable charge separated state is unprecedented. Based on such synthetic strategies it can be possible to fabricate photochromic devices for practical applications.

4A.5 References

1. a) S. Kitagawa, R. Kitaura, S. –I. Noro, *Angew. Chem. Int. Ed.* **2004**, *43*, 2334; b) O. M. Yaghi, *Nature. Mater*. **2007**, *6*, 92.

2. a) A. Zukal, I. Dominguez, J. Mayerová, J. Cezka, *Langmuir*. **2009**, *25*, 10314; b) R. V. Siriwardane, M.S. Shen, E. P. Fisher, J. Losch, *Energy Fuels*. **2005**, *19*, 1153.

3. a) Y. Belmabkhout, A. Sayari, *Adsorption*. **2009**, *15*, 318; b) S. Kim, J. Ida, V. V. Guliants, J. Y. S. lin, *J. Phys. Chem. B*. **2005**, *109*, 6287; c) S. N. Kim, W. J. Son, J. S. Choi, W. S. Ahn, *Microporous Mesoporous. Mater*. **2008**, *116*, 394.

4. a) R. Banerjee, A. Phan, B. Wang, C. Knobler, H. Furukawa, M. O'Keeffe, O. M. Yaghi, *Science*. **2008**, *319*, 939; b) H. Hayashi, A. P. Côté, H. Furukawa, M. O'Keeffe, O. M. Yaghi, *Nat. Mater*. **2007**, *6*, 501; c) J. A. R. Navarro, E. barea, A. Rodríguez-Diéguez, J. M. Salas, C. O. Ania, J. B. Parra, N. Masciocchi, S. Galli, A. Sironi, *J. Am. Chem. Soc*. **2008**, *130*, 3978; d) F. Debatin, A. Thomas, A. Kelling, N. Heddin, Z. Bacsik, I. Senkovska, S. Kaskel, M. Junginger, H. Müller, U, Schilde, C. Jäger, A. Friedrich, H.-J. Holdt, *Angew. Chem. Int. Ed*. **2010**, *49*, 1258; e) J. An, S. J. Geib, N. L. Rosi, *J. Am. Chem. Soc*. **2008**, *132*, 38; f) R. Vaidhyanathan, S. S. Iremonger, K. W. Dawson, G. K. H. Shimizu, *Chem. Comm.* **2009**, *35*, 5230; g) C. A. Fernandez, J. Liu, P. K. Thallapally and D. M. Strachan, *J. Am. Chem. Soc*. **2012**, *134*, 9046; h) L. Pan, D. H. Olson, L. R. Ciemnolonski, R. Heddi and J. li, *Angew. Chem. Int. Ed*. **2006**, *45*, 616; i) J. Y. Lee, D. H. Olson, L. Pan, T. J. Emge, J. Li, *Adv. Funct. Mater*. **2007**, *17*, 1255; j) J. R. Li, R. J. Kuppler, H.-C. Zhou, *Chem. Soc. Rev*. **2009**, *38*, 1477; k) L. J. Murray, M. Dincă, J. R. Long, *Chem. Soc. Rev*. **2009**, *38*, 1294.

5. a) J. Y. Lee, O. K. Farha, J. Roberts, K. A. Scheidt, S. T. Nguyen, J. T. Hupp, *Chem. Soc. Rev*. **2009**, *38*, 1450; b) R. K. Das, A. Aijaz, M. K. Sharma, P. Lama, P. K. Bharadwaj, *Chem. Eur. J*. **2012**, *18*, 6866.

6. a) M. Kim, J. F. Cahill, H. Fei, K. A. Prather, S. M. Cohen, *J. Am. Chem. Soc*. **2012**, *134*, 18082; b) T. K. Maji, R. Matsuda, G. Mostafa, S. Kitagawa, *Nature. Mater*. **2007**, *6*, 142; c) T. K. Prasad, D. H. Hong, M. P. Suh, *Chem. Eur. J*. **2010**, *16*, 14043.

7. a) B. Chen, S. Xiang, G. Qian, *Acc. Chem. Res*. **2010**, ***43***, 1115; b) M. D. Allendorf, C. A. Bauer, R. K. Bhakta, R. J. T. Houk, *Chem. Soc. Rev*. **2009**, *38*, 1330; c) R. Haldar, K. V. Rao, S. J. George, T. K. Maji, *Chem. Eur. J*. **2012**, *18*, 5848; d) K. Jayaramulu, P. Kanoo, S. J. George, T. K. Maji, *Chem. Commun*. **2010**, *49*, 7906; e) C. A. Kent, B. P. Mehl, L. Ma, J. M. Papanikolas, T. J. Meyer, W. Lin, *J. Am. Chem. Soc*. **2010**, *132*, 12767.

8. a) P. Kanoo, K. L. Gurunatha, T. K. Maji, *Cryst. Growth. Des*. **2009**, *9*, 4147; b) P. Kanoo, K. L. Gurunatha, T. K. Maji, *J. Mater. Chem*. **2010**, *20*, 1322; c) J. J. Perry, J. A. Perman, M. J. Zaworotko, *Chem. Soc. Rev*. **2009**, *38*, 1400; d) J. P. Zhang, S. Kitagawa, *J. Am. Chem. Soc*. **2008**, *130*, 907.

9. a) P. K. Thallapally, J. Tian, M. R. Kishan, C. A. Fernandez, S. J. Dalgarno, P. B. McGrail, J. E. Warren, J. L. Atwood, *J. Am. Chem. Soc*. **2008**, *130*, 16842; b) K. L. Mulfort, O. K. Farha, C. D. Malliakas, M. G. Kanatzidis, J. T. Hupp, *Chem. Eur. J*. **2010**, *16*, 276; c) J. –H. Wang, M. Li, D. Li, *Chem. Sci*. **2013**, *4*, 1793.

10. a) R. Haldar, T. K. Maji, *CrystEnggCommun*. **2012**, *14*, 684; b) W. Yang, A. J. Davies, X. Lin, M. Suyetin, R. Matsuda, A. J. Blake, C. Wilson, W. Lewis, J. E. Parker, C. C. Tang, M. W. George, P. Hubberstay, S. Kitagawa, H. Sakamoto, E. Bichoutskaia, N. R. Champness, S. Yang, M. Schroder, *Chem. Sci*. **2012**, *3*, 2993; c) P. Kanoo, R. Matsuda, M. Higuchi, S. Kitagawa, T. K. Maji, *Chem. Mater*. **2009**, *21*, 5860; d) H. –L. Jiang, T. Makal, H. –C. Zhou, *Coord. Chem. Rev*. **2013**, *15*, 2232.

11. a) K. Sumida, D. L. Rogow, J. A. Mason, T. M. McDonald, E. D. Bloch, Z. R. Herm, T. –H. Bae, J. R. Long, *Chem. Rev*. **2012**, *112*, 724; b) R. Vaidhyanathan, S. S. Iremonger, G. K. H. Shimizu, P. G. Boyd, S. Alavi, T. K. Woo, *Science*, **2010**, *330*, 650; c) C. M. Nagaraja, R. Haldar, T. K. Maji, C. N. R. Rao, *Cryst. Growth. Des*. **2012**, *12*, 975; d) W. Lu, J. P. Scully. D. Yuan, R. Krishna, Z. Wei, H. –C. Zhou, *Angew. Chem. Int. Ed*. **2012**, *51*, 1; e) T. M. McDonald, W. R. Lee, J. A. Mason,B. M. Wiers, C. S. Hong, J. R. Long, *J. Am. Chem. Soc.* **2012**, *134*, 7056; f) T. M. McDonald, D. M. D'Alessandro, R. Krishna, J. R. Long, *Chem. Sci*. **2011**, *2*, 2022.

12. a) T. Ahnfeldt, N. Guillou, D. Gunzelmann, I. Margiolaki, T. Loiseau, G. Férey, J. Senker, N. Stock, *Angew. Chem. Int. Ed*. **2009**, *48*, 5163; b) X. -Y. Chen, B. Zhao, W. Shi, J. Xia, P. Cheng, D. –Z. Liao, S. –P. Yan, Z. –H. Jiang, *Chem. Mater*. **2005**, *17*, 2866; c) A. L. Grzesia, F. J. Uribe, N. W. Ockwig, O. M. Yaghi, A. J. Matzger, *Angew. Chem. Int. Ed*. **2006**, *45*, 2553; d) X. Si, C. Jiao, F. Li, J. Zhang, S. Wang, S. Liu, Z. Li, L. Sun, F. Xu, Z. Gabelica and C. Schick, *Energy Environ Sci*. 2011, **4**, 4522; e) J. An, S. J. Geib, N. L. Rosi, *J. Am. Chem. Soc*. **2010**, *132*, 38; f) Y, Zhao, H. Wu, T. J. Emge, Q, Gong, N, Nijem, Y. S. Chabal, L. Kong, D. C. Langreth, H. Liu, H. Zeng and J. Li, *Chem. Eur. J*. **2011**, *17*, 5101; g) Z. Zhang, Y, Zhao, Q, Gong and J. Li, *Chem Commun*. **2013**, *49*, 653.

13. SMART (V 5.628), SAINT (V 6.45a), XPREP, SHELXTL; Bruker AXS Inc. Madison, Wisconsin, USA, **2004**.

14. G. M. Sheldrick, Siemens Area Detector Absorption Correction Program, University of Götingen, Götingen, Germany, **1994**.

15. A. Altomare, G. Cascarano, C. Giacovazzo, A. Gualaradi, *J. Appl. Cryst*., **1993**, *26*, 343.

16. G. M. Sheldrick, SHELXL-97, Program for Crystal Structure Solution and Refinement; University of Götingen, Götingen, Germany, **1997**.

17. A. L. Spek. *J. Appl. Crystallogr*. **2003**, *36*, 7.

18. G. M. Sheldrick, SHELXS 97, Program for the Solution of Crystal Structure, University of Götingen, Germany, **1997**.

19. L. J. Farrugia, WinGX-A Windows Program for Crystal Structure Analysis, *J. Appl. Cryst*. **1999**, *32*, 837.

20. J. Chocholoušová, V. Špirko, P. Hobza, *Phys. Chem. Chem. Phys*. 2004, 6, 37.

21. E. D. Glendening, A. E. Reed, J. E. Carpenter, F. Weinhold, NBO Version 3.1

22. M. J. Frisch, G. W. Trucks, H. B. Schlegel, Gaussian 09, Revision A.1, Gaussian, Wallingford Conn, USA, **2009**.

23. M. Szafran, A. Komasa, E. Bartoszak-Adamska, *J. Mol. Str*. **2007**, *827*, 101.

24. R. Dennington, T. Keith, J. Millam, GaussView, Version 5, Semichem, Shawnee Mission, Kan, USA, 2009.

25. The sizes of the channels were calculated considering the van der Waals radii of the atoms.

26. a) A. Shigematsu, T. Yamada, H. Kitagawa, *J. Am. Chem. Soc*. **2012**, *134*, 13145; b) R. Plessius, R. Kromhout, A, L. D. Ramos, M. Farbinteanu, M. C. Mittelmeijer-Hazeleger, R. Krishna, R. Rothenberg, S. Tanase, *Chem. Eur. J*. **2014**, *20*, 1; c) H. Furukawa, H. Gandara,

Y.-B. Zhang, J. Jiang, W. L. Queen, M. R. Hudson, O. M. Yaghi, *J. Am. Chem. Soc.* **2014**, *136*, 4369.

Part 4B

Anionic porous metal-organic framework with reversible electron transfer induced by guest responsive structural change

Summary

An anionic framework $\{[Zn_4(O)(H_2O)(1,4\text{-ndc})_{3.5}(H_2O)](C_8H_{12}N)(2DMF)\}_n$ (**1**) has been synthesized using Zn^{2+} and 1,4-naphthalenedicarboxylate (1,4-ndc) as a linker in a solvothermal condition. Used template *N*,*N*′-dimethylaniline (DMA) gets protonated ($HDMA^+$) in the reaction condition and remains as a cationic counterpart in the 3D framework. **1** shows blue emission and also ground state interaction (CT) which is possibly formed between one of the 1,4-ndc and $HDMA^+$. Upon desolvation (**1a**) a structural rearrangement enforces generation of radical ion pairs; 1,4-ndc and $1,4\text{-ndc}^{-\cdot}$ and $HDMA^{+\cdot}$ which remains stable at ambient condition. Resolvation with DMF, the framework changes the structure to as-synthesized structure with only ground state CT interaction between 1,4-ndc and $HDMA^+$ and thus the electron transfer process is reversible by desolvation-resolvation process. **1a** possess sufficient void space and shows H_2 uptake of 1.5 wt% at 77 K at 40 bar pressure.

1. R. Haldar, T. K. Maji, To be Submitted.

4B.1 Introduction

Organization of donor and acceptor chromophores in a confined space to achieve interesting photophysical properties are of paramount importance for fabrication of optical devices, transistors or solar cells etc are very important topic of study.[1] In recent years, using organic polymers such as dendrimers or conjugated polymers many such self-assembled systems have been reported and their photophysical properties such as excimer/exciplex or charge transfer or electron transfer properties have been studied.[2] Electron transfer in such donor-acceptor assembly is an important topic of study as they can be directly correlated to nature's photosynthetic systems and hence based on such processes artificial photosynthetic systems can be developed. Moreover solar cell, photovoltaics and related optical devices are primarily dependent on spatial organization of donor acceptor chromophores for stimuli responsive electron transfer or redox behaviour.[3] Heat or light mediated redox properties are thus an extremely challenging area for study.[4] As mentioned before, efforts have been directed in this path using organic polymers but use of hybrid organic-inorganic systems are rare. The previous section of this chapter is based on strut-to-strut stable charge separated state, but guest responsive reversible charge separated state in PCPs is yet to be explored which will be main focus of this section.

PCPs are periodic permanently porous hybrid materials that contain merits of organic as well as inorganic units.[5] Hence, exploiting such crystalline system it is possible to organize donor and acceptor chromophores in same matrix to see their redox or electron transfer behaviour induced by external stimuli. There are few studies on coordination polymers those show photochromic behaviour based on electron transfer but stability of the charge separated states and reversibility are rare.[6] In this chapter, we envisage to study of such electron transfer process in an anionic PCP. Using 1,4-naphthalenedicarboxylic acid (1,4-ndc) linker, Zn^{2+} and a template *N*,*N*′-dimethylaniline (DMA) using a solvothermal condition we could synthesize an anionic porous 3D structure which contains $HDMA^{+}$ cation as a guest. The as-synthesized framework shows weak ground state charge transfer (CT) interaction between 1,4-ndc and $HDMA^{+}$ cation but also shows emission due to presence of another 1,4-ndc linker that does not participate in ground state CT formation. Upon desolvation of **1** (**1a**) structural rearrangement enables electron transfer from 1,4-ndc to the $HDMA^{+}$ cation leading to a colour change from colourless to green. Moreover, upon resolvation the structure reverts back to its original phase and thus it shows only CT process. This sort of reversible electron transfer process in a PCP mediated by structural rearrangement is unprecedented in literature.

1a also shows CO_2 (195 K) uptake property and high H_2 uptake capacity at 77 K at 40 bar pressure.

4B.2 Experimental Section

4B.2.1 Materials

All the reagents employed were commercially available and used as provided without further purification. The $Zn(NO_3)_2 \cdot 6H_2O$ was obtained from Spectrochem, 1,4-naphthalenedicarboxylic acid was obtained from Sigma Aldrich chemicals. *N*,*N*′-dimethyl aniline was obtained from Spectrochem India.

4B.2.2 Physical Measurements

The elemental analysis was carried out using a Thermo Fischer Flash 2000 Elemental Analyzer. FT-IR spectra were recorded on a Bruker IFS 66v/S spectrophotometer using KBr pellets in the region 4000-400 cm^{-1}. Powder XRD pattern of the products were recorded by using Cu-K_α radiation (Bruker D8 Discover; 40 kV, 30 mA). Electronic absorption spectra were recorded on a Perkin Elmer Lambda 900 UV-VIS-NIR Spectrometer and emission spectra were recorded on Perkin Elmer Ls 55 Luminescence Spectrometer. UV-Vis and emission spectra were recorded in 1 mm path length cuvette. NMR spectra were obtained with a Bruker AVANCE 400 (400 MHz) Fourier transform NMR spectrometer with chemical shifts reported in parts per million (ppm).

4B.2.3 Synthesis of $\{[Zn_4(O)(H_2O)(1,4\text{-ndc})_{3.5}(H_2O)](C_8H_{12}N)(2DMF)\}_n$ (1)

0.l mmol (0.0293 g) of $Zn(NO_3)\cdot 6H_2O$ and 0.3 mmol (0.064 g) of 1,4-naphthalenedicarboxylic acid were dissolved in 5 mL of DMF and mixed for 15 min to get a homogeneous slurry. In this slurry 1 mL of water and 1 mL of *N*,*N*′-dimethylaniline (DMA) were added and again stirred for 15 min. This solution mixture was kept in 120 °C oven for 2 days to get colourless block shaped crystals of **1**. In open atmosphere crystals are highly unstable and show a colour change from colourless to fade green. Yield: 63%, relative to Zn^{2+}. Anal. Calcd. for $C_{56}H_{40}Zn_4N_3O_{17}$: C, 52.13; H, 3.18; N, 3.25. Found: C, 52.77; H, 3.09; N, 3.79. FT-IR (KBr pellet, 4000-400 cm^{-1}) (Figure 1): 1659(s), 1596(s), 1513(s), 1409(s), 1361(s), 1263(s), 1213(s), 1163(s), 1096(s), 798(s).

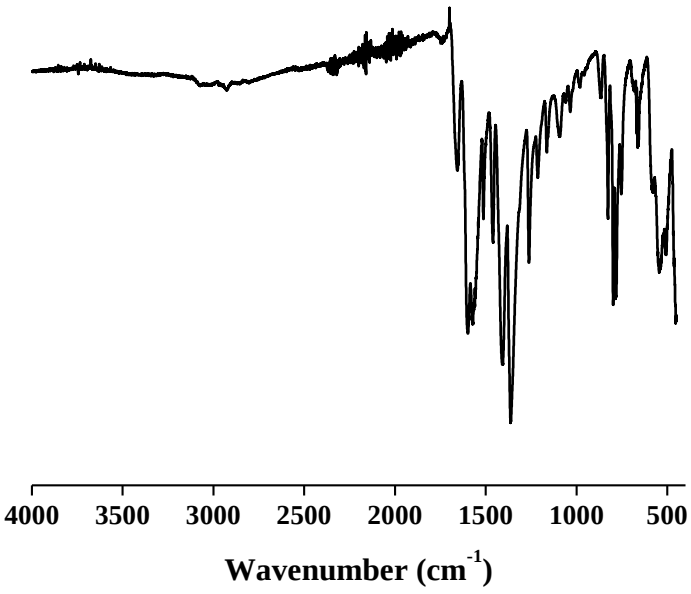

Figure 1: FT-IR spectrum of **1**.

4B.2.4 X-ray Crystallography

X-ray single crystal structural data of **1** was collected on a Bruker Smart-CCD diffractometer equipped with a normal focus, 2.4 kW sealed tube X-ray source with graphite monochromated Mo-*Kα* radiation (λ = 0.71073 Å) operating at 50 kV and 30 mA. The program SAINT[7] was used for integration of diffraction profiles and absorption correction was made with SADABS[8] program. All the structures were solved by SIR 92[9] and refined by full matrix least square method using SHELXL-97.[10] All the hydrogen atoms were geometrically defixed and placed in ideal positions. All crystallographic and structure refinement data of **1** is summarized in Table 1. Selected bond lengths and angles for **1** is given in Table 2. Due to weak diffraction and instability of the crystals we could not locate all the solvent molecules and few atoms of the 1,4-ndc linker. However, using ^{1}H-NMR we have shown presence of the guest molecules and the linker 1,4-ndc. All calculations were carried out using SHELXL 97,[10] PLATON,[11] SHELXS 97[12] and WinGX system, Ver 1.70.01.[13]

4B.2.5 Adsorption measurements

The adsorption isotherms of N_2 (77 K) and CO_2 (195 K) for compound **1a** were measured by using QUANTACHROME QUADRASORB *SI* analyzer. The adsorbent sample (~100–150 mg) was placed in the sample chamber (~17.5 mL) maintained at T = 473 K ± 0.03 K under vacuum for about 10 h prior to measurement of the isotherm. Helium gas at a

certain pressure was introduced in the gas chamber and allowed to diffuse into the sample chamber by opening the valve. The change in pressure allowed an accurate determination of the volume of the total gas phase. The amount of gas adsorbed was calculated readily from pressure difference ($P_{cal} - P_e$), where P_{cal} is the calculated pressure with no guest adsorption and P_e is the observed equilibrium pressure. High pressure H_2 adsorption measurement at 77 K was carried out on a fully computer controlled volumetric BELSORP-HP, BEL JAPAN high pressure instrument. H_2 gas used for the measurement is scientific/research grade with 99.999% purity. For the measurements, approximately 300 mg sample was taken in a stainless-steel sample holder and degassed at 473 K for a period of 10 h under vacuum. Dead volume of the sample cell was measured with He gas of 99.999% purity. Non-ideal correction for H_2 gas was made by applying virial coefficients at 77 K.

4B.3 Results and discussion

4B.3.1 Structural description of $\{[Zn_4(O)(H_2O)(ndc)_{3.5}(H_2O)](C_8H_{12}N)(2DMF)\}_n$ (1)

Compound **1** crystallizes in monoclinic $P2_1/n$ spacegroup. The asymmetric unit contains four Zn^{2+} (Zn1, Zn2, Zn3 and Zn4) centers, one water, three and half 1,4-ndc linkers, one $HDMA^+$ cation and two DMF guest molecules. The four Zn^{2+} centers remain in four corners of a tetrahedral anionic secondary building unit $\{Zn_4(O)(COO)_7(H_2O)\}^-$ (Figure 2); these metal ions are connected through bridging carboxylate groups from seven 1,4-ndc linkers. One O^{2-} (O100) remains at the center of the tetrahedron and is connected to all four Zn^{2+} centers. Among the four Zn^{2+}, Zn1 and Zn2 are four coordinated, Zn4 is pentacoordinated and Zn3 is octahedral (Figure 2). The Zn3 center contains one coordinated water (O1w) molecule. Such formed tetrahedral SBU is connected to all three directions by seven 1,4-ndc linkers. Among seven, six of the 1,4-ndc linkers connect the SBUs in *ac* plane to form a thick 2D layer (Figure 3a). This 2D layer is further connected by remaining 1,4-ndc linker along *b*-direction to form a 3D framework structure (Figure 3b). Interestingly the $HDMA^+$ cation remains in the confined 2D layer space and undergoes C-H$\cdots\pi$ interactions (3.786 and 3.623 Å) with the neighbouring 1,4-ndc linkers (Figure 3a). The 1,4-ndc linker connecting the 2D layers along *b*-axis does not have any close interaction with the cation.

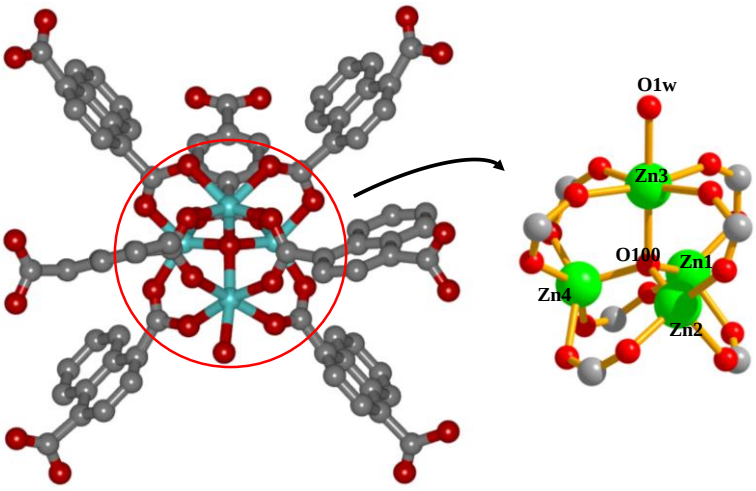

Figure 2: Coordination environment of Zn^{2+} in the tetrahedral SBU of compound **1**.

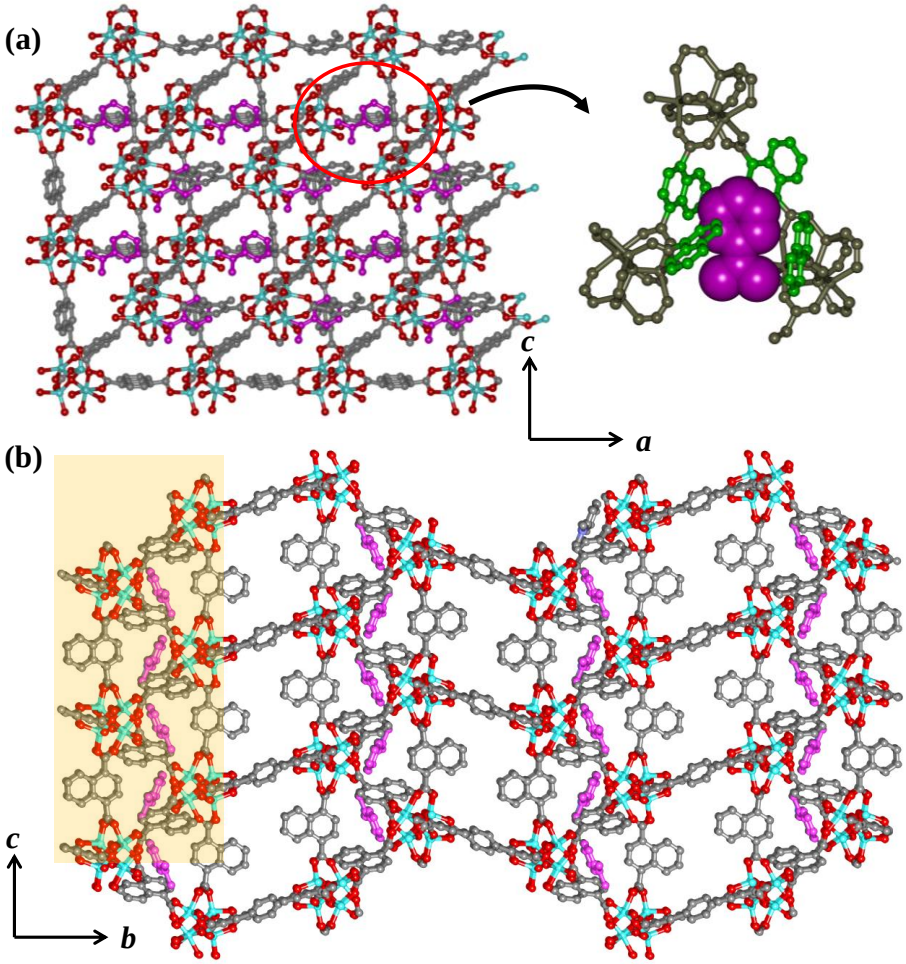

Figure 3: Structural details of compound **1**: (a) 2D sheet like structure in *ac* plane and position of $HDMA^+$ in the 2D layer; (b) View of the 3D structure along *a*-axis.

View along *a* and *c*-axes shows irregular dumbell shaped channels of dimensions 1.2×3.5 $Å^2$ which are occupied by guest DMF molecules (Figure 4).[14] Presence of solvent molecules is confirmed from ^{1}HNMR spectroscopy (Figure 5). The void space calculated using PLATON

was found to be 44% of total cell volume.[11] Topological analysis using TOPOS 4.0 suggests a 2,7-connected four nodal net with Schläfli symbol $\{8^{17}.12^{4}\}2\{8\}7$ (Figure 6).[15]

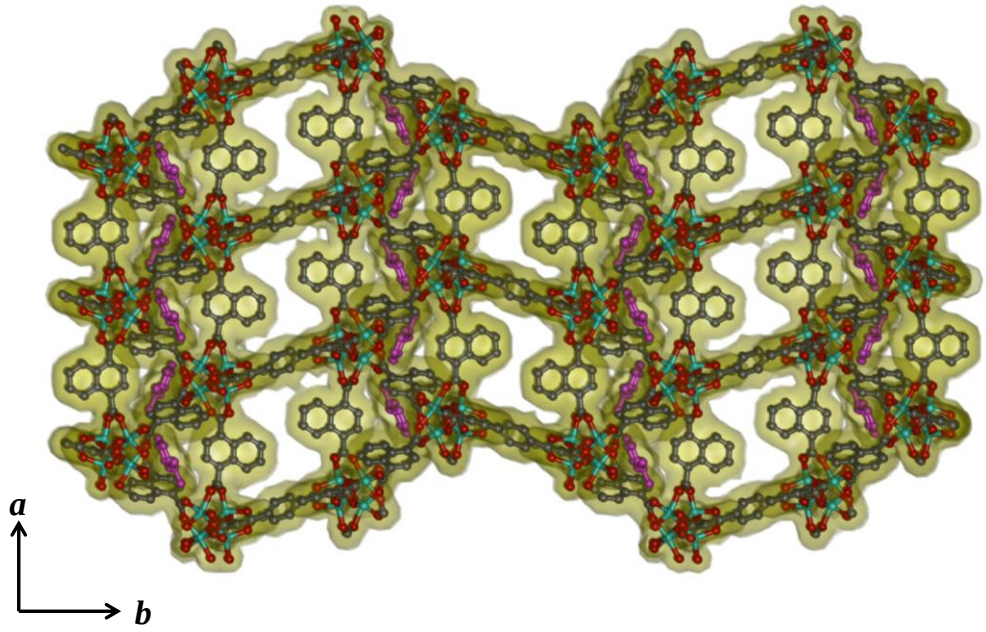

Figure 4: Van der Waals surface added view of the channels along *c*-axis in compound **1**.

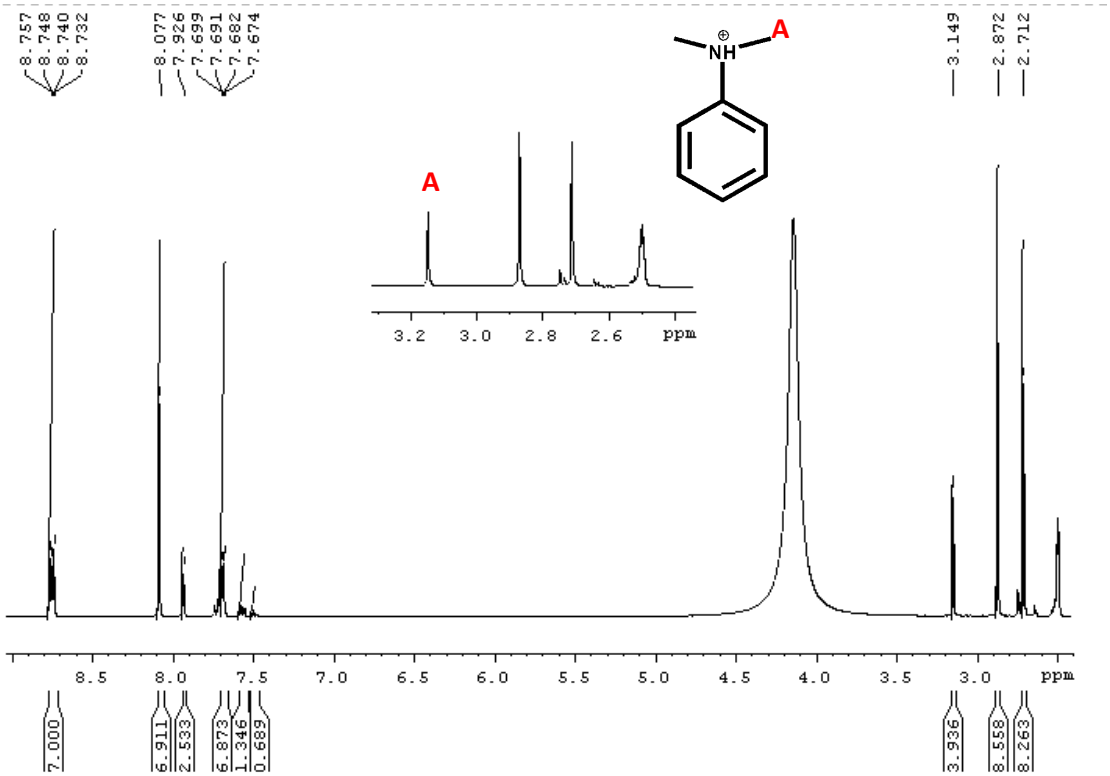

Figure 5: ^{1}H-NMR spectrum of compound **1** in d_6-DMSO.

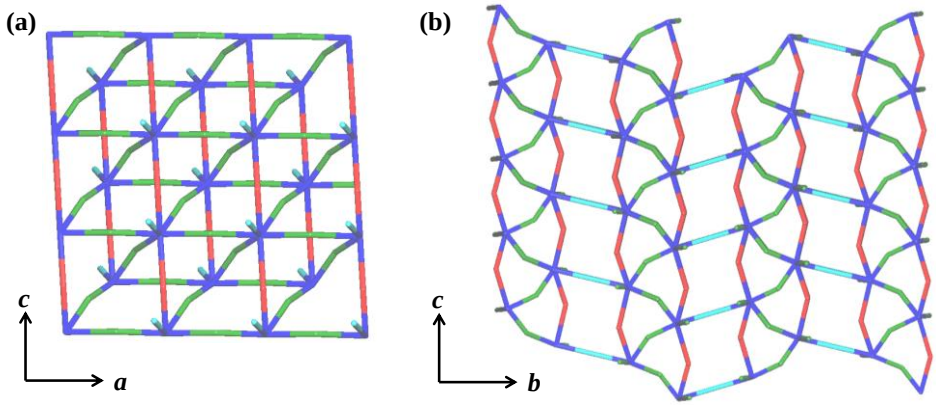

Figure 6: View of the (a) 2D and (b) 3D net topologies in compound **1**.

Table 1: Crystal data and structure refinement parameters of compound **1**.

Parameters	1
Empirical formula	$C_{56}H_{40}ZnN_3O_{17}$
M	1141.31
Cryst. system	Monoclinic
space group	$P2_1/n$ (No. 14)
***a* (Å)**	12.369(4)
***b* (Å)**	41.156(5)
***c* (Å)**	12.283(7)
***α* °**	90.0
***β* °**	93.94
***γ* °**	90.0
***V* (Å^3)**	6939.05(5)
Z	4
***T*(K)**	100
***λ* (Mo K$_α$)**	0.71073
***D*$_c$ (g cm^{-3})**	1.092
***μ* (mm^{-1})**	1.421
***θ*$_{max}$ (deg)**	23.9
total data	19589
unique reflection	6593

R_{int}	0.093
data [$I > 2\sigma(I)$]	2591
R^a	0.096
R_w^b	0.2362
GOF	1.19

^{a} $R = \Sigma||F_o| - |F_c||/\Sigma|F_o|$. ^{b} $R_w = [\Sigma\{w(F_o^2 - F_c^2)^2\}/\Sigma\{w(F_o^2)^2\}]^{1/2}$.

Table 2: Summary of crystal data and refinement results.

Zn1-O14	2.002(3)	Zn1-O100	1.917(3)
Zn1-O12_c	2.011(4)	Zn1-O4_d	1.961(4)
Zn2-O2	1.914(4)	Zn2-O10	1.993(4)
Zn2-O13	1.998(4)	Zn2-O100	1.935(3)
Zn3-O1W	2.088(4)	Zn3-O6	2.126(4)
Zn3-O3_d	2.126(4)	Zn3-O8_h	2.042(4)
Zn4-O1	2.077(4)	Zn4-O5	1.988(4)
Zn4-O100	1.887(3)	Zn4-O11_c	2.093(4)
Zn4-O7_h	1.990(4)		
O14-Zn1-O100	108.28(14)	O12_c-Zn1-O14	98.86(15)
O1-Zn4-O11_c	84.25(15)	O4_d-Zn1-O14	101.41(15)
O1-Zn4-O7_h	145.12(16)	O12_c -Zn1-O100	114.93(13)
O5-Zn4-O11_c	145.96(16)	O4_d-Zn1-O12_c	107.80(16)
O5-Zn4-O7_h	92.87(15)	O2-Zn2-O10	106.33(16)
O11_c-Zn4-O100	104.19(13)	O2-Zn2-O13	99.26(15)
O7_h-Zn4-O100	107.03(14)	O2-Zn2-O100	114.74(13)
O7_h-Zn4-O11_c	81.44(15)	O10-Zn2-O13	103.10(15)
O10-Zn2-O100	121.76(13)	O13-Zn2-O100	108.74(14)

c = x,y,1+z; d = 1+x,y,z; h = 1/2+x,1/2-y,1/2+z

4B.3.2 Thermal stability and porosity

TGA profile of **1** shows that till ~ 100 °C there is no loss of guest molecules (Figure 7a). In the temperature range 100-250 °C ~ 13 weight% loss is attributed to the guest DMF and coordinated water molecules. The desolvated framework (**1a**) remains stable till ~ 350 °C. The PXRD pattern of **1a** shows clear difference compared to that of as-synthesized **1** suggesting a structural rearrangement after desolvation (Figure 7b). Removal of coordinated

water molecule from the SBU might change the geometry of the SBU and hence the final structure also rearranges. Resolvation of **1a** using DMF shows similar PXRD pattern as that of **1** suggesting that structural change is reversible.

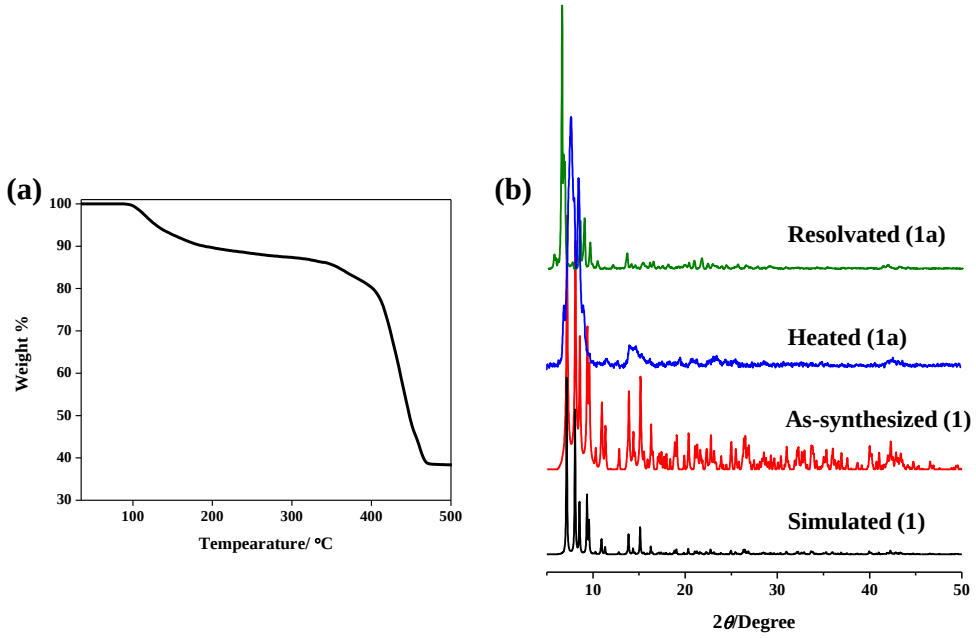

Figure 7: (a) TGA profile of compound **1** in the temperature range of 30-500 °C at heating rate of 3 °C/min under N_2 atmosphere; (b) PXRD patterns of **1** and different phases.

4B.3.3 Photophysical properties of 1: Electron transfer induced by structural change

The UV-vis spectrum of **1** shows a broad absorption band from 200 to 390 nm and a weak band in 500-600 nm range (Figure 8a). Absorption corresponding to π-π* or n-π* appears in the UV region of the spectrum (200-390 nm), but appearance of a small band in the visible region is due to ground state CT interaction between one of the 1,4-ndc (donor) and $HDMA^+$ (acceptor) cation. It is worth to mention that none of the 1,4-ndc linker is in face-to-face interaction with $HDMA^+$. Upon excitation at 330 nm **1** shows blue emission with emission maximum at 430 nm which is due to the 1,4-ndc linkers (Figure 8b). Here, the CT band is originated from the 2D layer of the framework in the *ac* plane while the 1,4-ndc connecting the 2D layers along *b*-axis is the source of blue emission. Presence of such ground state CT and emission in the same matrix is unusual but is present in this case due to unique structural features of **1**. Surprisingly, upon desolvation the **1a** becomes dark green in colour indicating some strong ground state interaction between the 1,4-ndc (donor) and $HDMA^+$ (acceptor) cation (Inset, Figure 9a). The UV-vis spectrum shows broad absorption band from

200 to 390 nm and in addition to that two clear peaks in the visible region of the spectrum at 460 and 610 nm (Figure 9a). To confirm the extent of charge separation EPR measurement of **1a** was carried out which clearly indicates presence of radical ion (Figure 9c). Hence the two distinct peaks in the visible spectrum are due to the radical ion pairs generated upon desolvation. As mentioned before, desolvation brings structural change and hence the electron transfer process becomes feasible in the 2D layer of the framework. Possibly one of the 1,4-ndc comes in a suitable position for electron transfer to occur from 1,4-ndc to $HDMA^{+}$. While the 1,4-ndc linker connecting the 2D layers remain unaffected as blue emission from **1a** state can be seen, similar to that of **1** (Figure 9b).

To check the reversibility of the process I have exposed **1a** in DMF vapour and within few hours the green colour slowly changes to colourless and the absorption spectrum clearly shows diminishing radical ion peaks in the visible region of the spectrum (Figure 9a). The EPR spectrum shows no peak indicating absence of electron transfer process in the resolvated phase. This can be correlated with the PXRD patterns as resolvation reverts back the **1a** structure to a phase similar to as-synthesized **1**. Hence, this electron transfer process is mediated by structural rearrangement and reversible in nature (Scheme 1). It must be noted that the radical ion pair generated is stable at room temperature and does not reverts back unless solvation process changes the structure to as-synthesized phase.

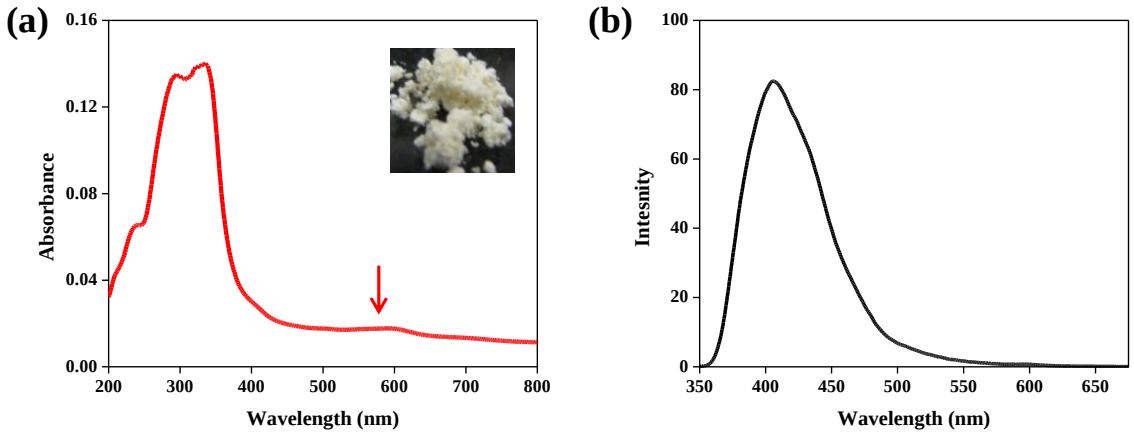

Figure 8: (a) Absorption spectrum of 1; inset shows compound colour in daylight; (b) Emission spectrum of 1 upon excitation at 330 nm.

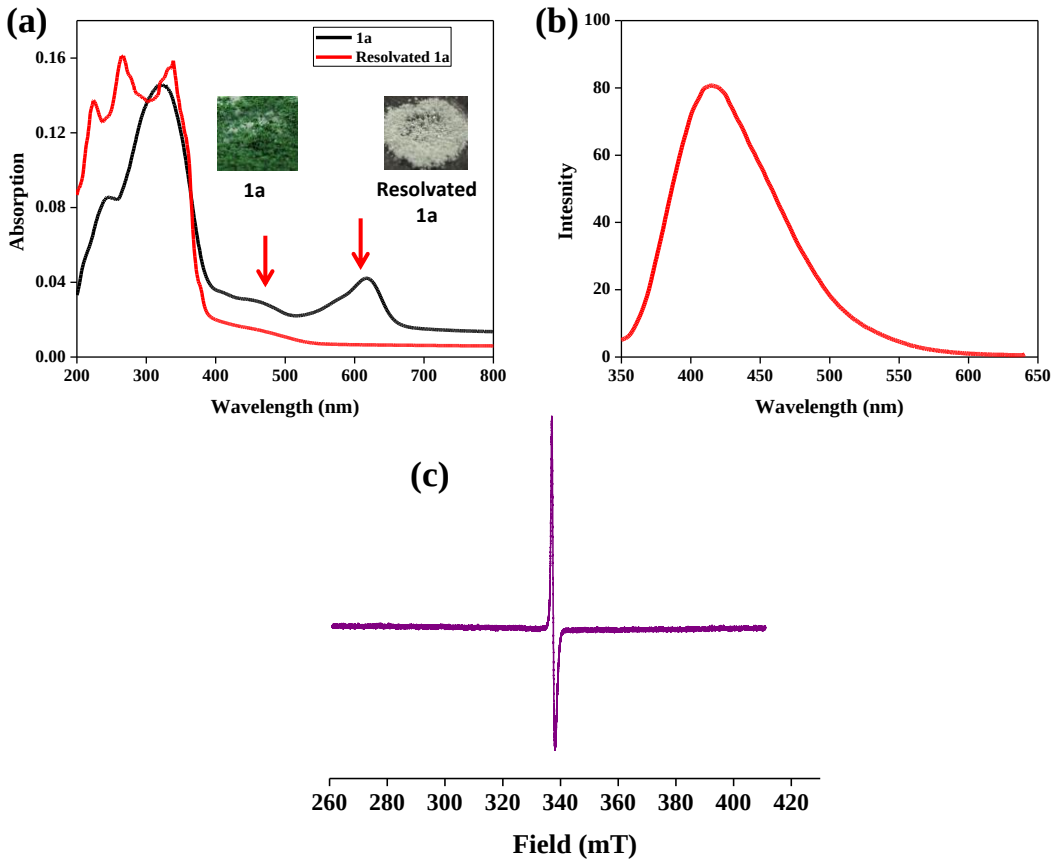

Figure 9b: (a) Absorption spectra of **1a** and resolvated **1a**, Inset shows the photographs of **1a** and resolvated **1a** in daylight; (b) Emission spectrum of **1a** upon excitation at 330 nm; (c) EPR spectrum of **1a** at RT.

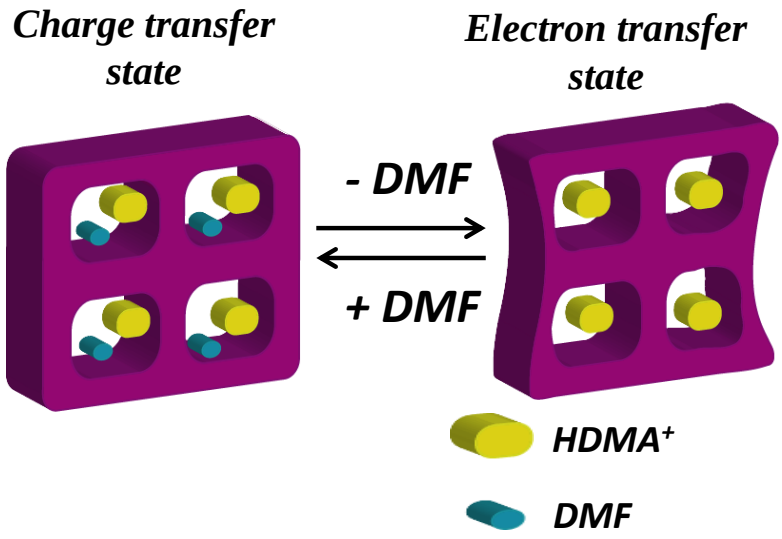

Scheme 1: Schematic of structural transformation induced reversible electron transfer in compound **1**.

4B.3.4 Adsorption properties of 1a

To establish the permanent porosity of compound **2a** N_2 and CO_2 adsorption isotherms were measured at 77 and 195 K, respectively. **1a** does not show any uptake of N_2 due to smaller pore size which is not sufficient for N_2 (Kinetic diameter ~ 3.64 Å) diffusion (Figure 10a). But it shows type-I uptake profile for CO_2 at 195 K with final uptake amount of ~ 77 mL/g (~ 15.1 wt%) and uptake does not saturate in 1 atm pressure range (Figure 10b). This selectivity for CO_2 over N_2 is due to smaller kinetic diameter of CO_2 (3.3 Å) and also specific interaction between CO_2 and aromatic π clouds of the pore the surface. Such sort of CO_2 selectivity is reported in the literature. At 77 K, compound **1a** showed an appreciable uptake amount of 1.48 wt% of H_2 at 40 bar pressure. Initial uptake of H_2 is steep and within 25 bar pressure uptake saturates. The micropores present in **1a** along *a* and *c*-axes are potential attributes for such high H_2 uptake capacity.

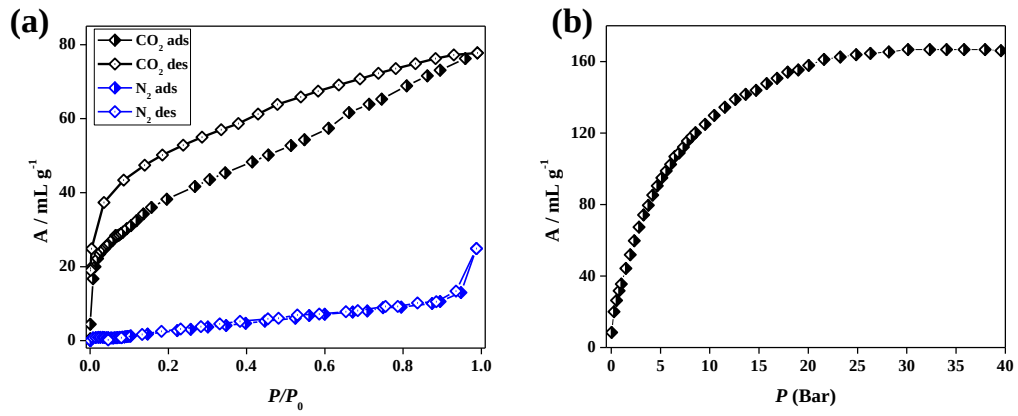

Figure 10: (a) CO_2 and N_2 adsorption isotherms of compound **1a** at 195 and 77 K; (b) H_2 adsorption profile at 77 K at 40 bar pressure for **1a**.

4B.4 Conclusions

In conclusion, this chapter shows synthesis of an anionic framework $\{[Zn_4(O)(H_2O)(1,4\text{-ndc})_{3.5}(H_2O)](C_8H_{12}N)(2DMF)\}_n$ (**1**) which contains a tetrahedral SBU and extended in three dimension to form 3D porous structure. The 2D channels are filled with guest DMF molecules and one $HDMA^+$ cation resides in the framework void to satisfy the charge balance of the framework. As-synthesized framework shows weak CT interaction between 1,4-ndc and $HDMA^+$, whereas upon desolvation electron transfer occurs from 1,4-ndc to $HDMA^+$. Such process is reversible upon resolvation and completely driven by structural change. Generation of radical ion pairs in a reversible fashion in PCPs are unprecedented and can pave the way to fabricate advance redox active or photochromic

materials for applications in solar cell or light harvesting. The desolvated framework also shows CO_2 uptake at 195 K and high H_2 uptake capacity at 77 K at 40 bar pressure.

4B.5 References

1. N. Kishi, M. Akita, M. Yoshizawa, *Angew. Chem. Int. Ed.* **2014**, *53*, 3604.

2. a) M. Irie, T. Fukaminato, T. Sasaki, N. Tamai, T. Kawai, *Nature.* **2002**, *420*, 759; b) P. H. M. Lee, C. C. Ko, N. Zhu, V. W. W. Yam, *J. Am. Chem. Soc.* **2007**, *129*, 6058; c) Q. L. Zhu, T. L. Sheng, R. B. Fu, S. M. Hu, L. Chen, C. J. Shen, X. Ma, X. T. Wu, *Chem. Eur. J.* **2011**, *17*, 3358.

3. a) D. Y. Lee, C. Y. Shin, S. J. Yoon, H. Y. Lee, W. Lee, N. K. Shrestha, J. K. Lee, S.-H. Han. *Sci. Rep*. **2014**, ***4***, 3930; b) D. Y. Lee, D. V. Shinde, S. J. Yoon, K. N. Cho, W. Lee, N. K. Shrestha, S.-H. Han. *J. Phys. Chem. C.* **2014**, *118*, 16328.

4. Thematic issue on Phtochromism: Memories and switches: *Chem. Rev*. **2010**, *100*, 6-1890.

5. a) S. Kitagawa, R. Kitaura, S. Noro, *Angew. Chem., Int. Ed.* **2004**, *43*, 2334; b) C. Janiak, *Dalton Trans.* **2003**, 2781; c) T. K. Maji, S. Kitagawa, *Pure App. Chem.* **2007**, *79*, 2155; d) G. Férey, *Chem. Soc. Rev.* **2008**, *37*, 191; e) J. C. Tan, A. K. Cheetham, *Chem. Soc. Rev.* **2011**, *40*, 1059; f) K.-L. Zhang, H.-Y. Gao, N. Qiao, F. Zhou, G.-W. Diao, *Inorg. Chim. Acta*. **2008**, *361*, 153; g) M. K. Bhunia, S. K. Das, M. M. Seikh, K. V. Domasevitch, A. Bhaumik, *Polyhedron*. **2011**, *30*, 2218; h) Y.-N. Zhang, Y.-Y. Wang, L. Hou, P. Liu, J.-Q. Liu, Q.-Z. Shi, *CrystEngComm*. **2010**, *12*, 3840.

6. a) L. Han, L. Qin, L. Xu, Y. Zhou, J. Sunb, X. Zou, *Chem. Commun.* **2013**, *49*, 406; b) Y.Takashima1, V. M. Martínez, S. Furukawa, M. Kondo, S. Shimomura , H. Uehara , M. Nakahama , K. Sugimoto, S. Kitagawa, *Nat. Commun*. **2011**, *2*, 168; c) S. V. Bhosale, C. H. Jani, S. J. Langford, *Chem. Soc. Rev.* **2008**, *37*, 331; d) B. Q. Ma, K. L. Mulfort, J. T. Hupp, *Inorg. Chem.* **2005**, 44, 4912.

7. SMART (V 5.628), SAINT (V 6.45a), XPREP, SHELXTL; Bruker AXS Inc. Madison, Wisconsin, USA, **2004**.

8. G. M. Sheldrick, Siemens Area Detector Absorption Correction Program, University of Götingen, Götingen, Germany, **1994**.

9. A. Altomare, G. Cascarano, C. Giacovazzo, A. Gualaradi, *J. Appl. Cryst*. **1993**, *26*, 343.

10. G. M. Sheldrick, SHELXL-97, Program for Crystal Structure Solution and Refinement; University of Götingen, Götingen, Germany, **1997**.

11. A. L. Spek, *J. Appl. Cryst*. **2003**, *36*, 7.

12. G. M. Sheldrick, SHELXS 97, Program for the Solution of Crystal Structure, University Götingen, Germany, **1997**.

13. L. J. Farrugia, WinGX-A Windows Program for Crystal Structure Analysis, *J. Appl. Cryst.* **1999**, *32*, 837.

14. The sizes of the channels were calculated considering the van der Waals radii of the atoms.

15. V. A. Blatov, A. P. Shevchenko, V. N. Serezhkin, *J. Appl. Crystallogr.* **2000**, *33*, 1193.

Chapter 5

Rigid and flexible porous coordination polymers for selective CO_2 adsorption

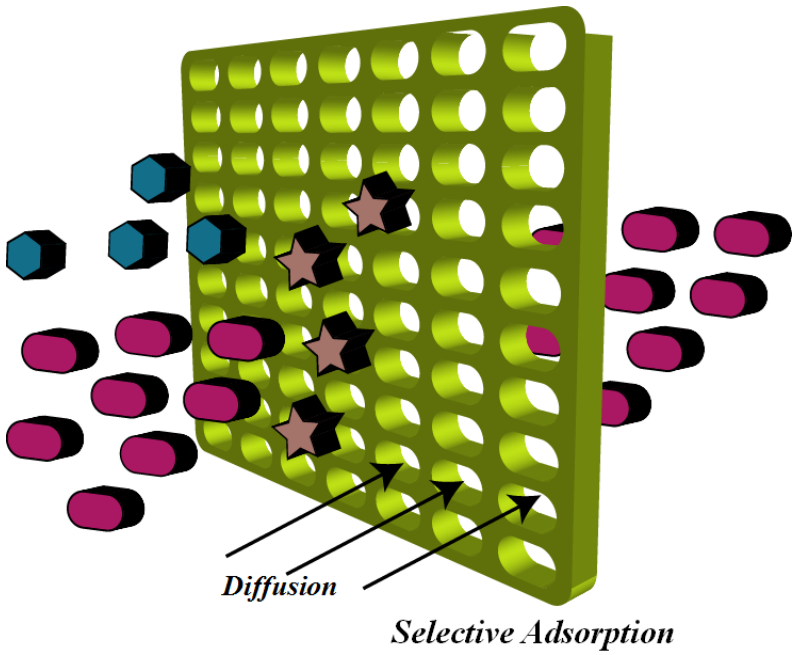

Part: 5A

Selective carbon dioxide uptake and crystal-to-crystal transformation: Porous 3D framework to 1D chain triggered by conformational change of the spacer

Summary

In this chapter, α-Polonium type 3D porous frameworks, $\{[M(bpe)_2(N(CN)_2)](N(CN)_2)(xH_2O)\}_n$, (M = Zn^{2+} (x = 5) (**1**) / Co^{2+} (x = 4) (**2**)) **(**bpe = 1,2-bis(4-pyridyl)ethane, $N(CN)_2^-$ = dicyanamide anion) composed of mixed ligand system have been synthesized and structurally characterized. Upon two–fold interpenetration both 3D frameworks (**1** and **2**) show bimodal channel structure; small channel contains non-coordinated $N(CN)_2^-$ anions and the bigger channels occupied by guest water molecules. High framework stability for both compounds was realized by similarity in PXRD pattern in dehydrated state and even in reversible single-crystal-to-single-crystal transformation for framework **1**. Both the PCPs display unprecedented structural transformation from 3D framework to 1D $\{[M(bpe)(N(CN)_2)_2]\}_n$ (M= Zn^{2+} (**1b**) / Co^{2+} (**2b**)) coordination chain upon removal of one molecule of bpe and concomitant bridging of non-coordinated $N(CN)_2^-$ and conformational change (*anti* to *gauche*) by another bridging bpe linker. Moreover, the dehydrated solid $\{[Co(bpe)_2(N(CN)_2)]N(CN)_2\}_n$,(**2a**) exhibits highly selective CO_2 uptake characteristic among the number of adsorbates (H_2, N_2, O_2 and Ar) at 195 K.

1. R. Haldar, T. K. Maji, ***CrystEnggComm***. **2012**, *14*, 684.

5A.1 Introduction

Porous coordination polymers (PCPs) are a new class of solid state material featuring regular and designable channel structure with permanent porosity composed of flexible coordination bonds.[1] The last couple of decades have witnessed enormous growth in the field of PCPs and many interesting properties and applications have been unveiled including gas storage and separation,[2] heterogeneous catalysis,[3] ion exchange[4] and drug delivery.[5] Apart from these critical applications single-crystal-to-single-crystal transformation[6] and solid state structural conversion is one of the key observation in flexible PCPs induced by external stimuli, e.g., light, heat, pressure, guest etc.[7] Much effort has been devoted for preparing environmentally responsive materials and varieties of crystal-to-crystal transformations like 0D→1D/2D, 1D→2D, 2D→3D have been documented.[8] These type of structural transformations are associated with the cleavage and generation of new coordination bonds and the corresponding change in dimensionality is realized by the subtle change in porosity, optical and magnetic properties.[9] But crystal-to-crystal transformations like 3D→2D, 3D→1D or 2D→1D are yet to be realized in PCPs.

The recognition and selective adsorption of gas molecules by PCPs are of paramount importance in particular environmental and industrial fields. The rapid growth of the atmospheric carbon dioxide (CO_2) level, mainly from the emission of fossil fuel based power plants demands an urgent strategy that can selectively sequester and store the greenhouse gas CO_2. The current conventional techniques for flue gas sequestrations, like amine absorbers and cryogenic coolers are not a permanent solution for a long run due to low efficacy and economic drawbacks.[10] In this context PCPs are being studied to address these challenges because it is possible to design a framework which can selectively recognize specific molecule by various host-guest interactions resulting in selective adsorption characteristic.[11] Already, few examples of PCPs with selective CO_2 uptake have been reported by tuning the pore size and introducing the specific functionality in the organic spacer which interact effectively with the CO_2 molecule.[12]

This chapter describes synthesis, structural characterization and crystal-to-crystal transformation of two isostructural two–fold interpenetrated α-polonium type 3D porous PCPs, $\{[M(bpe)_2(N(CN)_2)](N(CN)_2(xH_2O)\}_n$ (M= Zn^{2+} (x= 5) (**1**) / Co^{2+} (x = 4) (**2**)) (bpe = 1,2-bis(4-pyridyl)ethane, $N(CN)_2^-$= dicyanamide), which are isostructural to earlier reported $\{[Ni(bpe)_2(N(CN)_2)](N(CN)_2(6H_2O)\}_n$.[13] Both the frameworks exhibit

unprecedented 3D→1D structural transformation by release of one bpe and concomitant conformational change from *anti* to *gauche* by another bpe linker and coordination by free $N(CN)_2^-$ anion triggered by temperature. Dehydrated compound **2** (**2a**) shows excellent selective CO_2 gas uptake among other gases (N_2, H_2, O_2 and Ar) at 195 K.

5A.2 Experimental Section

5A.2.1 Materials

All the reagents employed were commercially available and used as provided without further purification. All the metal salts were obtained from Spectrochem, 1,2-bis(4-pyridyl)ethane and sodium dicyanamide were obtained from Sigma Aldrich chemicals.

5A.2.2 Physical Measurements

Elemental analyses were carried out using a Thermo Fischer Flash 2000 Elemental Analyzer. IR spectra were recorded on a Bruker IFS 66v/S spectrophotometer using KBr pellets in the region 4000-400 cm^{-1}. Thermogravimetric analysis (TGA) was carried out (Metler Toledo) in nitrogen atmosphere (flow rate = 50 ml min^{-1}) in the temperature range 30–500 °C (heating rate = 3°C min^{-1}). Powder XRD pattern of the products were recorded by using Cu-K_α radiation (Bruker D8 Discover; 40 kV, 30 mA). The pattern was agreed with those calculated from single crystal structure determination.

5A.2.3 Synthesis of $\{[M(bpe)_2(N(CN)_2)](N(CN)_2)(xH_2O)\}_n$ (M= Zn^{2+} (*x*= 5) (1) / Co^{2+} (*x*= 4) (2))

An aqueous solution (25 mL) of $NaN(CN)_2$ (1mmol, 0.089 g) was mixed with an ethanolic solution (25 mL) of bpe (1mmol, 0.184 g) and stirred for 30 min to mix well. $Zn(NO_3)_2{\cdot}6H_2O$ (0.5 mmol, 0.146 g) (for compound **2**, $Co(NO_3)_2{\cdot}6H_2O$) was dissolved in 50 mL of water and added to the ligand solution dropwise. White (for **1**) and orange (for **2**) powder sample was isolated after 1-2 days of continuous stirring. Just by keeping the filtrate solution in room temperature for 4-5 days beautiful colorless (for **1**) and orange colored (for **2**) block shaped crystals were obtained. Crystals were separated, washed with water and dried. Good quality single crystals were picked up from the mother liquor and immediately covered with paraffin oil and crystal data was collected at 293 K. Compound **1**: Yield: 68%, relative to Zn. FT-IR (KBr pellet, 4000-400 cm^{-1}): 3492(b), 3234(w),

3070(w), 2330(s), 2232(m), 2126(m), 1610(s), 1568(s), 1502(s), 1424(s), 1311(w), 1223(s), 1065(s), 1021(s), 910(w), 872(w), 829(s). Anal. Calcd. for $C_{28}H_{34}ZnN_{10}O_5$: C, 51.26; H, 5.19; N, 21.35. Found: C, 52.11; H, 5.17; N, 21.01. Compound **2**: Yield: 70%, relative to Co. FT-IR (KBr pellet, 4000-400 cm^{-1}: 3490(b), 3234(w), 3072(w), 2326(s), 2238(m), 2128(m), 1614(s), 1562(s), 1502(s), 1428(s), 1310(w), 1228(s), 1068(s), 1020(s), 912(w), 874(w), 820(s). Anal. Calcd. for $C_{28}H_{32}CoN_{10}O_4$: C, 53.24; H, 5.07; N, 22.18. Found: C, 52.91; H, 5.03; N, 21.79.

5A.2.4 Preparation of $\{[Zn(bpe)_2(N(CN)_2)](N(CN)_2(H_2O)\}_n$ (1′) and $[Zn(bpe)_2(N(CN)_2)](N(CN)_2(5H_2O)\}_n$ (1′′)

Few good quality single crystals of compound **1** were kept in a quartz sample cell and heated at 70 °C under dynamic vacuum (10^{-1} pa) for 12 h. A good quality single crystal was separated and immediately covered with paraffin oil and crystal data was collected. The same dehydrated crystal **(1′)** was again exposed to water vapour for 1-2 days to get **1′′** and crystal data was collected at 293 K.

5A.2.5 Synthesis of $\{M(bpe)(N(CN)_2)_2\}_n$ (M= Zn^{2+} (1b) / Co^{2+} (2b)) from $\{[M(bpe)_2(N(CN)_2)](N(CN)_2)(xH_2O)\}_n$ (M= Zn^{2+} (x= 5) (1) / Co^{2+} (x = 4) (2))

As-synthesized compound **1** (or **2**) (about 0.15 g) was heated in a glass tube at 200 °C under dynamic vacuum (10^{-1} pa) for about 6 hours. The white to light brown for **1** and orange to red for **2** color change was observed. The heated compounds were characterized by the elemental analyses, IR and powder X-ray diffraction study. Compound **1b**: FT-IR (KBr pellet, 4000-400 cm^{-1}): 3232(w), 3067(w), 2296(s), 2247(s), 2181(s), 1610(s), 1560(s), 1500(s), 1429(s), 1347(s), 1215(s), 1071(s), 1021(s), 928(m), 810 (s). Anal. Calcd. for $C_{16}H_{12}ZnN_8$: C, 50.39; H, 3.14; N, 29.39. Found: C, 50.82; H, 3.54; N, 29.75. Compound **2b:** FT-IR (KBr pellet, 4000-400 cm^{-1}): 3237(w), 3057(w), 2298(s), 2240(s), 2180(s), 1616(s), 1561(s), 1503(s), 1423(s), 1349(s), 1216(s), 1074(s), 1024(s), 928(m), 807(s). Anal. Calcd. for $C_{16}H_{12}CoN_8$: C, 51.16; H, 3.31; N, 29.84. Found: C, 51.51; H, 3.39; N, 29.09.

5A.2.6 X-ray Crystallography

X-ray single crystal structural data of **1**, **1′, 1″** and **2** were collected on a Bruker Smart-CCD diffractometer equipped with a normal focus, 2.4 kW sealed tube X-ray source with graphite monochromated Mo-*Kα* radiation (λ = 0.71073 Å) operating at 50 kV and 30 mA. The program SAINT[14] was used for integration of diffraction profiles and absorption correction was made with SADABS[15] program. All the structures were solved by SIR 92[16] and refined by full matrix least square method using SHELXL-97.[17] In compound **1** the nitrogen atom (N5) of guest $N(CN)_2^-$ are in positional disorder and have been resolved in terms of their occupancy. In compound **1'** and **1''** N4 and N5 and, for compound **2** N2 and N6 atoms of bridging and guest $N(CN)_2^-$ are in positional disorder respectively and has been resolved in terms of their occupancy. All the hydrogen atoms were geometrically defixed and placed in ideal positions. Potential solvent accessible area or void space was calculated using the PLATON multipurpose crystallographic software.[18] All crystallographic and structure refinement data of **1**, **1′, 1″** and **2** are summarized in Table 1. Selected bond lengths and angles for **1**, **1′, 1″** and **2** are given in Table 2-5 respectively. All calculations were carried out using SHELXL 97,[17] PLATON,[18] SHELXS 97[19] and WinGX system, Ver 1.70.01.[20]

5A.2.7 Adsorption Study

The adsorption isotherm of CO_2, H_2, N_2, Ar and O_2 (195 K) using the dehydrated sample of **2** were measured by using QUANTACHROME QUADRASORB-*SI* analyzer. In the sample tube the adsorbent sample **2** (~100-150 mg) was placed which had been prepared at 348 K under a 1×10^{-1} Pa vacuum for about 6 h prior to measurement of the isotherms. Helium gas (99.999% purity) at a certain pressure was introduced in the gas chamber and allowed to diffuse into the sample chamber by opening the valve. The amount of gas adsorbed was calculated readily from pressure difference (P_{cal} - P_e), where P_{cal} is the calculated pressure with no gas adsorption and P_e is the observed equilibrium pressure. All operations were computer-controlled and automatic.

The adsorption of different solvents like MeOH at 293K and H_2O, EtOH at 298 K were measured in the dehydrated sample of **2** in the gaseous state by using BELSORP-aqua-3 analyzer. The sample of about ~100–150 mg was prepared by heating at 348 K for about 10 hours under vacuum (1×10^{-1} Pa) prior to measurement of the isotherms. The different solvent molecules used to generate the vapor were degassed fully by repeated

evacuation. Dead volume was measured with helium gas. The adsorbate was placed into the sample tube, then the change of the pressure was monitored and the degree of adsorption was determined by the decrease in pressure at the equilibrium state. All operations were computer controlled and automatic.

5A.3 Results and discussion

5A.3.1 Structural description of $\{[M(bpe)_2(N(CN)_2)](N(CN)_2)(xH_2O)\}_n$ (M= Zn^{2+} (*x*= 5) (1) / Co^{2+} (*x*= 4) (2))

Compound **1** and **2** both crystallize in monoclinic *C*2/*c* space group (Table 1) and structure determination by X-ray crystallography reveals a 3D *α*-Po type coordination framework of M^{2+} (M= Zn^{2+} (**1**) / Co^{2+} (**2**)) bridged by the bpe and $N(CN)_2^-$ linkers and is found to be isostructural with Ni^{2+} analogue.[13] Each slightly distorted octahedral M^{2+}

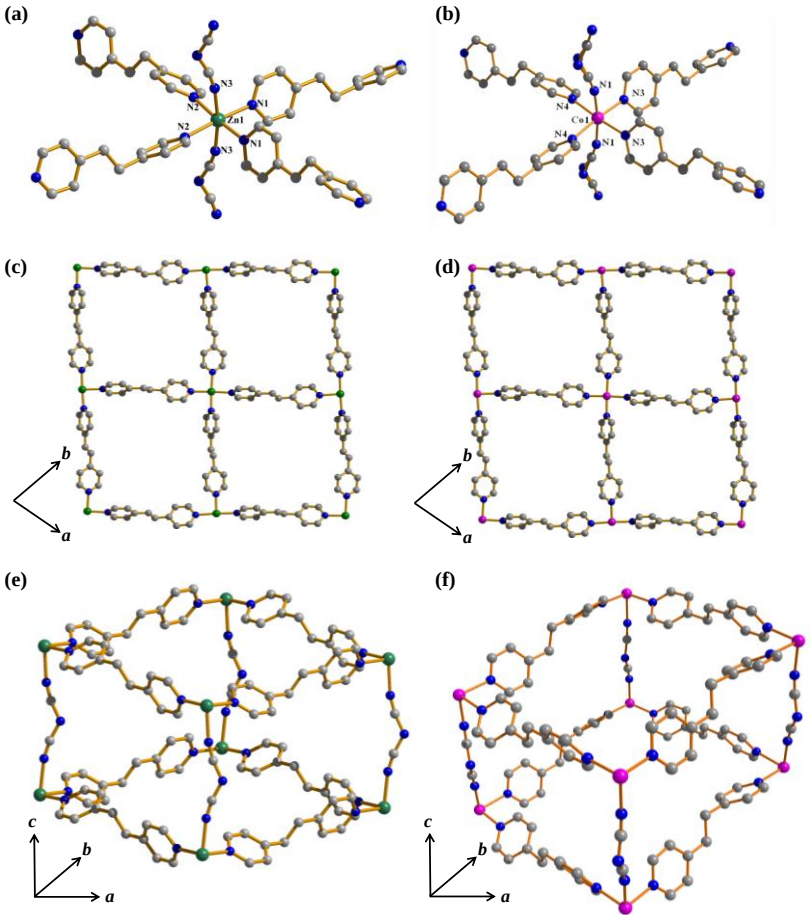

Figure 1: Structural details of **1** and **2**: View of the coordination environment of (a) Zn^{2+} in **1** and (b) Co^{2+} in **2**; (c) 2D sheet of $\{Zn(bpe)_2\}^{2+}$ along crystallographic *ab* plane; (d) 2D sheet of $\{Co(bpe)_2\}^{2+}$ along crystallographic *ab* plane, *α*-Po type 3D building unit of (e) Compound **1** and (f) **2**.

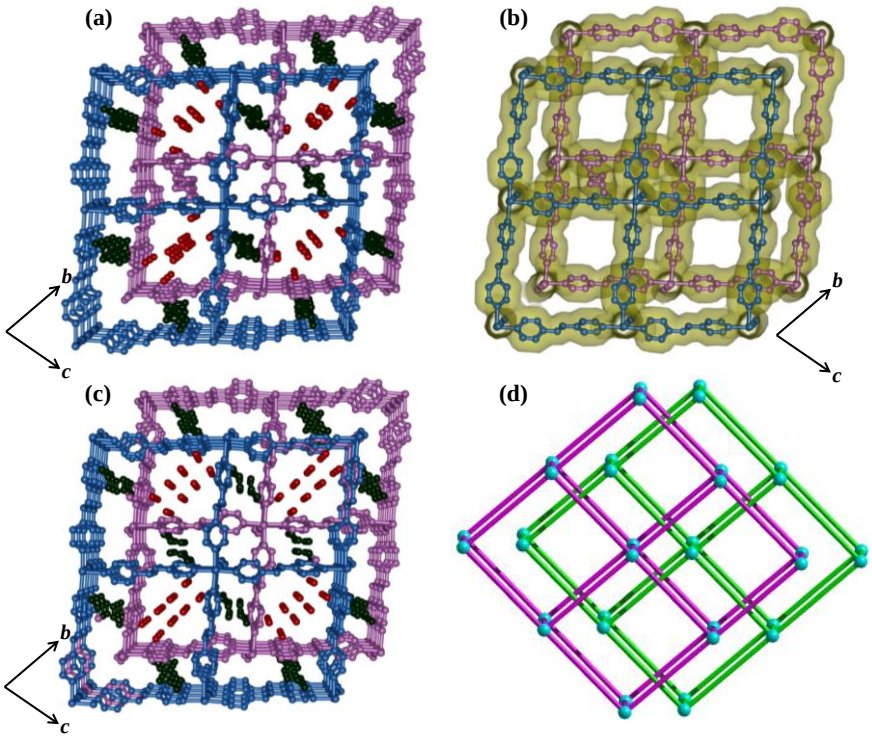

Figure 2: Structural details of **1** and **2**: (a) Perspective view of 3D framework of **1** along *c*-axis showing two fold interpenetrated bimodal channel structure; (b) Van der Walls surface added view of **1** along *c*-axis; (c) Perspective view of 3D framework of **2** along *c*-axis showing two fold interpenetrated bimodal channel structure; (d) α-Polonium type topology of **1** and **2**.

center ligated with four nitrogen atoms from four bpe and two nitrogen atoms of two $N(CN)_2^-$ linkers (Figure 1a-b) and the Zn^{2+}-N bond lengths are in the range of 2.155(5) Å-2.212(5) Å (Table 2). Similarly, for compound **2**, Co^{2+}-N bond lengths are in the range 2.113(3) Å-2.189(2) Å (Table 3). The four bpe linkers linked to M^{2+} center forms a 2D sheet of $\{M(bpe)_2\}^{2+}$ along crystallographic *ab* plane which is pillared by $N(CN)_2^-$ resulting in a α-polonium type 3D framework (Figure 1c-f). The 3D framework undergoes two-fold interpenetration ensuing two distinct channels; hexagonal channel having dimension of 5.5 × 4.5 $Å^2$ (6 × 4.5 $Å^2$ for compound **2**)[21] houses guest water molecules and the rectangular one with dimension of 2.0 × 0.5 $Å^2$ (2.5 × 0.5 $Å^2$, for compound **2**) shelters $N(CN)_2^-$ anions (Figure 2a-2d). The conformationally flexible bpe remains in *anti* conformation with a dihedral angle of 176.37° **(**178.14° for compound **2**) along ethane C-C bond. The Zn^{2+}–Zn^{2+} separation along the $N(CN)_2^-$ and bpe are 8.773 Å and 13.669 Å, respectively (8.709 Å & 13.630 Å respectively, for compound **2**). The effective solvent accessible void space was calculated using the PLATON[21] and it shows 20.9% (for **1**) and 21.1 % void space (for **2**) to the total crystal volume.

Table 1: Crystal data and structure refinement parameters of compound **1**, **1′**, **1′′** and **2**.

Parameters	**1**	**1′**	**1′′**	**2**
Empirical formula	$C_{28}H_{34}ZnN_{10}O_5$	$C_{28}H_{26}ZnN_{10}O$	$C_{28}H_{34}ZnN_{10}O_5$	$C_{28}H_{32}CoN_{10}O_4$
M	655.96	583.96	655.96	631.50
Cryst. system	Monoclinic	Monoclinic	Monoclinic	Monoclinic
space group	*C2/c*	*C2/c*	*C2/c*	*C2/c*
***a* (Å)**	18.5219(3)	18.7806(5)	18.5462(9)	18.5114(7)
***b* (Å)**	20. 0552(3)	19.9045(5)	20.0824(10)	20.0115(8)
***c* (Å)**	8.7707(1)	8.7871(2)	8.7759(5)	8.7093(3)
***β* (deg)**	100.993(1)	100.981(1)	101.244(3)	100.555(2)
***V* (Å^3)**	3198.19(8)	3224.64(14)	3205.9(3)	3171(2)
Z	4	4	4	4
***T*(K)**	293	150	283	293
***λ* (Mo K_α)**	0.71073	0.71073	0.71073	0.71073
***D*$_c$ (g cm^{-3})**	1.342	1.199	1.338	1.306
***μ* (mm^{-1})**	0.820	0.797	0.818	0.589
***θ*$_{max}$ (deg)**	25.5	26.4	27.5	32.1
total data	18296	19272	17049	23902
unique reflection	2979	3285	3683	1950
***R*$_{int}$**	0.040	0.039	0.090	0.051
data [*I* > 2σ(*I*)]	2583	2644	2444	4115
***R*^{a}**	0.0587	0.0815	0.0809	0.0669
***R*$_w^b$**	0.1836	0.2764	0.2649	0.2256
GOF	1.11	1.15	1.07	1.07

^{a} $R = \Sigma||F_o| - |F_c||/\Sigma|F_o|$. ^{b} $R_w = [\Sigma\{w(F_o^2 - F_c^2)^2\}/\Sigma\{w(F_o^2)^2\}]^{1/2}$.

Table 2: Selected bond lengths (Å) and angles (°) for $\{[Zn(bpe)_2(N(CN)_2)](N(CN)_2)(5H_2O)\}_n$ **(1)**.

Zn1-N1	2.162(3)	Zn1-N3	2.153(3)
Zn1 -N1_b	2.162(3)	Zn1-N3_b	2.153(3)
Zn1-N2_c	2.213(3)	Zn1-N2_e	2.213(3)
N1-Zn1-N3	91.95(13)	N1-Zn1-N1_b	86.38(11)
N1-Zn1-N3_b	94.23(13)	N1-Zn1-N2_c	176.04(12)
N1-Zn1-N2_e	90.11(12)	N1_b-Zn1-N3	94.23(13)
N3-Zn1-N3_b	171.52(13)	N2_c-Zn1-N3	86.47(13)
N2_e-Zn1-N3	87.72(13)	N1_b-Zn1-N3_b	91.95(13)
N1_b-Zn1-N2_c	90.11(12)	N1_b-Zn1-N2_e	176.04(12)
N2_c-Zn1-N3_b	87.72(13)	N2_e-Zn1-N3_b	86.47(13)
N2_c-Zn1-N2_e	93.45(12)	Zn1-N1-C1	124.1(3)
Zn1-N1-C5	118.7(3)	Zn1_d-N2-C11	122.8(3)
Zn1_d-N2-C12	120.8(3)	Zn1-N3-C13	168.3(3)

Symmetry codes: b = 2-x,y,3/2-z; c = -1/2+x,-1/2+y,z; e = 5/2-x,-1/2+y,3/2-z.

Table 3: Selected bond lengths (Å) and angles (°) for $\{[Co(bpe)_2(N(CN)_2)](N(CN)_2)(4H_2O)\}_n$ **(2)**.

Co1 -N1	2.113(3)	Co1-N3	2.189(2)
Co1 -N4	2.149(2)	Co1-N1_b	2.113(3)
Co1 -N3_b	2.189(2)	Co1-N4_b	2.149(2)
N1-Co1-N3	86.95(8)	N1-Co1-N4	91.83(8)
N1-Co1-N1_b	172.45(9)	N1-Co1-N3_b	87.90(8)
N1-Co1-N4_b	93.69(8)	N3-Co1-N4	175.67(8)
N1_b-Co1-N3	87.90(8)	N3-Co1-N3_b	93.95(8)
N3-Co1-N4_b	90.16(8)	N1_b-Co1-N4	93.69(8)
N3_b-Co1-N4	90.16(8)	N4-Co1-N4_b	85.78(8)
N1_b-Co1-N3_b	86.95(8)	N1_b-Co1-N4_b	91.83(8)
N3_b-Co1-N4_b	175.67(8)		

Symmetry code: b = 2-x,y,3/2-z

5A.3.2 Framework stability: Thermogravimetric and PXRD analysis

TG analysis of compound **1** carried out under nitrogen atmosphere shows a weight loss of 10 % (calc. wt. loss ~12%) in the range 30-75 °C corresponding to the five guest water molecules and the dehydrated framework is stable up to ~145 °C (Figure 3a). The slight discrepancy in the weight loss can be correlated to the release of loosely bound water molecules at RT in the powder sample. Then, in the range of 150-200 °C a significant weight loss of 26 % was observed which corresponds to the loss of one bpe linker and this particular phase is stable up to 280 °C without further weight loss. Upon further heating another bpe was released at ~340 °C and then decomposed to unidentified product. TG analysis of compound **2** (Figure 3b) also shows a weight loss of 10 % (calc. wt. loss ~11%) in the range 30-80 °C corresponding to the four guest water molecules and the dehydrated framework is stable up to ~140 °C. Then, in the range of 150-210 °C a significant weight loss of 26 % was observed which corresponds to the loss of one bpe linker. Upon further heating another bpe was released at ~350 °C and decomposed to unidentified product. The PXRD patterns of dehydrated solids $\{[M(bpe)(N(CN)_2)_2]N(CN)_2\}_n$ of **1** (*i.e* **1a**) and **2** (*i.e* **2a**) exhibit no significant change compared to that of as-synthesized **1** suggesting structural rigidity of the framework (Figure 4).

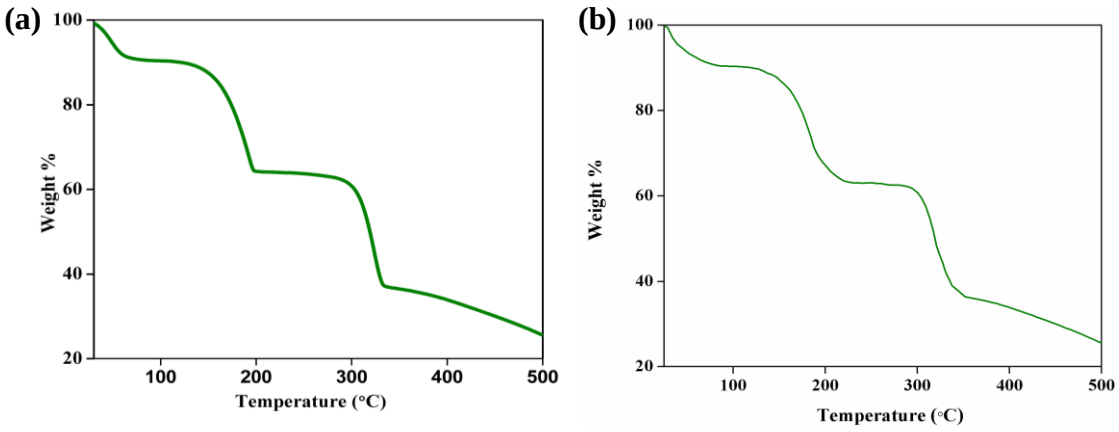

Figure 3: TGA of compound (a) **1** and (b) **2** in the temperature range of 30-500 °C at heating rate of 3 °C/min under N_2 atmosphere.

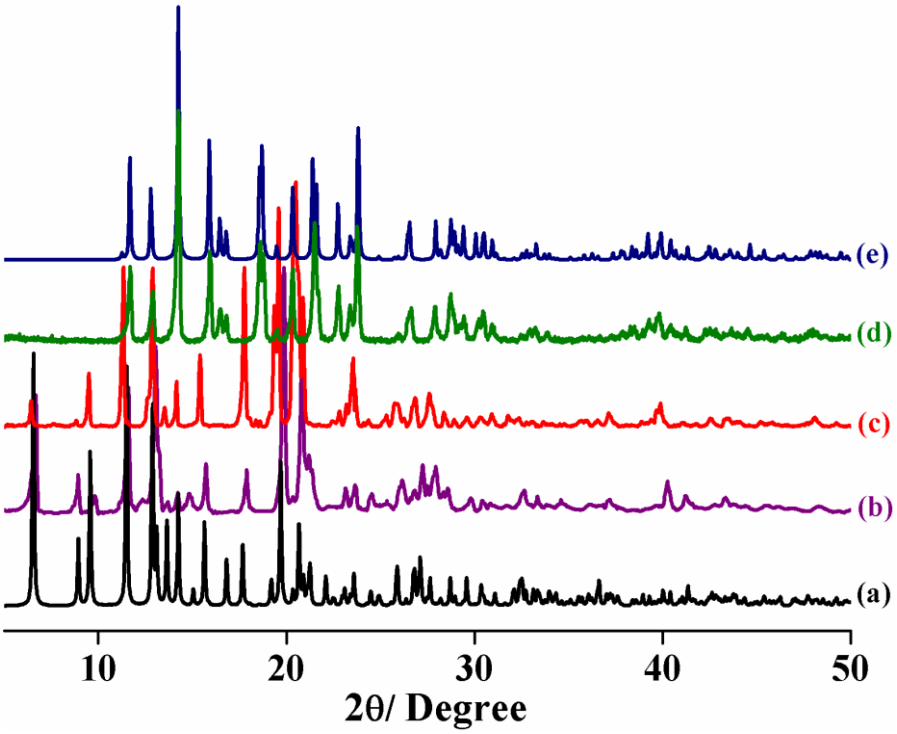

Figure 4: PXRD patterns of **2** in different state: (a) Simulated; (b) As-synthesized; (c) Heated at 75 °C; (d) Heated at 200 °C; (e) Simulated **2b**.

5A.3.3 Crystal-to-Crystal transformation: 3D to 3D and 3D to 1D

Encouraged by the high thermal stability and structural rigidity we carried out single-crystal-to-single-crystal transformation experiment for compound **1**. Few good quality block shaped single crystals of **1** were heated at 70 °C under vacuum for 12 hours and we obtained a partially guest removed structure, $\{[Zn(bpe)_2(N(CN)_2)](N(CN)_2(H_2O)\}_n$ (**1′**). Except a negligible change in cell volume other cell parameters (Table 1) remain unchanged and single crystal structure

determination suggests that three guest water molecules were removed from hexagonal channels of the 3D porous framework. The Zn^{2+}–N bond length of the metal coordination sphere varies as 2.162(5) Å -2.217(4) Å (Table 4), indicating slight increase compared to its as-synthesized solvated analogue. Here, each Zn^{2+} centre is more close to the perfect octahedral geometry compared to the parent compound **1** which is reflected to the *cisoid* and *transoid* angles. The nearest neighbour Zn^{2+}-Zn^{2+} separation along dicyanamide and bpe bridges are 8.787 Å and 13.683 Å, respectively and slight increase in the distances compared to **1** suggesting some relaxation in the framework after removal of partial guests water molecules. Similar to the parent crystal structure there is a disorder in guest and bridged $N(CN)_2^-$ linkers. It is worth mentioning that complete removal of water molecules did not materialize due to instability of the single crystals. When the partially dehydrated crystals were exposed to water vapour for 1-2 days the virgin as-synthesized $\{[Zn(bpe)_2(N(CN)_2)](N(CN)_2)(5H_2O)\}_n$ (**1′′**) compound regenerated with the similar composition of the parent compound **1**. X-ray structure determination shows almost similar cell parameter (Table 1) with preserving overall 3D framework structure as of compound **1** suggesting a reversible single-crystal-to-single-crystal structural transformation. This structural reversibility strongly correlates the robustness of the 3D framework.

Table 4. Selected bond lengths (Å) and angles (°) for $\{[Zn(bpe)_2(N(CN)_2)](N(CN)_2)(H_2O)\}_n$ (**1′**).

Zn1-N1	2.174(4)	Zn1-N2	2.217(4)
Zn1-N3	2.162(5)	Zn1-N1_a	2.174(4)
Zn1-N2_a	2.217(4)	Zn1-N3_a	2.162(5)
N1-Zn1-N2	176.47(15)	N1-Zn1-N3	91.92(17)
N1-Zn1-N1_a	87.05(15)	N1-Zn1-N3_a	93.92(17)
N1-Zn1-N2_a	89.74(14)	N2-Zn1-N3	86.86(17)
N1_a-Zn1-N2	89.74(14)	N2-Zn1-N2_a	93.51(15)
N2-Zn1-N3_a	87.50(17)	N1_a-Zn1-N3	93.92(17)
N2_a-Zn1-N3	87.63(17)	N3-Zn1-N3_a	171.96(16)
N1_a-Zn1-N2_a	176.47(15)	N1_a-Zn1-N3_a	91.92(17)
N2_a-Zn1-N3_a	86.86(17)		

Symmetry code: a = 1-x, y, 1/2-z

Table 5. Selected bond lengths (Å) and angles (°) for $\{[Zn(bpe)_2(N(CN)_2)](N(CN)_2)(5H_2O)\}_n$ (**1″**).

Zn1-N1	2.217(4)	Zn1-N2	2.168(4)
Zn1-N3	2.158(4)	Zn1-N1_a	2.217(4)
Zn1-N2_a	2.168(4)	Zn1-N3_a	2.158(4)
N1-Zn1-N2	175.93(15)	N1-Zn1-N3	86.69(17)
N1-Zn1-N1_a	93.57(15)	N1-Zn1-N2_a	90.07(14)
N1-Zn1-N3_a	87.26(17)	N2-Zn1-N3	91.66(17)
N1_a-Zn1-N2	90.07(15)	N2-Zn1-N2_a	86.36(15)
N2-Zn1-N3_a	94.83(17)	N1_a-Zn1-N3	87.47(17)
N2_a-Zn1-N3	94.78(17)	N3-Zn1-N3_a	171.16(16)
N1_a-Zn1-N2_a	175.93(15)	N1_a-Zn1-N3_a	86.69(17)
N2_a-Zn1-N3_a	91.66(17)		

Symmetry code: a = 1-x, y, 1/2-z

Furthermore, the stepwise release of the coordinated bpe linkers in **1** and **2** prompted to characterize the thermally isolated product after removal of the one bpe linker. As TGA suggests a large plateau in the range of ~200-300 °C after removal of one bpe in both cases, we have able to isolate the compound after heating **1** and **2** at ~200°C under vacuum for 6 h. We observed a distinct color change from white to fade brownish (for **1**) and orange to pink (for **2**) after removal of one bpe and elemental analysis suggests the formulation of $[M(bpe)(N(CN)_2)_2]_n$ ($M=Zn^{2+}$(**1b**)/Co^{2+}(**2b**)) (*vide supra*). IR spectrum of the thermally isolated product of **1** shows significant changes in peak positions in particular ν(CN) which shifted to higher wavenumber indicating the coordination of both $N(CN)_2^-$ anions (Figure 5). PXRD pattern of thermally isolated product (**1b** and **2b**) is completely different compared to the as-synthesized product **1** and **2**), suggesting structural transformation and reorganization after removal of the one bpe molecule (Figure 4 and 6). To get a better insight of the structures of **1b** and **2b**, the powder patterns of thermally isolated products at 200 °C were indexed by TREOR 90 program[22] and it suggests similar cell parameter to the 1D coordination chain of $[M(bpe)(N(CN)_2)_2]_n$ (($M=Zn^{2+}$(**1b**)/Co^{2+}(**2b**)) (cell parameters for compound **1b**: a = 16.5107(4) Å, b = 9.5342(5) Å, c = 12.8793(7) Å , β = 123.444(7)°, V = 1699.39(9) Å^3; compound **2b**: a = 16.5034(9) Å, b = 9.5213(4) Å, c = 12.8964(6) Å, β = 123.484(3)°, V = 1690.15(6) Å^3), which have been reported earlier.[23] Single crystals were also prepared following the same composition of **1b** and **2b** and good quality crystals were isolated

after one week. Most interestingly X-ray single crystal diffraction suggests that the structure of **1b** or **2b** is a 1D linear coordination chain bridge by two $N(CN)_2^-$ and one bpe linkers where the bpe linker adopts *gauche* conformation to connect two Zn^{2+}/Co^{2+} centers (Figure 7). The torsion angle between ethane C-C bond is about 46.93(4) ° (torsion angle ~ 46.93(4) °, for compound **2b**). This unprecedented structural transformation is realized by the release of one bpe linker and concurrent coordination of the non-coordinated $N(CN)_2^-$ anion and conformational change to *gauche* from *anti* of the other bpe linker for the stabilization of the resulting 1D structure.

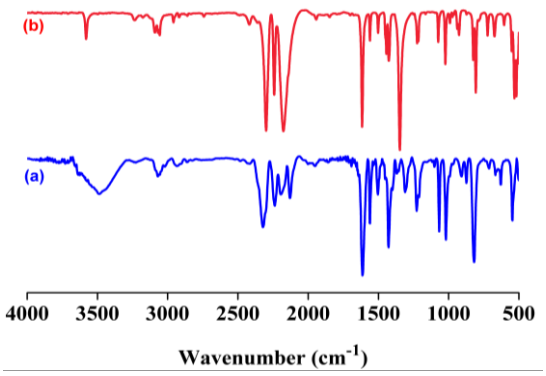

Figure 5: FT-IR spectra (a) Compound $\{[Zn(bpe)_2(N(CN)_2)](N(CN)_2)(5H_2O)\}_n$ **(1)** and (b) $\{Zn(bpe)(N(CN)_2)_2\}_n$ **(1b)**.

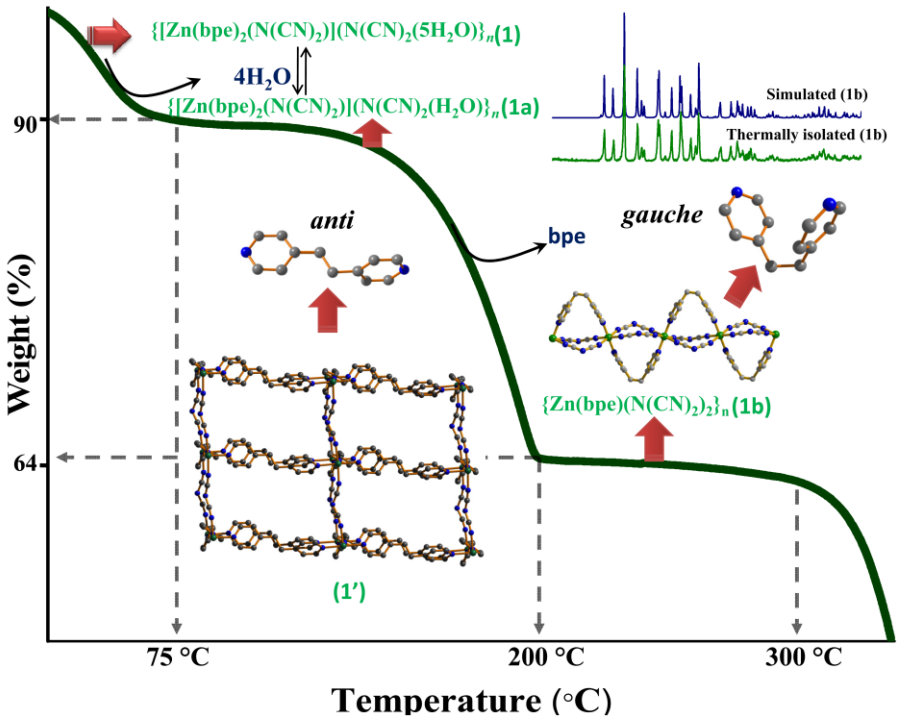

Figure 6: Schematic representation of 3D $(\{[Zn(bpe)(N(CN)_2)_2]N(CN)_2(5H_2O)\}_n$ (**1**) to 1D $\{[Zn(bpe)(N(CN)_2)_2]\}_n$ (**1b**) crystal-to-crystal transformation triggered by release of the one coordinated bpe linker. PXRD pattern of thermally isolated product and as-synthesized compound **1b**. 1D coordination chain of $\{Zn(bpe)(N(CN)_2)_2\}_n$ (**1b**).

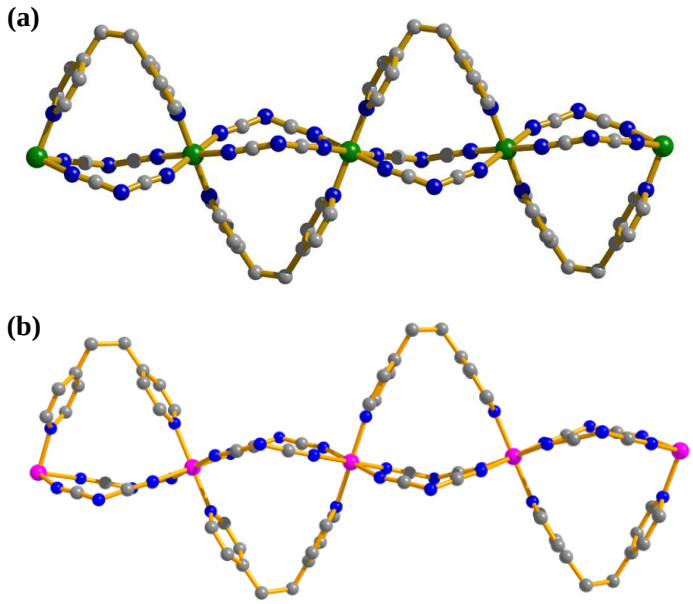

Figure 7: View of the 1D coordination chains of (a) $\{[Zn(bpe)(N(CN)_2)_2]\}_n$ (**1b)** and (b) $\{[Co(bpe)(N(CN)_2)_2]\}_n$ (**2b)**.

Indexing result of the powder pattern of the compound **1b** after heating at 200 °C.

H	K	L	SST-OBS	SST-CALC	DELTA	2TH-OBS	2TH-CALC	D-OBS	FREE PARAM.
0	1	1	.010318	.010320	-.000002	11.660	11.661	7.5834	0
			.011795			12.470		7.0926	0
0	0	2	.015535	.015538	-.000003	14.320	14.321	6.1802	0
2	1	0		.018730			15.732		
-2	1	1	.018844	.018845	-.000001	15.780	15.781	5.6115	0
-2	0	2	.020294	.020293	.000001	16.380	16.380	5.4073	0
-1	1	2	.021290	.021278	.000012	16.780	16.775	5.2793	0
2	1	1	.026395	.026384	.000011	18.700	18.696	4.7413	0
1	2	0	.028796	.028817	-.000021	19.540	19.547	4.5394	0
1	1	2		.028817			19.547		
-1	2	1	.030814	.030816	-.000003	20.220	20.221	4.3882	0
3	1	0	.034091	.034097	-.000006	21.280	21.282	4.1720	0
2	0	2	.035369	.035371	-.000002	21.680	21.680	4.0959	0
-2	2	1		.038152			22.527		
-3	1	2	.038261	.038327	-.000066	22.560	22.580	3.9381	0
-2	1	3	.042379	.042382	-.000002	23.760	23.761	3.7418	0
-3	2	1		.051635			26.268		
-4	1	1	.051912	.051957	-.000045	26.340	26.352	3.3809	0
-3	1	3		.052095			26.387		
0	3	0		.057922			27.852		
-1	2	3	.058117	.058123	-.000006	27.900	27.901	3.1953	0

0	2	3	.060703		28.527				
3	1	2	.060943		28.584				
1	3	0	.061009	.060996	.000013	28.600	28.597	3.1186	0
2	2	2	.061114		28.625				
2	1	3	.064994	.064998	-.000004	29.540	29.541	3.0215	0
1	3	1	.066765		29.949				
4	1	1	.066987	.067035	-.000048	30.000	30.011	2.9762	0

NUMBER OF LINES

INPUT DATA = 22

CALCULATED = 39

MEAN ABSOLUTE DISCREPANCIES

<Q> = .1400E-03

<DELTA(2-THETA)> = .0179E-01

MAX. ERROR ACCEPTED (DEG. 2-THETA) = .4524E-01

5A.3.4 Selective CO_2 adsorption

Encouraged by high thermal stability and structural rigidity, dehydrated solid **2a** was subjected to gas adsorption study. After heating the compound at 75 °C under vaccum a CO_2 (kinetic diameter, 3.3 Å)[24] adsorption isotherm was run at 195 K and observed rapid onset of CO_2 adsorption at very low pressure attributed to the microporosity of the compound (Figure 8). The final CO_2 uptake volume is 36 mL/g at P/P_0 ~ 1 which corresponds to 70 mg/g of CO_2. The Langmuir surface area is about 180 m^2/g and the corresponding BET surface area is 137 m^2/g. A distinct hysteresis in adsorption-desorption isotherm suggests stronger interaction of CO_2 with pore surfaces which is also reflected in considerably high isosteric heat of adsorption (~ 35 kJ/mol) as calculated from Dubinin-Radushkevich (DR) equation.[25] Stronger interaction can be attributed to the presence of nitrogen atoms of $N(CN)_2^-$ and pyridine groups of bpe on the pore walls which can interact effectively with the quadruple moment of CO_2. To our surprise, at 195 K compound **2a** shows negligible uptake of N_2 (kinetic diameter, 3.64 Å), O_2 (3.46 Å), H_2 (2.83 Å) and Ar (3.5 Å) (Figure 8). Although the channel size is large compared to the kinetic diameter of each adsorbate, arguing the observed selectivity is pore size independent. It is worth mentioning that N_2 and H_2 uptake was also not observed at 77 K. This is one of rare example where the diffusion of CO_2 inside the pore is solely depending upon the adsorbate-adsorbent interactions.

Excellent selectivity in gas uptake prompted us to study the vapor sorption in **2a** of different solvent molecules having different polarity and size; H_2O (kinetic diameter, 2.65 Å),[24] MeOH (4.0 Å) and EtOH (4.3 Å) (Figure 9). H_2O adsorption profile exhibits a two-step uptake; up to relative pressure P/P_0 ~ 0.58 it shows almost type-I profile and then steep uptake is observed up to P/P_0 ~ 0.9 (Figure 9a). The final uptake amount is ~ 110 mL/g without saturation which corresponding ~ 2.7 molecules of H_2O per formula unit of **2a**. MeOH profile exhibits single-step gated adsorption whereas EtOH profile reveals gradual uptake with increasing pressure (Figure 9b-c). Up to P/P_0 ~ 0.42, MeOH profile shows almost negligible uptake and the adsorption amount increases with increasing pressure and finishes with a final amount of 80 mL/g suggesting about 2.14 molecules occluded into the framework per formula unit. The 1.57 molecules of EtOH included per formula unit of **2a** correlating that the uptake amount is in accordance to the size and polarity of the guest molecules. The desorption curve in all cases does not follow the adsorption one and unveil distinct hysteresis indicating strong interaction with the pore walls. It is worth noting that such guest dependent two step or gated adsorption behaviour may be correlated to the different adsorption sites in the framework and not related to the 'pore blocking' or 'structural breathing affect' observed in other PCP systems exhibiting stepwise or gated adsorption profile.[26]

5A.4 Conclusion

In conclusion, two isostructural flexible porous two–fold interpenetrated 3D frameworks (**1** and **2**) with bimodal channels were synthesized and upon heating both the frameworks show stepwise release of guest water molecules and bpe linkers. Compound **1** shows reversible single-crystal-to-single-crystal transformation upon removal and inclusion of guest water molecules. Most significantly for the first time we have observed a 3D to 1D structural transformation by removing of a metal bound bridging bpe linker and concomitant bridging of non-coordinated $N(CN)_2^-$ anion and conformational change from *anti* to *gauche* of the another bpe linker. Such kind of structural and dimensionality change by external stimuli in a PCP would pave the way for fabrication of novel coordination framework having substantial importance in the field of crystal growth and engineering. The dehydrated phase of cobalt compound **2a** shows excellent selectivity of CO_2 over a number of adsorbates (N_2, O_2, H_2 and Ar) at 195 K.

5A.5 References

1. a) G. Férey, *Chem. Soc. Rev*. **2008**, *37*, 191; b) S. Kitagawa, R. Kitaura, S. -I. Noro, *Angew. Chem. Int. Ed*. **2004**, *43*, 2334; c) T. K. Maji, S. Kitagawa, *Pure App. Chem.* **2007**, *79*, 2155.

2. a) H. K. Chae, M. Eddaoudi, J. Kim, S. I. Hauck, J. F. Hartwig, M. O'Keeffe, O. M. Yaghi, *J. Am. Chem. Soc.* **2001**, *123*, 11482; b) M. Eddaoudi, D. B. Moler, H. L. Li, B. L. Chen, T. M. Reineke, M. O'Keeffe, O. M. Yaghi, *Acc. Chem. Res.* **2001**, *34*, 319; c) L. Pan, B. Parker, X. Huang, D. H. Olson, J. Y. Lee, J. J. Li, *J. Am. Chem. Soc.* **2006**, *128*, 4180; d) R. Matsuda, R. Kitaura, S. Kitagawa, Y. Kubota, R. V. Belosludov, T. C. Kobayashi, H. Sakamoto, T. Chiba, M. Takata, Y. Kawazoe, Y. Mita, *Nature.* **2005**, *436*, 238; e) P. Kanoo, R. Matsuda, M. Higuchi, S. Kitagawa, T. K. Maji, *Chem. Mater.* **2009**, 5861; f) P. Kanoo, K. L. Gurunatha, T. K. Maji, *J. Mater. Chem.* **2010**, *20*, 1322; g) S. Q. Ma, D. F. Sun, J. M. Simmons, C. D. Collier, D. Q. Yuan, H. C. Zhou, *J. Am. Chem. Soc.* **2008**, *130*, 1012; h) Z. Q. Wang, S. M. Cohen, *J. Am. Chem. Soc.* **2009**, *131*, 16675; i) H. J. Choi, M. Dincá, J. R. Long, *J. Am. Chem. Soc.* **2008**, *130*, 7848; j) T. Ahnfeldt, N. Guillou, D. Gunzelmann, I. Margiolaki, T. Loiseau, G. Férey, J. Senker, N. Stock, *Angew. Chem. Int., Ed.* **2009**, *48*, 5163.

3. a) H. K. Liu, W. Y. Sun, W. X. Tang, T. Yamamoto, N. Ueyama, *Inorg. Chem.* **1999**, *38*, 6313; b) N. Guillou, P. M. Forster, Q. Gao, J. S. Chang, M. Nogues, S. E. Park, A. K. Cheetham, G. Férey, *Angew. Chem., Int. Ed.* **2001**, *40*, 2831; c) S. Horike, M. Dincá, K. Tamaki, J. R. Long, *J. Am. Chem. Soc.* **2008**, *130*, 5854; d) S. Hasegawa, S. Horike, R. Matsuda, S. Furukawa, K. Mochizuki, Y. Kinoshita, S. Kitagawa, *J. Am. Chem. Soc.* **2007**, *129*, 2607; e) S. R.Venna, M. A. Carreon, *J. Am. Chem. Soc.* **2010**, *132*, 76; f) Y. S. Li, F. Y. Liang, H. Bux, A. Feldhoff, W. S. Yang, J. Caro, *Angew. Chem. Int., Ed.* **2010**, *49*, 548; g) S. Couck, J. F. M. Denayer, G. V. Baron, T. Remy, J. Gascon, F. Kapteijn, *J. Am. Chem. Soc.* **2009**, *131*, 6326.

4. a) J. Fan, W. Y. Sun, T. –A. Okamura, J. Xie, W. –X. Tang, N. Okamura, *New J. Chem.* **2002**, *26***,** 199; b) A. N. Parvulescu, G. Marin, K. Suwinska, V. C. Kravtsov, M. Andruh, V. Parvulescu, V. I. J. Parvulescu, *J. Mater. Chem.* **2005**, *15*, 4234; c) S. Muthu, J. H. K. Yip, J. J. Vittal, *Dalton Trans.* **2002**, 4561; d) M. H. Alkordi, Y. L. Liu, R. W. Larsen, J. F. Eubank, M. Eddaoudi, *J. Am. Chem. Soc.* **2008**, *130*, 12639; e) C. Y. Sun, S. X. Liu, D. D. Liang, K. Z. Shao, Y. H. Ren, Z. M. Su, *J. Am. Chem. Soc.* **2009**, *131*, 1883.

5. a) P. Horcazada, C. Serre, M. Sebban, F. Taulelle, G. Férey, *Angew. Chem., Int. Ed.* **2006**, *45*, 5974; b) P. Horcazada, C. Serre, G. Maurin, N.A. Ramsahye, F. Balas, M. Vallet-Regi, M. Sebban, F. Taulelle, G. Férey, *J. Am. Chem. Soc.* 2008**, 130**, 6774; c) J. Y. An, S. J. Geib, N. L. Rosi, *J. Am. Chem. Soc.* **2009**, *131*, 8376; e) S. R. Miller, D. Heurtaux, T. Baati, P. Horcajada, J. M. Greneche, C. Serre, *Chem. Commun.* **2008**, *46*, 4526.

6. a) H. Liu, T.-H. Tsao, Y.-T. Zhang, C.-H. Lin, *CrystEngComm*, **2009**, *11*, 1462; b) M.-H. Zeng, X.- L. Feng, W.-X. Zhang, X.-M. Chen, *Dalton Trans.* **2006**, 5294; c) M. K. Sharma, P. Lama, P. K. Bharadwaj, *Cryst. Growth Des.* **2011**, *11*, 1411; d) M. K. Sharma, P. K. Bharadwaj, *Inorg. Chem.* **2011**, *50*, 1889; e) A. Aijaz, P. Lama, P. K. Bharadwaj, *Inorg. Chem.* **2010**, *49*, 5883; f) H. J. Choi, M. P. Suh, *J. Am. Chem. Soc.* **2004**, *126*, 15844; g) O. Ohmori, M. Kawano, M. Fujita, *J. Am. Chem. Soc.* **2004**, *126*, 16292; h) M. H. Zeng, X. L. Feng, M. X. Chen, *Dalton Trans.* **2004**, 2217; i) Y. X. Zhang, B. L. Chen, F. R. Fronczek, A. W. Maverick, *Inorg. Chem.* **2008**, *47*, 4433.

7. a) S. Henke, R. Schmidt, J. D. Grunwaldt, *Chem. Eur. J.* **2010**, *48*, 14296; b) Z. Q. Wang, S. M. Cohen, *J. Am. Chem. Soc.* **2009**, *46*, 16675.

8. a) G. Mahmoudi, A. Morsali, *Cryst. Growth Des.* **2008**, *10*, 1742; b) A. Aslani, A. Morsali, *Chem. Commun.* **2008**, 3402; c) A. Aslani, M. Zeller, A.Morsali, *Dalton Trans.* **2002**, 5173; d) M. Khanpour, A. Morsali, *CrystEngComm*, **2009**, *11*, 2585; *e*) K. J. Wei, J. Ni, Y. S. Xie, Q. L. Liu, *Inorg. Chem.* **2007**, *10*, 279; f) P. Kanoo, K. L Gurunatha, T. K. Maji, *Cryst. Growth Des.* **2009**, *9*, 4147.

9. a) C. Y. Chen, P. Y. Cheng, H. H. Wu, H. M. Lee, *Inorg. Chem.* **2007**, *46*, 5691; b) K. L. Gurunatha, G. Mostafa, D. Ghoshal, T. K. Maji, *Cryst. Growth Des.* **2010**, *10*, 2483; c) M. H. Zeng, X. L. Feng, X. M. Chen, *Dalton Trans.* **2004**, 2217; d) D. M. Shin, I. S. Lee, D. Cho, Y. K. Chung, *Inorg. Chem.* **2003**, *42*, 7722.

10. a) IPCC, IPCC Special Report on Carbon Dioxide Capture and Storage, Cambridge University Press, Cambridge, **2005**; b) R. S. Haszeldine, *Science*, **2009**, *325*, 1647.

11. a) J. R. Li, R. J. Kuppler, H. C. Zhou, *Chem. Soc. Rev.* **2009**, *38*, 1477; b) Y. Inubushi, S. Horika, T. Fukushima, G. Akiyama, R. Matsuda, S. Kitagawa, *Chem. commun.* **2010**, *46*, 9229; c) H. Wu, R. S. Reali, D. A. Smith, M. C. Trachtenberg, J. Li, *Chem. Eur. J.*, **2010**, *16*, 13951; d) S. Mohapatra, K. P. S. S. Hembram, U. Waghmore, T. K. Maji, *Chem. Mater.* **2009**, *21*, 5406.

12. a) T. Fukushima, S. Horike, Y. Inubushi, K. Nakagawa, Y. Kubota, M. Takata, S. Kitagawa, *Angew. Chem. Int. Ed.* **2010**, *49*, 4820; b) S. R. Caskey, A. G. Wong-Foy, A. J.

Matzger, *J. Am. Chem. Soc.* **2008**, *130*, 10870; c) R. Vaidhyanathan, S. S. Iremonger, K. W. Dawson, G. K. H. Shimizu, *Chem. Comm.* **2009**, *35*, 5230; d) R. Dey, R. Haldar, T. K. Maji, D. Ghoshal, *Cryst. Growth Des.* **2011**, *11*, 3905.

13. T. K. Maji, R. Matsuda, S. Kitagawa, *Nature Mater.* **2007**, *6*, 142.

14. SMART (V 5.628), SAINT (V 6.45a), XPREP, SHELXTL; Bruker AXS Inc. Madison, Wisconsin, USA, 2004.

15. G. M. Sheldrick, Siemens Area Detector Absorption Correction Program, University of Götingen, Götingen, Germany, **1994**.

16. A. Altomare, G. Cascarano, C. Giacovazzo, A. Gualaradi, *J. Appl. Cryst*. **1993**, *26*, 343.

17. G. M. Sheldrick, SHELXL-97, Program for Crystal Structure Solution and Refinement; University of Götingen, Götingen, Germany, **1997**.

18. A. L. Spek, *J. Appl. Crystallogr*. **2003**, *36*, 7.

19. G. M. Sheldrick, SHELXS 97, Program for the Solution of Crystal Structure, University of Götingen, Germany, **1997**.

20. L. J. Farrugia, WinGX-A Windows Program for Crystal Structure Analysis, *J. Appl. Cryst.* **1999**, *32*, 837.

21. The sizes of the channels were calculated considering the van der Waals radii of the atoms.

22. P. –E. Warner, L. Eriksson, M. Westdahl, *J. Appl. Crystallogr*. **1985**, *18*, 367.

23. a) N. D. Pinta, K. Urtiaga, M. G. Barandika, M. I. Arriortua, L. Lezama, G. Madariaga, R. Cartés, *Inorg. Chem.* **2010**, *49*, 10445; b) J. Carranza, C. Brennan, J. Sletten, F. Lloret, M. Julve, *Dalton Trans.* **2002**, 3164; c) S. C. Manna, E. Zangrando, J. Ribas, N. R. Chaudhuri, *Eur. J. Inorg. Chem.* **2008**, 1400.

24. C. E. Webster, R. S. Drago, M. C. Zerner, *J. Am. Chem. Soc.* **1998**, *120*, 5509.

25. M. M. Dubinin, *Chem. Rev.* **1960**, *60*, 235.

26. a) P. Kanoo, R. Sambhu, T. K. Maji, *Inorg. Chem.* **2011**, *50*, 400; b) J. T. Culp, M. R. Smith, E. Bittner, B. Bockroth, *J. Am. Chem. Soc.* **2008**, *130*, 12427.

Part: 5B

Flexible and rigid amine-functionalized microporous frameworks based on different secondary building units: supramolecular isomerism, selective CO_2 capture, and catalysis

Summary

In this chapter synthesis, structural characterization and porous properties of two structural supramolecular isomers of formula $\{[Cd(NH_2–bdc)(bphz)_{0.5}]\cdot DMF\cdot H_2O)\}_n$ (**1** & **2**) (NH_2–bdc = 2–aminobenzenedicarboxylic acid, bphz = 1,2-bis(4–pyridylmethylene)hydrazine) composed of mixed ligand system are presented. Compound **1**, having paddle-wheel type $\{Cd_2(COO)_4\}$ secondary building unit (SBU), is flexible in nature whereas the other isomer, compound **2** has rigid framework based on μ-oxo-bridged $\{Cd_2(\mu–OCO)_2\}$ SBU. Both the frameworks are two–fold interpenetrated and the pore surface is decorated with pendent $–NH_2$ and =N−N= functional groups. Both are nonporous to N_2 as revealed by the type–II adsorption profiles. However, compound **1** shows unusual double step hysteretic CO_2 adsorption profile and for **2** a typical type-I CO_2 profile is observed at 195 K. Moreover, at 195 K both the frameworks show excellent selectivity for CO_2 among other gases like N_2, O_2, H_2 and Ar which has been correlated to the specific interaction of CO_2 with the $–NH_2$ and =N–N= functionalized pore surface. Density functional theory (DFT) based calculations in **2** unveiled that $–NH_2$ group is the primary binding site for CO_2. High heat of CO_2 adsorption (ΔH_{ads} = 37.7 kJ/mol) in **2** is realized by $NH_2\cdots CO_2$ / aromatic–$\pi\cdots CO_2$ and cooperative $CO_2\cdots CO_2$ interactions. Further, postsynthetic modification of $–NH_2$ group to $–NHCOCH_3$ in **2** shows a reduced CO_2 uptake with lower binding energy which establishes the critical role of $–NH_2$ group for CO_2 capture. Presence of basic $–NH_2$ sites in **2** was further exploited for efficient catalytic activity towards Knoevenagel condensation reaction.

1. R. Haldar, S. K. Reddy, V. M. Suresh, S. Mohapatra, S. Balasubramanian, T. K. Maji, ***Chem. Eur. J***. **2014**, *20*, 4347.

5B.1 Introduction

Inorganic-organic hybrid porous solids represent a new class of crystalline porous material, commonly known as metal-organic framework (PCP) or porous coordination polymer (PCP).[1] Possessing the merits of both organic and inorganic building units, it surmounts all the limitations that other contemporaries like zeolite[2] or activated carbons[3] could not. A hefty catalogue of metal ions and organic linkers makes it feasible to synthesize hybrid materials according to their versatile applications in gas storage and separation,[4] catalysis,[5] ion exchange,[6] and as opto-electronic materials.[7] A proper combination of metal ion and organic linker(s) initiates the self-assembly process and just by tuning the reaction conditions (like temperature, pH, solvent) of self-assembly process, a variety of structures with different network topologies and dimensionalities can be obtained. Use of same set of metal ions and linkers may yield compounds of identical stoichiometry but with different network superstructures and they are known as structural supramolecular isomers.[8] Such supramolecular isomers are expected to exhibit different porous properties based on their different network superstructures, which are yet to be properly explored.[9] Furthermore, to the best of our knowledge, the synthesis of catenated supramolecular isomers based on two different secondary building units (SBUs) and their porous properties based on structural flexibility and rigidity in two isomers are yet to be accounted.

The conceptual tactic used to enhance the surface area is the use of long linkers, but this tactic often ends up with framework interpenetration which significantly reduces the porosity. However, recent results suggest that interpenetrated framework shows better interactions with the small molecules like H_2 and CO_2 through the entrapment mechanism where such molecules would be in close proximity with several aromatic rings from different interpenetrating nets.[10] Furthermore, selective capture of CO_2 from flue or natural gas purification is of paramount importance in energy and environmental contexts. The current amine based technology of CO_2 capture from flue gas has major drawbacks of high energy cost for regeneration. Other related issues are corrosive, volatility and occasional decomposition of amines. One of the alternative approaches is to functionalize the pore surface of solid adsorbent with less basic amines like aryl amines which would provide strong physiosorption (30-50 kJ/mol) with CO_2 rather than chemisorption. Such amine ($-NH_2$) tethered/decorated PCP could give easy–on / easy–off reversible CO_2 uptake balanced with selectivity.[11] However, such functionalization is not a straight

forward in practice as these groups can easily interfere with the coordination chemistry associated with the assembly of nodes. Till date, there are only few reports of $–NH_2$ containing PCPs achieved by direct synthesis among more than ten thousand PCPs reported.[12] Not only incorporation of functionalities, increase of binding strength of CO_2 by modifying the as-synthesized pore surface is also a stimulating extension of such work. Extensive reports of postsynthetic modification of PCPs by Cohen *et al.* are good motivation to approach such challenges.[13] Inclusion of $–NH_2$ functionality in the pore surface also opens up the prospect of base catalysis.[14] Knoevenagel condensation, a base catalysed reaction can be studied with the help of such materials and literature survey points out very few reports of such kind.[14] Moreover, a multi-functional material apposite for storage as well as catalysis would be one of the rare examples of its class.[15] Designing materials with all the above mentioned measures is a stupendous task and a critical choice is important. It was envisioned that a framework containing linkers like 2–aminobenzenedicarboxylic acid (NH_2–bdc) and 1,2–bis–(4–pyridylmethylene)hydrazine (bphz) can be able to generate PCPs with backbone decorated with basic functional groups ($–NH_2$ and =N–N=) which will afford interaction sites for CO_2 and also creates a platform for base catalysis. In this work, I have assembled NH_2-bdc and bphz with Cd^{II} at two different reaction conditions to yield two catenane supramolecular isomers with the same molecular formula, $[\{Cd(NH_2–bdc)(bphz)_{0.5}\}\cdot DMF\cdot H_2O]_n$. Both the frameworks are two-fold interpenetrated and show SBU modulated structural flexibility and rigidity (Scheme 1). Compound **1** shows double step hysteretic CO_2 adsorption profile whereas **2** exhibits type-I profile at 195 K. Both the frameworks exhibit excellent selectivity for CO_2 among other gases like H_2, N_2, O_2 and Ar. High isosteric heat of adsorption (ΔH_{ads} = 37.7 kJ/mol) in **2** is supported by density functional theory (DFT) based calculations which suggest that $–NH_2$ group is the primary binding site for CO_2 and also demonstrates the cooperative interaction between CO_2 molecules. Further, **2** was exploited as a base catalyst for Knoevenagel condensation reaction and very good efficiency and size selectivity were realized with different substrates.

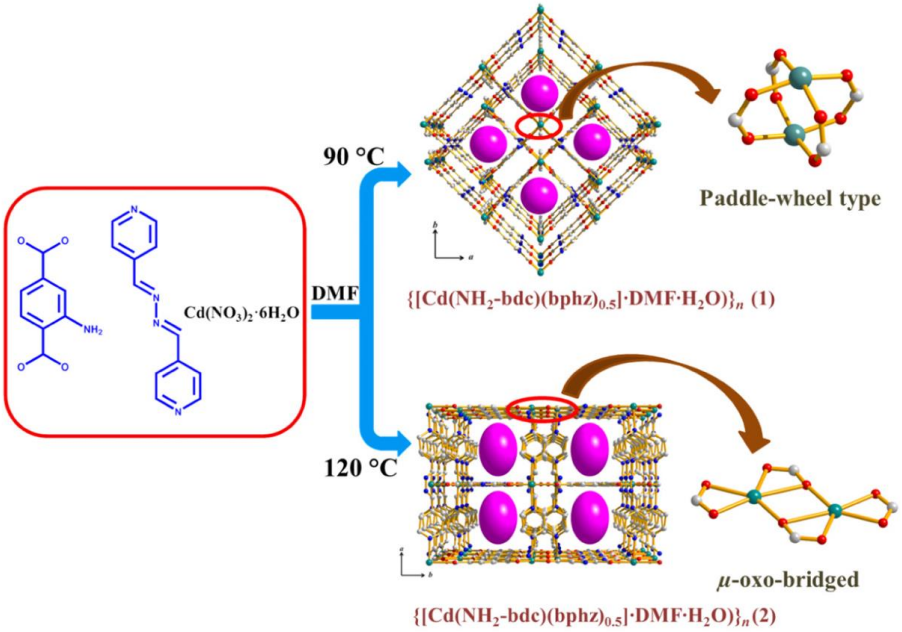

Figure 1: Schematic illustration of synthesis of structural (catenane) supramolecular isomers **1** and **2** based on different SBUs.

5B.2 Experimental Section

5B.2.1 Materials

All the reagents employed were commercially available and used as provided without further purification. $Cd(NO_3)_2 \cdot 6H_2O$ was obtained from Spectrochem. 2-aminobenzenedicarboxylic acid, acetic anhydride, malononitrile, methylcyano acetate, *p*-nitro and *p*-chloro benzaldehyde were obtained from Sigma Aldrich Chemicals Co. 1,2-bis-(4-pyridylmethylene)hydrazine (bphz) was synthesized following the method given in literature.[16]

5B.2.2 Physical Measurements

Elemental analyses were carried out using a Thermo Fischer Flash 2000 Elemental Analyzer. IR spectra were recorded on a Bruker IFS 66v/S spectrophotometer using KBr pellets in the region 4000-400 cm^{-1}. Thermogravimetric analysis (TGA) was carried out (Metler Toledo) in nitrogen atmosphere (flow rate = 50 mL min^{-1}) in the temperature range 30 – 500 °C (heating rate = 3 °C min^{-1}). Powder XRD patterns of the compound **1** and **2** were recorded by Bruker D8 Discover; 40 kV, 30 mA using Cu-K_α radiation. ^{1}H-NMR spectra were measured on a Bruker AV-400 spectrometer with chemical shifts reported as ppm (in DCl/d_6-DMSO, $CDCl_3$/CD_3CN, TMS as internal standard).

5B.2.3 Synthesis of $\{[Cd(NH_2\text{-}bdc)(bphz)_{0.5}]\cdot DMF\cdot H_2O)\}_n$ (1 and 2)

A 14 mL DMF solution of NH_2-bdc (0.2 mmol, 0.035 g) and bphz (0.2 mmol, 0.042 g) was prepared and $Cd(NO_3)_2\cdot 6H_2O$ (0.2 mmol, 0.049 g) was added and sonicated for 10-15 min to mix well. This solution was then equally divided in two glass *via*ls and kept at two different temperatures, 90 °C and 120 °C for 24 h. After cooling to RT rectangular block shaped yellow colored crystals were found at the walls of the *via*ls. From 90 °C reaction compound **1** and at 120 °C compound **2** were isolated. Crystals were separated from solution and then thoroughly washed with DMF. Crystals of both compounds were found to be weakly diffracting and hence for further characterization ^{1}H-NMR, elemental analysis and TGA were used (Figure 1-6). Compound **1**: Yield: 67%, relative to Cd. FT-IR (KBr pellet, 4000-400 cm^{-1}): 3490(b), 3234(w), 3072(w), 2326(s), 2238(m), 2128(m), 1614(s), 1562(s), 1502(s), 1428(s), 1310(w), 1228(s), 1068(s), 1020(s), 912(w), 874(w), 820(s). Anal. Calcd. for $C_{17}H_{19}CdN_4O_6$: C, 41.86; H, 3.92; N, 11.48. Found: C, 41.21; H, 4.41; N, 10.97. Compound **2**: Yield: 58%, relative to Cd. FT-IR (KBr pellet, 4000-400 cm^{-1}): 3490(b), 3234(w), 3072(w), 2326(s), 2238(m), 2128(m), 1614(s), 1562(s), 1502(s), 1428(s), 1310(w), 1228(s), 1068(s), 1020(s), 912(w), 874(w), 820(s). Anal. Calcd. for $C_{17}H_{19}CdN_4O_6$: C, 41.86; H, 3.92; N, 11.48. Found: C, 42.11; H, 4.17; N, 11.01.

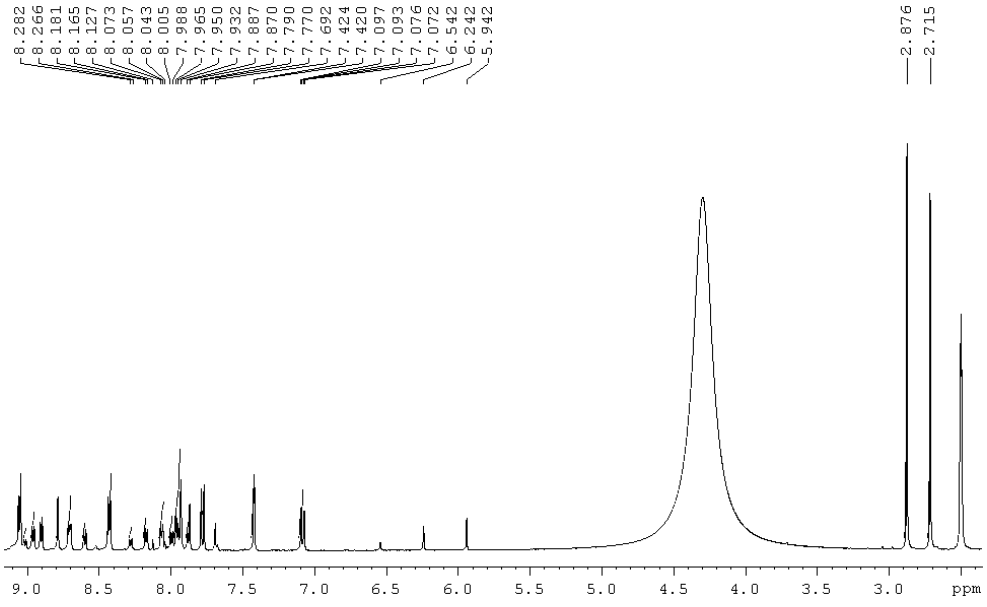

Figure 1: ^{1}H NMR spectrum of digested compound **1** (DCl/d_6-DMSO).

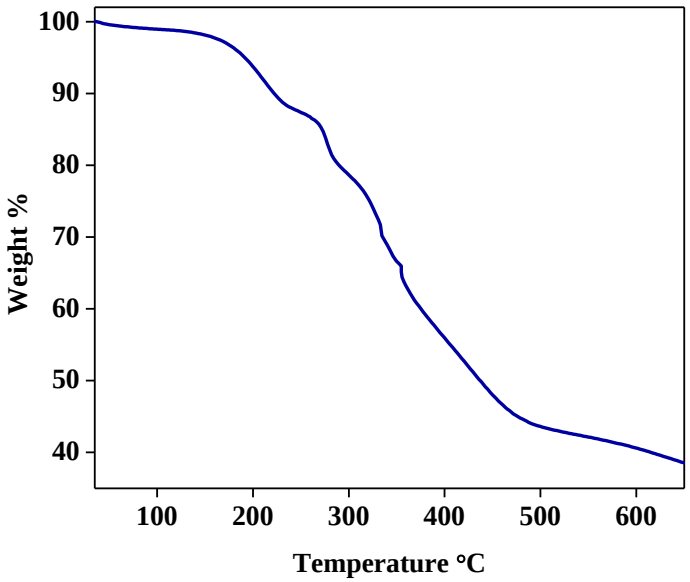

Figure 2: TGA profile of compound **1** in the temperature range of 30-650 °C at heating rate of 3 °C/min under N_2 atmosphere.

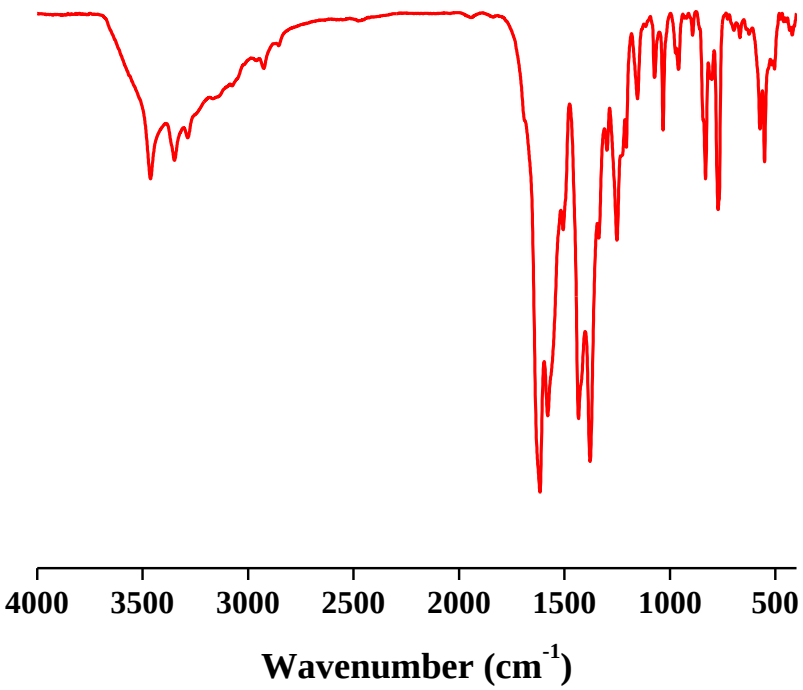

Figure 3: FT-IR spectrum of compound **1**.

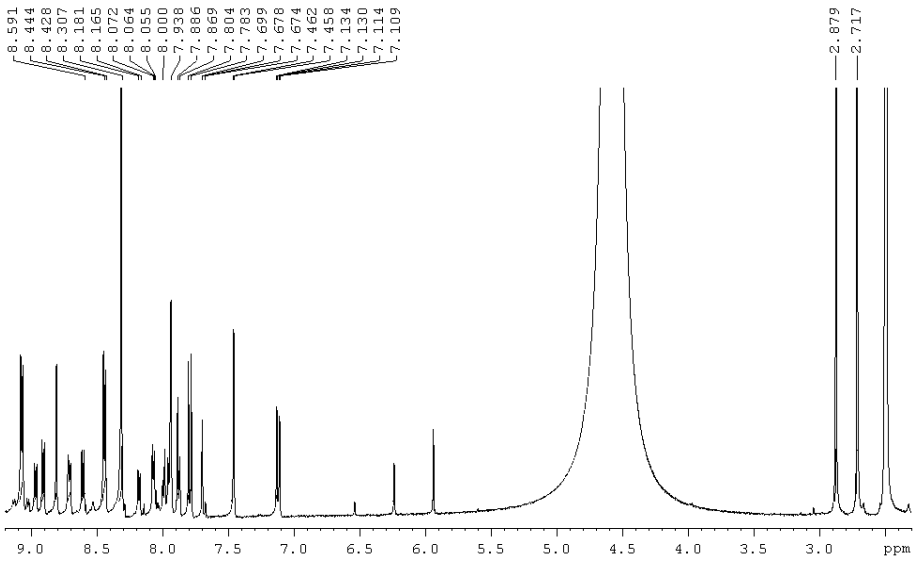

Figure 4: ^{1}H-NMR spectrum of digested compound **2** (DCl/d_6-DMSO).

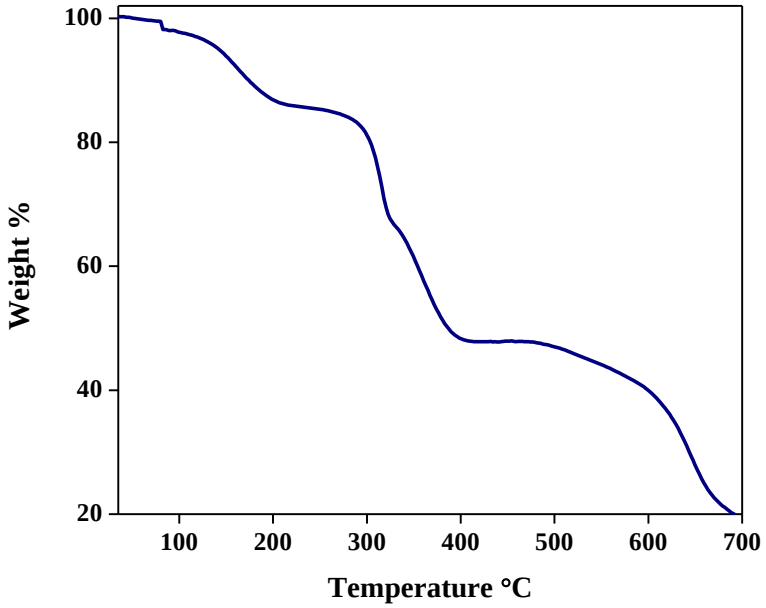

Figure 5: TGA profile of compound **2** in the temperature range of 30-650 °C at heating rate of 3 °C/min under N_2 atmosphere.

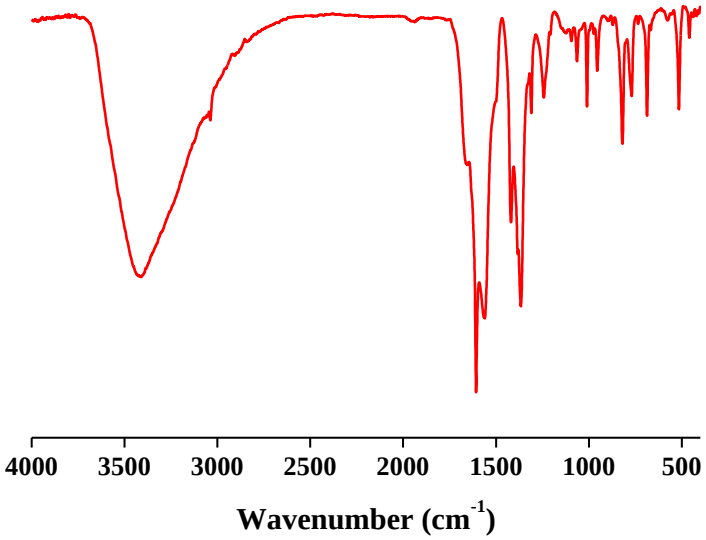

Figure 6: FT-IR spectrum of compound **2**.

5B.2.4 Synthesis of {[Cd(NH$_2$-bdc)$_{0.1}$(NHCOCH$_3$-bdc)$_{0.9}$(bphz)$_{0.5}$]·CHCl$_3$)}$_n$ (2a)

The activated (desolvated) compound **2** (~50 mg) is stirred with a chloroform solution of acetic anhydride (0.5 mmol in 5 mL of acetic anhydride) for 6-7 days at RT. The powder compound **2a** obtained was filtered and washed several times with $CHCl_3$ and dried in air. **2a** is characterized by ^{1}H-NMR studies (Figure 7). Anal. Calcd. for $C_{16.8}H_{12.8}CdN_4O_{4.9}$: C, 36.41; H, 2.31; N, 10.11. Found: C, 37.51; H, 3.01; N, 10.51.

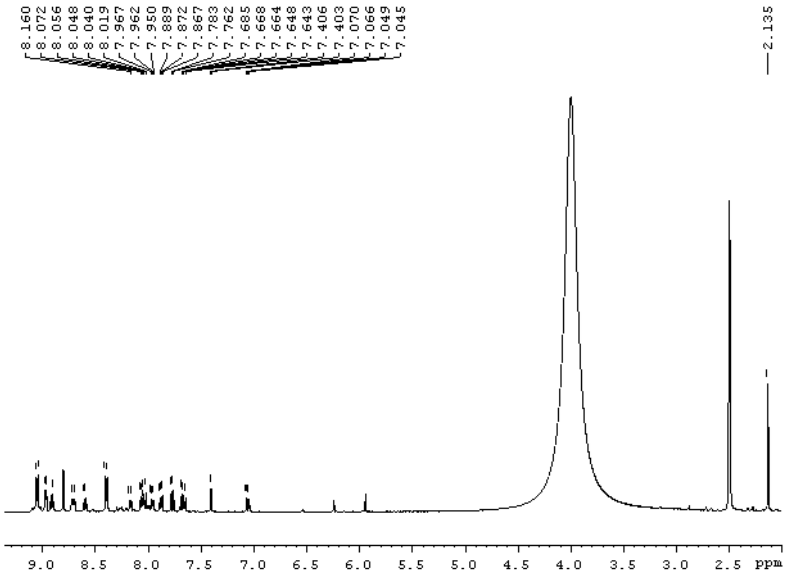

Figure 7: ^{1}H-NMR spectrum of digested postsynthetically modified compound **2a** (DCl/d_6-DMSO).

5B.2.5 X-ray Crystallography

X-ray single crystal structural data of **1** and **2** were collected on a Bruker Smart-CCD diffractometer equipped with a normal focus, 2.4 kW sealed tube X-ray source with graphite monochromated Mo-K_α radiation (λ = 0.71073 Å) operating at 50 kV and 30 mA. The program SAINT[17] was used for integration of diffraction profiles and absorption correction was made with SADABS[18] program. All the structures were solved by SIR 92[19] and refined by full matrix least square method using SHELXL-97.[20] All the hydrogen atoms were fixed by HFIX and placed in ideal positions. Due to weakly diffracting nature of the single crystals we could not locate the guest molecules and carried out ^{1}H-NMR, TGA, IR and CHN analysis to confirm the presence of guest molecules. Potential solvent accessible area or void space was calculated using the PLATON multipurpose crystallographic software.[21] All crystallographic and structure refinement data of **1** and **2** are summarized in Table 1. Selected bond lengths and angles for **1** and **2** are given in Table 2-3 respectively. All calculations were carried out using PLATON, and WinGX system, Ver 1.70.01.[22]

5B.2.6 Adsorption study

The adsorption isotherm of CO_2, H_2, N_2, Ar and O_2 (195 K) using the dehydrated sample of **1 (1′)**, **2 (2′)** and **2a** were measured by using QUANTACHROME QUADRASORB-*SI* analyzer. In the sample tube the adsorbent sample (~100-150 mg) was placed which had been prepared at 453 K under a 1×10^{-1} Pa vacuum for about 6 h prior to measurement of the isotherms. Helium gas (99.999% purity) at a certain pressure was introduced in the gas chamber and allowed to diffuse into the sample chamber by opening the valve. The amount of gas adsorbed was calculated readily from pressure difference (P_{cal} - P_e), where P_{cal} is the calculated pressure with no gas adsorption and P_e is the observed equilibrium pressure. All operations were computer-controlled and automatic.

5B.2.7 Computational details

All periodic calculations were carried out using density functional theory (DFT) as implemented in QUICKSTEP module in CP2K.[23] It uses a mixed basis set of which Kohn-Sham orbitals were expanded in an atom-centered basis Gaussian set and electronic charge density was described using an auxiliary plane wave basis set. Initial coordinates

were taken from the experimental structure and then its cell parameters and geometry were optimized iteratively until lowest energy structure was found. A super cell of size 1 × 1 × 1 was used. Goedecker-Teter-Hutter type norm conserving pseudo potentials were used to represent the combined effect of core electrons and nucleus.[24] Exchange and correlation interactions were accounted using the generalized gradient approximation (GGA) of Perdew, Burke, and Ernzerhof (PBE).[25] Long-range interactions were taken into account using dispersion corrections of Grimme for this functional.[26] Double-zeta single polarized molecularly optimized basis sets (DZVP) were used to describe valence electrons. Since this basis set is not available for cadmium, the shorter range version of the same type was used. Structural relaxation was carried out until forces on all atoms were less than 10^{-4} a. u. Binding energy (ΔE) of CO_2 with PCP was calculated using the formula,

$$\Delta E = E(PCP+CO_2) - E(PCP) - E(CO_2) \qquad (\mathbf{1})$$

where $E(PCP+CO_2)$, $E(PCP)$ and $E(CO_2)$ represents energy of PCP with CO_2, PCP and CO_2 respectively. All structures were visualized using VMD.[27]

5B.3 Results and discussion

5B.3.1 Structural description of $\{[Cd(NH_2\text{-bdc})(bphz)_{0.5}]\cdot DMF\cdot H_2O)\}_n$ (1 and 2)

Single crystal X-ray diffraction analysis illustrates that compound **1** and **2** both crystallize in orthorhombic crystal system with space groups *Cmcm* and *Cmca,* respectively (Table 1). Compound **1**, synthesized at 90 °C, has one metal center Cd^{2+}, half of bphz and one NH_2-bdc linker along with one molecule of DMF and H_2O in the asymmetric unit (Figure 8a). A paddle-wheel type $\{Cd_2(COO)_4\}$ SBU is the key component of the framework and this is further connected by NH_2-bdc in *ac* plane to furnish a 2D square sheet like structure (Figure 8b). These 2D sheets are pillared by bphz linkers to extend this network in three dimensions to provide a 3D *α*-polonium type pillared-layer porous framework (Figure 8c). The octahedral Cd^{2+} center slightly de*via*tes from perfect octahedral geometry and this is reflected in *cisoid* and *transoid* angles (Table 2). The Cd^{2+}-O bond distance is 1.995 Å and Cd^{2+}-N bond lengths are in the range of 2.022-2.036 Å. Pore size of the single net along *c*-direction is 8.4 × 8.4 $Å^2$ which reduces to 4 × 4 $Å^2$ due to a two-fold interpenetration (Figure 9).[28] These channels are occupied

by two different guest molecules, one water and one DMF. Presence of these guests was confirmed by elemental analysis, TGA, IR and ^{1}H-NMR studies (Figure 1-3). Removal of guest molecules creates a void volume of 2129 Å^3 (49 % of the unit cell volume).[21] Along with high void space, the pore surfaces are decorated with pendant –NH_2 groups.

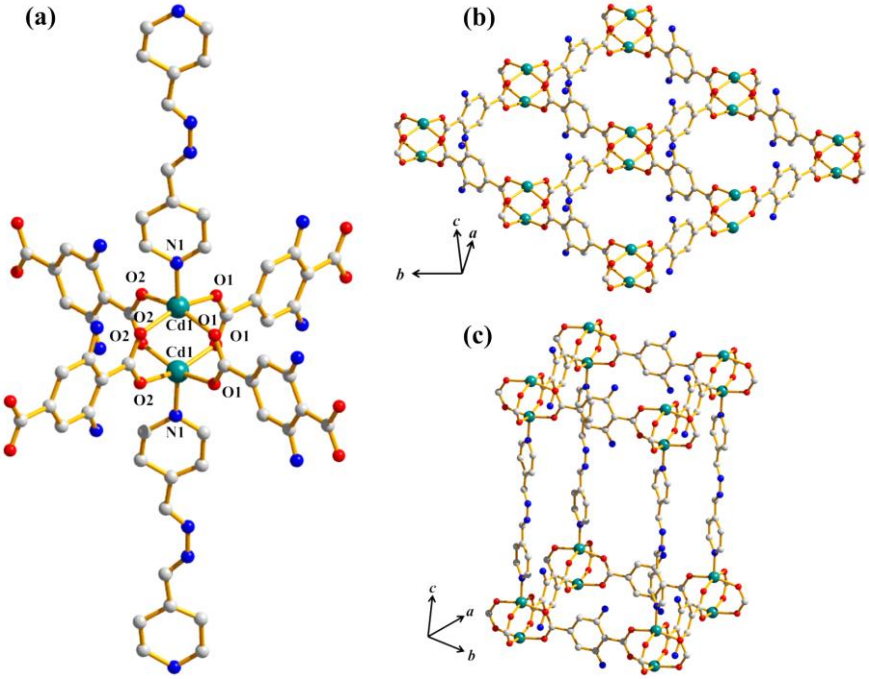

Figure 8: (a) Coordination environment of Cd^{2+} with paddle wheel building block in compound **1**, (b) 2D sheet of $\{Cd_2(NH_2\text{-bdc})_2\}_n$ unit on crystallographic *ab* plane, (c) 3D framework of compound **1** with α-Polonium type network topology. The two –NH_2 groups in the NH_2-bdc linker is due to its positional disorder.

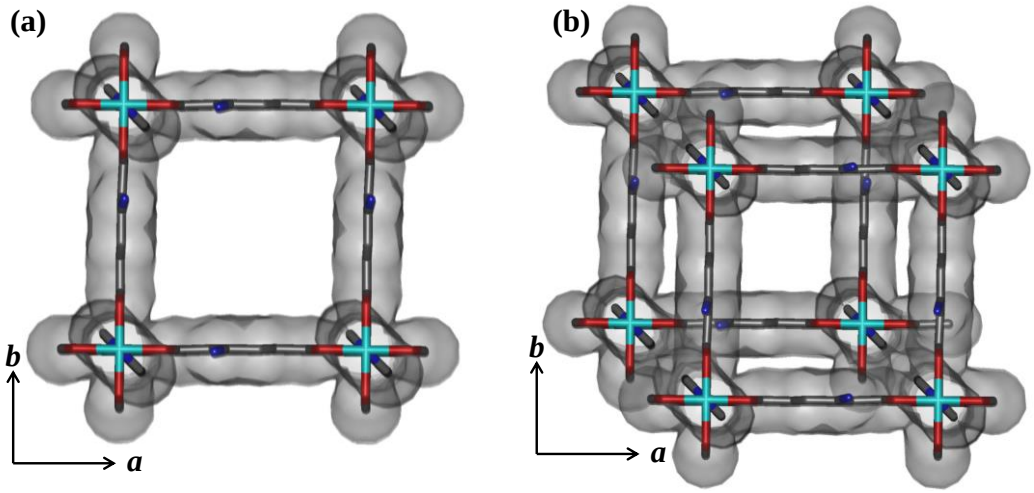

Figure 9: View of van der Waals surface added single net and interpenetrated net in compound **1** along *c* direction.

Unlike compound **1**, compound **2** is made of a different SBU, $\{Cd_2(\mu\text{-}OCO)_2\}$, where two Cd^{2+} centers are μ-oxo-bridged. NH_2-bdc linkers connect the SBUs along *bc* plane to furnish 2D sheets of $\{Cd_2(NH_2\text{-}bdc)_2\}_n$ (Figure 10a-b). These 2D sheets are then pillared by bphz to generate a 3D bi-pillared framework where the $–NH_2$ group remains pendant, similar to compound **1** (Figure 10c and Scheme 1). Here Cd^{2+} metal center is 7 coordinated; the Cd^{2+}-O bond lengths are in the range of 2.282-2.658 Å and Cd^{2+}-N bond length is 2.468 Å (Table 3). A two-fold interpenetration creates rectangular channels along *c*-direction with a dimension of 3×5 $Å^2$ and one water and one DMF molecules occupy the free space, identical to that of compound **1** (Figure 11 and Scheme 1). Presence of solvent molecules was confirmed by elemental analysis, TGA, IR and ^{1}H-NMR studies (Figure 4-6). Calculated solvent accessible volume was found to be ~ 28 % which is less in comparison to that of compound **1**. Striking similarity between both structures was the presence of pendant $–NH_2$ groups along the pore surfaces. Both the compounds have identical molecular formula but have different network super structure having different SBUs and hence they are structural supramolecular isomers (Scheme 1). They are two-fold catenated and can also be termed as catenane supramolecular isomers.

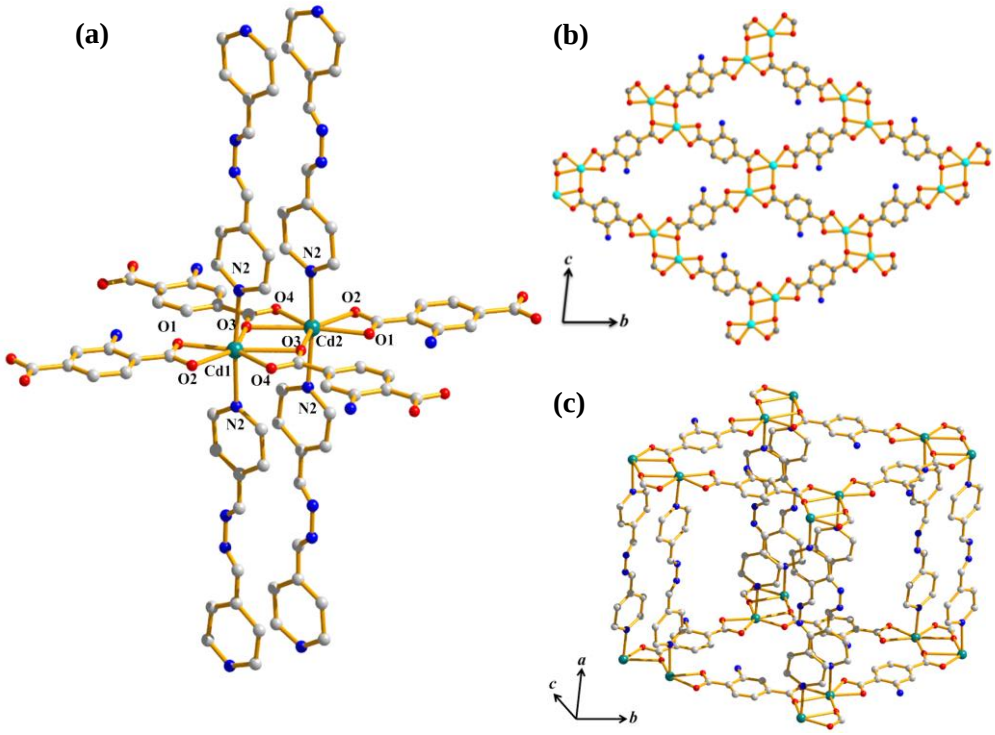

Figure 10: (a) Coordination environment of Cd^{2+} with μ-oxo bridge building block in compound **2**, (b) 2D sheet of $\{Cd_2(NH_2\text{-}bdc)_2\}_n$ unit on crystallographic *bc* plane, (c) 3D bi-pillared layer type framework of compound **2**.

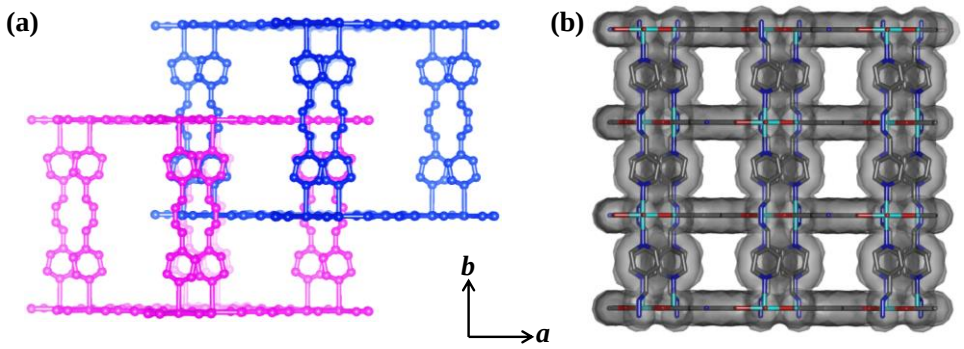

Figure 11: (a) Two-fold interpenetrated framework of **2**; (b) van der Waals surface added pore surface of **2**.

Table 1: Crystal data and structure refinement parameters of compound **1** and **2**.

Parameters	1	2
empirical formula	$C_{14}H_{10}CdN_3O$	$C_{14}H_{10}CdN_3O$
M	583.96	655.96
Cryst. system	Orthrhombic	Orthrhombic
space group	*Cmcm*	*Cmca*
***a* (Å)**	15.5918(15)	15.939(5)
***b* (Å)**	15.3726(14)	20.857(5)
***c* (Å)**	18.2802(16)	14.374(5)
***V* (Å^3)**	4381.5(7)	4779(3)
Z	8	8
***T*(K)**	293	293
λ (Mo K_α)	0.71073	0.71073
D_c (g cm^{-3})	1.287	1.183
μ (mm^{-1})	1.022	0.937
θ_{max} (deg)	24	25.8
total data	18132	20830
unique reflection	1732	2084
R_{int}	0.139	0.092
data [$I > 2\sigma(I)$]	1201	1081
***R*^{a}**	0.0781	0.0883
***R*$_w$^{b}**	0.1987	0.2349
GOF	1.272	1.76

^{a} $R = \Sigma||F_o| - |F_c||/\Sigma|F_o|$. ^{b} $R_w = [\Sigma\{w(F_o^2 - F_c^2)^2\}/\Sigma\{w(F_o^2)^2\}]^{1/2}$.

Table 2: Selected bond lengths (Å) and angles (°) for **1**.

Cd1-O1	2.037(6)	Cd1-N1	1.997(9)
Cd1-Cd1_b	2.9164(13)	Cd1-O1_e	2.037(6)
Cd1-O2_h	2.020(6)	Cd1-O2_j	2.020(6)

O1-Cd1-N1	101.2(2)	O1-Cd1-O1_e	88.0(2)
O1-Cd1-O2_h	88.3(2)	O1-Cd1-O2_j	160.2(2)
O1_e-Cd1-N1	101.2(2)	O2_h-Cd1-N1	98.7(2)
O2_j-Cd1-N1	98.7(2)	O1_e-Cd1-O2_h	160.2(2)
O1_e-Cd1-O2_j	88.3(2)	O2_h-Cd1-O2_j	88.6(3)

b = 1-x, y, 1/2-z; e = 1-x, y, z; h = 1/2-x, 1/2+y, 1/2-z; j = 1/2+x, 1/2+y, 1/2-z

Table 3: Selected bond lengths (Å) and angles (°) for **2**.

Cd1-O1	2.384(9)	Cd1-N2	2.590(18)
Cd1-O3_b	2.330(10)	Cd1-O3_d	2.658(9)
Cd1-O4_d	2.269(9)	Cd1-N2_i	2.590(18)
O1-Cd1-O2	55.1(3)	O1-Cd1-N2	94.5(3)
O1-Cd1-O3_b	144.6(3)	O1-Cd1-O3_d	138.5(3)
O1-Cd1-O4_d	86.7(3)	O1-Cd1-N2_i	94.5(3)
O2-Cd1-N2	92.3(3)	O2-Cd1-O3_b	89.4(3)
O2-Cd1-O3_d	166.4(3)	O2-Cd1-O4_d	141.9(3)
O2-Cd1-N2_i	92.3(3)	O3_b-Cd1-N2	86.2(4)
O3_d-Cd1-N2	86.9(3)	O4_d-Cd1-N2	90.6(3)
N2-Cd1-N2_i	171.0(5)	O3_b-Cd1-O3_d	77.0(3)
O3_b-Cd1-O4_d	128.7(3)	O3_b-Cd1-N2_i	86.2(4)
O3_d-Cd1-O4_d	51.7(3)	O3_d-Cd1-N2_i	86.9(3)
O4_d-Cd1-N2_i	90.6(3)		

b = 2-x, -1/2-y, 1/2+z; d = 2-x, -1/2+y, 1/2-z; i = 2-x, y, z

5B.3.2 Thermal stability and flexibility of 1 and 2

TG analysis of compound **1** (Figure 2) shows a weight loss in the range of 150 to 200 °C which indicates loss of DMF and water molecules. The desolvated framework $\{[Cd(NH_2\text{-bdc})(bphz)_{0.5}]\}_n$ **(1′)** is stable upto 250 °C without further weight loss. Upon further heating a rapid weight loss indicates decomposition of the compound. In case of compound **2**, the guest molecules are released at 200 °C (Figure 5) and the desolvated structure is stable upto 280 °C. Upon desolvation at 200 °C under vacuum, compound **1** undergoes structural transformation which is evident from the differences between PXRD patterns of desolvated and as-synthesized state (Figure 12a). First two peaks corresponding to (110) and (111) reflections are almost absent in the desolvated state

suggesting contraction in the framework. Refilling the pores with DMF alone shows further change in the PXRD pattern but it does return to its as-synthesized phase (Figure 12a). But PXRD pattern of desolvated framework **2** (**2′**) does not show any change and also retains its structural integrity upon exposure to solvent vapours like MeOH, EtOH, $CHCl_3$, and CH_3CN (Figure 12b). Upon desolvation the structural change associated with the framework **1** and the rigid nature of **2** can be explained on the basis of different SBUs and their orientations in the interpenetrated nets. In **1**, the axis passing through the metal centers of the paddle wheel SBU is parallel to the pillars bphz and NH_2-bdc plane and such orientation leaves enough space along *c* axis (Figure 13). Hence there is a possibility of net movements upon desolvation which is resulting in structural transformation in **1**.

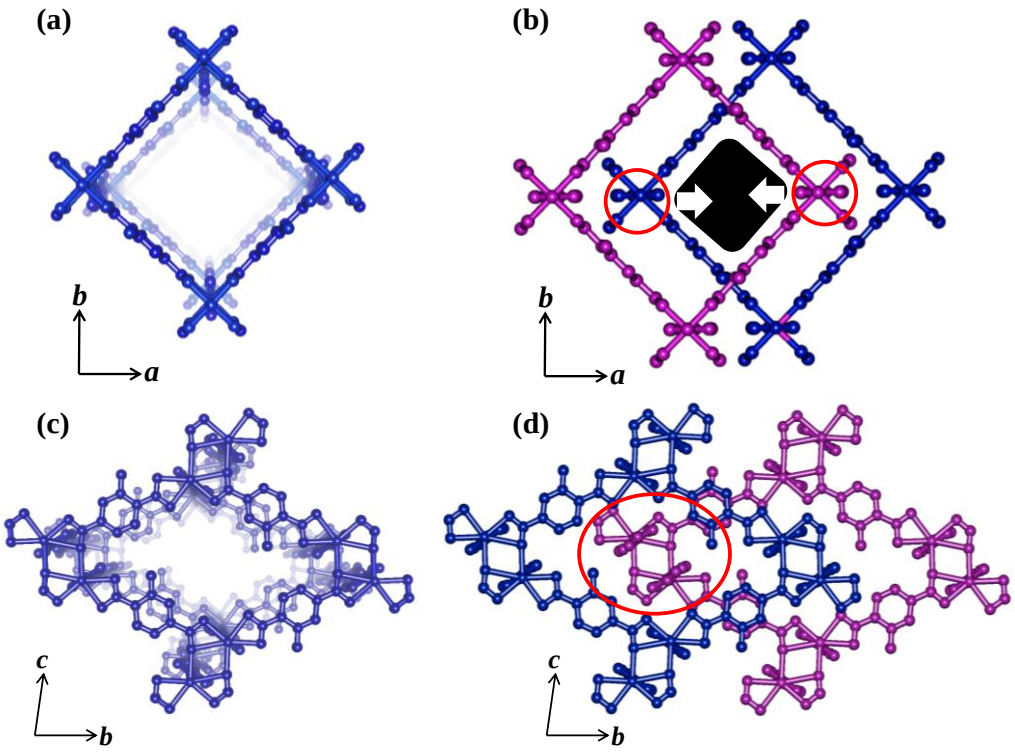

Figure 13: Top: View of compound **1** along *c*-axis: (a) Single net, (b) Interpenetrated net. Below: View of compound **2** along *a*-axis: (c) Single net, (d) Interpenetrated net.

But in case of **2** this sliding is not possible due to perfect fitting of the nets along the *a*–axis. Here the axis passing through the metal centers in μ-oxo bridged SBU is perpendicular to the pillars and further the bi-pillar nature leaves no space along *a* direction (Figure 13). In addition, in **2** the pendant $–NH_2$ (donor) of one net and =N–N= (acceptor) of other net are connected by hydrogen bonding interactions (N3-H⋯N1 = 3.253 Å) (Figure 13). Two other weak hydrogen bonds operate between hydrogen of –

CH=N- of one net with oxygen atom of carboxylate of other net (C14-H···O1=3.216 Å, C14-H···O1=3.402 Å). Due to these interactions, the two 3D nets are stabilized and do not move upon desolvation. But in case of **1**, no such interactions between the nets exist and the space for sliding of nets is available. Hence the structural flexibility in **1** and rigidity in **2** are realized.

5B.3.3 Selective CO_2 adsorption

Large void spaces and amine functionalized pore in both the compounds (**1** and **2**) lead us to carry out different gas adsorption measurements. Prior to measurement, compound **1** was activated by removing the guest molecules at 190 °C. At 77 K, compound **1** shows a typical type-II N_2 isotherm (Figure 14a) which indicates surface adsorption phenomenon. The calculated BET surface area is 82 m^2/g. To our surprise, at 195 K it shows a two-step commensurate uptake profile for CO_2 and the saturated uptake amount is ~ 118 mL/g which corresponds to 23 weight % (2 CO_2 molecules/formula) (Figure 14b). It also shows a unique hysteresis in the adsorption-desorption isotherm with withholding of ~ 9 wt % of CO_2 in the framework. With flexible framework, this kind of unusual adsorption behaviour is not uncommon.[29] The first step of uptake till pressure ~ P/P_0 ~ 0.5 equates to one molecule of CO_2 per formula and in the next step another CO_2 molecule is adsorbed. Initial steep uptake (Type-I) is probably due to the interaction with pendent $–NH_2$ present at the pore surface and it is reflected in the heat of adsorption ($q_{st,\varphi}$) value ~ 28.5 kJ/mol calculated using Dubinin−Radushkevich (DR) equation.[30] The second step is probably due to the sliding of the 3D nets which opens up more void space for CO_2 molecules to diffuse in. Using CO_2 uptake profile (till first step, P/P_0 ~ 0.5) calculated BET surface area is 185 m^2/g. Interestingly, it shows negligible uptake for other gases like H_2 (kinetic diameter- 2.83 Å),[31] Ar (3.5 Å), O_2 (3.46 Å) and N_2 (3.64 Å) at 195 K and thus it is very selective for CO_2 gas. Compound **2**, like compound **1**, shows no uptake of N_2 at 77 K (Figure 15a). But at 195 K, it shows a type-I adsorption profile for CO_2 and the final uptake amount is 101 mL/g which corresponds to ~ 19 weight % of CO_2 (1.8 molecules/formula) (Figure 15b). The BET surface area calculated using CO_2 adsorption profile was found to be ~ 298 m^2/g. The enthalpy of adsorption of CO_2 was obtained by measuring two isotherms at 273 and 293 K, followed by a fit of the data to virial equation.[32] At zero loading, ΔH_{ads} is 37.7 kJ/mol which clearly indicates the moderate interaction between framework **2** and CO_2. Remarkably, at maximum loading, ΔH_{ads} value is 39.6 kJ/mol. After initial loading, ΔH_{ads} falls slowly and again rises to a

value that is higher than that at zero loading (Figure 16). This is likely due to cooperative interaction between adsorbed CO_2 molecules. Similar to compound **1**, **2** is also found to be selective for CO_2 at 195 K among other gases like H_2, Ar, O_2 and N_2.

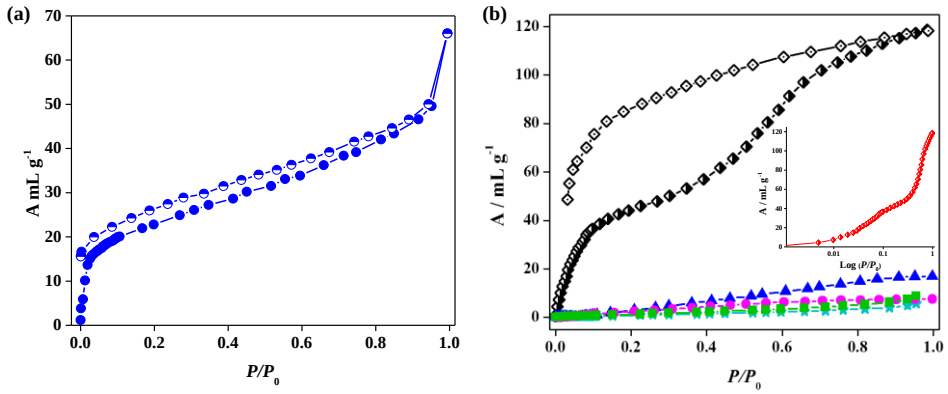

Figure 14: Adsorption isotherms of compound **1**: (a) N_2 adsorption at 77 K; (b) at 195 K: CO_2 (diamond), N_2 (star shape), H_2 (circle), Ar (triangle shape), O_2 (square); Inset: CO_2 adsorption profile at 195 K in log scale.

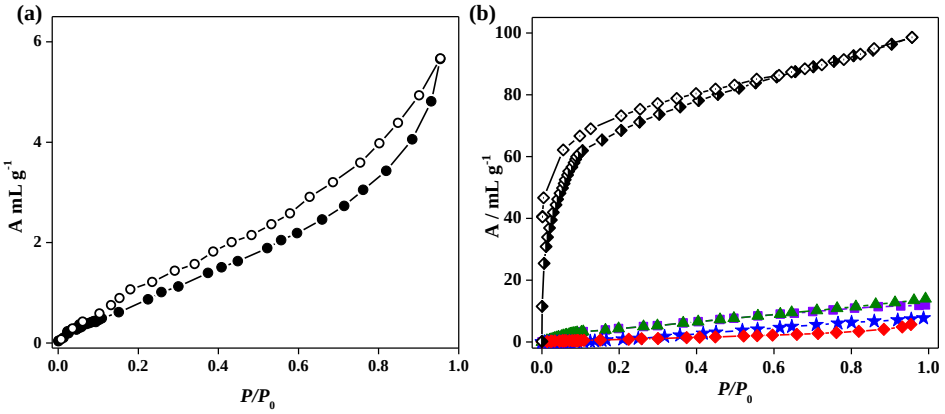

Figure 15: Adsorption isotherms of compound **2**: (a) N_2 adsorption at 77 K; (b) at 195 K: CO_2 adsorption (Half-filled diamond), CO_2 desorption (open diamond), N_2 (star shape), H_2 (Filled diamond), Ar (triangle), O_2 (square). (b) CO_2 adsorption profile at 273 and 293 K.

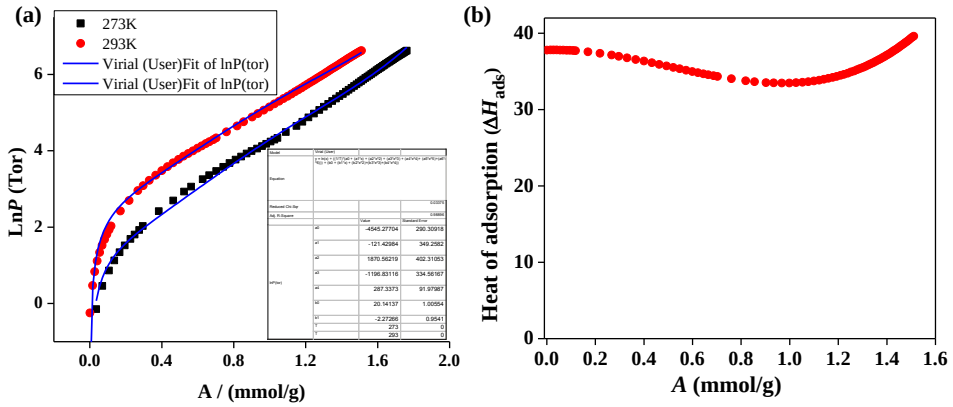

Figure 16: (a) Virial equation fitting of CO_2 adsorption isotherms of **2** at 293 and 273 K; (b) Plot of heat of adsoption (ΔH_{ads}) vs CO_2 loading.

5B.3.4 Computational study: Finding the adsorption sites in 2

After removal of guest molecules, compound **1** undergoes structural transformation; as we do not have any structural information of its desolvated phase, DFT calculations would not provide accurate insight of the CO_2 adsorption phenomena. Rather, we choose **2**, the rigid framework, to carry out density functional theory (DFT) based calculations to find out favourable binding sites. In order to find these sites, gas molecules were initially placed randomly inside the solvent removed framework of **2**. Geometry optimization of the gas loaded framework was carried out. Two favourable locations for CO_2 molecule, CO_2-I and CO_2-II were obtained. The former is near the $–NH_2$ group with its molecular axis passing through the bisector of amine, at a distance of 3.01 Å (Figure 17). The backbone angle of CO_2-I is marginally de*via*ted from linearity (177.7 °) suggesting a specific interaction between $–NH_2$ and CO_2-I. Electron density difference maps (i.e., the difference in electron density between the PCP with the gas molecule and that of the individual components – pure PCP and isolated gas molecule) over nitrogen of $–NH_2$ and carbon of CO_2-I indicates a moderate interaction of the quadrupole moment of CO_2-I with the lone pair of $–NH_2$ group (Figure 18). Positive difference map over one of the two oxygen atoms of CO_2 indicates a weak hydrogen bond formed with hydrogens of ligand bphz. The distances between O and H are 2.59, 2.79, 2.89 and 3.49 Å. The second CO_2 molecule (CO_2-II) is found to be present on top of bphz with its center at the midpoint between the aromatic ring and amino group, suggesting aromatic π interaction with CO_2 as shown in Figure 17. The distance between this midpoint and carbon of CO_2-II is 3.63 Å. It also interacts electrostatically with hydrogen atoms of the aromatic ring of bphz. The distances between O of CO_2-II and hydrogen atoms are 2.64, 2.89 and 3.13Å. Electron density difference map for this molecule is shown in Figure 18b which reveals two types of interactions: Lewis acid-base interaction where the carbon of CO_2-II which is electron deficient, loses some electronic charge to the aromatic ring and the weak hydrogen bonding between hydrogens of aromatic ring and oxygens of CO_2-II. Recently such aromatic $\pi\cdots CO_2$ interaction in PCP has been established by single crystal X-ray diffraction study.[33]

These two CO_2 molecules are also stabilized by a cooperative effect as is evident from the short distance (3.76 Å) between the carbon atom of CO_2–I and the oxygen atom of CO_2–II. This distance is comparable to that observed between two neighbouring CO_2 molecules in supercritical CO_2.[34] The angle between the backbone vectors of the two CO_2

molecules in the PCP is 59.5 ° while it is 70° in crystalline CO_2. This observation suggests that the dimer inside PCP is in a distorted T-shaped configuration, similar to that found in the crystalline phase and supercritical CO_2.[34] The interaction energy of CO_2 molecule with **2** is compared against the experimental heat of adsorptions. CO_2-I and CO_2-II molecules are interacting with the framework individually and give binding energies of 36.03 and 30.03 kJ/mol, respectively. When both these two molecules are present in **2**, the mean binding energy per molecule is calculated to be 33.94 kJ/mol. At low pressures, from the Boltzmann ratio, the most preferable binding site is the one that provides strong affinity for CO_2 molecule. So they prefer to bind near amino group (CO_2-I) (with an energy of 36.03 kJ/mol) which is comparable to that calculated from adsorption isotherms using the virial equation (37.7 kJ/mol). It is worth to mention that though there is an evident proof of $NH_2\cdots CO_2$ interaction and a moderate ΔH_{ads} value, we do not observe any distinct hysteresis in the adsorption isotherm. As it is a case of mere physiosorption, hysteresis is unlikely to occur[11b,11d-e] unless there is any structural transformation (rearrangement) which can act as barrier for gas molecules to diffuse out of the pores. In this case, compound **2** is rigid in nature and the observations found here are in line with the literature reports.[11b, 11d-e]

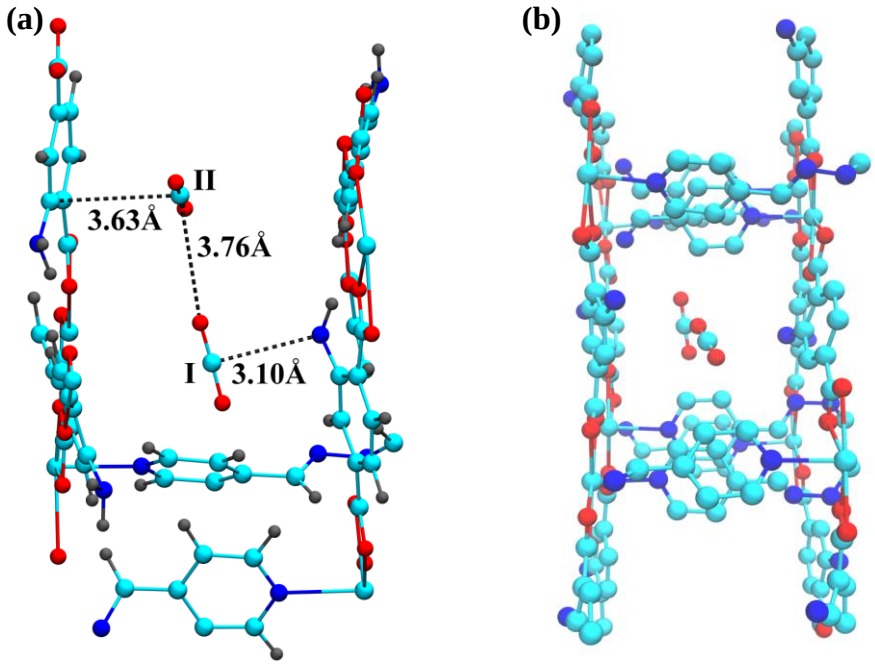

Figure 17: (a) Cooperativity between two adsorbed CO_2 molecules within framework **2**. Carbon of CO_2-I interacts with the lone pair of nitrogen of amino group and CO_2-II interacts with the π-cloud of benzene ring. Colour code: C, Cyan; H, Grey; N, Blue; O, Red; (b) View of the CO_2 molecules inside one pore of solvent removed **2**.

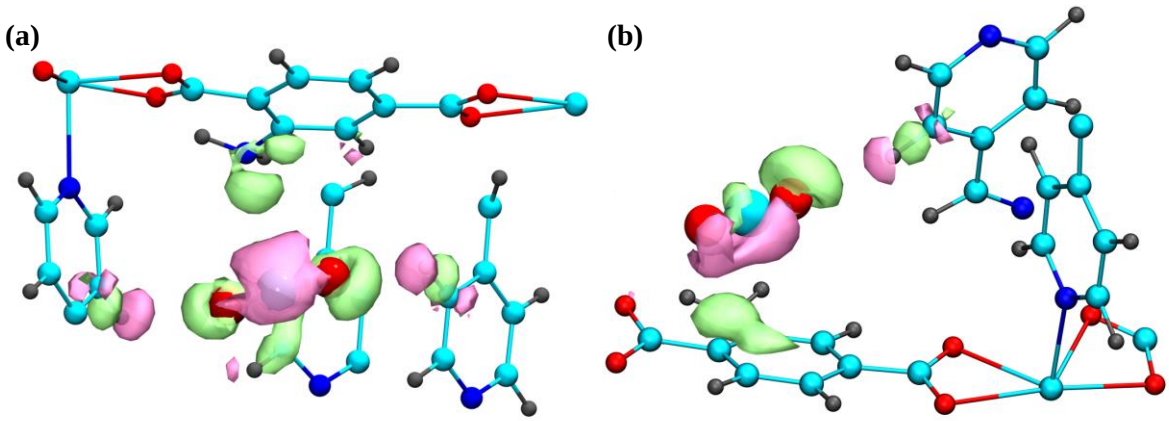

Figure 18: (a) Electron density difference maps for a) CO_2-I b) CO_2-II interacting with the PCP **2**, presented at isosurface values of 0.005 and 0.004 a. u. respectively. Only a portion of the PCP is shown for clarity. CO_2 molecules form weak hydrogen bonds with the PCP. Electron rich and deficient regions are shown in green and pink colours respectively. Colour code: C, Cyan; H, Grey; N, Blue; O, Red.

5B.3.5 Postsynthetic modification

As we could visualize the role of $–NH_2$ functional group from the DFT calculations, we also carried out an indirect experiment to establish its immense importance. We modified the $–NH_2$ group to $–NHCOCH_3$ group in a post-synthetic method and by doing so the polarity of the pore surface is altered. We obtained ~ 90 % conversion of **2** to $\{[Cd(NH_2\text{-bdc})_{0.1}(NHCOCH_3\text{-bdc})_{0.9}(bphz)_{0.5}]\cdot CHCl_3)\}_n$ (**2a**) as confirmed by ^{1}H-NMR spectroscopy (Figure 7). PXRD patterns of **2a** showed no distinct change compared to the parent compound **2** suggesting that the structure remains intact (Figure 19a). The CO_2 adsorption isotherm at 195 K showed interesting changes compared to the parent compound **2** (Figure 19b). The adsorption curve clearly indicates that up to relative pressure P/P_0 ~ 0.1, the uptake is not very sharp as that of the parent compound **2**; but in the high pressure range, CO_2 molecules enter into the pores and the uptake reaches a saturation amount of ~ 9 wt %. Heat of adsorption calculation using DR equation shows $q_{st,\phi}$ ~ 28 kJ/mol and BET surface area is 98 m^2/g which are lesser than those of **2**. Evidently absence of the strong Lewis base $–NH_2$ and less available space accounted for the low heat of adsorption and smaller uptake.

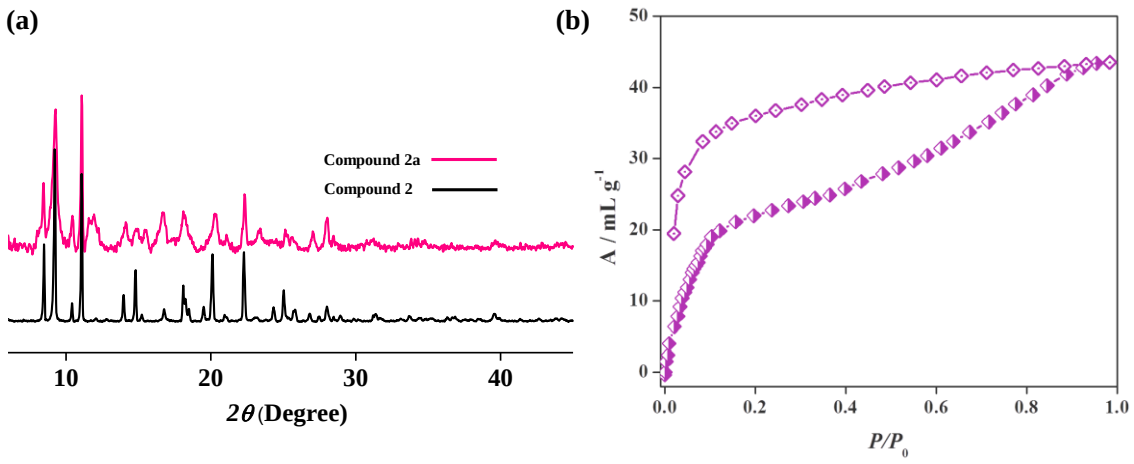

Figure 19: (a) PXRD patterns of compound **2** and **2a**; (b) CO_2 adsorption-desorption isotherm of postsynthetically modified **2** (**2a**) at 195 K.

5B.3.5 Knoevenagel condensation

Presence of pendent $–NH_2$ group, structural rigidity and high thermal stability of compound **2** encouraged us to carry out a base catalysed Knoevenagel condensation reaction. Prior to the catalytic reaction, we activated the catalyst by removing the guest DMF and water molecules from the pore and then carried out condensation of benzaldehyde derivatives (4-nitro and 4-chlorobenzaldehyde) with malononitrile using different solvents at 60 °C (Table 4, Figure 20-21). Using malononitrile and 4–nitro benzaldehyde, we observed ~ 99 % conversion within 6 h in acetonitrile but in methanol after 6 h, 85 % conversion was observed. Changing the solvent from non-protic to protic hampers the reaction rate. Reaction kinetics of malononitrile and nitro-benzaldehyde shows a very fast conversion within 2 h and ~ 99 % conversion is reached in 6 h (Figure 22a). Decreasing the reaction temperature to 40 °C decreases the conversion rate. We also observed excellent size selectivity by the catalyst as changing malononitrile to other substituent like methyl cyanoacetate. As the size increases, % conversion becomes only 41 and 52 % after 6 and 12 h, respectively (Table 4; Figure 22b). We have performed 5-6 catalytic cycles to see the efficiency of the catalyst and we observed no change in the conversion rate. Similar catalytic reactions with –CONH- functionalized PCPs have been reported by Kitagawa *et. al.* and Zhou *et. al.* and these show much slower conversion time (~ 12h) compared to our results.[14a,c] This is due to better diffusion of the reactants into the pores. But this higher diffusion of reactants also decreases the size selectivity in present case compared to the report by Kitagawa *et. al*. The PXRD pattern of the catalyst after 6 cycles of reaction was found to remain same as that of as-synthesized suggesting

high thermal and chemical stability of the framework (inset, Figure 22c). It is worth to mention, a reaction carried out using NH_2-bdc alone as a catalyst resulted negligible yield. Mixing of only malononitrile and 4–nitro benzaldehyde without any catalyst at 60 °C in acetonitrile does not yield any product.

Table 4: List of the substrates, reaction conditions and conversion achieved in catalytic reactions using desolvated compound **2** as a catalyst.

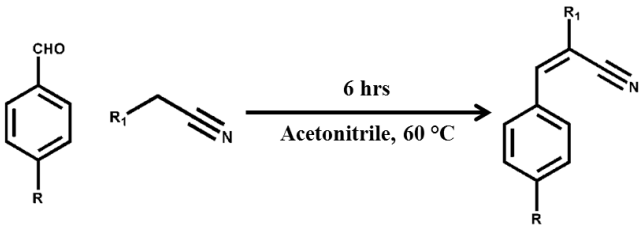

S. No.	R	R1	Temperature and solvent media	Time/hrs	Yield (%)
1	NO_2	CN	60 °C, Acetonitrile	6	~ 99
2	NO_2	CN	60 °C, Methanol	6 8	~ 85 ~ 98
3	NO_2	CN	40 °C, Acetonitrile	6 9	~ 81 ~ 99
4	NO_2		60 °C, Methanol	6 12	~ 41 ~ 52
5	Cl	CN	60 °C, Acetonitrile	6	~ 99
6	NO_2	CN	60 °C, Acetonitrile (Without Catalyst)	12	~ 0

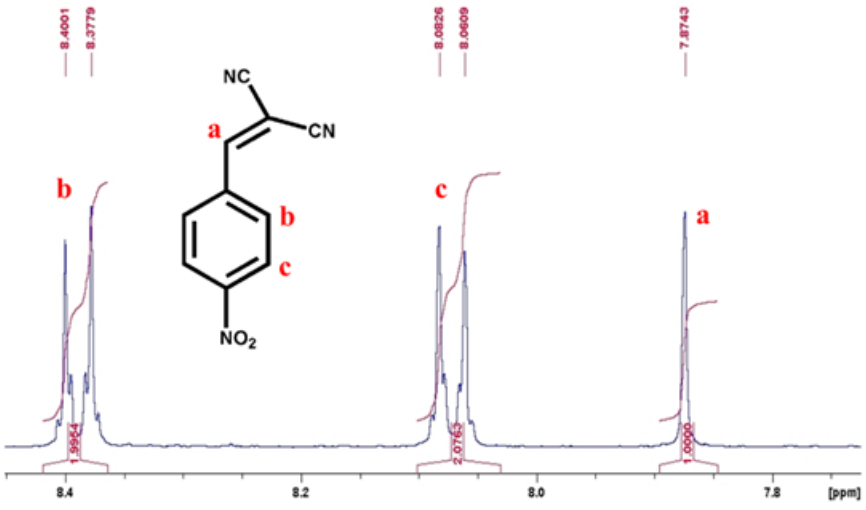

Figure 20: ^{1}H-NMR spectrum of recovered product (NO_2-derivative) after reaction.

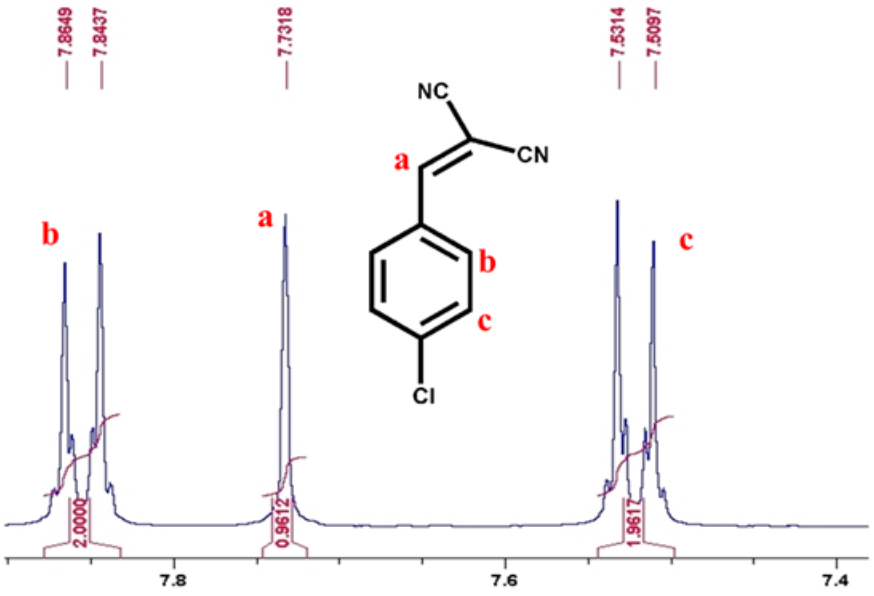

Figure 21: ^{1}H-NMR spectrum of recovered product (Cl-derivative) after reaction.

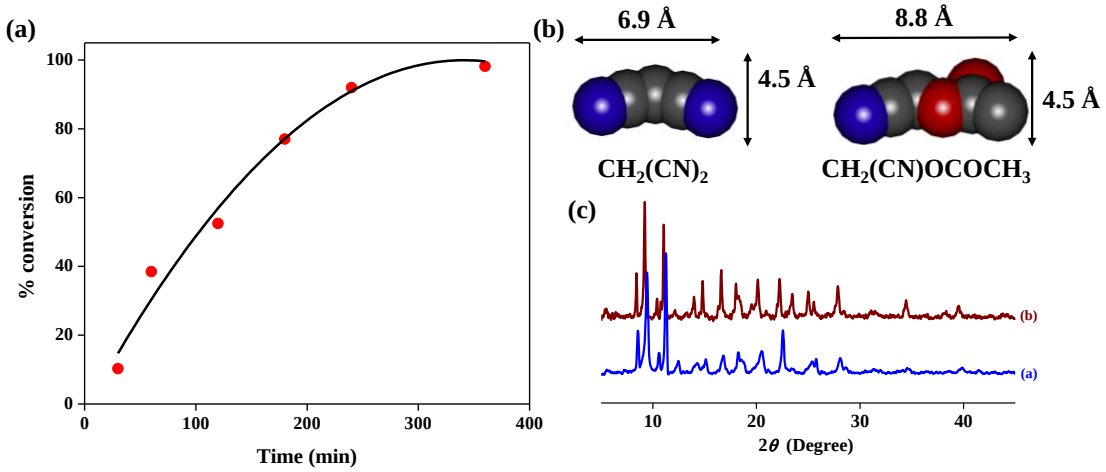

Figure 22: (a) Conversion (%) vs time (min) for Knoevenagel condensation reaction of NO_2-benzaldehyde and malononitrile at 60 °C in acetonitrile; (b) Molecular dimensions of the substrates used for Knoevenagel condensation; (c) PXRD patterns of compound **2**: (a) before catalysis, (b) after catalysis.

5B.4 Conclusions

In summary, two catenane supramolecular isomers of Cd^{2+} with 3D porous structures have been synthesized. Compound **1,** containing a paddle-wheel SBU shows structural flexibility upon guest removal but compound **2** is rigid in nature with μ-oxo bridge SBU. The origin of rigidity and flexibility arises from the orientation of the two interpenetrated nets in the framework controlled by different SBUs. Both the framework shows selective CO_2 uptake. **1** shows a two-step uptake profile with large hysteresis emphasizing the flexible nature of the framework. In contrast, **2** shows a type-I uptake

profile with moderate heat of adsorption (37.7 kJ/mol). DFT calculations further enlighten the $–NH_2\cdots CO_2$ and $CO_2\cdots CO_2$ cooperative interactions in the framework. Importance of $–NH_2$ group towards CO_2 capture was further realized through a postsynthetic modification of $–NH_2$ to $–NHCOCH_3$. Such modification drastically reduces the uptake amount and also binding energy. Compound **2** also acts as a very efficient base catalyst for Knoevenagel condensation reaction and shows size selectivity. The present study is significant as it displays elegant example of structural supramolecular isomerism with multifunctional properties; such as selective CO_2 uptake and catalysis.

5B.5 References

1. a) S. Kitagawa, R. Kitaura, S. –I. Noro, *Angew. Chem. Int. Ed.* **2004**, *43*, 2334; b) O. M. Yaghi, *Nature. Mater*. **2007**, *6*, 92.

2. a) A. Zukal, I. Dominguez, J. Mayerová, J. Cezka, *Langmuir*. **2009**, *25*, 10314; b) R. V. Siriwardane, M.S. Shen, E. P. Fisher, J. Losch, *Energy Fuels*. **2005**, *19*, 1153.

3. a) Y. Belmabkhout, A. Sayari, *Adsorption*. **2009**, *15*, 318; b) S. Kim, J. Ida, V. V. Guliants, J. Y. S. lin, *J. Phys. Chem. B.* **2005**, *109*, 6287; c) S. N. Kim, W. J. Son, J. S. Choi, W. S. Ahn, *Microporous Mesoporous. Mater*. **2008**, *116*, 394.

4. a) R. Banerjee, A. Phan, B. Wang, C. Knobler, H. Furukawa, M. O'Keeffe, O. M. Yaghi, *Science*. **2008**, *319*, 939; b) H. Hayashi, A. P. Côté, H. Furukawa, M. O'Keeffe, O. M. Yaghi, *Nat. Mater*. **2007**, *6*, 501; c) J. A. R. Navarro, E. barea, A. Rodríguez-Diéguez, J. M. Salas, C. O. Ania, J. B. Parra, N. Masciocchi, S. Galli, A. Sironi, *J. Am. Chem. Soc*. **2008**, *130*, 3978; d) F. Debatin, A. Thomas, A. Kelling, N. Heddin, Z. Bacsik, I. Senkovska, S. Kaskel, M. Junginger, H. Müller, U, Schilde, C. Jäger, A. Friedrich, H.-J. Holdt, *Angew. Chem. Int. Ed*. **2010**, *49*, 1258; e) J. An, S. J. Geib, N. L. Rosi, *J. Am. Chem. Soc*. **2008**, *132*, 38; f) R. Vaidhyanathan, S. S. Iremonger, K. W. Dawson, G. K. H. Shimizu, *Chem. Comm.* **2009**, *35*, 5230; g) C. A. Fernandez, J. Liu, P. K. Thallapally, D. M. Strachan, *J. Am. Chem. Soc*. **2012**, *134*, 9046; h) L. Pan, D. H. Olson, L. R. Ciemnolonski, R. Heddi, J. li, *Angew. Chem. Int. Ed*. **2006**, *45*, 616; i) J. Y. Lee, D. H. Olson, L. Pan, T. J. Emge, J. Li, *Adv. Funct. Mater*. **2007**, *17*, 1255; j) J. R. Li, R. J. Kuppler, H.-C. Zhou, *Chem. Soc. Rev*. **2009**, *38*, 1477; k) L. J. Murray, M. Dincă, J. R. Long, *Chem. Soc. Rev*. **2009**, *38*, 1294.

5. a) J. Y. Lee, O. K. Farha, J. Roberts, K. A. Scheidt, S. T. Nguyen, J. T. Hupp, *Chem. Soc. Rev*. **2009**, *38*, 1450; b) R. K. Das, A. Aijaz, M. K. Sharma, P. Lama, P. K. Bharadwaj, *Chem. Eur. J*. **2012**, *18*, 6866.

6. a) M. Kim, J. F. Cahill, H. Fei, K. A. Prather, S. M. Cohen, *J. Am. Chem. Soc*. **2012**, *134*, 18082; b) T. K. Maji, R. Matsuda, G. Mostafa, S. Kitagawa, *Nature. Mater*. **2007**, *6*, 142; c) T. K. Prasad, D. H. Hong, M. P. Suh, *Chem. Eur. J*. **2010**, *16*, 14043.

7. a) B. Chen, S. Xiang, G. Qian, *Acc. Chem. Res*. **2010**, ***43***, 1115; b) M. D. Allendorf, C. A. Bauer, R. K. Bhakta, R. J. T. Houk, *Chem. Soc. Rev*. **2009**, *38*, 1330; c) R. Haldar, K. V. Rao, S. J. George, T. K. Maji, *Chem. Eur. J*. **2012**, *18*, 5848; d) K. Jayaramulu, P. Kanoo, S. J. George, T. K. Maji, *Chem. Commun*. **2010**, *49*, 7906; e) C. A. Kent, B. P. Mehl, L. Ma, J. M. Papanikolas, T. J. Meyer, W. Lin, *J. Am. Chem. Soc*. **2010**, *132*, 12767.

8. a) P. Kanoo, K. L. Gurunatha, T. K. Maji, *Cryst. Growth. Des*. **2009**, *9*, 4147; b) P. Kanoo, K. L. Gurunatha, T. K. Maji, *J. Mater. Chem*. **2010**, *20*, 1322; c) J. J. Perry, J. A. Perman, M. J. Zaworotko, *Chem. Soc. Rev*. **2009**, *38*, 1400; d) J. P. Zhang, S. Kitagawa, *J. Am. Chem. Soc*. **2008**, *130*, 907.

9. a) P. K. Thallapally, J. Tian, M. R. Kishan, C. A. Fernandez, S. J. Dalgarno, P. B. McGrail, J. E. Warren, J. L. Atwood, *J. Am. Chem. Soc*. **2008**, *130*, 16842; b) K. L. Mulfort, O. K. Farha, C. D. Malliakas, M. G. Kanatzidis, J. T. Hupp, *Chem. Eur. J*. **2010**, *16*, 276; c) J. –H. Wang, M. Li, D. Li, *Chem. Sci*. **2013**, *4*, 1793.

10. a) R. Haldar, T. K. Maji, *CrystEnggCommun*. **2012**, *14*, 684; b) W. Yang, A. J. Davies, X. Lin, M. Suyetin, R. Matsuda, A. J. Blake, C. Wilson, W. Lewis, J. E. Parker, C. C. Tang, M. W. George, P. Hubberstay, S. Kitagawa, H. Sakamoto, E. Bichoutskaia, N. R. Champness, S. Yang, M. Schroder, *Chem. Sci*. **2012**, *3*, 2993; c) P. Kanoo, R. Matsuda, M. Higuchi, S. Kitagawa, T. K. Maji, *Chem. Mater*. **2009**, *21*, 5860; d) H. –L. Jiang, T. Makal, H. –C. Zhou, *Coord. Chem. Rev*. **2013**, *15*, 2232.

11. a) K. Sumida, D. L. Rogow, J. A. Mason, T. M. McDonald, E. D. Bloch, Z. R. Herm, T. –H. Bae, J. R. Long, *Chem. Rev*. **2012**, *112*, 724; b) R. Vaidhyanathan, S. S. Iremonger, G. K. H. Shimizu, P. G. Boyd, S. Alavi, T. K. Woo, *Science*, **2010**, *330*, 650; c) C. M. Nagaraja, R. Haldar, T. K. Maji, C. N. R. Rao, *Cryst. Growth. Des*. **2012**, *12*, 975; d) W. Lu, J. P. Scully. D. Yuan, R. Krishna, Z. Wei, H. –C. Zhou, *Angew. Chem. Int. Ed*. **2012**, *51*, 1; e) T. M. McDonald, W. R. Lee, J. A. Mason,B. M. Wiers, C. S. Hong, J. R. Long, *J. Am. Chem. Soc.* **2012**, *134*, 7056; f) T. M. McDonald, D. M. D'Alessandro, R. Krishna, J. R. Long, *Chem. Sci.* **2011**, *2*, 2022.

12. a) T. Ahnfeldt, N. Guillou, D. Gunzelmann, I. Margiolaki, T. Loiseau, G. Férey, J. Senker, N. Stock, *Angew. Chem. Int. Ed*. **2009**, *48*, 5163; b) X. -Y. Chen, B. Zhao, W. Shi, J. Xia, P. Cheng, D. –Z. Liao, S. –P. Yan, Z. –H. Jiang, *Chem. Mater*. **2005**, *17*, 2866; c) A. L. Grzesia, F. J. Uribe, N. W. Ockwig, O. M. Yaghi, A. J. Matzger, *Angew. Chem. Int. Ed*. **2006**, *45*, 2553; d) X. Si, C. Jiao, F. Li, J. Zhang, S. Wang, S. Liu, Z. Li, L. Sun, F. Xu, Z. Gabelica, C. Schick, *Energy Environ Sci*. **2011**, *4*, 4522; e) J. An, S. J. Geib, N. L. Rosi, *J. Am. Chem. Soc*. **2010**, *132*, 38; f) Y, Zhao, H. Wu, T. J. Emge, Q, Gong, N, Nijem, Y. S. Chabal, L. Kong, D. C. Langreth, H. Liu, H. Zeng, J. Li, *Chem. Eur. J*. **2011**, *17*, 5101; g) Z. Zhang, Y, Zhao, Q, Gong, J. Li, *Chem Commun*. **2013**, *49*, 653.

13. a) S. M. Cohen, *Chem. Soc. Rev*. **2012**, *112*, 970; b) K. K. Tanabe, C. Allen, S. M. Cohen, *Angew. Chem. Int. Ed*. **2010**, *49*, 9730; c) K. K. Tanabe, S. M. Cohen, *Chem. Soc. Rev*. **2011**, *40*, 498.

14. a) S. Hasegawa, S. Horike, R. Matsuda, S. Furukawa, K. Mochizuki, Y. Kinoshita, S. Kitagawa, *J. Am. Chem. Soc*. **2007**, *129*, 2607; b) Y. K. Hwang, D. –Y. Hong, J. –S. Chang, S. H. Jhung, Y. –K. Seo, J. Kim, A. Vimont, M. daturi, C. Serre, G. Férey, *Angew. Chem. Int. Ed*. **2008**, *47*, 4144; c) J. Park, J. –R. Li, Y. –P. Chen, J. Yu, A. A. Yakovenko, Z. U. Wang, L.-B. Sun, P. B. Balbuena, H. –C. Zhou, *Chem. Commun*. **2012**, *48*, 9995.

15. a) A. Hazra, P. Kanoo, G. Mostafa, T. K. Maji, *Chem Commun*. **2011**, *47*, 538; b) C. D. Wu, A. Hu, L. Zhang, W. Lin, *J. Am. Chem. Soc*. **2005**, *127*, 8940; c) S. Su, Y. Zhang, M. Zhu, X. Song, S. Wang, S. Zhao, S. Song, X. Yang, H. Zhang, *Chem Commun*. **2012**, *48*, 11118; d) R. –Q. Zou, H. Sakurai, Q. Xu, *Angew. Chem. Int. Ed*. **2006**, *45*, 2542.

16. A. R. Kennedy, K. G. Brown, D. Graham, J. B. Kirkhouse, M. Kittner, C. Major, C. J. Mchugh, P. Murdoch, E. E. Smith, *New. J. Chem*. **2005**, *26*, 826.

17. SMART (V 5.628), SAINT (V 6.45a), XPREP, SHELXTL; Bruker AXS Inc.: Madison, Wisconsin, USA, **2004**.

18. G. M. Sheldrick, Siemens area detector absorption correction program; University of Götingen, Germany, **1994**.

19. A. Altomare, G. Cascarano, C. Giacovazzo, A. Gualaradi, *J. Appl. Crystallogr*. **1993**, *26*, 343.

20. G. M. Sheldrick, SHELXL-97, Program for the crystal structure solution and refinement; University of Götingen, Germany, **1997**.

21. A. L. Spek. *J. Appl. Crystallogr*. **2003**, *36*, 7.

22. L. J. Farrugia, WinGX-A, Windows program for crystal structure analysis. *J. Appl. Crystallogr*. **1999**, *32*, 837.

23. J. VandeVondele, M. Krack, F. Mohamed, M. Parrinello, T. Chassaing, J. Hutter, *Comput. Phys. Commun*. **2005**, *167*, 103.

24. S. Goedecker, M. Teter, J. Hutter, *Phys. Rev. B.* **1996**, *54*, 1703.

25. J. P. Perdew, K. Burke, M. Ernzerhof, *Phys. Rev. Lett.* **1996**, *77*, 3865.

26. S. J. Grimme, *Comput. Chem.* **2006**, *27*, 1787.

27. W. Humphrey, A. Dalke, K. Schulten, *J. Mol. Graphics Modell*. **1996**, *14*, 33

28. The sizes of the channels were calculated considering the van der Waals radii of the atoms.

29. a) S. Yang, L. Liu, J. Sun, K. M. Thomas, A. J. Davies, M. W. George, A. J. Blake, A. H. Hill, A. N. Fitch, C. C. Tang, M. Schröder, *J. Am. Chem. Soc*. **2013**, *135*, 4954; b) M. K. Sharma, P. K. Bharadwaj, *Inorg. Chem*. **2011**, *50*, 1889; c) D. Tanka, K. Nakagawa, M. Higuchi, S. Horike, Y. Kubota, T. C. Kobayashi, M. Takata, S. Kitagawa, *Angew. Chem. Int. Ed*. **2008**, *47*, 3914.

30. M. M. Dubinin, *Chem. Rev*. **1960**, *60*, 235.

31. C. E. Webster, R. S. Drago, M. C. Zerner, *J. Am. Chem. Soc*. **1998**, *120*, 5509.

32. a) O. Talu, *Adv. Colloid Interface Sci*. **1998**, *227*, 76; b) J. Purewal, Hydrogen adsorption by alkali metal graphite intercalation compounds. Ph.D. Dissertation, California Institute of Technology, Pasadena, CA, **2010**.

33. A. M. Plonka, D. Banerjee, W. R. Woerner, Z. Zhang, N. Nijem, Y. J. Chabal, J. Li, J. B. Parise, *Angew. Chem. Int. Ed*. **2012**, *51*, 1.

34. M. Saharay, S. Balasubramanian, *J. Phys. Chem. B.* **2007**, *111*, 387.

Chapter 6

Selective adsorption of O_2 in a highly flexible porous solid of Cd^{2+}: ^{113}Cd NMR as a probe in guest induced geometry change and structural modifications

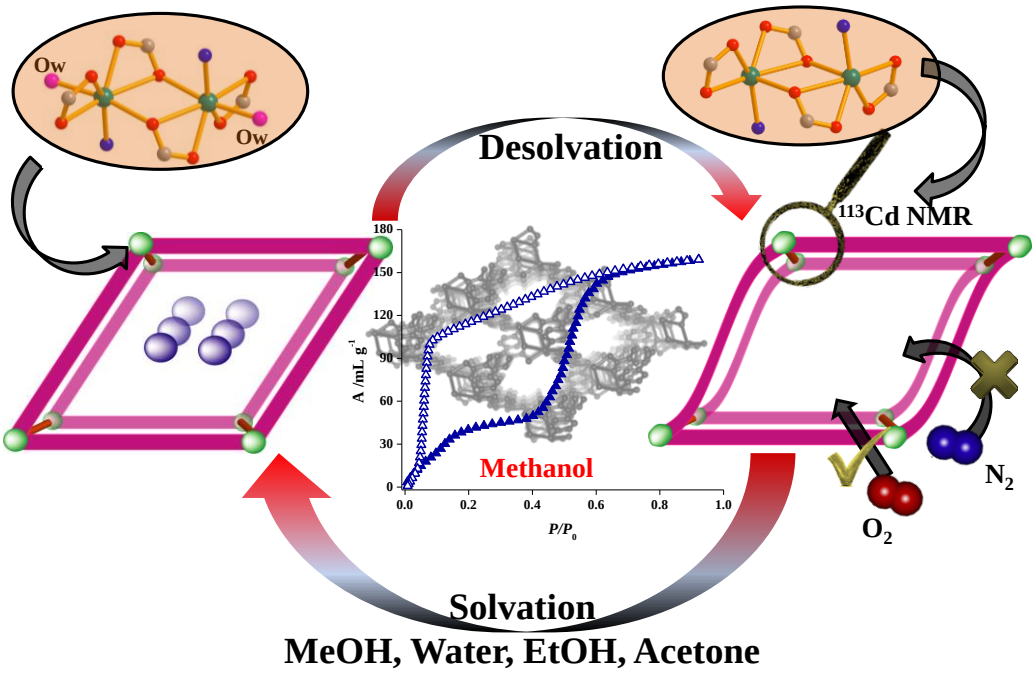

Summary

Two new isomorphous 3D porous coordination polymers, $\{[Cd(bpe)_{0.5}(bdc)(H_2O)]\cdot EtOH\}_n$ (**1**) and $\{[Cd(bpe)_{0.5}(bdc)(H_2O)]\cdot 2H_2O\}_n$ (**2**) (bpe = 1,2-bis(4-pyridyl)ethane and bdc = 1,4-benzenedicarboxylic acid) were synthesized by altering the solvent media. Both the structures contain 1D channels filled with metal coordinated and guest solvent molecules and desolvated frameworks show significant changes in the structure. But exposure to the solvent vapors (water and methanol) reverts back to the as-synthesized structure and thus a reversible flexible nature of the structure was comprehended. Further investigation was done by solid state ^{113}Cd NMR spectroscopy which unambiguously advocates the transformation "pentagonal-bipyramidal CdO_6N → octahedral CdO_5N" geometry in the desolvated state. The flexibility was further reinforced from the CO_2 adsorption profiles (195 and 273 K) which show stepwise uptake. Acetylene adsorption at 195 K also shows gate opening type uptake profile. Moreover, a high selectivity for O_2 over N_2 at 77 K was realized. The framework exhibits interesting solvent vapour adsorption behaviour depending upon size, polarity and coordination ability.

1. R. Haldar, M. Inukai, S. Horike, K. Uemura, S. Kitagawa, T. K. Maji, Submitted

6.1 Introduction

There is an upsurge of interest in the design and synthesis of porous coordination polymers (PCPs) or metal-organic frameworks (MOFs) with remarkable functions such as high degree of gas storage and seperation,[1] heterogeneous catalysis[2] ion exchange,[3] molecular sensing[4a-d] and other optical properties.[4e-j] A large number of rigid and stable functional PCPs have been accomplished by precisely designing the bridging ligands (shape, length, symmetry, and flexibility) and utilizing the versatile coordination of the metal ions.[5] Apart from H-bonding, $\pi\cdots\pi$ interactions also play crucial role to determine the final superstructure.[6]

In general, PCPs consist of repeated building units and provide uniform open spaces filled with guest molecules. Due to such regularities, in PCPs the extensive cooperativity would be expected among the molecules throughout the crystal, such that the small distortion/change around a metal center induces the overall framework's rearrangements in a well-concerted fashion to maintain its macroscopic integrity. Several numbers of unique framework transformation induced by adsorption/desorption of guest molecules have been reported and highlighted[7] and in few cases direct determination of the second structure through single-crystal-to-single-crystal structural transformation clarified the whole phenomena.[8] Although, there are difficulties to interpret the phenomenon related to guest induced structural transformation without proper structural information of second phases.[9] Nevertheless, the spectroscopy measurements for the later cases would give the information about the deformed metal or change in the organic linker. On the other hand, separation of gases, particularly O_2 from air is useful for oxyfuel combustion which is an alternative of fossil fuels. On industrial scale cryogenic methods are employed to separate O_2, but those are not cost effective. Hence a cheaper adsorptive based separation is in demand and PCP can be a potential candidate for the same. Till date there are very few reports those study O_2 *vs* N_2 selectivity in PCPs.[10] Based on these backgrounds, we focused on constructing porous frameworks by selecting Cd^{2+} as a metal node. Taking into account the d^{10} electronic configuration and flexible and versatile coordination geometry of Cd^{2+}, it was aimed to synthesize microporous framework of Cd^{2+} using mixed linker system. Here, the solid state ^{113}Cd NMR spectroscopy is exploited as a probe to understand the changes in Cd^{2+} environment during guest induced structural change. This chapter reports the synthesis, structural characterization, unique sorption properties and selectivity of three-dimensional (3D)

microporous frameworks, $\{[Cd(bpe)_{0.5}(bdc)(H_2O)]\cdot EtOH\}_n$ (**1**) and $\{[Cd(bpe)_{0.5}(bdc)(H_2O)]\cdot 2H_2O\}_n$ (**2**) (bpe = 1,2-bis(4-pyridyl)ethane and bdc = 1,4-benzenedicarboxylic acid). In both **1** and **2**, Cd^{2+} geometry shows the reversible change from pentagonal bipyramidal (hepta-coordinate, unsaturated) to octahedral (hexa-coordinate, saturated) upon desolvation and resolvation, respectively. The change in geometry of Cd^{2+} influences the pore deformation which is realized through XRD and solid state ^{113}Cd NMR studies. Interestingly, we observed that desolvated structure shows highly selective adsorption of O_2 over N_2 at 77 K and also a two-step uptake of CO_2 gas at 195 K. Such O_2 selectivity and also the unique CO_2 adsorption is very important in many aspects of seperation techniques.[11] It also shows gated adsorption profile for acetylene at 195 K. Moreover, we observed unique solvent vapour (H_2O and MeOH) adsorption profiles and also size exclusion effect of the desolvated framework.

6.2 Experimental section

6.2.1 Materials

All the reagents and solvents employed were commercially available and used as supplied without further purification. $Cd(ClO_4)_2\cdot H_2O$, 1,2-bis(4-pyridyl)ethane were obtained from the Aldrich Co, and Benzene-1,4-dicarboxylic acid was obtained from Tokyo Kasei Industrial.

6.2.2 Physical measurements

Elemental analyses were carried out on a Flash EA 1112 series, Thermo Finnigan instrument. Thermal gravimetric analysis (TG) was carried out with a Rigaku Instrument TG8120 in nitrogen atmosphere. X-ray powder diffraction (XRPD) data were collected on a Rigaku RINT-2200HF diffractometer with Cu-Kα radiation.

6.2.3 Synthesis of compound $\{[Cd(bpe)_{0.5}(bdc)(H_2O)]\cdot EtOH\}_n$ (1)

A 50 mL aqueous solution of Cd^{2+} was prepared by dissolving $Cd(ClO_4)_2\cdot H_2O$ (1 mmol, 0.311 g), and 50 mL ligand solution was prepared by mixing the 25 mL ethanol solution of bpe (0.5 mmol; 0.91 g) and 25 mL aqueous solution of Na_2bdc (1 mmol; 0.210 g). Then 2 mL of the ligand solution was carefully layered above the 2 mL metal solution using the 0.5 mL buffer solution (H_2O : EtOH = 2:1 (= v/v)). The colorless square shaped

crystals suitable for X-ray single crystal structure determination were obtained after one month. The crystals were separated and washed with MeOH and H_2O (= 1:1) mixture and dried (Yield 80 %). Elemental analysis calculated for $C_{16}H_{18}CdNO_6$: C, 44.40; H, 4.16; N, 3.23 Found: C, 43.20; H, 3.67; N, 3.23.

6.2.4 Synthesis of compound $\{[Cd(bpe)_{0.5}(bdc)(H_2O)].2H_2O\}_n$ (2)

The compound **2** was prepared adopting the same procedure of **1**, by changing the MeOH solvent instead of ethanol. Yield: 70 %. Elemental analysis calculated for $C_{14}H_{16}CdNO_7$: C, 42.42; H, 3.78; N, 3.33 Found: C, 41.78; H, 3.63; N, 4.11.

6.2.5 Adsorption measurements

The adsorption isotherm of N_2 (77 K), H_2 (77 K), C_2H_2 (195 K), CO_2 (195 K), and different solvent vapours (H_2O, MeOH, EtOH, Me_2CO and THF) were measured using BELSORP-18-Plus volumetric adsorption equipment from BEL, Osaka, Japan. In the sample chamber (17.5 mL) maintained at T (0.03 K was placed the adsorbent sample (100-150 mg), which had been prepared at 423 K for **1** and 383 K for **2** and 10^{-1} Pa for about 5 h prior to measurement of the isotherms. The adsorbate was placed into the sample tube, and then the change of the pressure was monitored and the degree of adsorption was determined by the decrease of the pressure at the equilibrium state. All operations were computer-controlled and automatic. Helium gas at a certain pressure was introduced in the gas chamber and was allowed to diffuse into the sample chamber by opening a valve. The change in pressure allowed an accurate determination of the volume of the total gas phase. The complexation was monitored in a similar manner by using a guest vapor in place of helium. The amount of guest adsorbed was calculated readily from pressure difference (P_{cal}-P_e), where P_{cal} is the calculated pressure with no guest adsorption and P_e is the observed equilibrium pressure. All operations were computer-controlled and automatic.

6.2.6 Solid state NMR spectroscopy

All NMR experiments were carried out on a Bruker ADVANCE 400 MHz spectrometer operating at resonance frequency of 88.754 MHz for ^{113}Cd at room temperature. A 7 mm MAS probe was used at spinning speeds of 6 kHz. Cross-polarization magic-angle spinning (CPMAS) method was used to improve the sensitivity

and resolution of the spectra. A 2 ms contact time for CP and a recycle delay of 5 second were used. ^{113}Cd chemical shifts were referenced indirectly to $Cd(NO_3)_2 \cdot 4H_2O$ (-102.2 ppm).

6.2.7 X-ray Crystallography

For each of **1** and **2**, a suitable single crystal was mounted on a glass fiber and coated with epoxy resin, and X-ray data collection was carried out on a Rigaku Mercury diffractometer with graphite-monochromated Mo Kα radiation (λ = 0.71069 Å) and a CCD 2D detector. In both cases the sizes of the unit cells were calculated from the reflections collected on the setting angles of seven frames by changing 0.5° for each frame. Three different settings were used and were changed by 0.5°/frame, and intensity data were collected with a scan width of 0.5°. Empirical absorption correction by using REQABA was performed for all data in both cases.[12] Both the structures of **1** and **2** were solved by direct methods by using the SIR-97 program[13] and expanded by using Fourier techniques.[14] All calculations were with the teXsan crystallographic software package from Molecular Structure Corporation.[15] For both the compounds, the non-hydrogen atoms were refined anisotropically and all hydrogen atoms placed in the ideal positions. For compound **1** the ethanol guest molecule atoms (O6, C15 and C16) and for compound **2** the H_2O molecules (O6 and O7) were refined isotropically. Potential solvent accessible area and void space were calculated using the PLATON multipurpose crystallographic software.[16] All crystallographic and refinement parameters for both complexes are summarized in Table 1. Selected bond lengths and angles for **1** and **2** are given in Table 2-3, respectively.

6.3 Results and discussion

6.3.1 Structural description of $\{[Cd(bpe)_{0.5}(bdc)(H_2O)]\cdot EtOH\}_n$ (1) and $\{[Cd(bpe)_{0.5}(bdc)(H_2O)]\cdot 2H_2O\}_n$ (2)

Single crystal X-ray diffraction analysis demonstrated that compound **1** crystallizes in triclinic *P*ī space group and is a 3D porous coordination polymer containing hepta-coordinated Cd^{2+} centers (Figure 1, Table 1). Each Cd^{2+} metal center is connected to three different bdc linkers through carboxylate oxygen atoms (O2, O3, O4, O5), one bpe (N1), and one H_2O molecule (O1), residing in a distorted pentagonal

bipyramidal environment (Figure 1). The Cd^{2+}–O and Cd^{2+}–N bond lengths are in the range of 2.273(5)–2.672(6) Å and 2.283(5) Å, respectively (Table 2). The degree of distortion from an ideal pentagonal bipyramidal geometry are reflected in the *transoid* and *cisoid* angles which are 133.09(9) - 169.91(9)° and 51.90(9)-114.12(9)°, respectively. The deviation of Cd^{2+} from the mean plane formed by the equatorial atoms is 0.311(2) Å and maximum deviation of equatorial oxygen atom is 0.803(1) Å. Interestingly, the carboxylate group of one of the bdc linkers act as chelating bidentate ligand and the other one functions as chelating as well as μ-oxo bridging. Such type of ligation creates a $Cd_2(\mu\text{-}O)_2$ cluster, acting as a secondary building unit (SBU) in the structure. Each of these SBU is connected to four other SBUs by four bdc linkers to generate two dimensional rectangular sheets lying on the crystallographic *ab* plane (Figure 2a). Such 2D sheets are connected by the bpe linkers to form a 3D microporous framework having one dimensional channels along *c*-axis (dimension is 5.4 × 4.4 $Å^2$) (Figure 2b-c).[17] These 1D channels are occupied by the ethanol molecules which are in close proximity to the coordinated (O1) water molecules and thus form strong H-bonds (O1(w)---O6(EtOH) = 2.717(7) Å) (Figure 2d). The H-bonding interactions plays very essential role for the overall conformation and stability of the 3D microporous framework. Void volume calculated after removal of the coordinated and guest solvent molecules were found to be 22.0 %[16] of total cell volume. Topology analysis by TOPOS shows bimodal (2,6)-connected net with *Schläfi* symbol $\{8^{12}.12^3\}\{8\}3$ (Figure 2e).

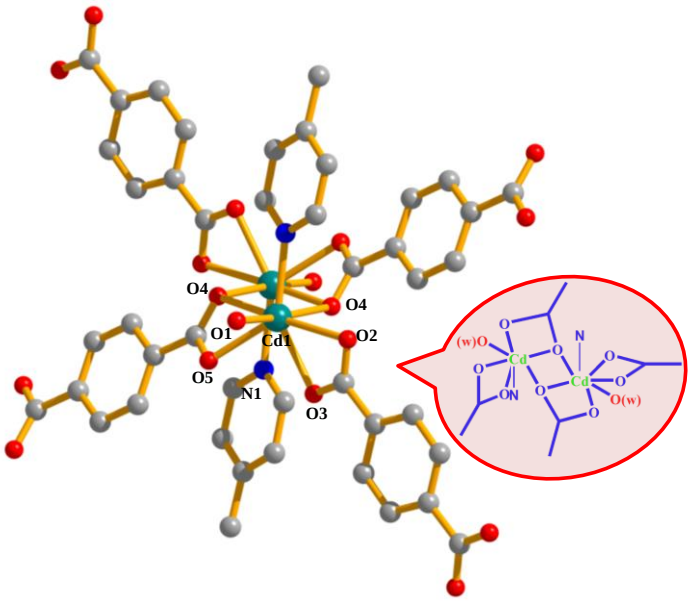

Figure 1: Coordination environment of Cd^{2+} metal center in compound **1**; inset figure showing the secondary building units.

Compound **2** is iso-structural to compound **1**, having identical SBU. The microporous channels of **2** are identical to that of **1** but the guest ethanol molecule is replaced by two water molecules (Figure 3). The guest H_2O molecules are H-bonded to O1w of the wall (O1w···O(H_2O) = 2.701(14) Å) (Figure 3). The void space calculated after removal of coordinated and guest water molecules is 22.0 %,[16] identical to that of compound **1**.

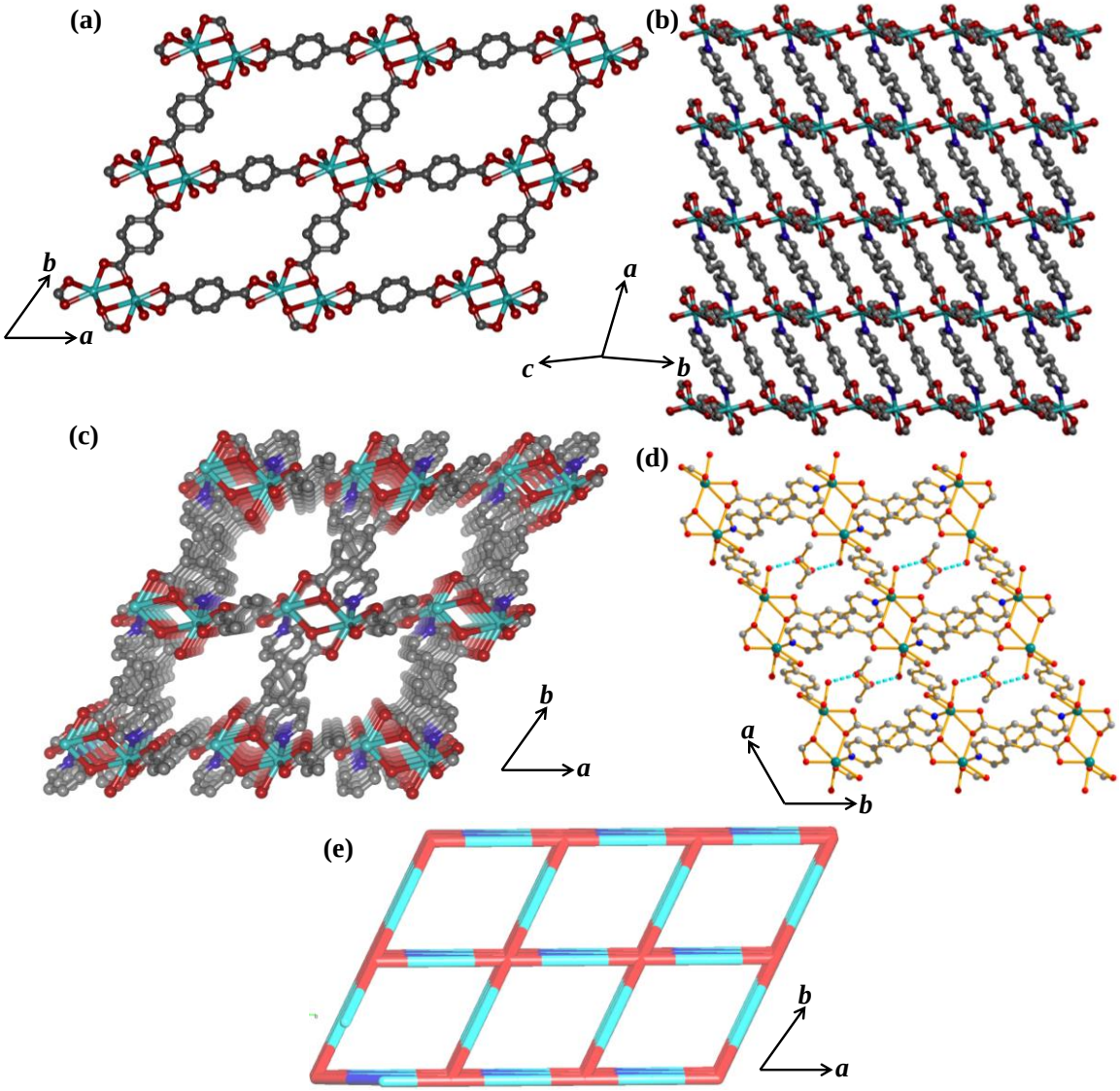

Figure 2: Structural details of **1**: (a) View of the 2D sheet on *ab* plane; (b) View of the bpe connected layers; (c) 1D channels along *c*-direction; (d) View of hydrogen bonding interactions between metal coordinated O1 and hydrogens of O6 from ethanol molecules. (Dotted cyan bonds represent hydrogen bonds); (e) 2,6-connected net along *c*-direction.

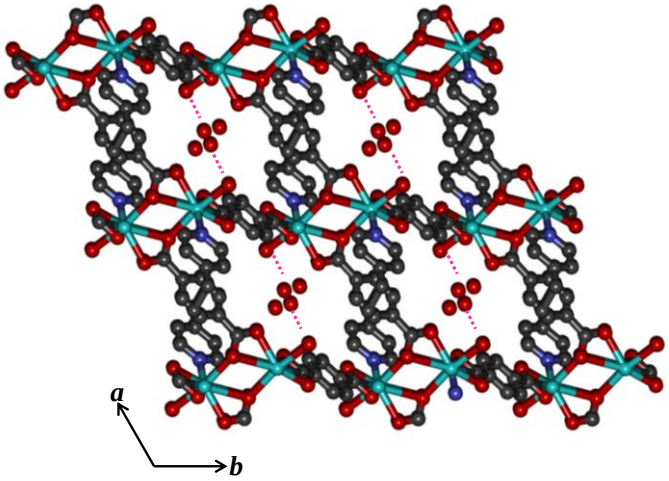

Figure 3: View of hydrogen bonded guest water molecules in compound **2** along *c*-direction (Hydrogen bonds shown in dotted pink lines).

Table 1: Crystal data and structure refinement parameters of compound **1** and **2**.

Parameters	**1**	**2**
Empirical formula	C_{16} $H_{19}CdNO_6$	$C_{14}H_{16}CdNO_7$
M	433.8	422.66
Cryst. system	Triclinic	Triclinic
space group	*P*ī (No. 2)	*P*ī (no. 2)
***a* (Å)**	9.75(2)	9.45(3)
***b* (Å)**	9.88(2)	9.75(2)
***c* (Å)**	9.88(1)	10.29(2)
α °	90.36(3)	96.11(3)
β °	92.73(3)	90.40(9)
γ °	117.33(5)	116.54(8)
***V* (Å^3)**	4381.5(7)	842(4)
Z	2	2
***T*(K)**	293	293
***λ* (Mo K$_α$)**	0.71073	0.71073
***D*$_c$ (g cm^{-3})**	1.703	1.651
***μ* (mm^{-1})**	1.325	0.329
***θ*$_{max}$ (deg)**	27.5	27.5
total data	9279	4680
unique reflection	1249	4578
***R*$_{int}$**	0.040	0.067
data [*I* > 2σ(*I*)]	3195	2374
***R*^{a}**	0.0276	0.0479
***R*$_w$^{b}**	0.0311	0.0642

GOF	0.83	0.96

^{a} $R = \Sigma||F_o| - |F_c||/\Sigma|F_o|$. ^{b} $R_w = [\Sigma\{w(F_o^2 - F_c^2)^2\}/\Sigma\{w(F_o^2)^2\}]^{1/2}$

Table 2: Bond length (Å) and angle (°) table for compound **1**.

Cd1-O1	2.319(5)	Cd1-O2	2.273(5)
Cd1-O3	2.502(6)	Cd1-O4	2.416(6)
Cd1-N1	2.283(5)	Cd1-O4_b	2.672(6)
O1-Cd1 -O2	95.78(10)	O1-Cd1-O3	78.62(8)
O1-Cd1-O4	169.91(9)	O1-Cd1-N1	90.61(10)
O1-Cd1-O4_b	114.12(9)	O1-Cd1-O5_b	83.18(10)
O2-Cd1-O3	54.55(10)	O2-Cd1-O4	85.12(10)
O2-Cd1-N1	147.70(12)	O2-Cd1-O4_b	120.54(10)
O2-Cd1-O5_b	85.25(11)	O3-Cd1-O4	93.89(9)
O3-Cd1-N1	96.24(10)	O3-Cd1-O4_b	167.24(8)
O3-Cd1-O5_b	133.09(9)	O4-Cd1-N1	83.44(10)
O4-Cd1-O4_b	73.55(9)	O4-Cd1-O5_b	106.92(10)
O4_b-Cd1-N1	84.72(10)	O5_b-Cd1-N1	127.00(10)
O4_b-Cd1-O5_b	51.90(9)		

b = -1-x,-1-y,-z

Table 3: Bond length (Å) and angle (°) table for compound **2**.

Cd1-O1	2.346(10)	Cd1-O2	2.404(10)
Cd1-O3	2.351(10)	Cd1-O4	2.377(10)
Cd1-N1	2.297(10)	Cd1-O4_c	2.754(11)
Cd1-O5_c	2.234(10)		
O1-Cd1-O2	97.5(3)	O1-Cd1-O3	86.1(3)
O1-Cd1-O4	170.5(2)	O1-Cd1-N1	86.9(3)
O1-Cd1-O4_c	109.8(2)	O1-Cd1-O5_c	82.8(3)
O2-Cd1-O3	54.8(3)	O2-Cd1-O4	87.9(3)
O2-Cd1-N1	152.7(3)	O2-Cd1-O4_c	119.5(3)
O2-Cd1-O5_c	82.6(3)	O3-Cd1-O4	90.6(2)
O3-Cd1-N1	99.0(3)	O3-Cd1-O4_c	164.1(2)
O3-Cd1-O5_c	134.0(2)	O4-Cd1-N1	84.8(3)

c = -x,-y,-z

6.3.2 Thermal stability and PXRD studies

From the TG analysis of compound **1** it was found that the guest ethanol and coordinated water molecules can be completely removed at ~ 80 °C (observed 14.3 %, calculated 14.8 %) and after removal of solvents the resultant $\{Cd(bpe)_{0.5}(bdc)\}_n$ (**3**), is stable up to 290 °C (Figure 4). Further heating gradually decomposes the compound. In case of compound **2** also, the guest and coordinated solvent molecules are removed at 80 °C and (observed 11.6 %, calculated 12.8 %) (Figure 4).

To understand the framework stability upon desolvation, PXRD measurements were carried out and these revealed interesting structural changes. Compound **1** was completely desolvated at 100 °C under vaccum to generate compound **3**. The X-ray diffraction peaks obtained from **3** were sharp indicating crystalline nature of the desolvated phase but those are different compared to that of **1** (Figure 5a). Indexing of the obtained PXRD pattern of **3** shows a clear change in the crystal system and cell parameters. In addition, the peak corresponding to (001) and (100) plane at 8.96° and 10.22° of as-synthesized **1** has shifted to lower angle of 8.67 and 9.85°, respectively in **3** (Figure 5b). When compound **3** was exposed to vapors of methanol it generates a framework structure similar to **1** as can be seen from the PXRD patterns. This shows that the structure is dynamic in nature and also reveals the reversible structural transformation. Further, exposure to the vapors of ethanol, water, acetonitrile and THF show that the structure again reverts back to similar structure as of compound **1** (Figure 6).

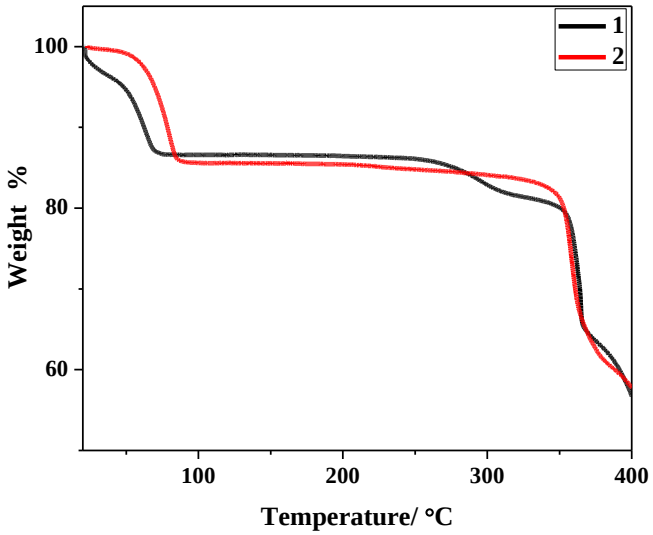

Figure 4: TG analysis of compound **1** and **2** under N_2 atmosphere with heating rate of 3 °C/min in the temperature range of 30-400 °C.

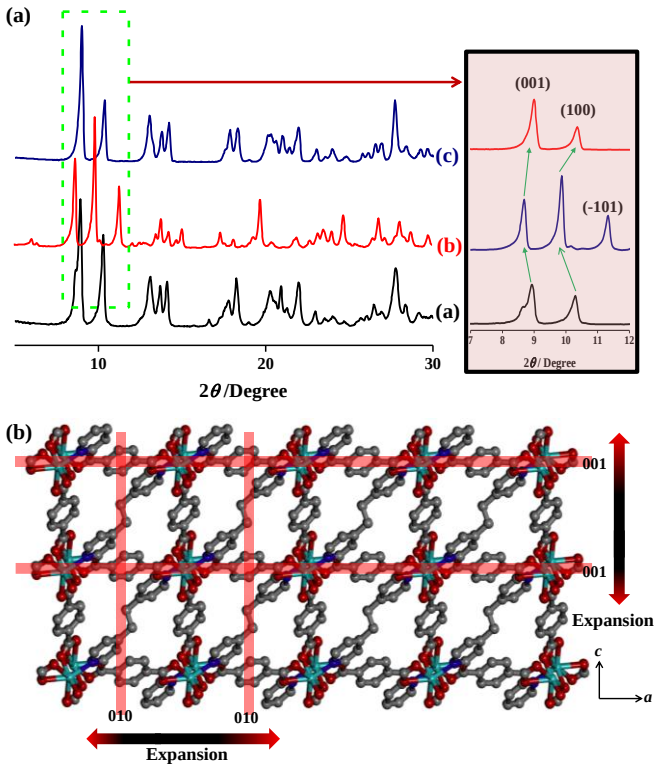

Figure 5: (a) PXRD patterns of compound **1** in different phase: (a) as-synthesized, (b) heated at 100 °C under reduced pressure, (c) methanol exposed; right hand side patterns show the peaks corresponding to (001), (100), and (-101) planes; (b) 001 and 010 planes (shown in red bar) in **1;** After desolvation these two planes show shift of Bragg intensity in the lower 2θ indicating structural expansion.

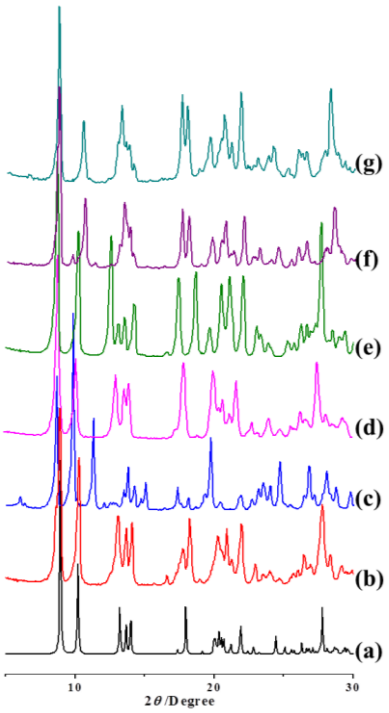

Figure 6: PXRD patterns of compound **1**: (a) simulated, (b) as-synthesized, (c) desolvated, (d) ethanol, (e) water, (f) acetonitrile, (g) THF.

Details of indexing of PXRD patterns of compound 3:

NUMBER OF SINGLE INDEXED LINES = 12

TOTAL NUMBER OF LINES = 17

a = 14.460(0.014678) Å; *b* = 14.594(0.021348) Å; *c* = 13.890280(0.010273) Å

α = 90.0 °; β = 98.349(0.101402) °; γ = 90.0 °

UNIT CELL VOLUME = 2900.27 A**3

H	K	L	SST-OBS	SST-CALC	DELTA	2TH-OBS	2TH-CALC	D-OBS	FREE PARAM.
0	1	0	.002761	.002786	-.000025	6.024	6.051	14.6593	0
1	0	0		.002899			6.173		
0	0	1	.003135	.003142	-.000007	6.419	6.426	13.7575	0
1	1	0	.005694	.005685	.000009	8.655	8.648	10.2083	0
.007346				9.833		8.9876		0	
1	1	1	.009727	.009703	.000024	11.320	11.306	7.8104	0
0	2	0	.011108	.011143	-.000035	12.100	12.119	7.3086	0
-1	0	2	.013815	.013712	.000103	13.500	13.450	6.5537	0
0	2	1		.014285			13.729		
2	1	0	.014433	.014381	.000051	13.800	13.775	6.4119	0
0	1	2	.015406	.015352	.000054	14.260	14.235	6.2060	0
-1	2	1		.016307			14.673		
2	0	1	.016455	.016490	-.000035	14.740	14.756	6.0050	0
-1	1	2		.016498			14.760		
1	0	2	.017173	.017218	-.000045	15.060	15.080	5.8781	0
2	2	0	.022776	.022739	.000037	17.360	17.346	5.1042	0
-2	1	2	.023405	.023442	-.000037	17.600	17.614	5.0351	0
-1	2	2	.024851	.024856	-.000005	18.140	18.142	4.8864	0
0	3	1	.028215	.028214	.000001	19.340	19.340	4.5858	0
0	0	3		.028275			19.361		
1	2	2		.028362			19.391		

-3 1 1 .029383 .029388 -.000006 19.740 19.742 4.4938 0

-1 1 3 .031298 .031330 -.000032 20.380 20.390 4.3541 0

NUMBER OF OBS. LINES = 17

NUMBER OF CALC. LINES = 22

M(17)= 11 AV.EPS.= .0000316

F 17 = 23.(.015796, 47)

M CF. J.APPL.CRYST. 1(1968)108

F CF. J.APPL.CRYST. 12(1979)60

6.3.3 Solid state ^{113}Cd NMR study

The structural changes realized from the PXRD experiments show that the structure is stimuli responsive and also reversible. To elucidate the detail changes occurring at the metal center we used ^{113}Cd NMR as a probe. The ^{113}Cd NMR shows considerable promise as a probe of metal ion environments with chemical shifts range of ~ 900 ppm.[18] ^{113}Cd CPMAS NMR spectra for as-synthesized **1**, **3**, and methanol exposed **3** are shown in Figure 7. The isotropic ^{113}Cd shifts in **1** is 5.0 ppm (Figure 7). As mentioned previously, the Cd^{2+} center in **1** is hepta-coordinated with the distorted pentagonal bipyramidal geometry with CdO_6N chromophore. Since the chemical shift of hepta-coordinated Cd^{2+} with CdO_7 chromophore remains in the range of 0 ~ 60 ppm,[19] the shift at 5.0 ppm is reasonable, resulting down field shift due to the deshielding by N-atom of the bpe ligand. Interestingly, in case of **3**, an isotropic chemical shift is observed at 58.0 ppm with a small shoulder peak at 50 ppm, which is quite different from that of **1**. This lower field signals are due to the geometry change of Cd^{2+}, "pentagonal-bipyramidal CdO_6N (**1**) → octahedral CdO_5N (**3**)",[20] because the coordinated H_2O molecule is removed. The isotropic Cd^{2+} shift with CdO_6 and CdN_6 chromophore is observed in the range +150 ~ 0 ppm and +200 ~ +380 ppm, respectively. The main peak with small shoulder peak would suggest that **3** has slightly different octahedral coordination environment. Clearly, it is difficult to address the isotropic shifts further as the Cd^{2+} is coordinated to the mixed N- and O- atoms and the polyhedra around Cd^{2+} is irregular. Importantly, the isotropic shift observed for Cd^{2+} in methanol exposed compound **3** is 4.0 ppm which is close to that of **1**. Hence, it can be concluded that the hexa-coordinated metal center is again hepta-coordinated upon exposure to solvent vapour. Upon exposure

to methanol vapour, a new heptacoordinated chromophore $CdO_5N(MeOH)$ is obtained which is structurally similar to that of **1** as realized by the MeOH exposed PXRD pattern of **3**. Moreover, the structural flexibility and reversibility of the framework were further confirmed.

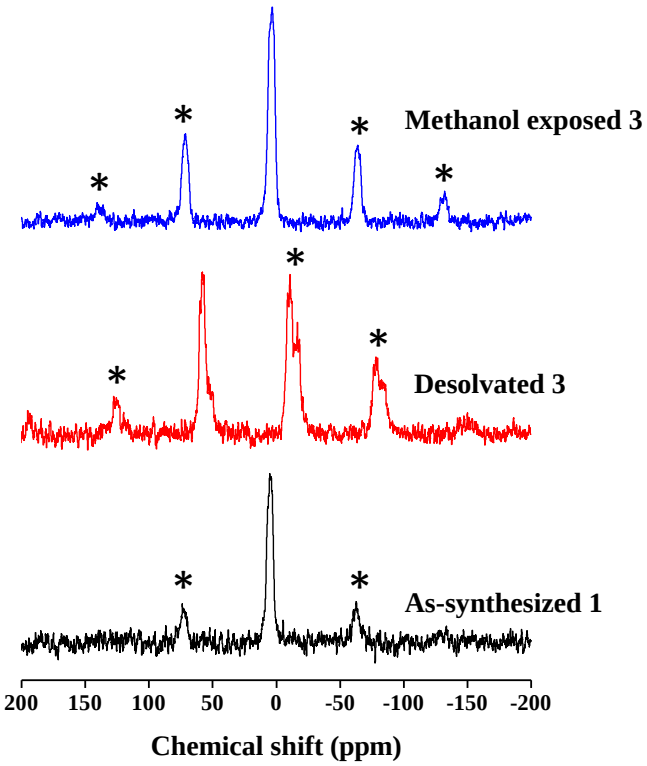

Figure 7: ^{113}Cd CPMAS spectra of as-synthesized **1**, desolvated **3** and MeOH exposed **3**. Asterisks in ^{113}Cd CPMAS spectra exhibit a spinning sideband.

Importantly, the isotropic shift observed for Cd^{2+} in methanol exposed compound **3** is 4.0 ppm which is close to that of **1**. Hence, it can be concluded that the hexa-coordinated metal center is again hepta-coordinated upon exposure to solvent vapour. Upon exposure to methanol vapour, a new heptacoordinated chromophore $CdO_5N(MeOH)$ is obtained which is structurally similar to that of **1** as realized by the MeOH exposed PXRD pattern of **3**. Moreover, the structural flexibility and reversibility of the framework were further confirmed.

6.3.4 Adsorption studies: Stepwise CO_2 uptake and O_2/N_2 selectivity

In order to check the porous property of compound **3**, N_2, O_2 (77 K) and CO_2 (195 K) gas adsorption measurements were carried out. Although compound **3** contains sufficient window dimension to allow the diffusion of N_2 (3.64 Å)[21] it shows very small

amount of N_2 at 77 K. It is probably due to higher diffusion barrier imposed on the 1D channel by structural transformation. But O_2 with slightly lesser kinetic diameter (3.2 Å) than that of N_2 diffuses into the pores of **3** at 77 K (Figure 8a). The surface area was calculated to be 232 m^2/g using O_2 adsorption profile, indicating that **3** maintain the permanent porosity. The final uptake amount at ~ 20 kPa was ~14 wt % while at the same pressure the N_2 uptake was 1.5 wt %. Such huge uptake difference (selectivity factor ~ 10) at low relative pressure region makes this framework a potential material for O_2/N_2 seperation. The amount of adsorption of N_2 and O_2 per Cd^{2+} atom calculated from the Langmuir analyses are 0.3 and 1.3, respectively. Apart from preferential O_2 adsorption over N_2, the CO_2 (Kinetic diameter ~ 3.4 Å) adsorption profile at 195 K shows interesting features (Figure 8b). The isotherm shows a two-step uptake and also a distinct hysteresis. There are two steps at relative pressures 0.05 and 0.12 as realized from logarithmic scale plot and at P/P_0 ~ 0.96 the final uptake amount is 75 mL/g. Further, at 273 K CO_2 uptake profile shows a distinct stepwise uptake with final uptake amount of 23 mL/g (Figure 8c). These stepwise adsorption again reflects the structural flexibility associated with CO_2 adsorption as the CO_2 molecule can interact with pore surface decorated with carboxylate oxygen and aromatic π cloud from bpe and bdc linkers. This type of gated and stepwise uptake of CO_2 is not very common and also very important in terms of seperation purposes.[22] Acetylene adsorption profile at 195 K also shows a gate opening type profile with a final uptake amount of 21 mL/g which is very unique in PCPs (Figure 8d).

The reversible structural transformation observed with exposure to different solvents such as water, methanol, and ethanol *etc* lead us to see the vapour adsorption properties of **3**. At 298 K the water vapour adsorption profile of **3** shows a type-I profile till P/P_0 ~ 0.45 with uptake amount 65 mL/g (~ 1.07 molecules/formula) and after that it rises sharply to reach final uptake amount of 292 mL/g (4.84 molecules/formula) (Figure 9a). The first step clearly indicates that water molecule coordinates to the metal center and this leads to transformation of $CdO_5N \rightarrow CdO_6N$ chromophore. In the second step, water molecules fill the pores and probably forms hydrogen bonded clusters. The desorption path clearly makes a hysteresis loop due to strong hydrogen bonded association of the water molecules. Interesting uptake profile was observed for MeOH at 293 K. During the initial adsorption process, the isotherm shows type-I curve and then suddenly rises at point A (P/P_0 ~ 0.39), and attains a saturated level at point B (P/P_0 ~ 0.92). In desorption process, MeOH molecules are gradually released till point C (P/P_0 ~ 0.08), and then drops immediately and thus adsorption/desorption isotherm shows a large hysteresis

curve. The amounts of MeOH molecules adsorbed per Cd^{2+} in the framework are about 0.82 (point A), 2.45 (point B), and 1.69 (point C) (Figure 9). The initial type-I uptake can be hence considered as

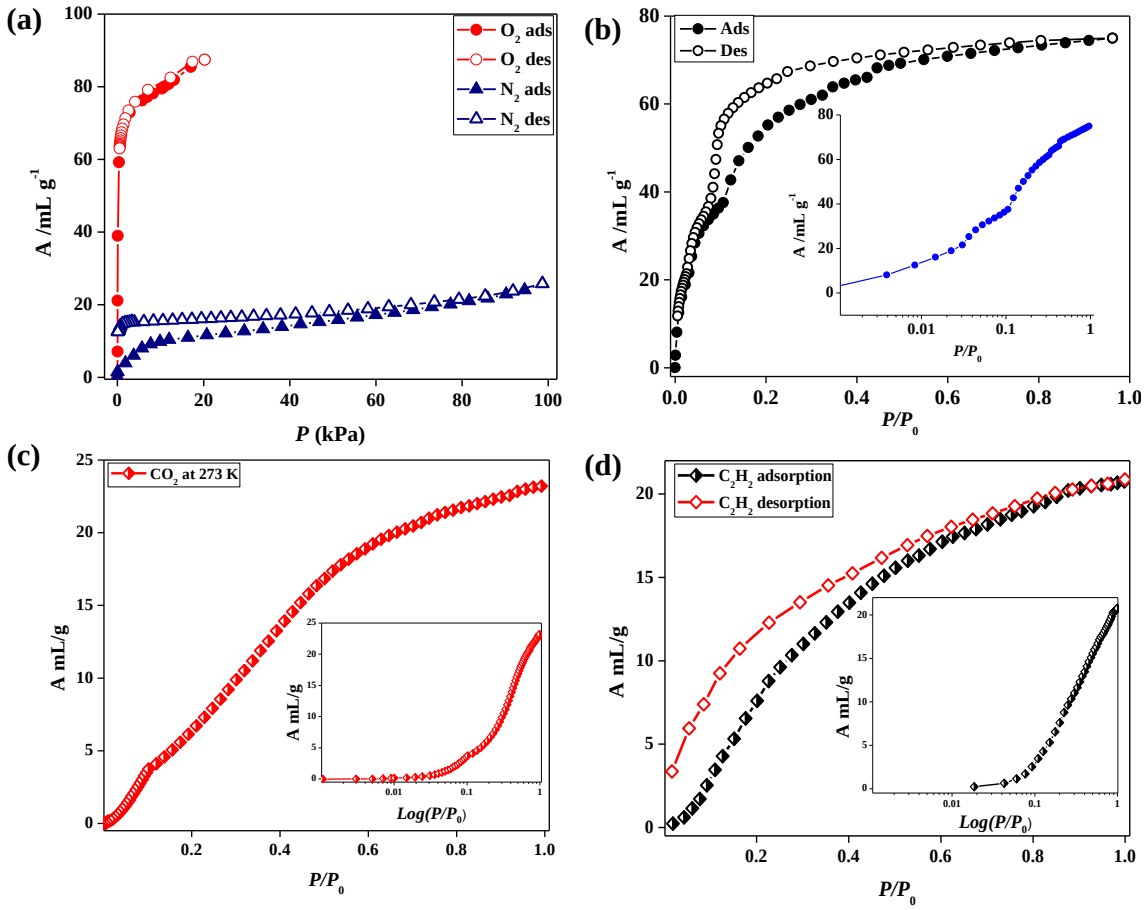

Figure 8: Adsorption studies of compound **3**: (a) N_2 and O_2 adsorption isotherms at 77 K, (b) CO_2 adsorption isotherm at 195 K; inset: logarithmic scale plot; (c) CO_2 adsorption isotherm at 273 K; Inset shows the logarithmic pressure scale plot; (d) C_2H_2 adsorption isotherm at 195 K; Inset shows the logarithmic pressure scale plot.

coordination of methanol to the Cd^{2+} center and thus a structural transformation occurs due to conversion of $CdO_5N \rightarrow CdO_5N(MeOH)$. After point A, additional MeOH molecules fill the pore as guest molecules. As the desorption curve does not trace the adsorption path, there must be some strong interaction between host and guest MeOH. Presence of H-bonding is prime reason and till point C there is very small amount of release of guest molecules. After this point H-bonding breaks which lead to rapid release of all the MeOH molecules. As the kinetic diameter increases from ethanol, acetone to THF, the uptake amount decreases significantly (Figure 9b). In case of ethanol and acetone the final uptake amounts are 26 and 30 mL/g. But THF shows a type-II uptake profile showing the size exclusion property of the framework.

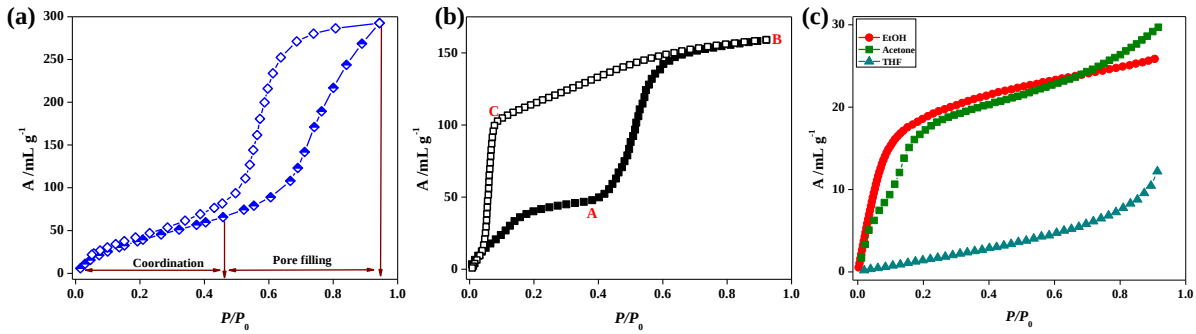

Figure 9: (a) Water vapour adsorption profile of **3** at 298 K, P_0 is 3.169 kPa; (b) Methanol vapour adsorption profile at 293 K; Points A, B and C in methanol adsorption profile show different stages of adsorption, P_0 is 12.927 kPa; (c) Ethanol, acetone and THF vapour adsorption profile of **3** at 298 K, P_0 values are 7.84, 30.59 and 21.622 kPa.

6.4 Conclusions

In conclusion, we have synthesized Cd^{2+} based two 3D PCPs, $\{[Cd(bpe)_{0.5}(bdc)(H_2O)]\cdot EtOH\}_n$ (**1**) and $\{[Cd(bpe)_{0.5}(bdc)(H_2O)]\cdot 2H_2O\}_n$ (**2**) which differs only in terms of solvent molecules. Removal of coordinated solvent molecules brings drastic change in the framework and this has been characterized by solid state ^{113}Cd NMR probe which confirms the transformation of $CdO_5N \rightarrow CdO_6N$ chromophore. The desolvated framework shows preferential adsorption of O_2 over N_2 at 77 K and this property makes it a promising material for N_2/O_2 seperation. The CO_2 adsorption isotherm at 195 K shows a two-step adsorption process which again reveals the flexible characteristics of the framework. Further, the water and methanol solvent vapour adsorption profiles show unique characteristics indicating the reversible structural changes during adsorption process and confirm the spectroscopic observation. Such spectroscopic characterization of metal ion geometry could open up a new path for characterization of flexible PCPs and their guest responsive behaviour and this can have huge implications in catalysis (e.g. Lewis acid catalyst) and separation.

6.5 References

1. a) O. K. Farha, C. E. Wilmer, I. Eryzici, B. G. Hauser, P. A. Parilla, K. O'Neill, A. A. Serjeant, S. T. Nguyen, R. Q. Snurr, J. T. Hupp, *J. Am. Chem. Soc*. **2012**, *134*, 9860; b) J. L. C. Rowsell, O. M. Yaghi, *Angew. Chem. Int. Ed*. **2005**, *44*, 4670; c) O. K. Farha, I. Eryzici, N. C. Jeong, B. G. Hauser, C. E. Wilmer, A. A. Serjeant, R. Q. Snurr, S. T. Nguyen, A. Ö. Yazaydin, J. T. Hupp, *J. Am. Chem. Soc.* **2012**, *134*, 15016; d) L. J. Murray, M. Dincă, J. R. Long, *Chem. Rev*. **2009**, *38*, 1294; e) J. Duan, M. Higuchi, R.

Krishna, T. Kiyonaga, Y. Tsutsumi, Y. Sato, Y. Kubota, M. Takata, S. Kitagawa, *Chem. Sci*. **2014**, *5*, 660; f) M. C. Das, Q. Guo, Y. He, J. Kim, C. –G. Zhao, K. Hong, S. Xiang, Z. Zhang, K. M. Thomas, R. Krishna, B. Chen, *J. Am. Chem. Soc*. **2012**, *134*, 8703; g) J. Liu, P. K. Thallapally, D. Strachan, *Langmuir*, **2012**, *28*, 11584; h) S. Kitagawa, R. Kitaura, S.-I. Noro, *Angew. Chem. Int. Ed*. **2004**, *43*, 2334.

2. a) S. Hasegawa, S. Horike, R. Matsuda, S. Furukawa, K. Mochizuki, Y. Kinoshita, S. Kitagawa, *J. Am. Chem. Soc*. **2007**, *129*, 2607; b) R. K. Das, A. Aijaz, M. K. Sharma, P. Lama, P. K. Bharadwaj, *Chem. Eur. J*., **2012**, *18*, 6866; c) R. Haldar, S. K. Reddy, M. V. Suresh, S. Mohapatra, S. Balasubramian, T. K. Maji, *Chem. Eur. J*., **2014**, *20*, 4347; d) Y. Li, L. Xie, Y. Li, J. Zheng, X. Li, *Chem. Eur. J*. **2009**, *15*, 8951; e) Y. Chen, T. Hoang, S. Ma, *Inorg. Chem*. **2012**, *51*, 12600.

3. a) D. N. Dybtsev, H. Chun, S. H. Yoon, D. Kim, K. Kim, *J. Am. Chem. Soc*. **2004**, *126*, 32; b) S. Muthu, J. H. K. Yip, J. J. Vittal, *J. Chem. Soc. Dalton Trans*. **2002**, 4561; c) B. –C. Tzeng, T. – H. Chiu, B. –S. Chen and G. –H. Lee, *Chem. Eur. J*., **2008**, *14*, 5237; d) J. Tian, L. V. Saraf, B. Schwenzer, S. M. Taylor, E. K. Brechin, J. Liu, S. J. Dalgarno, P. K. Thallapally, *J. Am. Chem. Soc*. **2012**, *134*, 9581; e) S. Bhattacharya, A. Chakraborty, K. Jayaramulu, A. Hazra, T. K. Maji, *Chem. Commun*, **2014**, DOI: 10.1039/C4CC05991C.

4. a) L. E. Kreno, K. Leong, O. K. Farha, M. Allendorf, R. P. V. Duyne, J. T. Hupp, *Chem. Rev*. **2012**, *112*, 1105; b) R. Haldar, R. Matsuda, S. Kitagawa, S. J. George, T. K. Maji, *Angew. Chem. Int. Ed.* **2014**, DOI: 10.1002/anie.201405619; c) B. Chen, S. Xiang, G. Qian, *Acc. Chem. Res*. 2010, *43*, 1115; d) B. Chen, Y. Yang, F. Zapata, G. Lin, G. Qian, E. B. Lobkovsky, *Adv. Mater*. **2007**, *19*, 1963; e) S. Das, P. K. Bharadwaj, *Inorg. Chem*. **2006**, *45*, 5257; f) Y. Cui, Y. Yue, G. Qian, B. Chen, *Chem. Rev*. **2012**, *112*, 1126; g) M. D. Allendorf, C. A. Bauer, R. K. Bhakta, R. J. T. Houk, *Chem. Soc. Rev*. **2009**, *38*, 1330; h) C. A. Kent, B. P. Mehl, J. M. Papanikolas, T. J. Meyer, W. Lin, *J. Am. Chem. Soc*. **2010**, *132*, 12676; i) R. Haldar, K. V. Rao, S. J. George, T. K. Maji, *Chem. Eur. J*. **2012**, *18*, 5848; j) V. M. Suresh, S. J. George, T. K. Maji, *Adv. Funct. Mater*. **2013**, *23*, 5585.

5. a) M. O'keeffe, O. M. Yaghi, *Chem. Rev*. **2012**, *112*, 675; b) M. O'keeffe, *Chem. Soc. Rev*. **2009**, *38*, 1215; c) D. J. Tranchemontagne, J. L. Mendoza-Cortés, M. O'keeffe, O. M. Yaghi, *Chem. Soc. Rev*. **2009**, *38*, 1257; d) R. Haldar, T. K. Maji, *CrystEngComm*. **2013**, *15*, 9276.

6. a) J. J. Perry IV, J. A. Perman, M. J. Zaworotko, *Chem. Soc. Rev*. **2009**, *38*, 1400; b) B. D. Wagner, G. J. McManus, B. Moulton, M. J. Zaworotko, *Chem. Commun*. **2002**, 2176;

c) A. Hazra, P. Kanoo, T. K. Maji, *Chem. Commun*. **2011**, *47*, 538; d) Y. Hijikata, S. Horike, M. Sugimoto, S. Kitagawa, *Chem. Eur. J*. **2011**, *17*, 5138.

7. a) R. Kitaura, K. Seki, G. Akiyama, S. Kitagawa, *Angew. Chem. Int. Ed*. **2003**, *4*, 428; b) K. S. Walton, A. R. Millward, D. Dubbeldam, H. Frost, J. J. Low, O. M. Yaghi, R. Q. Snurr, *J. Am. Chem. Soc*. **2007**, *2*, 406; c) P. Kanoo, G. Mostafa, R. Matsuda, S. Kitagawa, T. K. Maji, *Chem. Commun*. **2011**, *28*, 8106; d) A. Demessence, J. R. Long, *Chem. Eur. J*. **2010**, *16*, 5902; e) Z.-Q. Jiang, G. –Y. Jiang, F. Wang, Z. Zhou, J. Zhang, *Chem. Eur. J*. **2012**, *18*, 10525; f) K. L. Gurunatha, T. K. Maji, *Inorg. Chem*. **2009**, *48*, 10886.

8. a) T. K. Maji, G. Mostafa, R. Matsuda, S. Kitagawa, *J. Am. Chem. Soc*. **2005**, *127*, 17152; b) W. Kosaka, K. Yamagishi, H. Yoshida, R. Matsuda, S. Kitagawa, M. Takata, H. Miyasaka, *Chem. Commun*. **2013**, *49*, 1594; c) V. Bon, I. Senkovska, D. Wallacher, D. M. Tobbens, I. Zizak, R. Feyerherm, U. Mueller, S. Kaskel, *Inorg. Chem*. **2014**, *53*, 1513.

9. a) P. Kanoo, S. K. Reddy, G. Kumari, R. Haldar, C. Narayana, S. Balasubramanian, T. K. Maji, *Chem. Commun*. **2012**, *48*, 8487; b) H. J. Choi, M. Dincă, J. R. Long, *J. Am. Chem. Soc*. **2008**, *130*, 7848; c) S. B. Choi, H. Furukawa, H. J. Nam, D.-Y. Jung, Y. H. Jhon, A. Walton, D. Book, M. OKeeffe, O. M. Yaghi, J. Kim, *Angew. Chem. Int. Ed*. **2012**, *51*, 1.

10. a) E. D. Bloch, L. J. Murray, W. L. Queen, S. Chavan, S. N. Maximoff, J. P. Bigi. R. Krishna, V. K. Peterson, F. Grandjean, G. J. Long, B. Smit, S. Bordiga, C. M. Brown, J. R. Long, *J. Am. Chem. Soc*. **2011**, *133*, 14814; b) H. B. T. Jeazet, C. Staudt, C. Janiak, *Chem. Commun*. **2012**, *48*, 2140; c) S. Shimomura, M. Higuchi, R. Matsuda, K. Yoneda, Y. Hijikata, Y. Kubota, Y. Mita, J. Kim, M. Takata, S. Kitagawa, *Nature. Chem*. **2010**, *2*, 633.

11. a) T. M. McDonald, W. R. Lee, J. A. Mason, B. M. Wiers, C. S. Hong, J. R. Long, *J. Am. Chem. Soc*. **2012**, *134*, 7056; b) P. Kanoo, A.C. Ghosh, S. T. Cyriac, T. K. Maji, *Chem. Eur. J*. **2012**, *18*, 237; c) J. Park, D. Yuan, K. T. Pham, J. –R. Li, A. Yakovenko, H.-C. Zhou, *J. Am. Chem. Soc*. **2012**, *99*, 7056.

12. R. A. Jacobson, *REQABA Empirical Absorption Correction*, version 1.1-0301998; Molecular Structure Corp.: The Woodlands, TX, **1996-1998**.

13. A. Altomare, M. C. Burla, M. Camalli, G. L. Cascarano, C. Giacovazzo, A. Guagliardi, A. G. G. Moliterni, G. Polidori, R. Spagna, *J. Appl. Crystallogr*. **1999**, *32*, 115.

14. P. T. Beurskens, G. Admiraal, G. Beurskens, W. P. Bosman, R. deGelder, R. Israel, Smits, J. M. M. *The DIRDIF-94 Program System*; Technical Report of the Crystallography Laboratory; University of Nijmegen: Nijmegen, The Netherlands, **1994**.

15. *TeXsan Crystal Structure Analysis Package*; Molecular Structure Corp.: The Woodlands, TX, **2000**.

16. A. L. Spek, *PLATON*. The University of Utrecht: Utrecht, The Netherlands, **1999**.

17. The sizes of the channels were calculated considering the van der Waals radii of the atoms.

18. Multinuclear Solid-State Nuclear Magnetic Resonance of Inorganic Materials, K. MacKenzie, M. E. Smith, **2002**, Pergamon Materials series.

19. R. S. Honkonen, P. D. Ellis, *J.* Am. *Chem. Soc.***1986**, *108*, 912

20. E. Rivera, M. A. Kennedy, R. D. Adams, P. D. Ellis, *J. Am. Chem. Soc.* **1990**, *11*, 1400.

21. C. E. Webster, R. S. Drago, M. C. Zerner, *J. Am. Chem. Soc*. **1998**, *120*, 5509.

22. a) H. J. Park, M. P. Suh, *Chem. Commun*. **2010**, *46*, 610; b) Z. Q. Jiang, G. Y. Jiang, F. Wang, Z. Zhou, J. Zhang, *Chem. Eur. J*. **2012**, *18*, 10525; c) T. K. Maji, G. Mostafa, R. Matsuda, S. Kitagawa, *J. Am. Chem. Soc*. **2005**, *127*, 17152; d) Y. Inubushi, S. Horike, T. Fukushima, G. Akiyama, R. Matsuda, S. Kitagawa, *Chem. Commun*. **2010**, *46*, 9229.

Chapter 7

In situ C-N bond formation in coordination polymers: Porosity and chirality from achiral precursors

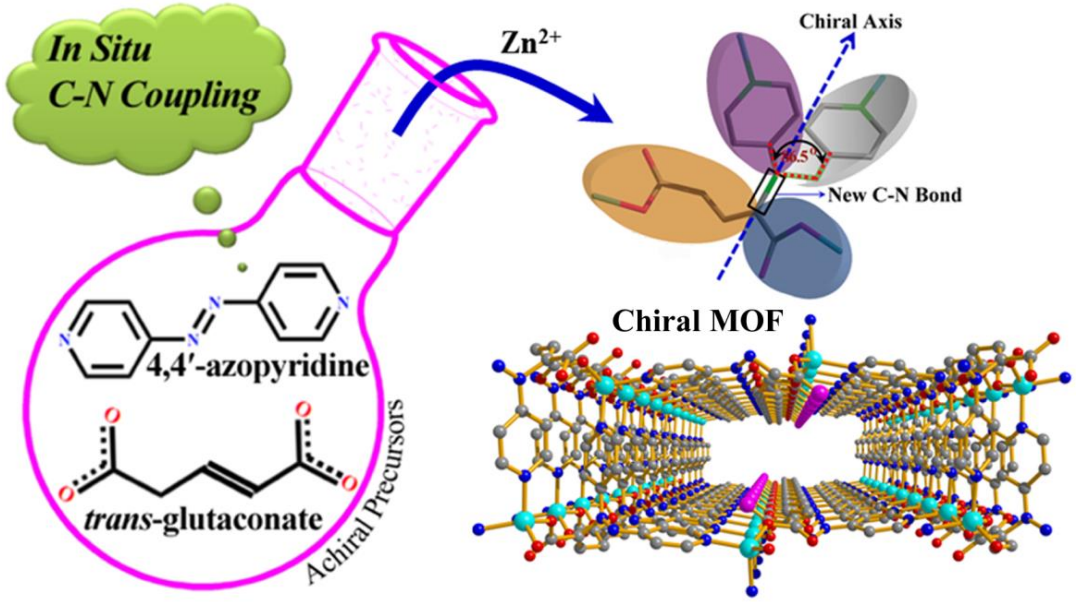

Summary

In this chapter an unprecedented in situ C-N coupling phenomena during synthesis of coordination polymers has been shown. Metal mediated in situ C-N coupling between 4,4′-azobipyridine (azpy) and disodium-*trans*-glutaconate (Na_2tga) at room temperature has resulted a new multifunctional linker *Z*-dhpe (*Z*-dhpe = (*Z*)-2-(1,2-(dipyridin-4-yl)hydrazinyl)pent-2-enedioate) which subsequently self-assembles with Zn^{2+} or Cd^{2+} resulting in a chiral, $\{Zn(Z\text{-dhpe})\cdot 3H_2O\cdot EtOH\}_n$ (**1**) or an achiral porous coordination polymer (PCP), $\{Cd_2(Z\text{-dhpe})_2\cdot 5H_2O\cdot 2EtOH\}_n$ (**2**) depending on its different coordination modes. Both the PCPs are highly porous and show appreciable amount CO_2 uptake properties. Changing the azpy linker to 1,2-bis(4-pyridyl) ethylene (bpee) yields another in situ generated linker 1-pyridyl-2-(N-3-(pent-1,5-dioate)pyridinium)ethylene (pnpe) which forms a 2D cationic structure coordination polymer with Cd^{2+}, $\{[Cd(pnpe)(bpee)(H_2O)_2]\cdot(NO_3)\}_n$ (**3**).

1. P. Kanoo, R. Haldar, S. T. Cyriac, T. K. Maji, ***Chem. Commun***. **2011**, *47*, 11038.

2. R. Haldar, P. Kanoo, T. K. Maji, To be submitted.

7.1 Introduction

Metal mediated in situ coupling between two organic components for generating new ligands and their subsequent coordination with metal ions is an elegant method for fabrication of novel coordination compounds which are otherwise inaccessible in direct preparation from the components.[1] In situ ligand synthesis, being very important in the context of organic chemistry, have also become an important approach in the crystal engineering of porous coordination polymers[2] (PCPs) exhibiting interesting properties like porosity, photoluminescence, magnetism, sensing etc.[3] The hydro(solvo)-thermal method has been found to be very promising for many in situ metal/organic reactions towards the construction of PCPs of different dimensionalities.[1b,4] Recently, Feller *et. al*. have reported dimerization of L-aspartic acid involving in situ C-N coupling to imminodisuccinic acid *via* a postulated fumaric acid intermediate, precisely coupling between a $–NH_2$ and a reactive alkene group, which leads to the formation of a coordination polymer at high temperature.[3e]

Here we have shown an interesting observation of in situ C-N coupling between two organic components, 4,4′-azobipyridine (azpy) and disodium-*trans*-glutaconate (Na_2tga) that leads to the formation of a new linker *Z*-dhpe (*Z*-dhpe = (*Z*)-2-(1,2-(dipyridin-4-yl)hydrazinyl)pent-2-enedioate) in a H_2O/EtOH medium at room temperature. On many occasions, spatial arrangement of in situ generated ligands becomes decisive in dictating the fate of the final structure. Chirality is one such property which may arise in solids because of the asymmetric arrangement of linkers in space.[5] Instead of high temperature we have preferred metal based coupling at RT which is well known in synthetic organic chemistry. In the course of our study, we have found that *Z*-dhpe is capable of generating both a chiral and an achiral solid depending on its different coordination mode with d^{10}-metal ions Zn^{2+} and Cd^{2+}, respectively. Self-assembly of *Z*-dhpe with Zn^{2+} results in a chiral PCP, $\{Zn(Z\text{-dhpe})\cdot 3H_2O\cdot EtOH\}_n$ (**1**) while with Cd^{2+} an achiral PCP $\{Cd_2(Z\text{-dhpe})_2\cdot 5H_2O\cdot 2EtOH\}_n$ (**2**) at RT. The type of chirality found here is axial and the chiral axis passes through the newly formed C-N bond as shown in Scheme 1. These compounds represent the first examples in PCPs where tga has been used as a component to assemble framework structures. Despite having bulky structure of *Z*-dhpe, its unique distorted tetrahedral geometry allows to grow the polymeric structure in three crystallographic directions upon coordination with tetrahedral Zn^{2+} resulting in a porous chiral 3D structure. It has a BET surface area of 870 m^2/g and shows excellent selective

adsorption of CO_2 over other gases (H_2, N_2, Ar, O_2) at 195 K. Compound **2** is achiral but shows high surface area (481 m^2/g) and appreciable amount of CO_2 uptake. Further, changing the azpy linker to 1,2-bis(4-pyridyl)ethylene (bpee) and self-assembly with Cd^{2+} and tga generates a new in situ formed linker, 1-pyridyl-2-(N-3-(pent-1,5-dioate)pyridinium)ethylene (pnpe) and the polymer thus formed, $\{[Cd(pnpe)(bpee)(H_2O)_2]\cdot(NO_3)\}_n$ (**3**) is 2D cationic in nature.

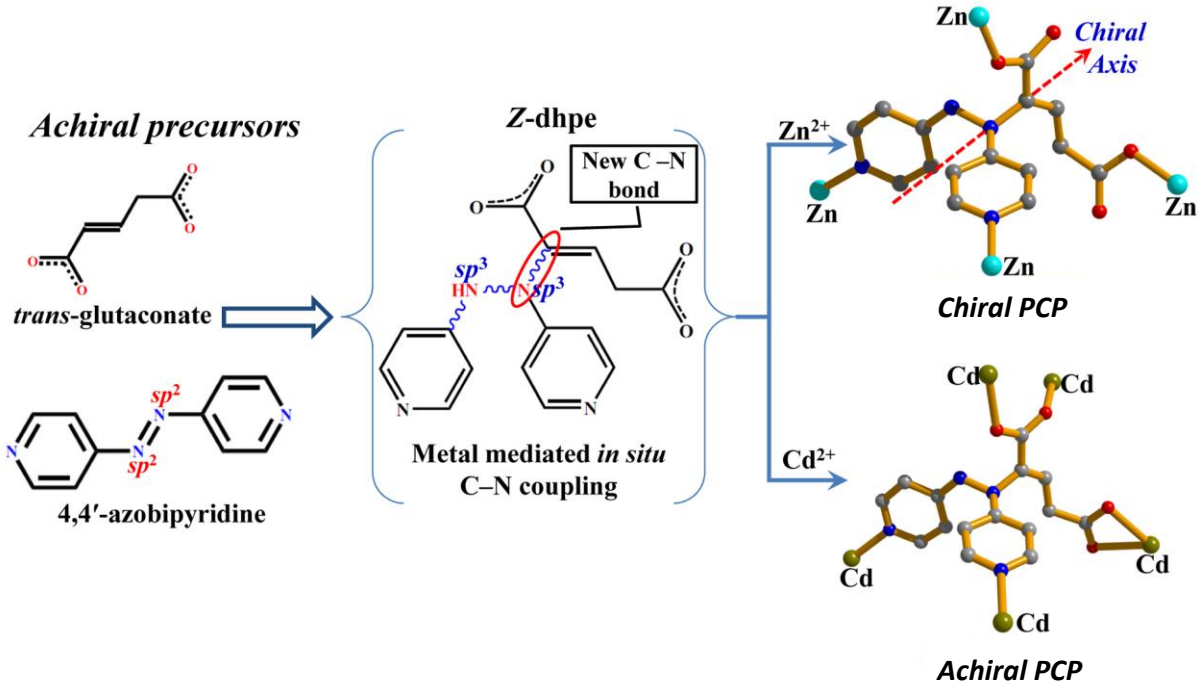

Scheme 1: Coordination driven self-assembly towards a chiral and an achiral PCP from an in situ generated organic linker (*Z*-dhpe) *via* metal mediated C-N coupling reaction.

7.2 Experimental section

7.2.1 Materials

All the reagents and solvents employed were commercially available and used as supplied without further purification. $Zn(NO_3)_2\cdot6H_2O$, $Cd(NO_3)_2\cdot6H_2O$ and *trans*-glutaconic acid were obtained from Aldrich Chemical Co. 4,4′-azobipyridine has been synthesised following literature procedure.[6]

7.2.2 Physical measurements

Elemental analyses were carried out using a Thermo Scientific Flash 2000 CHN analyzer. IR spectrum was recorded on a Bruker IFS 66v/S spectrophotometer using the KBr pellets in the region 4000-400 cm^{-1}. Thermogravimetric analysis (TGA) was carried

out on a METTLER TOLEDO TGA850 instrument in the temperature range of 30-600 °C under nitrogen atmosphere (flow rate of 50 mL min^{-1}) at a heating rate of 5 °C min^{-1}. Powder X-ray diffraction (PXRD) pattern in different state of the samples were recorded on a Bruker D8 Discover instrument using Cu-Kα radiation. ^{1}H and ^{13}C NMR were recorded on a Bruker AV-400 spectrometer (in DCl/[D_6]-DMSO, TMS as internal standard). Mass spectrum was recorded on a Bruker Ultraflex II MALDI/TOF spectrometer.

7.2.3 Synthesis of {Zn(*Z*-dhpe)·3H_2O·EtOH}$_n$ (1) and {Cd_2(*Z*-dhpe)$_2$·7H_2O·2EtOH}$_n$ (2):

An aqueous solution (50 mL) of disodium *trans*-glutaconate (Na_2tga) (1mmol, 0.174 g) was mixed with ethanolic solution (50 mL) of 4,4′-azobipyridine (azpy) (0.5 mmol, 0.078 g) and the resulting solution was stirred for 20 min. to mix well. $Zn(NO_3)_2·6H_2O$ (1mmol, 0.297 g) was dissolved in 100 mL water and 2 mL of this Zn^{2+} solution was slowly and carefully layered with the above mixed ligand solution using 1 mL buffer (1:2 of water and EtOH) solution. Good quality orange colour block shaped crystals were isolated after 45 days. The crystals were separated and washed with EtOH/water (1:1) mixture and air dried. (Yield 53 %). Anal. calcd. for $C_{17}H_{24}ZnN_4O_8$: C, 42.74; H, 5.06; N, 11.73. Found: C, 42.31; H, 4.61; N, 11.02 %. FT-IR (KBr pellet, 4000-400 cm^{-1}) (Figure 1): 3430(s), 3244(s), 1612(s), 1445(m), 1114(m). Compound **2** was prepared by similar procedure, except Cd^{2+} was used instead of Zn^{2+}. Anal. calcd. for $C_{34}H_{44}Cd_2N_8O_{17}$: C, 49.58; H, 4.16; N, 12.36. Found: C, 49.29; H, 4.52; N, 12.62 %. FT-IR (KBr pellet, 4000-400 cm^{-1}) (Figure 2): 3430(s), 3244(s), 1612(s), 1445(m), 1114(m).

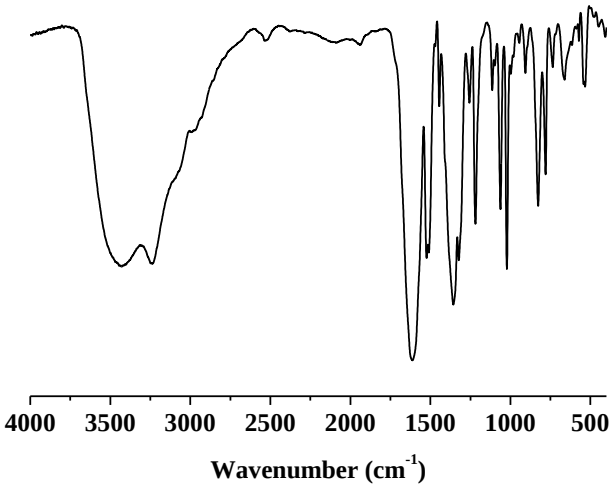

Figure 1: FT-IR spectrum of **1**.

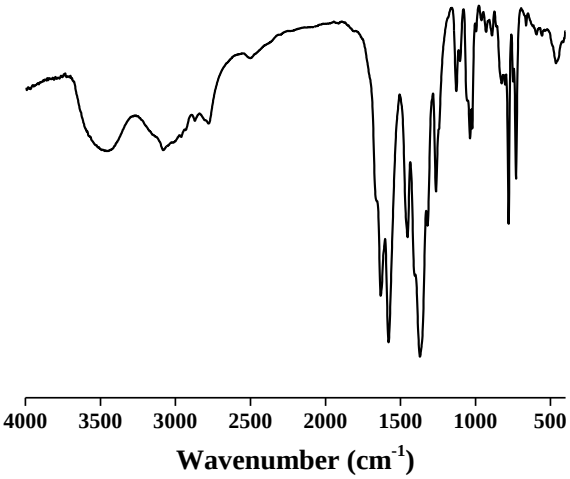

Figure 2: FT-IR spectrum of **2**.

7.2.4 Synthesis of $\{[Cd(pnpe)(bpee)(H_2O)_2]\cdot(NO_3)\}_n$ (3)

An aqueous solution (50 mL) of disodium *trans*-glutaconate (Na_2tga) (1mmol, 0.174 g) was mixed with ethanolic solution (50 mL) of 1,2-bispyridyl ethylene (bpee) (0.5 mmol, 0.072 g) and the resulting solution was stirred for 20 min. to mix well. $Cd(NO_3)_2\cdot 6H_2O$ (1 mmol, 0.301 g) was dissolved in 100 mL water and 2 mL of this Cd^{2+} solution was slowly and carefully layered with the above mixed ligand solution using 1 mL buffer (1:2 of water and EtOH) solution. Colorless rod shaped crystals were isolated after 10-12 days. The crystals were separated and washed with EtOH/water (1:1) mixture and air dried. (Yield 48 %). Anal. calcd. for $C_{29}H_{34}CdN_5O_9$: C, 40.39; H, 6.11; N, 13.41. Found: C, 40.59; H, 5.90; N, 13.29 %. FT-IR (KBr pellet, 4000-400 cm^{-1}) (Figure 3): 3589(s), 3450(s), 1619(s), 1431(m), 1119(m).

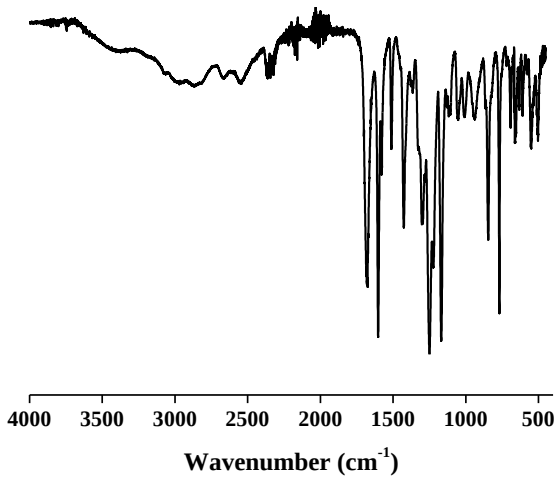

Figure 3: FT-IR spectrum of **2**.

7.2.5 X-ray Crystallography

X-ray single crystal structural data of **1-3** were collected on a Bruker Smart-CCD diffractometer equipped with a normal focus, 2.4 kW sealed tube X-ray source with graphite monochromated Mo-$K\alpha$ radiation (λ = 0.71073 Å) operating at 50 kV and 30 mA. The program SAINT[7] was used for integration of diffraction profiles and absorption correction was made with SADABS[8] program. All the structures were solved by SIR 92[9] and refined by full matrix least square method using SHELXL-97.[10] All the hydrogen atoms were geometrically defixed and placed in ideal positions. All crystallographic and structure refinement data of **1**-**3** are summarized in Table 1. All calculations were carried out using SHELXL 97,[10] PLATON,[11] SHELXS 97[12] and WinGX system, Ver 1.70.01.[13]

7.2.6 Adsorption measurements

Adsorption isotherms of N_2 (at 77 K) and CO_2, N_2, H_2, Ar, O_2 (at 195 K) gases were recorded using the dehydrated samples of **2** (**2′**) by using a QUANTACHROME QUADRASORB-*SI* analyzer. In the sample tube the adsorbent samples (~ 100-150 mg) were placed which had been prepared at 100 °C under a 1×10^{-1} Pa vacuum for about 12 h prior to measurement of the isotherms. Helium gas (99.999% purity) at a certain pressure was introduced in the gas chamber and allowed to diffuse into the sample chamber by opening the valve. The amount of gas adsorbed was calculated from the pressure difference (P_{cal}-P_e), where P_{cal} is the calculated pressure with no gas adsorption and P_e is the observed equilibrium pressure. All the operations were computer-controlled.

Adsorption isotherms of water (298 K) and methanol (293 K) vapours were measured using a BELSORP-aqua-3 analyzer. A sample of about ~ 100–150 mg was prepared by heating at 100 °C for about 12 h under vacuum (1×10^{-1} Pa) prior to measurement of the isotherms. The solvent molecules used to generate the vapour were degassed fully by repeated evacuation. Dead volume was measured with helium gas. The adsorbate was placed into the sample tube, then the change of the pressure was monitored and the degree of adsorption was determined by the decrease in pressure at the equilibrium state. All operations were computer controlled and automatic.

7.3 Results and discussion

7.3.1 Structural description of $\{Zn(Z\text{-dhpe})\cdot 3H_2O\cdot EtOH\}_n$ (1) and $\{Cd_2(Z\text{-dhpe})_2\cdot 7H_2O\cdot 2EtOH\}_n$ (2):

Single crystal X-ray diffraction analysis suggests that compound **1** crystallizes in a chiral space group $P2_12_12_1$. The asymmetric unit of **1** comprises of one *Z*-dhpe, one Zn^{2+} atom with a distorted tetrahedral geometry, three water and one ethanol guest molecules (Figure 4). Four *Z*-dhpe coordinate to a tetrahedral Zn^{2+} center *via* two oxygen atoms (O1 and O4) from two different carboxylate groups and two nitrogen atoms (N1 and N4) from two pyridyl groups (Figure 5a). The loss of molecular symmetry of azpy because of the change in hybridization of two nitrogen atoms N2 and N3 from sp^2 to sp^3 *via* C-N coupling provides the sufficient angle (~ 86.5 °) to the pyridyl rings to bend away from each other, which gives rise to a distorted tetrahedral geometry in *Z*-dhpe linker (Figure 5b). This nonlinear spatial disposition of pyridyl groups of *Z*-dhpe in its *Z*-configuration helps to grow the polymeric structure along crystallographic *b* and *c*-axes while the alkyl dicarboxylate chain part allows to extend along *a*-direction resulting in a 3D framework structure (Figure 6). The chiral axis in **1** passes through the newly formed C-N bond as shown in Scheme 1. Single crystal of **1** is homochiral as suggested by Flack parameter obtained from X-ray crystallographic data (Table 2). Successively, we collected single crystal data of four different crystals from different reaction batches and found all are homochiral but have mixed handedness. As a consequence, the bulk sample was found to be heterochiral. Chirality in the present structure is completely coordination driven and very unique. The most probable explanation for occurrence of chirality in **1** is the presence of a tetrahedral Zn^{2+} centre with four different ligand groups that resembles an asymmetric carbon. Three water and one ethanol guest molecules reside in the 1D channels of **1** extending along crystallographic *a*-axis decorated with pendant oxygen atoms of carboxylate group. The approximate dimension of the dumble shaped channel is 12.5 × 5.25 $Å^2$ (Figure 6).[14] Calculation using PLATON[11] shows that the framework **1** possesses ~ 50% void space to the total crystal volume after removing the guest molecules. Topological analysis with TOPOS 4.0 software[15] suggests a 4-connected uninodal net in line with observed geometry of *Z*-dhpe with Schläfli symbol $\{4^2.6^3.8\}$ (Figure 7).

Tetrahedral coordination geometry of Zn^{2+} is the key to chirality as the assembly

of the same ligand with octahedral Cd^{2+} results in an achiral solid which crystallizes in *C*2/*c* space group (Scheme 1). The asymmetric unit of compound **2** contains one Cd^{2+}, one *Z*-dhpe linker, 3.5 molecules of guest water and one ethanol molecule (Figure 8). Unlike **1**, the geometry around Cd^{2+} in **2** is octahedral (Figure 8) and the presence of an inversion centre in the structure renders the compound achiral. Here, one *Z*-dhpe linker connects five Cd^{2+} centers through its versatile coordination modes (Figure 9). The coordination sites of Cd^{2+} are filled by four oxygens (O1, O2, O3 and O4) from three *Z*-dhpe linkers and two nitrogens (N1 and N4) from other two *Z*-dhpe linkers. Here also the *Z*-dhpe linker adopts a tetrahedral arrangement and thus leads to a 3D porous structure. View along *b*-axis and (10-1) plane shows rectangular shaped channels with dimensions 4×2.2 and 2.8×1.8 $Å^2$, respectively (Figure 10a-b).[14] Total void space calculated was found to be ~ 37% of total cell volume. Topological analysis with TOPOS 4.0 software suggests a 5-connected uninodal net with *Schläfli* symbol $\{4^6.6^4\}$ (Figure 11).

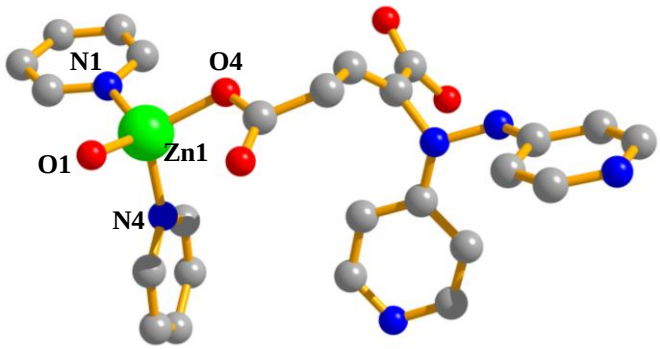

Figure 4: Coordination environment of Zn^{2+} in compound **1**.

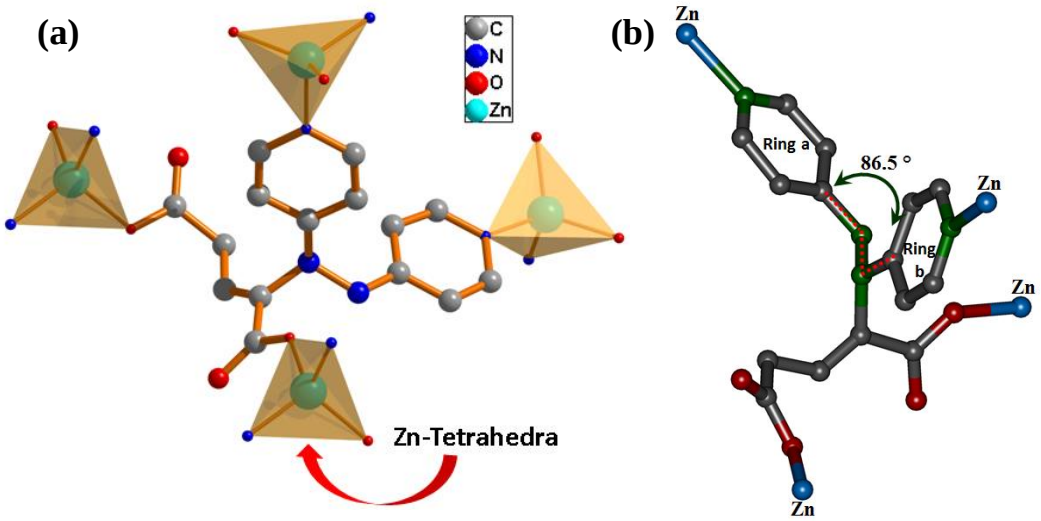

Figure 5: Structural details of **1**: (a) Coordination modes of the bi-functional ligand *Z*-dhpe; (b) Spatial disposition of *Z*-dhpe.

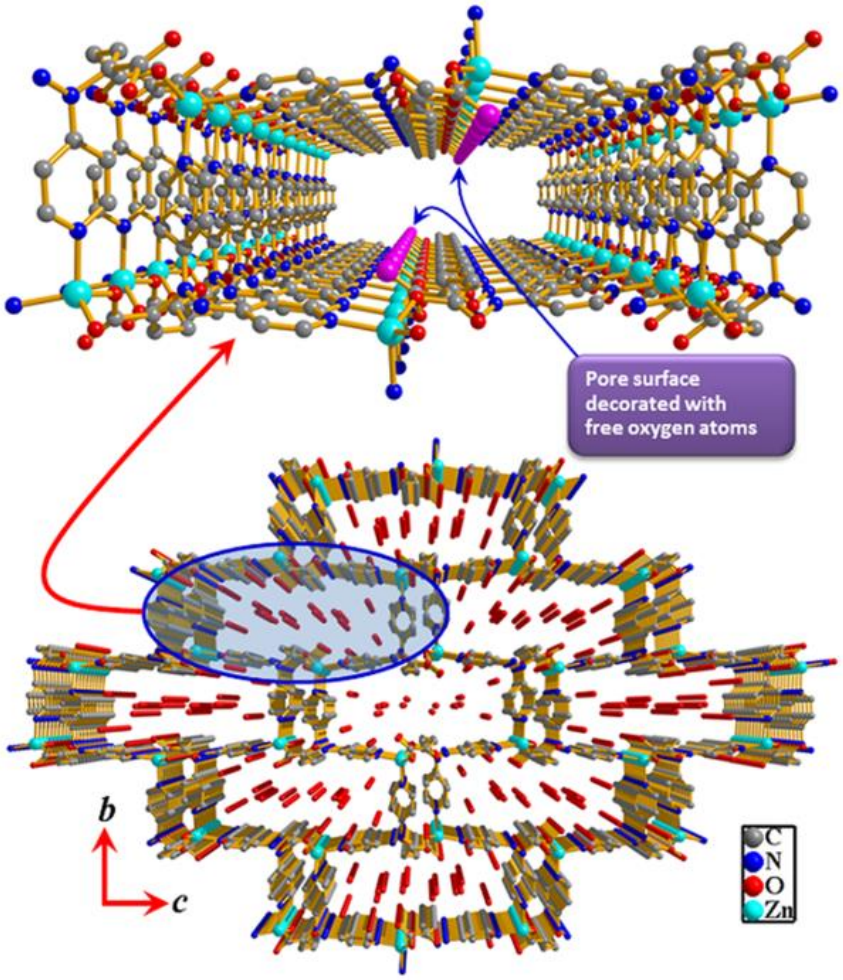

Figure 6: View of the 3D framework of **1** along *a*-direction. The channels are occupied by guest water (green balls) and ethanol (pink color) molecules.

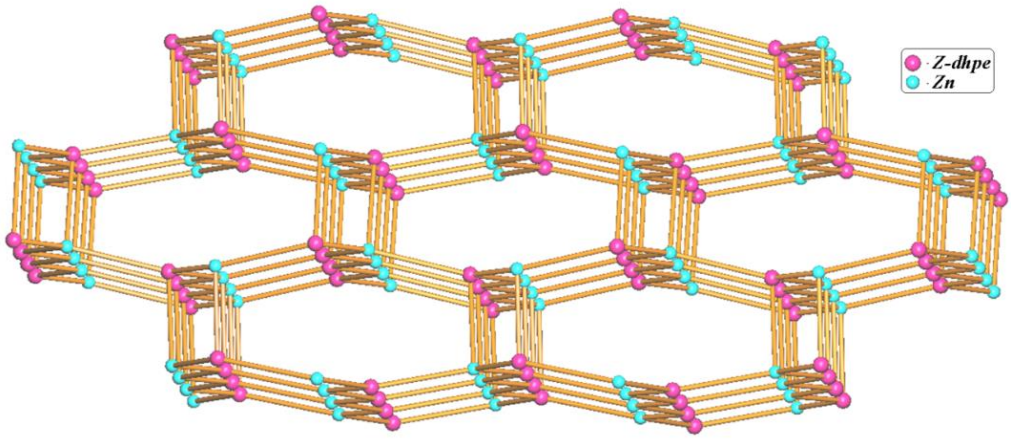

Figure 7: Topological view of 4-connected uninodal net in **1**.

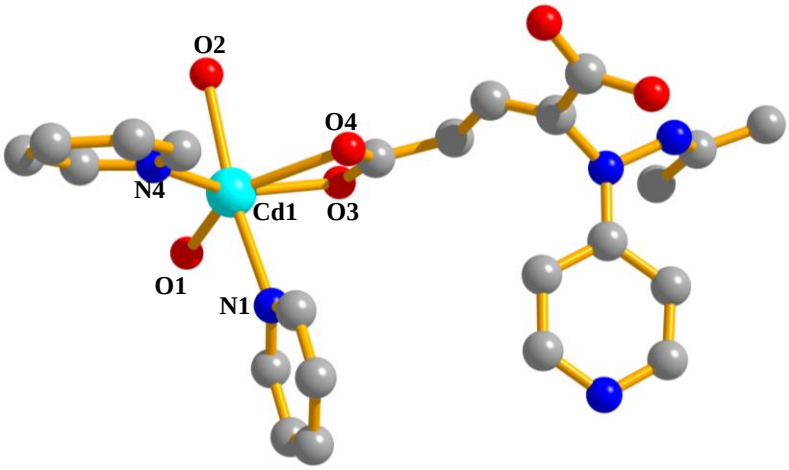

Figure 8: Coordination environment of Cd^{2+} in compound **2**.

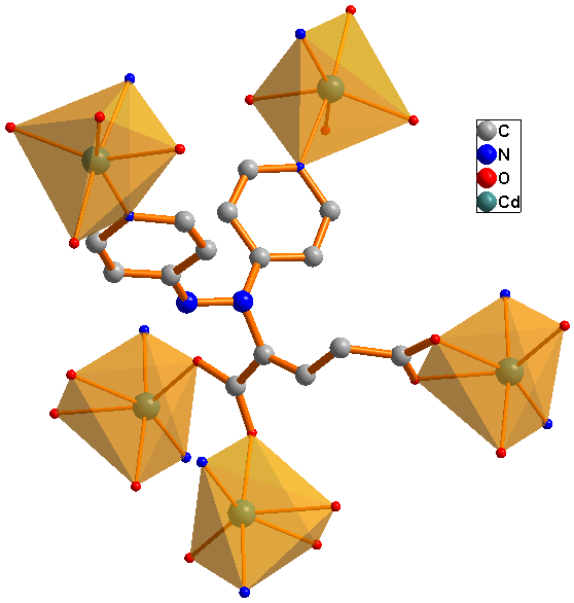

Figure 9: Coordination modes of the bi-functional ligand *Z*-dhpe in compound **2**.

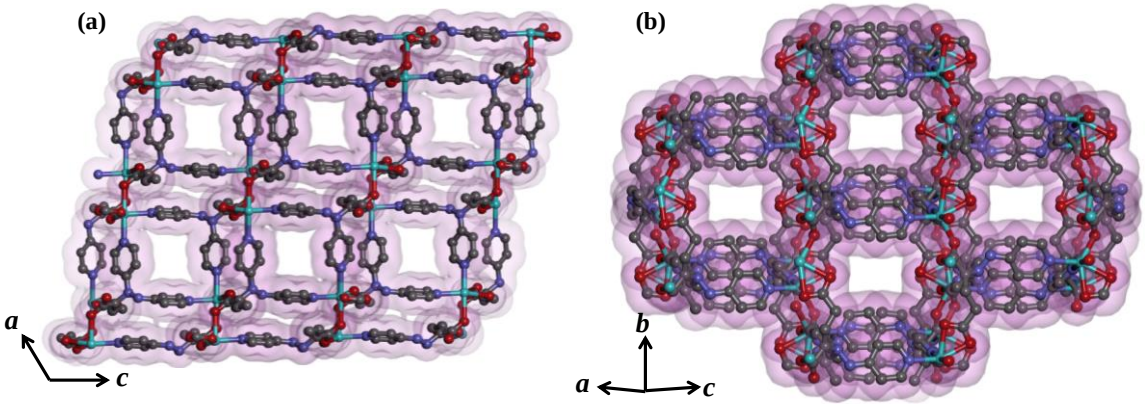

Figure 10: View of the channels in compound **2**: (a) Along *b*-axis; (b) Along (10-1) plane.

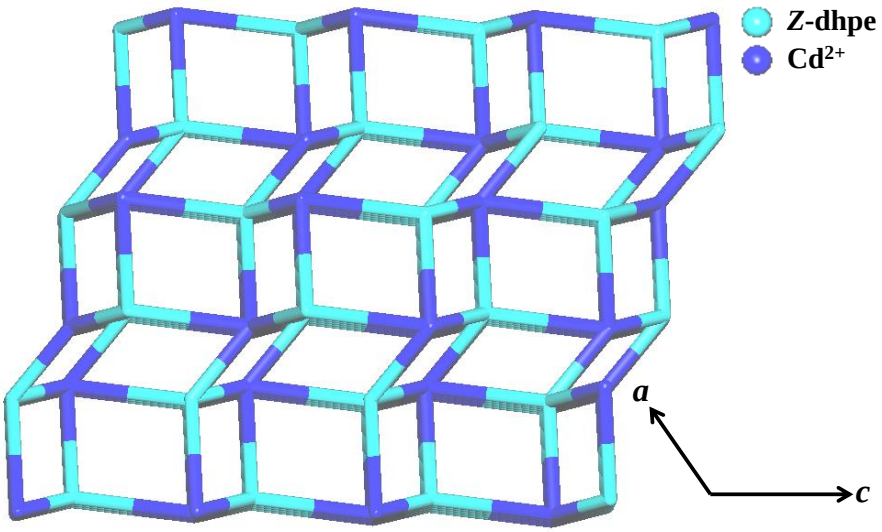

Figure 11: Topological view of 5-connected uninodal net along *b*-axis in compound **2**.

Single crystal structure of the compound **1** clearly indicates the presence of a C-N bond (C2-N2 distance, 1.45 Å) in *Z*-dhpe. The ligand has been further characterized by IR, ^{1}H-NMR, ^{13}C NMR and mass spectra to establish the presence of a C-N bond (Figure 2 and 12-14). Strong evidence comes up from ^{1}H-NMR spectra which suggest absence of

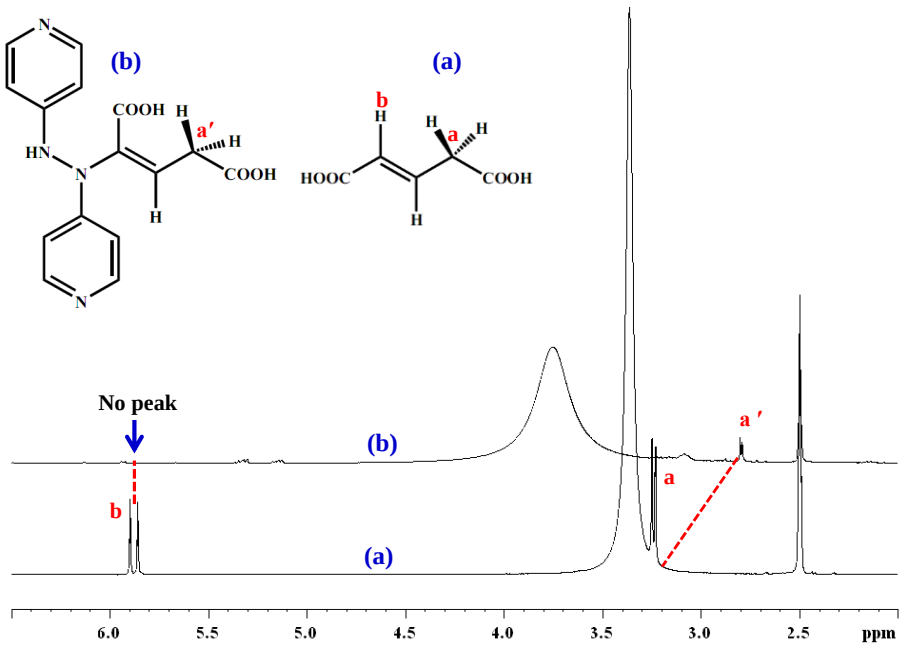

Figure 12: ^{1}H-NMR spectra of digested compound 1 (DCl/[D_6]-DMSO). Absence of proton in *marked carbon atom and chemical shift of a protons to a′ confirm the C-N coupling. Dotted lines represent correlation of the peaks.

the ethylene proton peak in *Z*-dhpe at the point where C-N coupling has occurred (Figure 12). Moreover, a medium intensity peak at 1114 cm^{-1} in the IR spectrum corroborates to

the presence of a C-N bond in **1** (Figure 2). A blank reaction was carried out between Na_2tga and azpy under similar condition in the absence of Zn^{2+}/Cd^{2+}. No reaction occurred between the two organic components up to 90 days which confirms the critical role of Zn^{2+}/Cd^{2+} in the formation of *Z*-dhpe. A proposed mechanism for the formation of the ligand is shown in Figure 15.

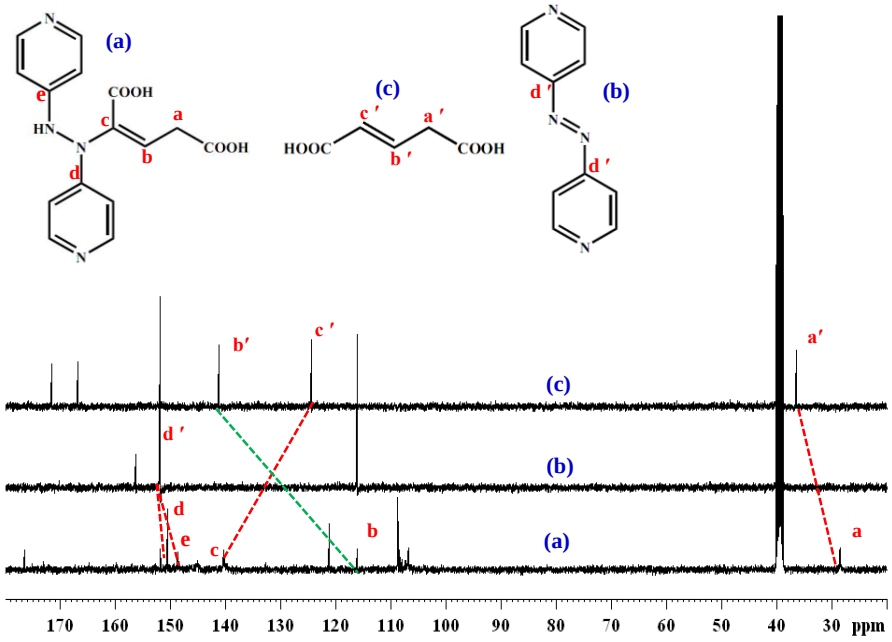

Figure 13: ^{13}C NMR spectra of digested compound **1** (DCl/D_6-DMSO).Chemical shifts of a, b, c and d carbons and appearance of a new peak e confirm the formation of *Z*-dhpe via C-N coupling.

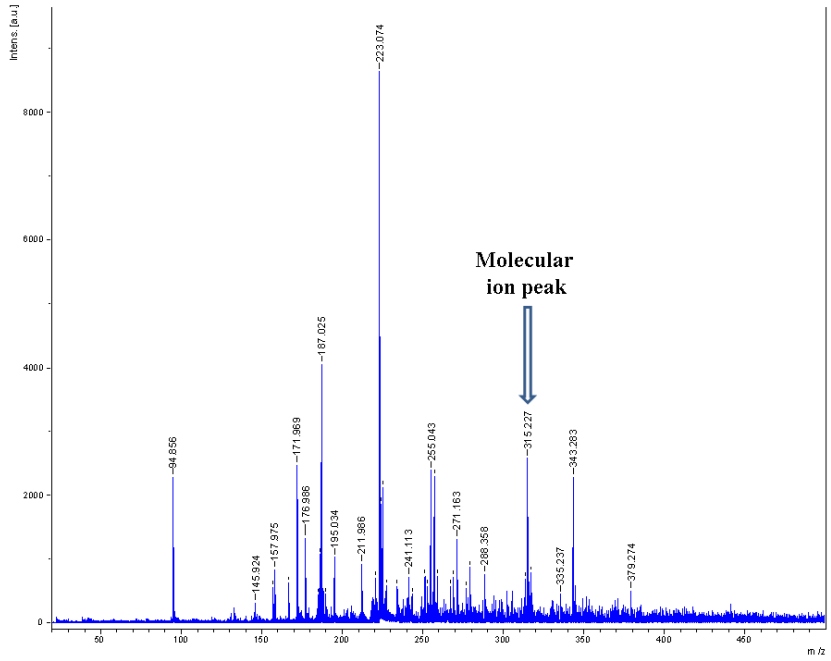

Figure 14: ESI-MS analysis of digested compound **1** which shows the presence of molecular ion peak for the ligand *Z*-dhpe.

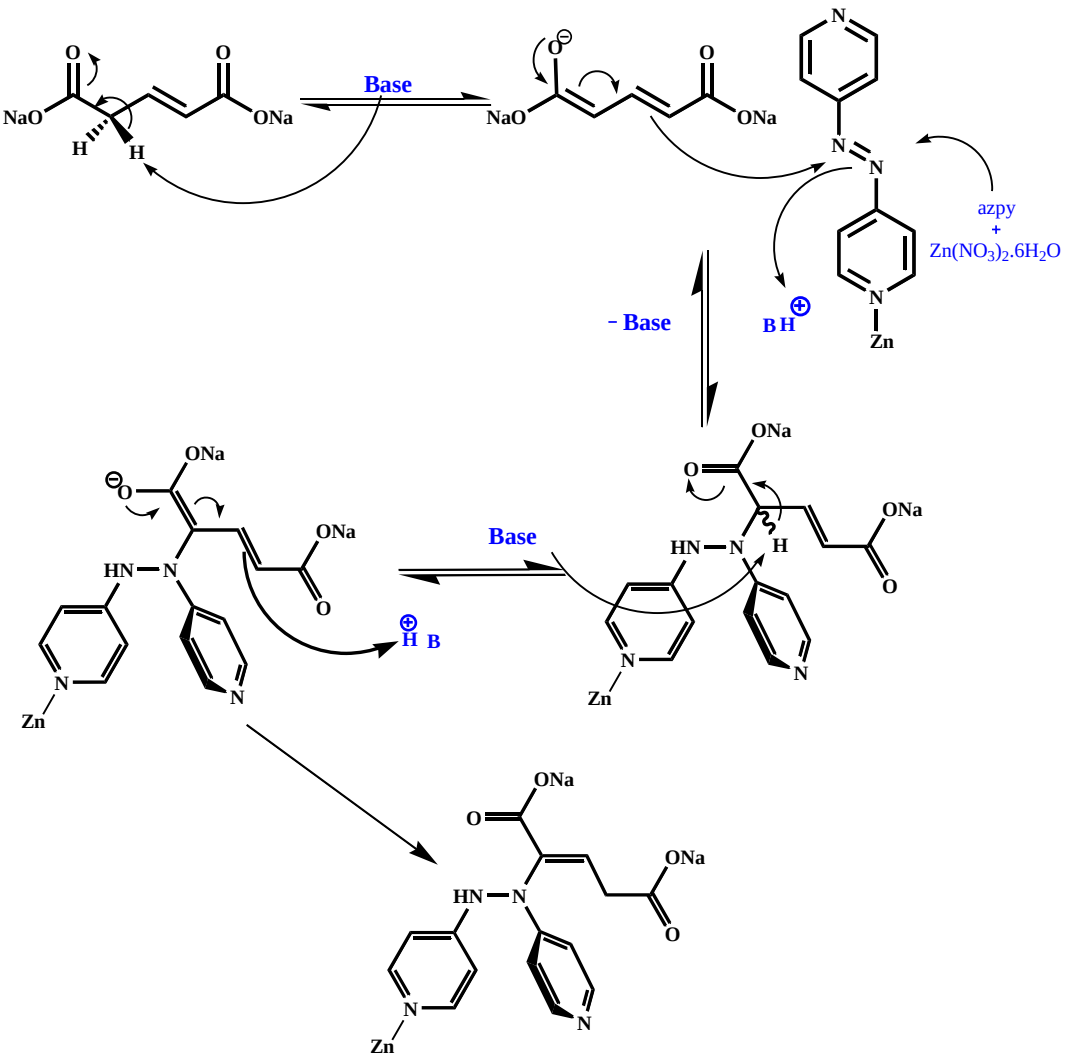

Figure 15: Proposed mechanism for the formation of the ligand *Z*-dhpe.

7.3.2 Structural description of $\{Cd(pnpe)(bpee)(H_2O)_2(NO_3)\}_n$ (3):

Compound **3** crystallizes in monoclinic $P2_1/c$ spacegroup. The asymmetric unit contains one Cd^{2+}, one in situ formed linker pnpe, one bpee, two coordinated water molecules and one guest nitrate anion (Figure 16). Here, due to the change in the –N=N- (in **1** and **2**) functionality to –C=C- functionality, the C-N coupling occurs at pyridyl nitrogen. Thus one extra positive charge is generated in the linker. The newly formed C-N bond distance is 1.500(2) Å. The Cd^{2+} metal center is octahedral; four equatorial positions are occupied by four oxygens, two from coordinated water molecules (O5 and O6), rest of the two oxygens (O1 and O3) are from two pnpe linkers; two axial sites are satisfied by two nitrogens (N1 and N2) from two bpee. The pnpe linker connects the metal centers through carboxylate groups along *b*-direction to form a chain like structure (Figure 17a). These chains are connected further along *a*-direction by the bpee linkers to generate a 2D

sheet like structure in *ab* plane (Figure 17b). As a counter ion NO_3^- anions resides in between the 2D layers (Figure 17c). Interestingly, one of the pyridyl nitrogen of pnpe linker remains uncoordinated and exposed in the 2D layer (Figure 17b).

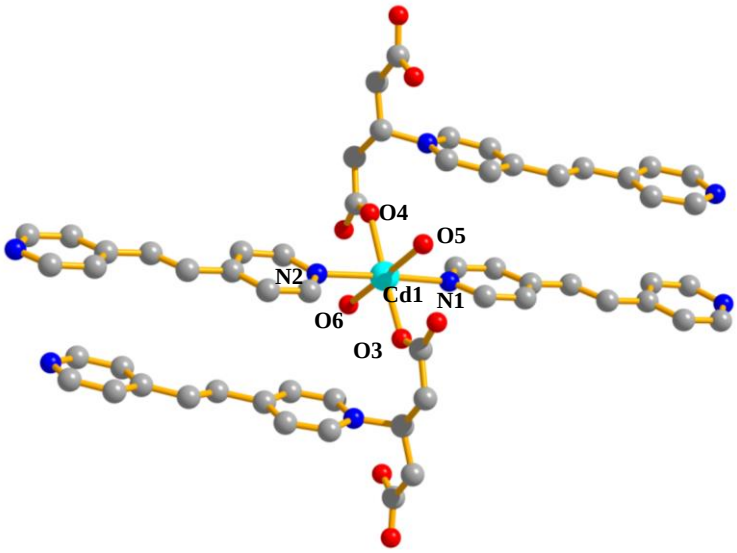

Figure 16: Coordination environment of Cd^{2+} in compound **3**.

7.3.3 Thermal stability and PXRD:

To analyze the stability and integrity of compounds **1-3** thermogravimetric analysis was carried out under nitrogen atmosphere (Figure 18). There is a rapid weight loss of ~ 21% in the temperature range of 35-120 °C corresponding to the presence of guest water and ethanol molecules in compound **1**. Slight discrepancy in the weight loss is due to the release of some guest molecules at RT itself. Afterwards, a plateau was observed up to 200 °C and then an abrupt weight loss occurs which suggests collapse of the framework structure. In case of compound **2**, weight loss in the temperature range of 35-50 °C indicates loss of ethanol guest molecules; further weight loss in the temperature range 50-110 °C is attributed to the guest water molecules. Heating beyond 220 °C shows rapid weight loss indicating disintegration of the framework. Compound **3** remains stable till ~ 210 °C and further heating probably disintegrates the 2D structure. PXRD pattern of the desolvated compound **1** (**1′**) [Zn(*Z*-dhpe)] shows negligible shift in peak positions suggesting 3D framework structure remains intact even it sustains loss of guest molecules (Figure 19). However, broadening of some low angle peaks indicates loss of single crystallinity upon desolvation. Compound **2** upon desolvation (**2′**) shows subtle changes

in the PXRD patterns indicating structural rearrangement in the framework (Figure 20a). Figure 20b shows the phase purity of the bulk compound **3**.

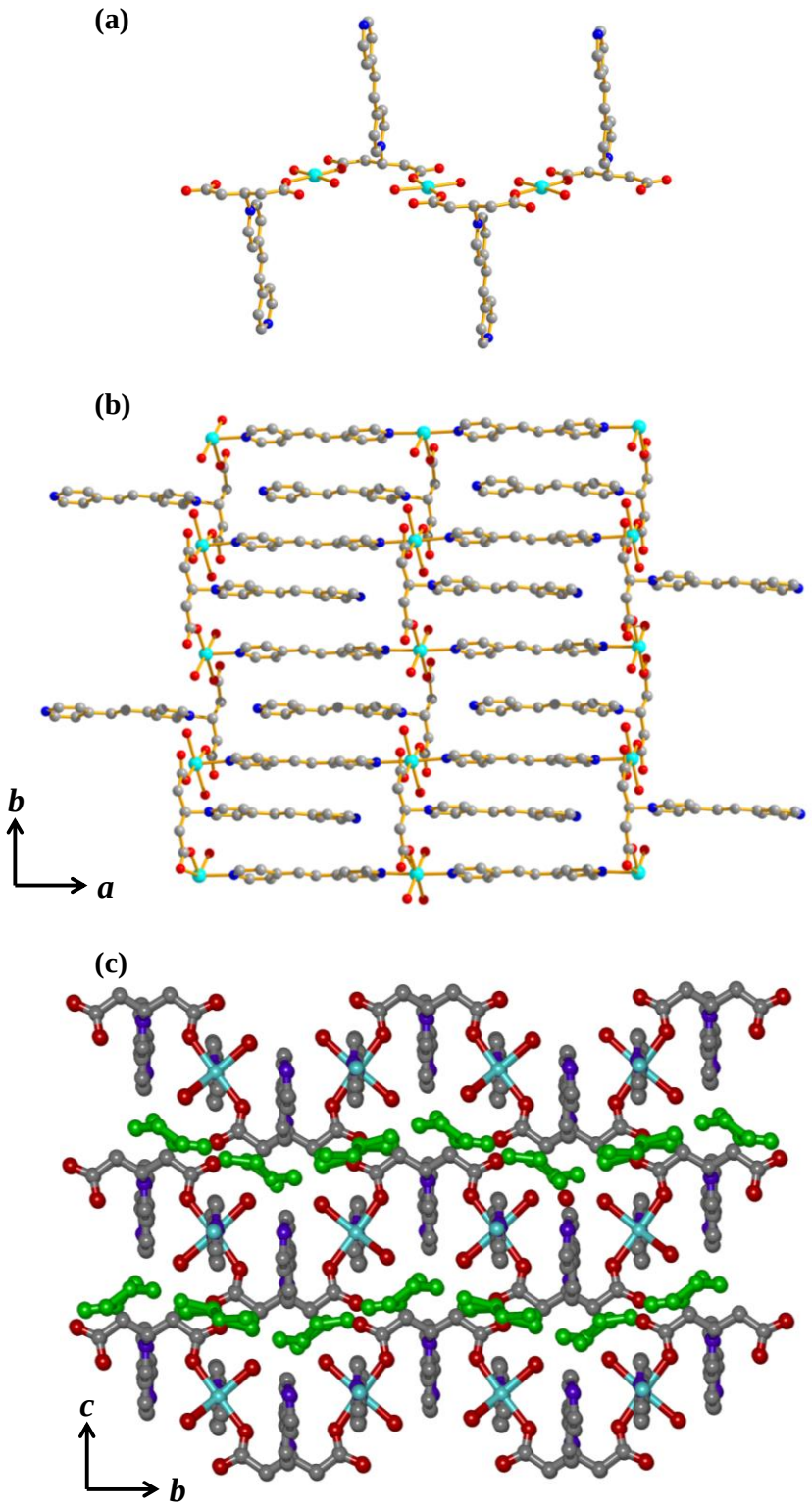

Figure 17: Structural details of compound **3**: (a) 1D chain formed by Cd^{2+} and pnpe; (b) 2D sheet; (c) NO_3^- anions between the 2D layers (shown in green).

Table 1: Crystal data and structure refinement parameters of compound **1-3**.

Parameters	**1**	**2**	**3**
Empirical formula	$C_{17}H_{24}ZnN_4O_8$	$C_{34}H_{44}Cd_2N_8O_{17}$	$C_{29}H_{34}CdN_5O_9$
M	477.74	1065.51	709.19
Cryst. system	Orthorhombic	Monoclinic	Monoclinic
space group	$P2_12_12_1$ (No. 19)	*C*2/*c* (no. 15)	*P*21/*c* (no. 14)
***a* (Å)**	8.741(5)	25.4628(7)	14.5698(9)
***b* (Å)**	14.796(5)	9.8868(3)	14.7853(4)
***c* (Å)**	19.340(5)	20.2318(6)	17.1269(2)
***α* °**	90.0	90.0	90.0
***β* °**	90.0	93.44(9)	111.793(9)
***γ* °**	90.0	90.0	90.0
***V* (Å^3)**	2501.3(2)	4223.8(3)	3384.7(2)
Z	4	4	4
***T*(K)**	100	100	100
***λ* (Mo K$_α$)**	0.71073	0.71073	0.71073
***D*$_c$ (g cm^{-3})**	1.253	1.654	1.617
***μ* (mm^{-1})**	1.024	1.087	0.726
***θ*$_{max}$ (deg)**	31.9	22.1	32
total data	15504	21220	55173
unique reflection	8008	2633	11781
***R*$_{int}$**	0.077	0.053	0.077
data [*I* > 2σ(*I*)]	3074	2342	8181
***R*^{a}**	0.086	0.0385	0.0969
***R*$_w$^{b}**	0.2689	0.098	0.2757
GOF	0.92	1.1	1.15

^{a} $R = \Sigma||F_o| - |F_c||/\Sigma|F_o|$. ^{b} $R_w = [\Sigma\{w(F_o^2 - F_c^2)^2\}/\Sigma\{w(F_o^2)^2\}]^{1/2}$.

Table 2: Summary of crystal data of compound **1** and refinement results.

Samples	**Space group**	***a* (Å)**	***b* (Å)**	***c* (Å)**	***R***	***R*$_w$**	**Flack parameter**
Crystal 1	$P2_12_12_1$	8.741(5)	14.796(5)	19.340(5)	0.086	0.2689	0.00(3)
Crystal 1a	$P2_12_12_1$	8.7423(6)	14.7183(11)	19.3742(15)	0.0843	0.2300	0.01(6)
Crystal 1b	$P2_12_12_1$	8.7726(4)	14.7582(9)	19.3159(10)	0.0797	0.2428	0.02(4)
Crystal 1c*	$P2_12_12_1$	8.7611(8)	14.7839(16)	19.353(2)	0.0811	0.2286	0.05(5)
Crystal 1d*	$P2_12_12_1$	8.7562(6)	14.8244(11)	19.3329(14)	0.0798	0.2285	-0.01(5)

Crystals with and without *mark have opposite handedness.

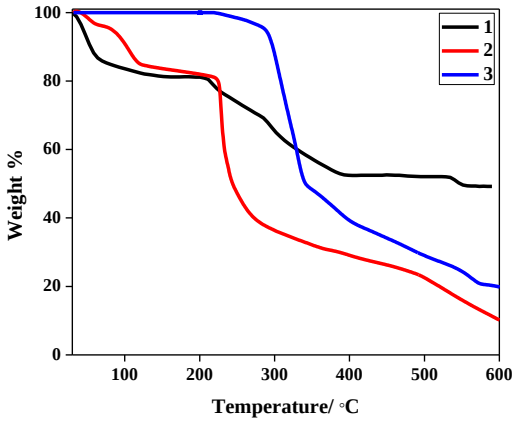

Figure 18: TG analysis of compound **1-3** under N_2 atmosphere with heating rate of 3 °C/min in the temperature range of 30-600 °C.

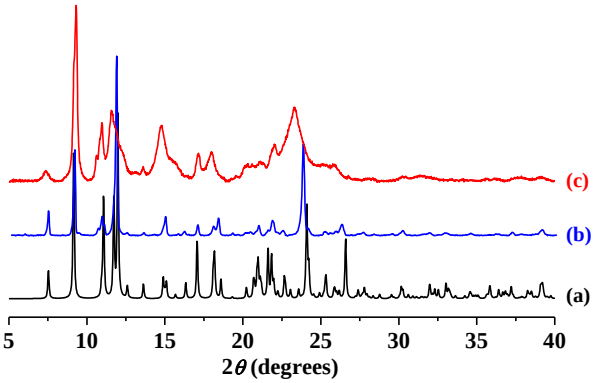

Figure 19: PXRD patterns of compound **1** in different phase: (a) Simulated (b) As-synthesized, (c) heated at 100 °C under reduced pressure.

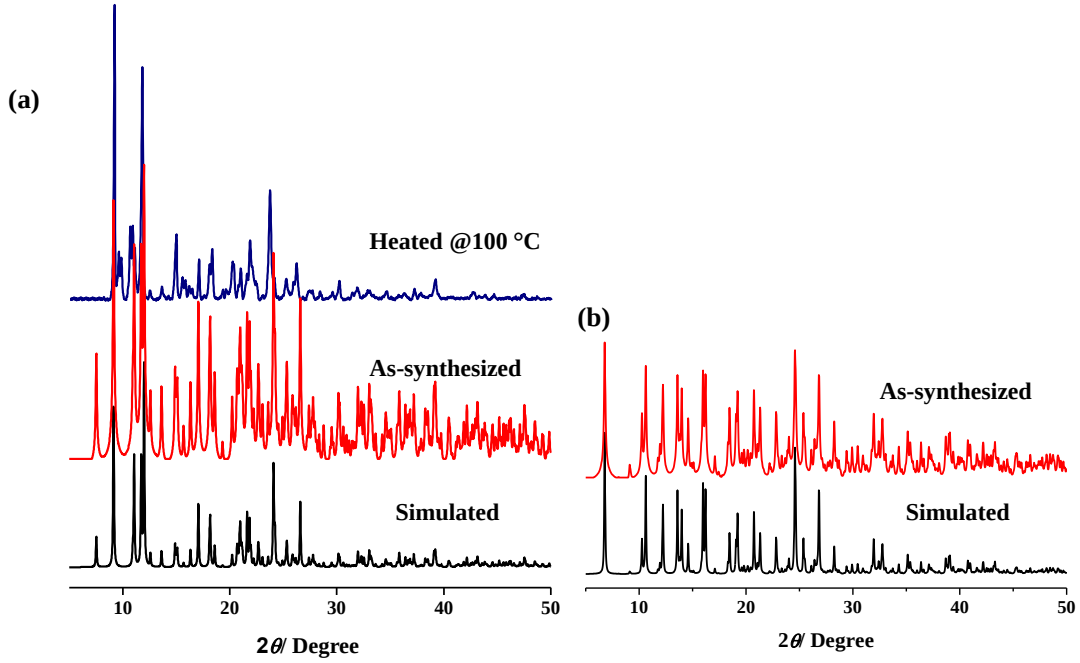

Figure 20: (a) PXRD patterns of compound **2** in different phases; (b) PXRD patterns of compound **3**.

7.3.4 Porous properties of compounds 1, 2 and 3

Structural descriptions clearly indicate that compound **1** and **2** are potentially porous compounds while compound **3** does not contain any void space. To establish permanent porosity of **1′** and **2′**, N_2 adsorption experiment was carried out at 77 K. Prior to the adsorption measurement, as-synthesized compounds were evacuated under vacuum at 100 °C for ~16 h to remove water and ethanol guest molecules to produce activated compounds **1′** and **2′**. The isotherms show typical type-I profiles with uptake volume of 190 and 110 mL/g, for **1′** and **2′**, respectively suggesting microporous nature of the frameworks (Figure 21). Calculation using the measured isotherms suggest that frameworks **1′** and **2′** have Brunauer–Emmett–Teller (BET) surface area of 870 and 481 m^2/g. Surface area of **1′** draws comparison with some of the popular zeolitic PCPs like, ZIF-95 (1050 m^2/g) and ZIF-100 (595 m^2/g) bearing tetrahedral Zn^{2+} nodes.[16]

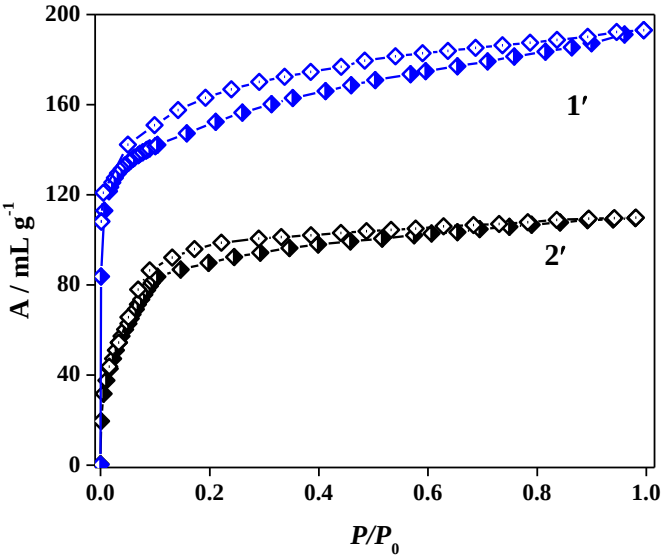

Figure 21: N_2 adsorption isotherms of compound **1′** and **2′** at 77 K.

After the permanent porosity of the frameworks has been established from N_2 adsorption studies, I have tested the compounds for their uptake capacities for other gases. CO_2 adsorption-desorption profile of **1′** measured at 195 K also exhibits a type-I curve similar to N_2 isotherm. The framework shows an appreciable uptake of ~42 weight % CO_2 (9.96 mmol/g at STP) without saturation in the measurement pressure range (Figure 22a). Analysis of the isotherm with Dubinin-Radushkevich[17] (DR) equation suggests the value of isosteric heat of adsorption, ($q_{st,\phi}$) to be 32 kJ/mol. At 298 K and 1 atm pressure the framework captures ~9 weight % of CO_2 (1.96 mmol/g) which is very close to the value reported for MOF-5 (2.1 mmol/g) and much higher than activated

carbon- MAXSORB (0.5 mmol/g) and BPL carbon (0.4 mmol/g) (Figure 22b).[18,19] Measurement of adsorption isotherms at 195 K for other gases, such as H_2, N_2, O_2 and Ar shows negligible uptake suggesting the framework is highly selective towards CO_2 gas. This type of selective adsorption phenomena is unique in PCPs. Abrupt decrease in N_2 uptake from 77 K to 195 K could be accounted for higher thermal energy of the inert gas molecules which significantly decreases interaction with the pore surfaces. Moreover, the structural analysis suggests that pore surfaces in **1** are decorated with free pendant oxygen atoms from the carboxylate groups as well as Zn^{2+} sites that makes the pore wall polar in nature. Since CO_2 molecule has large quadrupole moment (-1.4 x 10^{-39} C/m^2) compare to other gas molecules, it interacts with the pore surface strongly resulting in high uptake at 195 K. Similar to compound **1′**, **2′** also shows high CO_2 uptake capacity; it adsorbs ~ 30 weight% of CO_2 (6.78 mmol/g at STP) at 195 K (Figure 23). At 298 K and 1 atm pressure it can adsorb 5.3 weight% (1.2 mmol/g) CO_2 (Figure 23). Although the uptake amounts are low compared to those of compound **1′**, the isosteric heat of adsorption calculated using DR equation is slightly higher (33.1 kJ/mol) than in case of compound **1′**. This might be due to smaller pore dimension of the two dimensional channels available in compound **2′**. Confined pore can induce stronger interaction between CO_2 and pore surface of the framework.

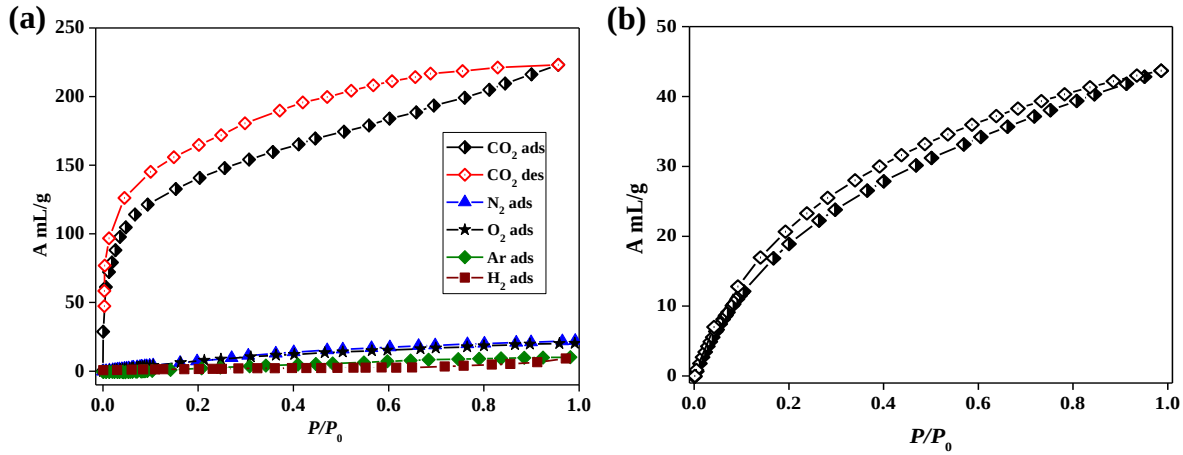

Figure 22: (a) Selective CO_2 gas adsorption over H_2, N_2, O_2 and Ar by **1′** at 195 K; (b) CO_2 adsorption isotherm at 298 K.

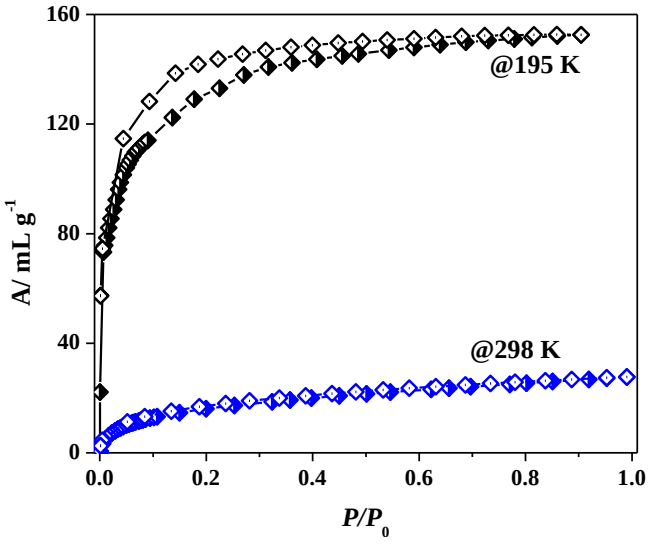

Figure 23: CO_2 adsorption isotherms of compound **2′** at 195 and 298 K.

Although compound **3** does not show any potential void space, the water (298 K) and methanol (293 K) solvent vapour adsorption were carried out (Figure 24). We have carried out the measurements after activating compound **3** at 220 °C for 6 h. Water vapor uptake profile is two-step; first step till P/P_0 ~ 0.32 shows 1.3 molecules of water per formula uptake indicating that approximately one water molecule coordinates to the Cd^{2+} center. In the second step total uptake reaches 3 molecules of water per formula which might be due to one more water molecule coordinates to the metal center and hydrogen bonding between adsorbed water molecules. In case of methanol, due to bulkier size and weak coordination ability compared to water, initial uptake starts at P/P_0 ~ 0.17 and with a stepwise process it reaches to 2.6 molecules per formula.

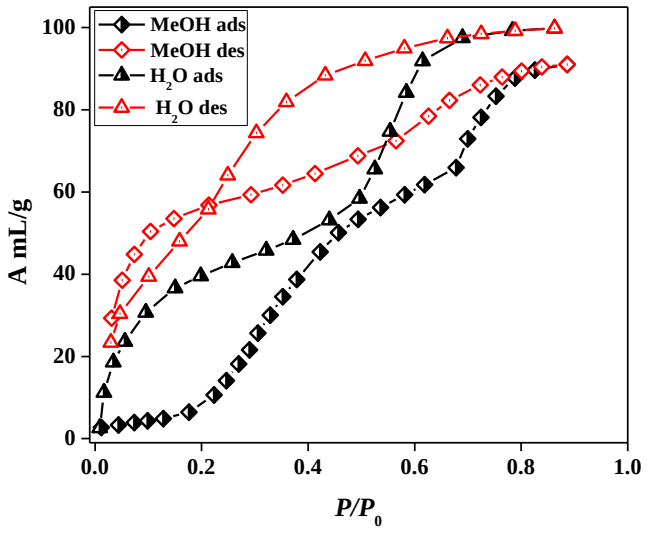

Figure 24: Water and methanol vapour adsorption isotherms of compound **3** at 298 and 293 K, respectively.

7.4 Conclusions

In conclusion, Zn^{2+}/Cd^{2+} can mediate in situ C-N coupling reaction during construction of PCPs. The unusual distorted tetrahedral geometry of the newly in situ formed ligand, obtained by coupling of azpy and Na_2tga, with a *Z*-configuration, and its asymmetric coordination with Zn^{2+} directs the structure in all three crystallographic axes to generate a chiral 3D framework structure. The chirality in compound **1** is of axial type and is completely coordination driven. In case of octahedral Cd^{2+} an achiral structure was obtained. The microporous nature of both the frameworks has been established by gas adsorption studies. More interestingly, compound **1** shows selective adsorption of CO_2 gas over H_2, N_2, O_2 and Ar at 195 K. It also shows 9 weight % of CO_2 uptake at 298 K. Hence this can be a CO_2 selective material in presence of other gases and may find application for separating CO_2 gas from flue gas components. Further, changing the linker functionality from –N=N- (azpy) to –C=C- (bpee) also renders a new linker pnpe. This is formed *via* new C-N bond formation between pyridine nitrogen and C3 of tga linker. Following this work, efforts can be directed towards synthesis of homochiral PCPs for chiral separation or asymmetric catalysis. .

7.5References

1. a) X.-M. Chen, M.-L. Tong, *Acc. Chem. Res.* **2007,** *40*, 162; b) E. C. Constable, *Metals and Ligand Reactivity; VCH: Weinheim* **1996**, 245; c) J. Burgess, C. D. Hubbard, *Ligand substitution reactions. Adv. Inorg. Chem.* **2003**, *54*, 71.

2. a) S. Kitagawa, R. Kitaura, S. Noro, *Angew. Chem., Int. Ed.* **2004**, *43*, 2334; b) C. Janiak, *Dalton Trans.* **2003**, 2781; c) T. K. Maji, S. Kitagawa, *Pure App. Chem.* **2007**, *79*, 2155; d) G. Férey, *Chem. Soc. Rev.* **2008**, *37*, 191; e) J. C. Tan, A. K. Cheetham, *Chem. Soc. Rev.* **2011**, *40*, 1059; f) K.-L. Zhang, H.-Y. Gao, N. Qiao, F. Zhou, G.-W. Diao, *Inorg. Chim. Acta*. **2008**, *361*, 153; g) M. K. Bhunia, S. K. Das, M. M. Seikh, K. V. Domasevitch, A. Bhaumik, *Polyhedron*. **2011**, *30*, 2218; h) Y.-N. Zhang, Y.-Y. Wang, L. Hou, P. Liu, J.-Q. Liu, Q.-Z. Shi, *CrystEngComm*. **2010**, *12*, 3840; i) B. Gil-Hernández, H. A. Höppe, J. K. Vieth, J. Sanchiz, C. Janiak, *Chem. Commun.* **2010**, *46*, 8270.

3. (*a*) O. R. Evans, W. -B. Lin, *Acc. Chem. Res.* **2002**, *35*, 511; b) J. Y. Lu, *Coord. Chem. Rev.* **2003**, *246*, 327; c) X. -M. Zhang, *Coord. Chem. Rev.* **2005**, *249*, 1201; d) J. -P. Zhang, X. -M. Chen, *Chem. Commun.* **2006**, 1689; e) R. K. Feller, P. M. Forster, F. Wudl, A. K. Cheetham, *Inorg. Chem.* **2007**, *46*, 8717.

4. a) R. G. Xiong, X. Xue, H. Zhao, X. Z. You, B. F. Abrahams, Z. L. Xue, *Angew. Chem., Int. Ed.* **2002**, *41*, 3800; b) D. S. Liu, X. H. Huang, C. C. Huang, G. S. Huang, J. Z. Chen, *J. Solid State Chem.* **2009**, *182*, 1899; c) G. B. Li, J. M. Liu, Z. Q. Yu, W. Wang, C. Y. Su, *Inorg. Chem.* **2009**, *48*, 8659; d) S. T. Zheng, M. H. Wang, G. Y. Yang, *Inorg. Chem.* **2007**, *46*, 9503; e) J. Wang, S. L. Zheng, S. Hu, Y. H. Zhang, M. L. Tong, *Inorg. Chem.* **2007**, *46*, 795.

5. R. E. Morris, X. Bu, *Nat. Chem.* **2010**, *2*, 353.

SMART (V 5.628), SAINT (V 6.45a), XPREP, SHELXTL; Bruker AXS Inc. Madison, Wisconsin, USA, **2004**.

6. G. M. Sheldrick, Siemens Area Detector Absorption Correction Program, University of Götingen, Götingen, Germany, **1994**.

7. A. Altomare, G. Cascarano, C. Giacovazzo, A. Gualaradi, *J. Appl. Cryst*., **1993**, *26*, 343.

8. G. M. Sheldrick, SHELXL-97, Program for Crystal Structure Solution and Refinement; University of Götingen, Götingen, Germany, **1997**.

9. A. L. Spek. *J. Appl. Crystallogr*. **2003**, *36*, 7.

10. G. M. Sheldrick, SHELXS 97, Program for the Solution of Crystal Structure, University of Götingen, Germany, **1997**.

11. L. J. Farrugia, WinGX-A Windows Program for Crystal Structure Analysis, *J. Appl. Cryst*. **1999**, *32*, 837.

12. A. L. Spek, *J. Appl. Crystallogr*. **2003**, *36*, 7.

13. a) V. A. Blatov, L. Carlucci, G. Ciani, D. M. Proserpio, *CrystEngComm*. **2004**, *6*, 377; b) V. A. Blatov, A. P. Shevchenko, V. N. Serezhkin, *J. Appl. Crystallogr*. **2000**, *33*, 1193.

14. B. Wang, A. P. Côté, H. Furukawa, M. OKeeffe, O. M. Yaghi, *Nature*. **2008**, *453*, 207.

15. M. M. Dubinin, *Chem. Rev.* **1960**, *60*, 235.

16. A. R. Millward, O. M. Yaghi, *J. Am. Chem. Soc.* **2005**, *127*, 17998.

17. K. B. Lee, M. G. Beaver, H. S. Caram, S. Sircar, *Ind. Eng. Chem. Res.* **2008**, *47*, 8048.

18. a) R. Vaidhyanathan, S. S. Iremonger, G. K. H. Shimizu, P. G. Boyd, S. Alavi, T. K. Woo, *Science*. **2010**, *330*, 650; b) L. Pan, K. M. Adams, H. E. Hernandez, X. Wang, C. Zheng, Y. Hattori, K. Kaneko, *J. Am. Chem. Soc.* **2003**, *125*, 3062; c) A. Comotti, S. Bracco, P. Sozzani, S. Horike, R. Matsuda, J. Chen, M. Takata, Y. Kubota, S. Kitagawa,

J. Am. Chem. Soc. **2008**, *130*, 13664; d) J. An, S. J. Geib, N. L. Rosi, *J. Am. Chem. Soc.* **2010**, *132*, 38.